

NONDESTRUCTIVE EVALUATION OF PRESTRESSED CONCRETE
STRUCTURES BY MEANS OF ACOUSTIC
EMISSIONS MONITORING

Except where reference is made to the work of others, the work described in this dissertation is my own or was done in collaboration with my advisory committee. This dissertation does not include proprietary or classified information.

Jiangong Xu

Certificate of Approval:

Anton K. Schindler
Gottlieb Associate Professor
Civil Engineering

Robert W. Barnes, Chair
James J. Mallett Associate Professor
Civil Engineering

Mary L. Hughes
Instructor
Civil Engineering

George E. Ramey
Professor Emeritus
Civil Engineering

George T. Flowers
Dean
Graduate School

NONDESTRUCTIVE EVALUATION OF PRESTRESSED CONCRETE
STRUCTURES BY MEANS OF ACOUSTIC
EMISSIONS MONITORING

Jiangong Xu

A Dissertation

Submitted to

the Graduate Faculty of

Auburn University

in Partial Fulfillment of the

Requirements for the

Degree of

Doctor of Philosophy

Auburn, Alabama
December 19, 2008

NONDESTRUCTIVE EVALUATION OF PRESTRESSED CONCRETE
STRUCTURES BY MEANS OF ACOUSTIC
EMISSIONS MONITORING

Jiangong Xu

Permission is granted to Auburn University to make copies of this dissertation at its discretion, upon requests of individuals or institutions and at their expense. The author reserves all publication rights.

Signature of Author

Date of Graduation

VITA

Jiangong Xu, son of Guoan Xu and Peizhen Luo, was born in the city of Cixi, Zhejiang, China. He received a B.S. and an M.S. in Civil Engineering in 1997 and 2000, respectively, both from Tianjin University in Tianjin, China. He entered the Graduate School at Auburn University in January, 2004 to seek his Ph.D. in Civil Engineering (Structures). After graduate school, he began work as bridge engineer for Whitney Bailey Cox & Magnani, LLC in Baltimore, Maryland.

DISSERTATION ABSTRACT
NONDESTRUCTIVE EVALUATION OF PRESTRESSED CONCRETE
STRUCTURES BY MEANS OF ACOUSTIC
EMISSIONS MONITORING

Jiangong Xu

Doctor of Philosophy, December 19, 2008
(M. S. Tianjin University, China, 2000)
(B. S. Tianjin University, China, 1997)

340 Typed Pages

Directed by Robert W. Barnes

The acoustic emission (AE) technique has been found to be an informative nondestructive testing (NDT) method for evaluation of structures constructed with certain materials. While AE evaluation procedures and evaluation criteria have been proposed for nonprestressed concrete structures, standardized AE evaluation criteria for prestressed concrete beams are not available. The main objective of the study described in this dissertation was to develop and evaluate practical AE methods for integrity assessment of in-service prestressed concrete structures. The study encompassed a laboratory investigation of the AE response of prestressed concrete beams as well as a field investigation of the AE response of an in-service prestressed concrete bridge. The results of this study indicate that AE monitoring holds promise for nondestructive evaluation of

prestressed concrete structures. For the laboratory study, AE was monitored while sixteen prestressed concrete T-beams—twelve beams constructed with self-consolidating concrete (SCC) and four beams constructed with conventionally consolidated concrete—were loaded in cycles of increasing intensity to failure. Several AE parameters, such as amplitude, duration, and signal strength, were investigated in relation to the structural integrity of the beams. Three previously proposed AE criteria for integrity evaluation of reinforced concrete members were evaluated with respect to the behavior of these prestressed concrete specimens. A new evaluation method based on the signal strength moment was proposed and proved effective for indicating the integrity of the prestressed concrete beams. The behavior and AE response of the SCC beams were compared with those of conventionally consolidated prestressed concrete beams. In addition, the effectiveness of the recently proposed ACI 437 Cyclic Load Test (CLT) NDT method for concrete structures was evaluated vis-à-vis the behavior of the laboratory specimens. Results indicated good agreement between the CLT assessment criteria and two of the AE evaluation criteria for prestressed concrete beams. For the field investigation, two spans of a damaged highway bridge were load tested to investigate the practical effectiveness of AE monitoring for in-service prestressed concrete bridges. Procedures for in-situ AE evaluation of prestressed concrete bridges were proposed and evaluated by comparing the AE results from the load tests with the corresponding structural deformations.

ACKNOWLEDGEMENTS

I would like to express my deepest gratitude and appreciation to my advisor, Dr. Robert Barnes for his support, guidance, generous time and patience throughout my Ph.D. studies. The experience of working with him in Auburn leaves me wonderful memories to appreciate for the rest of my life.

I would like to express special thanks to Dr. Paul Ziehl, for his valuable advice and technical guidance during the course of this study.

In addition, special thanks to my committee members, Dr. Anton Schindler, Dr. Mary Hughes, and Dr. Ramey for their reviewing of this work and constructive comments.

I would like to acknowledge Graduate Research Assistants Kelly Levy, Mustafa Gurbuz, Jason Meadows, Bill Fason, Kelly Shapiro, and the concrete lab technician Billy Wilson for helping me during my doctoral work.

Finally, I would also like to thank my friends and family for their support and love.

Style manual used Kate L. Turabian A Manual for Writers of Term Papers, Theses,
and Dissertations. 6th ed.

Computer software used Microsoft Word & Excel 2003, Origin 7.0, AutoCAD 2004

TABLE OF CONTENTS

LIST OF TABLES	xv
LIST OF FIGURES	xvii
CHAPTER 1: INTRODUCTION	
1.1 INTRODUCTION.....	1
1.2 OBJECTIVE AND SCOPE.....	3
1.3 ORGANIZATION OF DISSERTATION.....	4
CHAPTER 2: THEORY OF ACOUSTIC EMISSION.....	7
2.1 INTRODUCTION.....	7
2.2 AE PARAMETERS	9
2.3 AE MONITORING PROCEDURE.....	19
2.4 AE FROM REINFORCED CONCRETE	24
2.5 AE FROM PRESTRESSED CONCRETE.....	28
CHAPTER 3: EVALUATION OF PRESTRESSED CONCRETE BEAMS USING A PARAMETER-BASED ACOUSTIC EMISSION TECHNIQUE	32
3.1 INTRODUCTION.....	32
3.2 RESEARCH SIGNIFICANCE.....	34
3.3 AE PARAMETERS	35
3.3.1 AMPLITUDE	36

3.3.2 DURATION	36
3.3.3 SIGNAL STRENGTH	37
3.3.4 SIGNAL ENERGY.....	37
3.4 EXPERIMENTAL INVESTIGATION	38
3.4.1 SPECIMEN DESCRIPTION	38
3.4.2 TEST PROCEDURE AND MEASUREMENT.....	39
3.5 EXPERIMENTAL RESULTS AND DISCUSSION	47
3.5.1 DURATION/AMPLITUDE CROSSPLOT	47
3.5.1.1 BEAM STD-M-B	47
3.5.1.2 BEAM STD-M-C	50
3.5.1.3 BEAM STD-M-D	54
3.5.1.4 BEAM STD-M-A	58
3.5.2 RELATIONSHIP BETWEEN SIGNAL STRENGTH AND DAMAGE	61
3.6 CONCLUSIONS	65
CHAPTER 4: DAMAGE ASSESSMENT CRITERIA FOR AE TESTING OF PRESTRESSED CONCRETE BEAMS.....	67
4.1 INTRODUCTION.....	67
4.2 RESEARCH SIGNIFICANCE	69
4.3 AE EVALUATION CRITERIA	69
4.3.1 NDIS-2421 CRITERION	69
4.3.2 RELAXATION RATIO	71
4.3.3 PEAK CSS RATIO.....	72

5.5 EXPERIMENTAL RESULTS AND DISCUSSION	108
5.5.1 STRUCTURAL RESPONSE	108
5.5.2 AE SIGNAL STRENGTH	111
5.5.3 CUMULATIVE SIGNAL STRENGTH.....	114
5.5.4 DURATION/AMPLITUDE CROSSPLOT	115
5.5.5 AE EVALUATION CRITERIA.....	120
5.6 CONCLUSIONS	128
CHAPTER 6: NONDESTRUCTIVE STRENGTH EVALUATION OF	
PRESTRESSED CONCRETE BEAMS.....	130
6.1 INTRODUCTION	130
6.2 RESEARCH SIGNIFICANCE	131
6.3 LOAD TEST METHODS.....	132
6.3.1 CYCLIC LOAD TEST METHOD.....	132
6.3.2 ACOUSTIC EMISSION METHOD.....	136
6.4 EXPERIMENTAL INVESTIGATION	138
6.4.1 SPECIMEN DESCRIPTION.....	138
6.4.2 LOADING PATTERNS.....	139
6.4.3 MEASUREMENT OF DISPLACEMENTS	142
6.4.4 AE TESTING	142
6.5 EXPERIMENTAL RESULTS AND DISCUSSION	143
6.5.1 STD-M-B.....	143
6.5.2 STD-M-C.....	151
6.5.3 STD-M-D	155

6.5.4 STD-M-A.....	159
6.6 CONCLUSIONS.....	166
CHAPTER 7: IN-PLACE ACOUSTIC EMISSIONS MONITORING OF DAMAGED PRESTRESSED CONCRETE BRIDGE GIRDERS.....	167
7.1 INTRODUCTION.....	167
7.2 RESEARCH SIGNIFICANCE.....	169
7.3 AE EVALUATION CRITERIA.....	170
7.3.1 NDIS-2421 CRITERION.....	170
7.3.2 SIGNAL STRENGTH MOMENT RATIO EVALUATION.....	170
7.4 EXPERIMENTAL PROCEDURE.....	171
7.4.1 PRELIMINARY INVESTIGATION.....	171
7.4.2 AE TESTING PROCEDURE.....	174
7.4.3 CONVENTIONAL MEASUREMENT.....	180
7.4.4 LOADING PATTERNS FOR AE MONITORING.....	181
7.5 EXPERIMENTAL RESULTS AND DISCUSSION.....	184
7.5.1 CRACK OPENING DISPLACEMENT ANALYSIS.....	184
7.5.2 ACOUSTIC EMISSION EVALUATION RESULTS.....	187
7.5.2.1 NDIS-2421 CRITERION.....	187
7.5.2.2 SIGNAL STRENGTH MOMENT RATIO EVALUATION.....	190
7.5.3 CRACK LOCATION USING AE 2D-LOC ANALYSIS TECHNIQUE.....	192

7.6 SUMMARY AND CONCLUSIONS	195
CHAPTER 8: SUMMARY, CONCLUSIONS AND RECOMMENDATIONS	197
8.1 SUMMARY	197
8.2 CONCLUSIONS FROM LABORATORY TESTING	199
8.3 CONCLUSIONS FROM FIELD TESTING.....	200
8.4 RECOMMENDATIONS FOR FUTURE STUDY.....	201
REFERENCES.....	202
APPENDIX A: NOTATION	210
APPENDIX B: LOAD, DEFLECTION, AND STRAND SLIP PLOTS.....	212
APPENDIX C: DURATION VERSUS AMPLITUDE CROSSPLOTS.....	229
APPENDIX D: LOAD AND SIGNAL STRENGTH VERSUS TIME PLOTS	275
APPENDIX E: SUMMARY OF EVALUATION CRITERIA RESULTS.....	284
APPENDIX F: NDIS ASSESSMENTS	288
APPENDIX G: SSM DURING HOLD PLOTS	297
APPENDIX H: CUMULATIVE SIGNAL STRENGTH VERSUS TIME DURING CYCLE 5	306

LIST OF TABLES

Table 2-1: K factor for Historic Index (ASTM E 2478 - 06)	17
Table 3-1: Test specimen properties.....	39
Table 3-2: Load step value.....	42
Table 4-1: Test specimen properties.....	76
Table 4-2: AE test parameters.....	79
Table 4-3: Load step value.....	83
Table 4-4: Summary of evaluation criteria results	87
Table 5-1: Concrete mixture proportions.....	104
Table 5-2: Summary of fresh property test results	105
Table 5-3: Hardened concrete property summary	105
Table 5-4: Summary of test specimens and results	110
Table 6-1: Test specimen properties.....	139
Table 6-2: Summary of calculated load step values.....	140
Table 6-3: Load step value.....	142
Table 6-4: Summary of calculation for STD-M-B beam.....	147
Table 6-5: Summary of AE evaluation criteria results	149
Table 6-6: Summary of calculation for STD-M-C beam.....	153
Table 6-7: Summary of CLT calculation for STD-M-D beam	157

Table 6-8: Summary of calculation for STD-M-A beam	160
Table 6-9: Summary of evaluation criteria results	165
Table 7-1: AE test parameters for prestressed concrete girder	175
Table 7-2: Test truck loads	182
Table 7-3: AE evaluation results	191
Table E-1: Summary of Evaluation Criteria Results for Beam STD-M.....	284
Table E-2: Summary of Evaluation Criteria Results for Beam SCC-MA.....	285
Table E-3: Summary of Evaluation Criteria Results for Beam SCC-MS	286
Table E-4: Summary of Evaluation Criteria Results for Beam SCC-HS	287

LIST OF FIGURES

Figure 2-1: Principles of AE technology (adapted from Pollock 1995).....	8
Figure 2-2: AE signal features	10
Figure 2-3: Emission on repeated loading (Pollock 1995)	16
Figure 2-4: Historic Index and cumulative signal strength for prestressed concrete beam.....	19
Figure 2-5: Calibration of AE equipment	22
Figure 3-1: AE signal features	35
Figure 3-2: T-Beam cross section detail.....	38
Figure 3-3: Test setup.....	40
Figure 3-4: Load cycles and steps	41
Figure 3-5: Linear potentiometers used to monitor beam deflection	45
Figure 3-6: AE sensor locations	46
Figure 3-7: Load and deflection versus time for beam STD-M-B.....	48
Figure 3-8: Crack pattern for STD-M-B at failure (Levy 2007).....	48
Figure 3-9: Crossplot of amplitude and duration of AE signals from loadset 3-4 for beam STD-M-B.....	49
Figure 3-10: Crossplot of amplitude and duration of AE signals from loadset 7-8 for beam STD-M-B.....	50

Figure 3-11: Load and deflection versus time for beam STD-M-C	51
Figure 3-12: Crack pattern for STD-M-C at failure (Levy 2007)	52
Figure 3-13: Crossplot of amplitude and duration of AE signals from loadset 3-4 for beam STD-M-C	53
Figure 3-14: Crossplot of amplitude and duration of AE signals from loadset 5-6 for beam STD-M-C	53
Figure 3-15: Load and deflection versus time for beam STD-M-D.....	55
Figure 3-16: STD-M-D shear-tension failure (Levy 2007)	55
Figure 3-17: Crack pattern for STD-M-D at failure (Levy 2007).....	56
Figure 3-18: Crossplot of amplitude and duration of AE signals from loadset 3-4 for beam STD-M-D.....	57
Figure 3-19: Crossplot of amplitude and duration of AE signals from loadset 5 for beam STD-M-D.....	57
Figure 3-20: Load and deflection versus time for beam STD-M-A.....	58
Figure 3-21: Crack pattern for STD-M-A at failure (Levy 2007).....	59
Figure 3-22: Crossplot of amplitude and duration of AE signals from loadset 3-4 for beam STD-M-A	60
Figure 3-23: Load and signal strength versus time for beam STD-M-C.....	62
Figure 3-24: Load and signal strength versus time on Cycle 5 for beam STD-M-C	63
Figure 3-25: Load and signal strength versus time on Cycle 5 for beam STD-M-B	64
Figure 3-26: Load and signal strength versus time on Cycle 5 for beam STD-M-D	65
Figure 4-1: Classification of damages by two ratios recommended by NDIS-2421.....	71
Figure 4-2: Beam cross section detail.....	76

Figure 4-3: Load test setup and sensor location.....	77
Figure 4-4: Photo of an AE testing set-up	79
Figure 4-5: Attenuation curve for prestressed concrete beam	80
Figure 4-6: Load cycles and steps	81
Figure 4-7: NDIS assessment for beams STD-M-B, STD-M-C, and STD-M-D.....	88
Figure 4-8: Signal strength moment during holds for beam STD-M-C	93
Figure 4-9: Signal strength moment during holds for beam STD-M-A	94
Figure 5-1: T-Beam cross section	103
Figure 5-2: Specimen identification system	103
Figure 5-3: Load test setup and AE sensor locations	106
Figure 5-4: Load cycles and steps	107
Figure 5-5: Load and signal strength versus time for beam STD-M-C.....	112
Figure 5-6: Load and signal strength versus time for beam SCC-MS-C.....	113
Figure 5-7: Cumulative signal strength versus time for “C” beams during load cycle 5	114
Figure 5-8: Crossplot of amplitude and duration of AE signals from loadset 3-4 for beam SCC-MS-C.....	116
Figure 5-9: Crossplot of amplitude and duration of AE signals from loadset 5-6 for beam SCC-MS-C.....	117
Figure 5-10: Crossplot of amplitude and duration of AE signals from loadset 3-4 for beam STD-M-C.....	118
Figure 5-11: Crossplot of amplitude and duration of AE signals from loadset 5-6 for beam STD-M-C.....	119

Figure 5-12: Calm ratios for Loadset/Specimen combinations.....	123
Figure 5-13: Load ratios for Loadset/Specimen combinations.....	123
Figure 5-14: Relaxation ratios for Loadset/Specimen combinations	125
Figure 5-15: CSS ratios for Loadset/Specimen combinations	126
Figure 5-16: SMM ratio for Loadset/Specimen combinations	127
Figure 6-1: Load cycles and steps	133
Figure 6-2: Example of load-versus-deflection curve for two cycles	134
Figure 6-3: Schematic load-versus-deflection curve for six cycles	135
Figure 6-4: Crack pattern for STD-M-B at failure	144
Figure 6-5: Time history of CLT for STD-M-B	145
Figure 6-6: Load versus deflection curve for STD-M-B	146
Figure 6-7: Load and deviation from linearity versus time for STD-M-B beam.....	148
Figure 6-8: NDIS assessment for beams STD-M-B, STD-M-C, and STD-M-D.....	149
Figure 6-9: Signal strength moment during holds for beam STD-M-B	151
Figure 6-10: Crack pattern for STD-M-C at failure (Kelly 2007)	152
Figure 6-11: Time history of CLT for STD-M-C	152
Figure 6-12: Load versus deflection curve for STD-M-C	153
Figure 6-13: Load and deviation from linearity versus time for STD-M-C beam.....	154
Figure 6-14: Signal strength moment during holds for beam STD-M-C	155
Figure 6-15: Crack pattern for STD-M-D at failure (Kelly 2007)	156
Figure 6-16: Time history of CLT for STD-M-D	157
Figure 6-17: Load versus deflection curve for STD-M-D.....	158
Figure 6-18: Crack pattern for STD-M-A at failure (Kelly 2007)	159

Figure 6-19: Time history of CLT for STD-M-A	161
Figure 6-20: Load versus deflection curve for STD-M-A	161
Figure 6-21: Load and deviation from linearity versus time for STD-M-A beam.....	162
Figure 6-22: Signal strength moment during holds for beam STD-M-A	163
Figure 7-1: Bridge cross section and transverse position of test truck.....	172
Figure 7-2: Girder cross section dimensions.....	172
Figure 7-3: I-565 girder layout and numbering system.....	173
Figure 7-4: Types of cracking	174
Figure 7-5: Steel sheet and crack measurement.....	176
Figure 7-6: Cable mounting pad and magnetic hold-down	176
Figure 7-7: Array of sensors on the east face of Girder 8.....	177
Figure 7-8: Sensor location on Span 10 Girder 8.....	178
Figure 7-9: Array of Girder 7 sensors	179
Figure 7-10: Plan view of test truck location on span 10	182
Figure 7-11: Two test trucks on span 10.....	183
Figure 7-12: Plan view of test truck locations on Span 11	184
Figure 7-13: Crack opening displacement during second night.....	185
Figure 7-14: COD of Girder 8 Span 10 during first night	186
Figure 7-15: Example of calculation of calm ratio of Span 10 Girder 8	188
Figure 7-16: Damage qualification of bridge based on NDIS method.....	189
Figure 7-17: Signal strength moment during holds.....	190
Figure 7-18: AE Event location and crack pattern of Span 11 Girder 8	193
Figure 7-19: AE Event location and crack pattern of Span 11 Girder 7	194

Figure B-1: Applied Load and deflection versus time for STD-M-A	212
Figure B-2: Applied load and end slip versus deflection for STD-M-A	213
Figure B-3: Applied Load and deflection versus time for STD-M-B	213
Figure B-4: Applied load and end slip versus deflection for STD-M-B	214
Figure B-5: Applied Load and deflection versus time for STD-M-C	214
Figure B-6: Applied load and end slip versus deflection for STD-M-C	215
Figure B-7: Applied Load and deflection versus time for STD-M-D	215
Figure B-8: Applied load and end slip versus deflection for STD-M-D	216
Figure B-9: Applied Load and deflection versus time for SCC-MA-A	216
Figure B-10: Applied load and end slip versus deflection for SCC-MA-A	217
Figure B-11: Applied Load and deflection versus time for SCC-MA-B.....	217
Figure B-12: Applied load and end slip versus deflection for SCC-MA-B.....	218
Figure B-13: Applied Load and deflection versus time for SCC-MA-C.....	218
Figure B-14: Applied load and end slip versus deflection for SCC-MA-C.....	219
Figure B-15: Applied Load and deflection versus time for SCC-MA-D	219
Figure B-16: Applied load and end slip versus deflection for SCC-MA-D	220
Figure B-17: Applied Load and deflection versus time for SCC-MS-A.....	220
Figure B-18: Applied load and end slip versus deflection for SCC-MS-A.....	221
Figure B-19: Applied Load and deflection versus time for SCC-MS-B	221
Figure B-20: Applied load and end slip versus deflection for SCC-MS-B	222
Figure B-21: Applied Load and deflection versus time for SCC-MS-C	222
Figure B-22: Applied load and end slip versus deflection for SCC-MS-C	223
Figure B-23: Applied Load and deflection versus time for SCC-MS-D.....	223

Figure B-24: Applied load and end slip versus deflection for SCC-MS-D.....	224
Figure B-25: Applied Load and deflection versus time for SCC-HS-A.....	224
Figure B-26: Applied load and end slip versus deflection for SCC-HS-A.....	225
Figure B-27: Applied Load and deflection versus time for SCC-HS-B.....	225
Figure B-28: Applied load and end slip versus deflection for SCC-HS-B.....	226
Figure B-29: Applied Load and deflection versus time for SCC-HS-C.....	226
Figure B-30: Applied load and end slip versus deflection for SCC-HS-C.....	227
Figure B-31: Applied Load and deflection versus time for SCC-HS-D.....	227
Figure B-32: Applied load and end slip versus deflection for SCC-HS-D.....	228
Figure C-1: Crossplot of amplitude and duration of AE signals from loadset 1-2 for beamSTD-M-A.....	229
Figure C-2: Crossplot of amplitude and duration of AE signals from loadset 3-4 for beam STD-M-A	230
Figure C-3: Crossplot of amplitude and duration of AE signals from loadset 5-6 for beam STD-M-A	230
Figure C-4: Crossplot of amplitude and duration of AE signals from loadset 7-8 for beam STD-M-A	231
Figure C-5: Crossplot of amplitude and duration of AE signals from loadset 9-10 for beam STD-M-A.....	231
Figure C-6: Crossplot of amplitude and duration of AE signals from loadset 1-2 for beam STD-M-B	232
Figure C-7: Crossplot of amplitude and duration of AE signals from loadset 3-4 for beam STD-M-B	232

Figure C-8: Crossplot of amplitude and duration of AE signals from loadset 5-6 for beam STD-M-B	233
Figure C-9: Crossplot of amplitude and duration of AE signals from loadset 7-8 for beam STD-M-B	233
Figure C-10: Crossplot of amplitude and duration of AE signals from loadset 9-10 for beam STD-M-B.....	234
Figure C-11: Crossplot of amplitude and duration of AE signals from loadset 1-2 for beam STD-M-C.....	234
Figure C-12: Crossplot of amplitude and duration of AE signals from loadset 3-4 for beam STD-M-C.....	235
Figure C-13: Crossplot of amplitude and duration of AE signals from loadset 5-6 for beam STD-M-C.....	235
Figure C-14: Crossplot of amplitude and duration of AE signals from loadset 7-8 for beam STD-M-C.....	236
Figure C-15: Crossplot of amplitude and duration of AE signals from loadset 9-10 for beam STD-M-C.....	236
Figure C-16: Crossplot of amplitude and duration of AE signals from loadset 1-2 for beam STD-M-D	237
Figure C-17: Crossplot of amplitude and duration of AE signals from loadset 3-4 for beam STD-M-D	237
Figure C-18: Crossplot of amplitude and duration of AE signals from loadset 5 for beam STD-M-D.....	238
Figure C-19: Crossplot of amplitude and duration of AE signals from loadset 1-2 for	

beam SCC-MA-A.....	238
Figure C-20: Crossplot of amplitude and duration of AE signals from loadset 3-4 for beam SCC-MA-A.....	239
Figure C-21: Crossplot of amplitude and duration of AE signals from loadset 5-6 for beam SCC-MA-A.....	239
Figure C-22: Crossplot of amplitude and duration of AE signals from loadset 7-8 for beam SCC-MA-A.....	240
Figure C-23: Crossplot of amplitude and duration of AE signals from loadset 9-10 for beam SCC-MA-A.....	240
Figure C-24: Crossplot of amplitude and duration of AE signals from loadset 11-12 for beam SCC-MA-A.....	241
Figure C-25: Crossplot of amplitude and duration of AE signals from loadset 1-2 for beam SCC-MA-B.....	241
Figure C-26: Crossplot of amplitude and duration of AE signals from loadset 3-4 for beam SCC-MA-B.....	242
Figure C-27: Crossplot of amplitude and duration of AE signals from loadset 5-6 for beam SCC-MA-B.....	242
Figure C-28: Crossplot of amplitude and duration of AE signals from loadset 7-8 for beam SCC-MA-B.....	243
Figure C-29: Crossplot of amplitude and duration of AE signals from loadset 9-10 for beam SCC-MA-B.....	243
Figure C-30: Crossplot of amplitude and duration of AE signals from loadset 11-12 for beam SCC-MA-B.....	244

Figure C-31: Crossplot of amplitude and duration of AE signals from loadset 1-2 for beam SCC-MA-C.....	244
Figure C-32: Crossplot of amplitude and duration of AE signals from loadset 3-4 for beam SCC-MA-C.....	245
Figure C-33: Crossplot of amplitude and duration of AE signals from loadset 5-6 for beam SCC-MA-C.....	245
Figure C-34: Crossplot of amplitude and duration of AE signals from loadset 7-8 for beam SCC-MA-C.....	246
Figure C-35: Crossplot of amplitude and duration of AE signals from loadset 9-10 for beam SCC-MA-C.....	246
Figure C-36: Crossplot of amplitude and duration of AE signals from loadset 11-12 for beam SCC-MA-C.....	247
Figure C-37: Crossplot of amplitude and duration of AE signals from loadset 1-2 for beam SCC-MA-D.....	247
Figure C-38: Crossplot of amplitude and duration of AE signals from loadset 3-4 for beam SCC-MA-D.....	248
Figure C-39: Crossplot of amplitude and duration of AE signals from loadset 5-6 for beam SCC-MA-D.....	248
Figure C-40: Crossplot of amplitude and duration of AE signals from loadset 7-8 for beam SCC-MA-D.....	249
Figure C-41: Crossplot of amplitude and duration of AE signals from loadset 9-10 for beam SCC-MA-D.....	249
Figure C-42: Crossplot of amplitude and duration of AE signals from loadset 11-12 for	

beam SCC-MA-D.....	250
Figure C-43: Crossplot of amplitude and duration of AE signals from loadset 1-2 for	
beam SCC-MS-A	250
Figure C-44: Crossplot of amplitude and duration of AE signals from loadset 3-4 for	
beam SCC-MS-A	251
Figure C-45: Crossplot of amplitude and duration of AE signals from loadset 5-6 for	
beam SCC-MS-A	251
Figure C-46: Crossplot of amplitude and duration of AE signals from loadset 7-8 for	
beam SCC-MS-A	252
Figure C-47: Crossplot of amplitude and duration of AE signals from loadset 9-10 for	
beam SCC-MS-A	252
Figure C-48: Crossplot of amplitude and duration of AE signals from loadset 11-12 for	
beam SCC-MS-A	253
Figure C-49: Crossplot of amplitude and duration of AE signals from loadset 1-2 for	
beam SCC-MS-B	253
Figure C-50: Crossplot of amplitude and duration of AE signals from loadset 3-4 for	
beam SCC-MS-B	254
Figure C-51: Crossplot of amplitude and duration of AE signals from loadset 5-6 for	
beam SCC-MS-B	254
Figure C-52: Crossplot of amplitude and duration of AE signals from loadset 7-8 for	
beam SCC-MS-B	255
Figure C-53: Crossplot of amplitude and duration of AE signals from loadset 9-10 for	
beam SCC-MS-B	255

Figure C-54: Crossplot of amplitude and duration of AE signals from loadset 11-12 for beam SCC-MS-B	256
Figure C-55: Crossplot of amplitude and duration of AE signals from loadset 1-2 for beam SCC-MS-C	256
Figure C-56: Crossplot of amplitude and duration of AE signals from loadset 3-4 for beam SCC-MS-C	257
Figure C-57: Crossplot of amplitude and duration of AE signals from loadset 5-6 for beam SCC-MS-C	257
Figure C-58: Crossplot of amplitude and duration of AE signals from loadset 7-8 for beam SCC-MS-C	258
Figure C-59: Crossplot of amplitude and duration of AE signals from loadset 9-10 for beam SCC-MS-C	258
Figure C-60: Crossplot of amplitude and duration of AE signals from loadset 11-12 for beam SCC-MS-C	259
Figure C-61: Crossplot of amplitude and duration of AE signals from loadset 1-2 for beam SCC-MS-D	259
Figure C-62: Crossplot of amplitude and duration of AE signals from loadset 3-4 for beam SCC-MS-D	260
Figure C-63: Crossplot of amplitude and duration of AE signals from loadset 5-6 for beam SCC-MS-D	260
Figure C-64: Crossplot of amplitude and duration of AE signals from loadset 7-8 for beam SCC-MS-D	261
Figure C-65: Crossplot of amplitude and duration of AE signals from loadset 9-10 for	

beam SCC-MS-D	261
Figure C-66: Crossplot of amplitude and duration of AE signals from loadset 11-12 for beam SCC-MS-D	262
Figure C-67: Crossplot of amplitude and duration of AE signals from loadset 1-2 for beam SCC-HS-A	262
Figure C-68: Crossplot of amplitude and duration of AE signals from loadset 3-4 for beam SCC-HS-A	263
Figure C-69: Crossplot of amplitude and duration of AE signals from loadset 5-6 for beam SCC-HS-A	263
Figure C-70: Crossplot of amplitude and duration of AE signals from loadset 7-8 for beam SCC-HS-A	264
Figure C-71: Crossplot of amplitude and duration of AE signals from loadset 9-10 for beam SCC-HS-A	264
Figure C-72: Crossplot of amplitude and duration of AE signals from loadset 11-12 for beam SCC-HS-A	265
Figure C-73: Crossplot of amplitude and duration of AE signals from loadset 1-2 for beam SCC-HS-B	265
Figure C-74: Crossplot of amplitude and duration of AE signals from loadset 3-4 for beam SCC-HS-B	266
Figure C-75: Crossplot of amplitude and duration of AE signals from loadset 5-6 for beam SCC-HS-B	266
Figure C-76: Crossplot of amplitude and duration of AE signals from loadset 7-8 for beam SCC-HS-B	267

Figure C-77: Crossplot of amplitude and duration of AE signals from loadset 9-10 for beam SCC-HS-B	267
Figure C-78: Crossplot of amplitude and duration of AE signals from loadset 11-12 for beam SCC-HS-B	268
Figure C-79: Crossplot of amplitude and duration of AE signals from loadset 1-2 for beam SCC-HS-C	268
Figure C-80: Crossplot of amplitude and duration of AE signals from loadset 3-4 for beam SCC-HS-C	269
Figure C-81: Crossplot of amplitude and duration of AE signals from loadset 5-6 for beam SCC-HS-C	269
Figure C-82: Crossplot of amplitude and duration of AE signals from loadset 7-8 for beam SCC-HS-C	270
Figure C-83: Crossplot of amplitude and duration of AE signals from loadset 9-10 for beam SCC-HS-C	270
Figure C-84: Crossplot of amplitude and duration of AE signals from loadset 11-12 for beam SCC-HS-C	271
Figure C-85: Crossplot of amplitude and duration of AE signals from loadset 1-2 for beam SCC-HS-D	271
Figure C-86: Crossplot of amplitude and duration of AE signals from loadset 3-4 for beam SCC-HS-D	272
Figure C-87: Crossplot of amplitude and duration of AE signals from loadset 5-6 for beam SCC-HS-D	272
Figure C-88: Crossplot of amplitude and duration of AE signals from loadset 7-8 for	

beam SCC-HS-D.....	273
Figure C-89: Crossplot of amplitude and duration of AE signals from loadset 9-10 for beam SCC-HS-D.....	273
Figure C-90: Crossplot of amplitude and duration of AE signals from loadset 11-12 for beam SCC-HS-D.....	274
Figure D-1: Load and signal strength versus time for beam STD-M-A.....	275
Figure D-2: Load and signal strength versus time for beam STD-M-B.....	276
Figure D-3: Load and signal strength versus time for beam STD-M-C.....	276
Figure D-4: Load and signal strength versus time for beam STD-M-D.....	277
Figure D-5: Load and signal strength versus time for beam SCC-MA-A.....	277
Figure D-6: Load and signal strength versus time for beam SCC-MA-B.....	278
Figure D-7: Load and signal strength versus time for beam SCC-MA-C.....	278
Figure D-8: Load and signal strength versus time for beam SCC-MA-D.....	279
Figure D-9: Load and signal strength versus time for beam SCC-MS-A.....	279
Figure D-10: Load and signal strength versus time for beam SCC-MS-B.....	280
Figure D-11: Load and signal strength versus time for beam SCC-MS-C.....	280
Figure D-12: Load and signal strength versus time for beam SCC-MS-D.....	281
Figure D-13: Load and signal strength versus time for beam SCC-HS-A.....	281
Figure D-14: Load and signal strength versus time for beam SCC-HS-B.....	282
Figure D-15: Load and signal strength versus time for beam SCC-HS-C.....	282
Figure D-16: Load and signal strength versus time for beam SCC-HS-D.....	283
Figure F-1: NDIS assessment for beam STD-M-A.....	288
Figure F-2: NDIS assessment for beam STD-M-B.....	289

Figure F-3: NDIS assessment for beam STD-M-C	289
Figure F-4: NDIS assessment for beam STD-M-D	290
Figure F-5: NDIS assessment for beams SCC-MA-A.....	290
Figure F-6: NDIS assessment for beams SCC-MA-B.....	291
Figure F-7: NDIS assessment for beams SCC-MA-C.....	291
Figure F-8: NDIS assessment for beams SCC-MA-D.....	292
Figure F-9: NDIS assessment for beams SCC-MS-A	292
Figure F-10: NDIS assessment for beams SCC-MS-B	293
Figure F-11: NDIS assessment for beams SCC-MS-C	293
Figure F-12: NDIS assessment for beams SCC-MS-D	294
Figure F-13: NDIS assessment for beams SCC-HS-A.....	294
Figure F-14: NDIS assessment for beams SCC-HS-B	295
Figure F-15: NDIS assessment for beams SCC-HS-C	295
Figure F-16: NDIS assessment for beams SCC-HS-D.....	296
Figure G-1: Signal strength moment during holds for beam STD-M-A	297
Figure G-2: Signal strength moment during holds for beam STD-M-B	298
Figure G-3: Signal strength moment during holds for beam STD-M-C	298
Figure G-4: Signal strength moment during holds for beam STD-M-D	299
Figure G-5: Signal strength moment during holds for beam SCC-MA-A	299
Figure G-6: Signal strength moment during holds for beam SCC-MA-B.....	300
Figure G-7: Signal strength moment during holds for beam SCC-MA-C.....	300
Figure G-8: Signal strength moment during holds for beam SCC-MA-D	301
Figure G-9: Signal strength moment during holds for beam SCC-MS-A	301

Figure G-10: Signal strength moment during holds for beam SCC-MS-B	302
Figure G-11: Signal strength moment during holds for beam SCC-MS-C	302
Figure G-12: Signal strength moment during holds for beam SCC-MS-D	303
Figure G-13: Signal strength moment during holds for beam SCC-HS-A.....	303
Figure G-14: Signal strength moment during holds for beam SCC-HS-B.....	304
Figure G-15: Signal strength moment during holds for beam SCC-HS-C.....	304
Figure G-16: Signal strength moment during holds for beam SCC-HS-D.....	305
Figure H-1: Cumulative signal strength versus time for “A” beams during Cycle 5.....	306
Figure H-2: Cumulative signal strength versus time for “B” beams during Cycle 5.....	307
Figure H-3: Cumulative signal strength versus time for “C” beams during Cycle 5.....	307
Figure H-4: Cumulative signal strength versus time for “D” beams during Cycle 5.....	308

CHAPTER 1

INTRODUCTION

1.1 INTRODUCTION

Because prestressed concrete flexural members are critical to the integrity of a large share of existing buildings and bridges, the need has arisen for effective nondestructive testing (NDT) techniques to evaluate the integrity of prestressed concrete beams.

Nondestructive testing comprises those methods used to test a part or material or system without impairing its future usefulness (ASNT 1996). Since the 1920s, the art of testing without destroying the test object has developed from a laboratory theory to an indispensable tool of construction, fabrication, manufacturing and maintenance processes. Modern nondestructive tests are used widely by manufacturers to ensure product integrity and reliability and to avoid failure, prevent accidents and save human life. NDT can be categorized into two groups: active and passive methods (ASNT 1996). Active NDT techniques involve sending energy in some form into or onto the specimen. Examples of active NDT include ultrasonic, impact-echo, and eddy-current testing, as well as radiography. Passive NDT involves monitoring acoustic or visual changes in a structure under certain load conditions with the hope that a defect will reveal itself naturally. Passive methods include acoustic emission (AE) testing, visual inspection, dye-penetrant testing, and leak detection (Bray and Stanley 1997).

Current inspections of prestressed concrete structures are mainly based on visual observations, with occasional attempts to use ultrasonic and radiographic nondestructive testing to locate inclusions and delaminations (Ohtsu 1989; Pollock 1995; Tinkey and Fowler 2002). The low degree of reliability and the high cost of current prestressed concrete bridge inspection procedures indicate that a more reliable and efficient system must be developed and utilized. Acoustic emission (AE) monitoring technology has shown promise as an NDT method in laboratory testing of prestressed concrete members (Yepez Roca 1999).

Acoustic emission is defined by the American Society of Testing and Materials (ASTM) in its *Standard Terminology for Nondestructive Evaluations* (ASTM E 1316) as “the class of phenomena whereby transient elastic waves are generated by the rapid release of energy from localized sources within a material, or the transient elastic waves so generated.” AE testing differs from most other NDT methods in two key aspects: 1) the signal originates in the material itself, not in an external source; 2) AE monitoring detects movements or condition changes as they occur, while most other methods simply detect existing geometrical discontinuities.

The initial published studies of acoustic emission phenomena, in the early 1940s, dealt with the problem of predicting rock bursts in mines (ASNT 1996). The first significant investigation of acoustic emission from different metals was carried out by Kaiser (ASNT 1996). He observed what has since become known as the Kaiser Effect. It is a very important observation, and will be referred to again later in this dissertation. Following his work, scientists in the United States started applying this method. Many nondestructive testing applications of the acoustic emission technique have been

successfully demonstrated. This method appears to be very suitable for the evaluation of the mechanical stability of large-scale geological structures such as petroleum reservoirs and underground gas storage reservoirs (Hardy 1975). Also, it has been used to monitor various welding processes (Drouillard et al. 1975), and to check the integrity of fiber-reinforced polymer vessels (Ziehl and Fowler 2003). More recently, AE technology has been successfully used as a nondestructive testing tool to inspect concrete structures such as bridges and buildings (Pollock 1995; Yopez Roca 1999; Ohtsu et al. 2002).

1.2 OBJECTIVE AND SCOPE

The main objective of this investigation was to investigate the feasibility of using AE monitoring to assess the performance of prestressed concrete beams. Since application of AE techniques is relatively new for concrete structures, there remains an incomplete understanding of the meaning of AE activity, which impedes correct interpretation of AE data. The resulting specific objectives of this research are summarized as follows:

1. Use AE parameter-based analysis methods to determine a correlation between AE parameters and structural integrity of prestressed concrete beams.
2. Determine whether various AE evaluation criteria can be used to assess the integrity of prestressed concrete beams.
3. Compare the AE from loading of prestressed self-consolidating concrete (SCC) beams to the AE from loading of similar conventionally consolidated concrete beams.
4. Compare the accuracy of the ACI 437 Cyclic Load Test (CLT) assessment criteria to the accuracy of AE evaluation criteria for prestressed concrete beams.

5. Develop and evaluate a practical NDT method using AE monitoring technology to determine the integrity of in-service prestressed concrete bridge girders.

In order to gain further insight into the AE response of prestressed concrete members over a full range of loading, a series of laboratory tests were conducted. The AE monitoring technique was also applied in the field to an actual damaged prestressed concrete girder bridge.

1.3 ORGANIZATION OF DISSERTATION

In Chapter 2, background information about acoustic emission is presented. A description of key terms relating to AE is provided and the current state of knowledge about the acoustic emission technique in reinforced (nonprestressed) and prestressed concrete is reviewed.

Chapters 3 to 7 have been prepared in the form of a collection of five papers to be submitted for publication. Therefore, some descriptions of experimental procedures and AE evaluation criteria are repeated in some of these chapters.

Chapter 3 is titled “Evaluation of Prestressed Concrete Beams Using a Parameter-Based Acoustic Emission Technique”. In order to determine a correlation between acoustic emission (AE) parameters and the structural integrity of prestressed concrete beams, a twenty-four sensor monitoring system was used to collect AE data from four prestressed concrete T-Beams—one damaged beam, and three undamaged beams—that were loaded in cycles up to failure. AE parameters of amplitude, duration, and signal strength were analyzed for all beams, and relationships were found between these parameters and the damage experienced by the specimens. The results indicate that AE parameter-based analysis can be an effective nondestructive tool for damage detection in

prestressed concrete beams.

Chapter 4 is the paper “Damage Assessment Criteria for AE Testing of Prestressed Concrete Beams”. Several AE evaluation criteria have been proposed previously for reinforced concrete structures. This chapter describes an evaluation of the effectiveness of these criteria when applied to the same prestressed concrete flexural specimens described in Chapter 3. In addition, a new AE evaluation criterion for prestressed concrete—“Signal Strength Moment Ratio”—is proposed, evaluated, and compared to the other AE evaluation criteria.

Chapter 5 provides a “Comparison of Acoustic Emission Activity in Prestressed Conventionally Consolidated and SCC Beams”. In this research, the AE signals from conventionally consolidated and SCC concrete beams during the entire flexural loading process were analyzed. The main objectives of the research were to investigate the feasibility of the AE technique for prestressed SCC beams and to compare the response from SCC beams to that from similar conventionally consolidated concrete beams.

Chapter 6 addresses “Nondestructive Strength Evaluation of Prestressed Concrete Beams”. In this work, the relative performance of two distinct nondestructive testing techniques, the ACI 437 Cyclic Load Test (CLT) and AE monitoring, was evaluated when applied to the laboratory test specimens described in Chapter 3. The CLT assessment criteria are compared to two AE evaluation criteria, and a modification to one CLT criterion is proposed for prestressed concrete structures.

Chapter 7 is focused on “In-Place Acoustic Emissions Monitoring of Damaged Prestressed Concrete Bridge Girders”. To investigate the possibilities of acoustic emission monitoring as a practical nondestructive testing method for prestressed concrete

bridges, two spans of the elevated Interstate Highway 565 bridge structure in Huntsville, Alabama, U.S.A. were instrumented with AE testing. AE was monitored in the damaged regions of four girders while the bridge was load tested. Based on measurements of strains and crack opening displacements in the girders, the effectiveness of two AE evaluation criteria for prestressed concrete beams was evaluated. The effectiveness of a commercial two-dimensional AE source location software package was also investigated. The predicted position of cracks using this AE 2D-LOC analysis technique agreed well with the visually observed pattern of cracking. This indicates that AE methods hold promise for evaluation of the structural integrity of prestressed concrete bridge girders in situ.

Chapter 8 includes a summary of the dissertation and as well as conclusions and recommendations based on the work described herein. Recommendations for further research are also provided within this chapter.

CHAPTER 2

THEORY OF ACOUSTIC EMISSION

2.1 INTRODUCTION

Acoustic emission (AE) is defined by the ASTM in its *Standard Terminology for Nondestructive Examinations* (ASTM E 1316) as “the class of phenomena whereby transient elastic waves are generated by the rapid release of energy from localized sources within a material, or the transient elastic waves so generated.” AE is a kind of microseismic wave generated from dislocations, microcracking, and other irreversible changes in a stressed material. The monitoring of stress waves is accomplished by piezoelectric transducers, which convert these mechanical waves to electrical signals.

AE technique is based on the detection and conversion of these high frequency elastic waves to electrical signals. This is accomplished by directly coupling piezoelectric transducers on the surface of the structure under test and loading the structure. The AE monitoring process is depicted in Figure 2-1. It begins with forces acting on a body; the resulting stress is the stimulus that acts on the material and produces local plastic deformation, i.e. breakdown of the material at specific places. The material breakdown produces acoustic emission in the form of an elastic wave that travels outward from the source, directly or indirectly arriving at a remote sensor. The sensor translates the wave into an electrical signal, which is passed to electronic equipment for further processing.

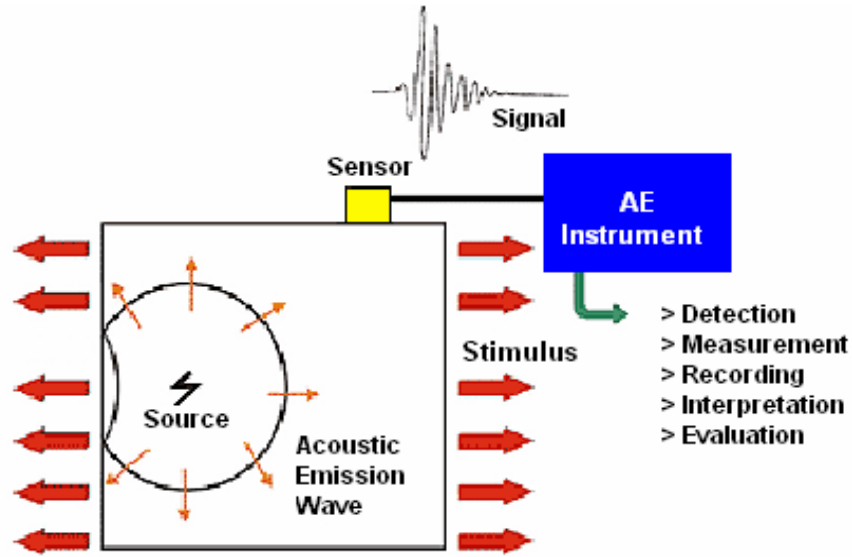


Figure 2-1: Principles of AE technology (adapted from Pollock 1995)

When a structure is loaded, it changes shape: it elongates, contracts, or shears. The resulting strain may have an elastic, reversible component and also a plastic, permanent component. The elastic component of the strain occurs immediately when the load is applied. The stress/strain field inside the structure is quickly redistributed such that all the forces are balanced. Actually, this redistribution takes place at the speed of sound, through the propagation of elastic waves. Unlike the elastic component, the plastic component of the strain often takes considerable time to develop. Some of the deformation is immediate but some of it is delayed. Some researchers (Robinson 1965; Dunegan et al 1968; Pollock 1995) have stated that acoustic emission is a very sensitive indicator that will reveal time-dependent behavior that might otherwise go unnoticed.

This chapter provides a description of key parameters related to AE, a simplified sketch of the AE monitoring procedure, and background information regarding previous

studies involving AE monitoring techniques for prestressed and reinforced (nonprestressed) concrete applications.

2.2 AE PARAMETERS

This section introduces a few basic definitions required to begin the discussion of AE behavior. In AE testing a number of parameters are measured from the emitted signals. From these parameters, the AE behavior of concrete beams tested under loading may be used to characterize and identify different sources of damage (Pollock 1981; Ohtsu 1988). Important signal parameters include amplitude, duration, signal strength, and signal energy. Features of a typical AE signal are shown in Figure 2-2.

Figure 2-2 shows a typical AE electrical signal as a voltage versus time curve. AE parameters in the time domain are used to characterize the AE source mechanism, e.g. crack growth, and to determine the degree of its severity. Due to the complexity of AE signals, it is usually advantageous to study a combination of these parameters to establish source characterization correlations. Some parameters that are commonly used for signal processing are described here:

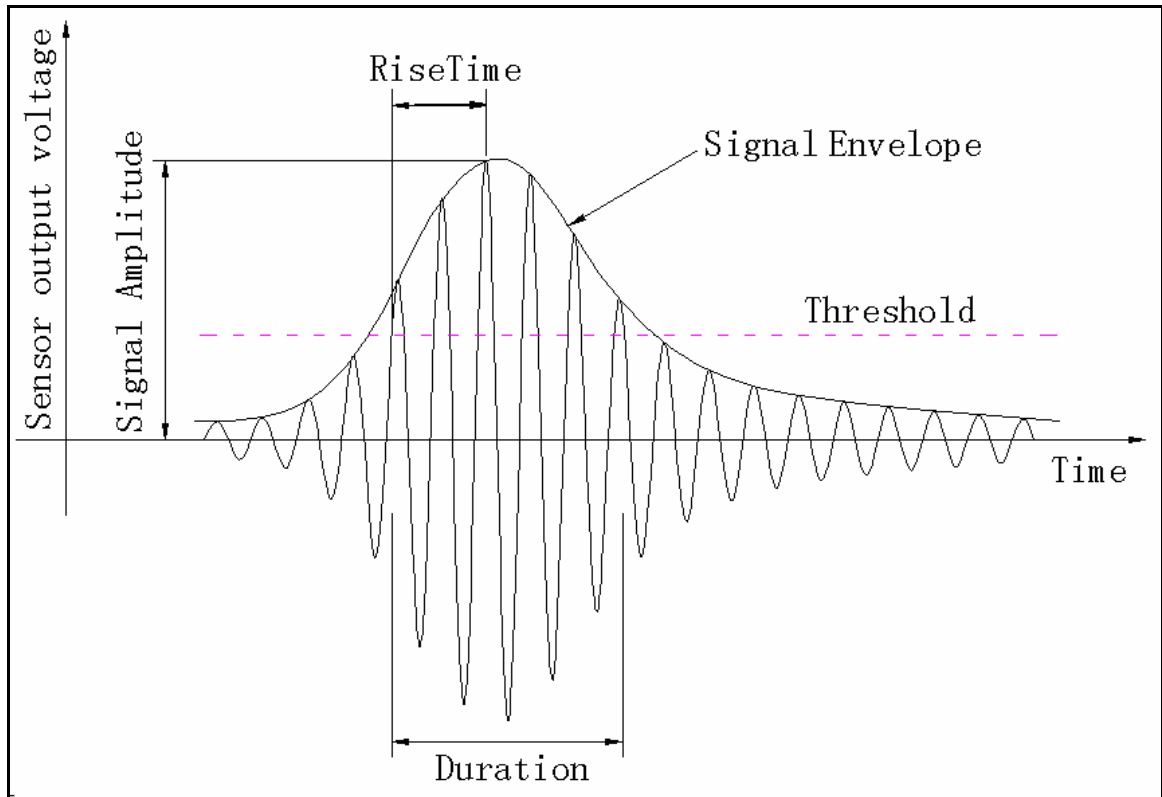


Figure 2-2: AE signal features

1) **Hit**

Hit is defined as the detection and measurement of an AE signal on an individual sensor channel (ASTM E 1316).

2) **Event**

Event is defined as a local material change giving rise to acoustic emission (ASTM E 1316). A single event can result in multiple hits (at one or more sensors).

3) **Voltage threshold**

Voltage threshold is defined as the voltage level on an electronic comparator such that signals with amplitudes larger than this level will be recognized. The voltage threshold may be user-adjustable, fixed, or automatic floating (ASTM E 1316). It is usually used to selectively reject signals with smaller amplitudes, which may not

provide useful information because they often correspond to ambient, electronic, or electromagnetic noise. Background noise may be effectively eliminated during AE data acquisition by rejecting those signals that have a peak amplitude voltage levels lower than a suitable threshold level, which is usually set slightly above the normal background noise level (Fowler et al. 1989).

4) **Signal amplitude**

Signal amplitude is defined as the magnitude of the peak voltage of the largest excursion attained by the signal waveform from a single emission event (ASTM E 1316). Because it is a magnitude, it is taken as the absolute value of this peak voltage. Amplitude, which is one of the most important measures of signal size, is usually reported in decibels (dB). Decibels are a relative measure; each decibel increment corresponds to an increase of 12.2%. Voltage is converted to decibels using the following equation:

$$A = 20 \log\left(\frac{V}{V_{ref}}\right)$$

Where:

A = Amplitude in decibels,

V = Voltage of peak excursion, and

V_{ref} = Reference voltage.

A decibel scale runs from 0 to 100.

Peak amplitude of an acoustic emission signal is an indication of the source intensity (Pollock 1995). Due to the various factors that may affect a transducer's response, peak amplitude of an individual signal may not provide significant information with

regard to the source. However, when the amplitude-related data are evaluated by means of statistical methods it could yield useful information (Pollock 1981).

Analysis of amplitude distribution may be used to increase the degree of reliability of the acoustic emission data (Fowler and Gray 1979). In accordance with common practice, the term amplitude will henceforth be used to describe the signal amplitude in this dissertation.

5) **Duration**

Duration is defined as the time between AE signal start and AE signal end (ASTM E 1316). It is the length of time from the first threshold crossing to the last threshold crossing of the signal. It is usually reported in microseconds. Duration of a signal is affected by the selection of the threshold level. Other parameters may also affect the signal duration during a test. The various sources of AE may produce different signal duration. Mechanical noise sources normally generate long-duration signals while the signal duration for an electrical pulse is generally less than 10 microseconds (Pollock 1995). The relationship between duration and amplitude is an indication of the signal's shape.

6) **Risetime**

Risetime is defined as the time between AE signal start and the peak amplitude of that AE signal (ASTM E 1316). It is measured in microseconds. Risetime measurement for AE signals may yield information similar to that obtained from signal duration.

7) **Signal strength**

Signal strength is defined as the measured area of the rectified AE signal, with units proportional to volt-sec (ASTM E 1316). Signal strength—sometimes referred to as

relative energy—relates to the amount of energy released by the specimen. Signal strength is a function of both the amplitude and duration of the signal. As such, it is a much better measure of total acoustic emission than duration or amplitude alone. It is often used in evaluation criteria for AE testing of structures. Specifically, the signal strength is defined as (Fowler et al. 1989):

$$S_0 = \frac{1}{2} \int_{t_1}^{t_2} f_+(t) dt + \frac{1}{2} \left| \int_{t_1}^{t_2} f_-(t) dt \right|$$

Where:

S_0 = Signal strength,

f_+ = positive signal envelope function,

f_- = negative signal envelope function,

t_1 = time at first threshold crossing, and

t_2 = time at last threshold crossing.

8) Signal energy

Signal energy is defined as the energy contained in a detected acoustic emission burst signal, with units usually reported in joules or values that can be expressed in logarithmic form (dB, decibels) (ASTM E 1316).

Specifically, AE *signal energy* (E_t) is defined as (Fowler et al. 1989):

$$E_t = \frac{1}{2} \int_{t_1}^{t_2} f_+^2(t) dt - \frac{1}{2} \int_{t_1}^{t_2} f_-^2(t) dt$$

9) Count

Count is defined as the number of times the acoustic emission signal exceeds a preset threshold during any selected portion of a test (ASTM E 1316). The total number of

counts and the *count rate*, which is the number of counts during a fixed period of time, are common parameters used for acoustic emission studies. This parameter is associated with the AE monitoring procedure known as ring-down counting. Ring-down counts are a complicated function of the frequency response of the transducer as well as the delay characteristics of the event, the propagation media, and the amplitude of the signal. In addition, the counts are sensitive to changes in the amplifier gain, threshold level, and coupling efficiency of the transducer (Ohtsu 1988). It is known that true AE signals are of complex forms and they may not be assumed to have a simple waveform (Robinson 1965). This arises from the fact that a transducer's response is heavily dependent on several factors. These include the frequency content of the true event, the resonance and damping of the transducer, and attenuation in the medium. Therefore, the information corresponding to the measurements of the counts can only be used in qualitative data evaluation (Ohtsu 1988).

Counts are the comparator output pulses corresponding to the threshold crossing. A single hit might give only a few counts or it might give hundreds of counts, depending on the size and shape of the signal. This is the easiest measurement to make and process; therefore, counts were the most common way to describe and report AE quantities in the early years of AE (Uomoto 1987). During the 1980's energy quantities replaced counts as the preferred measure of AE activity.

Nonetheless, counts are still useful for data interpretation; taken in conjunction with amplitude or duration, counts can give valuable information about signal shape (ASNT 1996).

10) Frequency

Frequency is the number of cycles per second of the pressure variation in a wave.

Commonly, an AE wave consists of several frequency components.

11) Kaiser Effect

Kaiser Effect is defined as the absence of detectable acoustic emission, at a fixed sensitivity level, until previously applied stress levels are exceeded (ASTM E 1316).

12) Felicity Effect

Felicity Effect is defined as the presence of detectable acoustic emission, at a fixed predetermined sensitivity level, at stress levels below those previously applied (ASTM E 1316). The Felicity Effect is a breakdown of the Kaiser Effect. The Felicity Effect means that the structure generates emission during reloading before the previous maximum stress is reached.

The *Felicity Ratio* has been used as an indication of the amount of damage.

Specifically, the Felicity Ratio (Fowler et al. 1989) is defined as:

$$\text{Felicity Ratio} = \text{Load at which emissions occur} / \text{Previous maximum load}$$

Thus, smaller Felicity Ratio values indicate increased levels of damage. The Kaiser Effect and Felicity Effect are illustrated in Figure 2-3. Here cumulative acoustic emission is plotted directly against applied load. The load is increased (to B), decreased (to C), increased again to a higher level (D), decreased (to E), and finally increased to an even higher level (G). Emission is generated during the first load rise (AB), but as the load is lowered (BC) and raised again (CB), there is no further emission until the previous load maximum (B) is exceeded. Emission continues as the

load is raised further (BD), and stops as the load is lowered for the second time (DE). On raising the load for the last time, a different emission pattern is observed: the emission begins (F) before the previous maximum load (D) is attained. Emission continues as the load is increased (FG) (Pollock 1995).

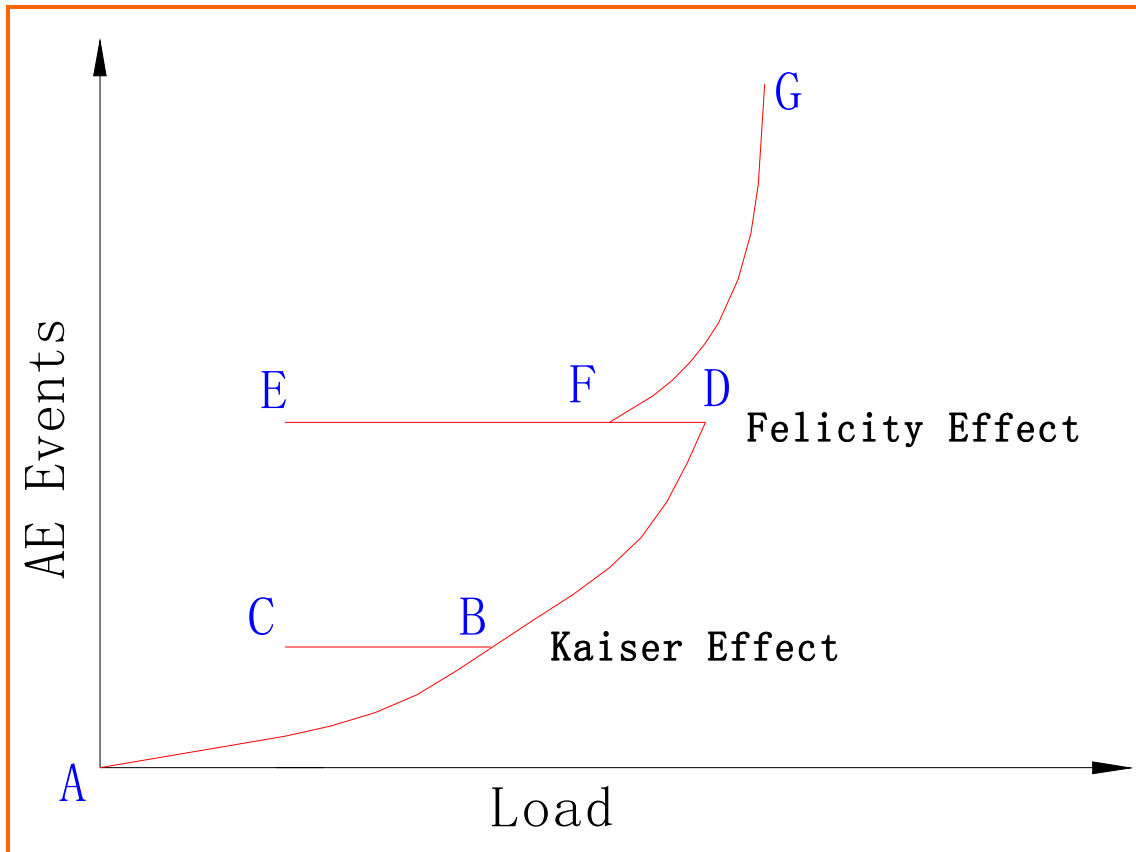


Figure 2-3: Emission on repeated loading (Pollock 1995)

The behavior observed at B (no emission until previous maximum load is exceeded) is known as the Kaiser Effect. The behavior observed at F (emission at a load less than the previous maximum) is known as the Felicity Effect. Insignificant flaws tend to exhibit the Kaiser Effect while structurally significant flaws tend to exhibit the Felicity Effect (Pollock 1995).

13) Historic index

Historic index is a parameter used to determine the change of signal strength rate throughout a test (ASTM E 2478). Specifically, it measures changes in slope of the cumulative signal strength versus hits plot. The historic index is sometimes used to establish the onset of significant acoustic emission. The historic index is defined by ASTM E 2478:

$$H(t) = \frac{N}{N - K} \frac{\sum_{i=K+1}^N S_{oi}}{\sum_{i=1}^N S_{oi}}$$

Where

$H(t)$ = the historic index at time t ,

N = the number of hits (ordered by time) up to and including time t ,

S_{oi} = the signal strength value of the i th hit, and

K = an empirically derived factor that varies with the number of hits. Values for K are given in Table 2-1.

TABLE 2-1: K Factor for Historic Index (ASTM E 2478 - 06)

Number of Hits, N	K
<20	Not applicable
20 to 100	0
101 to 500	0.8N
>500	N - 100

Historic index has been found to be a sensitive method of detecting a change in slope in the cumulative signal strength versus time curve. This change in slope is often referred to as the “knee in the curve”. Normally historic index is low at the beginning

of a test, and increases when the load increases. Once the structure starts to experience significant damage, the cumulative signal strength curve will show a rapid change of slope. At this point, a jump of historic index occurs. Historic index is particularly valuable for determining onset of new damage mechanisms and is essentially independent of specimen size. Historic index is a form of trend analysis, and is updated continuously after each hit. The greater the number of hits on a channel, the more significant the results. An analysis requires a minimum number of data points, and is not valid when only a small number of hits are recorded (ASTM E 2478).

Figure 2-4 is an example plot of historic index versus time of a prestressed concrete beam subjected to flexural load. The plot also superimposes cumulative signal strength. A peak value on the historic index versus time plot represents an important change in the magnitude of emission, which can normally be seen as rapid increases on the cumulative signal strength versus time plot.

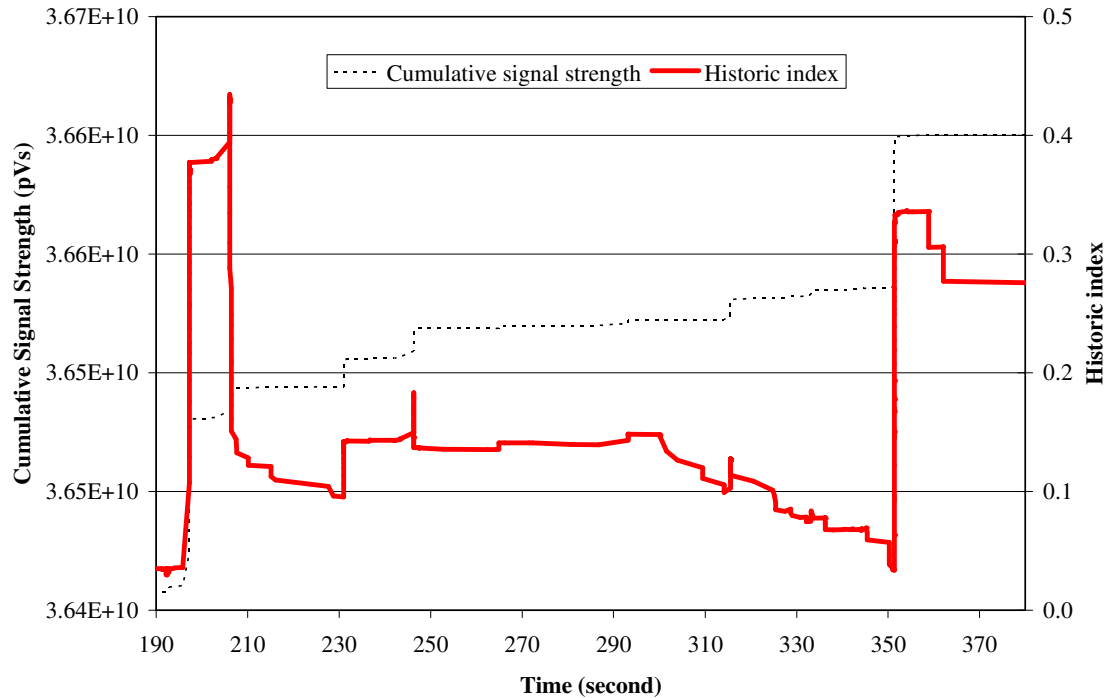


Figure 2-4: Historic Index and cumulative signal strength for prestressed concrete beam

2.3 AE MONITORING PROCEDURE

The technology used in AE monitoring can be very sophisticated, but its application is relatively simple. AE monitoring is easy to set up. A simplified overview of the AE monitoring procedure includes the following steps:

1) Preliminary survey

A preliminary visual survey of the structure is always of fundamental importance to establish a first view of the state of the structure. Structural drawings should be examined to identify the inspection areas. Arrangements should be made to make sure that there are no major obstacles to AE monitoring.

Prior to arrival on site, an appropriate day and time must be selected for monitoring, considering traffic and weather conditions; plans must be made for any necessary traffic control and equipment checkout must be performed in the laboratory (Pollock 1995).

2) Equipment Selection

The equipment used for the tests must have adequate capacity to handle large quantities of information at high data acquisition rates. This means that large disk storage capacity and a fast processor are essential. The most important technical choice to be made for AE monitoring is the choice of operating frequency (Pollock 1995). Sensors are available with resonant or broadband responses covering various frequency ranges. Resonant sensors give the advantage of operating in a known and well-established frequency band, which can be chosen to optimize system performance in the face of wave attenuation and background noise. Resonant sensors are generally more sensitive and less expensive than broadband types. Broadband types, by definition, deliver additional information, but the utilization of this information is not easy outside of the research laboratory (PCI-8 based AE system user's manual 2002). In most practical AE monitoring, resonant sensors are preferred over broadband types (Pollock 1995).

3) Sensor mounting

The first step in the sensor mounting process is surface preparation. Sensors must be attached to the surface carefully in order to avoid bad or damaged areas on the element. The surface must be clean and smooth. Dirty surfaces are undesirable because the dirt may include gritty particles that will hold the sensor away from the concrete surface and reduce the acoustic contact (Pollock 1995).

The second step is the actual placing of the sensor. When a sensor has simply been placed on the bare surface of the concrete containing the acoustic wave, it is found that the sensors produce a very weak signal. If a thin layer of a fluid is placed between the sensor and the concrete surface, a much larger signal is obtained. This can be explained

by looking at the acoustic wave as a pressure wave transmitted across two surfaces in contact (Pollock 1995). On a microscopic scale the surfaces of the concrete are quite rough, so only a few locations are actually in contact when sensors are placed directly on the concrete surface. In the aforementioned case the actual force-transmitting area is very small. If the microscopic gaps are filled with a fluid couplant, the pressure will be more effectively transferred between the surfaces. So the purpose of a couplant is to insure good contact between two surfaces on a microscopic level. High silicone vacuum grease has been successfully used to obtain good contact between the sensors and concrete beam surfaces (Yepez 1999). When the sensor is pressed into position, the couplant should ooze out all sides, driving out all the air and producing good acoustic continuity between the concrete surface and sensor face (Pollock 1995).

The third step in the sensor mounting process is to secure the connecting cable. The cables connecting the sensors to the acquisition system may be secured using mounting pads and cable ties to prevent movement, interference, and rubbing against the specimen, which could generate false AE signals.

The fourth step is to apply the sensor hold-down device to keep the sensor in place throughout the duration of the test. This device can also protect the sensor from environmental hazards and act as an insulator against external noise that may influence the test procedure (Pollock 1995; Yepez 1999).

With these steps completed, the sensor's installation is ready for checking.

4) Calibration

All the AE equipment must be kept in calibration prior to a test to recognize channels or sensors with low or high sensitivity. The preferred technique for conducting performance

verification is a pencil-lead break (PLB). Lead should be broken on the material surface at a specified distance from each sensor as illustrated in Figure 2-5. A standard calibration procedure for the sensors is specified in ASTM E 2374, using a 2H lead, 0.3-mm diameter mechanical pencil. As the lead is pressed against the specimen, the applied force produces a local deformation and this is suddenly relieved when the lead breaks; with good technique, the resulting stress wave is adequately reproducible. The breaking of the lead creates a very short-duration, localized impulse that is quite similar to a natural acoustic emission source such as a crack (ASNT 1996). Furthermore, the amplitude of the lead break source is well within the range associated with typical crack sources (CARP 1999).

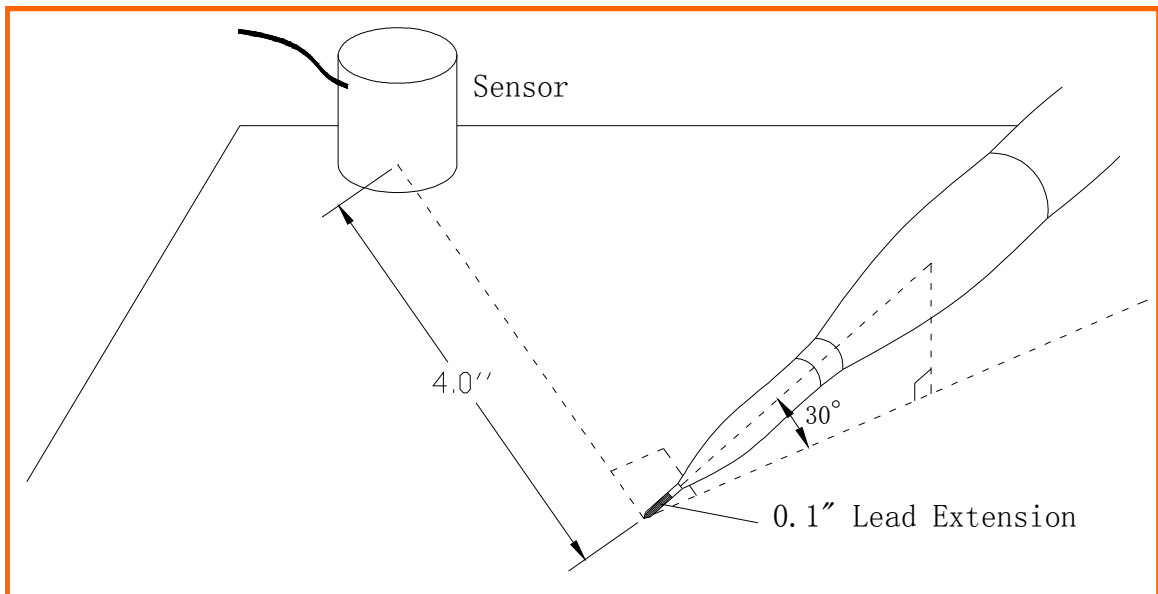


Figure 2-5: Calibration of AE equipment

5) Complementary measurements and environment

Ambient noise must be determined and, during the test, all significant changes must be noted in the test log for later interpretation. The degree of detail depends on the situation

and on the available equipment. As a minimum, the operator should record overall conditions as the monitoring proceeds. Beyond that, it can be useful for the operator to record during the test any specific traffic or weather incidents that were seen to produce emission; these incidents can be keyed to the time of test, so that the corresponding data can be reviewed in detail during post-test analysis (Pollock 1995).

6) Load application

Because acoustic emission is a measure of damage growth, it is load-history dependent (Ohtsu 1989). Therefore, the method of live load application is important to generate the proper data for interpretation.

7) Background check

A background check lasting at least 4 minutes should be performed prior to loading the test specimen (Ridge and Ziehl 2006). The specimen should remain undisturbed during this time. However, normal ambient noise (produced by conversations, testing equipment, etc.) can continue.

8) Data acquisition

During the AE test, AE data could be displayed in real time on a monitor with various screen options. These displays give an idea of the progression of the beam to failure. At the same time, the data can be stored for post-test analysis. During post-test analysis more time is available to perform more complex analytical operations and time can be used for AE data interpretation.

9) Sensor removal

Sensors should be removed prior to anticipated failure of the test specimen. This is necessary as the sensors could be damaged as the specimen fails.

2.4 AE FROM REINFORCED CONCRETE

Although the AE technique is relatively new, significant research has recently been conducted on the use of the AE technique in reinforced concrete structures.

The cracking process in a reinforced concrete beam was studied by Schechinger and Vogel (2007) using an AE techniques. A reinforced beam was loaded in a four-point-bending test to monitor the deterioration process inside the beam using AE analysis. The beam length was 4.5 m (14.8 ft) in total, and the cross section was 440 mm × 440 mm (17.3 in. × 17.3 in.). The experimental results showed that there were difficulties in assessing the regions of active damage due to cracking. The damage location capability decreased when cracking of the concrete occurred. Thus, it was determined that location results might not represent all ongoing deterioration processes.

Results obtained with AE techniques depend on such factors as loading rates, material properties, and type of structure. These might restrict the wide use of AE technique in reinforced concrete.

AE monitoring was performed in steel-reinforced concrete specimens by Li et al. (1998). The experimental results indicated that there was a clear relationship between the AE rate and the rebar corrosion rate. The primary advantage AE offered over other conventional nondestructive evaluation techniques was that it could directly detect the process of a flaw growth. When corrosion products were formed on a corroding rebar, they swelled and applied pressure to the surrounding concrete. Microcracks formed, and stress waves were generated during the expansion process. The growth of the microcracks was directly related to the amount of corrosion products of a corroding rebar. Thus, by detecting the AE event rate and the corresponding amplitudes, the degree of the

corrosion could be interpreted. Also, AE monitoring could detect the onset of rebar corrosion earlier than other conventional nondestructive evaluation methods. It was also determined that the true locations of rebar corrosion in concrete could be provided by AE techniques.

AE behavior of a concrete sample under unconfined compression was studied by Suzuki and Ohtsu (2004). The number of AE events, which corresponded to the generation of microcracks, increased due to the accumulation of cracks. It appeared that this process was dependent on the number of cracks at a certain stress level and the progress rate of the fracture, and thus could follow a stochastic process. The AE rate process theory was introduced to quantify AE behavior under unconfined compression. The degrees of damage in concrete samples were quantitatively evaluated by the AE rate process analysis.

The main challenge for structural integrity evaluation by AE testing is to interpret the AE data recorded. To assess the damage levels of reinforced concrete beams, several evaluation criteria have been proposed.

The NDIS-2421 quantitative assessment criterion was proposed by Ohtsu et al. (2002). To apply this method, the structure is subjected to load cycles during which AE activities are measured. The damage level of the structure is classified based on two parameters: the *load ratio* and the *calm ratio*, which are defined in the NDIS-2421 document as follows:

Load ratio = Load at the onset of AE activity in the subsequent loading/
the previous load;

Calm ratio = The number of cumulative AE activities during the unloading process/

Total AE activities during the last loading cycle up to the maximum

Ohtsu et al. proposed the damage classification boundaries of 0.05 for the calm ratio and 0.9 for the load ratio. This recommendation resulted from laboratory tests of reinforced concrete beams in which crack mouth opening displacement (CMOD) was used to define the level of damage in each specimen. A CMOD of 0.1 mm (0.004 in.) was selected as the transition value from “Minor” to “Intermediate” damage. A CMOD larger than 0.5 mm (0.02 in.) was associated with the “Heavy” damage label.

Colombo et al. (2005) used a relaxation ratio to predict the degree of damage of reinforced concrete beams. This method was focused on the AE activity recorded during the unloading phase of a load cycle. The relaxation ratio was expressed in terms of energy and defined as:

$$\text{Relaxation ratio} = \frac{\text{Average energy during unloading}}{\text{Average energy during loading phase}}$$

where the average energy was calculated as the cumulative AE energy recorded during each phase divided by the number of recorded sensor hits.

The use of average energy overcame the problem of the different time duration of the various cycles that could affect the results. This method was based on the principle that the presence of AE energy during the unloading phase of an AE test is generally an indication of structural damage of the material under study. According to the reported results of experiments on several reinforced concrete beams, the values of the relaxation ratio appeared to be related to the percentage of failure load reached in a specific cycle and were therefore related to the degree of damage of the beam. A value of relaxation ratio greater than one implied beam experienced damage. The results also were affected

by the concrete strength and loading rate used during the experiments.

Ridge and Ziehl (2006) proposed an evaluation criterion for strengthened reinforced concrete beam specimens based on the ratio of peak cumulative signal strength (peak CSS) recorded during a sustained load period (load hold) to the peak CSS recorded during a previous initial load hold at a slightly higher load. This evaluation criterion relies on AE data recorded only during load holds rather than during periods of increasing (loading) or decreasing (unloading) load, which is particularly useful in the field of AE testing where the genuine emission may be obscured by background noise. The ratio of peak CSS recorded during the reload hold to the peak CSS recorded during the initial load hold was calculated for each loadset and the results were used to determine a suitable acceptance criterion. This ratio was expressed as a percentage as defined in the following:

$$\text{Peak CSS Ratio} = \left(\frac{\text{Peak CSS at the end of reload hold period}}{\text{Peak CSS at the end of initial load hold period}} \right) * 100\%$$

To provide a suitable period for evaluation of the rate of AE activity during the hold period and to avoid nongenuine AE, each load hold was maintained for 4 minutes. To avoid having the second load level accidentally surpass the level of the first hold—which could introduce new cracks in the specimen—the peak load held during the second (reload) cycle of each loadset was slightly less than that of the initial cycle. AE data were analyzed for two strengthened specimens, one strengthened with precured FRP strips and the other with unidirectional FRP fabric. The experimental results indicated that when the Peak CSS Ratio was more than 40%, the strengthened reinforced concrete beam was damaged.

2.5 AE FROM PRESTRESSED CONCRETE

Although AE monitoring is increasingly widely used for monitoring concrete structures (Ohtsu et al. 2002; Colombo et al. 2003; Ridge and Ziehl 2004), its application for prestressed concrete bridges is currently very limited. However, in contrast to reinforced concrete, prestressed concrete is either uncracked, or the cracks are closed due to the applied compressive load. Accordingly, noises from nonstructural cracking are much less of a problem, and AE monitoring techniques show promise as NDT methods for prestressed concrete structures. Previous research work related to application of AE monitoring techniques for prestressed concrete are reviewed here.

An AE monitoring technique was developed to detect damage in prestressed concrete pipe (Travers 1997). Investigations showed that the concept of detecting AE generated by a prestressing wire failure was practical. Although the propagation of the acoustic energy along the pipe length was complicated by multiple reflections off the inside walls of the pipe, which made determination of the arrival time of signals at the sensors difficult and limited the certainty of the precise origin of the acoustic emission, the accuracy was acceptable for this application. The experimental results were validated by excavating sites indicated by field testing and locating distressed pipe based on the data.

Hearn and Shield (1997) studied the differences in AE behavior between ordinary reinforced and prestressed concrete. This study involved the AE monitoring of three large-scale ordinary reinforced beams and two prestressed concrete beams. The loading consisted of loading/unloading cycles with gradually increasing deflections until failure occurred. The loading/unloading ramp rates were set so that it took between 30 and 90 seconds to reach the prescribed deflection level from the unloaded state. The specimen

was then kept at the prescribed deflection level for a minimum of 30 seconds. This time was used to ensure that all AE activity that was going to occur during the loading cycle had time to occur, and to check the specimens for the formation of new cracks, or the propagation of pre-existing cracks. Tests showed differences in AE behavior between the ordinary reinforced and prestressed concrete specimens. In ordinary reinforced specimens, AE activity continued when the load was held constant. This activity was not observed in the prestressed specimens. The authors thought this was most likely due to the continuing transfer of tensile forces between the concrete and reinforcing steel for ordinary reinforced concrete. In order for the reinforcing steel to resist the tensile stresses the surrounding concrete must crack. Additionally, there was significant AE activity during crack closure for the prestressed specimens. The ordinary reinforced specimens had only limited AE activity during crack closure. This was most probably due to effect of the prestressing force acting to close the cracks, causing the surfaces to rub together during closure.

AE monitoring of load testing of high-strength prestressed concrete girders was performed by Luis Yopez (1999) at the University of Texas at Austin. The specimens tested were AASHTO Type I prestressed concrete girders with a 165 mm (6.5 in.) thick concrete slab cast on top. The girders were tested by applying load in a stepwise manner. Hydraulic pressure was applied to an actuator until the desired load was obtained. The load was held constant while measurements were taken of the principal test parameters including load, deflection, and concrete strains. AE was monitored during the loading stage and during a two-minute hold period immediately following attainment of the specified load. Following the two-minute load hold, data acquisition was paused and a

visual inspection of the girder undertaken. After marking cracks, the AE equipment was restarted, and the cycle continued again. The ability of the AE monitoring technique to predict and locate cracks before their appearance at the surface was indicated from the results. A significant increase in cumulative energy shortly before shear and flexural cracking was measured on the surface. This increase was thought to correspond to the formation of the microcrack network within the prestressed concrete. The AE parameter Historic Index was used to define the onset of emission because it could be used to define the load corresponding to the change in energy release clearer than a cumulative energy versus time plot. The moment tensor analysis technique (Ohtsu 1988) was used by Yopez to predict the position and growth of cracks. The results from the moment tensor analysis showed a good agreement with the actual crack patterns visible at the surface of the beam. Many sensors, however, were needed in order to compensate for the attenuation of the signal and to obtain three-dimensional source location.

Brian Tinkey (2000) and Piya Chotichai (2001) studied the application of acoustic emission to prestressed concrete girders. The full-scale prestressed concrete box girder and full-scale Type C prestressed girder had experienced premature concrete deterioration due to alkali-silica reaction and delayed ettringite formation. Acoustic emission experiments were performed on a full-scale prestressed concrete box girder under shear-dominated fatigue loading. The results showed that the progressive deterioration in the specimens could be identified by AE. Felicity ratio was the most powerful AE parameter for evaluating the damage level in a prestressed concrete girder. A decrease in the Felicity ratio indicated an increased damage level. Three criteria, the curvature, slope, and historic index were proposed to determine the onset of significant

emission. Strand pull-out tests were performed on two slices removed from the prestressed concrete girders. These tests showed that the acoustic emission monitoring technique could be used as a tool to identify strand slip. At the maximum pull-out load, as the strand started to slip, hits with long duration were detected. This characteristic could be used during in-service tests of prestressed concrete girders to identify strand slip. If an AE sensor mounted on the end region could detect the slip between prestressing strands and concrete, it would provide an engineer with important information about the condition of the structure.

Field tests carried out on six different in-service structures showed that acoustic emission could be used effectively in a noisy traffic environment. Traffic noise was filtered from genuine acoustic emission data by using the guard sensor technique. Background noise tests were carried out on in-service bridges. A procedure based on AE parameters was proposed for acoustic emission field monitoring of prestressed concrete bridge girders. Their works contributed to a better understanding of AE on prestressed concrete girders with premature cracking.

CHAPTER 3

**EVALUATION OF PRESTRESSED CONCRETE BEAMS USING A
PARAMETER-BASED ACOUSTIC EMISSION TECHNIQUE**

3.1 INTRODUCTION

Acoustic emissions are transient elastic stress waves resulting from a sudden release of elastic energy, caused by mechanical deformations, initiation and propagation of microcracks, dislocation movement, and other irreversible changes in a material (ASTM E 1316). These waves radiate from the source and can be detected by piezoelectric sensors mounted on the surface of the material. Studies of AE from concrete structures have been numerous, and a considerable number of articles have been published on this topic (Ohtsu 1989; Ohtsu et al. 2002; Colombo et al. 2005; Ridge and Ziehl 2006). AE has been measured in prestressed concrete structures in only a few studies (Hearn et al. 1997; Yopez 1999; Chotichai 2001).

AE is generated during both the initiation and propagation of cracks in prestressed concrete structures. Information about the existence and location of possible damage sources can be obtained by collecting and examining the characteristics of the AE surface waves (Pollock 1989). Among structural nondestructive tests, the AE monitoring technique is the only one that is able to detect a damage process as it occurs (ASNT 1996). The AE monitoring technique represents a potentially rapid, economic, and

reliable method to nondestructively test prestressed concrete structures.

Although the AE technique has been more widely used as a nondestructive evaluation method for concrete structure testing, the technique may be better suited for prestressed concrete structures than for reinforced concrete structures. This is because cracking in the tension zones of reinforced concrete members is normal under service loads and does not necessarily indicate a structural problem. This type of non-critical cracking is a significant source of AE that tends to mask more significant AE as structural damage develops. Filtering of unwanted data is problematic because AE characteristics associated with minor and significant cracking are similar (Pollock 1989; Yezpez 1999). Furthermore, the attenuation of the elastic stress waves induced by the tension-zone cracking is severe (Pollock 1989). This attenuation can severely decrease the AE monitoring sensitivity. These two main problems, tension-zone cracking and severe attenuation, make the application of the AE technique to reinforced concrete structures difficult.

In contrast to reinforced concrete, the results of AE monitoring of prestressed concrete beam tests are encouraging. The prestressed concrete is initially under compression and is either uncracked or prior cracks are closed. Thus, the existence of emission sources under service-level loads generally indicates a developing structural problem such as bond distress, shear cracking, flexural cracking, or internal microcracking. In addition, the absence of open cracks reduces attenuation and makes accurate source location more likely (Yezpez 1999). Because extraneous noises from noncritical cracking are much less of a problem in prestressed concrete structures, the AE technique shows promise as a nondestructive structural integrity test for these structures.

Because only limited studies have been performed on AE techniques for prestressed concrete structures, considerable shortcomings in the interpretation of AE data and parameters still exist (Hearn and Shield 1997; Yepez 1999). For the study described in this chapter, laboratory testing was performed to gain further insight into AE behavior in prestressed specimens prior to extensive implementation of AE techniques in practice. AE was monitored during cyclic tests of four prestressed concrete T-beams, including one beam that was damaged prior to testing.

AE data acquired from a carefully designed loading sequence provided real-time information concerning the integrity of each specimen. Correlations were established between AE activities and specific types of damage. Based on the experimental studies of prestressed concrete beams, several AE parameters, such as amplitude, duration and signal strength, were investigated. The main goal of these experiments was to determine a correlation between AE parameters and structural integrity of prestressed concrete beams.

3.2 RESEARCH SIGNIFICANCE

Although much research has been conducted on AE monitoring of concrete structures, few research results are available for prestressed concrete structures. Some problems exist regarding correct interpretation of AE data and understanding of AE parameters. In order to aid in solving these problems, several AE parameters were investigated based on cyclic load tests of prestressed concrete beams. The results reported in this chapter demonstrate that AE can be used to reliably detect cracks in prestressed concrete and can also identify their imminent occurrence.

3.3 AE PARAMETERS

In AE testing, a number of parameters are measured from the sensor-emitted signals.

When the signal rises above the threshold, which is defined in ASTM E 1316 as a voltage level on an electronic comparator such that signals with amplitudes larger than this level will be recognized, the sensor is said to have received a “hit”. Commonly employed parameters include amplitude, duration, signal strength, and signal energy. Through measurement and analysis of these parameters, the AE produced when prestressed concrete beams are subjected to loads may be used to characterize and identify different sources and types of damage. Features of a typical AE signal are shown in Figure 3-1.

Commonly used AE parameters are defined in the rest of this section.

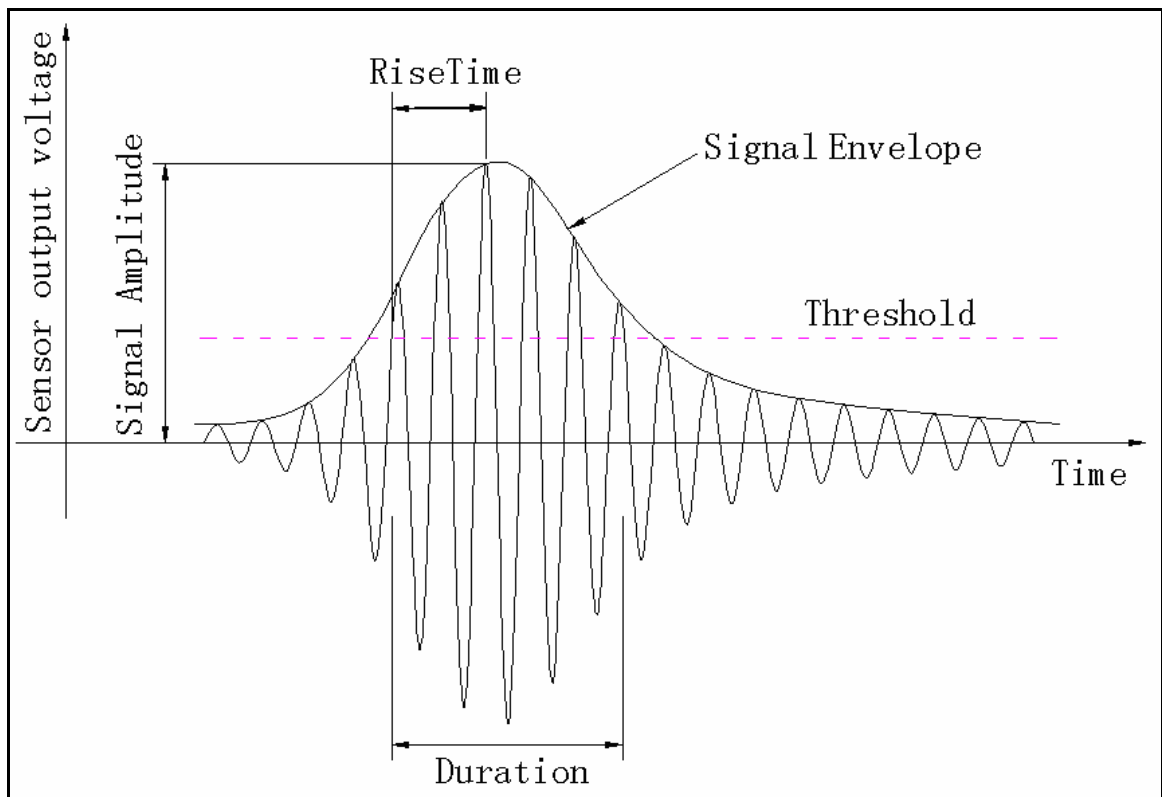


Figure 3-1: AE signal features

3.3.1 AMPLITUDE

The amplitude is defined as the peak voltage magnitude of the largest excursion attained by the signal waveform from an emission event (ASTM E 1316). It is taken as the absolute value of the maximum voltage of a waveform, and it is one of the most important measures of signal size. Amplitude is usually recorded in decibels (dB).

Peak amplitude of an AE signal is an indication of the source intensity. Due to the various factors that may affect a transducer's response, peak amplitude of an individual signal may not provide significant information with regard to the source. However, when the amplitude-related data are evaluated by means of statistical methods, some useful information can be obtained (Pollock 1981). Analysis of the amplitude distribution may be used to increase the degree of reliability of the AE data. Some researchers have stated that there are distinct regions of amplitude corresponding to beam damage in beams strengthened with fiber-reinforced polymers (FRP) (Fowler and Gray 1979) and steel (Pollock 1995).

3.3.2 DURATION

Duration is defined as the time between AE signal start and AE signal end (ASTM E 1316). It is the length of time between the first and the last threshold crossing of the signal. It is usually measured in microseconds. Duration of a signal is affected by the selection of the threshold level. Other parameters may also affect the signal duration during a test. Thus, proper and consistent experiment design is necessary to allow effective, reliable AE evaluation using duration as a parameter. The various sources of AE may produce different signal durations. Mechanical noise sources normally generate long-duration signals, while the signal duration for an electrical pulse is generally less

than 10 microseconds (Pollock 1995). The relationship between duration and amplitude is an indication of the signal shape. Long-duration events are important AE data descriptors. Fowler and Gray (1979) stated that the signal duration (relative to normal values for a material) is a good indicator of the severity of damage.

3.3.3 SIGNAL STRENGTH

Signal strength is the measured area of the rectified AE signal with units proportional to volt-seconds (ASTM E 1316). Signal strength—sometimes referred to as relative energy—relates to the amount of energy released by the specimen. It is a function of both the amplitude and duration of the signal. The signal strength (S_0) is defined as (Fowler et al. 1989):

$$S_0 = \frac{1}{2} \int_{t_1}^{t_2} f_+(t) dt + \frac{1}{2} \left| \int_{t_1}^{t_2} f_-(t) dt \right| \quad (\text{Eq. 3.1})$$

Where:

f_+ = positive signal envelope function,

f_- = negative signal envelope function,

t_1 = time at first threshold crossing, and

t_2 = time at last threshold crossing.

3.3.4 SIGNAL ENERGY

Signal energy is defined as the energy contained in a detected acoustic emission burst signal, with units usually reported in joules and values which can be expressed in logarithmic form (dB) (ASTM E 1316). Specifically, AE signal energy (E_i) is defined as (Fowler et al. 1989):

$$E_t = \frac{1}{2} \int_{t_1}^{t_2} f_+^2(t) dt - \frac{1}{2} \int_{t_1}^{t_2} f_-^2(t) dt \quad (\text{Eq. 3.2})$$

3.4 EXPERIMENTAL INVESTIGATION

3.4.1 SPECIMEN DESCRIPTION

In this study, four prestressed concrete T-beams, denoted as STD-M-A, STD-M-B, STD-M-C, and STD-M-D, cast in the Auburn University Structural Research Laboratory were instrumented with sensors to monitor their AE under various levels of loading. Figure 3-2 shows the cross section details for all four T-beams tested.

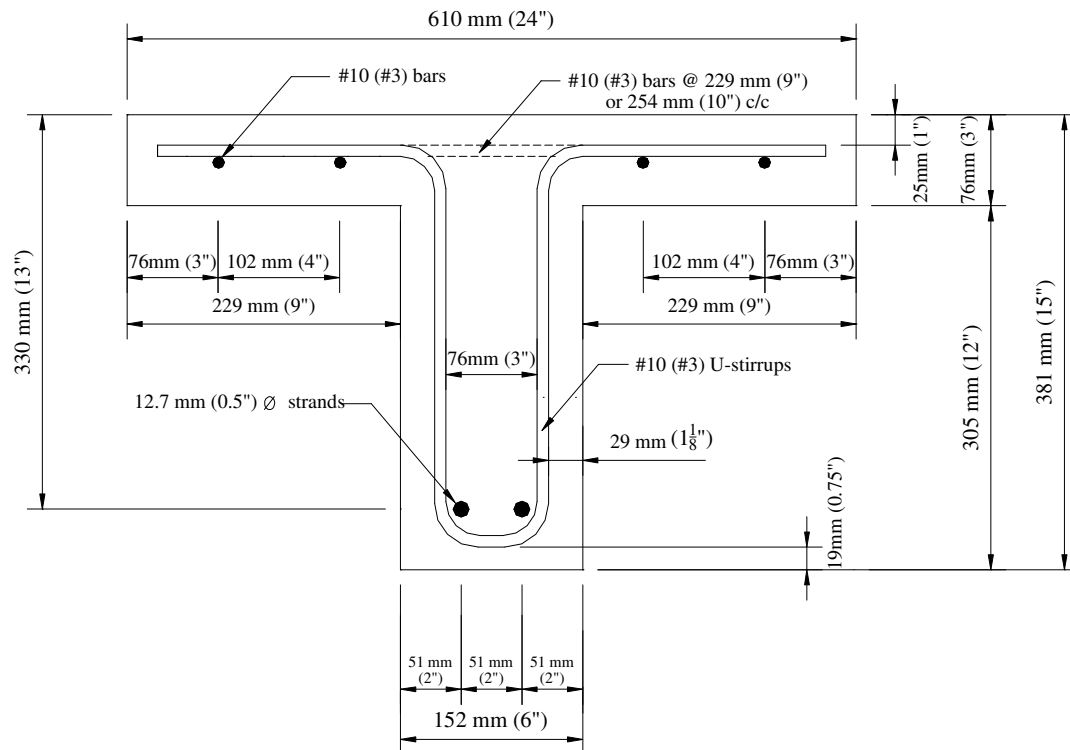


Figure 3-2: T-Beam cross section detail

The four specimens differed primarily in span length and the fact that STD-M-A was subjected to a large and damaging load prior to AE testing. The other three beams experienced no significant applied loading prior to testing. The specimens were

prestressed with two seven-wire, low-relaxation, Grade 270, 1/2-in. “special” prestressing strands. Four Grade 60 No. 3 reinforcing bars were provided as top-flange longitudinal reinforcement. In addition, Grade 60 No. 3 reinforcing bars were used for the shear reinforcement. For each beam length, a slightly different stirrup layout was used. Each specimen had the minimum shear reinforcement required to resist the anticipated flexural failure load for each specimen. The properties of the test specimens are listed in Table 3-1. Detailed information about the test specimens has been reported by Levy (2007).

Table 3-1: Test specimen properties

Beam	Span m (in.)	$\frac{a}{d_p}$	f'_c MPa (psi)	P_s kN (kips)	P_n kN (kips)	$M_{n,calc}$ kN-m (kip-ft)	M_{max} kN-m (kip-ft)	Failure Type
STD-M-A	7.01 (276)	9.23	43.6 (6320)	37.7 (8.5)	74.0 (16.6)	130 (96.0)	145 (107)	Flexure
STD-M-B	4.98 (196)	6.15		61.7 (13.9)	121 (27.1)		138 (102)	Flexure
STD-M-C	3.96 (156)	4.62		87.8 (19.7)	169 (38.0)		154 (113)	Flexure
STD-M-D	2.95 (116)	3.08		148 (33.3)	272 (61.2)		141 (104)	Shear- tension

Note:

f'_c = 28-day compressive strength of concrete,

d_p = Effective depth,

a = Shear span,

P_s = Service-level design load calculated prior to flexural load testing,

P_n = Ultimate load predicted based on nominal flexural capacity,

$M_{n,calc}$ = Calculated nominal moment capacity, and

M_{max} = Ultimate moment resisted during flexural test.

3.4.2 TEST PROCEDURE AND MEASUREMENT

Four beams were tested in flexure under symmetric four-point loading. The test setup, shown in Figure 3-3, consisted of a simply supported beam loaded by two equal concentrated loads. A 0.91-m (3.0-ft) length of uniform bending moment was induced at midspan by means of a spreader beam which transferred the load from the actuator (P) through steel cylinders to steel plates attached to the beam with a gypsum plaster.

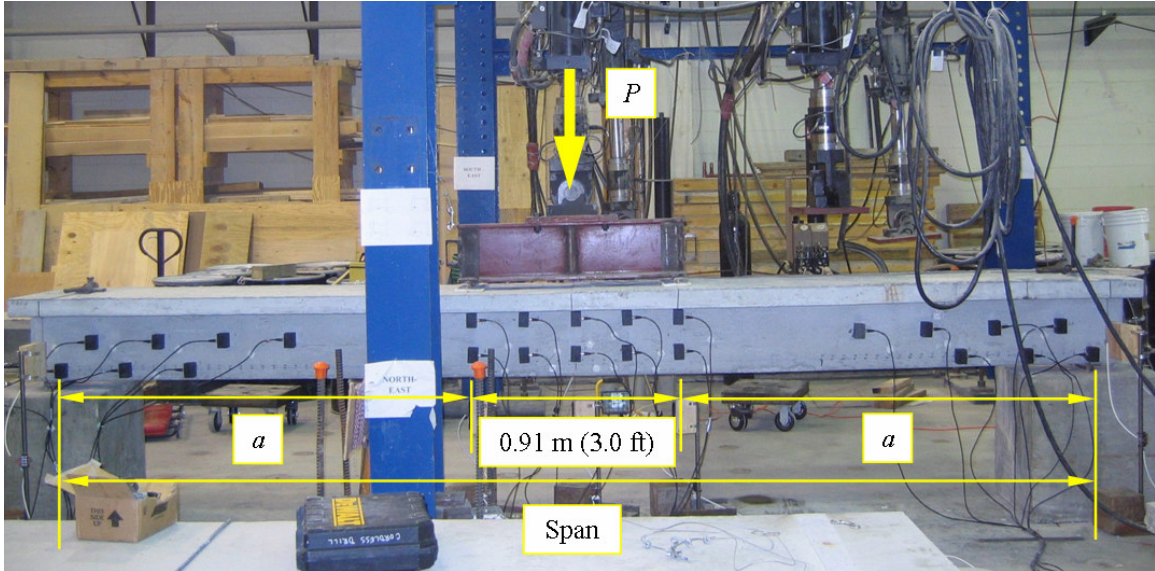


Figure 3-3: Test setup

While undergoing AE monitoring, all specimens were subjected to Cyclic Load Testing (CLT) (ACI 437R-03). The AE load cycles and the CLT cycles were grouped together. Therefore, the AE data and CLT data were collected simultaneously in one test sequence. An examination of the CLT results is presented in Chapter 6 of this dissertation.

The applied load was measured using a calibrated force transducer between the hydraulic actuator and the spreader beam. Figure 3-4 depicts the load cycles versus time. The ten numbered load cycles are paired into five load sets, e.g. Loadset 1-2 includes the similar Load Cycles 1 and 2. Thus the loading pattern is made up of five pairs of load sets, and each load set is made of two similar load cycles. Each load step marked by an ellipse was maintained for four minutes. Each of the other loading/unloading steps had an elapsed time of two minutes. All loads were applied and maintained via manual displacement control using a closed-loop hydraulic testing system.

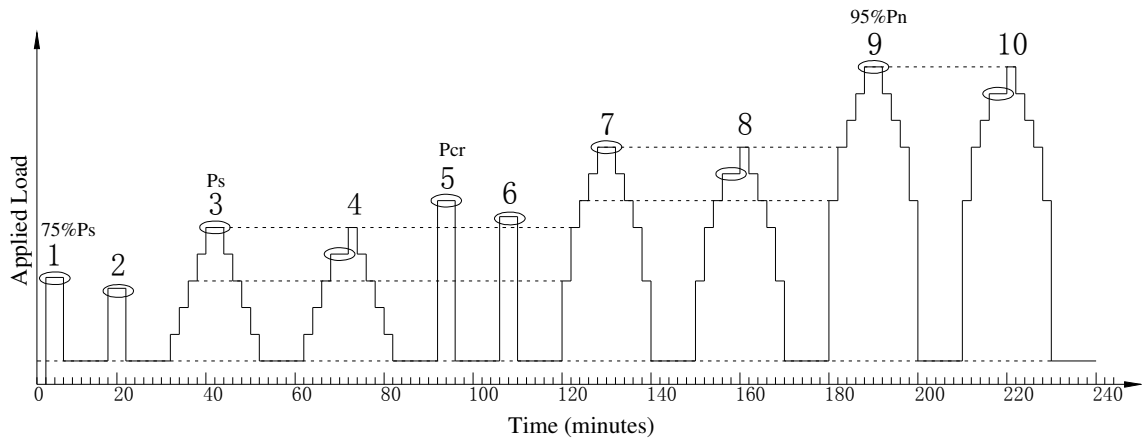


Figure 3-4: Load cycles and steps

All levels of loading applied in the load cycles were functions of four independent load values P_{min} , P_s , P_{cr} , and P_n . P_{min} was the minimum load, 2.2 kN (500 lbs), that was maintained after the start of the test. P_s was the applied load computed to cause zero net flexural stress in the bottom fiber of the beam at the load points (Table 3-1). This corresponds to the service-level design load for Alabama Department of Transportation (ALDOT) bridge girders. P_{cr} , unlike the other three load values, was not computed before the test. During the 5th load cycle, the load was applied at a rate of approximately 0.4 kN/sec (100 lbs/sec) until first cracking occurred. Achievement of this cracking load was signaled by a slight drop in load, accompanied by visible cracking. This actual cracking load, P_{cr} , was used to determine the peak load for the 6th cycle. P_n (Table 3-1) was the load required to cause a bending moment equal to the computed nominal moment capacity, M_n , in the midspan region. This nominal moment capacity was computed using the AASHTO LRFD procedures (AASHTO 2006).

The load step values for the five loadsets are detailed in Table 3-2.

Table 3-2: Load step value

Load set	Cycle	Load Step				
1-2	1	$P_1 = 0.75P_s$				
	2	$P_2 = 0.90P_1$				
3-4	3	$P_{31} = 0.25P_s$	$P_{32} = 0.50P_s$	$P_{33} = 0.75P_s$	$P_{34} = 0.90P_s$	$P_{35} = P_s$
	4	$P_{41} = P_{31}$	$P_{42} = P_{32}$	$P_{43} = P_{33}$	$P_{44} = P_{34}$	$P_{45} = P_{35}$
5-6	5	$P_5 = P_{cr}$				
	6	$P_6 = 0.90P_5$				
7-8	7	$P_{71} = 0.75P_s$	$P_{72} = P_s$	$P_{73} = (P_{72} + P_{74})/2$	$P_{74} = 0.90P_{75}$	$P_{75} = (P_s + P_{95})/2$
	8	$P_{81} = P_{71}$	$P_{82} = P_{72}$	$P_{83} = P_{73}$	$P_{84} = P_{74}$	$P_{85} = P_{75}$
9-10	9	$P_{91} = P_{73}$	$P_{92} = P_{75}$	$P_{93} = (P_{92} + P_{94})/2$	$P_{94} = 0.90P_{95}$	$P_{95} = 0.95P_n$
	10	$P_{101} = P_{91}$	$P_{102} = P_{92}$	$P_{103} = P_{93}$	$P_{104} = P_{94}$	$P_{105} = P_{95}$

For the first Loadset 1-2, Cycle 1 and Cycle 2 each consisted of only one loading step followed by an unloading step. The maximum load level for Cycle 1, P_1 , is equal to 75 percent of P_s . Therefore, it is also equal to 75 percent of the maximum load level for Cycle 3. P_1 is estimated to roughly correspond to a frequently occurring level of service load. Cycle 1 began by loading the beam to P_1 . This load was maintained for at least four minutes, during which time the specimen was not disturbed. Shortly after the end of this “load hold”, the load was decreased to P_{min} , which was maintained for 10 minutes. The maximum load level for Cycle 2, P_2 , corresponds to 90 percent of the previous peak load of Cycle 1. Cycle 2 began by reloading the specimen to P_2 . This load level was maintained for four minutes without disturbance, after which the load was again reduced

to P_{min} . Once again, the minimal load was maintained for 10 minutes, and the specimen remained undisturbed for at least the first 4 minutes.

For Loadset 3-4, Cycle 3 (corresponding to Cycle A of the ACI 437R-03 CLT) consisted of five load steps. The load was increased in steps until P_s was reached. Then the load was decreased through the same steps to P_{min} . Each loading/unloading step, including the sustained portion, was 2 minutes long, except the maximum load level, P_s , which was maintained for at least four minutes without disturbance. The maximum load level was maintained until the structural response parameters, such as strain and deflections, stabilized. After unloading, P_{min} was again held for 10 minutes. Response measurements were recorded during both the loading and the unloading phases. Cycle 4 (corresponding to Cycle B of the ACI 437R-03 CLT) was a repeat of Cycle 3, but the load of the fourth of five steps (P_{44}) was maintained at least four minutes while the beam was undisturbed. All other loading/unloading steps, including the sustained phase, were 2-minute long. After unloading, P_{min} was again held for 10 minutes.

For Loadset 5-6, Cycle 5 and Cycle 6 each consisted of only one load step (followed by a single unloading step). The maximum load level for Cycle 5 (P_5) was equal to P_{cr} , the actual first cracking load experienced in the test (For beam STD-M-A, it corresponded to the estimated cracking load since the beam was already cracked before testing. For beam STD-M-B, it corresponded to calculated cracking load, $P_{cr,calc}$ instead of actual cracking load, P_{cr}). Cycle 5 began by loading the beam to P_5 . This load was maintained for at least four minutes, during which time the specimen was undisturbed. Shortly after the end of this “load hold”, the load was decreased to P_{min} . This minimal load was held for 10 minutes. Cycle 6 began by reloading the specimen to P_6 . The

maximum load level for Cycle 6 (P_6) corresponded to 90 percent of the previous peak load, P_5 . This load level was maintained for at least four minutes without beam disturbance, after which the load was again reduced to P_{min} . This minimal load was held for 10 minutes, with the specimen remaining undisturbed for at least 4 minutes.

For Loadset 7-8, Cycles 7 and Cycle 8 represent ACI 437R-03 CLT Cycles C and D, respectively. They were identical in load magnitude and achieved a maximum load level (P_{75}) that was halfway between the maximum load level applied in Cycle 3 (P_3) and the maximum load planned for Cycle 9 ($P_{95} = 0.95P_n$). The load-step timing of Loadset 7-8 was similar to that of Loadset 3-4. For Cycle 7 (and 8), the first of the five load steps corresponded to the load level of the third step of Cycle 3 and the peak of Cycle 1 ($P_{71} = P_{33} = P_1$). The second step corresponded to the level of maximum load attained in Cycle 3 ($P_{72} = P_{35} = P_3$). The third step corresponded to P_5 , and was a load halfway between P_{72} and P_{74} . The fourth step was equal to 90 percent of P_{75} .

For Loadset 9-10, Cycle 9 and Cycle 10 represented ACI 437R-03 CLT Cycles E and F, respectively. They were identical in peak load magnitude, which corresponded to 95 percent of P_n . For Cycle 9, the first of five steps was at the load level of the third step of Cycle 7 and the peak of Cycle 5 ($P_{91} = P_{73} = P_5$). The load of the second step was at the level of maximum load applied in Cycle 7 ($P_{92} = P_{75}$). The load of the third step was halfway between the second and fourth load level. The load of the fourth of five steps was equal to 90 percent of the maximum load level of Cycle 9. The load-step timing of Loadset 9-10 was similar to that of Loadset 3-4 and Loadset 7-8.

At the conclusion of Cycle 10, the test load was reduced to P_{min} and maintained for 10 minutes.

Linear potentiometers were used to measure the displacements. Vertical deflections relative to the floor under the supports, as well as directly under midspan, were measured. All displacement values reported in this chapter refer to the vertical midspan displacement relative to any vertical movement of the support sections. Figure 3-5 shows the use of linear potentiometers to monitor displacement.

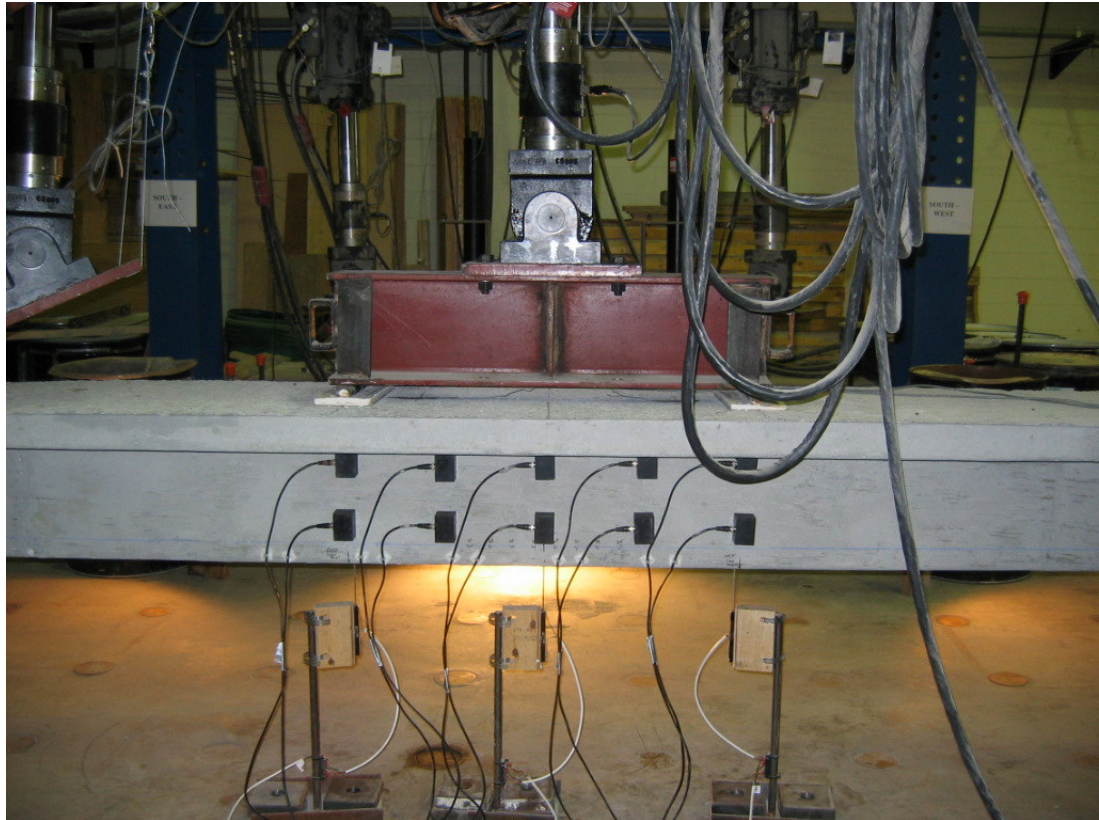


Figure 3-5: Linear potentiometers used to monitor beam deflection

All AE signals were monitored with a 24-channel "Sensor based Acoustic Multi-channel Operation Systems" (SAMOS) manufactured by Physical Acoustics Corporation (PAC). The SAMOS was powered by AE-Win Software, which can record AE parameters as well as AE wave data. PAC R6I-AST 50-kHz integral resonant sensors were used.

The AE system had the following characteristics: 16-bit analog-to-digital-converter resolution, 0.25- μ sec time-of-hit resolution, 200- μ sec hit definition time (HDT), 50- μ sec peak definition time (PDT), 300- μ sec hit lockout time (HLT), 45-dB threshold, and 40-dB preamplifier (R6I).

Twenty-four sensors were surface-mounted on three zones of each beam as shown in Figure 3-6: two parallel rows of five sensors to monitor flexural cracking in the zone of maximum moment, a row of three sensors along the prestressing strand depth near each support to monitor strand slippage in the anchorage zone (along the transfer length), and a row of four sensors near the mid-depth of the beam in each shear span (between load point and support). All sensors were placed on one face of the beam. This is necessary as the sensors could be damaged as the specimen fails.

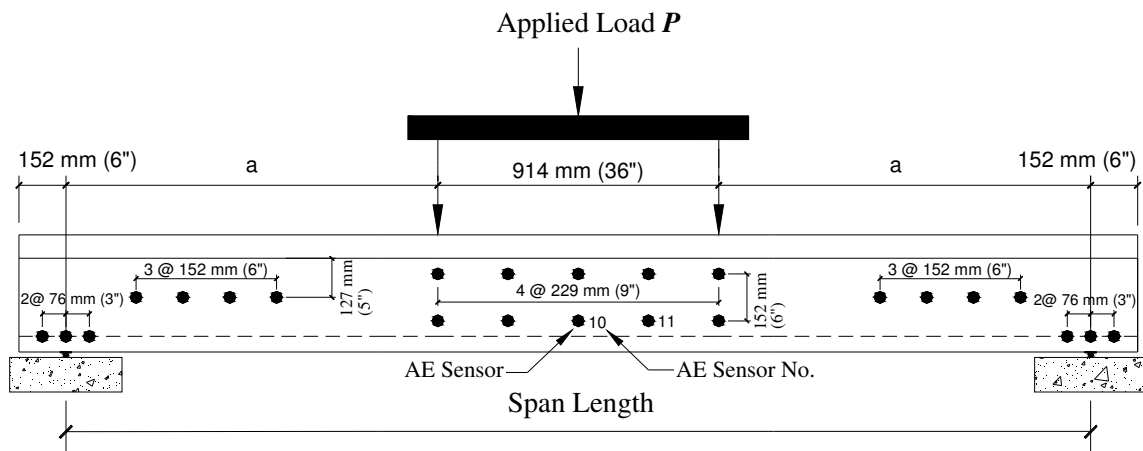


Figure 3-6: AE sensor locations

Prior to each test, the system was calibrated using the conventional pencil-lead break test (ASTM E976). A background check lasting about 4 minutes was performed prior to loading the test specimen. During each load cycle, the AE parameters recorded for each channel included signal energy, duration, amplitude, and signal strength. At the end of

the AE monitoring load cycles, the AE sensors were removed from the beam prior to loading to failure.

3.5 EXPERIMENTAL RESULTS AND DISCUSSION

3.5.1 DURATION/AMPLITUDE CROSSPLOT

The duration/amplitude crossplot features each AE sensor hit plotted as a single data point in a Cartesian coordinate system with the hit duration as the abscissa and amplitude as the ordinate. This crossplot demonstrates the relationship between duration and amplitude. It is an effective way to analyze the features of an entire AE signal for the purpose of distinguishing signal characteristics.

3.5.1.1 BEAM STD-M-B

Figure 3-7 shows a plot of applied load versus time superimposed with the deflection for beam STD-M-B. This specimen failed in a flexural manner; no strand end slip was detected during this test. For beam STD-M-B, Loadset 5-6 was only taken to the *calculated* cracking load, but the beam did not actually crack during this loadset. The first flexural cracking was observed during Cycle 7 at an applied load of 95.6 kN (21.5 kips), corresponding to a deflection of 5.6 mm (0.22 in.). The cracking moment, M_{cr} , was 10 percent greater than the calculated cracking moment, $M_{cr,calc}$. The maximum load reached for this specimen was 141.0 kN (31.7 kips), corresponding to a deflection of 102 mm (4.0 in.), when the beam lost its load-carrying capacity due to strand rupture. The maximum moment resisted by this beam, M_{max} , was 6 percent greater than $M_{n,calc}$. No web-shear cracking was observed in this specimen. The crack pattern corresponding to the maximum load for this beam is depicted in Figure 3-8.

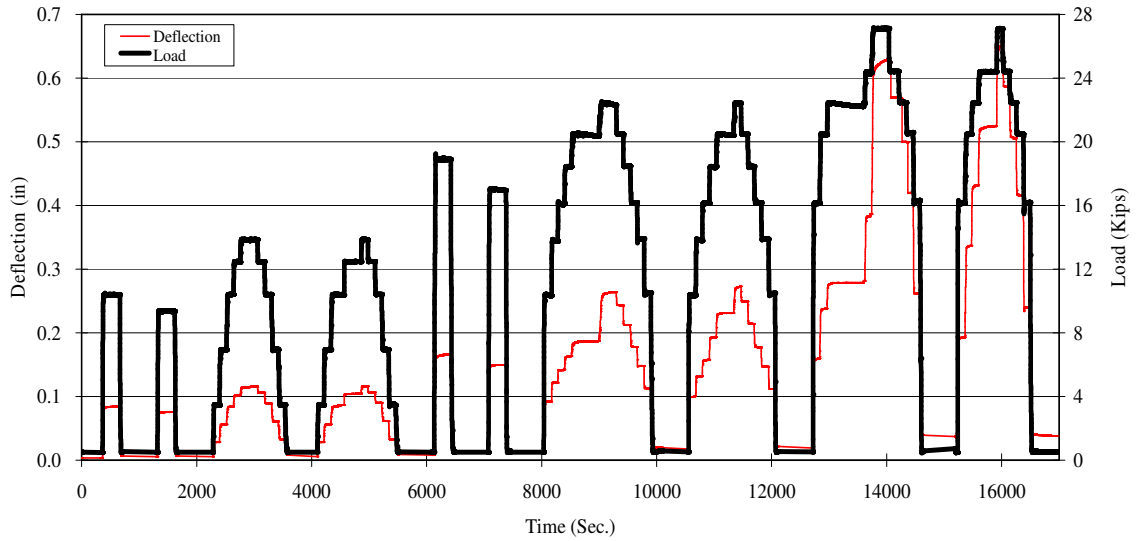


Figure 3-7: Load and deflection versus time for beam STD-M-B
(1 in. = 25.4 mm, 1 kip = 4.45 kN)

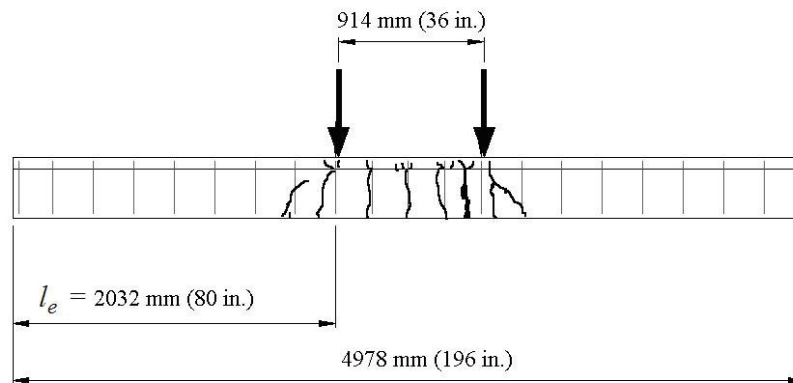


Figure 3-8: Crack pattern for STD-M-B at failure (Levy 2007)

Figure 3-9 shows the results of a crossplot of amplitude and duration of AE signals from channel 10 of beam STD-M-B during Loadset 3-4. This sensor, located in the flexure zone as shown in Figure 3-6, was the most active of all sensors. The left plot shows the AE data from load Cycle 3 and the right plot from load Cycle 4. The solid triangles indicate AE events from the loading stages of the cycle, whereas open circles indicate AE events from the unloading stages. Loadset 3-4 represents the applied load

computed to cause zero stress in the bottom fiber of the beam at the load points. This service-level design condition was reached with a load of 61.8 kN (13.9 kips) and a deflection of 2.8 mm (0.11 in.). There were no visible indications of cracking in beam STD-M-B during this loadset.

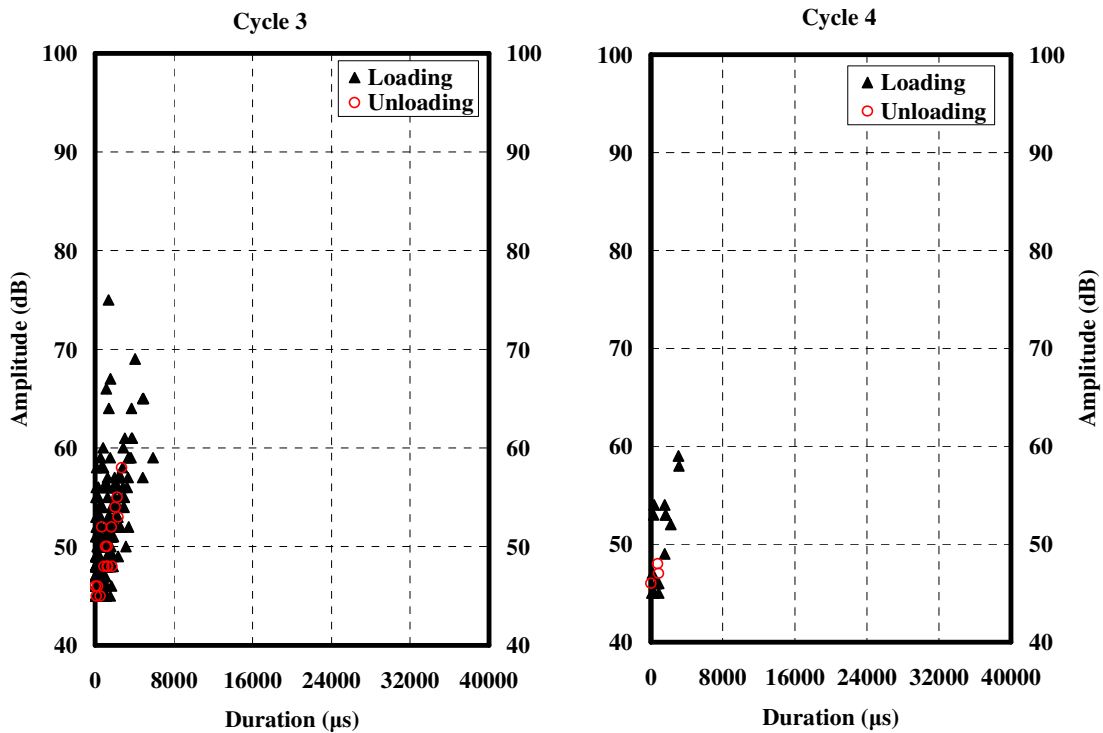


Figure 3-9: Crossplot of amplitude and duration of AE signals from Loadset 3-4 for beam STD-M-B

Figure 3-10 shows the results of a crossplot of amplitude and duration of AE signals from channel 10 of beam STD-M-B during Loadset 7-8. The left and right plots show the AE data from load Cycle 7 and 8, respectively. Again, the solid triangles indicate AE events from loading stage, whereas open circles indicate AE events from unloading stage. Comparing Figures 3-9 and 3-10, one can infer that the AE signals have a relatively short duration and low amplitude for both the loading and unloading stages at service-level loads prior to cracking, and the AE signals have a relatively long duration and high

amplitude for both the loading and unloading stages after the beam cracks. There appears to be fewer long-duration AE hits during the loading portion of the reload (8) cycle than during the loading portion of cycle 7 and similar AE duration during the unloading stage for the two cycles. This indicates that the mechanical rubbing of the interlocked faces (crack closing) generate low duration signals, while the initiation of cracks generate longer signal durations. Similar durations can also be produced from rubbing of crack surfaces as they close and grind in response to unloading.

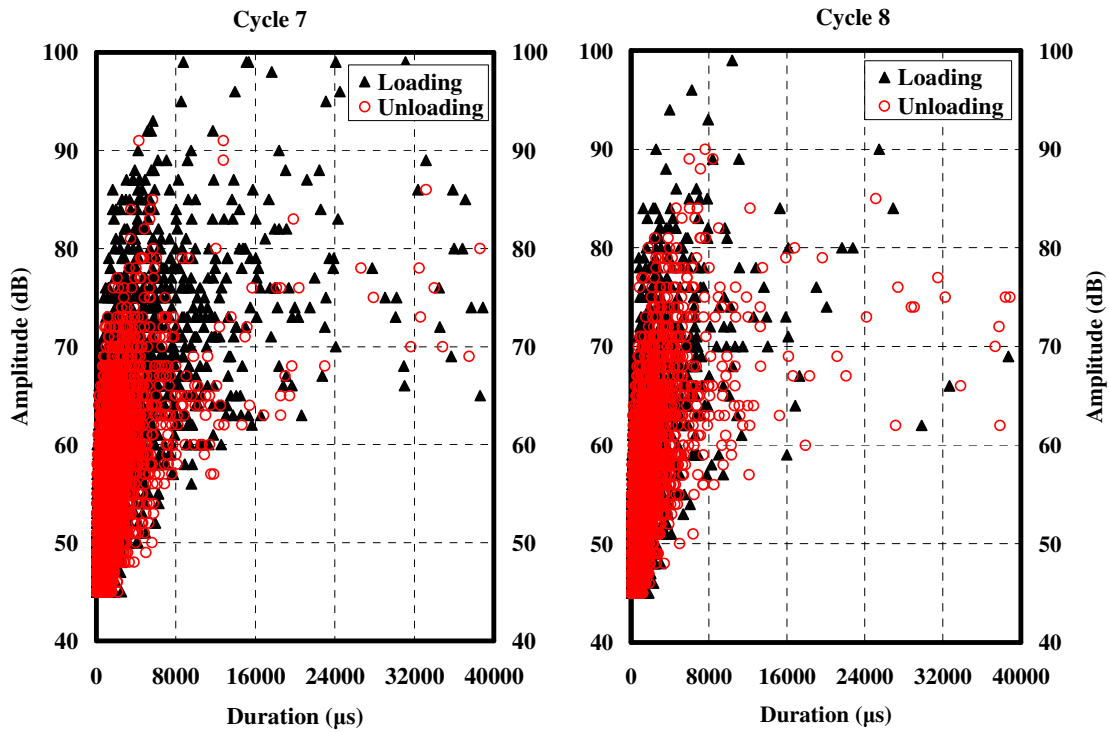


Figure 3-10: Crossplot of amplitude and duration of AE signals from Loadset 7-8 for beam STD-M-B

3.5.1.2 BEAM STD-M-C

Figure 3-11 shows a plot of applied load versus time superimposed with the deflection for beam STD-M-C. This specimen failed in a flexural manner with moderate strand slip.

The first flexural cracking was observed during Cycle 5 at the peak load of 142 kN (32.0

kips), corresponding to a deflection of 3.6 mm (0.14 in.). The cracking moment, M_{cr} , was 16 percent greater than the calculated cracking moment, $M_{cr,calc}$. The maximum load reached was 218 kN (49.1 kips), corresponding to a deflection of 86.4 mm (3.40 in.). The strand end slip experienced by the specimen at the peak load was 2.5 mm (0.10 in.). The maximum moment resisted by this beam, M_{max} , was 18 percent greater than $M_{n,calc}$. The beam lost its load-carrying capacity due to strand rupture. No web-shear cracking was observed in this specimen. The crack pattern corresponding to the maximum load for this beam is depicted in Figure 3-12.

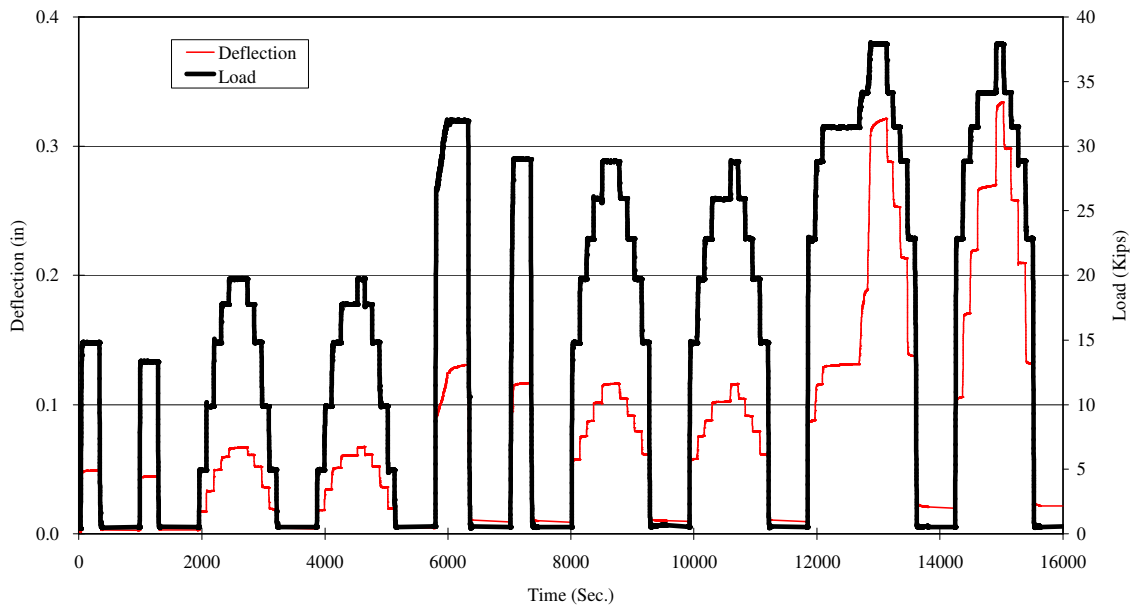


Figure 3-11: Load and deflection versus time for beam STD-M-C
(1 in. = 25.4 mm, 1 kip = 4.45 kN)

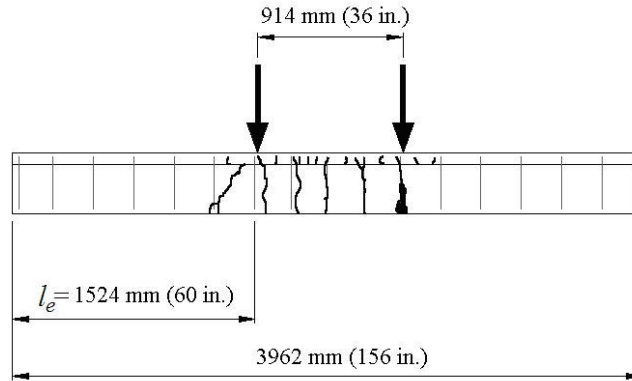


Figure 3-12: Crack pattern for STD-M-C at failure (Levy 2007)

Figure 3-13 and Figure 3-14 show crossplots of amplitude and duration of AE signals from channel 10 of beam STD-M-C during Loadset 3-4 and Loadset 5-6, respectively. Loadset 3-4 was the service-level load of 87.6 kN (19.7 kips), corresponding to a deflection of 1.8 mm (0.07 in.). The first flexural cracking was observed at the peak load of Loadset 5-6.

A definitive trend may be observed in Figures 3-13 and 3-14. In the early loading stages, as shown in Figure 3-13, the signals congregate in an area of low amplitude and low duration. However, as the loading approaches the cracking load, as shown in Figure 3-14, signals with large amplitude and longer duration begin to appear. These signals tend to indicate the beam condition near flexural cracking load levels.

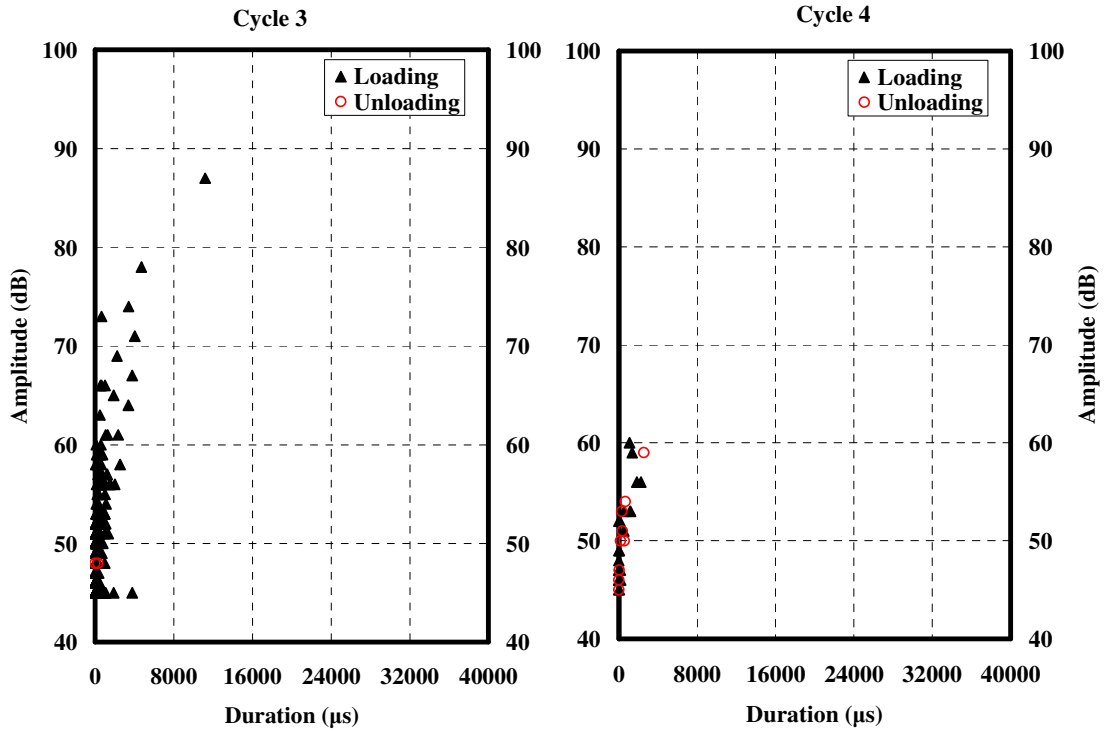


Figure 3-13: Crossplot of amplitude and duration of AE signals from Loadset 3-4 for beam STD-M-C

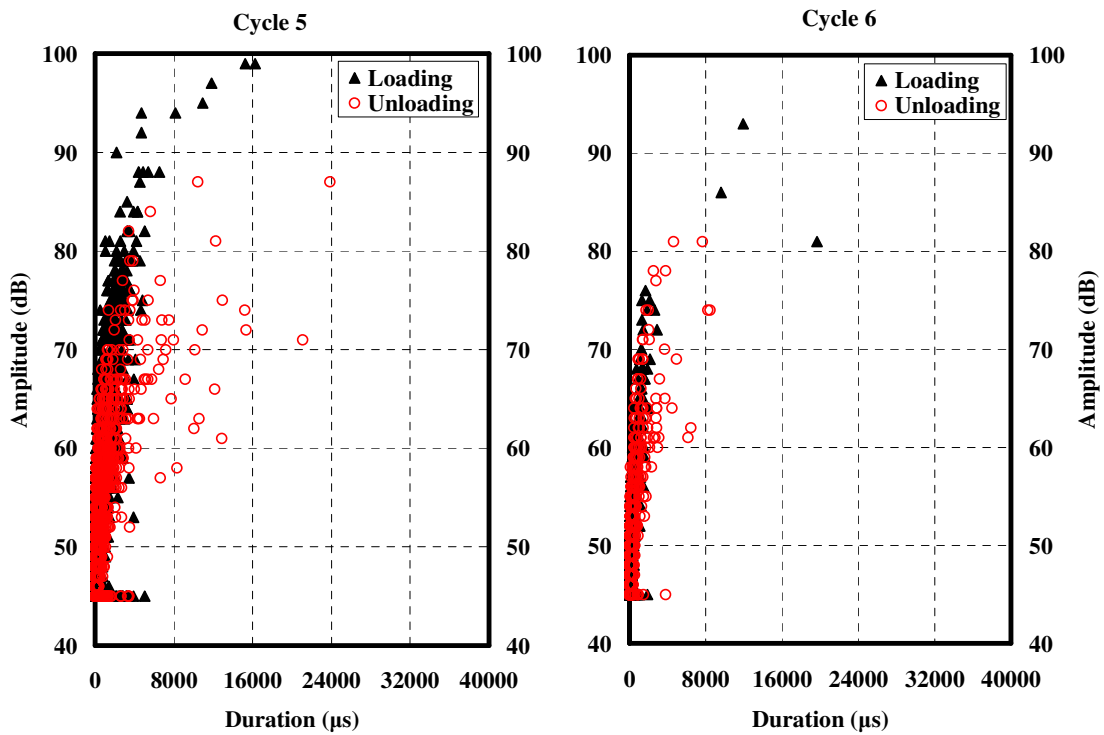


Figure 3-14: Crossplot of amplitude and duration of AE signals from Loadset 5-6 for beam STD-M-C

3.5.1.3 BEAM STD-M-D

Figure 3-15 shows a plot of applied load versus time superimposed with the deflection for beam STD-M-D. This specimen experienced a shear-tension failure during Cycle 5. The first crack was an inclined crack observed during Cycle 5 at an applied load of 218 kN (49.1 kips) and a midspan displacement of 1.8 mm (0.07 in.). The strands began to gradually slip with this cracking event, and the beam was only able to withstand a slightly higher load due to the gradual decrease in bond strength with increasing strand slip. The maximum load resisted was 223 kN (50.2 kips) at a displacement of 5.1 mm (0.20 in.). The strand end slip at the peak load was 2.5 mm (0.10 in.). Under increasing displacement, the resisted load gradually decreased until the concrete in the top flange crushed in compression at a displacement of approximately 14 mm (0.57 in.) and a strand slip of 11 mm (0.43 in.). Displacement application ceased at a final displacement of 58.4 mm (2.3 in.) at a load of 141 kN (31.7 kips). Figure 3-16 depicts the specimen at the end of the test. The crack pattern corresponding to the maximum load for this beam is depicted in Figure 3-17.

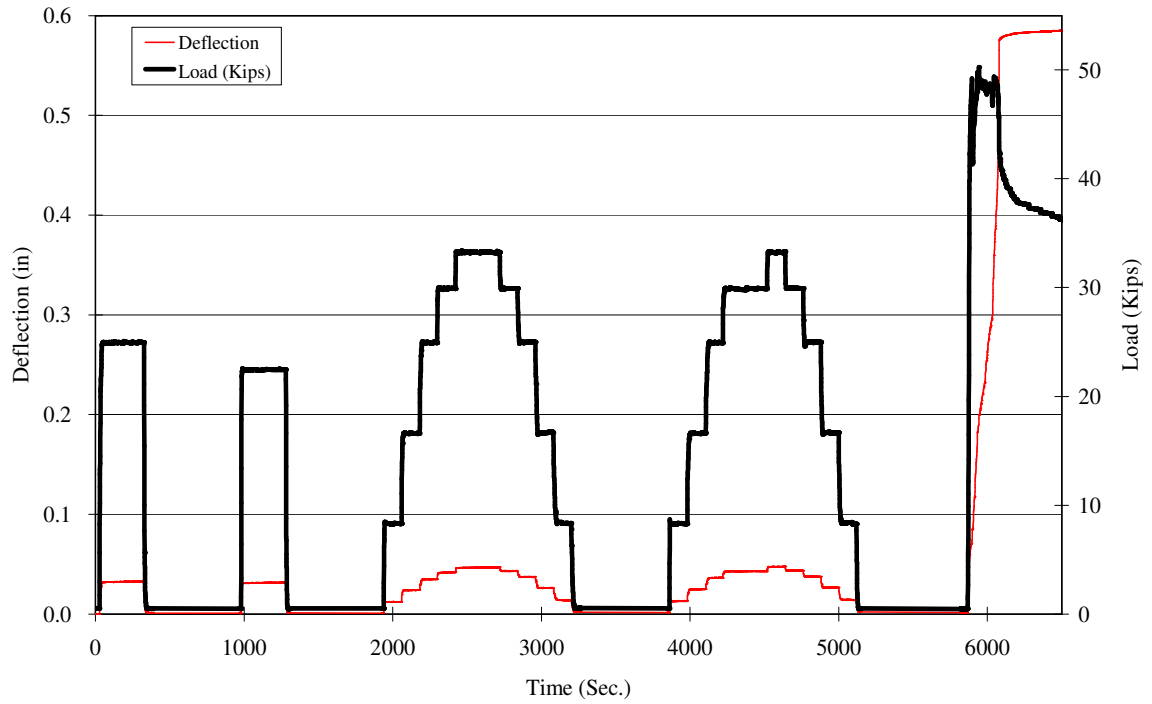


Figure 3-15: Load and deflection versus time for beam STD-M-D
(1 in. = 25.4 mm, 1 kip = 4.45 kN)



Figure 3-16: STD-M-D shear-tension failure (Levy 2007)

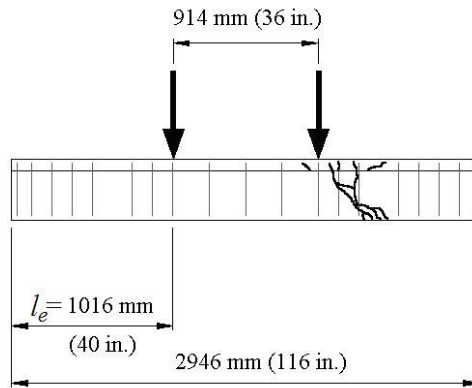


Figure 3-17: Crack pattern for STD-M-D at failure (Levy 2007)

Figure 3-18 and Figure 3-19 show the results of a crossplot of amplitude and duration of AE signals from channel 10 of beam STD-M-D during Loadset 3-4 and load Cycle 5, respectively. Loadset 3-4 was the service-level load of 148 kN (33.3kips), corresponding to a deflection of 1.3 mm (0.05 in.). The same trend as mentioned for the previous beams can be observed in Figures 3-18 and 3-19. The AE signals have a relatively short duration and low amplitude for both the loading and unloading stage before the beam cracked. After the beam cracked in Cycle 5, the AE signals exhibit a longer duration and higher amplitude.

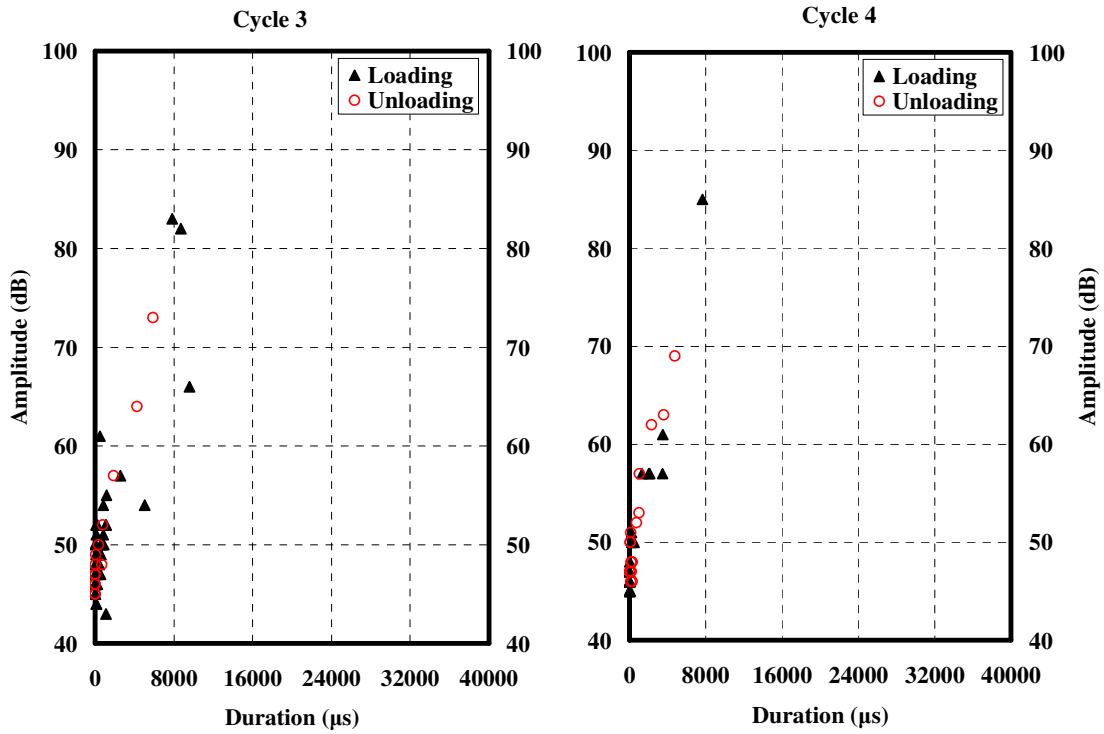


Figure 3-18: Crossplot of amplitude and duration of AE signals from Loadset 3-4 for beam STD-M-D

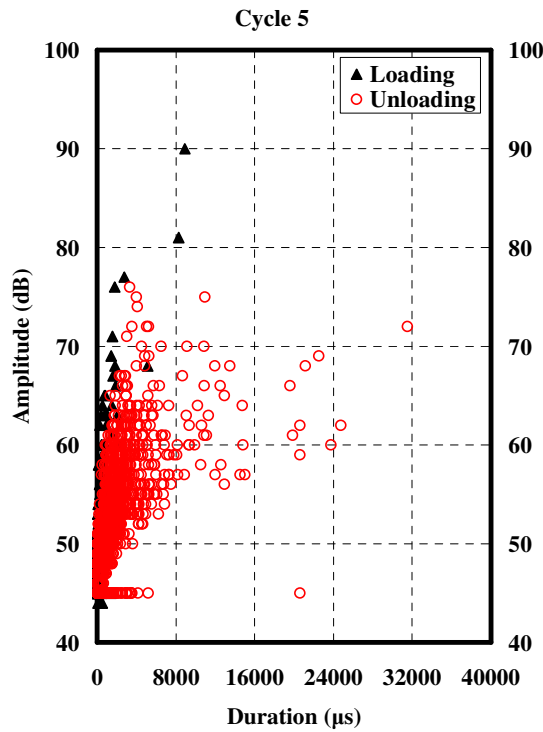


Figure 3-19: Crossplot of amplitude and duration of AE signals from Loadset 5 for beam STD-M-D

3.5.1.4 BEAM STD-M-A

Figure 3-20 shows a plot of applied load versus time superimposed with the deflection for beam STD-M-A. This specimen had been prematurely loaded beyond its cracking and yielding loads before the beginning of the AE testing. The specimen failed in a flexural manner after the end of the AE test. No strand end slip was measured during the test. The maximum load reached for this specimen was 91.2 kN (20.5 kips) at a maximum deflection of 188 mm (7.40 in.). The maximum moment resisted by this beam, M_{max} , was 11 percent greater than $M_{n,calc}$. The beam lost its load-carrying capacity due to strand rupture, and no web-shear cracking was observed in this specimen. The crack pattern corresponding to the maximum load for this beam is depicted in Figure 3-21.

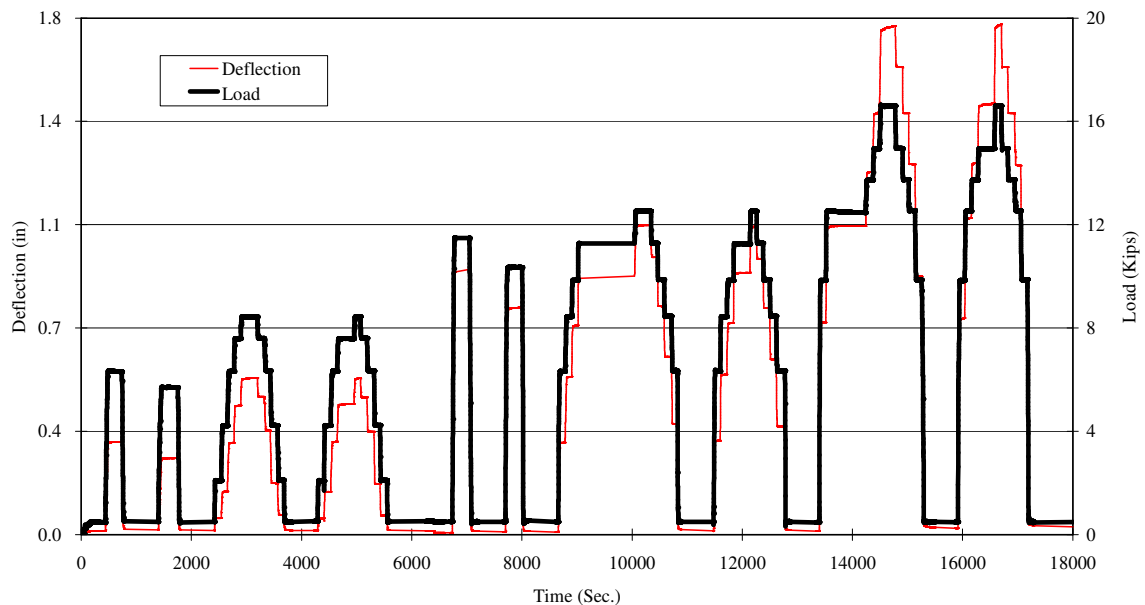


Figure 3-20: Load and deflection versus time for beam STD-M-A
(1 in. =25.4 mm, 1 kip = 4.45 kN)

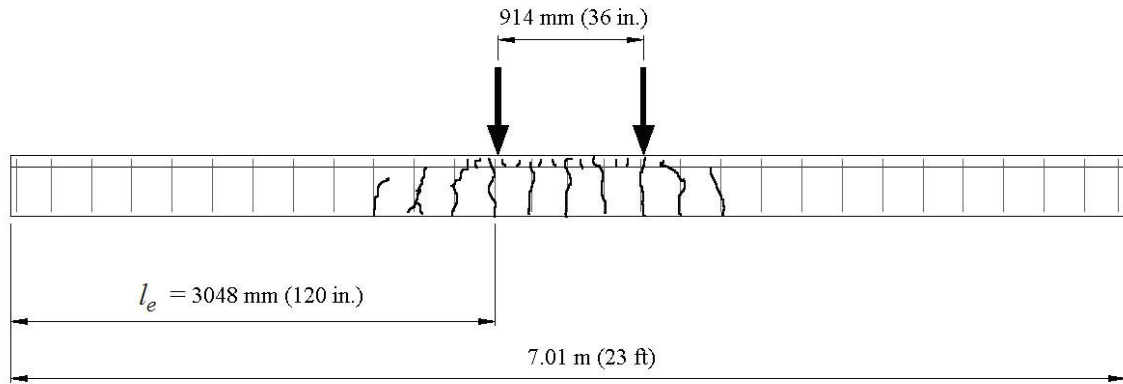


Figure 3-21: Crack pattern for STD-M-A at failure (Levy 2007)

Figure 3-22 shows crossplots of amplitude and duration of AE signals from channel 11 of beam STD-M-A during Loadset 3-4. This sensor was located in the flexure zone as shown in Figure 3-6, and the emissions are generated from the flexural cracks that were already present in the beam prior to beginning of the AE load cycles. The left and right plots show the AE data from the loading and unloading stages, respectively. The solid squares indicate AE events from Cycle 3; whereas open squares indicate AE events from the Cycle 4. Loadset 3-4 was the service-level load of 37.8 kN (8.50 kips), corresponding to a deflection of 5.3 mm (0.21 in.). Recall that the beam had been loaded well beyond this level prior to AE testing. From Figure 3-22, it can be seen that large-duration AE such as observed in the unloading stage is not present in the loading stage at load levels less than a previously applied peak. Thus an AE signal associated with crack growth and an AE signal associated with friction (or contact due to closing of cracks) may have similar amplitudes, but the friction/contact AE signal that is expected to be more prevalent during unloading could be characterized by a longer duration. This provides a possible way to recognize signals produced by friction/contact and to distinguish them from signals produced by crack growth.

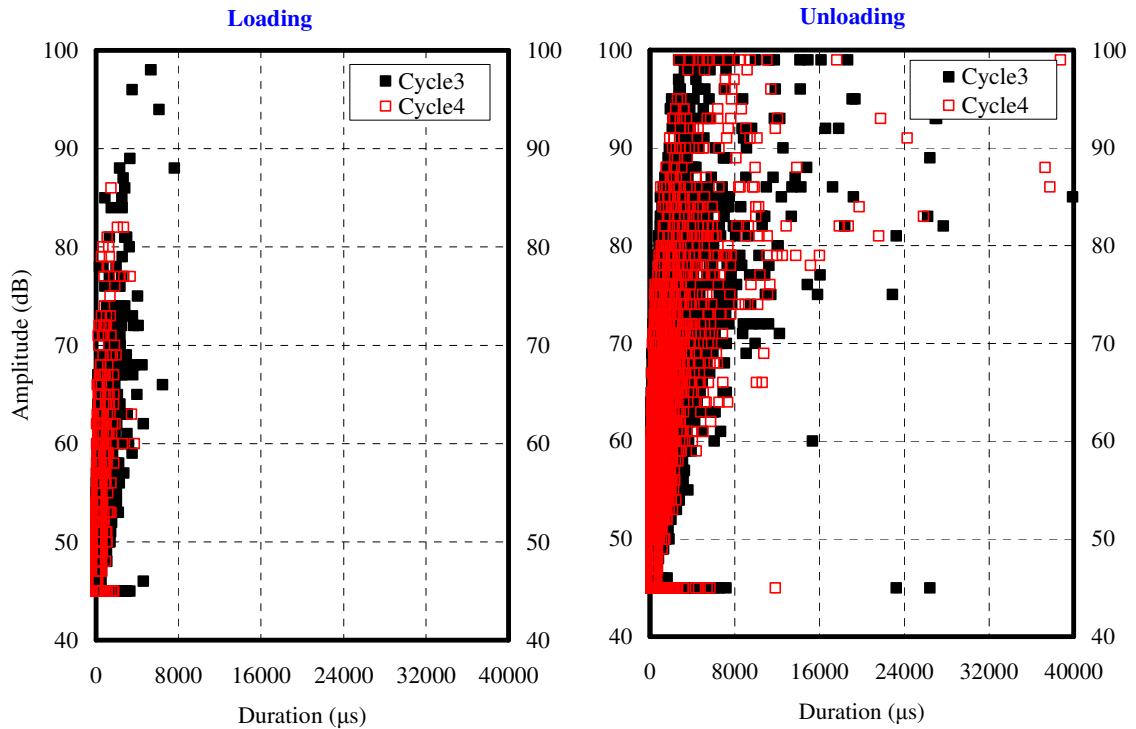


Figure 3-22: Crossplot of amplitude and duration of AE signals from Loadset 3-4 for beam STD-M-A

From the crossplots of AE signal amplitude versus duration, it was found that, in general, for all tests, the majority of the data in the duration-amplitude crossplot tend to fall into and above a diagonal band running from lower left to upper right. Along with this basic tendency, subtle variations exist. The initiation of early microcracks or local slips and the mechanical rubbing of the interlocked faces generate lower signal amplitude, while the initiation of the main tensile crack generates higher signal amplitude. AE signals can also be produced from rubbing of crack surfaces as they close and grind in response to unloading. Comparing Loadset 3-4 crossplots for the four beams, one can infer that the AE signals have a long duration during unloading from service-level loads for the previously damaged beam STD-M-A, and the AE signals have a

relatively short duration during unloading from service-level loads for three uncracked beams. The long duration may be attributed to the rubbing/contact of crack faces produced during the damage loading. Different AE sources can be distinguished by observing amplitude and duration data. Therefore, it seems that the structural integrity of prestressed concrete beams may be evaluated by comparing the AE parameters of hit duration and amplitude during cyclic flexural loading to different load levels.

3.5.2 RELATIONSHIP BETWEEN SIGNAL STRENGTH AND DAMAGE

Test results from beam STD-M-C are reported here because the data from this beam are typical for first-time loading of beams. Figure 3-23 shows a plot of signal strength versus time superimposed with the load cycles for beam STD-M-C. In order to assess the integrity of the beam, cumulative signal strength was also superimposed on the plot.

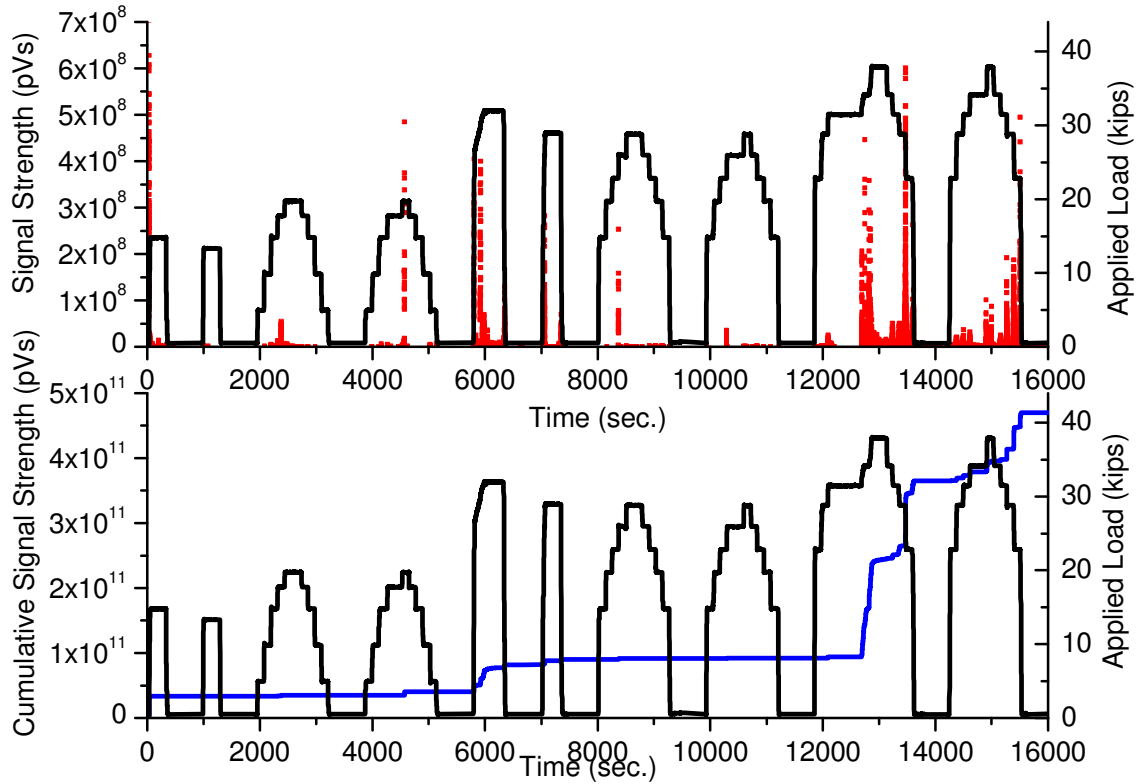


Figure 3-23: Load and signal strength versus time for beam STD-M-C

The plot demonstrates the AE signal strength to some degree corresponded to the various load conditions imposed on the beam. It offers visual clues to the beam condition. During the first load set, some AE activities attributed to the initial friction at the support were observed. It was typical for first-time loading of new beams. The AE activities diminished during the following loading cycles. During the service-load cycles, the beam was uncracked and the AE activities were limited. During Loadset 5-6, the first flexural cracking appeared, accompanied by a massive burst of AE. During the final load set, a sharp increase in AE activities accompanied a rapid increase in cracking and extension of cracks, particularly (1) during the application of loads higher than those previously applied and (2) during the unloading stages.

The AE testing showed indications of cracking in the prestressed concrete well before

the first observed crack. This indication of imminent cracking is easily seen in a plot of cumulative signal strength versus time for load cycle 5 of beam STD-M-C. As shown in Figure 3-24, a significant increase of AE, characterized as an abrupt increase in the cumulative AE signal strength versus time curve, began at time equal to 5,920 seconds at an applied load of 133 kN (30.0 kips).

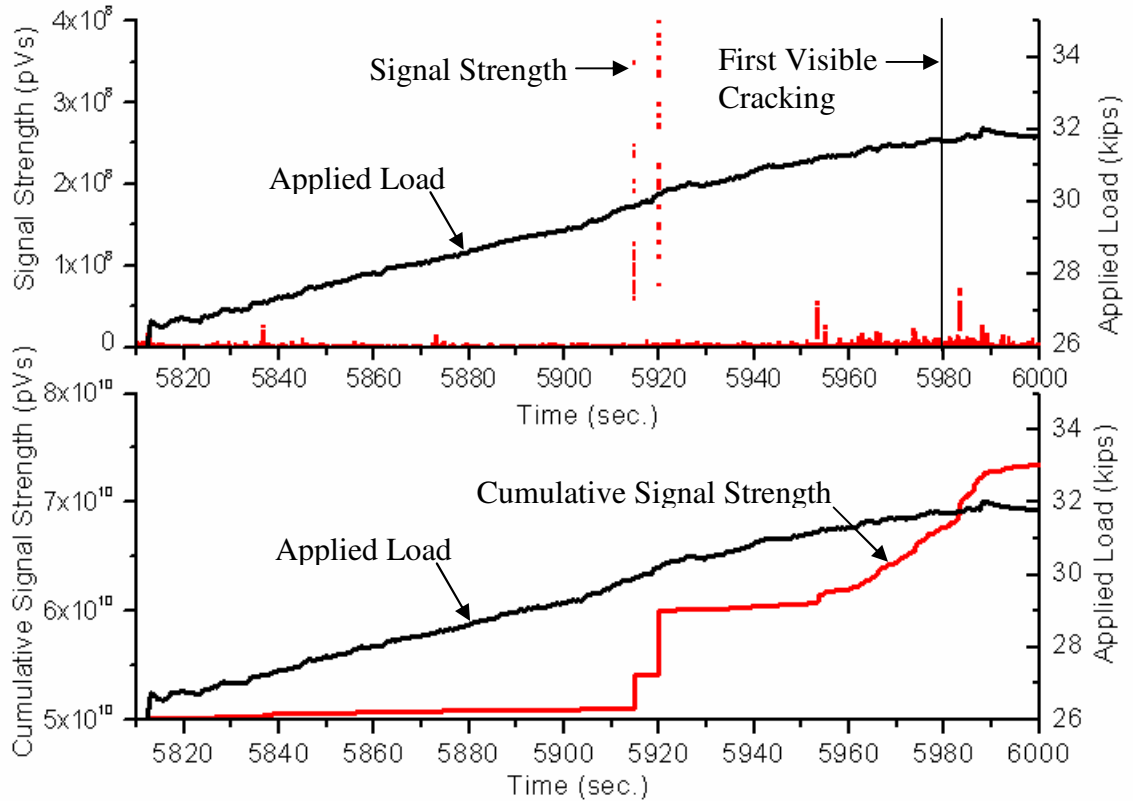


Figure 3-24: Load and signal strength versus time on Cycle 5 for beam STD-M-C

It is thought that this is the load at which internal microcracking began. Cracking was not visibly evident on the surface of the beam or on the load versus deflection plot until a time equal to 5,980 seconds, at an applied load of 141 kN (31.7 kips). Thus, the AE testing is capable of predicting imminent cracking in prestressed concrete structures slightly earlier than detection by visual inspection. A significant increase in AE signal

strength prior to visible cracking was also observed in beams STD-M-B and STD-M-D, which is shown in Figures 3-25 and 3-26. It is believed that the reason for these “jump” is a sharp increase in the amount of internal microcrack formation. The cracking becomes visible only when these microcracks coalesce and then the crack propagates to the surface.

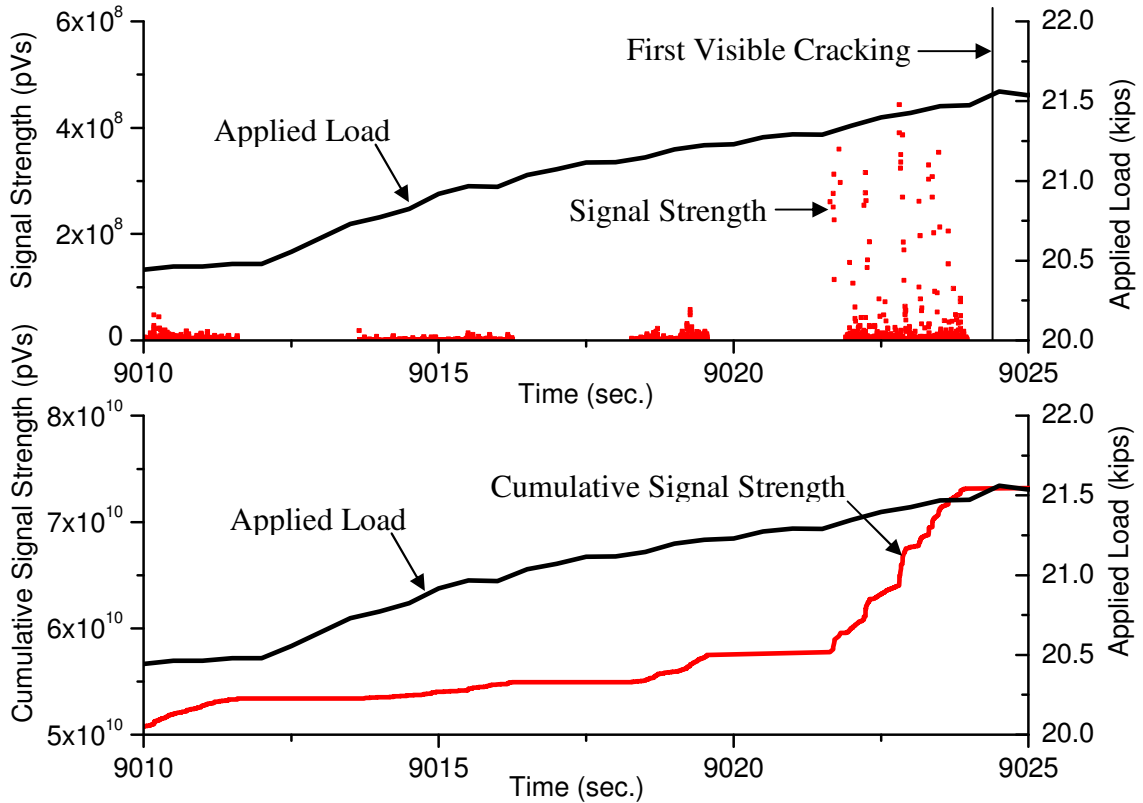


Figure 3-25: Load and signal strength versus time on Cycle 5 for beam STD-M-B

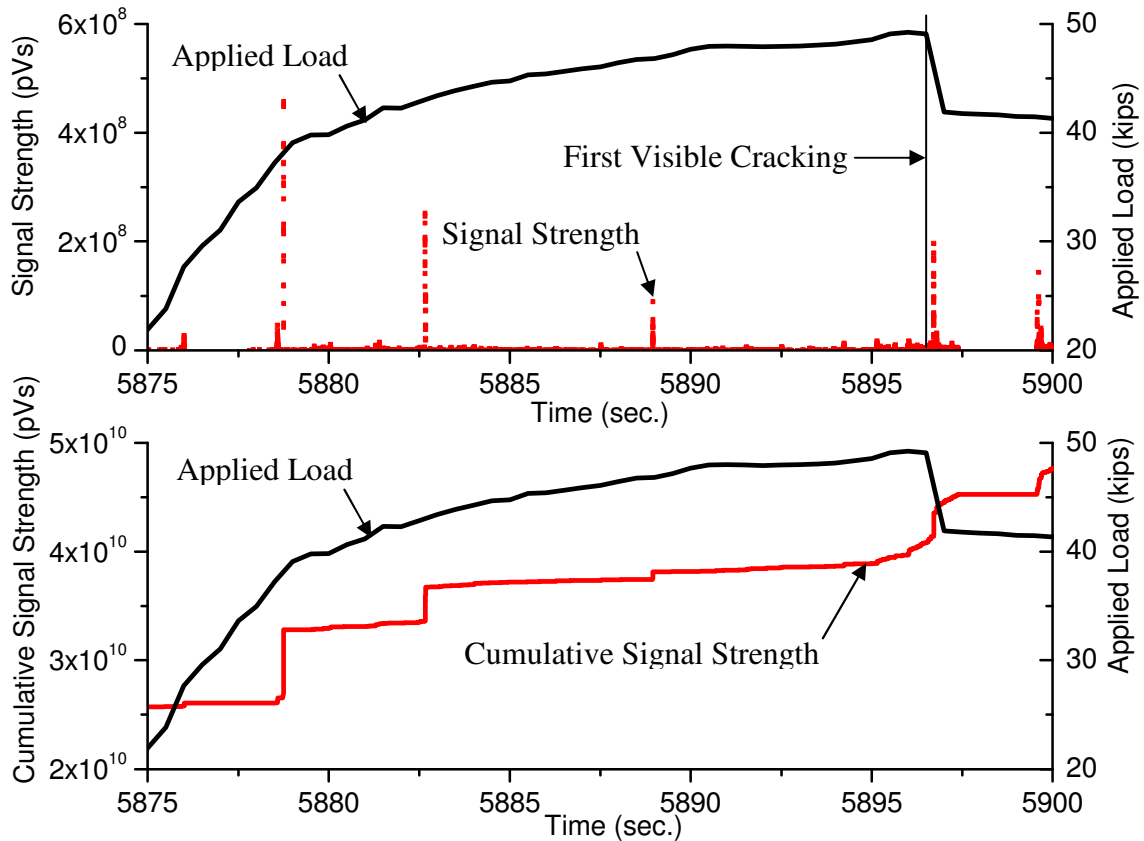


Figure 3-26: Load and signal strength versus time on Cycle 5 for beam STD-M-D

The test results indicate that the formation and propagation of cracks in a prestressed concrete beam are preceded by a significant increase in AE signal strength. The relationship between the AE behavior and tension zone distress make it possible to identify imminent cracking from the increased rate of AE signal strength. The data from these tests show that AE parameters, particularly signal strength, are associated with structurally significant damage.

3.6 CONCLUSIONS

In this chapter, the results of experiments on four prestressed concrete beams are described. The appearance and growth of cracks in concrete structures are compared with the occurrence of AE activities. The AE parameter analysis exhibited a favorable

correlation with the damage condition of the prestressed concrete beams. As a result, the AE monitoring technique exhibits promise as a method for estimating the integrity of prestressed concrete structures.

Several conclusions resulted from this experimental investigation:

1. The initiation of early microcracks or local slips and the mechanical rubbing of interlocked faces result in lower AE signal amplitude, while the initiation of primary flexural cracks produces higher signal amplitudes.
2. For a previously damaged beam, long signal duration is observed during unloading—even during unloading from lower (service-level) loads. This phenomenon is attributed to the closing and rubbing of interlocked faces produced during the previous loading.
3. The AE parameters of amplitude and duration are correlated with cracking processes. Different AE source damage processes can be distinguished by comparing the amplitude and duration data.
4. The formation and propagation of visible cracks in prestressed concrete beams is preceded by a significant increase in AE signal strength. Indication of imminent cracking is best indicated by a rapid increase in cumulative signal strength versus time.

Eventually, with further research effort, definite quantitative relationships of AE parameters to actual condition of prestressed beams may be possible.

CHAPTER 4
DAMAGE ASSESSMENT CRITERIA FOR AE TESTING OF PRESTRESSED
CONCRETE BEAMS

4.1 INTRODUCTION

Because prestressed concrete flexural members are critical to the integrity of a large share of existing buildings and bridges, the need has arisen for effective nondestructive testing (NDT) techniques to evaluate the integrity of prestressed beams. The acoustic emission (AE) technique has been found to be one of the most informative NDT methods for determining material behavior and structural performance (Ohtsu 1989; Pollock 1995).

The AE NDT technique is based on the detection of high-frequency elastic waves emitted by the structure and conversion of these waves to electrical signals. The application of load to a beam that exceeds the local strength of the beam may result in the growth of a crack defect. The release of stored energy that accompanies this growth creates a stress wave that propagates within the beam (ASNT 1996). The stress waves can be detected on the beam surface using transducers that convert mechanical wave energy into an electrical voltage. The voltage is then amplified and analyzed with respect to time and frequency using various numerical methods. By evaluating AE parameters from several transducers, an assessment of the integrity of the beam can be made.

AE studies of concrete materials have been numerous and a considerable number of articles have been published on this topic. In the case of prestressed concrete, however, a basic understanding is still limited.

Due to microcracks and its nonhomogeneous nature, concrete attenuates an AE signal more quickly than steel does. The high attenuation in concrete has hindered progress in the development of AE testing for concrete. A *prestressed* concrete beam, on the other hand, remains uncracked until it reaches a high percentage of its ultimate load. The precompression reduces the growth of initial cracks relative to nonprestressed concrete; therefore, attenuation of the AE signal in a prestressed concrete beam is less than in a comparable reinforced concrete beam. Effective evaluation by AE methods is expected to be more readily achievable in prestressed concrete than in reinforced concrete.

The main challenge for structural integrity evaluation using AE techniques is to accurately interpret the AE data recorded. Several evaluation criteria have been proposed. To assess the damage levels of reinforced concrete beams, the *NDIS-2421* quantitative assessment criterion was adopted by the Japanese Society for Nondestructive Inspections (JSNDI) (Ohtsu et al. 2002). A *relaxation ratio* was used by Colombo et al. to predict the degree of damage of reinforced concrete beams (Colombo et al. 2005). Ridge and Ziehl proposed an evaluation criterion based on the *ratio of peak cumulative signal strength* (peak CSS) (Ridge and Ziehl 2006).

In the study described in this chapter, acoustic emissions were monitored during cyclic tests of four prestressed concrete T-beams—including one beam that was damaged prior to testing. The effectiveness of extending three previously proposed AE evaluation criteria to prestressed concrete members was evaluated. In addition, a new evaluation

method based on ratios of signal strength moments was introduced and proved effective for indicating the integrity of the prestressed concrete beams.

4.2 RESEARCH SIGNIFICANCE

AE data can provide valuable insight into the behavior and damage mechanisms of passively reinforced, as well as prestressed, concrete structures (Ohtsu 1989). While AE evaluation procedures and evaluation criteria exist for concrete structures (Ohtsu et al. 2002; Colombo et al. 2005; Ridge and Ziehl 2006), standardized AE evaluation criteria for prestressed concrete beams are not available. In order to develop and evaluate a practical evaluation method to determine the integrity of a prestressed concrete beam, three previously proposed AE criteria for integrity evaluation of reinforced concrete members were evaluated with respect to the behavior of prestressed concrete specimens. A new evaluation method based on the signal strength moment was proposed and proved effective for indicating the integrity of the prestressed concrete beams.

4.3 AE EVALUATION CRITERIA

4.3.1 NDIS-2421 CRITERION

The NDIS-2421 quantitative assessment criterion was proposed by Ohtsu et al. (2002). To apply this method, the structure to be evaluated is subjected to load cycles during which AE activities are measured. The damage level of the structure is classified based on two parameters: the *load ratio* and the *calm ratio*, which are defined in the NDIS-2421 as follows:

$$\text{Load ratio} = \frac{\text{Load at the onset of AE activity in the subsequent loading/}}{\text{The previous load;}} \quad (\text{Eq. 4.1})$$

Calm ratio = The number of cumulative AE activities during the unloading process/

Total AE activities during the last loading cycle up to the maximum (Eq. 4.2)

Specific descriptions of how the load ratio and calm ratio were computed for the AE data in this study will be provided later in this chapter.

The criterion used to qualify the damage according to the combination of these two ratios is graphically depicted in Figure 4-1. Ohtsu et al. proposed the classification boundaries (dashed lines in Figure 4-1) of 0.05 for the calm ratio (horizontal boundary) and 0.9 for the load ratio (vertical boundary). Thus, if a structure's AE response for a particular load level is characterized by a calm ratio greater than 0.05 and a load ratio less than 0.9, the structure is classified as heavily damaged.

The AE data from the most active channel are used for calculation. This recommendation resulted from laboratory tests of nonprestressed, reinforced concrete beams in which crack mouth opening displacement (CMOD) was used to define the level of damage in each test specimen. A CMOD of 0.1 mm (0.004 in.) was selected as the transition value from "Minor" to "Intermediate" damage. A CMOD larger than 0.5 mm (0.02 in.) was associated with the "Heavy" damage label.

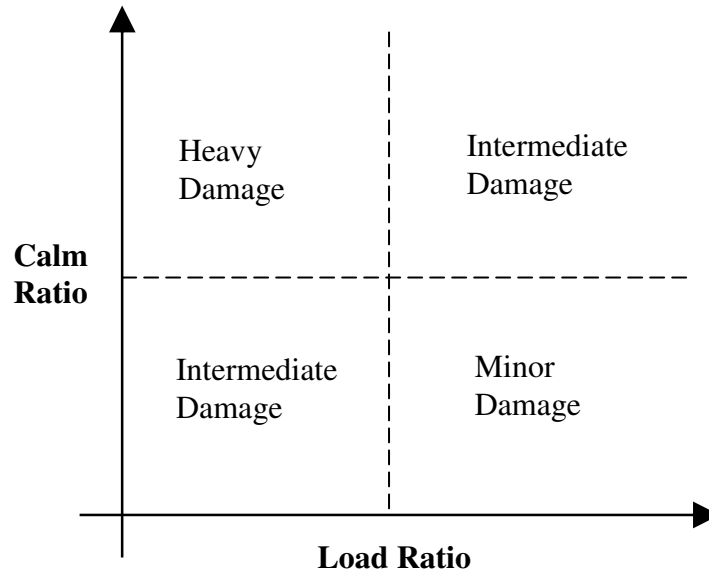


Figure 4-1: Classification of damage by two ratios recommended by NDIS-2421 (from Ohtsu 2002)

4.3.2 RELAXATION RATIO

Colombo et al. (2005) used a relaxation ratio to predict the degree of damage of reinforced concrete beams. This method is focused on the AE activity recorded during the unloading phase of a load cycle. During testing, AE signals were recorded using different types and model of AE sensors, resonant (R6I) and broadband (WD and UT-1000). The relaxation ratio is computed in terms of average energy per AE sensor “hit” and defined as:

$$\text{Relaxation ratio} = \frac{\text{Average energy during unloading}}{\text{Average energy during loading phase}} \quad (\text{Eq. 4.3})$$

where the average energy is calculated as the cumulative AE energy recorded during each phase divided by the number of recorded sensor hits.

In one set of tests, the value of the relaxation ratio became greater than one when approximately 45% of the ultimate bending load was reached. So the author concluded that a value of relaxation ratio greater than one is indicative of structural damage.

4.3.3 PEAK CSS RATIO

Ridge and Ziehl (2006) proposed an evaluation criterion based on the ratio of peak cumulative signal strength (peak CSS) recorded during a sustained load period (load hold) to the peak CSS recorded during a previous initial load hold of similar magnitude. This evaluation criterion relies on AE data recorded only during load holds rather than during periods of increasing (loading) or decreasing (unloading) load, which is particularly useful in the field of AE testing, where the genuine emission can be obscured by background noise.

Several loadsets of increasing magnitude were applied and the ratio of peak cumulative signal strength (CSS) recorded during the reload hold to the peak CSS recorded during the initial load hold was calculated for each loadset. The results were used to determine a suitable acceptance criterion. This ratio was expressed as a percentage defined by the following:

$$\text{Peak CSS Ratio} = (\text{Peak CSS at the end of reload hold period} / \text{Peak CSS at the end of initial load hold period}) * 100\% \quad (\text{Eq. 4. 4})$$

To ensure that the second load-hold (reload) level does not surpass the first load-hold level in a loadset, which could induce new damage in the specimen, the peak load held during the reload cycle is slightly less than the peak load of the initial cycle.

The AE data from four sensors are used for calculation. Based on the test results of six reinforced concrete beams—two unstrengthened beams, two beams strengthened with

pre-cured carbon fiber-reinforced polymer (CFRP), and two beams strengthened with unidirectional CFRP, Ridge and Ziehl recommended that the beam be considered damaged if the Peak CSS Ratio is more than 40 percent.

4.3.4 SIGNAL STRENGTH MOMENT RATIO

Hamstad et al. (1992) introduced the concept of using a time-weighted approach for analyzing the AE activity during load holds in composite materials. He developed the “cumulative event rate moment”, which is defined as the summation over the hold period of the quantities produced by multiplying the number of first (per event) hits (i.e. the number of events detected) at a given sensor during a fixed time interval by the time elapsed from the beginning of the load hold, to quantify AE behavior during the hold. Thus, the cumulative moment (M) can be defined as:

$$M = \sum_{i=1}^n t_i N_i \quad (\text{Eq. 4.5})$$

where t_i is the time from the beginning of the hold to the i th time interval and N_i is the number of events occurring in interval i . For a 4-minute hold and 1-second intervals, $n = 240$.

To extend this concept to damage assessment in prestressed concrete beams, a new method was developed to calculate the “Signal Strength Moment (SSM)”, which is the summation over the hold period of the quantities produced by multiplying the signal strength associated with each hit by the time elapsed from the beginning of the load hold.

The signal strength moment for a load hold is defined as:

$$SSM = \sum_i^n t_i S_i \quad (\text{Eq. 4. 6})$$

Where:

n — the total number of hits occurring during the load hold,

t_i — the time from the beginning of the load hold to the i th hit, and

S_i — the signal strength occurring in the i th hit.

Signal strength is the measured area of the rectified AE signal with units proportional to volt-seconds (ASTM E 1316).

In the SSM, AE activity occurring later in a load hold is given more weight than AE activity occurring immediately after attainment of the held load. This is based on the assumption that sustained (or increasing) emission over time is indicative of a beam that is experiencing continued damage under the sustained load. A constant or accelerating rate of AE activity occurring during a hold would characterize a beam in which internal load-resistance mechanisms are shifting due to ongoing damage. Thus, a greater SSM value indicates a beam that is experiencing continued internal distress at a certain load level.

In order to make the method less dependent on the characteristics of specific sensors, an evaluation criterion based on the *ratio* of SSM recorded during a second (reload) load hold to the SSM recorded during a first load hold was evaluated. To be consistent, the same time length for the two load holds must be used. In this study, a hold period of 240 seconds was used for evaluation. If the actual hold duration exceeded this limit, only the first 240 seconds of AE data were used. This ratio can be expressed as a percentage:

$$\text{SSM Ratio} = (\text{SSM of the second hold period} / \text{SSM of the first hold period}) \times 100\% \quad (\text{Eq. 4.7})$$

The evaluation focused on SSM during load holds for three reasons: a) signal strength is a function of both the amplitude and duration of signal, which makes it a better measure of total AE than other parameters; b) using AE data from a load hold minimizes the influence of loading/unloading rate; c) the hypothesis that having a larger proportion of AE activity occurring later after load application is a sign of increased material damage.

4.4 EXPERIMENTAL INVESTIGATION

4.4.1 SPECIMEN DESCRIPTION

Four 0.38-m (15-in.) deep pretensioned concrete T-beams that were cast and prestressed in the Auburn University Structural Research Laboratory were instrumented with sensors to monitor their acoustic emissions under various levels of loading. Geometry and properties of the test specimens are summarized in Table 4-1 and Figure 4-2. The four specimens, denoted STD-M-A, STD-M-B, STD-M-C, and STD-M-D, had the same cross section, and differed primarily in span length and the fact that STD-M-A was subjected to a damaging applied load prior to testing. The other three beams experienced no significant applied loading prior to testing. All four specimens were cast from the same batch of concrete; the mixture was representative of concrete regularly used in Alabama precast, prestressed bridge girders.

Figure 4-2 shows the cross-sectional details for the four T-beams. The specimens were prestressed with two seven-wire, low-relaxation, Grade 270, 1/2-in. “special” diameter strands. Each specimen had the minimum transverse reinforcement required to resist the anticipated flexural failure load for each specimen. Detailed information about the design, fabrication, and testing of these specimens has been reported by Levy (2007).

Table 4-1: Test specimen properties

Beam	Span m (in.)	$\frac{a}{d_p}$	f'_c MPa (psi)	P_s kN (kips)	P_n kN (kips)	$M_{n,calc}$ kN-m (kip-ft)	M_{max} kN-m (kip-ft)	Failure Type
STD-M-A	7.01 (276)	9.23	43.6 (6320)	37.7 (8.5)	74.0 (16.6)	130 (96.0)	145 (107)	Flexure
STD-M-B	4.98 (196)	6.15		61.7 (13.9)	121 (27.1)		138 (102)	Flexure
STD-M-C	3.96 (156)	4.62		87.8 (19.7)	169 (38.0)		154 (113)	Flexure
STD-M-D	2.95 (116)	3.08		148 (33.3)	272 (61.2)		141 (104)	Shear- tension

Note:

f'_c = 28-day compressive strength of concrete

d_p = Effective depth

a = Shear span

P_s = Service-level design load calculated prior to flexural load testing

P_n = Ultimate load predicted based on nominal flexural capacity

$M_{n,calc}$ = Calculated nominal moment capacity

M_{max} = Ultimate moment resisted during flexural test

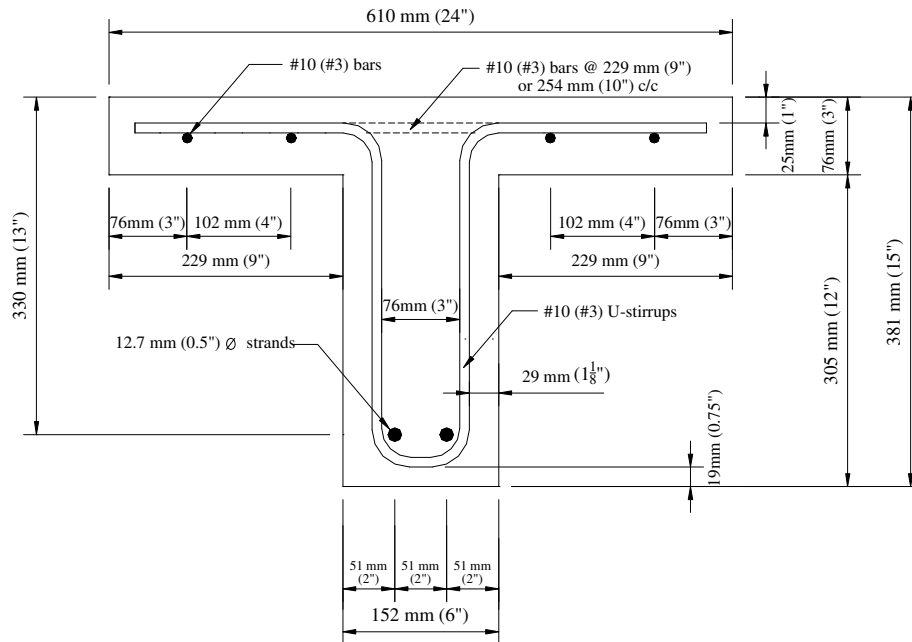


Figure 4-2: T-Beam cross section detail

The details of the load testing geometry are shown in Figure 4-3. Four beams were tested in flexure under symmetric four-point loading. Loading was applied by

displacement of a hydraulic actuator. A 0.9-m (3-ft) length of uniform bending moment was induced at midspan by means of a spreader beam, which transferred the load to steel plates attached to the beam with a gypsum plaster.

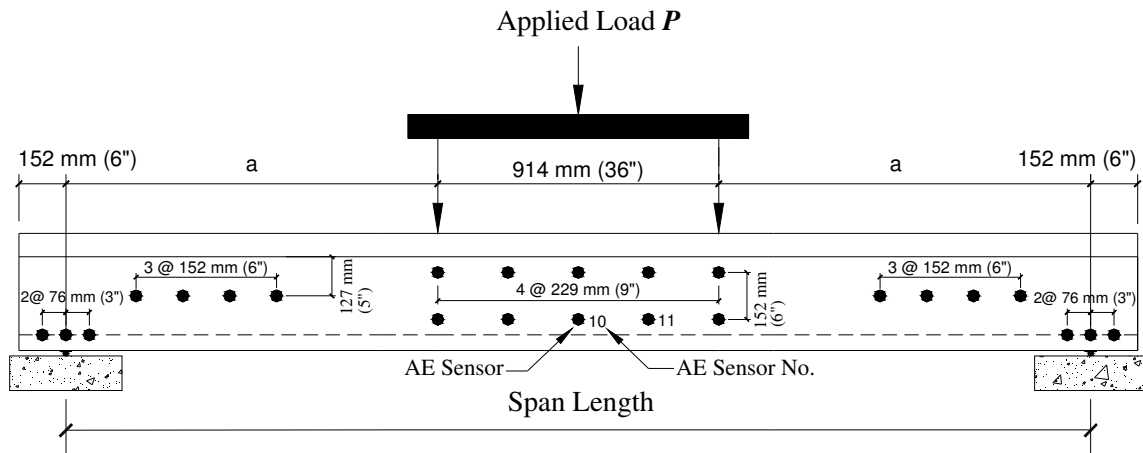


Figure 4-3: Load test setup and sensor location

4.4.2 AE TESTING PROCEDURE

A 24-channel SAMOS[®] manufactured by Physical Acoustic Corporation (PAC) was used to perform AE monitoring during the load testing of the prestressed concrete beams. Because a large number of sensors were used, the data gathered provided an opportunity for a close look at local variations in the AE generated during these tests. The AE testing setup is shown in Figures 4-3 and 4-4. A simplified outline of the AE testing procedure follows.

First, before load testing began, the beam surface where the sensors were to be mounted was cleaned and smoothed with sandpaper. Twenty-four PAC R6I-AST 50-kHz integral resonant AE sensors were mounted on three zones of the beam: ten sensors in the flexure zone in the region of maximum moment; three sensors in each anchorage zone (along the transfer length) to monitor strand slippage, and four sensors in each shear span.

The cables connecting the sensors to the acquisition system were secured with tape so that the cables would not pull on the sensors or move against the beam. All AE signals were monitored with a 24-channel "Sensor-based Acoustic Multi-channel Operation Systems" (SAMOS). SAMOS multi-channel systems were powered by AE-Win Software, which can record AE parameters as well as AE wave data. Specific setup information, including the hardware setup, graph setup, acquisition setup, filters, and location setup, is summarized in Table 4-2.

A standard calibration test was performed prior to the beam test (Pollock 1995). Instead of the standard Pentel[®] 0.3-mm 2H lead, a Pentel[®] 0.5-mm 2H lead was used for calibration because it gives a bigger pulse that is more suitable for prestressed concrete monitoring (Yepez 1999). A background check lasting about 4 minutes was performed prior to loading each test specimen. The specimen remained undisturbed during this time. This pre-test procedure was used to check the effectiveness of the mounted sensors and to reveal any weak channels that need corrections before data acquisition. During the beam test, AE data were displayed in real time on a monitor with various screen options. These displays gave a visual indication of the progression of the beam to failure. At the same time, the data were stored on hard disk for post-test analysis. AE sensors were removed prior to application of the expected failure load. The recorded data were then converted to ASCII (American Standard Code for Information Interchange) format. The ASCII files were imported into the commercial statistical analysis software Origin[®] and were analyzed using procedures written for this project within this software.

Table 4-2: AE test parameters

Parameter	Value
Hit Definition Time (HDT)	200 μ sec
Peak Definition Time (PDT)	50 μ sec
Hit Lockout Time (HLT)	300 μ sec
Threshold	45 dB
Preamplifier (R6I)	40 dB
Bandpass Data Acquisition Filter	100-400 kHz

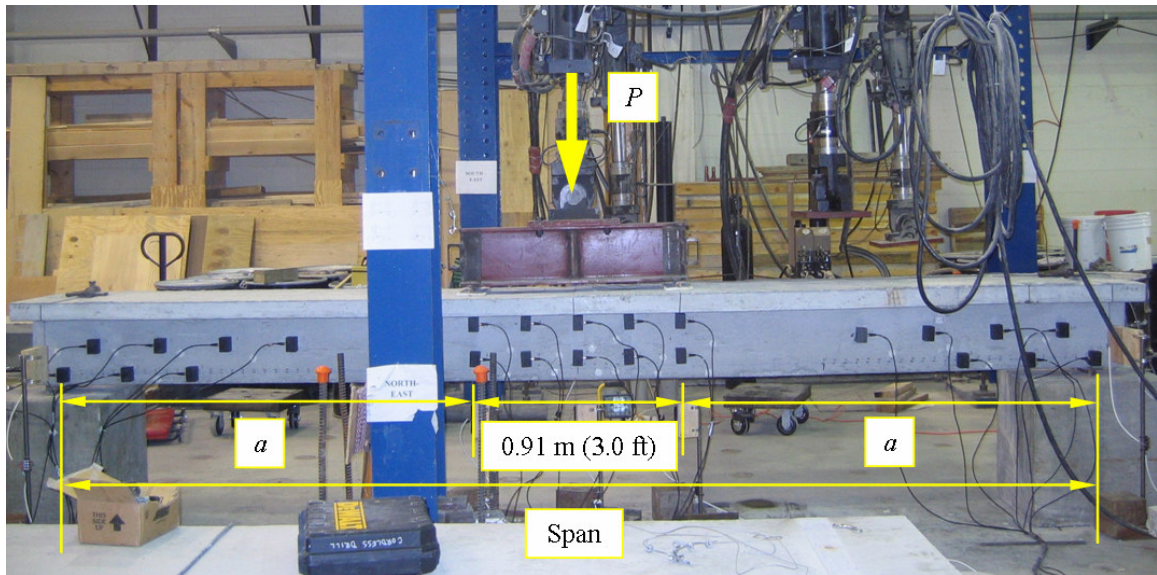


Figure 4-4: Photo of an AE testing setup

4.4.3 ATTENUATION

As the acoustic wave travels through the structure, its amplitude decreases. This phenomenon is called attenuation, and is illustrated in Figure 4-5.

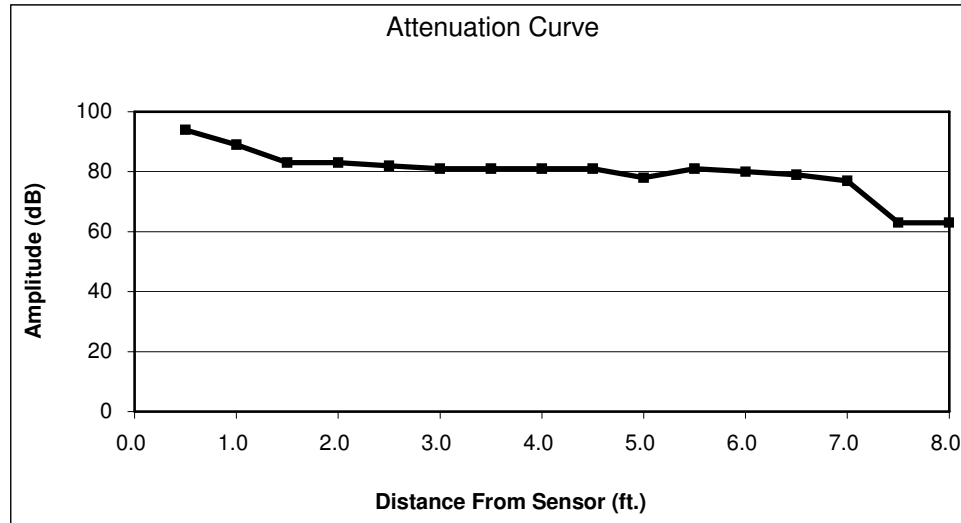


Figure 4-5: Attenuation curve for prestressed concrete beam

Due to its heterogeneity and microcracks, concrete attenuates the AE more quickly than steel. Typical amplitude reduction in plain concrete specimens is approximately 100 dB/m (Uomoto 1987). AE attenuation in the prestressed beams was assessed by breaking a 0.5-mm Pentel[®] 2H pencil lead on the beam web at 0.15-m (6-in.) intervals from an R6I sensor for a total 2.44 m (8 ft). Amplitudes of the resulting sensor hits were then plotted to generate the attenuation curve for prestressed concrete beam STD-M-C as shown in Figure 4-5. It can be seen that there was a loss of 30 dB over the 2.44 m (8 ft). Therefore, amplitude reduction in these prestressed concrete specimens was approximately 12 dB/m.

In contrast to reinforced concrete, prestressed concrete is uncracked under service-level loads, or pre-existing cracks are closed due to precompression. Accordingly, prestressed concrete beams experience low signal attenuation. The force exerted by the prestressing strands also prevents the growth of initial cracks, resulting in lower attenuation compared to reinforced concrete. Thus, any acoustic emissions exhibited under service-level loads are more likely to correspond to significant structural damage rather than to insignificant nonstructural cracking, of the type which occurs in reinforced

concrete beams. The AE monitoring technique shows promise as a NDT for prestressed concrete structures.

4.4.4 LOADING PATTERNS FOR AE MONITORING

Figure 4-6 depicts the load patterns used for AE monitoring. The ten numbered load cycles are paired into five load sets, e.g. Loadset 1-2 includes the similar Load Cycles 1 and 2. So the loading pattern is made up of five pairs of load sets, and each load set is made of two identical load cycles. The load steps marked by an ellipse were maintained for four minutes. All other loading/unloading steps had an elapsed time of two minutes. All loads were applied via manual displacement control using a closed-loop hydraulic testing system. All loads were applied via manual displacement control using a closed-loop hydraulic testing system.

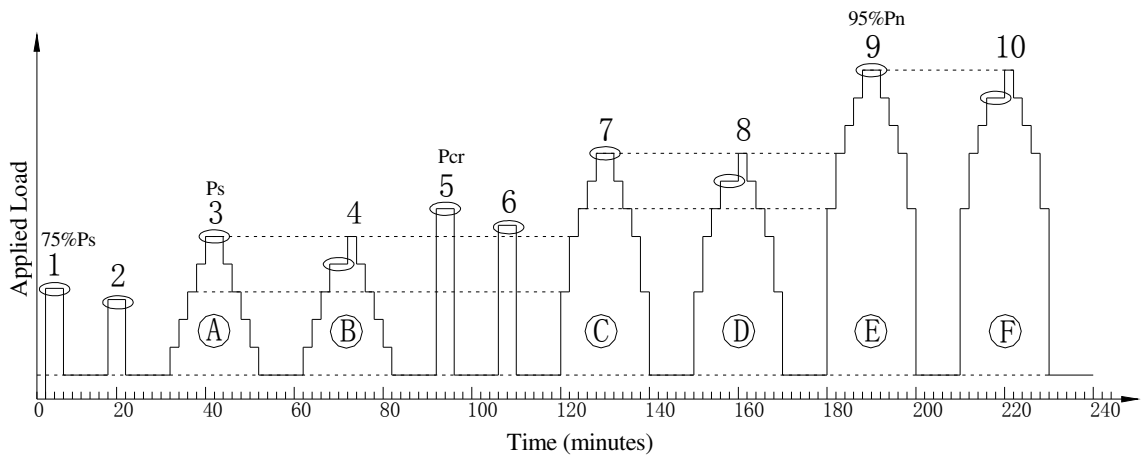


Figure 4-6: Load cycles and steps

All levels of applied loading that were used in the various load steps were functions of four values of load (P_{min} , P_s , P_{cr} , and P_n) determined prior to the test for each specimen. The first of these four loads, P_{min} , was the minimum load, 2.2 kN (500 lbs), that was maintained after the start of the test. This minimum load was needed to keep loading

equipment and sensors engaged throughout the test. The next of the four loads, P_s , was the applied load computed to cause zero net flexural stress in the bottom fiber of the beam at the load points. This corresponded to the service-level design load for Alabama Department of Transportation (ALDOT) bridge girders. Values of P_s for each beam are shown in Table 4-1. The next load value which was critical to the loading cycles was the flexural cracking load, P_{cr} . This load value, unlike the other three, was not determined before the test. The load was applied at a rate of approximately 0.4 kN/sec (100 lb/sec) until first cracking occurred. Achievement of the cracking load was signaled by a slight drop in load, accompanied by visible cracking. The actual cracking load, P_{cr} , was used to determine the peak load value for the AE testing. Finally, the last of the four load values determined prior to testing, P_n , was the applied load computed to cause a bending moment equal to the nominal moment capacity, M_n , at the critical section. The nominal moment was computed using AASHTO LRFD procedures (AASHTO 2006).

For the first Loadset 1-2, Cycle 1 and Cycle 2 each consisted of only one loading step followed by an unloading step. The maximum load level for Cycle 1 was equal to 75 percent of P_s . The maximum load level for Cycle 2 corresponded to 90 percent of the previous peak load of Cycle 1 to allow for evaluation of the Felicity effect (Ridge and Ziehl 2006). Both were held four minutes.

For the second Loadset 3-4, Cycles 3 and 4 (corresponding to Cycles A and B of the CLT Method of ACI 437R-03) each consisted of five load steps. As prescribed for the CLT method, these cycles consisted of five load steps increasing in value until P_s was reached. Then the load was decreased in steps to P_{min} . Each step including the sustained portion was 2 minutes long except the maximum load level for Cycle 3 and the fourth

load step for Cycle 4, which were each sustained for four minutes. P_{min} was held for 10 minutes at the end of each cycle. The values of the five load steps of Cycle 3 are detailed in Table 4-3. Load Step P_{33} is equal to the prior peak load (Cycle 1).

Table 4-3: Load step value

Cycle	Load Step				
3	$P_{31} = 0.25P_s$	$P_{32} = 0.50P_s$	$P_{33} = 0.75P_s$	$P_{34} = 0.90P_s$	$P_{35} = P_s$
7	$P_{71} = 0.75P_s$	$P_{72} = P_s$	$P_{73} = (P_{72}+P_{74})/2$	$P_{74} = 0.90P_{75}$	$P_{75} = (P_{35}+P_{95})/2$
9	$P_{91} = P_{73}$	$P_{92} = P_{75}$	$P_{93} = (P_{92}+P_{94})/2$	$P_{94} = 0.90P_{95}$	$P_{95} = 0.95P_n$

For the third Loadset 5-6, Cycle 5 and Cycle 6 each consisted of only one load step (followed by a single unloading step). The maximum load level for Cycle 5 (P_5) was intended to allow capture of the beam behavior shortly after flexural cracking. (For beam STD-B-M, it corresponded to the calculated cracking load, $P_{cr,calc}$ instead of the actual cracking load, P_{cr}). This load was maintained for four minutes. The maximum load level for Cycle 6 (P_6) corresponds to 90 percent of the previous peak load P_5 ($P_6 = 0.90P_5$). This load level was also maintained for four minutes.

For the fourth Loadset 7-8, Cycle 7 and 8 (corresponding to Cycles C and D of the CLT Method of ACI 437R-03) were identical in load magnitude and achieved a maximum load level (P_{75}) that was half-way between the maximum load level achieved in Cycle 3 (P_s) and the maximum load planned for Cycle 9 (P_{95}). The loading procedure of Cycle 7 and Cycle 8 was similar to that of Cycle 3 and Cycle 4 respectively. The values of the five load steps of Cycle 7 were detailed in Table 4-3. Cycle 8 is a repeat of Cycle 7, but the load of the fourth of five steps during loading phase, P_{84} , was maintained

four minutes and all other loading/unloading steps were two minutes long, including the sustained phase.

For the fifth Loadset 9-10, Cycle 9 and 10 (corresponding to Cycles E and F of the CLT Method of ACI 437R-03) were identical in load magnitude, and they reached 95 percent of P_n . The values of the load steps of Cycle 9 were detailed in Table 4-3. Cycle 10 was a repeat of Cycle 9, but the load of the fourth of five steps was maintained for four minutes and all other loading/unloading steps, including the sustained phase, were 2 minutes long.

At the conclusion of Cycle 10, the test load was reduced to P_{min} , which was maintained for 10 minutes. The AE sensors were removed and the test beam was then loaded to failure.

4.5 EXPERIMENTAL RESULTS AND DISCUSSION

4.5.1 SPECIMEN BEHAVIOR

STD-M-A—Before the beginning of the AE testing, this specimen was prematurely loaded beyond its cracking load and the load initiating yielding in the prestressing strands. After completion of the AE testing, the specimen failed in a flexural manner when loaded to its ultimate strength. No strand end slip was measured during the test. The maximum load reached for this specimen was 91.2 kN (20.5 kips) at a maximum deflection of 188 mm (7.40 in.). The maximum moment resisted by this beam, M_{max} , was 11 percent greater than $M_{n,calc}$. The beam lost its load-carrying capacity due to strand rupture. No web-shear cracking was observed in this specimen.

STD-M-B—This specimen failed in a flexural manner. No strand end slip was detected during this test. The first flexural cracking was observed during load Cycle 7 with a

value of 95.6 kN (21.5 kips), corresponding to a deflection of 5.6 mm (0.22 in.). The cracking moment, M_{cr} , for this specimen was 10 percent greater than the calculated cracking moment, $M_{cr,calc}$. The maximum load reached for this specimen was 141.0 kN (31.7 kips), corresponding to a deflection of 102 mm (4.0 in.). The maximum moment resisted by this beam, M_{max} , was 6 percent greater than $M_{n,calc}$. The beam lost its load-carrying capacity due to strand rupture. No web-shear cracking was observed in this specimen.

STD-M-C—This specimen failed in a flexural manner with moderate strand slip. The first flexural cracking was observed during load Cycle 5 with a load of 142.3 kN (32.0 kips), corresponding to a deflection of 3.6 mm (0.14 in.). The cracking moment, M_{cr} , for this specimen was 16 percent greater than the calculated cracking moment, $M_{cr,calc}$. The maximum load reached for this specimen was 218.4 kN (49.1 kips), corresponding to a deflection of 86 mm (3.4 in.). The strand end slip experienced by the specimen at the peak load was 2.5 mm (0.1 in.). The maximum moment resisted by this beam, M_{max} , was 18% greater than $M_{n,calc}$. The beam lost its load-carrying capacity due to strand rupture. No web-shear cracking was observed in this specimen.

STD-M-D—This specimen was damaged in Cycle 5 suddenly and suffered a shear-tension failure, characterized by a gradual loss of strand anchorage due to bond deterioration after formation of a diagonal flexural-shear crack. The first flexural cracking was observed during load Cycle 5 at a load value of 218.4 kN (49.1 kips), corresponding to a deflection of 1.8 mm (0.07 in.). The cracking moment, M_{cr} , for this specimen was 8% greater than the calculated cracking moment, $M_{cr,calc}$. The maximum load reached for this specimen was 223.3 kN (50.2 kips), corresponding to a deflection of

5.1 mm (0.2 in.). The strand end slip experienced by the specimen at the peak load was 2.5 mm (0.1 in.). The maximum moment resisted by this beam, M_{max} , was 75 percent of $M_{n,calc}$.

4.5.2 AE EVALUATION RESULTS

4.5.2.1 NDIS-2421 CRITERION RESULT

The NDIS-2421 assessment procedure was carried out. To apply this criterion, the calm ratio and load ratio were calculated for each loadset for the four prestressed concrete beams. The calm ratio, defined previously in section 4.3.1, was computed using the loading and unloading portions of the first cycle of each loadset for all four beams, and the load ratio for STD-M-A was calculated differently from that for the three beams that were not damaged prior to testing.

For the beams that were undamaged prior to AE testing—STD-M-B, STD-M-C, and STD-M-D—the calm ratio was calculated using the first load cycle of each loadset. The load ratio was computed as the ratio of the load at the onset of AE activity in the second loading cycle to the previous maximum experienced load. At each loading stage, two parameters—calm ratio and load ratio were determined. The calculated values of the calm ratio and the load ratio are listed in Table 4-4. The data for specimens B, C, and D are plotted in Figure 4-7, with the load ratio and calm ratio on the horizontal and vertical axes, respectively. The label above each point represents the corresponding loadset number.

Since the values of the CMOD were not available, the region limits were determined graphically. To enable a comparison, the classification limits used by Ohtsu et al. (2002) are shown in Figure 4-7 as dashed lines. It can be seen in the figure that most of the

loadsets are classified as indicating “Heavy damage” by the Ohtsu limits. This includes several loadsets, such as Loadsets 5-6 and 7-8 of STD-M-B and Loadset 5-6 of STD-M-C, that correspond to loads less than or equal to the first flexural cracking load. For this reason, it was concluded that the Ohtsu limits are not accurate for these prestressed concrete specimens. New limits were proposed based on these test results, and these are indicated by the solid lines in Figure 4-7. The logic used to set these limits is explained below.

Table 4-4: Summary of evaluation criteria results

Beam	Criterion	Loadset Number				
		1-2	3-4	5-6	7-8	9-10
STD-M-A	Calm Ratio	2.36	12.54	19.17	36.59	13.07
	Load Ratio	0.08	0.06	0.04	0.04	0.03
	Relaxation Ratio	1.5	2.5	178.9	3.0	63.0
	Peak CSS Ratio	12.1%	114.8%	25.7%	8.4%	16.7%
	SSM Ratio	6.0%	4.2%	6.8%	4.1%	15.1%
STD-M-B	Calm Ratio	0.02	0.05	0.45	0.27	0.78
	Load Ratio	1.00	0.83	0.77	0.68	0.54
	Relaxation Ratio	0.2	1.2	13.1	0.5	0.5
	Peak CSS Ratio	0.2%	0.0%	0.4%	8.6%	5.1%
	SSM Ratio	0.4%	0.0%	0.8%	2.8%	4.9%
STD-M-C	Calm Ratio	0.00	0.00	0.12	0.07	0.79
	Load Ratio	1.00	0.75	0.52	0.79	0.52
	Relaxation Ratio	0.0	0.0	0.2	0.0	0.6
	Peak CSS Ratio	1.5%	0.0%	1.0%	0.0%	6.2%
	SSM Ratio	0.9%	0.0%	2.7%	0.0%	4.3%
STD-M-D	Calm Ratio	0.44	0.21			
	Load Ratio	1.00	0.41			
	Relaxation Ratio	0.0	0.2			
	CSS Ratio	1.0%	4.7%			
	SSM Ratio	1.3%	2.6%			

The new limits used to qualify the damage degree were determined after classifying the loadset before the first crack opening into “Minor damage” and classifying the loadset corresponding to the first crack opening into “Intermediate damage”. The resulting classification limits are set as 0.7 for load ratio and 0.5 for the calm ratio. According to

Figure 4-7, “Intermediate damage” corresponds to the first crack opening for beams STD-M-B and STD-M-C and one load cycle away from failure for beam STD-M-D.

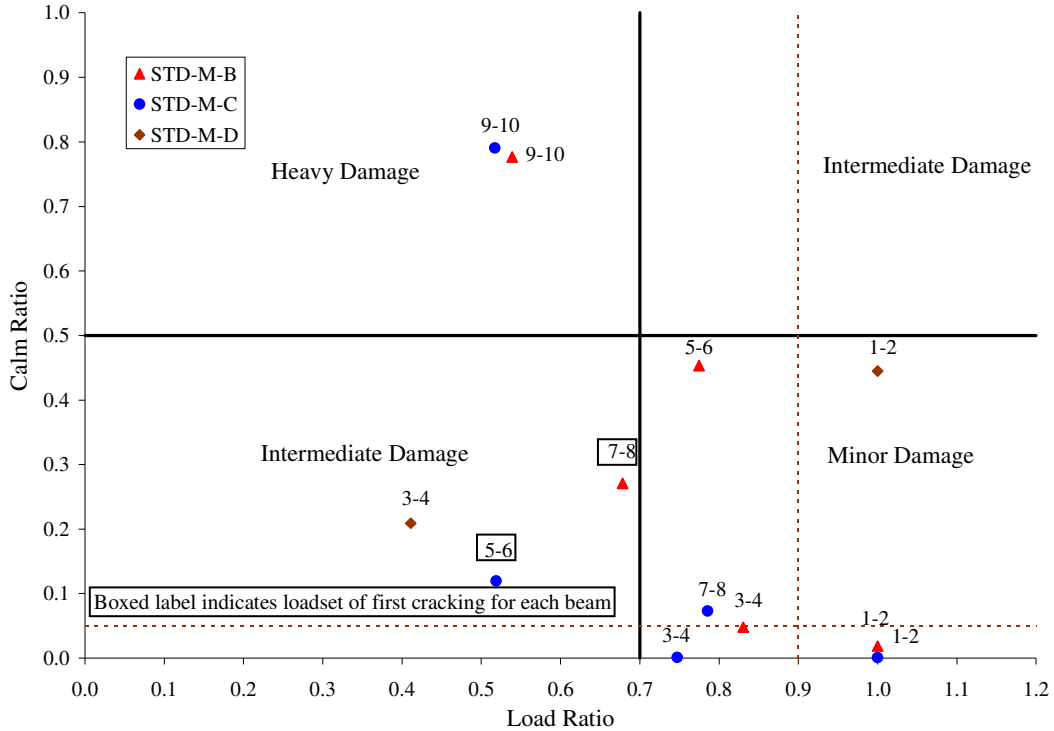


Figure 4-7: NDIS assessment for beams STD-M-B, STD-M-C, and STD-M-D

For beam STD-M-B, the first three loadsets were classified into the minor damage zone. Loadset 7-8 was classified into the intermediate damage zone. This was the first time the load reached its flexural cracking load. Loadset 9-10, which corresponds to 95 percent of P_n , was classified into the heavy damage zone. The maximum load reached at this load level was 121.0 kN (27.2 kips), which corresponds to 86 percent of the maximum load reached for this specimen, corresponding to a deflection of 15.5 mm (0.61in.). The cracks did not close when the load was removed from this load level, indicating that the beam had been loaded into the nonlinear response range, beyond yielding of the reinforcement.

For beam STD-M-C, the first two loadsets and Loadset 7-8 (which was less intense than Loadset 5-6) were classified into the minor damage zone. The Loadset 5-6 was classified into intermediate damage zone, which corresponds to the cracking load. Loadset 9-10 was classified into the heavy damage zone which corresponds to 95% of P_n . The maximum load reached at this load level was 169.0 kN (38.0 kips), which corresponds to 77 percent of the maximum load reached for this specimen, at a deflection of 8.1 mm (0.32 in.). The cracks did not close when the load was removed at this load level.

For beam STD-M-D, the first loadset was classified into the minor damage zone. Loadset 3-4, which corresponds to a service-level load, was classified into the intermediate damage zone. The maximum load reached at this load level was 148.6 kN (33.4 kips), which corresponds to 67 percent of the maximum load reached for this specimen, corresponding to a deflection of 1.3 mm (0.05 in.). According to the classification limits used above, there was more damage for Loadset 3-4 in this beam than there was for Loadset 3-4 in Beams STD-M-B and STD-M-C. There was no visual indication of distress, but this load level proved to be only one load cycle away from a sudden, nonductile failure. Therefore, the AE seems to have offered some an indication of increasing internal damage that was not evident from a visual observation.

In summary, with respect to the three levels of minor, intermediate, and heavy damage, the plotted data are classified in reasonable agreement with the actual beam conditions of these three previously undamaged beams.

For beam STD-M-A, which was damaged before the beginning of AE testing, the precise previous maximum load that the beam experienced was not available. This lack of

data is representative of the conditions that might be expected in a field assessment of an existing structure, where the previously applied maximum service load is unknown.

Therefore, a modified load ratio was computed by using the maximum (known) previous load applied during the AE testing period instead of the maximum (unknown) previous load that the beam experienced before the beginning of AE testing. Therefore the load ratio used in beam STD-M-A was the ratio of the load at the onset of AE activity in the second loading cycle to the previous maximum (known) load applied during the testing period. The calm ratio was calculated for the first load cycle of each loadset. The calculated values of the calm ratio and the load ratio are shown in Table 4-4. According to the classification limits used above, all loadsets of beam STD-M-A were classified into the heavy damage zone, which agrees well with the damage (cracking of concrete and yielding of reinforcement) induced in the beam prior to AE testing. The load ratios for STD-M-A were all very small because AE began at low loads in all of the post-damage load cycles.

The results above indicate that the damage levels of prestressed concrete beams can be qualified by the NDIS criterion using the modified load ratio and calm ratio limits proposed herein.

The limits chosen for damage classification can be used on practical in-situ applications after the applicability of the criterion had been examined and confirmed.

4.5.2.2 RELAXATION RATIO EVALUATION

The relaxation ratio, as discussed previously in Section 4.3.2, was computed for the first cycle of each load set. The calculated values for each load set are listed in Table 4-4.

For the pre-damaged beam STD-M-A, the relaxation ratios for all load sets were all more than the classification limit of 1.0, accurately indicating the beam damage. However, the value changed considerably from one loadset to the next. For beam STD-M-D, the relaxation ratios were all less than one before the beam suddenly cracked and subsequently failed. No clear trend can be identified in either of other two beams. As discussed by Colombo et al. (2005), the beam size, loading path, and the type of sensors used could all affect the results. Loadset 5-6 of STD-M-B was characterized by a relaxation ratio of 13 even though the beam had not yet cracked. The relaxation ratio evaluation method proposed for reinforced concrete could not be applied reliably for these prestressed concrete beams.

4.5.2.3 PEAK CSS RATIO EVALUATION

The Peak CSS Ratio, described in Section 4.3.3, was calculated for each load set. The calculated values are listed in Table 4-4. The Peak CSS Ratio for all load sets except Loadset 3-4 of pre-damaged beam STD-M-A were less than the acceptance criteria of 40% suggested by Ridge and Ziehl (2006), indicating that there should be no damage. No clear trend of Peak CSS ratio can be identified. The data were more scattered than the results reported by Ridge and Ziehl (2006). One possible explanation is the difference in sensitivity to AE signal recorded in prestressed concrete versus reinforced concrete. The low signal attenuation in the prestressed concrete beam, which could affect the AE activity during a load hold, may not be reflected in the Peak CSS ratio. Peak CSS ratio is only based on the simple summation of magnitude of the AE activity without considering the effect of the AE activity rate.

The results obtained from the AE data recorded did not reveal a clear trend. Thus, this approach appears to be less effective for indicating damage in prestressed concrete than for reinforced concrete beams. According to the tests results shown in Table 4-4, a difference in behavior between the beam STD-M-A, that had prior damage, and the undamaged beams, was not observed. Thus further work is needed to establish in which exact conditions the Peak CSS Ratio criteria is successful. The limits of its application and confirmation of its validity need to be investigated.

4.5.2.4 SIGNAL STRENGTH MOMENT RATIO EVALUATION

The newly proposed evaluation criterion based on the ratio of signal strength moment (SSM) recorded during the reload hold of a loadset to the initial load hold of that same loadset was applied. The resulting SSM ratio for each loadset is shown in Table 4-4.

For beam STD-M-B, the values of SSM for the first three cycles were close to zero. An SSM ratio of 2.8% corresponded to the actual flexural cracking load. For the final loadset, the SSM ratio increased to 4.9%.

For beam STD-M-C, the SSM values for first and second loading cycles of each loadset are shown in Figure 4-8. The SSM ratio for each loadset is also shown. The SSM ratio of 2.7% corresponded to the actual flexural cracking load; this value is very close to the STD-M-B value of 2.8%. An SSM ratio of 0.0% for Loadset 7-8 is observed. The maximum load level applied in Loadset 7-8 is less than the first flexural cracking load. For the final loadset, the SSM ratio was 4.3%.

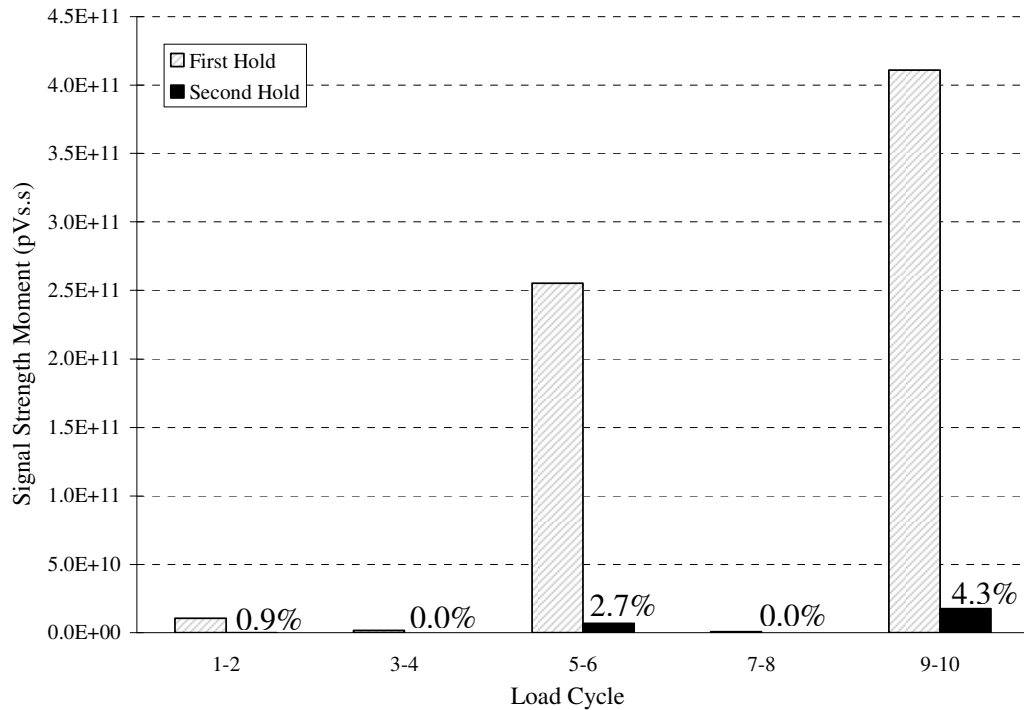


Figure 4-8: Signal strength moment during holds for beam STD-M-C

For beam STD-M-D, the SSM ratio for Loadset 3-4 (just prior to cracking and shear-tension failure) was 2.6%. This value is close to the SSM ratio at the first cracking load in STD-M-B and STD-M-C.

An acceptance criterion for this method may be determined from Table 4-4. It is clear that the trend of SSM ratio increases with increasing level of damage. During the load hold period for a beam that has experienced little or no previous damage, the SSM ratio is very small. When the SSM ratio is greater than 4%, the beam has experienced heavy damage.

For the pre-damaged beam STD-M-A, the SSM values and ratios are shown in Figure 4-9. The SSM ratios for all load cycles were more than 4%. According to the acceptance criterion used above, beam STD-M-A was heavily damaged, and this damage would have been indicated by the SSM ratio computed at any level of test load. This implies that the

damage levels of prestressed concrete beams can be qualified by the proposed criterion based on the SSM ratio.

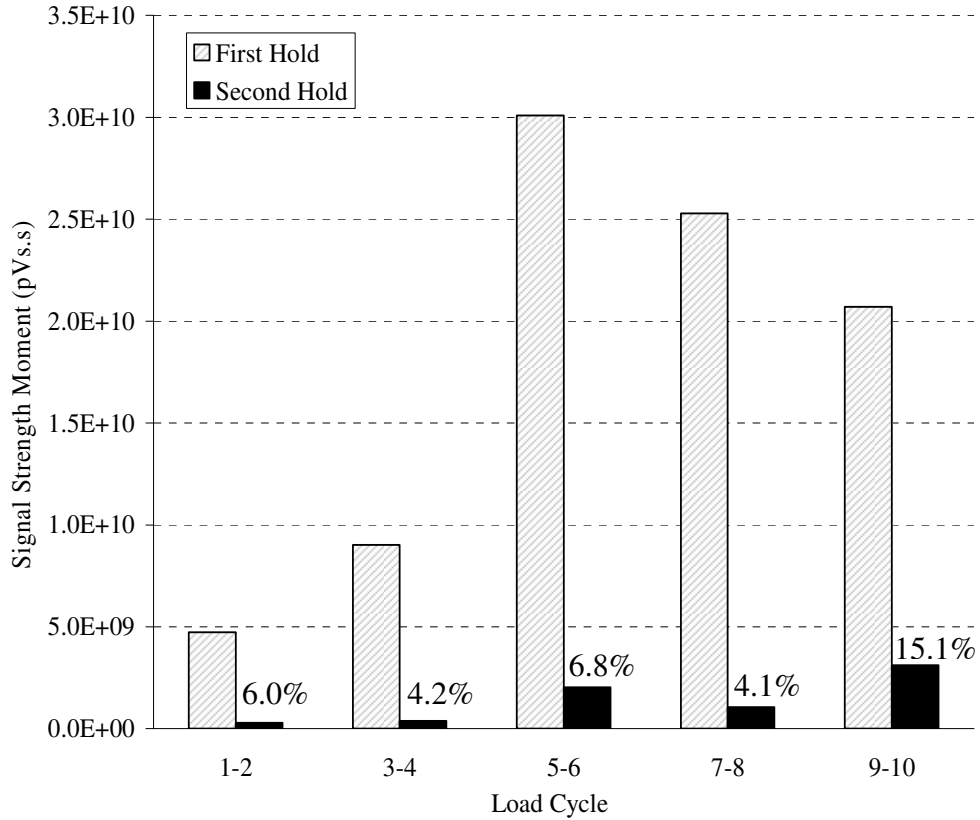


Figure 4-9: Signal strength moment during holds for beam STD-M-A

According to the SSM ratio analysis, STD-M-B and STD-M-C were damaged during Loadset 9-10. On the NDIS-2421 assessment table, that cycle corresponds to the one falling into the heavy damage area. The beam STD-M-A was classified as heavily damaged using both methods. So an SSM ratio of 4 percent or greater was a consistently accurate indicator of heavy damage in prestressed concrete beams and the results from SSM ratio appear to be supported by the modified NDIS method. This implies that the proposed procedure is practical and applicable in evaluating the integrity of the prestressed concrete beams.

4.6 CONCLUSIONS

The AE data acquired from a deliberately designed loading sequence provide insight into the behavior and integrity of prestressed concrete beams. The AE method provides a promising and effective means of investigating the condition of concrete bridges.

Although much research has been conducted on AE monitoring of concrete structures, there have been only limited applications to prestressed concrete, and no standardized procedures to evaluate the recorded data.

In this study, the results of experiments on four prestressed concrete beams were investigated. The effectiveness of various AE evaluation criteria for assessing structural damage was evaluated. A new type of analysis of AE signals based on a recommended SSM ratio was proposed, and the results were evaluated.

Several specific conclusions were drawn from this experimental investigation:

1. When applying NDIS-2421 evaluation criteria to prestressed concrete beams, reasonable results are obtained when the classification limits are set as 0.7 for the load ratio and 0.5 for the calm ratio.
2. Relaxation ratio is an unreliable AE evaluation measure for prestressed concrete beams.
3. The results from applying the Peak CSS AE evaluation criteria did not reveal a clear trend. This damage evaluation approach appears to be less effective for prestressed concrete than for reinforced concrete beams and the limits of its application need further investigation.

4. For the newly proposed SSM ratio evaluation criterion, an SSM ratio of 4 percent or greater was a consistently accurate indicator of heavy damage in prestressed concrete beams.
5. The results from the proposed SSM ratio evaluation criterion agreed with the results from the modified NDIS-2421 quantitative assessment criterion.

The AE method shows promise as a technique for nondestructive testing of prestressed concrete components. Further research is required to implement the evaluation criteria discussed in this chapter for evaluation of the performance of actual prestressed concrete structures.

CHAPTER 5

**COMPARISON OF ACOUSTIC EMISSION ACTIVITY IN CONVENTIONALLY
CONSOLIDATED AND SCC CONCRETE BEAMS**

5.1 INTRODUCTION

Many structures such as bridges, parking decks, and flooring systems are supported by prestressed concrete elements. For many years, vibration has been used to consolidate the fresh concrete in these elements. Though it has been used successfully for casting, several shortcomings exist with this conventionally consolidated concrete. One of the major problems with the use of vibrated concrete is the high amount of labor needed to ensure proper consolidation. Even after the vibration, voids are often present on the surfaces of the prestressed elements when the forms are stripped; thus, more labor is needed to patch the unwanted voids. Self-consolidating concrete (SCC), developed in Japan in the 1980s, is a highly fluid concrete that is able to deform under its own weight and to completely encapsulate any reinforcement, in the absence of vibration, without exhibiting defects due to segregation or bleeding (Khayat 1999). SCC can be placed without internal or external vibration. As a result, the use of SCC for construction is increasing rapidly.

SCC differs significantly from conventionally consolidated concrete. SCC has a higher fine aggregate content and a smaller coarse aggregate size. SCC requires a higher content of high-range water-reducing admixture than does conventionally consolidated concrete.

SCC also incorporates a higher volume of powder than conventionally consolidated concrete in order to provide the concrete with the cohesiveness necessary for successful casting (Khayat, Hu, and Monty 1999). Because the performance and design of prestressed concrete is heavily influenced by the behavior of the constituent materials, it is crucial that accurate behavior characteristics of SCC be established prior to its widespread implementation in prestressed bridge construction.

At the present time, relatively little research has been conducted to investigate the use of SCC in prestressed concrete, especially comparing specimens cast from several different mixtures. The use of SCC has been restricted due to a lack of standardized test procedures and performance data, as well as uncertainty regarding the applicability of current design procedures to elements made with SCC. It is, therefore, necessary to evaluate the applicability of some of the popular nondestructive testing methods to evaluate the performance of SCC and the effect of the use of SCC in prestressed beams.

In recent years, acoustic emissions (AE) techniques have been applied in the study of mechanical behavior of concrete (Hearn and Shield 1997; Yopez Roca 1999; Ohtsu et al. 2002). AE is a passive nondestructive inspection technique that has been used to assess structural integrity. In the AE method, transient elastic stress waves generated by the rapid release of energy from localized sources within a material are detected by piezoelectric sensors attached to the surface of the structure. By recording and analyzing the output of these sensors, information about the existence and location of possible damage sources is obtained.

The AE technique differs from most other nondestructive methods in two significant aspects (Pollock 1989). First, the AE signal detected is released from the interior of the

tested specimens rather than from some external sources. Because of this characteristic, the AE technique enables effective detection of changes within the structure of the specimen being tested. Second, AE techniques are capable of detecting the dynamic processes associated with degradation of structural integrity. In other words, the AE monitoring technique is able to detect a damage process as it occurs.

In this study, AE was monitored during cyclic tests of sixteen prestressed concrete T-beams. Twelve of these T-beams were constructed with one of three SCC mixtures. The remaining four beams were constructed with a more conventional concrete mixture similar to that used in precast/prestressed bridge girders in which proper consolidation is obtained using internal vibration.

AE data acquired from a carefully designed loading sequence provided real-time information concerning the integrity of each specimen. In this research, the AE signals emitted from conventionally consolidated and SCC concrete beams during the entire flexural loading process were analyzed. The main objectives of the research were to investigate the feasibility of the AE technique for prestressed concrete beams and to compare the response from SCC beams with that for conventionally consolidated prestressed concrete beams.

5.2 RESEARCH SIGNIFICANCE

The use of SCC may help precast/prestressed plants to produce high-quality prestressed concrete members at reduced labor costs. Concerns about the effects of SCC properties have limited the widespread use of SCC in precast/prestressed concrete applications. In order to investigate the relative performance of SCC in prestressed applications, AE monitoring was employed during load testing of conventionally consolidated and SCC

prestressed beams. The behavior and AE response of the SCC beams were compared with those of conventionally consolidated prestressed concrete beams.

5.3 ACOUSTIC EMISSION METHOD

In AE testing, a number of parameters are measured from the sensor-emitted signals. Through measurement and analysis of these parameters, the AE produced when prestressed concrete beams are subjected to loads may be used to characterize and identify different sources and types of damage. Commonly employed parameters include amplitude, duration, signal strength, and signal energy. The amplitude, an important measure of signal size, is defined as the peak voltage of the largest excursion attained by the signal waveform from an emission event (ASTM E 1316), and is usually measured in decibels (dB). Duration, which is usually measured in microseconds, is defined as the time between the start and end of an AE signal (ASTM E 1316). Signal strength is the measured area of the rectified AE signal, with units proportional to volt-seconds (ASTM E 1316). Signal strength—sometimes referred to as relative energy—relates to the amount of energy released by the specimen. It is a function of both the amplitude and duration of the signal.

For the research described in this chapter, several AE evaluation criteria were applied to assess the relative response of SCC and conventionally consolidated concrete in prestressed concrete beams.

The *NDIS-2421* quantitative assessment criterion was adopted by the Japanese Society for Nondestructive Inspections (JSNDI). The damage level of the structure is classified based on two parameters: the *load ratio* and the *calm ratio*, which are defined in the *NDIS-2421* as follows (Ohtsu et al. 2002):

$$\text{Load ratio} = \frac{\text{Load at the onset of AE activity in the subsequent loading}}{\text{the previous load;}} \quad (\text{Eq. 5.1})$$

Calm ratio = The number of cumulative AE activities during the unloading process/

$$\text{Total AE activities during the last loading cycle up to the maximum} \quad (\text{Eq. 5.2})$$

A *Relaxation Ratio* was used by Colombo et al. (2005) to predict the degree of damage of reinforced concrete beams. The relaxation ratio is defined as:

$$\text{Relaxation ratio} = \frac{\text{Average energy during unloading}}{\text{Average energy during loading phase}} \quad (\text{Eq. 5.3})$$

Ridge and Ziehl proposed an evaluation criterion based on the *Ratio of Peak Cumulative Signal Strength* (Peak CSS) (Ridge and Ziehl 2006). This ratio was expressed as a percentage as defined in the following:

$$\text{Peak CSS Ratio} = \frac{\text{Peak CSS at the end of reload hold period}}{\text{Peak CSS at the end of initial load hold period}} * 100\% \quad (\text{Eq. 5.4})$$

Signal Strength Moment Ratio Evaluation method is based on a time-weighted parameter —signal strength moment (SSM)—based on AE response during a load hold. The signal strength moment (SSM) is defined as:

$$SSM = \sum_i^n t_i S_i \quad (\text{Eq. 5.5})$$

where n is the total number of AE hits recorded during the load hold period, t_i is the time from the beginning of the hold period to the i th hit, and S_i is the signal strength for the i th hit.

A ratio of SSM from two consecutive load holds of similar intensity and duration is used for assessment purposes. The SSM Ratio is expressed as:

$$\text{SSM Ratio} = (\text{SSM for the second hold period} / \text{SSM for the first hold period}) \times 100\% \quad (\text{Eq. 5.6})$$

5.4 EXPERIMENTAL PROCEDURE

5.4.1 DESCRIPTION OF TEST SPECIMENS

The test specimens for this study consisted of sixteen prestressed T-beams. One standard (conventionally consolidated) mixture and three SCC mixtures were each placed in four T-beams. Each of these four beams had a different length: 2.95 m (116 in.), 3.96 m (156 in.), 4.98 m (196 in.) and 7.01 m (276 in.). The lengths were varied within each set to allow for development-length testing as described by Levy (2007). Figure 5-1 shows the cross section details for all sixteen T-beams tested. Each specimen was prestressed with two seven-wire, low-relaxation, Grade 270, ½-in.-special (oversize) strands. Grade 60 No. 3 reinforcing bars were used for U-shaped shear reinforcement. For each beam length, a slightly different stirrup layout was used in order to provide adequate, but not excessive, shear capacity. Complete test details are described by Levy (2007).

The three SCC mixtures consisted of a moderate-strength mixture using a 30% cement replacement with Class C fly ash (SCC-MA), a moderate-strength mixture using a 50% cement replacement with Grade 100 ground, granulated blast-furnace (GGBF) slag (SCC-MS), and a high-strength mixture using a 30% cement replacement with Grade 100 GGBF slag (SCC-HS). The actual proportions of the mixtures are shown in Table 5-1. The admixtures used in these mixtures include a high-range water-reducing admixture (HRWRA), a viscosity-modifying admixture (VMA), a mid-range water-reducing admixture (WRA), and an air-entraining admixture (AEA). Table 5-2 provides a summary of the fresh property test results for all four mixtures. Table 5-3 provides a summary of the hardened concrete property results.

Table 5-1: Concrete Mixture Proportions

Mixture Constituents	Mixtures			
	STD-M	SCC-MA	SCC-MS	SCC-HS
Water (pcy)	270	270	270	260
Cement (pcy)	640	525	375	650
Fly Ash (pcy)	0	225	0	0
GGBF Slag (pcy)	0	0	375	279
Coarse Agg. (pcy)	1964	1607	1613	1544
Fine Agg. (pcy)	1114	1316	1323	1265
AEA (oz/cwt)	0.33	0.00	0.00	0.00
WRA (oz/cwt)	4.0	4.0	6.0	6.0
HRWRA (oz/cwt)	3.5	4.0	4.5	5.0
VMA (oz/cwt)	0.0	2.0	2.0	2.0

Where:

GGBF = Ground Granulated Blast Furnace,

AEA = Air-Entraining Admixture,

WRA = Water-Reducing Admixture.

HRWRA = High-Range Water-Reducing Admixture, and

VMA = Viscosity-Modifying Admixture.

Table 5-2: Summary of Fresh Property Test Results

FRESH PROPERTIES	MIXTURES			
	STD-M	SCC-MA	SCC-MS	SCC-HS
Slump Flow (in.)	9.5	29	28.5	26
Unit Weight (lb/ft ³)	142.2	151.8	148.4	155.2
Air content (%)	11.0	2.0	5.0	3.0
VSI	-	1.0	1.0	1.0
T-50 (sec.)	-	2.47	1.54	3.75
J-Ring Difference (in.)	-	1.5	2	2.5
L-Box (H ₂ /H ₁)	-	0.84	0.92	0.63
Temperature (°F)	82	62	89	95

Table 5-3: Hardened Concrete Property Summary

PROPERTY	MIXTURES			
	STD-M	SCC-MA	SCC-MS	SCC-HS
f'_{ci} (psi)	5000	5500	5300	9990
E_{ci} (ksi)	4900	4900	4950	6050
f'_c (psi)	6320	8540	9170	13380
E_c (ksi)	5150	5400	6950	7050
f_r (psi)	1050	1250	1280	1520

Where:

f'_{ci} = Specified compressive strength of concrete at transfer of prestress force,

E_{ci} = Modulus of Elasticity of concrete at transfer of prestress force,

f'_c = Specified compressive strength of concrete,

E_c = Modulus of Elasticity of concrete, and

f_r = Modulus of rupture.

5.4.2 TEST SETUP

The beams were tested in flexure under symmetric four-point loading. The test setup, shown in Figure 5-3, consisted of a simply supported beam loaded by two equal

concentrated loads. A 0.9-m (3-ft) length of uniform bending moment was induced at midspan by means of a spreader beam which transferred the load from the actuator through steel cylinders to steel plates attached to the beam with a gypsum plaster. The applied load was measured using a calibrated force transducer between the hydraulic actuator and the spreader beam.

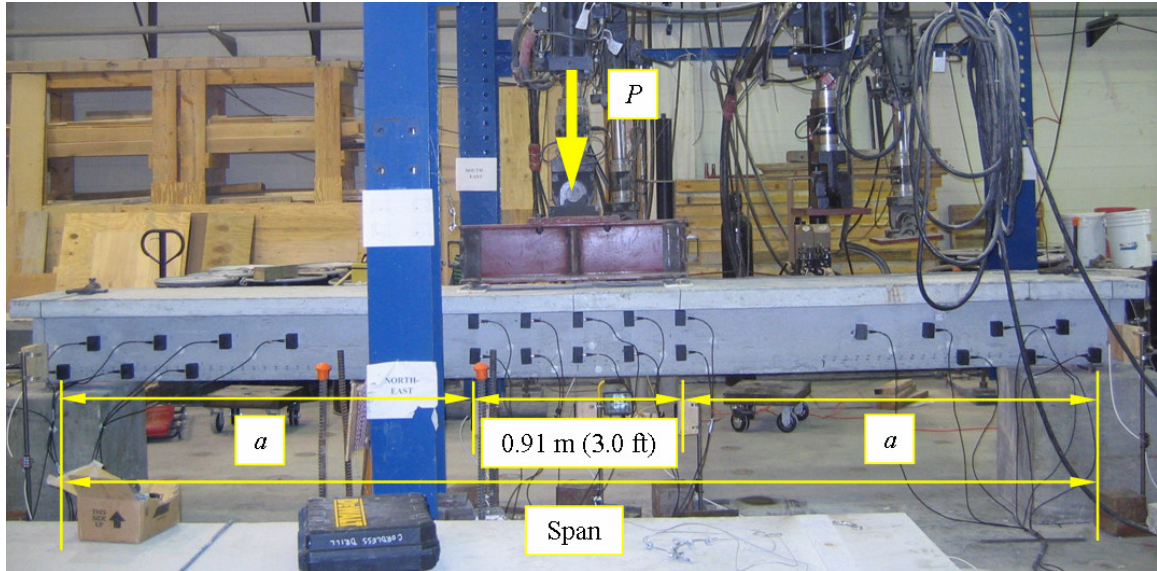


Figure 5-3: Load test setup and AE sensor locations

Figure 5-4 depicts the load cycles used for AE testing for SCC beams. The twelve numbered load cycles are paired into six load sets, e.g. Loadset 1-2 includes the similar Load Cycles 1 and 2. For the conventionally consolidated concrete (STD-M) beams, AE monitoring was performed for only the first ten numbered load cycles. Each load step marked by an ellipse was maintained for four minutes. Each of the other loading/unloading steps had an elapsed time of two minutes. All loads were applied and maintained via manual displacement control using a closed-loop hydraulic testing system.

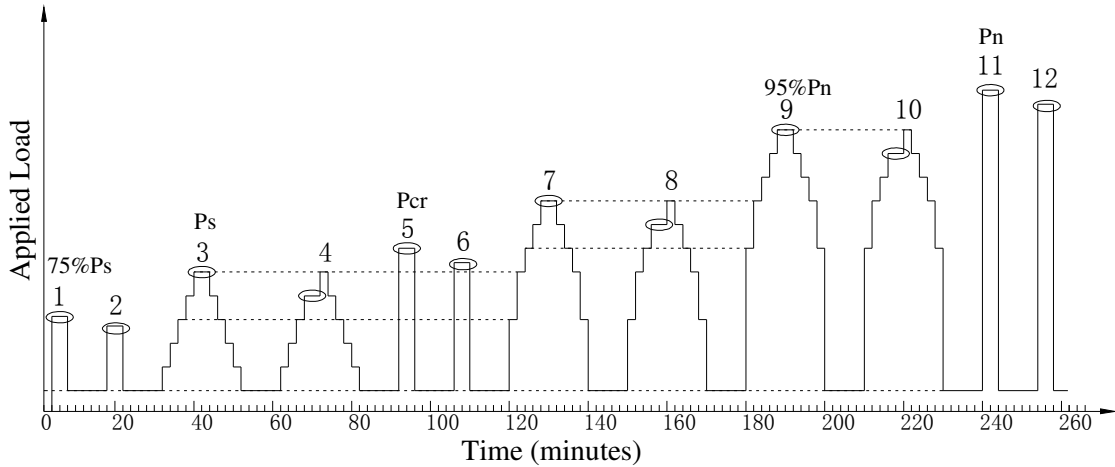


Figure 5-4: Load cycles and steps

All loading levels were functions of four independent load values: P_{min} , P_s , P_{cr} , and P_n determined for each specimen. P_{min} was the minimum load, 2.2 kN (500 lbs), that was maintained after the start of each test. P_s was the applied load computed to cause zero net flexural stress in the bottom fiber of the beam at the load points. This corresponds to the service-level design criteria for Alabama Department of Transportation (ALDOT) bridge girders. P_{cr} was not computed before the test. During the 5th load cycle, the load was applied at a rate of approximately 0.4 kN/sec (100 lbs/sec) until first cracking occurred. Achievement of this cracking load was signaled by a slight drop in load, accompanied by visible cracking. This actual cracking load, P_{cr} , was used to determine the peak load for the 6th cycle. P_n was the load required to cause a bending moment equal to the computed nominal moment capacity, M_n , in the midspan region.

Linear potentiometers were used to measure displacements. Displacement values reported in this chapter refer to the vertical midspan displacement relative to any vertical displacement of the support sections.

AE signals were monitored with a 24-channel "Sensor-based Acoustic Multi-channel Operation Systems" (SAMOS) manufactured by Physical Acoustics Corporation (PAC). PAC R6I-AST 50-kHz integral resonant sensors were used.

Twenty-four sensors were surface-mounted on three zones of each beam as shown in Figure 5-3: two parallel rows of five sensors to monitor flexural cracking in the zone of maximum moment, a row of three sensors along the prestressing strand depth near each support to monitor strand slippage in the anchorage zone (along the transfer length), and a row of four sensors near the mid-depth of the beam in each shear span (between load point and support). All sensors were placed on one face of the beam.

Prior to each test, the system was calibrated using the conventional pencil-lead break test (ASTM E976). A background check lasting about 4 minutes was performed prior to loading the test specimen. During each load cycle, the AE parameters recorded for each channel included duration, amplitude, and signal strength. At the end of the load cycles, the AE sensors were removed from the beam prior to loading to failure.

5.5 EXPERIMENTAL RESULTS AND DISCUSSION

5.5.1 STRUCTURAL RESPONSE

Flexural testing was conducted on sixteen specimens. Table 5-4 summarizes the structural response characteristics of the sixteen specimens. Because STD-M-A was cracked prior to flexural testing, the flexural cracking data are not reported in Table 5-4. Three failure modes were observed: flexural failure, flexural with slip failure, and shear-tension failure. The flexural failure mode was characterized by a pure flexural failure in which no end slip was measured throughout the entire loading process. The first cracks were observed at or between the load points. The crack pattern was generally symmetric

for this failure mode. For all flexural failures, both strands ruptured at a stress beyond their predicted ultimate capacity. Strand rupture occurred between the load points for all flexural failures. Failure was also accompanied by crushing of the concrete in the compression flange between the load points.

The flexural with strand slip failure mode was characterized by flexural failure with moderate strand slip. For a flexural failure with slip, the cracking patterns varied among different specimens more for this type of failure than for pure flexural failures. For each of these failures, the strand slip did not significantly affect the failure load of the beam. Concrete crushing of the extreme compression fiber was experienced by all specimens reaching this failure mode. For specimens characterized by this failure mode, the only case in which the strands did not rupture was specimen SCC-MA-D. In that case, the load required to cause failure of the beam exceeded the maximum load capacity for the actuator.

The shear-tension failure mode was characterized by extreme strand slip, leading to a premature shear failure. This failure began with the virtually simultaneous occurrence of a diagonal crack and large strand slip on one end of the beam, resulting in a dramatic loss of load-carrying capacity of the section. The crack pattern was asymmetric with the large diagonal crack forming just within the transfer length of the end of the beam which experienced strand slip. The stress in the strand at failure was much lower than its ultimate strength and strand rupture was not achieved.

Fifteen of sixteen specimens exhibited a flexural failure; only three of these were accompanied by moderate bond slip. The shear-tension failure was observed in only one specimen, STD-M-D.

Table 5-4: Summary of test specimens and results

	P _{cr} kN (kips)	M _{cr} kN-m (kip-ft)	Δ _{cr} mm (in.)	P _{max} kN (kips)	M _{max} kN-m (kip-ft)	Δ _{max} mm (in.)	Failure Type
STD-M-A	-	-	-	91.2 (20.5)	144.6 (106.3)	188.0 (7.4)	Flexural
SCC-MA-A	61.4 (13.8)	101.2 (74.4)	8.38 (0.33)	91.6 (20.6)	145.1 (106.7)	221.0 (8.7)	Flexural
SCC-MS-A	64.1 (14.4)	105.1 (77.3)	9.14 (0.36)	93.9 (21.1)	148.4 (109.1)	198.1 (7.8)	Flexural
SCC-HS-A	62.7 (14.1)	103.2 (75.9)	6.86 (0.27)	93.4 (21.0)	147.7 (108.6)	195.6 (7.7)	Flexural
STD-M-B	95.6 (21.5)	95.9 (70.5)	5.59 (0.22)	141.0 (31.7)	138.7 (102.0)	101.6 (4.0)	Flexural
SCC-MA-B	103.2 (23.2)	103.1 (75.8)	5.33 (0.21)	153.9 (34.6)	150.8 (110.9)	119.4 (4.7)	Flexural
SCC-MS-B	105.0 (23.6)	104.7 (77.0)	4.83 (0.19)	146.8 (33.0)	144.2 (106.0)	134.6 (5.3)	Flexural
SCC-HS-B	105.4 (23.7)	105.1 (77.3)	4.32 (0.17)	149.5 (33.6)	146.6 (107.8)	134.6 (5.3)	Flexural
STD-M-C	142.3 (32.0)	101.3 (74.5)	3.56 (0.14)	218.4 (49.1)	153.4 (112.8)	86.4 (3.4)	Flex.w/Slip
SCC-MA-C	141.5 (31.8)	100.8 (74.1)	3.05 (0.12)	224.2 (50.4)	157.6 (115.9)	88.9 (3.5)	Flexural
SCC-MS-C	145.0 (32.6)	103.2 (75.9)	3.05 (0.12)	211.3 (47.5)	148.8 (109.4)	86.4 (3.4)	Flexural
SCC-HS-C	152.6 (34.3)	108.4 (79.7)	2.54 (0.10)	213.5 (48.0)	150.6 (110.7)	83.8 (3.3)	Flexural
STD-M-D	218.4 (49.1)	96.3 (70.8)	1.78 (0.07)	221.1 (49.7)	97.4 (71.6)	5.1 (0.2)	Shear- tension
SCC-MA-D	221.5 (49.8)	97.6 (71.8)	2.29 (0.09)	368.3 (82.8)	161.2 (118.5)	45.7 (1.8)	Flex.w/Slip
SCC-MS-D	238.0 (53.5)	104.7 (77.0)	2.03 (0.08)	364.3 (81.9)	159.4 (117.2)	55.9 (2.2)	Flex.w/Slip
SCC-HS-D	241.5 (54.3)	106.2 (78.1)	1.78 (0.07)	355.4 (79.9)	155.6 (114.4)	55.9 (2.2)	Flexural

Table 5-4 indicates that SCC specimens performed as well as specimens constructed with a conventionally consolidated concrete mixture. For specimens which were designed to have a 60-in. embedment length and given the designation “C”, the only

specimen to experience general bond slip was STD-M-C, which was constructed with a conventional concrete mixture. Likewise, for specimens which were designed to have a 40-in. embedment length and given the designation “D”, the only specimen to experience a shear-tension failure was STD-M-D, which was constructed with a conventional concrete mixture. Therefore, it can be concluded that the use of SCC mixtures did not have an adverse effect on the overall flexural performance of these specimens.

5.5.2 AE SIGNAL STRENGTH

One form of analyzing AE data is to look at the timing and intensity of AE activities that occur during a test. An increase in the AE activities indicates a change in the condition of the specimen. AE signal strength was one of the most useful parameters in the study of AE characteristics of prestressed concrete beams. Signal strength relates to the amount of energy released by the specimen. Appendix D contains plots that show the AE signal strength versus time superimposed with the load cycles for all sixteen beams. Figures 5-5 and 5-6 show examples of the relationships between AE signal strength and load history for STD-M-C and SCC-MS-C, respectively. Test results from beam STD-M-C and SCC-MS-C are reported here because the data from these two beams are representative of the other beams. The solid line in each figure represents the applied load, while the dots represent the individual signal strength of each hit recorded.

The AE signal strength reflected the specimen response to the various load conditions imposed. Comparison of Figure 5-5 and Figure 5-6 indicates that the SCC specimen behaved similarly to the conventionally consolidated concrete beam. Both figures illustrate several typical phenomena and offer visual clues to the beam condition. First, some AE activities likely produced by the initial friction at the support were observed at

the onset of testing. This was typical for first-time loading of new beams. The AE activities diminished during Cycle 2. Second, while the beam was uncracked during the service-load cycle, the AE activities were small. Third, during Loadset 5-6, in which the first flexural cracking was observed, a massive burst of AE occurred. Last, as the specimen neared its ultimate strength, new surface-breaking cracks grew and a rapid increase in cracking was observed, accompanied by a sharp increase in AE signal strength.

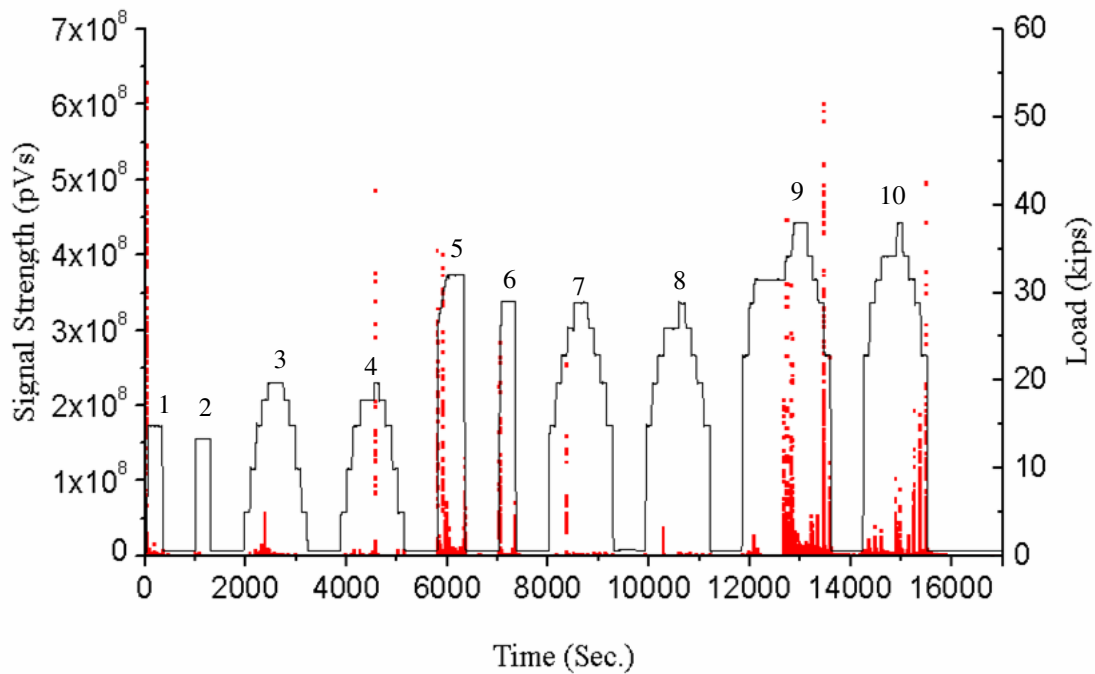


Figure 5-5: Load and signal strength versus time for beam STD-M-C

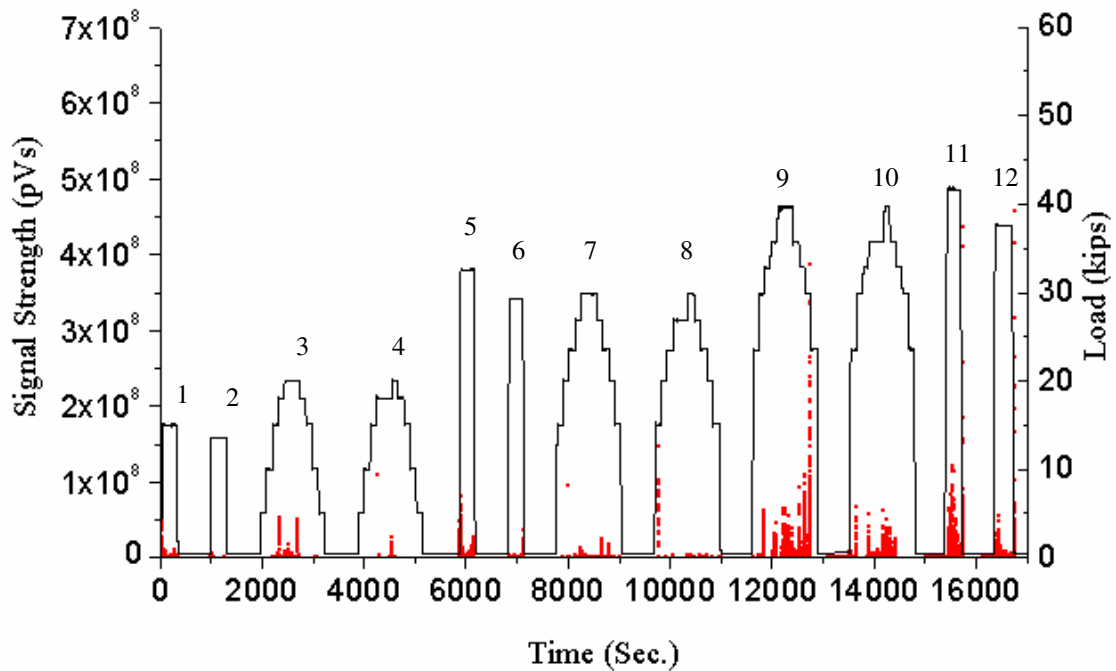


Figure 5-6: Load and signal strength versus time for beam SCC-MS-C

It was also noted that in all specimens, a significant increase in AE signal strength occurred *prior to* observation of visible cracking on the beam surface. This increase likely corresponded to the formation and propagation of the internal microcrack network within the concrete tensile zone. The cracking becomes visible only when these microcracks coalesce to form a flexural crack.

The data from these tests show that AE signal strength is associated with structurally significant damage in SCC beams. The experimental results indicated that there is a clear relationship between the AE activities and the behavior of both SCC beams and conventionally consolidated concrete beams. However, further research is needed to quantify and calibrate the relationship between the AE signal strength and behavior of SCC beams before applying this technique to field practice.

5.5.3 CUMULATIVE SIGNAL STRENGTH

Since high signal strength is normally associated with damage in a specimen, a graph of cumulative signal strength versus time is sometimes used to describe damage processes in specimens tested in a controlled environment (Pollock 1998). Figure 5-7 shows the cumulative signal strength versus time for the entire loading, holding, and unloading process of Load Cycle 5 (when first flexural cracking was observed) of the C specimens. The plots of cumulative signal strength versus time during Load Cycle 5 for all of the specimens are reported in Appendix H. The solid line in the figure represents the cumulative signal strength during loading; the dashed line represents the cumulative signal strength during the load hold; the dotted line represents the cumulative signal strength during unloading.

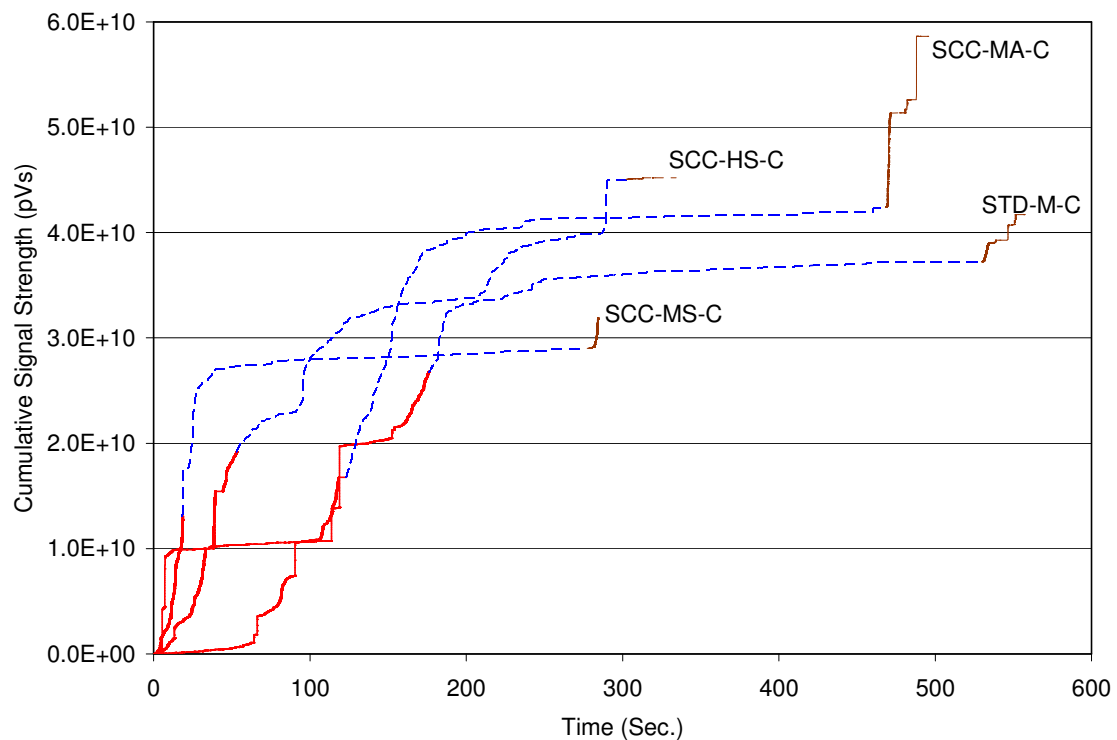


Figure 5-7: Cumulative signal strength versus time for “C” beams during Load Cycle 5

As shown in Figure 5-7, SCC-HS-C and SCC-MA-C emitted more total signal strength than STD-M-C during the cycle, and SCC-MS-C emitted less signal strength than STD-M-C. The SCC beams exhibit trends similar to the conventionally consolidated concrete beams. There was no consistent difference evident in the signal strength emitted during the whole Cycle 5 (first flexural cracking) when comparing beams cast with SCC to beams cast with conventionally consolidated concrete.

In some SCC beams, the cumulative signal strength emitted during the first cracking period was greater than in the companion conventionally consolidated concrete beams, while the opposite was true for other SCC beams. The cumulative signal strengths of SCC concrete beams were not significantly different from conventionally consolidated beams. As a result, it can be concluded that AE response of SCC and conventionally consolidated prestressed concrete beams were similar.

5.5.4 DURATION/AMPLITUDE CROSSPLOT

The AE signal itself may provide information about the damage level of structures (Yoon et al. 2000). One method that can be used to illustrate the features of the AE signal is a duration/amplitude crossplot. The duration/amplitude crossplot features each AE sensor hit plotted as a single data point in a Cartesian coordinate system with the hit duration as the abscissa and hit amplitude as the ordinate.

Duration/amplitude crossplots for each loadset for sixteen beams are shown in Appendix C. Figure 5-8 shows a typical crossplot of amplitude and duration of AE signals from the most active sensor of beam SCC-MS-C during Loadset 3-4. The left plot shows the AE data from Cycle 3 and the right plot from Cycle 4. The solid triangles indicate AE events from the loading stages of the cycle, whereas open circles indicate AE

events from the unloading stages. The peak load of loadset 3-4 represents the applied load computed to cause zero stress in the bottom fiber of the beam at the load points. This service-level design condition was reached with a load of 89.4 kN (20.1 kips) and a midspan displacement of 1.5 mm (0.06 in.). There were no visible indications of cracking in beam SCC-MS-C during this load set.

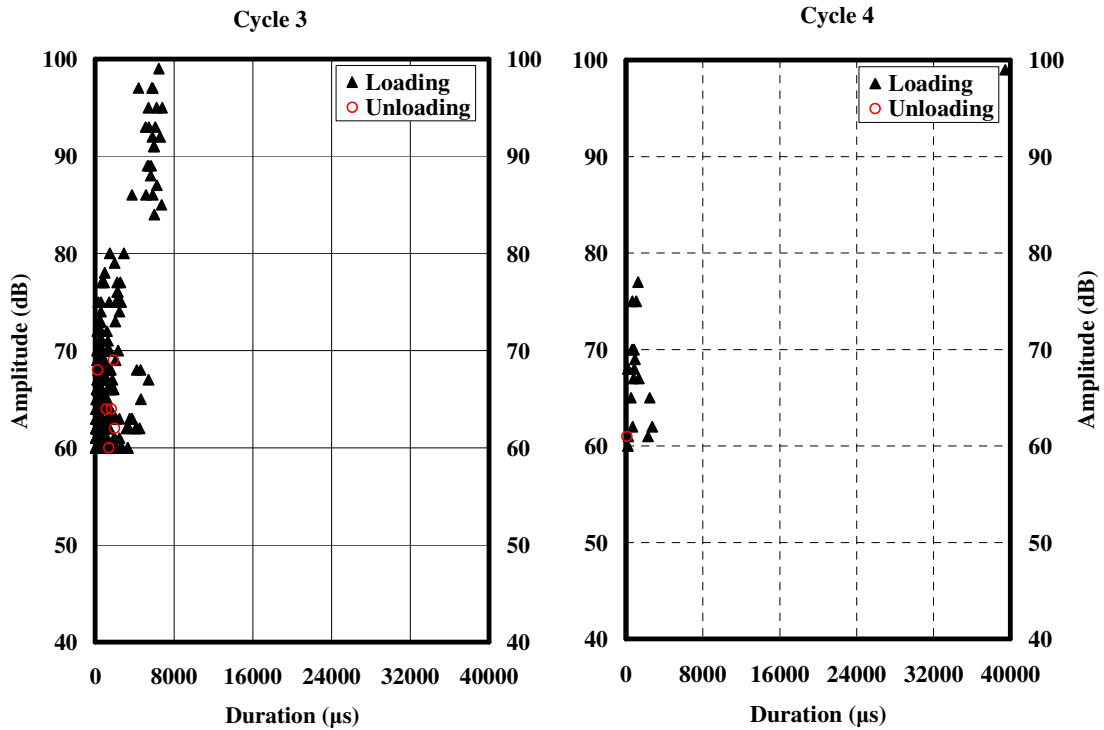


Figure 5-8: Crossplot of amplitude and duration of AE signals from Loadset 3-4 for beam SCC-MS-C

Figure 5-9 shows the results of a crossplot of amplitude and duration of AE signals of beam SCC-MS-C during Loadset 5-6. The left and right plots show the AE data from load Cycle 5 and 6, respectively. The first flexural cracking was observed during the 5th load cycle at an applied load of 145.0 kN (32.6 kips) and a corresponding midspan displacement of 3.0 mm (0.12 in.). Compared to the crossplots for Loadset 3-4 in Figure 5-8, the AE signals plotted in Figure 5-8 have a characteristically long duration and high

amplitude for both the loading and unloading stages. Thus, the AE signals associated with flexural cracking exhibit a longer duration and higher amplitude. The AE signals have a relatively short duration and low amplitude for both the loading and unloading stages at service-level loads prior to cracking, and the AE signals have a relatively long duration and high amplitude for both the loading and unloading stages after the beam cracks.

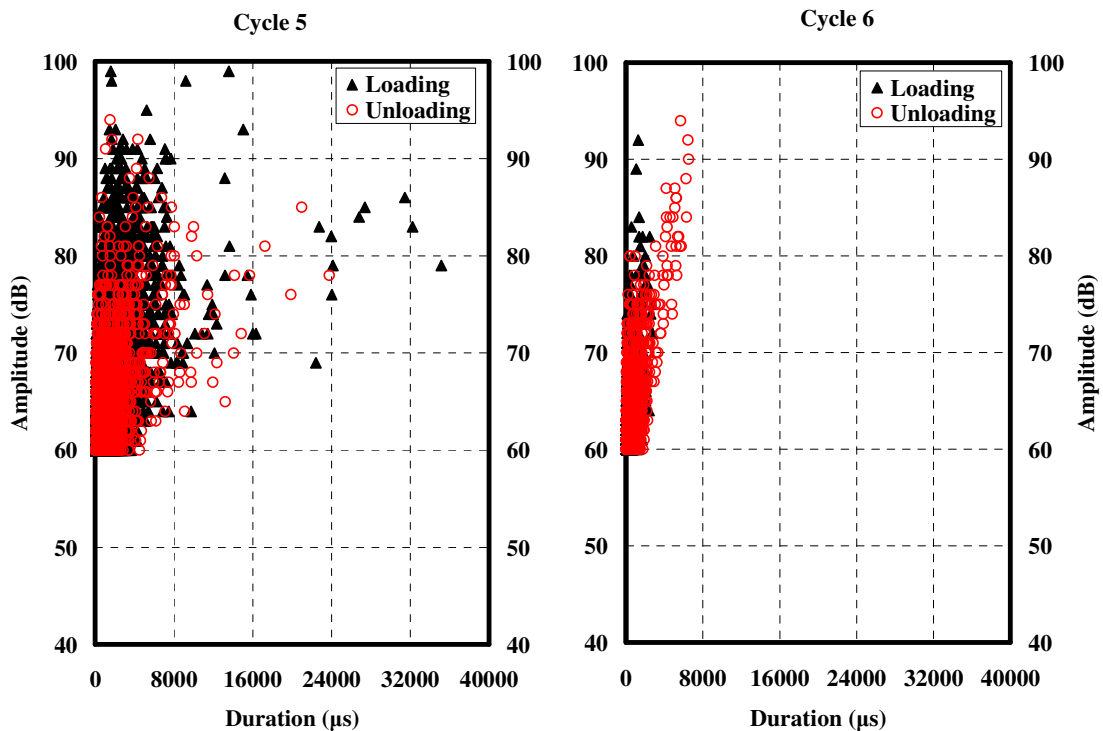


Figure 5-9: Crossplot of amplitude and duration of AE signals from Loadset 5-6 for beam SCC-MS-C

This same behavior observed for the SCC beams can be observed in conventionally consolidated concrete beams. Figure 5-10 and Figure 5-11 show the results of a duration/amplitude crossplot of beam STD-M-C during Loadsets 3-4 and 5-6, respectively. Loadset 3-4 was the service-level load of 87.6 kN (19.7 kips), corresponding to a deflection of 1.8 mm (0.07 in.). Again, the AE signals have a

relatively short duration and low amplitude for both the loading and unloading stage before the beam cracked. After the beam cracked in Cycle 5, the AE signals exhibit a longer duration and higher amplitude.

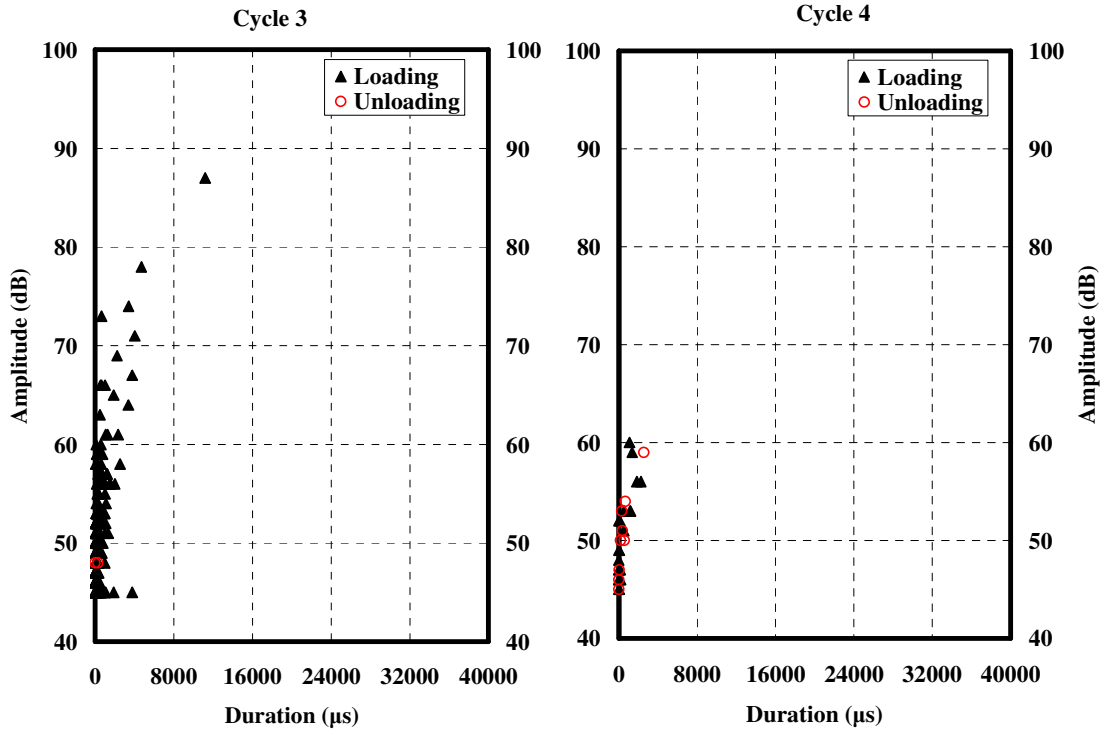


Figure 5-10: Crossplot of amplitude and duration of AE signals from Loadset 3-4 for beam STD-M-C

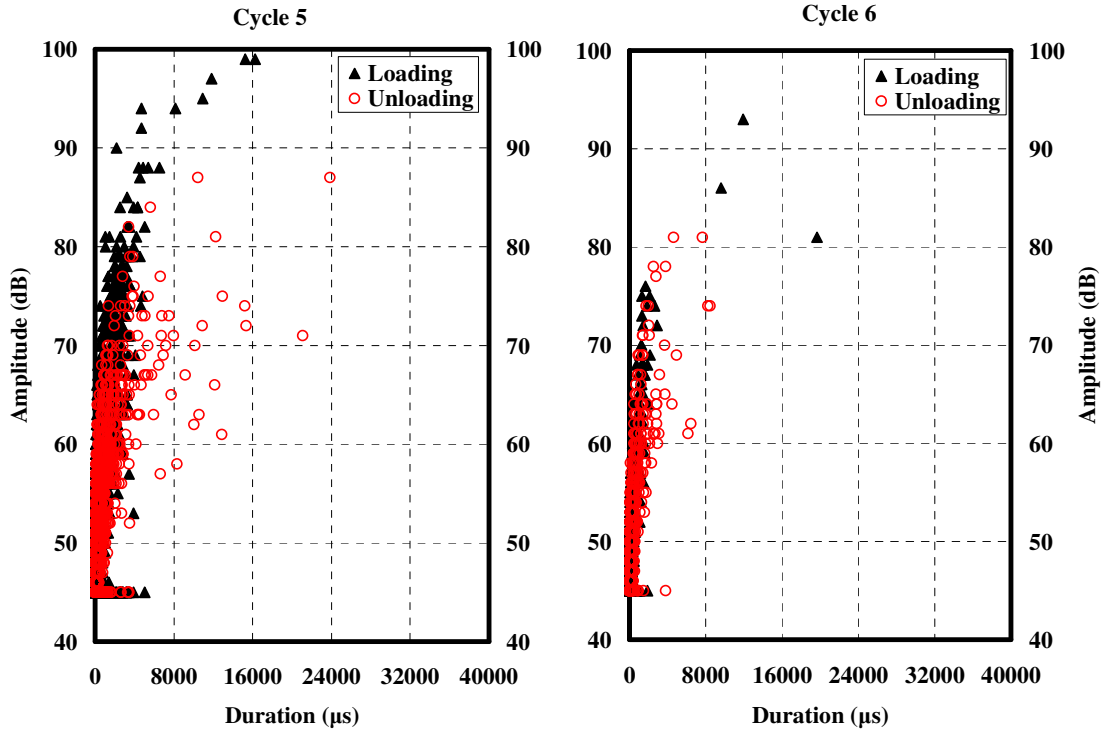


Figure 5-11: Crossplot of amplitude and duration of AE signals from Loadset 5-6 for beam STD-M-C

From the crossplots of AE signal amplitude versus duration, it was found that the initiation of early microcracks or the local slips and the mechanical rubbing of the interlocked faces generates lower signal amplitude, while the initiation of the main tensile crack generates higher signal amplitude. AE signals can also be produced from rubbing of crack surfaces as they close and grind in response to unloading. The long duration was attributed to the rubbings of interlocked faces produced during the previous loading. Different AE sources can be distinguished by the amplitude and duration data. Therefore, it seems that the structural integrity of both SCC prestressed concrete beams and conventionally consolidated prestressed concrete beams may be evaluated by comparing the AE parameters of duration and amplitude produced during cyclic flexural loading tests with different load levels.

5.5.5 AE EVALUATION CRITERIA

The main challenge for structural integrity evaluation using AE techniques is to accurately and quantitatively evaluate the AE data recorded. To assess the damage levels of prestressed concrete beams, several evaluation criteria—*calm ratio* and *load ratio* (of the *NDIS-2421* quantitative assessment criterion), *relaxation ratio* (Colombo et al. 2005), *CSS ratio* (Ridge and Ziehl 2006) and *SSM ratio* were calculated for comparison. The calculated values of AE evaluation criteria for each load set for sixteen prestressed concrete beams are listed in Appendix E.

To apply the *NDIS-2421* assessment criterion, the calm ratio and load ratio were calculated for each load set for the sixteen prestressed concrete beams. The calm ratio was computed using the loading and unloading portions of the first cycle of each load set for all specimens. For all fifteen of sixteen specimens (excluding STD-M-A), the load ratio used was the ratio of the load at the onset of AE activity in the second loading cycle to the previous maximum experienced load. For beam STD-M-A, which was damaged before the beginning of AE testing, the precise maximum load that the beam had previously experienced was not available. Therefore, a modified load ratio was computed by using the relative maximum (known) previous load applied during the AE testing period instead of the maximum (unknown) previous load that the beam experienced before the beginning of AE testing. The data for all specimens are plotted in Appendix F with the load ratio and calm ratio on the horizontal and vertical axes, respectively. The label above each point represents the corresponding loadset number.

Among the conventional (STD) specimens, beam A was damaged before testing, and beam B had a different load progression than its comparison SCC specimens. Thus, for

equitable comparison between SCC and conventionally consolidated beams, only the C and D beams are discussed in this section. The values of the calm ratio and load ratio for specimens C and D are indicated in Figures 5-12 and 5-13 by the height of each vertical bar, respectively. The horizontal axis of the bar graph consists of six loadset regions, and each loadset region is subdivided into two subgroups that represent the two test geometries (specimens C and D). Within each subgroup, there is one vertical bar per concrete mixture, and each mixture is distinguished by different hatching patterns. Based on the analysis in Chapter 4, the classification limits are set as 0.5 for the calm ratio and 0.7 for load ratio. As shown in Figure 5-12, for conventionally consolidated concrete beams, like beam STD-M-C, the calm ratio of the first three loadsets is less than 0.5 and the calm ratio of Loadset 9-10 is greater than 0.5; like beam STD-M-D, the calm ratio of the first two loadsets are less than 0.5. For SCC beams, for example beam SCC-MS-C, the calm ratio of the first three loadsets is less than 0.5, while the calm ratio of Loadsets 7-8 and 9-10 is greater than 0.5. High values of calm ratio were observed in SCC-HS-D for Loadset 1-2 and SCC-MS-C in Loadset 7-8, while small values were observed in SCC-MS-D and SCC-HS-D for Loadsets 9-10 and 11-12. Therefore, comparison of the calm ratio to the actual SCC beam damage resulted in relatively poor correlation.

According to the NDIS criterion, smaller load ratios are indicative of increased damage. As shown in Figure 5-13, the load ratio for conventionally consolidated concrete beams, like beam STD-M-C, in the Loadsets 5-6 and 9-10 is less than 0.7 and in the other loadsets is greater than 0.7; in beam STD-M-D, the first loadset is greater than 0.7 and the second loadset is less than 0.7. For SCC beams, all load ratios are less than 0.7 during Loadsets 9-10 and 11-12. In the remaining specimens, some values are less than 0.7

while others are greater than 0.7, but without a constant trend. While better correlation existed between load ratio and beam damage in specimens cast with SCC than for clam ratio, it was still poor. The material properties and load history investigated in this study may have contributed to this poor correlation.

According to the NDIS-2421 criterion, for beam STD-M-C, the first two loadsets and Loadset 7-8 (which was less intense than Loadset 5-6) were classified into the minor damage zone. The Loadset 5-6 was classified into the intermediate damage zone, which corresponds to the cracking load. For prestressed concrete beam, it is reasonable to classify them into intermediate. The Loadset 9-10 was classified into heavy damage zone which corresponds to 95% of P_n . For beam SCC-MS-C, the Loadset 9-10 was classified into the heavy damage zone but the Loadset 11-12 classified into the intermediate damage zone. The data collected in this study revealed that the limits classified for qualification can be used on conventionally consolidated concrete beams but the data of calm ratio and load ratio for the SCC beams are more scattered.

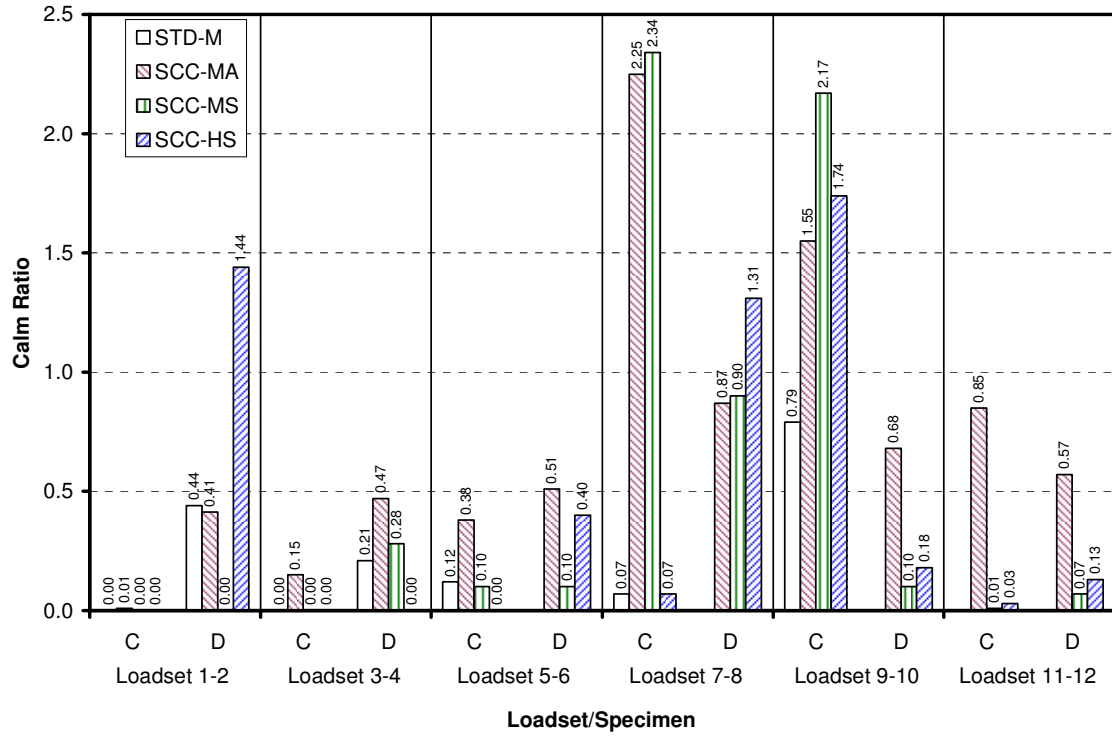


Figure 5-12: Calm ratios for loadset/specimen combinations

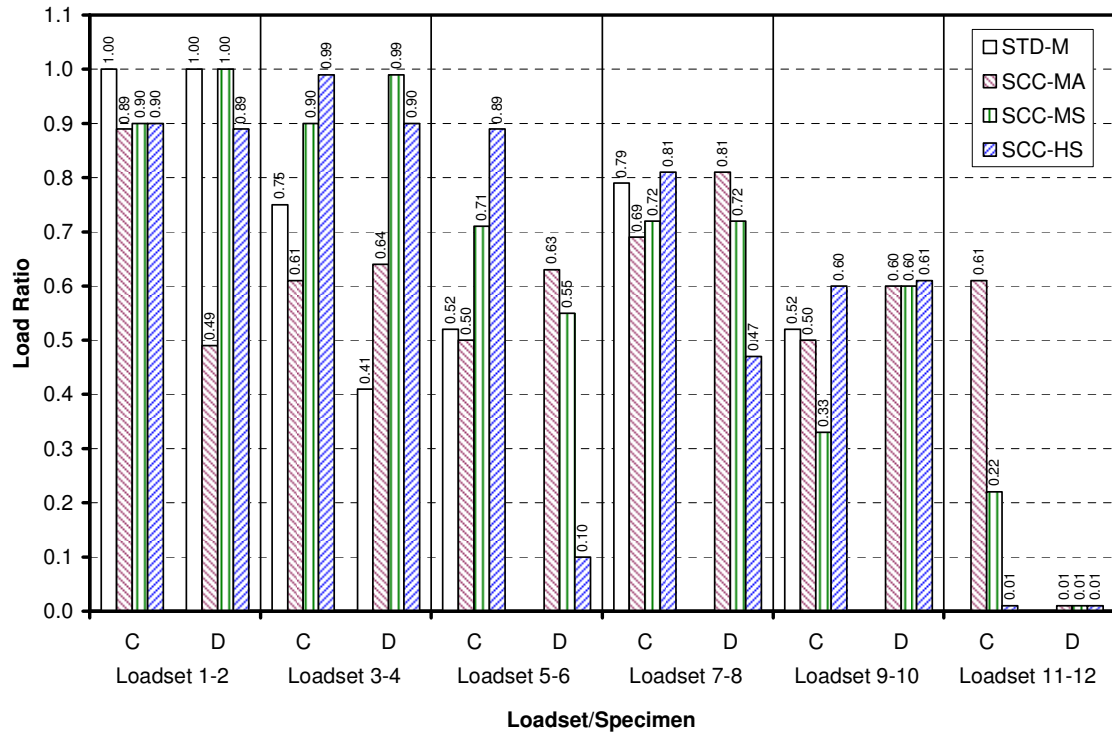


Figure 5-13: Load ratios for loadset/specimen combinations

Relaxation Ratio was computed for the first cycle of each load set. The calculated values for each load set are listed in Appendix E. The results of relaxation ratio for beams C and D are shown in Figure 5-14. For conventionally consolidated concrete beams STD-M-C and STD-M-D, the relaxation ratio never exceeded the threshold value of 1.0 for indicating beam damage (Colombo et al. 2005). On the other hand, for Beam SCC-MA-D, the relaxation ratio exceeded the threshold value of 1.0 in all loadsets. For beams SCC-MS-C and SCC-MS-D, the relaxation ratios for first four loadsets were less than 1.0 and for the final two loadsets were greater than 1.0. In the remaining cases, some values are greater than 1.0 and some values are less than 1.0, without an identifiable trend. As discussed by Colombo et al. (2005), the beam size, loading path, and the properties of concrete could all affect the results. The relaxation ratio evaluation method proposed for reinforced concrete could not be applied reliably for either SCC or conventionally consolidated concrete beams.

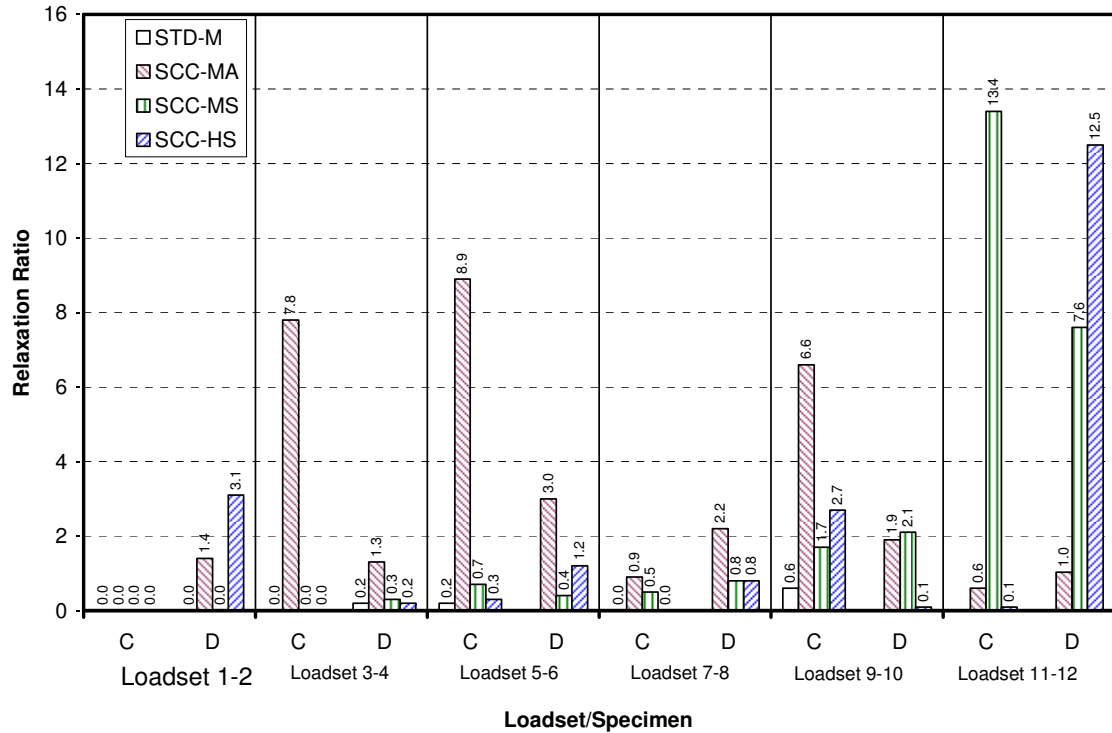


Figure 5-14: Relaxation ratios for loadset/specimen combinations

The peak cumulative signal strength ratio, *Peak CSS Ratio*, was calculated for each load set. The calculated values for each load set are listed in Appendix E. The results of CSS ratio calculations for beams C and D are shown in Figure 5-15. No clear trend can be identified. There are extremely high values in Loadset 7-8 for SCC-HS-D and in Loadset 11-12 for SCC-HS-D. The high values of CSS ratio were caused by a sudden increase in AE activity during the load hold at the second load hold in the loadset. It is difficult to determine what caused the increased AE activities. As previously discussed, AE activities are dependent on material properties, specimen size, load history and other factors. There was no AE signal strength recorded for SCC-HS-C during the load hold in load Cycle 10, so the CSS ratio for this loadset is zero. The CSS ratio values for both conventionally consolidated prestressed concrete beams and SCC prestressed concrete beams were more scattered than in research reported by Ridge and Ziehl (2006). The

results obtained from the AE data recorded did not reveal a clear trend. Therefore, this approach appears to be less effective for prestressed concrete than for reinforced concrete beams. The limits of CSS ratio application need to be further investigated.

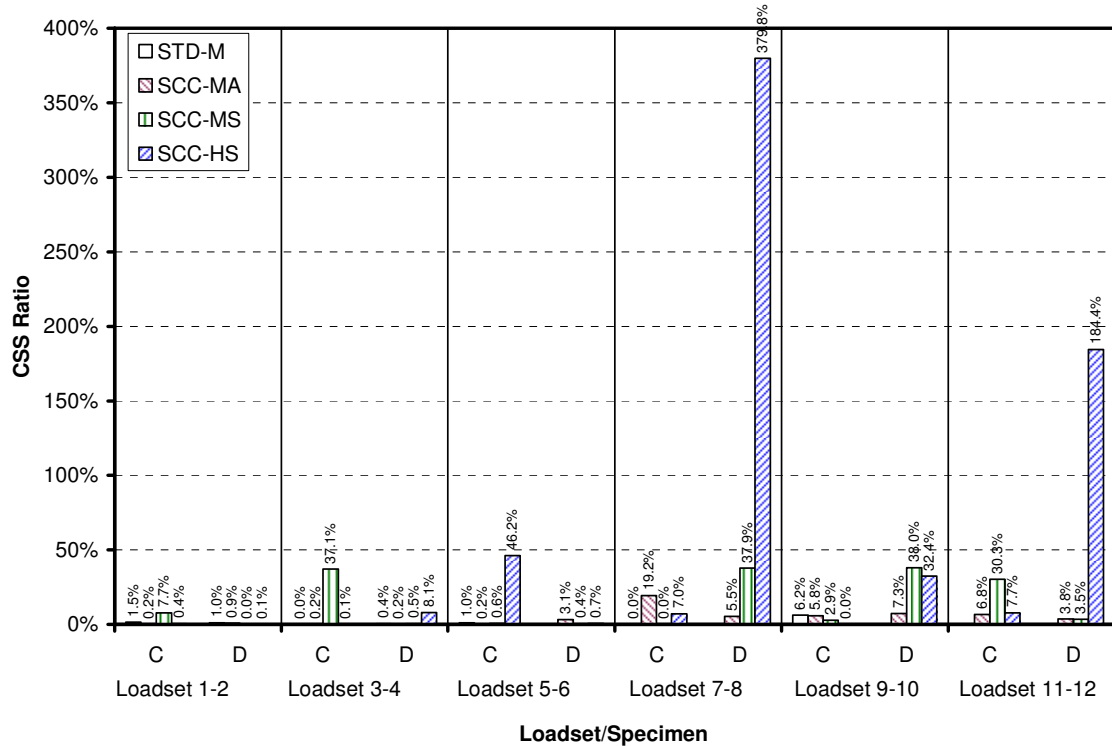


Figure 5-15: Peak CSS ratios for loadset/specimen combinations

The signal strength moment ratio, *SSM Ratio*, was calculated for each loadset based on the ratio of signal strength moment (SSM) recorded during the reload hold of a loadset to the initial load hold of that same loadset. The SSM ratio results for each loadset are reported in Appendix E. The relationship of SSM for first and second loading cycles of each loadset is shown in Appendix G.

The results of SSM ratio for beams C and D are shown in Figure 5-16. For beam STD-M-C, the SSM ratio of 2.7% corresponded to the actual flexural cracking load. The SSM ratio value of 0.0% for Loadset 7-8 is observed. The maximum load level applied in Loadset 7-8 is less than the first flexural cracking load. For the final loadset, the SSM

ratio was 4.3%. For beam STD-M-D, the SSM ratio for Loadset 3-4 was 2.6%. This value was close to SSM ratio at the first cracking load in STD-M-C. For conventionally consolidated concrete beams, it is clear that the trend of SSM ratio increases with increasing level of damage. During the load hold period for a beam that has experienced little or no previous damage, the SSM ratio is very small. When the SSM ratio is greater than 4%, the beam has experienced heavy damage.

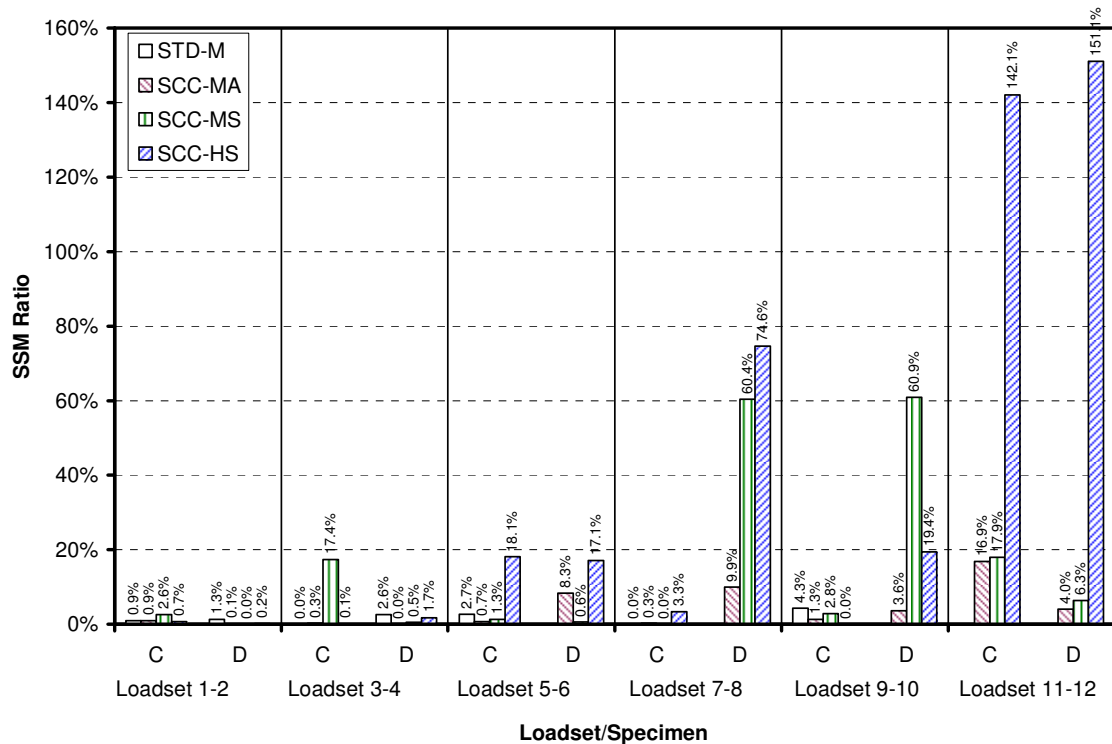


Figure 5-16: SSM ratios for loadset/specimen combinations

As shown in Figure 5-16, the SSM ratio obtained from SCC prestressed beams did not reveal as clear a trend. High values for SCC-MS-C in Loadset 3-4 and for SCC-HS-C and SCC-HS-D in Loadset 5-6 were observed. There are high values in Loadsets 9-10 and 11-12 for SCC-HS-D which were caused by sudden increases in AE activity during the second load hold of each cycle. The value of 0% for SCC-HS-C in Loadset 9-10 was observed due to no AE activity being recorded during this load hold. From the analysis of

all of the SSM ratio data, it can be concluded that very little reliable relationship existed between SSM ratio and beam damage for all SCC specimens in the study. From the results above, reasonable correlation between the specimen damage level and SSM evaluation criterion was observed for conventionally consolidated concrete beams; however, the relationship was not as reliable for SCC beams.

In summary, the results using the AE evaluation criteria *Relaxation Ratio* and *CSS Ratio* did not reveal a clear trend for both the conventionally consolidated concrete beams and SCC beams. A reasonably good correlation between specimen damage level and both the NDIS-2421 quantitative assessment criterion and SSM ratio evaluation criterion was observed for the conventionally consolidated concrete beams; however, the correlation was relatively poor for the SCC beams. Further work is needed to establish in which conditions the AE evaluation criteria can be applied reliably.

5.6 CONCLUSIONS

The results of this study support the following primary conclusions:

1. Flexural testing results indicated that SCC specimens performed as well as specimens constructed with standard concrete. Therefore, it can be concluded that the SCC mixtures did not have an adverse effect on the overall flexural bond performance of these specimens.
2. The experimental results indicated that there is a clear relationship between the AE signal strength and the behavior of SCC beams. AE signal strength could be used as an approach for assessing the structural condition of a prestressed concrete beams with SCC.

3. The cumulative signal strength emitted by SCC concrete beams was not significantly different from that emitted by conventionally consolidated concrete beams. As a result, it can be concluded that the cumulative AE activities of SCC beams were similar to conventionally consolidated concrete beams.
4. Different AE sources can be distinguished by comparing amplitude and duration data. For both SCC prestressed concrete beams and conventionally consolidated prestressed concrete beams, the initiation of early microcracks or local slips and the mechanical rubbing of interlocked faces resulted in lower AE signal amplitude, while the initiation of primary main flexural cracks produced higher signal amplitudes.
5. The AE evaluation criteria *Relaxation Ratio* and *CSS Ratio* did not reliably indicate the damage level of prestressed beams constructed of conventionally consolidated concrete or SCC.
6. Good correlation between specimen damage level and the modified NDIS-2421 AE assessment criterion and the SSM ratio AE evaluation criterion was observed for the conventionally consolidated concrete beams; however, the correlation was relatively poor for the SCC beams. The limits of application for these criteria need to be further investigated.

The findings of this research indicate that AE parameters can provide a useful tool to study the behavior of both conventionally consolidated concrete beams and SCC beams. Future research needs to focus on defining the limits of AE application and on confirmation of its validity.

CHAPTER 6
NONDESTRUCTIVE STRENGTH EVALUATION OF PRESTRESSED
CONCRETE BEAMS

6.1 INTRODUCTION

Prestressed concrete beams are widely used in highway bridges, parking garages, floor systems and other building applications. Through the years, some sections have deteriorated, and repairs must be made for safety. There is a clear need for evaluation of the structural performance of prestressed concrete beams.

The American Concrete Institute (ACI) recommends a static load test (ACI 318) and is also considering a cyclic load test (ACI 437) to evaluate the structural performance of existing structures. The static load test requires load to be sustained for 24 hours and behavior to be monitored for another 24 hours after the load has been removed. The Cyclic Load Test (CLT) described by ACI 437 (Appendix A of ACI 437R-03) is a relatively new technique that offers some advantages over the static load test outlined in Chapter 20 of ACI 318 (2008). The CLT method not only reduces the time required to perform an in-place load test, but it also provides more complete insight into structural behavior than the existing static load test method.

Another method for evaluation of existing prestressed concrete structures uses the acoustic emission (AE) signal monitoring technique. AE is defined by the American

Society of Testing and Materials (ASTM) in its *Standard Terminology for Nondestructive Evaluations* (ASTM E 1316) as “the class of phenomena whereby transient elastic waves are generated by the rapid release of energy from localized sources within a material, or the transient elastic waves so generated.” The AE monitoring technique differs from the static load test and CLT method. Instead of using the mechanical behavior of the beam to assess its condition, the AE monitoring technique uses the energy released by the structure during loading to assess its integrity. The AE technique can detect and evaluate integrity throughout an entire structure during a single test (Ohtsu 1989).

In this study, four prestressed concrete T-beams—one damaged beam and three undamaged beams—were loaded in cycles of increasing intensity to failure in an attempt to investigate the feasibility of using CLT and AE techniques to assess the performance of prestressed concrete beams. The resulting effectiveness of the ACI 437 CLT method and various AE evaluation criteria for prestressed concrete beams is discussed in this chapter.

6.2 RESEARCH SIGNIFICANCE

Although extensive research has been conducted on the evaluation of integrity of reinforced concrete beams (Mettemeyer 1999; Ohtsu et al. 2002; Masetti 2005; Ridge and Ziehl 2006), only a limited number of investigations have been focused on the damage monitoring of prestressed concrete structures (Hearn et al. 1997; Yopez 1999; Chotichai 2001). In this paper, two nondestructive testing techniques, CLT and AE, were employed to evaluate prestressed concrete beams. The CLT method, proposed in Appendix A of ACI 437R (2003), can significantly reduce the required time to perform a load test evaluation relative to static load testing. The AE technique can also provide rapid and

valuable insight into the behavior and damage mechanisms of prestressed concrete structures. The results from CLT assessment criteria were compared to the results from the AE evaluation criteria, and both methods show promise as techniques for nondestructive testing of prestressed concrete beams.

6.3 LOAD TEST METHODS

6.3.1 CYCLIC LOAD TEST METHOD

The CLT involves applying load in quasi-static load cycles. The full test sequence for a beam consists of six load cycles; each load cycle includes five load steps. Each of the six CLT load cycles is denoted on Figure 6-1 by a circled letter from A to F. The additional cycles (numbered 1, 2, 5 and 6), which are not part of the CLT protocol, were used only for AE testing. In Figure 6-1, the vertical axis corresponds to the applied test load and the horizontal axis indicates the cumulative time during the testing sequence. Each load cycle starts at a minimum load level; loading is increased in steps up to the cycle's maximum load level and then decreased to the minimum value using the same load steps. Each load cycle is repeated one time (ACI 437R 2003). Each load step marked by an ellipse was maintained for four minutes. Each of the other loading/unloading steps had an elapsed time of two minutes. All loads were applied and maintained via manual displacement control using a closed-loop hydraulic testing system.

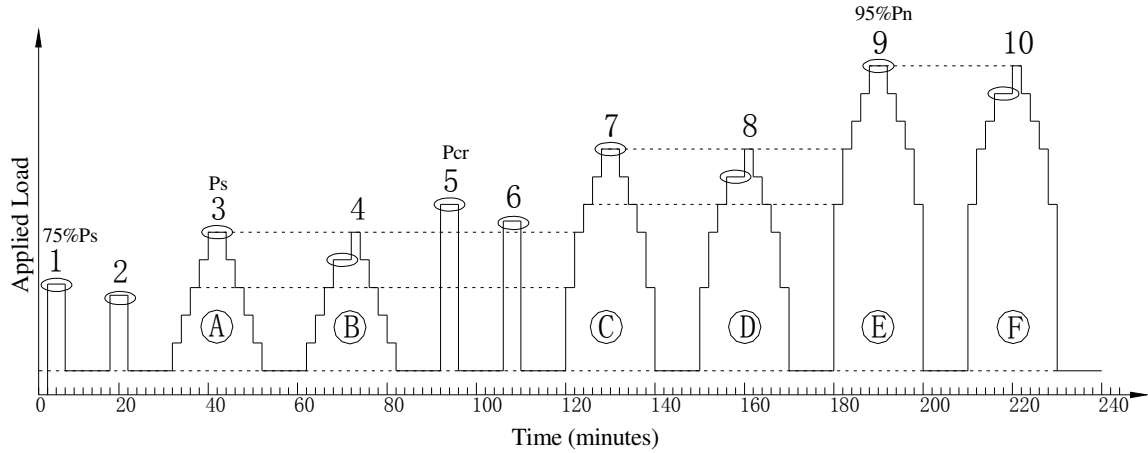


Figure 6-1: Load cycles and steps

The evaluation criteria defined for CLT are repeatability, permanency, and deviation from linearity (ACI 437R 2003). These three parameters that have been established to analyze the behavior of a tested beam are computed based on the displacement-response of the beam as described below:

Repeatability is the ratio of the difference between the maximum and residual deflections recorded during the second of two identical load cycles to the same difference in the first cycle of the pair. It is calculated using the following equation, referring to Figure 6-2:

$$\text{Repeatability} = \frac{\Delta_{\max}^B - \Delta_r^B}{\Delta_{\max}^A - \Delta_r^A} \times 100\% \quad (\text{Eq. 6.1})$$

Where:

Δ_{\max}^B = Maximum deflection in Cycle B under a load of P_{\max} ,

Δ_r^B = Residual deflection in Cycle B after unloading to a load of P_{\min} ,

Δ_{\max}^A = Maximum deflection in Cycle A under a load of P_{\max} , and

Δ_r^A = Residual deflection in Cycle A after unloading to a load of P_{\min} .

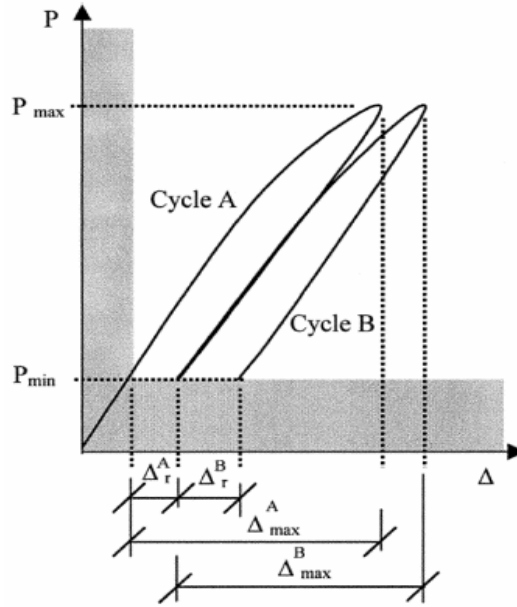


Figure 6-2: Example of load-versus-deflection curve for two cycles
(From ACI 437R 2003)

Based on the work of Mettemeyer (1999), ACI 437 date recommends that 95 percent is the lower limit deemed acceptable to indicate repeatability in an in-service structure.

Permanency is the amount of permanent change resulting from a loading. It is expressed as the ratio of residual deflection to maximum cycle deflection, both measured during the second of two identical load cycles. This computation is summarized by Equation (6.2):

$$\text{Permanency} = \frac{\Delta_r^B}{\Delta_{\max}^B} \times 100\% \quad (\text{Eq. 6.2})$$

Based on the work of Mettemeyer (1999), ACI 437 recommends that 10 percent is the upper limit deemed acceptable to indicate deflection permanency in an in-service structure.

Deviation from linearity represents the amount of nonlinear behavior of the beam being tested. As the damage increases, the beam response becomes more nonlinear. For

the purpose of measuring the deviation from linearity, the linearity of the response is computed for each load level as indicated in Figure 6-3. The linearity for a particular load level is defined relative to the slope of the load versus deflection curve for the first load cycle. The load-deflection envelope is constructed by connecting the points corresponding to only those loads that are greater than or equal to all previously applied loads. The linearity of any point i on the load-deflection envelope is the percent ratio of the slope of that point's secant line to the slope of the reference secant line as shown in the figure:

$$\text{Linearity} = \frac{\tan(\alpha_i)}{\tan(\alpha_{ref})} \times 100\% \quad (\text{Eq. 6.3})$$

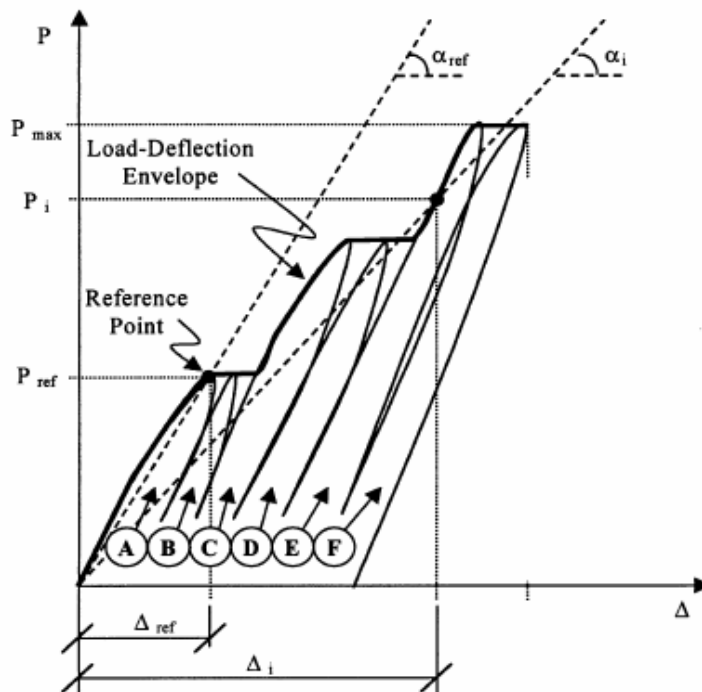


Figure 6-3: Schematic load-versus-deflection curve for six cycles (from ACI 437R 2003)

The deviation from linearity of any point on the load-deflection envelope is the complement of the linearity of that point, as shown in Equation (6.4):

$$\text{Deviation from Linearity}_i (I_{DL}) = 100\% - \text{Linearity}_i \quad (\text{Eq. 6.4})$$

Based on the work of Mettemeyer (1999), ACI 437 recommends 25 percent as the upper limit deemed acceptable to indicate deviation-from-linearity in an in-service structure.

If a beam is initially uncracked and becomes cracked during loading, the change in flexural stiffness as a result of a drastic change in moment of inertia at the cracked locations can produce a very high deviation from linearity that is not necessarily related to degradation in strength (Masetti 2005). For such a case, deviation from linearity should be computed relative to the deflection behavior in the cracked condition.

6.3.2 ACOUSTIC EMISSION METHOD

The AE nondestructive testing technique is based on the detection and conversion of high frequency elastic waves to electrical signals. By evaluating AE parameters from one or more transducers, an assessment of the integrity of the beam can be made.

Several AE evaluation criteria have been proposed to evaluate structural integrity (Ohtsu et al. 2002; Colombo et al. 2005; Ridge and Ziehl 2006). In this paper, two evaluation criteria, NDIS-2421 criterion (Ohtsu et al. 2002) and the newly proposed Signal Strength Moment Ratio Evaluation, were applied to assess the damage levels of prestressed concrete beams.

NDIS-2421 Criterion—The NDIS-2421 quantitative assessment criterion was adopted by the Japanese Society for Nondestructive Inspections (JSND). Based on the observed AE Kaiser effect (Ohtsu et al 2002), two ratios, the load ratio and the calm ratio, are established to assess the damage incurred by a reinforced concrete beam. The load ratio for a cycle, which is basically the same as the Felicity ratio (Ridge and Ziehl 2006), is

defined as the load at the onset of AE activity in the subsequent loading divided by the maximum previous load. The calm ratio is defined as the number of cumulative AE activities during the unloading process of a cycle divided by the total AE activities during the last loading cycle up to the maximum. When the calm ratio is plotted versus the load ratio, the general extent of damage can be classified according to the ratio values relative to prescribed limit values for each damage state. For reinforced concrete beams, the limits of the classification were based on the basis of crack mouth opening displacement (CMOD) in tests (Ohtsu et al. 2002). Values of 0.05 for the calm ratio and 0.9 for the load ratio are used to classify the beam damage.

Signal Strength Moment Ratio Evaluation—This evaluation method is based on a time-weighted parameter, signal strength moment (SSM), which is recorded during the load hold. Since the AE signal strength is a function of amplitude and duration of signal, it is a better measure of beam condition than other AE parameters. Having a larger proportion of AE activities occurring later rather than earlier during a period of sustained load (“load hold”) is taken as an indication of ongoing damage (Hamstad et al. 1992). SSM is the summation over the hold period of the quantities produced by multiplying the signal strength associated with each AE sensor hit by the time elapsed from the beginning of the load hold.

SSM is computed using the following equation:

$$SSM = \sum_i^n t_i S_i \quad (\text{Eq. 6.5})$$

where n is the total number of hits occurring during the load hold, t_i is the time from the beginning of the hold to the i th hit and S_i is the signal strength occurring in the i th hit.

SSM ratio is expressed as:

$$\text{SSM Ratio} = (\text{SSM for the second hold period} / \text{SSM for the first hold period}) \times 100\% \quad (\text{Eq. 6.6})$$

To be consistent, the same time length for the two load holds should be used. In this study, a hold period of 240 seconds was used for evaluation. If the actual hold period exceeded this limit, only the first 240-second period of the AE data were used.

6.4 EXPERIMENTAL INVESTIGATION

6.4.1 SPECIMEN DESCRIPTION

The test specimens consisted of four T-beams, denoted STD-M-A, STD-M-B, STD-M-C and STD-M-D, had the same cross section, and differed primarily in span length. The properties of the test specimens are listed in Table 6-1. The beam STD-M-A was subjected to a damaging applied load prior to testing, while the other three beams experienced no significant applied loading prior to testing. The specimens were prestressed with two seven-wire, low-relaxation, Grade 270 ½-in. “special” diameter strands. Four Grade 60 No.3 reinforcing bars were provided as top-flange longitudinal reinforcement. Transverse reinforcement was also provided in the form of No.3 reinforcing bars. In addition, Grade 60 No. 3 reinforcing bars were also used for the shear reinforcement. For each beam length, a slightly different stirrup layout was used. Details of specimens were reported by Levy (2007).

Table 6-1: Test specimen properties

Beam	Span m (in.)	Section m (in.)	$\frac{a}{d_p}$	f'_c MPa (psi)	$M_{n,calc}$ kN-m (kip-ft)	M_{max} kN-m (kip-ft)	Failure Type
STD-M-A	7.01 (276)	610×381×152 (24×15×6)	9.2	43.6 (6320)	130 (96.0)	145 (107)	Flexure
STD-M-B	4.98 (196)		6.1			138 (102)	Flexure
STD-M-C	3.96 (156)		4.6			154 (113)	Flexure
STD-M-D	2.95 (116)		3.1			141 (104)	Shear- tension

Note:

f'_c = 28-day compressive strength of concrete.

d_p = Effective depth.

a = Shear span.

$M_{n,calc}$ = Calculated nominal moment capacity.

M_{max} = Ultimate moment resisted during flexural test.

Four beams were tested in flexure under symmetric four-point loading in a laboratory. Loading was applied by displacement of a hydraulic actuator attached to a reaction frame. A spreader beam was used to divide this applied load equally between two load points via rollers. In this manner, a 0.9-m (3-ft) length of uniform applied bending moment was induced between the load points, with a region of uniform applied shear between each load point and the adjacent support.

6.4.2 LOADING PATTERNS

In addition to the load cycles prescribed for the CLT method, two extra pairs of load cycles (Cycles 1, 2, 5, and 6 – see Figure 6-1) were added to the beam test regimen for use in AE testing. AE data was collected and interpreted for all five pairs of load cycles, which were completed in the sequence indicated in Figure 6-1. In this manner, the AE data and CLT data for each specimen were collected in a single test sequence.

All loads were applied via manual displacement control using a closed-loop hydraulic testing system. The load steps marked by an ellipse in Figure 6-1 were maintained for four minutes. All other loading and unloading steps had a duration of 2 minutes.

The levels of applied loading that were used in the various load steps were functions of four values of load, P_{min} , P_s , P_{cr} and P_n , which were determined prior to the test for each specimen. The load values for each specimen are detailed in Table 6-2.

Table 6-2: Summary of calculated load step values

Beam	P_s , kN (kips)	P_{cr} , kN (kips)	P_n , kN (kips)
STD-M-A	37.7 (8.5)	51.2 (11.5)	74.0 (16.6)
STD-M-B	61.7 (13.9)	84.2 (18.9)	121 (27.1)
STD-M-C	87.8 (19.7)	118 (26.6)	169 (38.0)
STD-M-D	148 (33.3)	197 (44.2)	272 (61.2)

Note:

P_s = Service-level design load calculated prior to flexural load testing,

P_{cr} = Cracking load calculated using strain compatibility prior to flexural load testing, and

P_n = Ultimate load predicted based on nominal flexural capacity.

The first of these four loads, P_{min} , was the minimum load, 2.2 kN (500 lbs), that was maintained after the start of the test. This minimum load was needed to keep loading equipment and sensors engaged throughout the test. The next of the four loads, P_s , was the applied load computed to cause zero net flexural stress in the bottom fiber of the beam at the load points. This corresponded to the service-level design load for Alabama Department of Transportation (ALDOT) bridge girders. The next load value which was critical to the loading cycles was the flexural cracking load, P_{cr} . This load value, unlike the other three, was not determined before the test. The load for cycle 5 was applied at a

rate of approximately 0.4 kN/sec (100 lb/sec) until the cracking load was reached.

Achievement of the cracking load was signaled by a slight drop in load, accompanied by visible cracking. The actual cracking load, P_{cr} , was used to determine the load value for the AE testing. Finally, the last of the four load values determined prior to testing, P_n , was the applied load computed to cause a bending moment equal to the nominal moment capacity, M_n , at the critical section. The nominal moment was computed using AASHTO LRFD procedures (AASHTO 2006).

The values of load for the five loadsets are detailed in Table 6-3. For the first loadset 1-2, cycle 1 and 2 each consisted of only one loading step followed by an unloading step. The maximum load level for Cycle 1 was equal to 75 percent of P_s . The maximum load level for Cycle 2 corresponded to 90 percent of the previous peak load of Cycle 1 to allow for evaluation of the Felicity effect (Ridge and Ziehl 2006). Both were held four minutes. For the second Loadset 3-4, Cycles 3 and 4 (corresponding to Cycles A and B of the CLT Method of ACI 437R 2003) each consisted of five load steps. For the third loadset 5-6, cycle 5 and 6 each consisted of only one loading step followed by an unloading step. For the fourth loadset 7-8, cycle 7 and cycle 8 (corresponding to Cycles C and D of the CLT Method of ACI 437R 2003) each consisted of five load steps. For the fifth loadset, cycle 9 and cycle 10 represented ACI 437R 2003 CLT Cycles E and F, respectively.

Table 6-3: Load step value

Load set	Cycle	Load Step				
1-2	1	$P_1 = 0.75P_s$				
	2	$P_2 = 0.90P_1$				
3-4	3	$P_{31} = 0.25P_s$	$P_{32} = 0.50P_s$	$P_{33} = 0.75P_s$	$P_{34} = 0.90P_s$	$P_{35} = P_s$
	4	$P_{41} = P_{31}$	$P_{42} = P_{32}$	$P_{43} = P_{33}$	$P_{44} = P_{34}$	$P_{45} = P_{35}$
5-6	5	$P_5 = P_{cr}$				
	6	$P_6 = 0.90P_5$				
7-8	7	$P_{71} = 0.75P_s$	$P_{72} = P_s$	$P_{73} = (P_{72} + P_{74})/2$	$P_{74} = 0.90P_{75}$	$P_{75} = (P_s + P_{95})/2$
	8	$P_{81} = P_{71}$	$P_{82} = P_{72}$	$P_{83} = P_{73}$	$P_{84} = P_{74}$	$P_{85} = P_{75}$
9-10	9	$P_{91} = P_{73}$	$P_{92} = P_{75}$	$P_{93} = (P_{92} + P_{94})/2$	$P_{94} = 0.90P_{95}$	$P_{95} = 0.95P_n$
	10	$P_{101} = P_{91}$	$P_{102} = P_{92}$	$P_{103} = P_{93}$	$P_{104} = P_{94}$	$P_{105} = P_{95}$

After the final load of Cycle 10 had been applied, the test load was reduced to P_{min} and maintained for 10 minutes. All instruments were then removed before test beam was loaded to failure.

6.4.3 MEASUREMENT OF DISPLACEMENTS

Linear displacement potentiometers were used to measure all displacements.

Potentiometers were used to measure vertical deflection relative to the floor under each of the load points, as well as directly under midspan. Using the resulting measurements, the midspan displacement of the beam relative to the supports was computed. Complete details of displacement-measuring process have been reported by Levy (2007).

6.4.4 AE TESTING

A 24-channel SAMOS[®] manufactured by Physical Acoustic Corporation (PAC) was used to perform AE monitoring during the load testing of the prestressed concrete beams.

Twenty-four PAC R6I-AST 50-kHz integral resonant AE sensors were mounted on three zones of the beam: ten sensors in the flexure zone in the region of maximum moment; three sensors in each anchorage zone (along the transfer length) to monitor strand slippage, and four sensors in each shear span. Specific information, including the hardware setup, graph setup, acquisition setup, filters, and location setup can be found in previous chapters.

The AE system was calibrated prior to a test, to recognize channels or sensors with low or high sensitivity. A background check lasting about 4 minutes was performed prior to loading the test specimen. The specimen remained undisturbed during this time. During the beam test, AE data was displayed in real time on a monitor with various screen options. These displays gave a visual indication of the progression of the beam to failure. At the same time, the data were stored on hard disk for post-test analysis. The recorded data were then converted to ASCII (American Standard Code for Information Interchange) format. The ASCII files were imported into the commercial statistical analysis software Origin[®] and analyzed using procedures written for this project within this software.

6.5 EXPERIMENTAL RESULTS AND DISCUSSION

The results of tests on the four prestressed concrete beams using the CLT Method and AE monitoring are discussed here.

6.5.1 STD-M-B

The beam STD-M-B failed in a flexural manner. No strand end slip was detected during this test. The first flexural cracking was observed during load cycle 7 with a value of 95.6 kN (21.5 kips), corresponding to a deflection of 5.6 mm (0.22 in.). The cracking

moment, M_{cr} , for this specimen was 10 percent greater than the calculated cracking moment, $M_{cr,calc}$. The maximum load reached for this specimen was 141.0 kN (31.7 kips), corresponding to a deflection of 102 mm (4.0 in.). The maximum moment resisted by this beam, M_{max} , was 6 percent greater than $M_{n,calc}$. The beam lost its load-carrying capacity due to strand rupture. No web-shear cracking was observed in this specimen. The crack pattern corresponding to the maximum load for this beam is depicted in Figure 6-4.

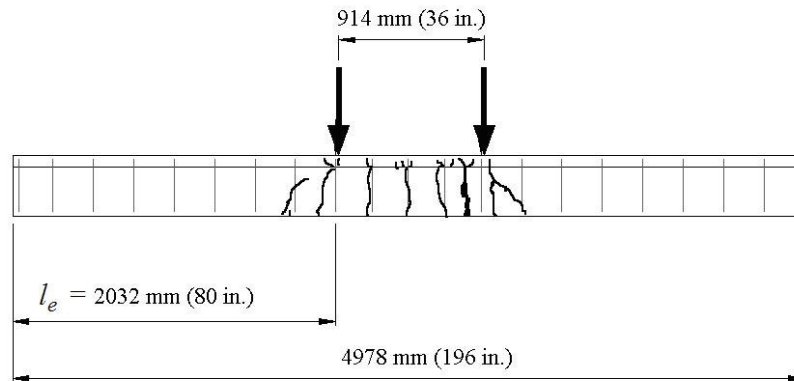


Figure 6-4: Crack pattern for STD-M-B at failure (Levy 2007)

Figure 6-5 is a time history of the load and deflection for the beam STD-M-B. The horizontal axis represents the cumulative time, in seconds, as the testing progressed. The right vertical axis shows the amount of load applied to the beams. The left vertical axis shows the deflection at the middle of the beam. The thick line represents the applied load and the thin line represents the deflection.

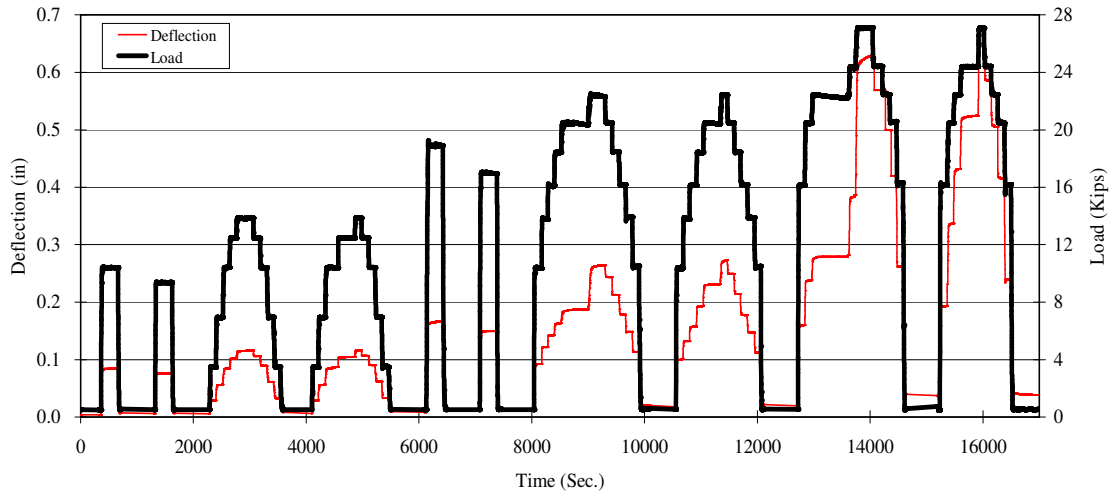


Figure 6-5: Time history of CLT for STD-M-B

(1 in. = 25.4 mm, 1 kip = 4.45 kN)

Figure 6-6 shows the portion of the load versus deflection curve corresponding to the ten load cycles. The thin line shows the behavior of the beam as it was loaded and unloaded repeatedly. The thick line represents the load-deflection envelope. This load deflection envelope was used to calculate the deviation from linearity for the CLT.

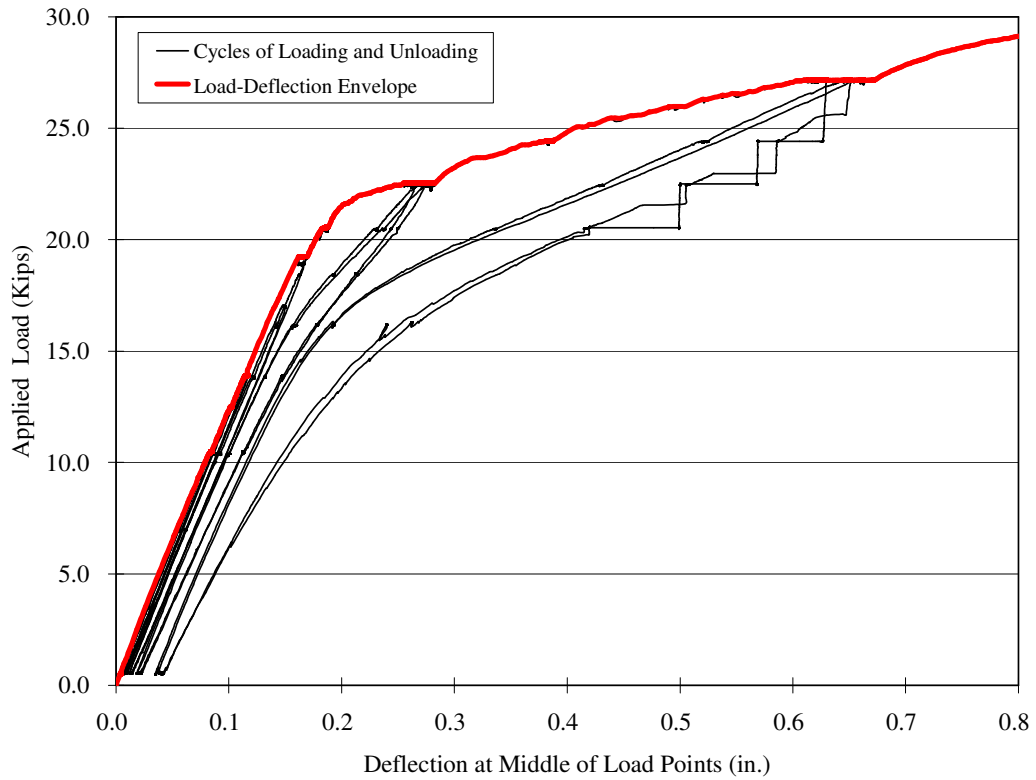


Figure 6-6: Load versus deflection curve for STD-M-B

The calculated numerical values for the three CLT evaluation criteria of repeatability, permanency, and maximum deviation from linearity are listed in Table 6-4; the acceptance limits recommended by ACI 437 are indicated in parentheses under each criterion. The repeatability and permanency criteria were satisfied for all load levels. The beam failed to satisfy the deviation-from-linearity criterion for the loads of Cycle 7 and higher.

Table 6-4: Summary of calculation for STD-M-B beam

Cycle	Δ_r (in.)	Δ_{max} (in.)	Permanency ($\leq 10\%$)	Repeatability ($\geq 95\%$)	Deviation ($\leq 25\%$)	Performance
Cycle 3(A)	0.0024	0.1097	0.7%	99.7%	4.2%	Pass
Cycle 4(B)	0.0007	0.1077			4.5%	Pass
Cycle 7(C)	0.0089	0.2520	1.5%	103.2%	28.8%	Failed
Cycle 8(D)	0.0038	0.2547			31.1%	Failed
Cycle 9(E)	0.0214	0.6102	1.2%	103.5%	64.0%	Failed
Cycle 10(F)	0.0072	0.6169			65.2%	Failed

The beam was uncracked initially and it became cracked as the load processed. The change in flexural stiffness as a result of a drastic change in moment of inertia at the crack location can produce a very high deviation from linearity that is not necessarily related to degradation in strength (Masetti 2005). For such a beam, deviation from linearity should be recalculated for the beam under a cracked condition.

To assess the adopted performance criteria for a damaged beam, two reference slopes were considered: α_{ref-1} , which was taken at the beginning of test when the beam was uncracked, and α_{ref-2} , which was taken at the beginning of the cycle right after the beam was cracked. In fact, it was possible to simulate the testing of a damaged structure by ignoring the cycles before the beam was cracked and thus start the load test at the cycle right after the beam cracked.

Figure 6-7 shows the deviation-from-linearity parameter versus time for two reference slopes considered for beam STD-M-B. The beam was uncracked initially and became cracked during Cycle 7. Using reference slope α_{ref-1} , the beam first failed to satisfy the criteria at a load of 99.6 kN (22.4 kips) during the ascending part of Cycle 7 (9041 seconds into the test). Using α_{ref-2} , the beam first failed at a load of 111.2 kN (25.0 kips)

during the ascending part of Cycle 9 (13,742 seconds). So, according to second reference slope, this CLT criterion indicates that the beam was failed to satisfy the assumed criteria in Cycle 9.

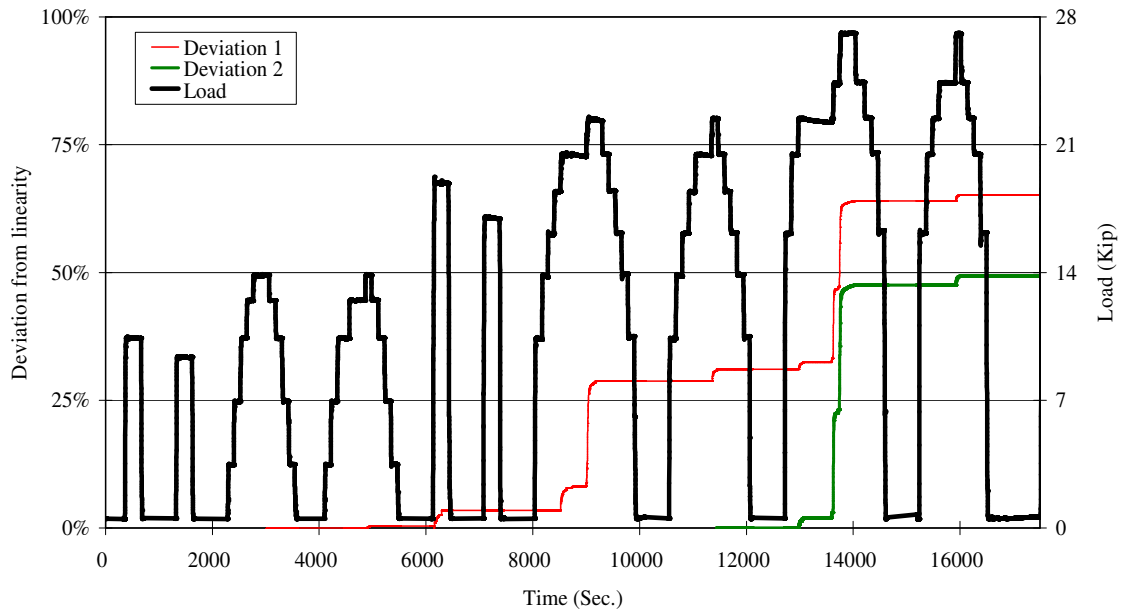


Figure 6-7: Load and deviation from linearity versus time for STD-M-B beam

In order to evaluate the effectiveness of AE methods for damage assessment, the NDIS-2421 assessment process was carried out. At each loading stage, two parameters—calm ratio and load ratio—were determined. The calculated values of the calm ratio and the load ratio are listed in the Table 6-5. For the previously undamaged beams (B, C, and D), the calm ratio was calculated only for the first load cycle of each loadset. The load ratio used was the ratio of the load at the onset of AE activity in the second loading cycle to the previous maximum experienced load. The data were plotted as shown in Figure 6-8, where the load ratio and calm ratio are indicated on the horizontal and vertical axes, respectively. The label above each point represents the corresponding loadset number.

Based on the work in Chapter 4, the classification limits are set as 0.7 for load ratio and 0.5 for the calm ratio. The areas of different damage are indicated.

Table 6-5: Summary of AE evaluation criteria results

Beam	Criterion	Loadset				
		1-2	3-4	5-6	7-8	9-10
STD-M-A	Calm Ratio	2.36	12.54	19.17	36.59	13.07
	Load Ratio	0.08	0.06	0.04	0.04	0.03
	SSM Ratio	6.0%	4.2%	6.8%	4.1%	15.1%
STD-M-B	Calm Ratio	0.02	0.05	0.45	0.27	0.78
	Load Ratio	1.00	0.83	0.77	0.68	0.54
	SSM Ratio	0.4%	0.0%	0.8%	2.8%	4.9%
STD-M-C	Calm Ratio	0.00	0.00	0.12	0.07	0.79
	Load Ratio	1.00	0.75	0.52	0.79	0.52
	SSM Ratio	0.9%	0.0%	2.7%	0.0%	4.3%
STD-M-D	Calm Ratio	0.44	0.21			
	Load Ratio	1.00	0.41			
	SSM Ratio	1.3%	2.6%			

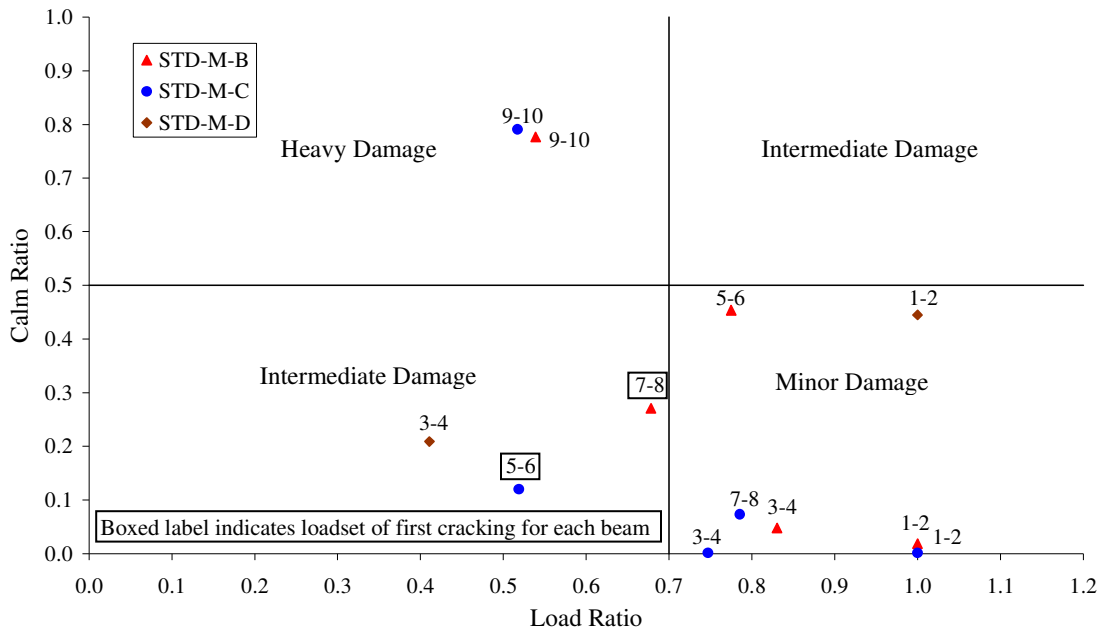


Figure 6-8: NDIS assessment for beams STD-M-B, STD-M-C, and STD-M-D

According to the NDIS-2421 criterion, for beam STD-M-B, the first three loadsets were classified into the minor damage zone. The loadset 7-8 was classified into the intermediate damage zone. These results agree with the actual observed beam condition because the first (flexural) cracking was experienced in loadset 7-8. Loadset 9-10 was classified into the heavy damage zone, which is in agreement with the actual beam condition as it had been subjected to 95 percent of its predicted capacity.

The SSM ratio was calculated for each loadset, and the results are shown in Table 6-5. The relationship of SSM for the first and second loading cycles of each loadset for beam STD-M-B is shown in Figure 6-9. The SSM ratio is given above each bar. For beam STD-M-B, the values of SSM for the first three cycles (minor damage) were close to zero. An SSM ratio of 2.8 corresponded to the loadset that included first flexural cracking (intermediate damage). For the final loadset (up to 95 percent of P_n and 89.5 percent of the actual ultimate strength) the SSM ratio increased to 4.9 percent. An acceptance criterion for use with this method may be determined from the values reported in Table 6-5. Based on the work described in Chapter 4, during the load hold period for beams that have experienced only minor or no damage, the SSM ratio is nearly zero. On the other hand, when the SSM ratio is greater than 4 percent, the beam has experienced significant damage. Application of this criterion indicates that this specimen was damaged in Cycle 9, which agrees with the observed state of the test specimen.

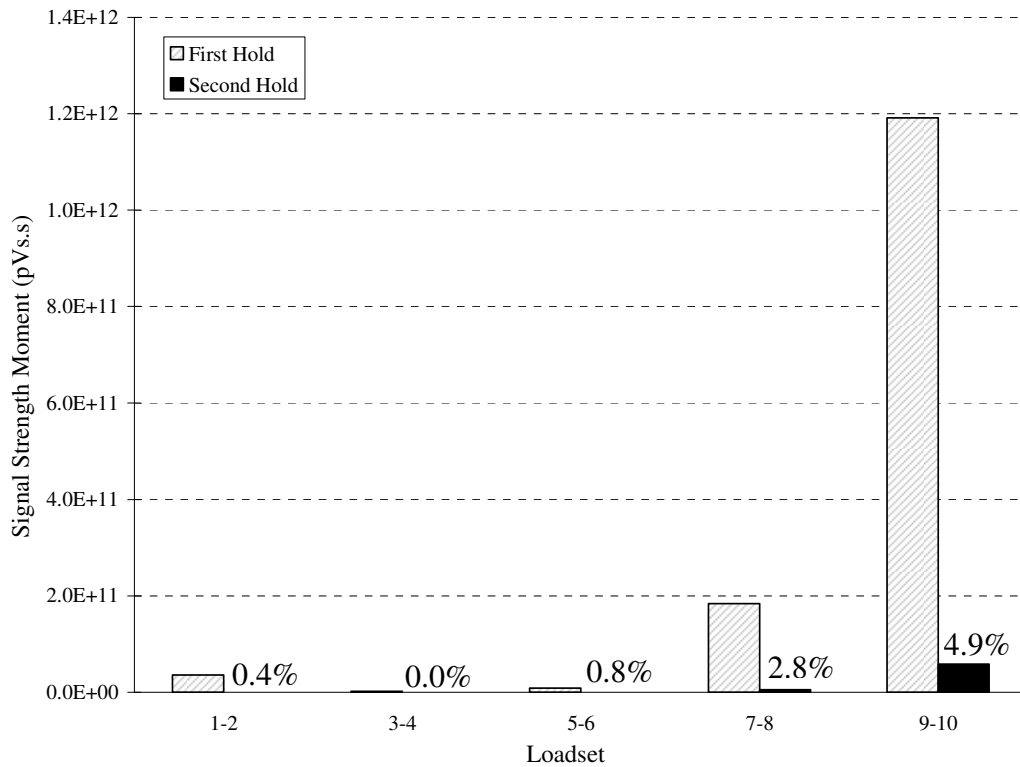


Figure 6-9: Signal strength moment during holds for beam STD-M-B

6.5.2 STD-M-C

This specimen failed in a flexural manner with moderate strand slip. The first flexural cracking was observed during load cycle 5 with a load of 142.3 kN (32.0 kips), corresponding to a deflection of 3.6 mm (0.14 in.). The cracking moment, M_{cr} , for this specimen was 16 percent greater than the calculated cracking moment, $M_{cr,calc}$. The maximum load reached for this specimen was 218.4 kN (49.1 kips), corresponding to a deflection of 86 mm (3.4 in.). The strand end slip experienced by the specimen at the peak load was 2.5 mm (0.1 in.). The maximum moment resisted by this beam, M_{max} , was 18 percent greater than $M_{n,calc}$. The beam lost its load-carrying capacity due to strand rupture. No web-shear cracking was observed in this specimen. The crack pattern corresponding to the maximum load for this beam is depicted in Figure 6-10.

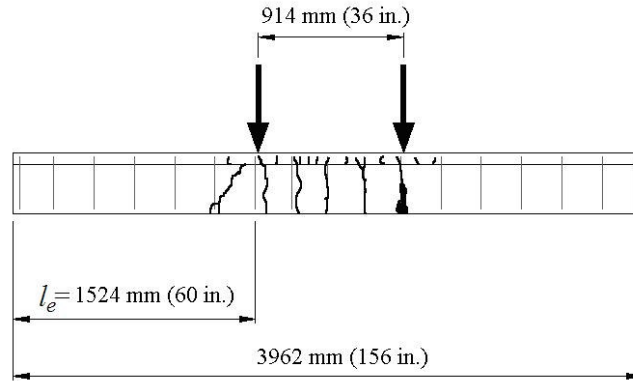


Figure 6-10: Crack pattern for STD-M-C at failure (Levy 2007)

Figures 6-11 is a time history of the load and deflection for the beam STD-M-C, and Figure 6-12 shows the portion of the load versus deflection curve corresponding to the ten load cycles. The calculated numerical values for the three CLT evaluation criteria of repeatability, permanency, and maximum deviation from linearity are listed in Table 6-6. The repeatability and permanency criteria were satisfied for all load levels. The beam failed to satisfy the deviation-from-linearity criterion for the loads of Cycle 9 and higher.

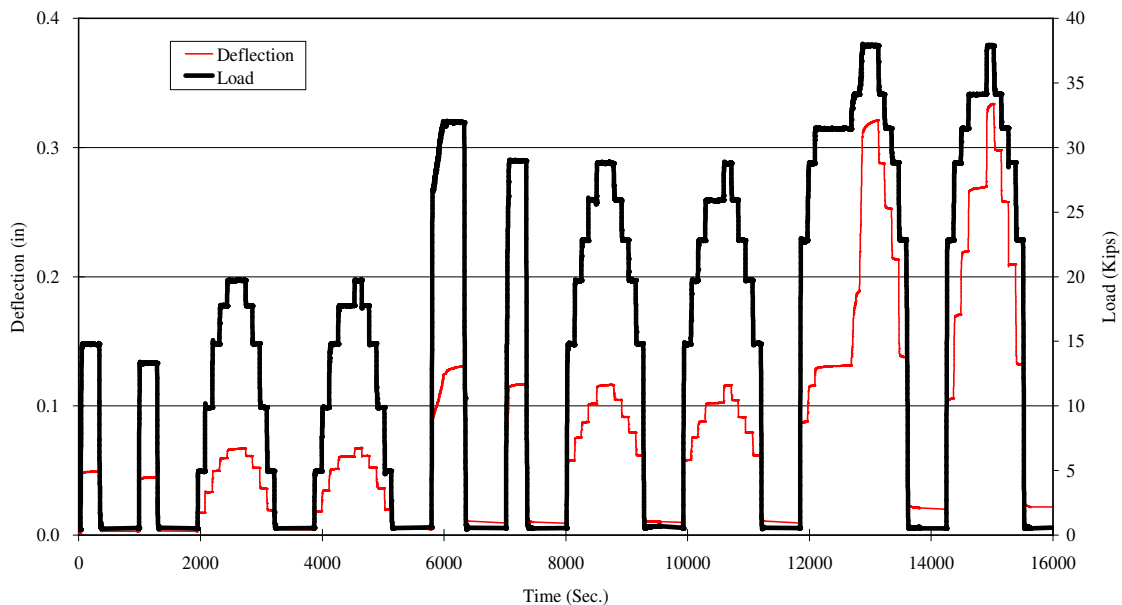


Figure 6-11: Time history of CLT for STD-M-C
(1 in. = 25.4 mm, 1 kip = 4.45 kN)

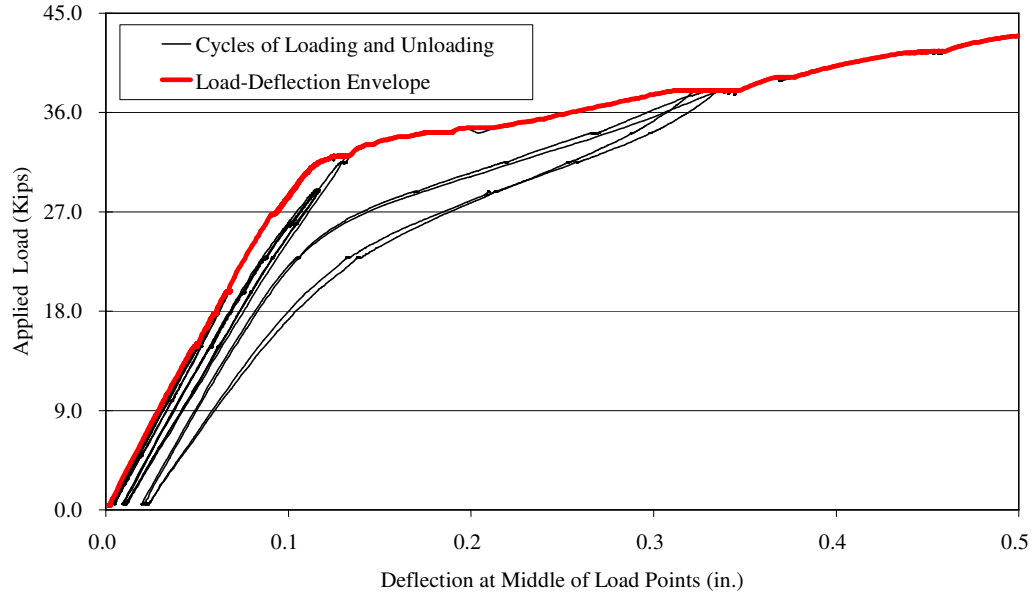


Figure 6-12: Load versus deflection curve for STD-M-C

Table 6-6: Summary of calculation for STD-M-C beam

Cycle	Δ_r (in.)	Δ_{max} (in.)	Permanency ($\leq 10\%$)	Repeatability ($\geq 95\%$)	Deviation ($\leq 25\%$)	Performance
Cycle 3(A)	0.0014	0.0641	1.4%	100.0%	1.6%	Pass
Cycle 4(B)	0.0009	0.0636			2.1%	Pass
Cycle 7(C)	0.0018	0.1073	1.8%	99.7%	18.1%	Pass
Cycle 8(D)	0.0019	0.1071			18.1%	Pass
Cycle 9(E)	0.0137	0.3119	1.1%	104.3%	60.4%	Failed
Cycle 10(F)	0.0035	0.3145			61.9%	Failed

The beam was uncracked initially and became cracked as the load increased. The deviation from linearity was accordingly recalculated. Figure 6-13 shows the deviation from linearity parameter versus time for two reference slopes considered for beam STD-M-C. The beam was uncracked initially and became cracked during load cycle 5. Using reference slope α_{ref-1} , the beam first failed at a load of 148.1 kN (33.3 kips) during the ascending part of Cycle 9 (12,710.5 seconds into the test). Using α_{ref-2} , the beam first failed at a load of 152.1 kN (34.2 kips) during the ascending part of cycle 9 (12,766.5

seconds). So, according to either reference slope, this CLT criterion indicates that the beam was beyond its usefulness in Cycle 9 at a load only slightly higher than the flexural cracking load.

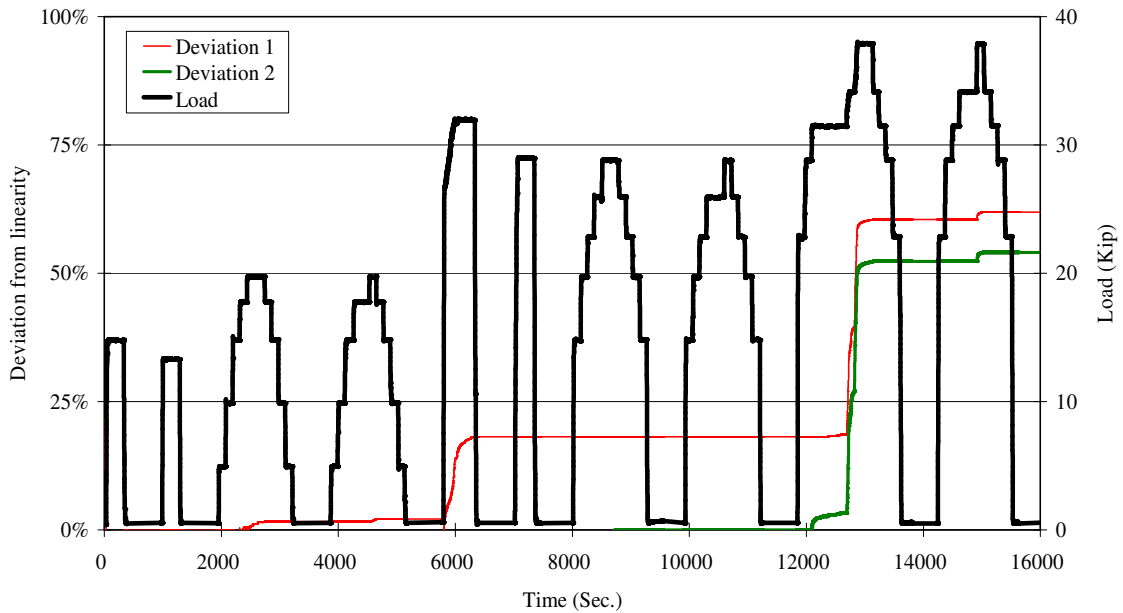


Figure 6-13: Load and deviation-from-linearity versus time for STD-M-C beam

The NDIS-2421 assessment process for beam STD-M-C was executed using the same procedure as for STD-M-B. The calculated values of the calm ratio and the load ratio are listed in Table 6-5. The areas of different damage for beam STD-M-C are indicated in Figure 6-8. The first two loadsets (before cracking) were classified into the minor damage zone. The loadset 5-6, in which flexural cracking occurred, was classified into the intermediate damage zone. Loadset 7-8, which was applied after cracking, but only up to a load less than the actual cracking load, falls in the minor damage zone. Loadset 9-10, which corresponded to 95 percent of P_n and 84.4 percent of the actual ultimate strength, was classified into the heavy damage zone.

The SSM ratio during loading was calculated for each loadset, and the results are shown in Table 6-5. For STD-M-C, the relationship of SSM for the first and second loading cycles of each loadset is shown in Figure 6-14. The SSM ratio is given above each bar. An SSM ratio of 2.7 percent corresponded to the first flexural cracking load, which is very close to the corresponding SSM ratio value of 2.8 percent for STD-M-B. For the final loadset (9-10), the SSM ratio was 4.3 percent, which indicates heavy damage according to the 4 percent limit proposed above.

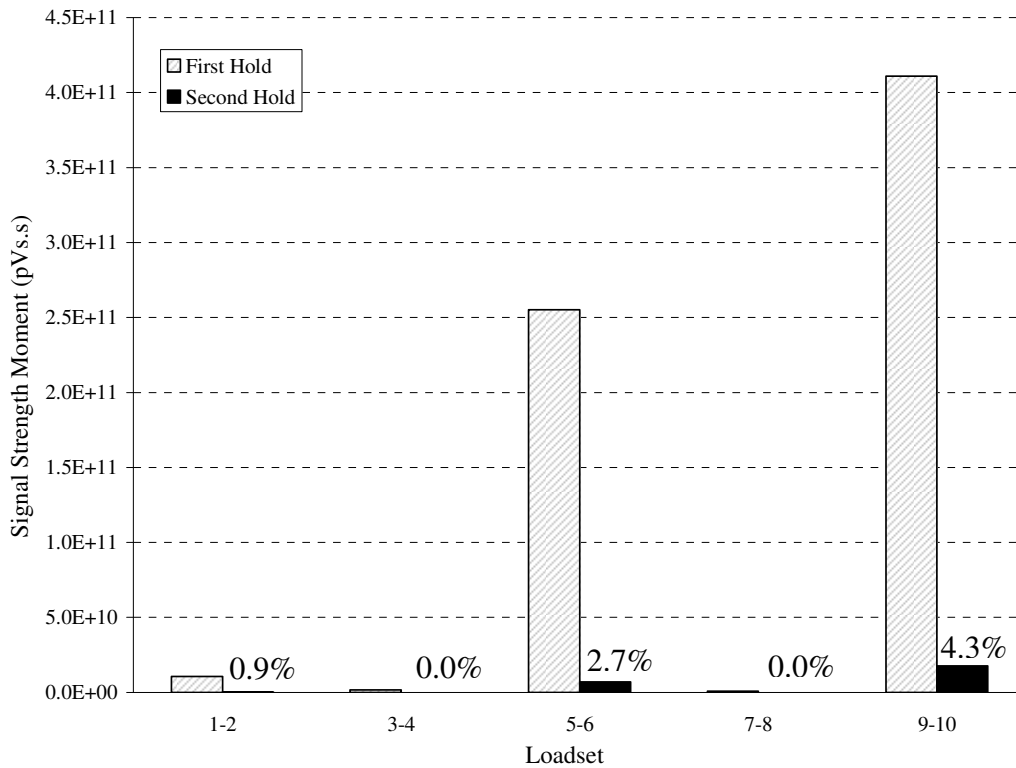


Figure 6-14: Signal strength moment during holds for beam STD-M-C

6.5.3 STD-M-D

The beam STD-M-D was suddenly damaged in Cycle 5 and suffered a shear-tension failure characterized by a gradual loss of strand anchorage due to bond deterioration after formation of a diagonal flexural-shear crack. The first cracking was observed in Cycle 5

with a value of 218.4 kN (49.1 kips), corresponding to a deflection of 1.8 mm (0.07 in.). The cracking moment, M_{cr} , for this specimen was 8 percent greater than the calculated cracking moment, $M_{cr,calc}$. The maximum load reached for this specimen was 223.3 kN (50.2 kips), corresponding to a deflection of 5.1 mm (0.2 in.). The strand end slip experienced by the specimen at the peak load was 2.5 mm (0.1 in.). The maximum moment resisted by this beam, M_{max} , was 75 percent of $M_{n,calc}$. The beam lost its load-carrying capacity due to concrete crushing after significant strand slip. Web-shear cracking was observed in this specimen. The crack pattern corresponding to the maximum load for this beam is depicted in Figure 6-15.

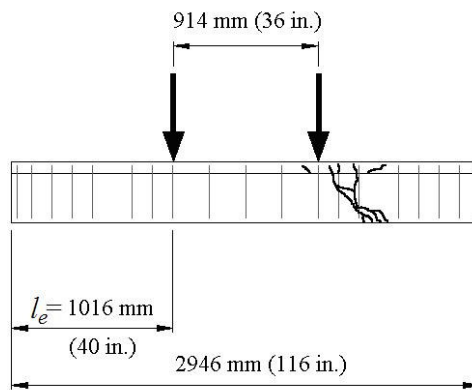


Figure 6-15: Crack pattern for STD-M-D at failure (Levy 2007)

Figures 6-16 is a time history of the load and deflection for the beam STD-M-D, and Figure 6-17 shows the portion of the load versus deflection curve corresponding to the four load cycles. The calculated numerical values for the three CLT evaluation criteria of repeatability, permanency, and maximum deviation from linearity are listed in Table 6-7. The repeatability, permanency and deviation-from-linearity criteria were satisfied for load Cycles 3 and 4.

Table 6-7: Summary of CLT evaluation for STD-M-D beam

Cycle	Δ_r (in.)	Δ_{max} (in.)	Permanency ($\leq 10\%$)	Repeatability ($\geq 95\%$)	Deviation ($\leq 25\%$)	Performance
Cycle 3(A)	0.0012	0.0462	1.7%	100.2%	7.3%	Pass
Cycle 4(B)	0.0008	0.0459			8.3%	Pass

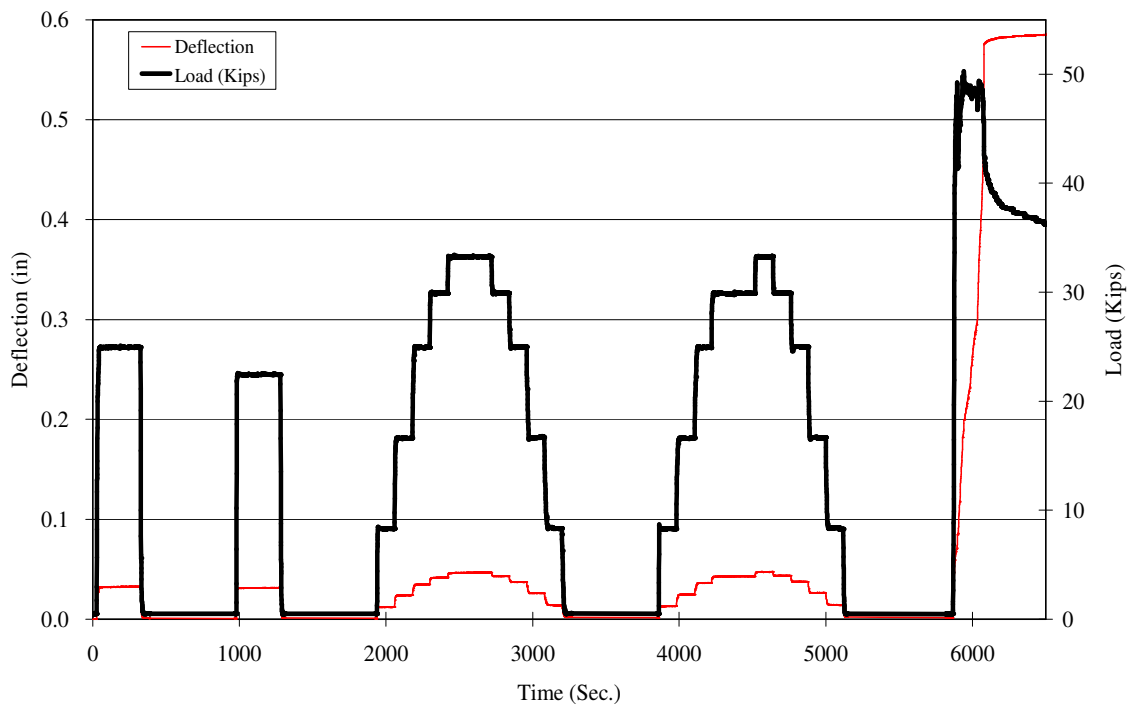


Figure 6-16: Time history of CLT for STD-M-D
(1 in. = 25.4 mm, 1 kip = 4.45 kN)

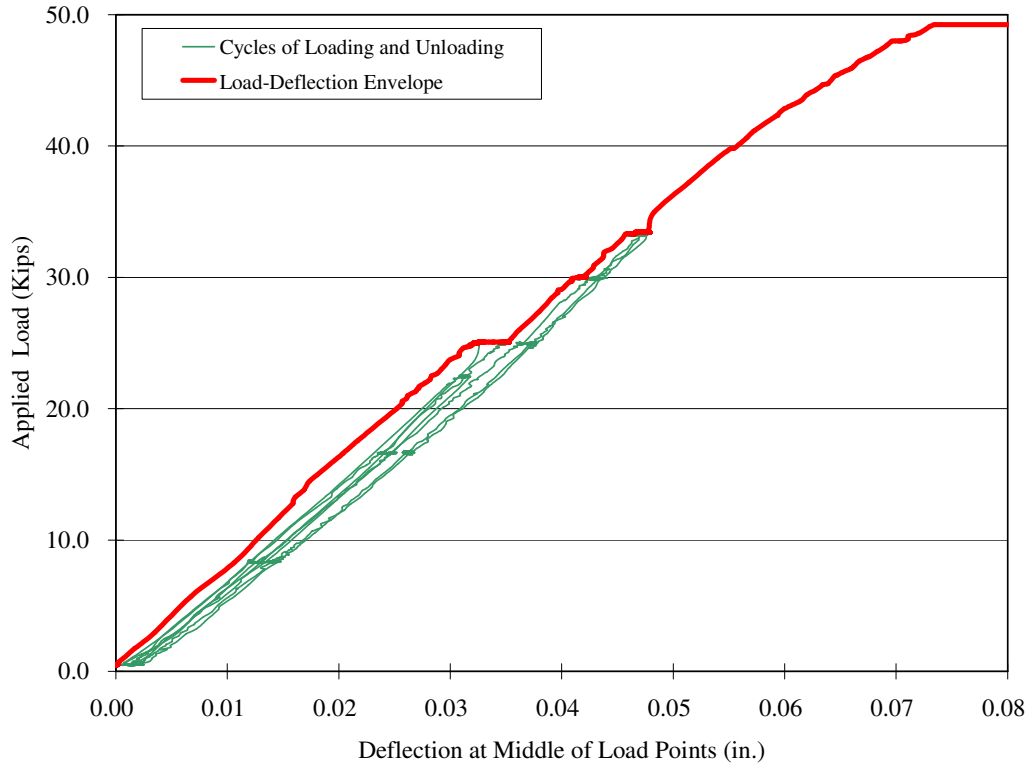


Figure 6-17: Load versus deflection curve for STD-M-D

The NDIS-2421 assessment process for beam STD-M-D was carried out in the same manner as for beam STD-M-B. The calculated values of the calm ratio and the load ratio are listed in Table 6-5. Using the limiting values mentioned in the discussion for STD-M-B, the areas of different damage for beam STD-M-D are indicated. The first loadset was classified into the minor damage zone. Although no cracking was evident from visual observation or inspection of the load versus deformation behavior, Loadset 3-4, which corresponded to the service-level load, was classified into the intermediate damage zone by the NDIS-2421 criterion.

The SSM ratio during loading was calculated for each loadset, and the results are shown in Table 6-5. For beam STD-M-D, the SSM ratio for loadset 3-4 was 2.6 percent.

This value was close to the SSM ratio at the first cracking load in STD-M-B and STD-M-C.

6.5.4 STD-M-A

Before the beginning of the AE testing, this specimen was prematurely loaded beyond its cracking load and the load initiating yielding in the prestressing strands. After completion of the AE testing, the specimen failed in a flexural manner when loaded to its ultimate strength. No strand end slip was measured during the test. The maximum load reached for this specimen was 91.2 kN (20.5 kips) at a maximum deflection of 188 mm (7.40 in.). The maximum moment resisted by this beam, M_{max} , was 11 percent greater than $M_{n,calc}$. The beam lost its load-carrying capacity due to strand rupture. No web-shear cracking was observed in this specimen. The crack pattern corresponding to the maximum load for this beam is depicted in Figure 6-18.

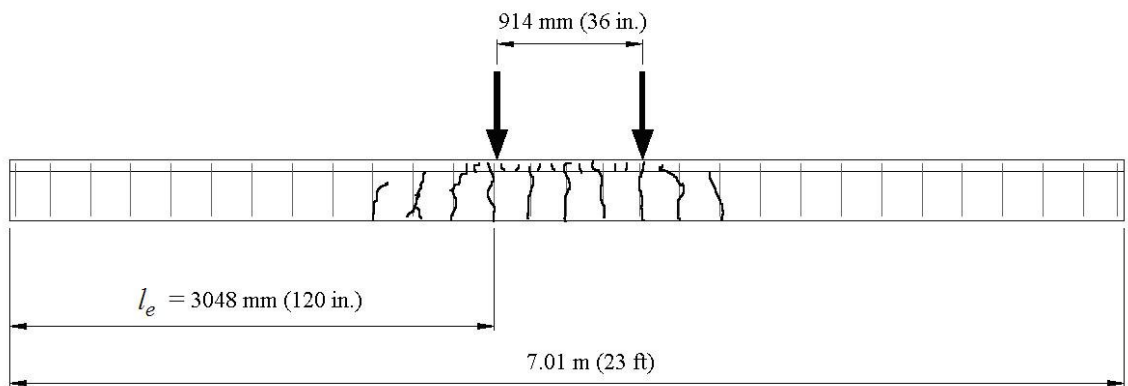


Figure 6-18: Crack pattern for STD-M-A at failure (Levy 2007)

The calculated numerical values for the three CLT evaluation criteria of repeatability, permanency, and maximum deviation from linearity are listed in Table 6-8. The repeatability and permanency criteria were satisfied for all load levels. The beam failed to satisfy the deviation-from-linearity criterion for the loads of Cycle 7 and higher.

Table 6-8: Summary of calculation for STD-M-A beam

Cycle	Δ_r (in.)	Δ_{max} (in.)	Permanency ($\leq 10\%$)	Repeatability ($\geq 95\%$)	Deviation ($\leq 25\%$)	Performance
Cycle 3(A)	0.0024	0.5313	0.3%	100.1%	8.4%	Pass
Cycle 4(B)	0.0017	0.5311			8.4%	Pass
Cycle 7(C)	0.0103	1.0711	0.6%	99.4%	26.3%	Failed
Cycle 8(D)	0.0061	1.0606			31.3%	Failed
Cycle 9(E)	0.0185	1.7606	0.7%	100.1%	44.4%	Failed
Cycle 10(F)	0.0129	1.7561			44.6%	Failed

Figure 6-19 is a time history of the load and deflection for the beam STD-M-A, and Figure 6-20 shows the portion of the load versus deflection curve corresponding to the ten load cycles. Figure 6-21 shows the deviation-from-linearity parameter versus time for two reference slopes considered for beam STD-M-A. The beam was already cracked before loading. According to α_{ref-1} , the beam failed at a load of 50.7 kN (11.4 kips) during the ascending part of Cycle 5 (6775 seconds). Since the beam is considered damaged in the cycle where deviation from linearity is more than 25 percent (Mettemeyer 1999), here, α_{ref-2} was calculated by ignoring the cycles before the beam was considered damaged (deviation from linearity is less than 25 percent.), i.e. cycle 1 to 5, and supposing to start the load test at the cycle right after the beam was considered damaged (deviation from linearity is more than 25 percent.), i.e. cycle 6. According to α_{ref-2} , the recalculated deviation from linearity is always less than 25 percent. The beam passed the test even at the end of cycle 10.

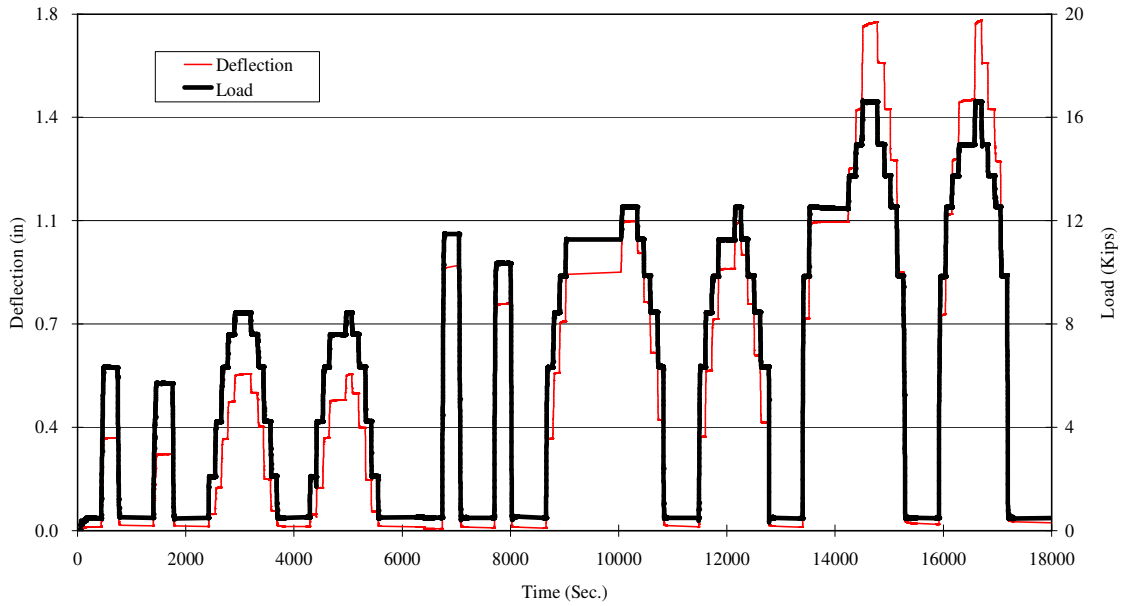


Figure 6-19: Time history of CLT for STD-M-A
 (1 in. = 25.4 mm, 1 kip = 4.45 kN)

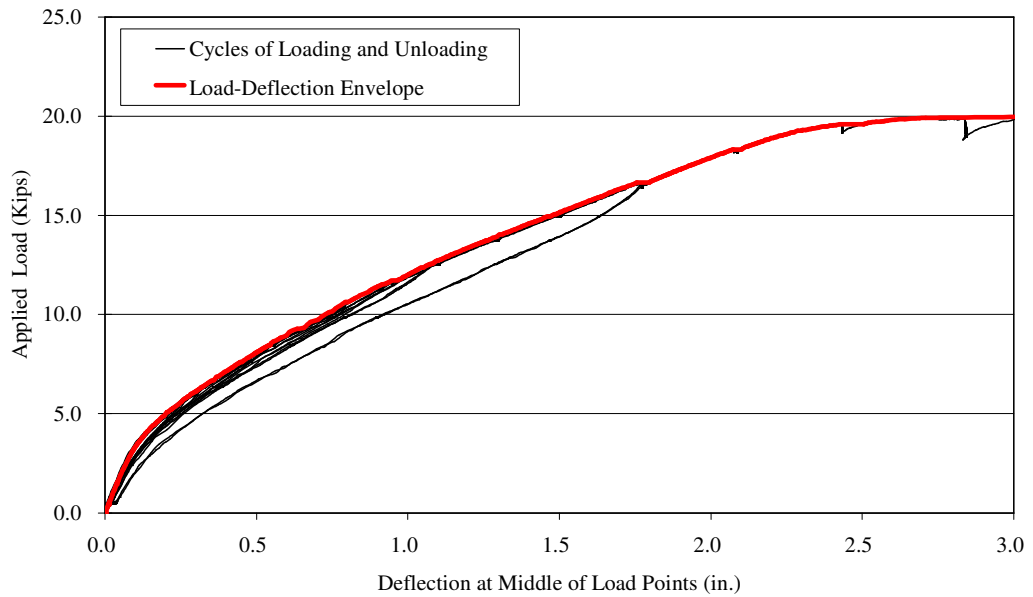


Figure 6-20: Load versus deflection curve for STD-M-A

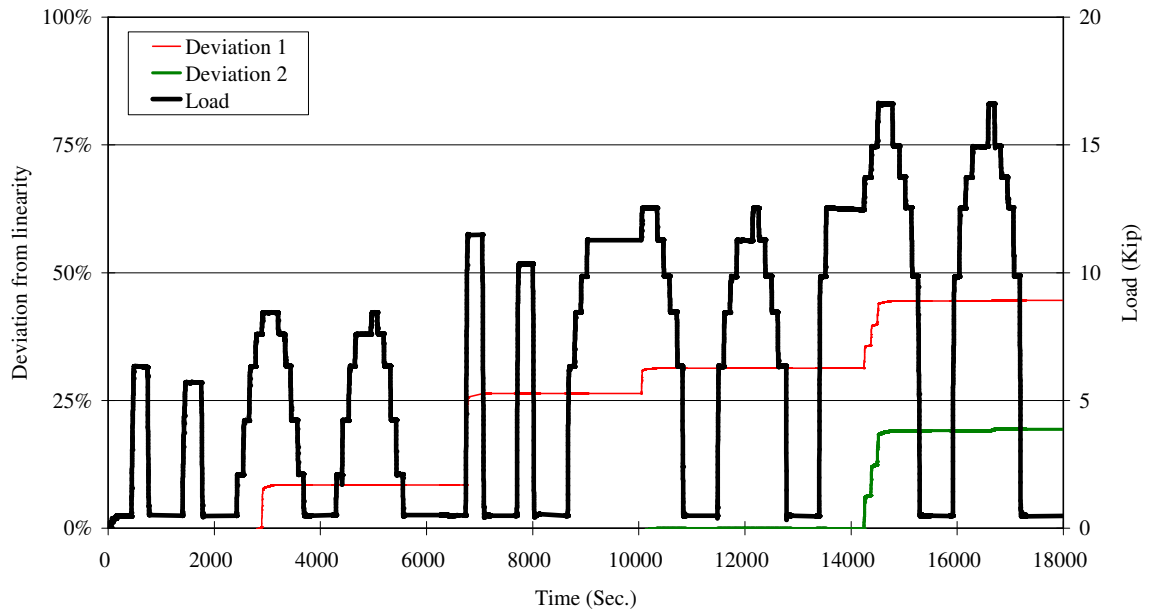


Figure 6-21: Load and deviation from linearity versus time for STD-M-A beam

The NDIS-2421 assessment procedure was carried out. To use this criterion, the calm ratio and the load ratio were calculated for each load set. The calm ratio used was calculated for the first cycle of each load set. For beam STD-M-A, which was damaged before the beginning of the AE testing, the previous maximum load the beam has experienced was not known. This represents the usual case in field testing of structures. Here the definition of “load ratio” was modified by using the known maximum previous load for the testing period instead of the (unknown) actual previous maximum load. Therefore, the load ratio used for beam STD-M-A was the ratio of the load at the onset of AE activity in the second loading cycle to the previous maximum load over the course of the entire testing period. The results are shown in Table 6-5. According to the classification limits proposed above, all loadsets of beam STD-M-A were classified into the heavy damage zone. These results are validated by the fact that the damaging preload pushed the load into the realm of nonlinear material behavior.

An evaluation criterion based on the ratio of signal strength moment (SSM) recorded during the reload hold of a loadset to the initial load hold of that same loadset was used. The SSM ratio during loading was calculated for each loadset, and the results are shown in Table 6-5. For the pre-damaged beam STD-M-A, the relationship of SSM for the first and second loading cycles of each loadset is shown in Figure 6-22. The SSM ratio is given above each bar. The SSM ratios for all load cycles were more than 4 percent. According to the acceptance criterion proposed above, all loadsets give results that indicate that STD-M-A was damaged. This implies that the damage level of a previously damaged prestressed concrete beam can be qualified by the proposed criterion based on the SSM ratio.

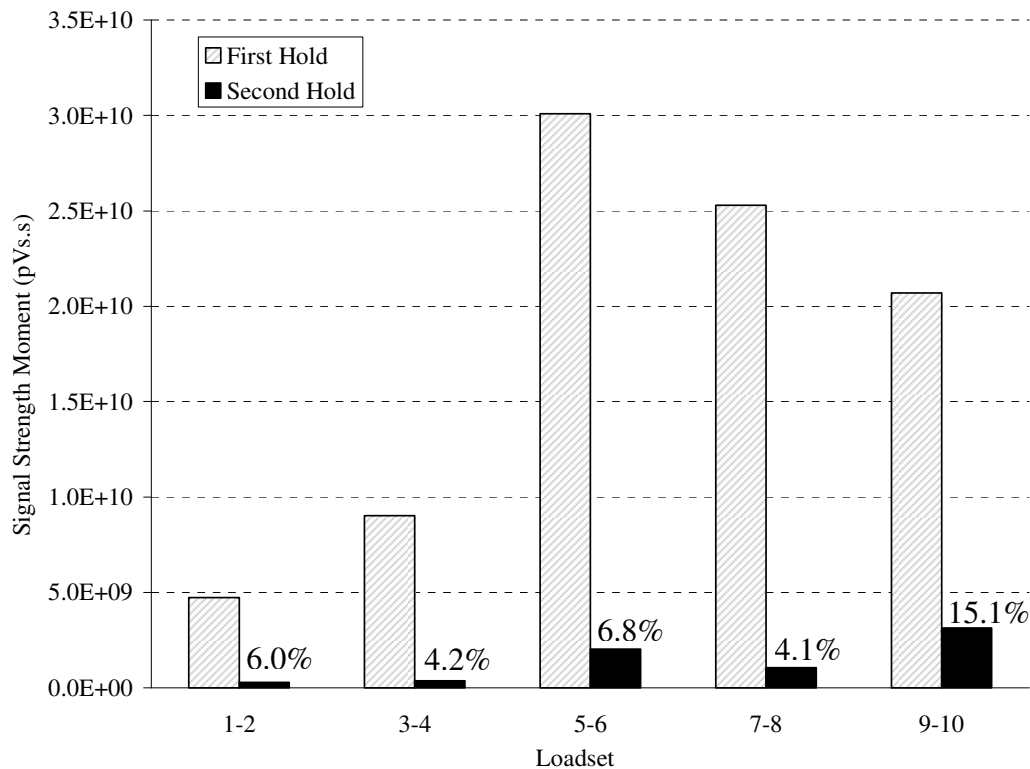


Figure 6-22: Signal strength moment during holds for beam STD-M-A

Table 6-9 offers a comparison of the outcomes of the various methods. For the CLT method, the parameters of permanency and repeatability were not sensitive to the accumulation of prestressed concrete beam damage up to 95 percent of the nominal flexural strength. The parameter of deviation from linearity is the most sensitive CLT criterion. The CLT deviation from linearity was recalculated to consider the drastic change in flexural stiffness for the beam after cracking. This criterion indicated failure in Cycle 9 for beams STD-M-B and STD-M-C, but STD-M-D still satisfied the criterion when it suddenly suffered a shear-tension failure. The deviation from linearity limit was exceeded after Cycle 4 (service-level load) for STD-M-A.

Table 6-9: Summary of evaluation criteria results

Specimen	Damage Evaluation		Loadset number				
			1-2	3-4	5-6	7-8	9-10
STD-M-A	Maximum load		75% of P_s	P_s	Calculated P_{cr}	$(P_s+95\%P_n)/2$	$95\%P_n$
	CLT	Permanency	N/A	Pass	N/A	Pass	Pass
		Repeatability	N/A	Pass	N/A	Pass	Pass
		Deviation	N/A	Pass	N/A	Failed	Failed
	AE	NDIS-2421	Heavy Damage	Heavy Damage	Heavy Damage	Heavy Damage	Heavy Damage
SSM Ratio		Failed	Failed	Failed	Failed	Failed	
STD-M-B	Maximum load		75% of P_s	P_s	Calculated P_{cr}	First cracking	$95\%P_n$
	CLT	Permanency	N/A	Pass	N/A	Pass	Pass
		Repeatability	N/A	Pass	N/A	Pass	Pass
		Deviation	N/A	Pass	N/A	Failed	Failed
	AE	NDIS-2421	Minor Damage	Minor Damage	Minor Damage	Intermediate Damage	Heavy Damage
SSM Ratio		Pass	Pass	Pass	Pass	Failed	
STD-M-C	Maximum load		75% of P_s	P_s	First cracking	$(P_s+95\%P_n)/2$	$95\%P_n$
	CLT	Permanency	N/A	Pass	N/A	Pass	Pass
		Repeatability	N/A	Pass	N/A	Pass	Pass
		Deviation	N/A	Pass	N/A	Pass	Failed
	AE	NDIS-2421	Minor Damage	Minor Damage	Intermediate Damage	Minor Damage	Heavy Damage
SSM Ratio		Pass	Pass	Pass	Pass	Failed	
STD-M-D	Maximum load		75% of P_s	P_s			
	CLT	Permanency	N/A	Pass			
		Repeatability	N/A	Pass			
		Deviation	N/A	Pass			
	AE	NDIS-2421	Minor Damage	Intermediate Damage			
SSM Ratio		Pass	Pass				

When applying NDIS-2421 evaluation criteria, the STD-M-B and STD-M-C beams were classified as heavily damaged during loadset 9-10, STD-M-D was classified as intermediately damaged before it suddenly failed, and STD-M-A was classified as heavily damaged from the first loadset (75 percent of service load). According to the SSM ratio analysis, STD-M-B and STD-M-C were damaged during loadset 9-10, STD-

M-D was not damaged (but approaching the damage limit) before sudden shear-tension failure, and STD-M-A was damaged before the beginning of the test.

6.6 CONCLUSIONS

In this study, the results of experiments on four prestressed concrete beams are described. The effectiveness of CLT and AE methods for evaluating damage were compared to the actual beam behavior. The damage assessments resulting from the CLT were compared to damage classifications according to two AE evaluation criteria: the NDIS-2421 evaluation criterion and the newly proposed SSM ratio evaluation criterion.

The specific conclusions drawn from this experimental investigation are:

1. The CLT repeatability and permanency criteria did not accurately indicate significant accumulated damage in prestressed concrete beams.
2. The CLT deviation from linearity is sensitive to damage in prestressed concrete beams, but the acceptance criterion needs to be further investigated and adjusted prior to implementation.
3. A good correlation between two AE evaluation criteria—the modified NDIS-2421 quantitative assessment criterion and the SSM ratio evaluation criterion—and the actual level of damages was observed for prestressed concrete beams.
4. The results from CLT assessment criteria were compared to the results from the AE evaluation criteria, and both methods show promise as techniques for nondestructive testing of prestressed concrete beams.

Further research is required to implement the evaluation criteria discussed in this chapter to evaluate the performance of prestressed concrete beams in real structures.

CHAPTER 7

**IN-PLACE ACOUSTIC EMISSIONS MONITORING OF DAMAGED
PRESTRESSED CONCRETE BRIDGE GIRDERS**

7.1 INTRODUCTION

Prestressed concrete girders are widely used in highway bridges. Through the years, the condition assessment of existing bridges has become increasingly important as some sections have started to deteriorate and repairs must be made for the sake of safety. So, a method for evaluating the condition of an existing bridge is badly needed. Conventional testing methods for concrete bridges do not provide full information about the severity of defects. Visual inspection is currently the predominant method for assessment of in-service bridge components, and it is limited to the detection of visible surface damage. Other nondestructive methods such as ultrasonic, thermal, and radiographic testing are capable of detecting defects of concern to local inspection, however, none of these methods are capable of determining the integrity of a bridge (Berger and Mordfin 1992).

Acoustic Emission (AE) refers to the generation of transient elastic waves during the rapid release of energy from localized sources within a material (ASTM E 1316 2006). AE monitoring can potentially allow detection and evaluation of the structural condition throughout an entire structure during a single test (Ohtsu 1989). Since only limited access is required, structural integrity assessment may be conducted in zones that are

inaccessible to the other traditional nondestructive methods (Pollock 1995). Due to the global nature of these emissions, a large volume of structure may be tested at the same time. The AE monitoring technique is able to detect a damage process as it occurs (Gong et al. 1992). AE data can provide valuable insight into the behavior and damage mechanisms of passively reinforced and prestressed concrete structures (Hearn and Shield 1997; Ohtsu et al. 2002). While conventional strain- and deflection-testing methods are helpful for calibrating analytical models and measuring mechanical behavior, the AE monitoring technique can provide a more direct measure of damage as it occurs in a structure. Therefore, it is often a more sensitive measure of damage than strain or displacement monitoring. In addition, the AE produced from damage processes is largely independent of temperature effects that affect conventional measurement techniques (ASNT 1996). For these reasons, the AE method is a promising nondestructive testing technique for integrity evaluations of concrete bridges.

This chapter describes a study of prestressed concrete girders located in Huntsville, Alabama, U.S.A. along northbound Spans 10 and 11 of the elevated I-565 bridge structures, which were constructed between January 1988 and March 1991. The bridge deck is supported by prestressed concrete bulb-tee bridge girders that were made continuous for live load. Wide cracks formed in the girder end regions close to the continuity diaphragms within 18 months after the completion of construction. This phenomenon has rarely been reported previously. Efforts by the Alabama Department of Transportation (ALDOT) personnel to relieve the potential danger caused by those cracks included the installation of extra supports to prevent a collapse of the structure if the girder ends fail, and injection of epoxy into the existing cracks to seal them and prevent

their growth. However, new cracks later appeared adjacent to some of the epoxy-injected cracks (Swenson 2003; Fason and Barnes 2004; Barnes et al. 2006).

In order to identify the most effective measurement techniques for assessing the integrity of the I-565 structure after cracking, in addition to the conventional strain-deflection testing technique, use of the AE technique for evaluating the structural integrity in prestressed concrete bridge beams in-situ was investigated.

The main problem for structural integrity evaluation using the AE technique is determining how to accurately interpret the AE data recorded. Standardized AE evaluation criteria for prestressed concrete beams are not available yet. Although several studies have been executed involving AE monitoring in concrete structures (Hearn et al. 1997; Yopez 1999; Colombo et al. 2005; Ridge and Ziehl 2006), successful results with respect to evaluation and prediction are few so far. In addition, almost all of the previous work has been performed in the laboratory. In this study, the AE generated during the truck loading of an actual in-service bridge was measured. The study had the objective of evaluating the overall effectiveness and practicality of using AE monitoring as a tool for the nondestructive testing of in-situ concrete bridges, as well as the accumulation of experience for the potential future implementation of AE monitoring of concrete bridges.

7.2 RESEARCH SIGNIFICANCE

Recently, extensive research has been conducted on the use of AE in a variety of civil engineering applications; however, almost all of this work has been done in a laboratory. Scarcely any studies have been performed on AE behavior in-situ. The main objective of the study described in this chapter is to develop a practical evaluation method using AE

technology to determine the integrity of prestressed concrete bridge girders loaded by moving truck loads. The strain, displacement, and AE data collected from the test were used to validate the AE results. These tests will help to establish standardized evaluation criteria for AE monitoring as a NDT technique in prestressed concrete bridges.

7.3 AE EVALUATION CRITERIA

7.3.1 NDIS-2421 CRITERION

The NDIS-2421 quantitative assessment criterion was adopted by the Japanese Society for Nondestructive Inspections (JSND) (Ohtsu et al. 2002). The damage levels of structures are classified based on two ratios related to AE activity under applied loads: the “Load Ratio” (the ratio of load at the onset of AE activity to the previous load) and the “Calm Ratio” (ratio of cumulative AE activities during the unloading process to that of the last maximum loading cycle).

7.3.2 SIGNAL STRENGTH MOMENT RATIO EVALUATION

The Signal-Strength Moment Ratio evaluation method uses a time-weighted approach for analyzing the AE signal strength during a load hold. Signal-Strength Moment is the summation over a period of sustained load (“load hold”) of the product of the signal strength associated with each hit by the time elapsed from the beginning of the load hold.

The signal strength moment (SSM) is defined as:

$$SSM = \sum_i^n t_i S_i \quad (\text{Eq. 7.1})$$

where n is the total number of hits occurring during the load hold, t_i is the time from the beginning of the hold to the i th hit and S_i is the signal strength occurring in the i th hit.

The SSM Ratio evaluation criterion is based on the ratio of SSM recorded during the reload hold of a loadset to SSM recorded during the initial load hold of that same loadset. As indicated by the laboratory research described in this dissertation, a greater SSM value is indicative of a situation in which the AE activity extends further into, or increases, during the hold period, as opposed to decreasing or remaining steady. The SSM ratio provides an indication of the progression of damage as the load intensity increases.

7.4 EXPERIMENTAL PROCEDURE

7.4.1 PRELIMINARY INVESTIGATION

In order to utilize the AE technique properly for detection and evaluation of the integrity of the damaged prestressed concrete bridge in service, a visual inspection was initially undertaken. The bridge segment investigated consists of a two-span unit, which is composed of nine prestressed concrete bridge girders, made continuous for live load, and a cast-in-place reinforced concrete (RC) bridge deck.

Figure 7-1 presents a cross-sectional view of the bridge. The bridge deck is 21.6 m (70.8 ft.) wide with a thickness of 165 mm (6.5 in.), not including the variable-depth build-up over each girder. The bridge deck was designed to act compositely with the girders by extending the girder stirrups into the deck slab (Swenson 2003). The nine girders are spaced 2.4 m (96 in.) center-to-center. Figure 7-2 shows the girder cross section.

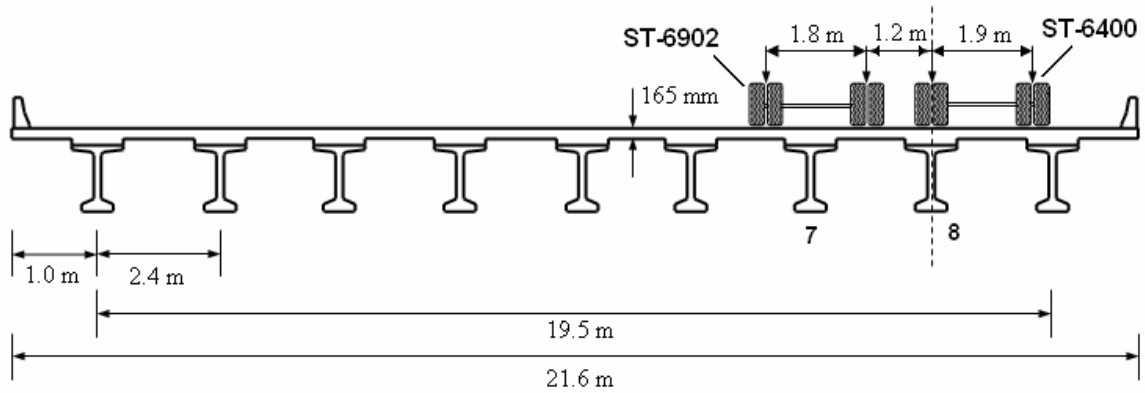


Figure 7-1: Bridge cross section and transverse position of test truck (from Fason and Barnes 2004)

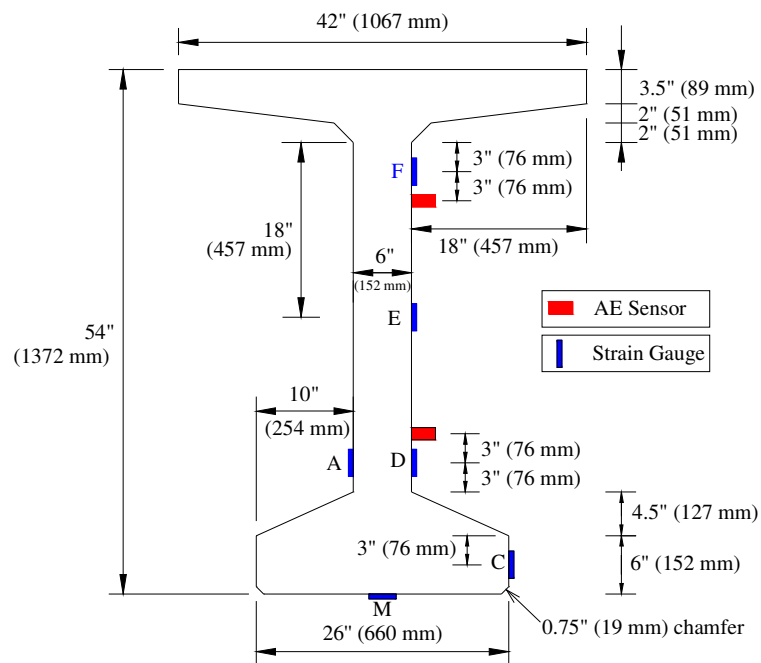


Figure 7-2: Girder cross section dimensions

The inspection was focused on assessing the current condition of girders supported by Bent 11 connecting northbound Spans 10 and 11. Figure 7-3 shows the basic layout and orientation of the girder lines and bents for I-565 Spans 10 and 11. A cast-in-place

continuity diaphragm connects girders from Span 10 with those from Span 11. Each of the nine girder lines supported by Bent 11 was visually inspected.

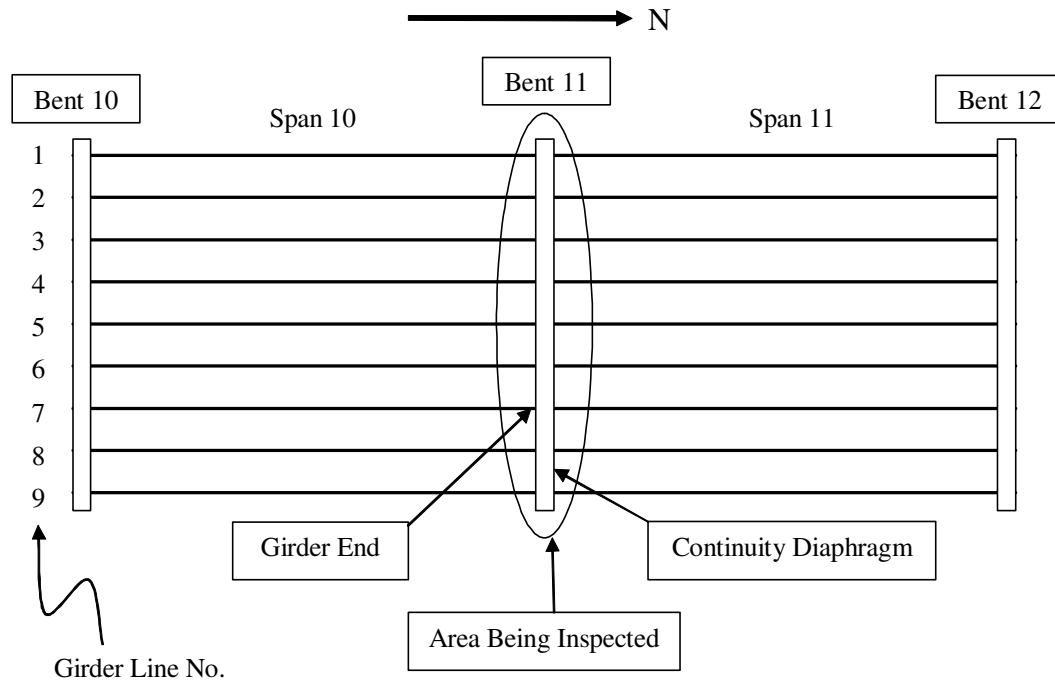


Figure 7-3: I-565 girder layout and numbering system

During the investigation of Bent 11, three types of cracks were encountered in the girder ends near the continuity diaphragm. The first type comprises large cracks that had previously been injected with an epoxy in order to seal each crack and prevent additional opening of the crack. These cracks are located in most girders. The second type of cracks is those that have not yet been repaired with epoxy. It is unknown whether these cracks opened before or after the epoxy injection of the first type of cracks. The third type is the cracks that cracked through, or immediately adjacent to, the epoxy since the initial cracking was repaired. Figure 7-4 shows the three types of cracks. The Cracks through epoxy and sealant are of the greatest concern, because they indicate that the bridge has

experienced damage since the initial repair. After the preliminary investigation, it was decided to focus the monitoring on Girders 7 and 8 on both sides of the continuity diaphragm.

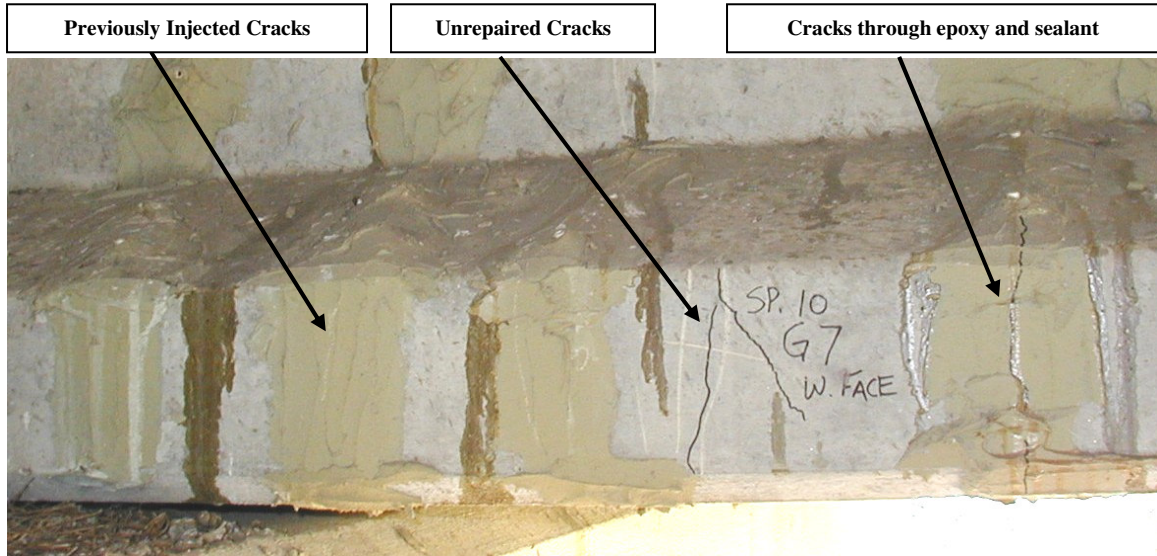


Figure 7-4: Types of cracking (from Fason and Barnes 2004)

7.4.2 AE TESTING PROCEDURE

A 24-channel SAMOS[®] manufactured by Physical Acoustic Corporation (PAC) was used to perform AE testing on the prestressed concrete bridge girders. On-site preparation for testing took one week, with the setup for AE installation taking only one day, and the actual testing took place during two nights. In order to save time and effort on site, some practice testing was performed in the Auburn University Structural Engineering Laboratory.

PAC R6I-AST 50 kHz integral resonant sensors were employed for the AE monitoring. Specific information, including the hardware setup, filters, and acquisition setup is summarized in Table 7-1.

Table 7-1: AE Test Parameters for Prestressed Concrete Girders

Parameters	Values
Hit Definition Time (HDT)	200 μ sec.
Peak Definition Time (PDT)	50 μ sec.
Hit Lockout Time (HLT)	300 μ sec.
Threshold	50 dB
Preamplifier (R6I)	40 dB
Bandpass Data Acquisition Filter	100-400kHz

Before AE sensors were mounted, the girder surface was cleaned and sanded until smooth to the touch. Dirty surfaces are undesirable because the dirt may include gritty particles that reduce the acoustic contact. The coupling media used to obtain good contact between the sensor and the surface was high silicone vacuum grease from Dow Corning. All the sensors were held on the surface of the girder using a magnetic hold-down device. In order to attract the magnetic hold-down to the surface of concrete, two steel sheets 32 mm \times 13 mm \times 0.5 mm (1.25 in. \times 0.5 in. \times 0.02 in.) were epoxied to the concrete surface as shown in Figure 7-5. Then, the magnetic hold-down device was used to exert contact pressure against the specimen by attraction to the steel sheets (Figure 7-6). Magnetic hold-downs kept the sensors in place throughout the test. This mounting system proved very flexible in that it allowed sensor placement in any desired position on the girder surface. The hold-downs also served to protect the sensors from environmental hazards and to act as insulators against external noise that may have influenced the test results. The cables connecting the sensors to the acquisition system were secured using mounting pads (Figure 7-6) and cable ties to prevent movements and interference.

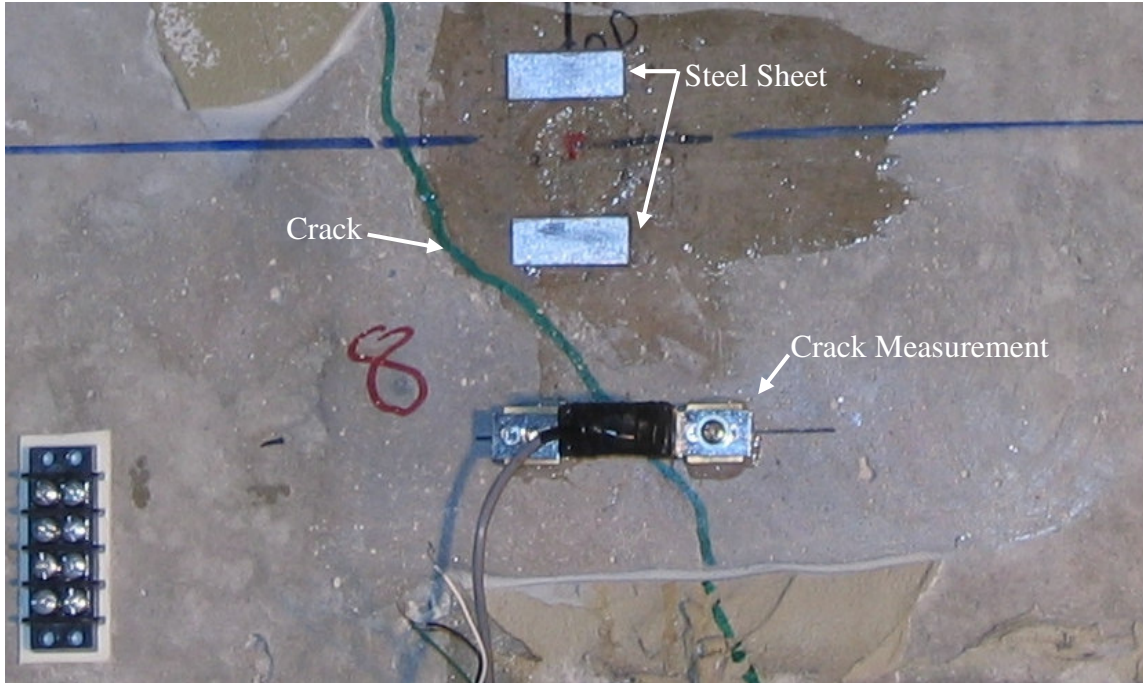


Figure 7-5: Steel sheet and crack measurement

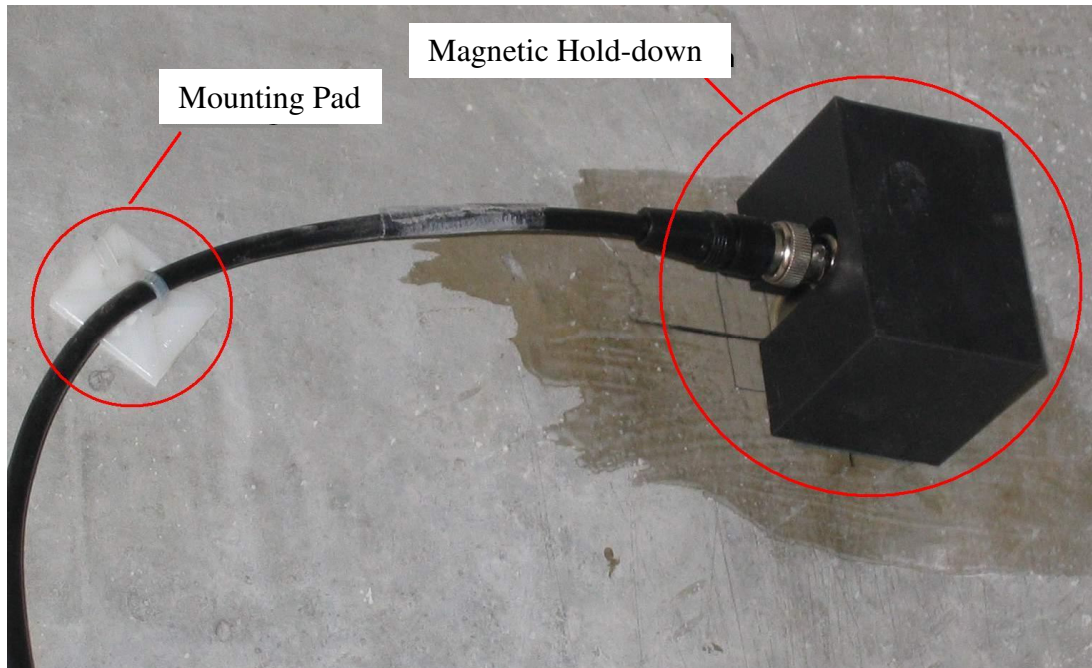


Figure 7-6: Cable mounting pad and magnetic hold-down

The sensors were located in different regions in order to capture the characteristic AE events. As stated above, it was decided to focus the monitoring on Girders 7 and 8 after

the preliminary inspection. There are a number of unsealed cracks on Girders 7 and 8. Girder 8 also has a large number of sealed cracks. Span 11 has long unsealed cracks, while Span 10 has shorter unsealed cracks with re-cracking of one previously sealed crack. Six sensors (1 to 6) were affixed to the east face of Span 10 of Girder 8 (S10G8) near the continuity diaphragm, and another six sensors (13 to 18) were affixed likewise to the adjacent end of Span 11 of Girder 8 (S11G8), as shown in Figure 7-7. The grid of AE sensors was 0.61 m high \times 0.91 m wide. The positions of Sensors 1 to 6 are shown in Figure 7-8.

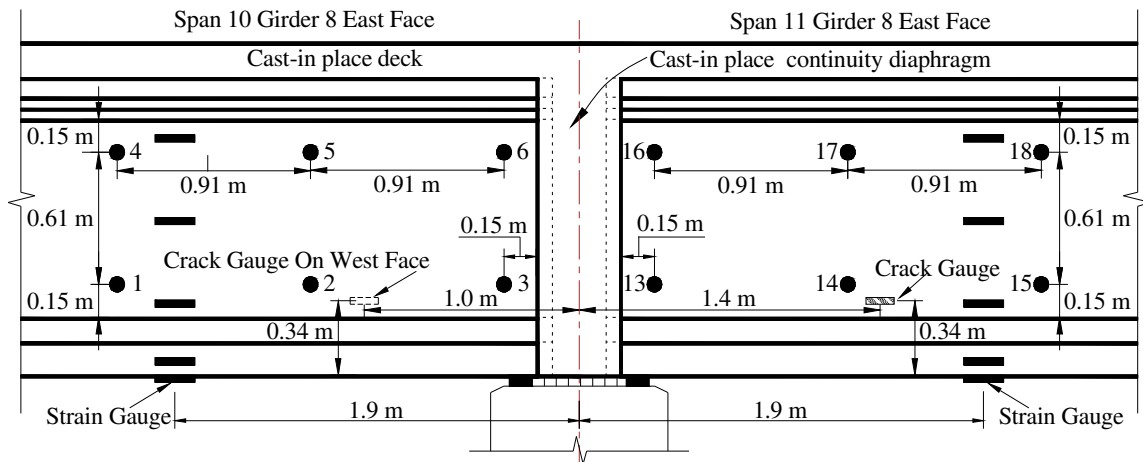


Figure 7-7: Array of sensors on the east face of Girder 8



Figure 7-8: Sensor locations on Span 10 Girder 8

Girder 7 exhibits a large number of both sealed and unsealed cracks. Span 11 has unsealed cracks paralleling sealed cracks and running nearly the entire depth of the beam. Span 10 has shorter unsealed cracks that remain in the bottom flange, as well as sealed cracks that have re-cracked through the seal. Six sensors (7 to 12) were affixed to the east face of Girder 7 at the end of Span 10 (S10G7) near the continuity diaphragm as shown in Figure 7-9. In order to avoid placing a sensor astride a crack, a few sensors were shifted slightly off the grid. Sensor 11 was moved down 51 mm (2.0 in.) to avoid a crack. Six sensors (19 to 24) were affixed to the adjacent end of Span 11 of Girder 7 (S11G7) as shown in Figure 7-9. Sensors 20 and 23 were shifted 25 mm (1.0 in.) to the right to avoid a crack.

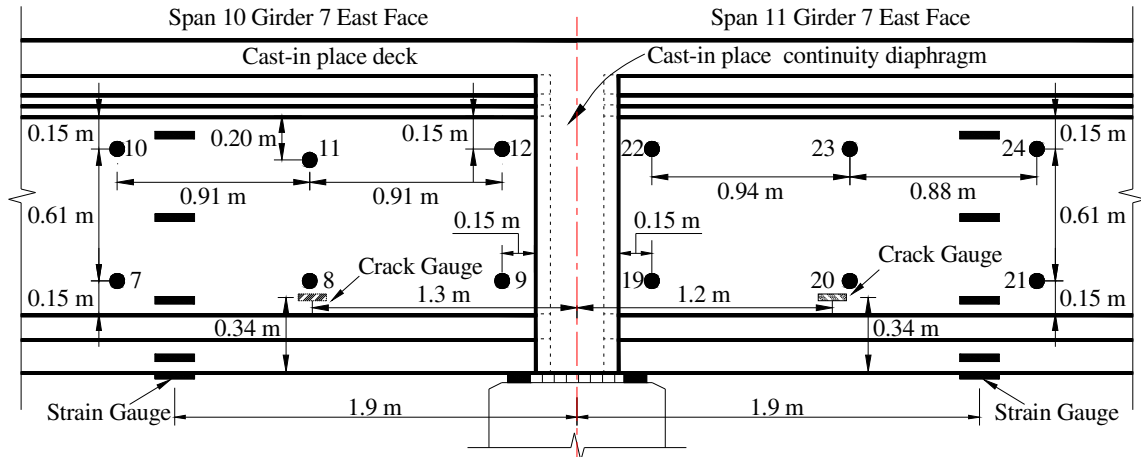


Figure 7-9: Array of Girder 7 sensors

To collect reliable AE data, it was essential that the channel sensitivities were well-matched and consistent. The hardware was checked in the Auburn University Structural Research Laboratory prior to use in the field. After the sensors were mounted, a system performance check was carried out using the pencil-lead break technique (Pollock 1995). This procedure was employed to check the effectiveness of the mounted sensors and to reveal any weak channels that needed correction. A re-check at the end of data acquisition was made to verify that there was no accidental loss of sensitivity during the test period (Pollock 1995). Calibration tests were performed prior to the test with 0.5-mm HB pencil lead breaks. All significant changes were noted in the test log for later interpretation.

One lane of the bridge was open to traffic during testing (over Girders 1 and 2, which are farthest from the tested Girders 7 and 8). The AE calibration test was performed on Girders 7 and 8 during 6 minutes of ambient traffic flow, and very few AE signals were detected. This indicated that AE emissions from ongoing traffic had no significant effect on the results from the subsequent controlled load tests.

7.4.3 CONVENTIONAL MEASUREMENTS

In order to evaluate the performance of the I-565 structure, the concrete surface strains on the girders were measured during the load testing. This was achieved by using electrical-resistance strain gauges (ERSGs), which were bonded with epoxy directly to the surface of the concrete. The ERSGs used in this test were 60-mm (2.4 in.), quarter-bridge strain gauges with a resistance of 350 Ω and temperature compensation appropriate for concrete or steel (Texas Measurements MFLA-60•350-1L). Strain gauge locations at instrumented cross sections near the AE sensors are depicted in Figure 7-2. Figures 7-7 and 7-9 show the locations of the instrumented cross sections.

Deflectometers were used to measure the amount of vertical movement that the bridge experienced under loads. These measurements were useful in determining the general behavior of the bridge. There were twelve deflectometers used in the load testing and they were placed at six different locations, including midspan, along each of the two girder lines. Detailed information about the deflectometers has been reported by Shapiro (2007).

Pre-existing cracks can generate AE due to the rubbing of crack surfaces as they open and close in response to changing traffic loads. Therefore, their presence has to be taken into account. Four crack-opening measurement devices were used to measure the crack opening displacements during the load tests. Metal attachment points were epoxied to the concrete on either side of the cracks. The cracks in the four positions were measured. One was on the west face of S10G8. The other three were on the east face of S11G8, S11G7, and S11G8, respectively. Each of the crack opening devices was installed 0.34 m (13.5 in.) above the girder bottom. Their locations relative to the AE sensors are shown in

Figures 7-7 and 7-9. Crack opening displacement was recorded throughout the entire monitoring period.

7.4.4 LOADING PATTERNS FOR AE MONITORING

The AE technique is a measure of damage growth, thus it is dependent on load history. In order to utilize the AE technique properly for detection and evaluation of the integrity of prestressed concrete bridges in service, live load application was designed to generate useful data for interpretation.

Loading of the girder was performed by moving trucks on the bridge. Two different load test trucks (ALDOT ST-6400 and ST-6902) were used for the test simultaneously. Application of truck loading occurred on two nights.

On the first night, the truck load configuration LC-6.5 was used to induce load effects slightly larger than values corresponding to the full service-level live load for which the bridge was designed. There were four loading application positions on the bridge; thus, the test was divided into two parts.

Initial reading of all sensors was recorded six minutes before the test trucks were brought onto the two-span unit. Part 1 was run first with test truck ST-6400 and ST-6902 on Span 10. The first test truck, ST-6400, with the load configuration LC-6.5 (Table 7-2) was gradually driven onto the bridge and placed at the predetermined position. The transverse positions of the test trucks on the bridge are shown in Figure 7-1. The first longitudinal stop position of the test truck placed the third axle of the truck (counting from the front) coincident with the position of Line 4 (1.8 m from the centerline of the continuity diaphragm), as shown in Figure 7-10. Two minutes later, the second test truck,

ST-6902, with the load case LC-6.5 (Table 7-2) was gradually driven to its predetermined position. Once the two test trucks were in the position indicated in Figure 7-10, they remained still for approximately nine minutes (Figure 7-11). The trucks were then driven off the bridge together and the bridge was monitored for approximately seven minutes afterward.

Table 7-2: Test Truck Loads

Load Case	Loading kN (kips)	
	ST-6400	ST-6902
LC-6.5	433.5 (97.45)	418.9 (94.18)
LC-6	416.4 (93.60)	405.9 (91.25)

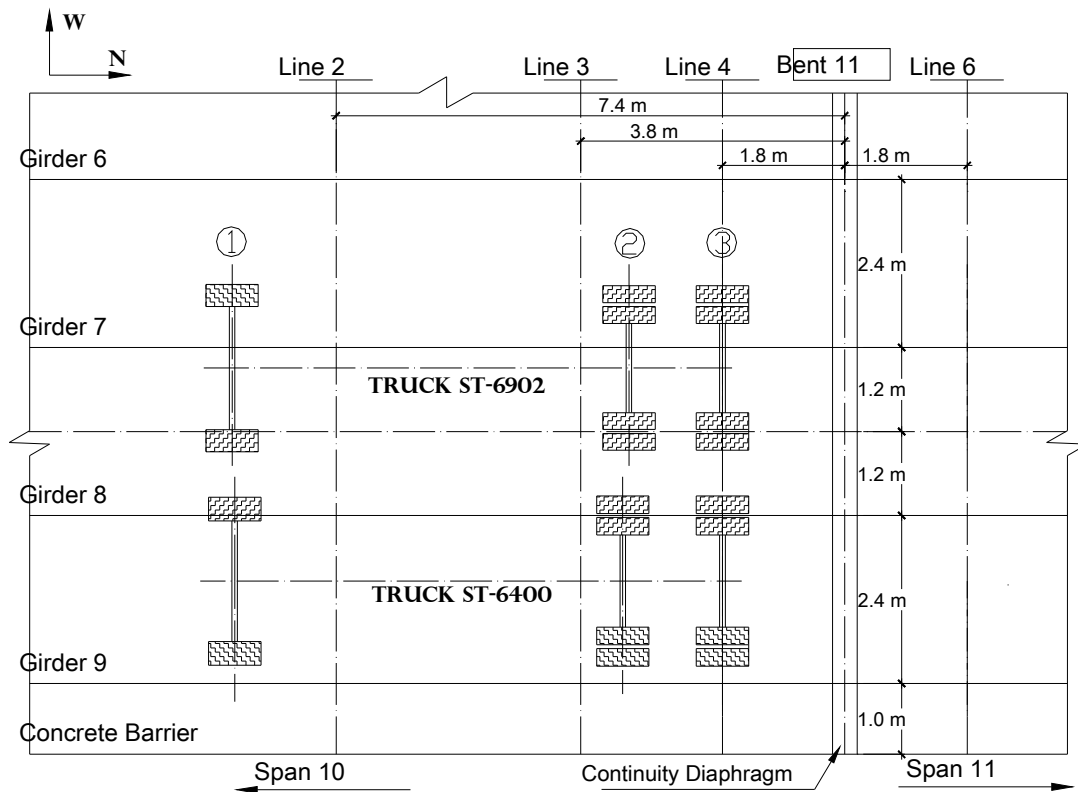


Figure 7-10: Plan view of test truck locations on Span 10



Figure 7-11: Two test trucks on Span 10

Part 2 was run with test truck ST-6400 and ST-6902 on Span 11. The load application was similar to that of Part 1. Six minutes' background testing was completed before the trucks were moved to place. The first test truck, ST-6400, with the load case LC-6.5 was then driven to the predetermined position on the bridge. The transverse position of this test truck on the bridge is shown in Figure 7-12. The longitudinal stop position of the test truck was placed such that the third axle of truck (counting from the front) was coincident with the position of Line 6 (1.8 m from the centerline of continuity diaphragm), as shown in Figure 7-12. About one minute later, the test truck ST-6902 with the load case LC-6.5 was driven to its predetermined position on the bridge. Once the two test trucks were in position, they remained motionless for approximately nine minutes. The trucks were then driven off the bridge together and the bridge was monitored for approximately seven minutes afterward.

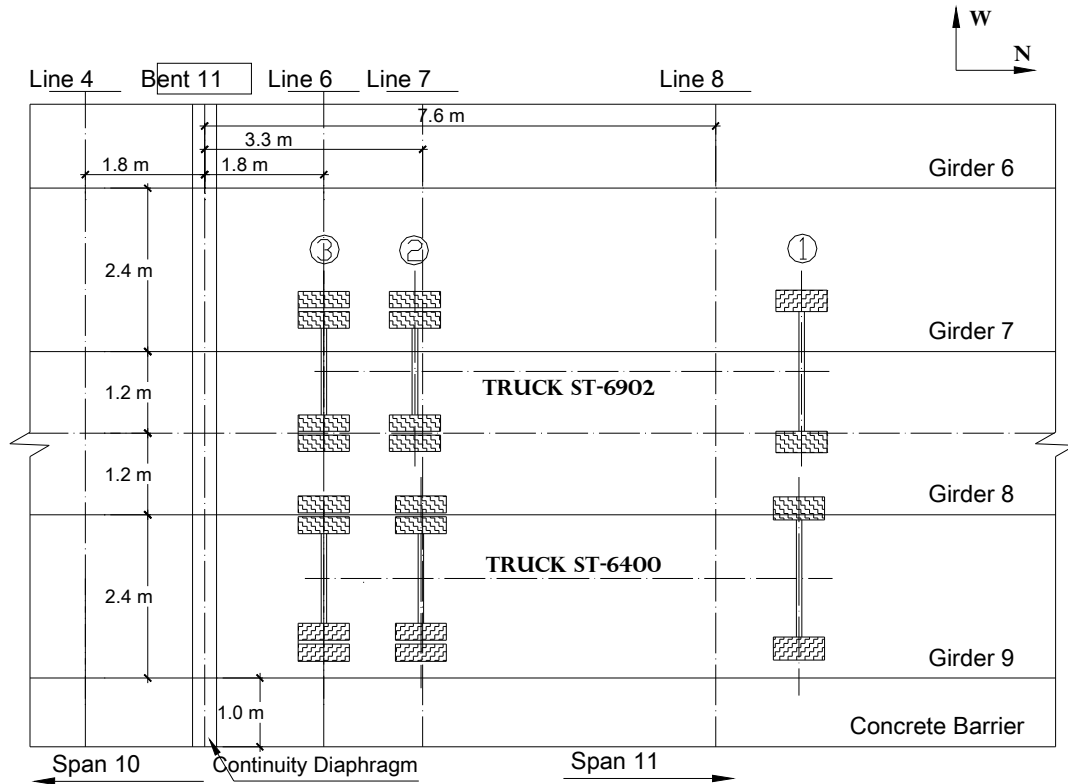


Figure 7-12: Plan view of test truck locations on Span 11

On the second night, the tests with the ST-6400 and ST-6902 trucks were similar to the tests run on the first night. However, on the second night is the truck load configuration LC-6 was used, representing approximately 96 percent of the first night loading (Table 7-2). This reduction was implemented to ensure that the second night's loading did not exceed the first night's loading. During the testing, the speed of trucks was kept as constant as possible.

7.5 RESULTS AND DISCUSSION

7.5.1 CRACK OPENING DISPLACEMENT ANALYSIS

Figure 7-13 shows the results of measurement of crack opening displacement (COD) produced in the four gauge locations during the first night's loading. The crack opening

device on S10G8 (span 10 of girder 8) was on the west face and other three were all on the east faces. Accordingly this, COD shows significantly different behavior from the other Span 10 CODs when the trucks are on Span 10. This is likely due to out-of-plane bending or twisting effects in the girders. The value of the COD in S11G8 (span 11 of girder 8) during the Span 11 load hold was much less than that in span 10 of girder 7 when Span 10 was loaded and in span 11 of girder 7 when Span 11 was loaded. Taking into account that the position of crack opening devices and dimensions of the girders were the same, it was thought that, relative to Girder S11G8, the integrity of Girder S10G7 and S11G7 was decreased for some reason. In addition, the values of the COD in S10G7 and S11G7 produced during the load hold in their respective spans was almost the same. This indicates that Girder 7 had similar condition in Spans 10 and 11.

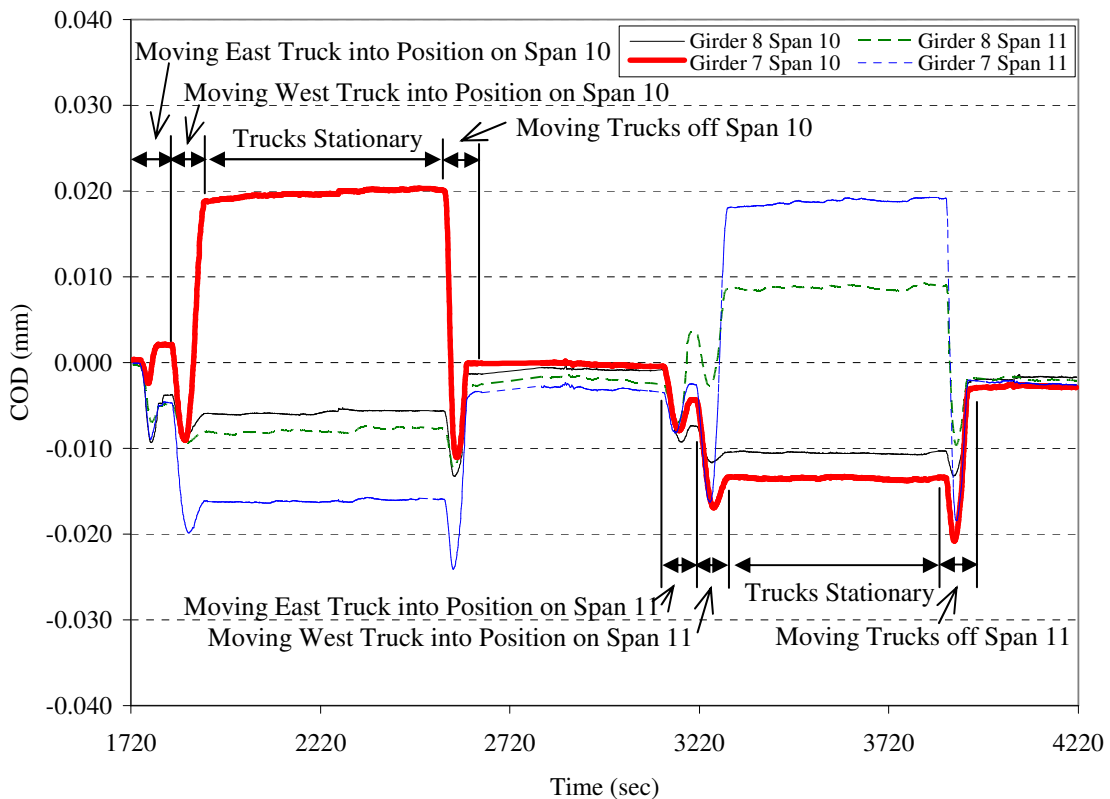


Figure 7-13: Crack opening displacement during second night

The AE activities under moving load were measured. The propagation of cracks could be traced by investigating the AE activities. Figure 7-14 shows the AE amplitude generated from all six sensors on S10G8 on the first night. The COD is superimposed on this plot. The graphs of AE amplitude versus time given in Figure 7-14 indicate that most AE activity took place when a large change of COD occurred. The amplitude distribution of the detected AE correlates well with the COD. This shows that the formation and propagation of cracks in the prestressed concrete girders was associated by a significant increase in AE activity.

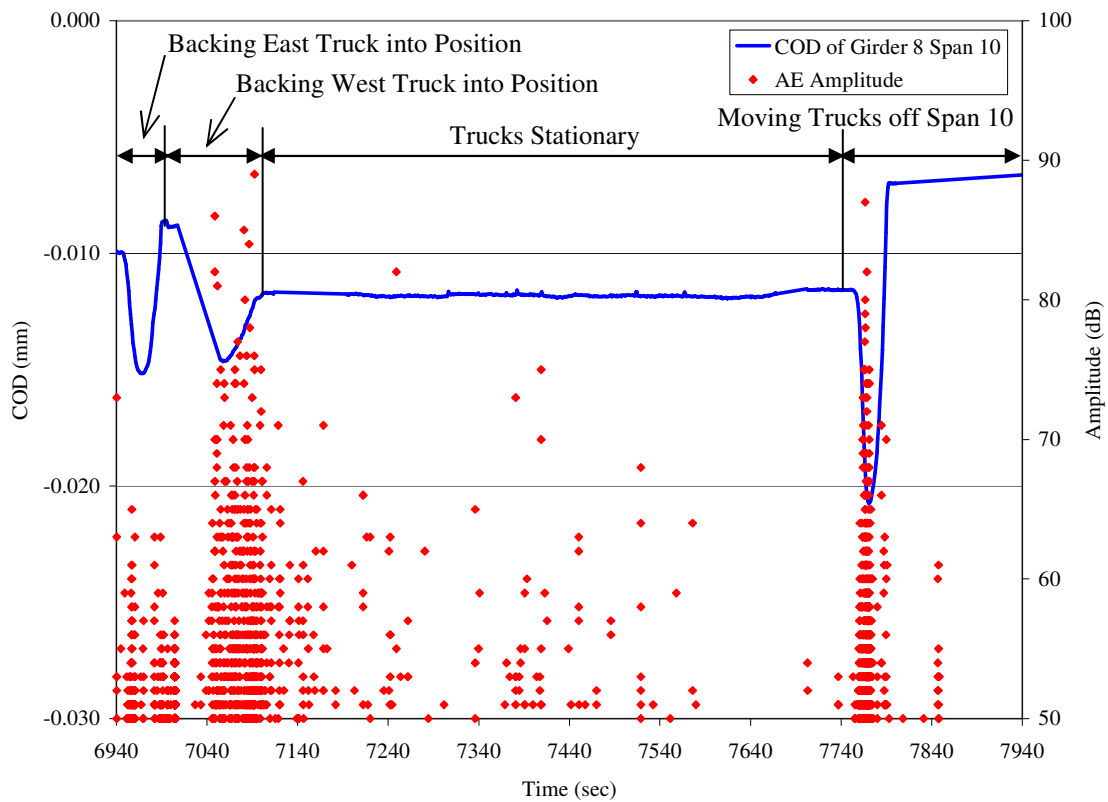


Figure 7-14: COD of Girder 8 Span 10 during first night

7.5.2 ACOUSTIC EMISSION EVALUATION RESULTS

7.5.2.1 NDIS-2421 criterion

The load ratio used in NDIS-2421 requires accurate control of loading because inaccuracies can render this method useless (Ohtsu et al. 2002). Since the load due to a truck moving is difficult to measure, the load ratio can not be used for evaluation of in-situ structures directly. Compared to the midspan deflections and crack opening displacements, the girder strain was more closely related to the truck loads. Thus, the load ratio might be replaced by the strain ratio, which could represent the variation of the load induced at the instrumented section by moving truck loads. In this study, the strain used was near the top of the girder, shown as “*Strain F*” in Figure 7-2. It is practically impossible to know the previous maximum strain the bridge had experienced during its service life. So the relative maximum strain for the testing period was used instead of the absolute previous maximum to compute the strain ratio. Here the strain ratio used for the prestressed concrete bridge was defined as the ratio of the strain at the onset of AE activity during the period when both trucks moved off the bridge to the relative maximum strain for the testing period.

The calm ratio was calculated using cumulative signal strength during the period that both trucks moved off the bridge.

The formulae for calculating the strain ratio and calm ratio are based on the variation of AE signal strength and strain, as follows:

$$\text{Strain Ratio} = \frac{\text{Strain}_{\text{onset of AE activity}}}{\text{Strain}_{\text{relative max strain}}} \quad (\text{Eq. 7.2})$$

$$Calm \ Ratio = \frac{Cumulative \ AE \ Signal \ Strength_{from \ max \ of \ strain \ to \ end}}{Cumulative \ AE \ Signal \ Strength_{from \ beginning \ to \ max \ strain}} \quad (Eq. \ 7.3)$$

Figure 7-15 shows example data used to calculate these two ratios for Girder 8, Span 10. The strain is superimposed on a plot of AE cumulative signal strength versus time in Figure 7-15. The plot of cumulative signal strength versus time is generated from all six sensors on Girder 8, Span 10. As the trucks drove away from the Span 10 loading position, the compressive strain gradually increased to a maximum value and then decreased until the trucks were completely off the structure. Within this truck-removal period, a loading phase and unloading phase were identified based on the measured strain change as indicated in Figure 7-15. In this manner, the CSS values for loading and unloading phases were determined. This procedure was repeated for Span 11 testing.

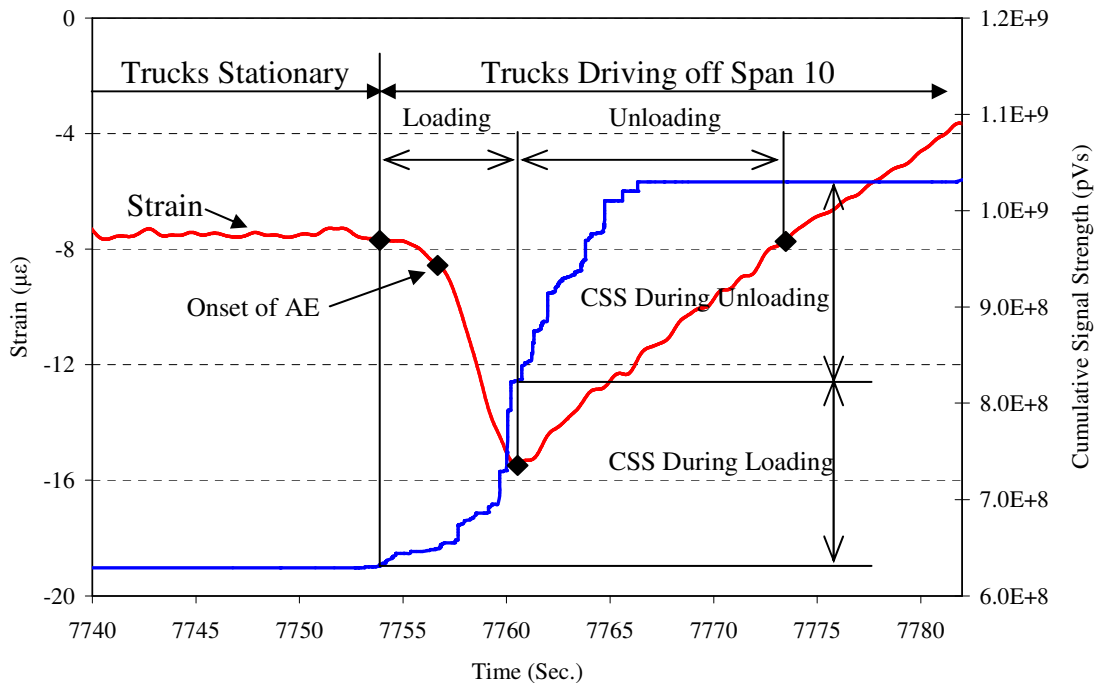


Figure 7-15: Example of calculation of calm ratio of Span 10 Girder 8

The degree of damage of the girders as determined using the NDIS criterion based on the strain ratio and calm ratio are plotted in Figure 7-16. The strain ratio and calm ratio are indicated on the horizontal and vertical axes, respectively. The solid markers and hollow markers represent the data from first night and second night, respectively. Based on the laboratory experiments described earlier in this dissertation, classification limits for prestressed concrete were set as 0.7 for strain ratio and 0.5 for the calm ratio. According to the classification limits used above, S10G8, S10G7 and S11G7 were classified into the heavy damage zone and S11G8 was classified into the intermediate damage zone. The classification showed a reasonable agreement with the COD results discussed earlier. This agreement indicates that the damage level of a prestressed concrete girder can be reasonably qualified by the criterion based on the strain ratio and the calm ratio.

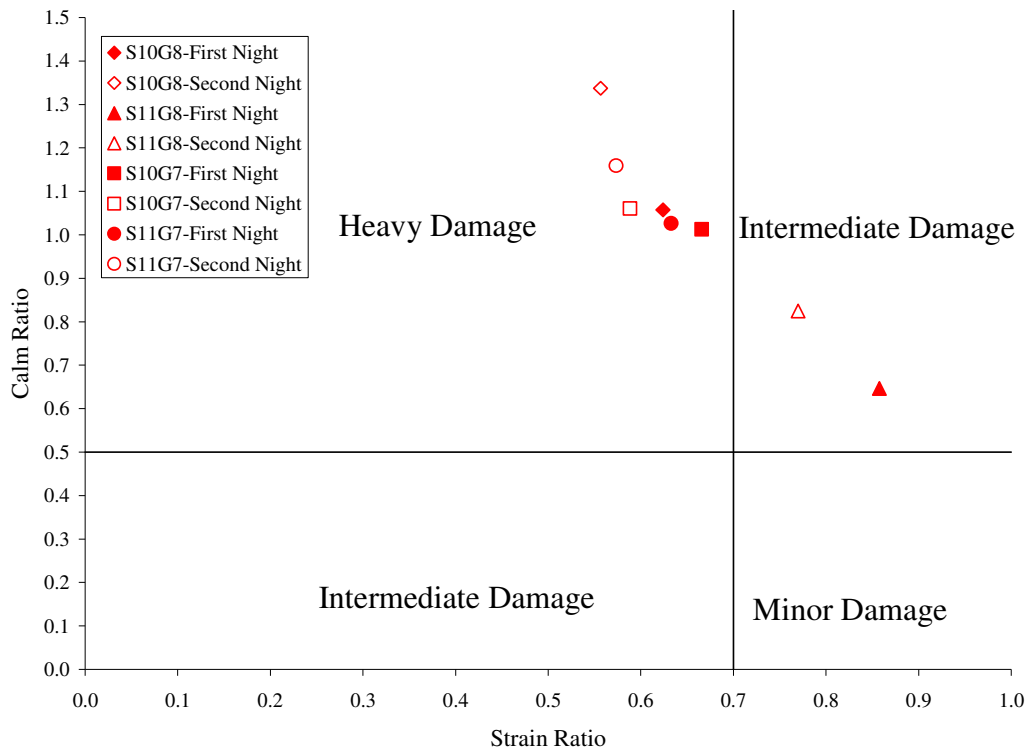


Figure 7-16: Damage qualification of bridge based on NDIS method

7.5.2.2 Signal Strength Moment Ratio Evaluation

An evaluation criterion that is based on the ratio of signal strength moment (SSM) was also employed. To use the evaluation criterion proposed based on the laboratory test program, the same time length used in the laboratory (240 seconds) for was used the two-truck load hold although the actual hold time was approximately 9 minutes. The SSM ratio can be expressed as a percentage as defined in the following:

$$SSM \text{ Ratio} = \frac{SSM_{\text{at the second night hold period}}}{SSM_{\text{at the first night hold period}}} \times 100\% \quad (\text{Eq. 7.4})$$

The results of SSM ratio evaluation are shown in Figure 7-17. The SSM ratio is given above each second night SSM bar.

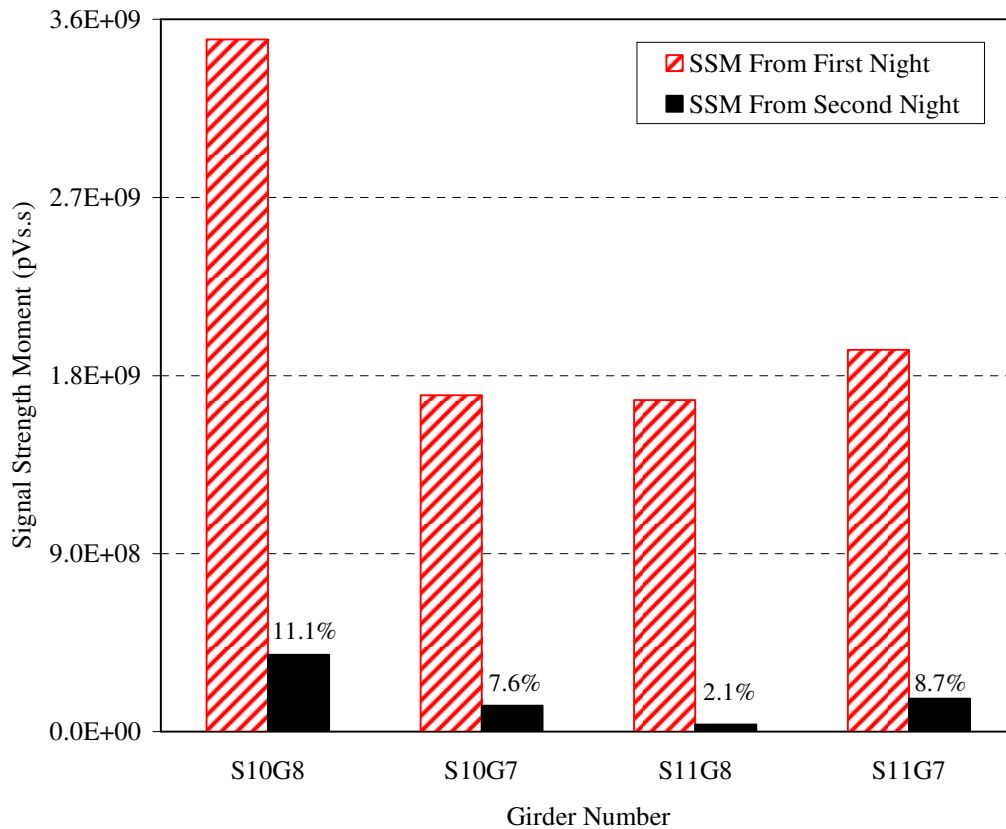


Figure 7-17: Signal strength moment during holds

The SSM ratio for Girder S10G8 is 11.1%, S11G7 is 8.7%, S10G7 is 7.6%, and S11G8 is 2.1. These values indicate the different damage levels. The results show that S10G8 was the most severely damaged and S11G8 was damaged the least. The laboratory experimental program indicated that prestressed concrete beams are heavily damaged when the SSM ratio exceeds 4%. According to this evaluation criterion, Girder S10G8, S10G7, and S11G7 were damaged and S11G8 was not heavily damaged.

Table 7-3 shows the AE evaluation results from the NDIS-2421 and the SMM Ratio method. As shown in this table, SSM ratio evaluation results agreed with the results from the NDIS-2421 assessment method, i.e. Girder S10G8, S10G7, and S11G7 were damaged and S11G8 was not heavily damaged. The results from two evaluation criteria support each other. The SSM ratio evaluation criteria can help an engineer to assess the present status of a bridge and can also provide information useful for deciding whether costly maintenance is necessary.

Table 7-3: AE evaluation results

Girder No.	AE Evaluation Criteria	
	NDIS-2421	SSM Ratio
S10G8	Heavy Damage	Damaged
S11G8	Intermediate Damage	Not Heavily damaged
S10G7	Heavy Damage	Damaged
S11G7	Heavy Damage	Damaged

7.5.3 CRACK LOCATION USING AE 2D-LOC ANALYSIS TECHNIQUE

The purpose of this portion of the AE data analysis is to compare the results of a two-dimensional source location analysis with the actual crack patterns which were visible at the surface of the beam.

The AE data presented in this section were generated from the load application on the first night. These AE data were processed using the AE 2D-LOC two-dimensional source location software from Physical Acoustic Corporation in order to obtain information on source location of the cracks. The location algorithm takes advantage of the sensor placement geometry and also uses information from each of the sensors that has detected an AE-producing event. The detection range of a given size source event can be visualized by using the integrated attenuation analysis (PCI-8 Based AE System User's Manual 2002).

Figure 7-18 shows the resulting event location produced by AE 2D-LOC for the end of Span 11 of Girder 8 which was represented by square dots. For comparison, the actual visible crack pattern is superimposed on the event location plot. Cracks from both girder faces, east and west, are labeled and are differentiated by the weight and type of the line. The sensors, which were located on the east face, are displayed with solid squares and are identified by numbers.

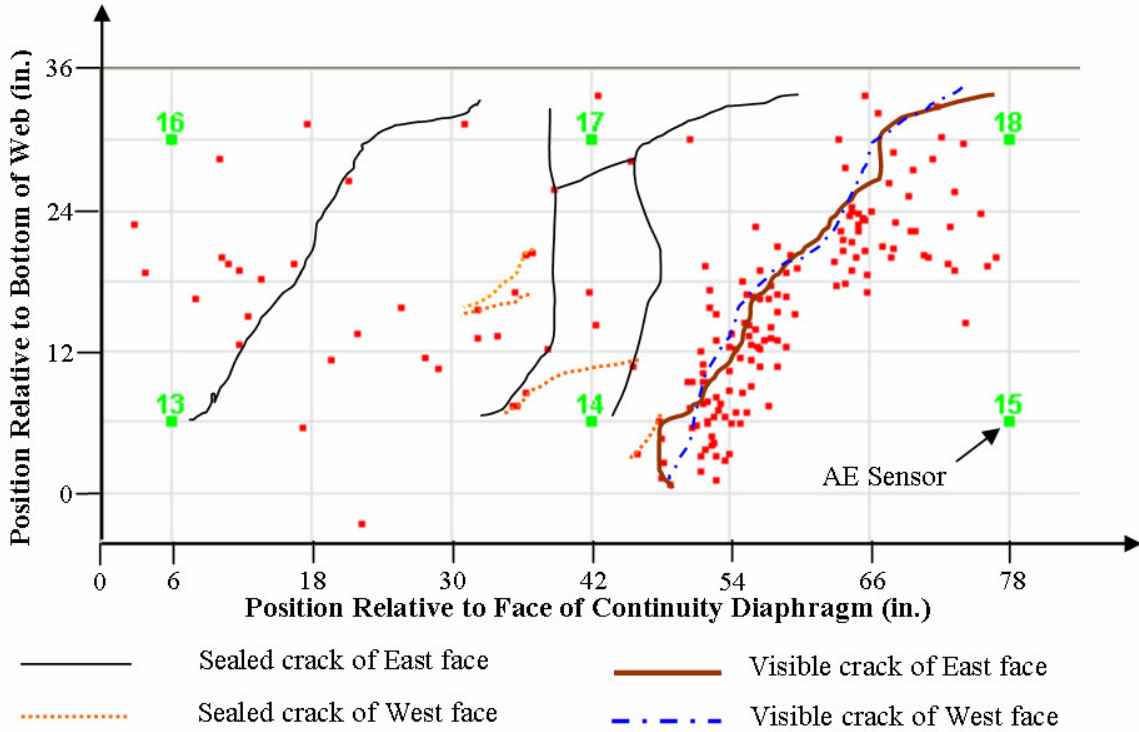


Figure 7-18: AE Event location and crack pattern of Span 11 Girder 8

Figure 7-19 shows the resulting event locations for the end of Span 11 of Girder 7 with the visible crack pattern superimposed. In Figures 7-18 and 7-19, the events plotted begin with the testing trucks moving onto Span 11 and end with the testing trucks moving off the bridge. The event locations plotted in Figures 7-18 and 7-19 correlate very well with the crack pattern visible at the surface of the beam.

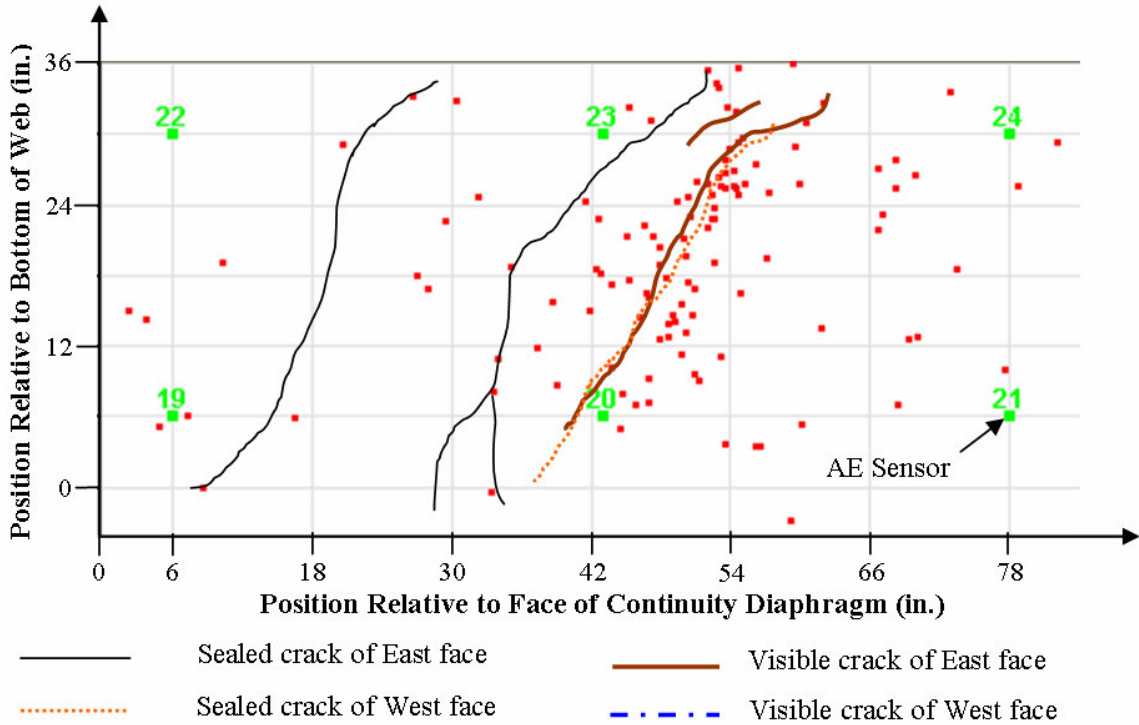


Figure 7-19: AE Event location and crack pattern of Span 11 Girder 7

Some events on the figures are scattered; this may be attributable to errors in the selection of the events or to friction between the prestressing strands and the concrete due to elongation or slip of the strands, which were located out of the sensor detection range.

From Figures 7-18 and 7-19, it may be observed that most events are concentrated in the middle region of the sensor layout. Very few events were located near the edges of the sensor pattern. This is attributed to the attenuation of the signals traveling from one extreme to the other. Once a crack is developed in the extreme of the monitored area, the signal is strong in the sensors near that extreme, but attenuates during its travel to the sensors near the other extreme.

7.6 SUMMARY AND CONCLUSIONS

Although much research has been conducted on AE monitoring of bridges, there are still no standard AE monitoring procedures for assessing the integrity of prestressed concrete members. In this study, AE evaluation procedures were evaluated under field testing conditions. The AE testing technique was carefully compared with other relevant data and evaluation criteria were developed.

The specific conclusions drawn from this experimental investigation are:

1. The AE method is a promising technique for nondestructive field testing of prestressed concrete girders.
2. The damage levels of prestressed concrete girder are reasonably qualified by a modified NDIS-2421 criterion. The recommended modified critical value for strain (load) ratio is 0.7; it is 0.5 for the calm ratio. These critical values are in reasonable agreement with interpretation of crack-opening displacements.
3. An evaluation criterion based on the ratio of signal strength moment (SSM) is proposed. A critical threshold value of 4 percent for the SSM ratio method was validated by comparison with the modified NDIS-2421 assessment criterion and COD measurements.
4. The AE 2D-LOC analysis technique was used successfully to locate the position of the cracks. The results showed a reasonable agreement with the crack pattern visible on the surface of the beam. The AE technique can be used to locate cracks by means of field testing.

The AE method is a promising and effective means of investigating the condition of prestressed concrete bridges. It can be used as a NDT tool to obtain an understanding of

the structural condition of prestressed concrete bridge girders subjected to a moving truck load.

Compared with other nondestructive techniques, AE monitoring still requires refinement to handle a number of difficulties encountered with in-situ testing. Background noise from protection of sensors and environmentally-induced emissions from wind and temperature should be considered in the AE testing. Further research should focus on implementation of evaluation criteria for the in-situ performance of prestressed concrete girders.

CHAPTER 8

SUMMARY, CONCLUSIONS, AND RECOMMENDATIONS

8.1 SUMMARY

Because prestressed concrete flexural members are critical to the integrity of many existing buildings and bridges, effective nondestructive testing (NDT) techniques are needed to evaluate the integrity of prestressed beams. The AE technique has been found to be one of the most informative NDT methods for determining material behavior and structure performance. The main objective of this study was to investigate the feasibility of using AE monitoring to assess the performance of prestressed concrete beams. In this research, laboratory testing was undertaken to gain insight into AE behavior on specimens in the laboratory environment. The AE technique was also applied in a field-test of a damaged prestressed concrete bridge.

This study consisted of an investigation of the AE behavior on sixteen prestressed concrete T-beams in the laboratory environment and one prestressed concrete bridge in the field. Twelve of these T-beams were constructed with one of three SCC mixtures. The remaining four beams were constructed with a concrete mixture similar to that used in precast/prestressed bridge girders in which proper consolidation is obtained using internal vibration. All specimens in this study were prestressed with two seven-wire, low-relaxation, and Grade 270 ½-in. “special” diameter strands.

The feasibility of using AE monitoring to assess the performance of prestressed concrete beams was investigated. The appearance and growth of cracks in concrete structures were compared with the occurrence of AE activities. Several AE parameters, such as amplitude, duration, and signal strength, were investigated in relation to the structural integrity of the beams.

The effectiveness of various AE evaluation criteria for assessing structural damage was evaluated. A new type of analysis of AE signals based on a proposed SSM ratio was proposed and the results were studied. AE signals from conventionally consolidated and SCC concrete beams during the entire flexural loading process were analyzed. The behavior and AE response of the SCC beams were compared with those of conventionally consolidated prestressed concrete beams. The effectiveness of the CLT method proposed in Appendix A of ACI 437 was investigated. The damage assessments resulting from the CLT were compared to damage classifications according to AE evaluation criteria.

Recently, extensive research has been conducted on the use of AE in a variety of civil engineering applications; however, almost all of this work has been done under controlled laboratory conditions. Scarcely any studies have been performed on AE behavior in-situ. A damaged prestressed concrete girder bridge was load tested in Huntsville, Alabama, U.S.A. The study had the objective of evaluating the overall effectiveness and practicality of using AE monitoring as a tool for the nondestructive testing of prestressed concrete bridges, as well as the accumulation of experience for the potential future implementation of AE monitoring of concrete bridges.

8.2 CONCLUSIONS FROM LABORATORY TESTING

Several conclusions were drawn based on the laboratory testing program described in this dissertation:

- Different AE sources can be distinguished by comparing the amplitude and duration of AE data. For both SCC prestressed concrete beams and conventionally consolidated prestressed concrete beams, the initiation of early microcracks or local slips and the mechanical rubbing of interlocked faces results in lower AE signal amplitude, while the initiation of primary flexural cracks produces higher signal amplitudes.
- For a damaged beam, long signal duration is observed during unloading even at lower (service-level) loads. This phenomenon is attributed to the closing and rubbing of interlocked faces produced during the previous loading.
- The formation and propagation of visible cracks in prestressed concrete beams is preceded by a significant increase in AE signal strength. Indication of imminent cracking is best indicated by a rapid increase in a plot of cumulative signal strength versus time.
- When applying NDIS-2421 evaluation criteria to conventionally consolidated prestressed concrete beams, reasonable results are obtained when the classification limits are set as 0.7 for the load ratio and 0.5 for the calm ratio.
- For the newly proposed SSM ratio evaluation criterion, an SSM ratio of 4 percent or greater was a consistently accurate indicator of heavy damage in conventionally consolidated prestressed concrete beams.

- A poor correlation between the actual specimen damage level and two AE evaluation criteria—the modified NDIS-2421 quantitative assessment criterion and the SSM ratio evaluation criterion—was observed for SCC beams. The application limits of these criteria need to be further investigated.
- The results of the AE evaluation criteria Relaxation Ratio and peak CSS Ratio did not reliably reflect the integrity of prestressed, conventionally consolidated concrete beams or prestressed SCC beams.
- The CLT repeatability and permanency criteria did not accurately indicate significant accumulated damage in prestressed concrete beams. The CLT deviation from linearity criterion is sensitive to damage in prestressed concrete beams, but the acceptance criterion needs to be further investigated and adjusted prior to implementation.

8.3 CONCLUSIONS FROM FIELD TESTING

The specific conclusions drawn from the field testing investigation are:

- AE testing of prestressed concrete structures can be successfully performed in the field.
- The damage levels of prestressed concrete girders are reasonably qualified using a modified NDIS-2421 criterion. The recommended critical value for strain (load) ratio is 0.7; it is 0.5 for the calm ratio.
- An evaluation criterion based on the ratio of signal strength moment (SSM) is proposed. A critical threshold value of 4 percent was adapted for practical application. The evaluation results from this SSM ratio method were validated by comparison with the assessment criterion suggested by the NDIS-2421.

- The AE 2D-LOC analysis technique can be used to locate cracks during field testing.

8.4 RECOMMENDATIONS FOR FUTURE STUDY

Since the T-beams tested in the laboratory were small-scale specimens, further research is required to implement the evaluation criteria discussed in this dissertation to evaluate the performance of prestressed concrete beams on larger scales.

The AE method is a promising and effective means of investigating the condition of prestressed concrete bridges. It can be used as a NDT tool to obtain understanding of the structural condition of prestressed concrete bridge girders subjected to a moving truck loads. A preliminary visual inspection of the bridge is of fundamental importance to perform AE monitoring. The presence of pre-existing cracks should be considered when deciding the sensor locations as these cracks affect the generation of AE. The cables should be fixed tightly in order to prevent excessive movement and avoid the generation of extraneous AE. Environmental factors such as wind, temperature, and traffic volume should be considered in order to obtain a comprehensive understanding of the AE data. Compared with other nondestructive techniques, AE monitoring still requires many refinements to handle a number of difficulties encountered with in-situ testing. Background noise from protection of sensors and environmentally-induced emissions from wind and temperature should be considered in the AE testing. Further research should focus on implementation of evaluation criteria for the in-situ performance of prestressed concrete girders.

REFERENCES

- AASHTO. 2006. *AASHTO LRFD Bridge Design Specifications: Customary U.S. Units*. 3rd ed. Washington D.C.: American Association of State Highway and Transportation Officials (AASHTO).
- ACI 437R-03. 2003. Strength evaluation of existing concrete buildings (ACI 437R-03). Farmington Hills, Michigan: American Concrete Institute (ACI). 28 pp.
- ACI 318-08. 2008. Building code requirements for structural concrete (ACI 318-08) and commentary (318R-08). Farmington Hills, Michigan: American Concrete Institute (ACI). 430 pp.
- ALDOT. 1994. Cracks in precast prestressed bulb tee girders on structure No.'s I-565-45-11.5 A. & B. on I-565 in Huntsville, Alabama. Report and attachments (A-L). Montgomery, Alabama: Alabama Department of Transportation (ALDOT).
- ASNT. 1996. Nondestructive testing handbook. 2nd ed. Columbus, OH: American Society for Nondestructive Testing (ASNT). 581 pp.
- ASTM E 1316-06. 2006. Standard terminology for nondestructive examinations. West Conshohocken, Pennsylvania: ASTM International. 30 pp.
- ASTM E 2374-04, 2004. Guide for acoustic emission system performance verification. West Conshohocken, Pennsylvania: ASTM International. 5 pp.
- ASTM E 2478-06, 2006. Standard practice for determining damage-based design stress for fiberglass reinforced plastic (FRP) materials using acoustic emission. West

- Conshohocken, Pennsylvania: ASTM International. 6 pp.
- Barnes, R. W., A. K. Schindler, K. S. Swenson, N. Gao, and W. E. Fason. 2006. Cracking and repair of prestressed concrete bridge girders made continuous for live loads. In *Extending the Life of Bridges: Concrete and Composites Buildings, Masonry and Civil Structures*, Proceedings of the 11th International Conference on Structural Faults and Repair. ed. M.C. Forde. Edinburgh, Scotland.
- Berger, H. and L. Mordfin. 1992. Nondestructive testing standards – present and future. West Conshohocken, Pennsylvania: ASTM STP 1151. 230 pp.
- Bray, D. E. and R. K. Stanley. 1997. Nondestructive evaluation: a tool in design, manufacturing, and service. New York: CRC Press. 586 pp.
- CARP. 1999. Recommended practice for acoustic emission evaluation of fiber reinforced plastic (FRP) tanks and pressure vessels. Columbus, Ohio: Committee on Acoustic Emission for Reinforced Plastics (CARP). 11 pp.
- Casadei, P. 2004. Assessment and improvement of capacity of concrete members: a case for in-situ load testing and composite materials. Ph.D. dissertation. Rolla, Missouri: University of Missouri-Rolla. 355 pp.
- Chotichai, P. 2001. Acoustic emission monitoring of prestressed bridge girders with premature concrete deterioration. M.S. thesis. Austin, Texas: University of Texas at Austin. 167 pp.
- Colombo, S., I. G. Main and M. C. Forde. 2003. Assessing damage of reinforced concrete beam using “b-value” analysis of acoustic emission signals. *Journal of Materials in Civil Engineering* 15 (3): 280–286.
- Colombo, S., M. C. Forde, I. G. Main and M. Shigeishi. 2005. Predicting the ultimate

- bending capacity of concrete beams from the “Relaxation Ratio” analysis of AE signals. *Construction and Building Materials* 19 (July): 746–754.
- Cole, T. A., M. Lopez and P. H. Ziehl. 2006. Fatigue behavior and nondestructive evaluation of full-scale FRP honeycomb bridge specimen. *Journal of Bridge Engineering* 11 (4): 420–429.
- Cross, N. O. 1972. Acoustic emission testing of pressure vessels for petroleum refineries and chemical plants. *Acoustic Emission*. ASTM STP 505: 270–296.
- Drouillard, T. F., R. G. Liptai and C. A. Tatro. 1975. Industrial use of acoustic emission for nondestructive testing. *Monitoring Structural Integrity by Acoustic Emission*. ASTM STP 571: 122–149.
- Dunegan H. L., D. O. Harris and C. A. Tatro. 1968. Failure analysis by use of acoustic emission. *Engineering Fracture Mechanics* 1 (1): 105–112.
- Fason, W. E. and R. W. Barnes. 2004. I-565 Visual inspection. Technical Report. Auburn, Alabama: Auburn University Highway Research Center. 31 pp.
- Fowler, T. J. and E. Gray. 1979. Development of an acoustic emission test for FRP equipment. Boston, MA: American Society of Civil Engineers Convention and Exposition. 22 pp.
- Fowler, T. J., J. A. Blessing and P. J. Conlisk. 1989. New direction in testing. In *Third International Symposium on Acoustic Emission from Composite Materials AECM-3*. 16–27. Paris, France.
- Gao, N. 2003. Investigation of cracking in precast prestressed girders made continuous for live load. M.S. thesis. Auburn, Alabama: Auburn University. 137 pp.
- Golaski, L., P. Gebiski and K. Ono. 2002. Diagnostics of reinforced concrete bridges by

- acoustic emission. *Journal of Acoustic Emission* 20 (1): 83–98.
- Gong, Z., E. O. Nyborg and G. Oommen. 1992. Acoustic emission monitoring of steel railroad bridges. *Materials Evaluation* 50 (7): 883–887.
- Hamstad, M. A., J. W. Whittaker and W. D. Brosey. 1992. Correlation of residual strength with acoustic emission from impact-damaged composite structures under constant biaxial load. *Journal of Composite Materials* 26 (15): 2307–2328.
- Hardy, H. R. 1975. Evaluation the stability of geological structures using acoustic emissions. *Monitoring Structural Integrity by Acoustic Emission*. ASTM-STP 571: 80–106.
- Hearn, S. W. and C. K. Shield. 1997. Acoustic emission monitoring as a nondestructive testing technique in reinforced concrete. *ACI Materials Journal* 94 (6): 510–519.
- Khayat, K. H. 1999. Workability, testing, and performance of Self-Consolidating Concrete. *ACI Materials Journal* 96 (3): 346-353.
- Khayat, K., C. Hu, and H. Monty. 1999. Stability of Self-Consolidating Concrete, advantages, and potential applications. In *Self-Compacting Concrete: Proceedings of the First International RILEM Symposium*, ed. A. Skarendahl and O. Petersson. Cachan Cedex, France: RILEM Publications, 143-152.
- Levy, K. R. 2007. Bond behavior of prestressed reinforcement in beams constructed with self-consolidating concrete. M.S. thesis. Auburn, Alabama: Auburn University. 277 pp.
- Li, Z., F. Li, A. Zdunek, E. Landis and S. Shah. 1998. Application of acoustic emission technique to detection of reinforcing steel corrosion in concrete. *ACI Materials Journal* 95 (1): 68–76.

- Ludovico, M. D., A. Nanni, A. Prota and E. Cosenza. 2005. Repair of bridge girders with composites: experimental and analytical validation. *ACI Structural Journal* 102 (5): 639–648.
- Luo, X., H. Haya, T. Inaba, T. Shiotani and Y. Nakanishi. 2004. Damage evaluation of railway structures by using train-induced AE. *Construction and Building Materials* 18: 215–223.
- MacGregor, J. G. and J. K. Wight. 2005. Reinforced concrete: mechanics and design. 4th Edition. New Jersey: Pearson Prentice Hall. 1132 pp.
- Masetti, F. 2005. Structural implications of field load testing using patch-loads. M.S. thesis. Rolla, Missouri: University of Missouri-Rolla. 118 pp.
- Matta, F., P. Rizzo, V. Karbhari and F. Scalea. 2006. Acoustic emission damage assessment of steel/CFRP bonds for rehabilitation. *Journal of Composites for Construction* 10 (3): 265–274.
- Mettemeyer, M. A. 1999. In situ rapid load testing of concrete structures. M.S. thesis. Rolla, Missouri: University of Missouri-Rolla. 112 pp.
- Ohtsu, M. 1988. Source inversion procedure for acoustic emission. *Progress in Acoustic Emission* 4 (1): 164–169.
- Ohtsu, M. 1989. A review of acoustic emission in civil engineering with emphasis on concrete. *Journal of Acoustic Emission* 8 (1): 93–98.
- Ohtsu, M., M. Uchida, T. Okamoto and S. Yuyama. 2002. Damage assessment of reinforced concrete beams qualified by acoustic emission. *ACI Structural Journal* 99 (4): 411–417.
- PCI-8 Based AE System User's Manual. 2002. Rev 0, Part #: 7030-1001. Physical

- Acoustics Corporation, Princeton Junction, NJ. 300 pp.
- Pollock, A. A. 1981. Acoustic emission amplitude distributions. *International Advances in Nondestructive Testing* 7: 215–239.
- Pollock, A. A. 1989. Acoustic emission inspection. *Metals Handbook* 17: 278–294.
- Pollock, A. A. 1995. Inspecting bridges with acoustic emission—inspection details about in-service steel bridges and monitoring weld operations: application guidelines.
Prepared by: Physical Acoustics Corporation.
- Ridge A. R. and P. H. Ziehl. 2006. Evaluation of strengthened reinforced concrete beams: cyclic load test and acoustic emission methods. *ACI Structural Journal* 103 (6): 832–841.
- Roberts, J. B. 2005. Evaluation of self-consolidating concrete for use in prestressed girder applications. M.S. thesis. Auburn, Alabama: Auburn University. 290 pp.
- Robinson, G. S. 1965. Methods of detecting the formation and propagation of microcracks in concrete. In *Proceedings of International Conference Structure of Concrete and Its Behaviour under Load*. London, England. 131–145.
- Schechinger, B. and T. Vogel. 2007. Acoustic emission for monitoring a reinforced concrete beam subject to four-point-bending. *Construction and Building Materials* 21 (March): 483–490
- Shapiro, K. A. 2007. Finite-element modeling of a damaged prestressed concrete bridge. M.S. thesis. Auburn, Alabama: Auburn University. 258 pp.
- Shield C. 1997. Comparison of acoustic emission activity in reinforced and prestressed concrete beams under bending. *Construction and Building Materials* 11(3): 189–194.
- Shiotani, T., K. Ikeda and M. Ohtsu. 2001. Detection and evaluation of AE waves due to

- rock deformation. *Construction and Building Materials* 15 (5): 235–246.
- Shiotani, T., N. Sakaino, M. Shingeishi, M. Ohtsu, Y. Asai and T. Hayashi. 1998. AE characteristics of full-scale concrete-pile under bending and shear Load. In *Proceedings of Sixth International Symposium on Acoustic Emission from Composite Materials*. 163–172. Tokyo, Japan.
- Skarendahl, A. 2003. The present - The Future”. In *Self-Compacting Concrete: Proceedings of the Third International RILEM Symposium*, ed. O. Wallevik and I. Nielsson. Bagnaux, France: RILEM Publications, 6-14.
- Suzuki, T. and M. Ohtsu. 2004. Quantitative damage evaluation of structural concrete by a compression test based on AE rate process analysis. *Construction and Building Materials* 18 (3): 197–202.
- Swenson, K. S. 2003. Feasibility of externally bonded FRP reinforcement for repair of cracked prestressed concrete girders. M.S. thesis. Auburn, Alabama: Auburn University. 257 pp.
- Swords J. S. 2005. Transfer length in prestressed self-consolidating concrete. M.S. thesis. Auburn, Alabama: Auburn University. 238 pp.
- Tinkey, B. V., T. J. Fowler and R. E. Klingner. 2002. Nondestructive testing of prestressed bridge girders with distributed load, Report No. FHWA/TX-03/1857-2, Austin, Texas. 20 pp.
- Travers, F. 1997. Acoustic monitoring of prestressed concrete pipe. *Construction and Building Materials* 11 (3): 175–187.
- Uomoto, T. 1987. Application of acoustic emission to the field of concrete engineering. *Journal of Acoustic Emission* 6 (3): 137–144.

- Yopez Roca, L.O. 1999. Acoustic emission examination of high strength prestressed concrete girders. M.S. thesis. Austin, Texas: University of Texas at Austin. 97 pp.
- Yoon, D., J. Weiss and S. Shah. 2000. Assessing damage in corroded reinforced concrete using acoustic emission. *Journal of Engineering Mechanics* 126 (3): 273–283.
- Yuyama, S., T. Okamoto and S. Nagataki. 1994. Acoustic emission evaluation of structural integrity in repaired reinforced concrete beams. *Materials Evaluation* 52 (1): 86–90.
- Yuyama, S., T. Okamoto, M. Shingeishi, M. Ohtsu and T. Kishi. 1999. A proposed standard for evaluating structural integrity of reinforced concrete beams by acoustic emission. *Acoustic Emission: Standards and Technology update*, ASTM STP 1353: 25–40.
- Yuyama, S., Z. Li, M. Yoshizawa, T. Tomokiyo and T. Uomoto. 2001. Evaluation of fatigue damage in reinforced concrete slab by acoustic emission. *Nondestructive Testing and Evaluation International* 34 (6): 381–387.
- Ziehl, P. H. and T. J. Fowler. 2003. Fiber reinforced polymer vessel design with a damage approach. *Journal of Composite Structures* 61 (4): 395–411.

APPENDIX A

NOTATION

Symbol	Description
A	Amplitude in decibels
d_b	nominal diameter of reinforcement
E_p	modulus of elasticity of prestressing reinforcement
ε_p	strain in prestressing reinforcement
f'_c	specified compressive strength of concrete 28 days
f_+	positive signal envelope function
f_-	negative signal envelope function
K	an empirically derived factor that varies with the number of hits
l_d	development length
l_e	embedment length
M_{cr}	actual cracking moment achieved by specimen during flexural testing
$M_{cr,calc}$	predicted cracking moment according to strain compatibility
M_{max}	maximum moment achieved by specimen during flexural testing
M_n	predicted nominal moment capacity
$M_{n,AASHTO}$	predicted nominal moment capacity according to AASHTO LRFD specifications

$M_{n,calc}$	predicted nominal moment capacity according to strain compatibility
N	the number of hits
P_{min}	minimum load used for AE load cycles
P_{cr}	cracking load experienced during flexural load testing
P_s	service load computed to cause zero stress in the bottom fiber of the beam at the load points
P_n	ultimate load predicted prior to flexural load testing
S_{oi}	the signal strength value of the i th hit
t_1	time at first threshold crossing
t_2	time at last threshold crossing
t_i	the time from the beginning of the hold to the i th hit
V	Voltage of peak excursion
V_{ref}	Reference voltage

APPENDIX B

LOAD, DEFLECTION, AND STRAND SLIP PLOTS

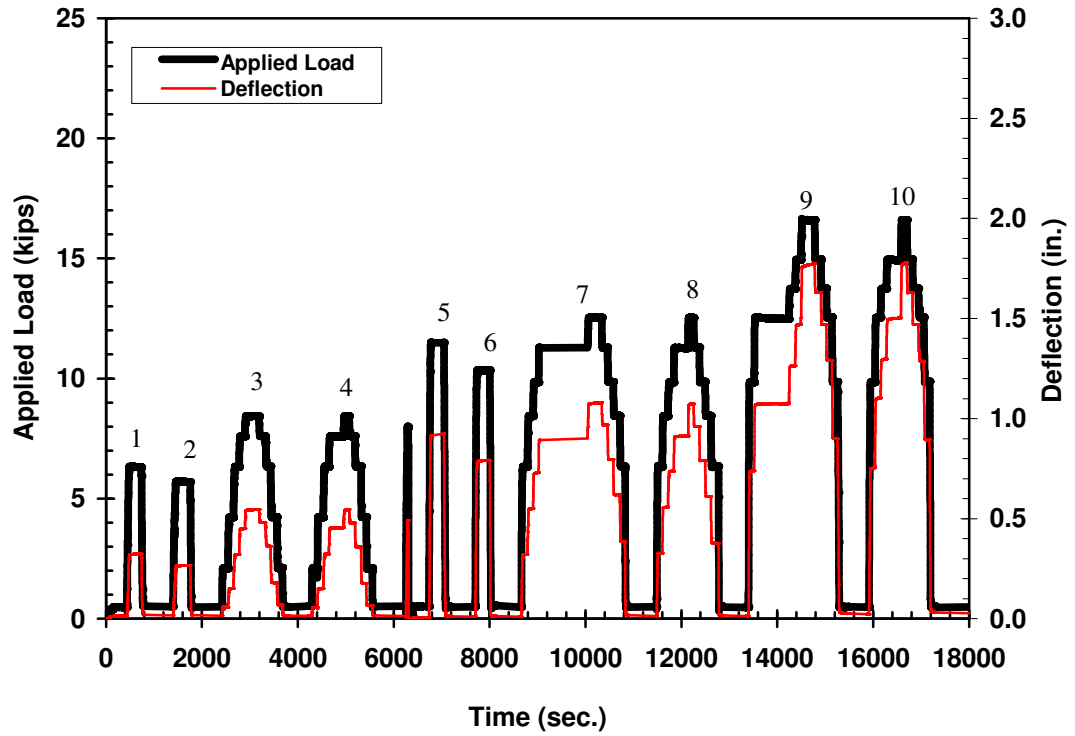


Figure B-1: Applied load and deflection versus time for STD-M-A

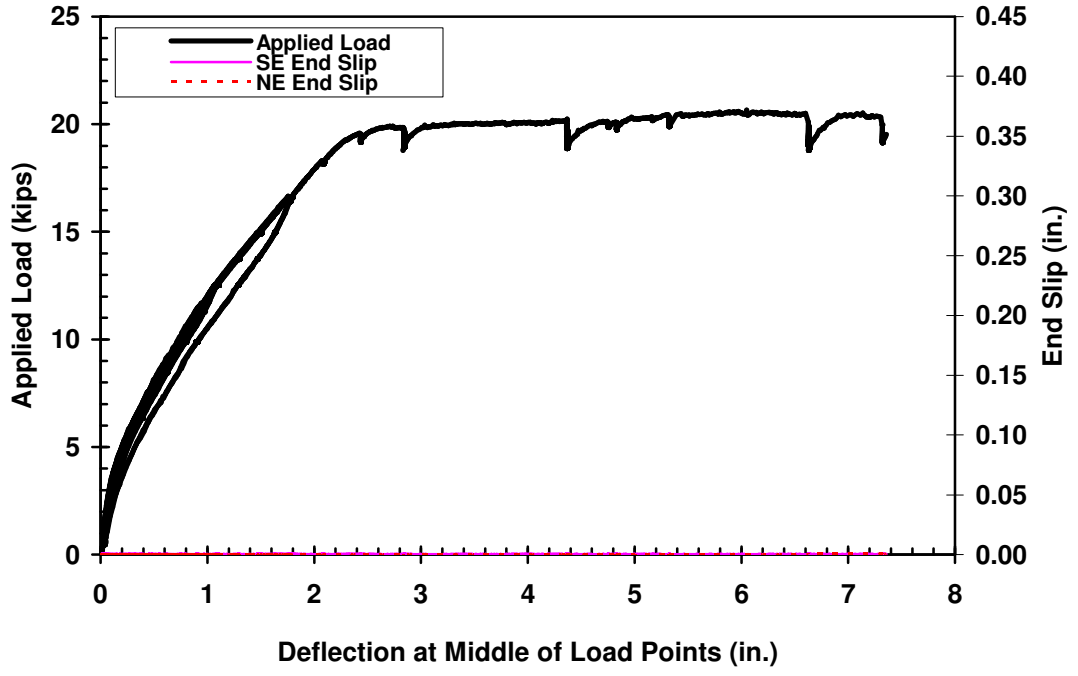


Figure B-2: Applied load and end slip versus deflection for STD-M-A

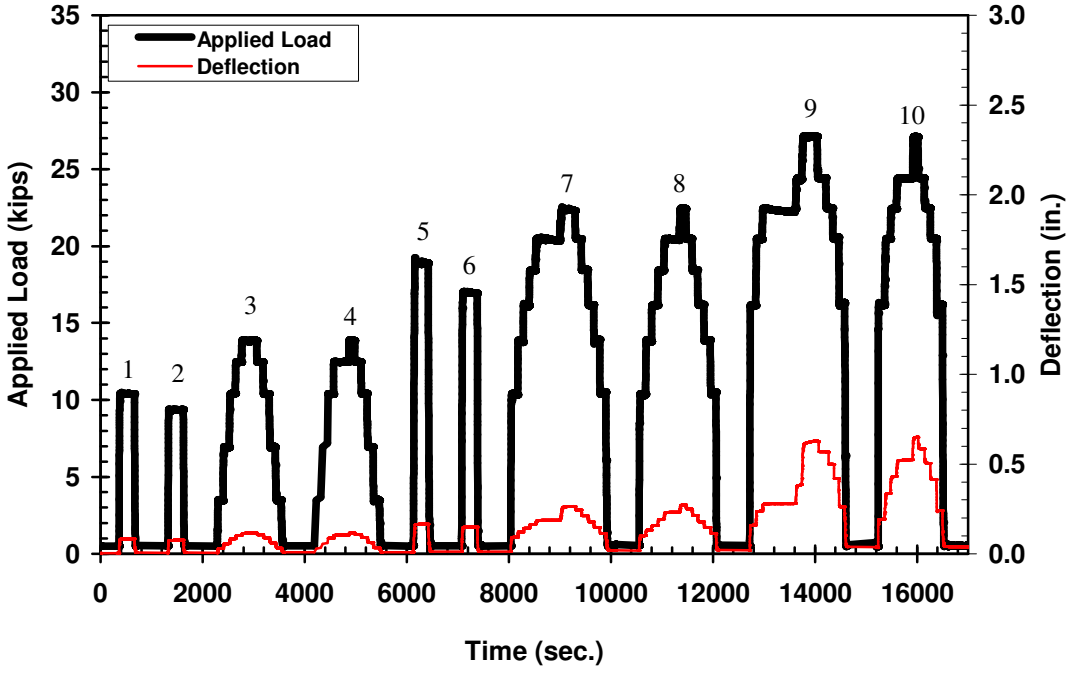


Figure B-3: Applied load and deflection versus time for STD-M-B

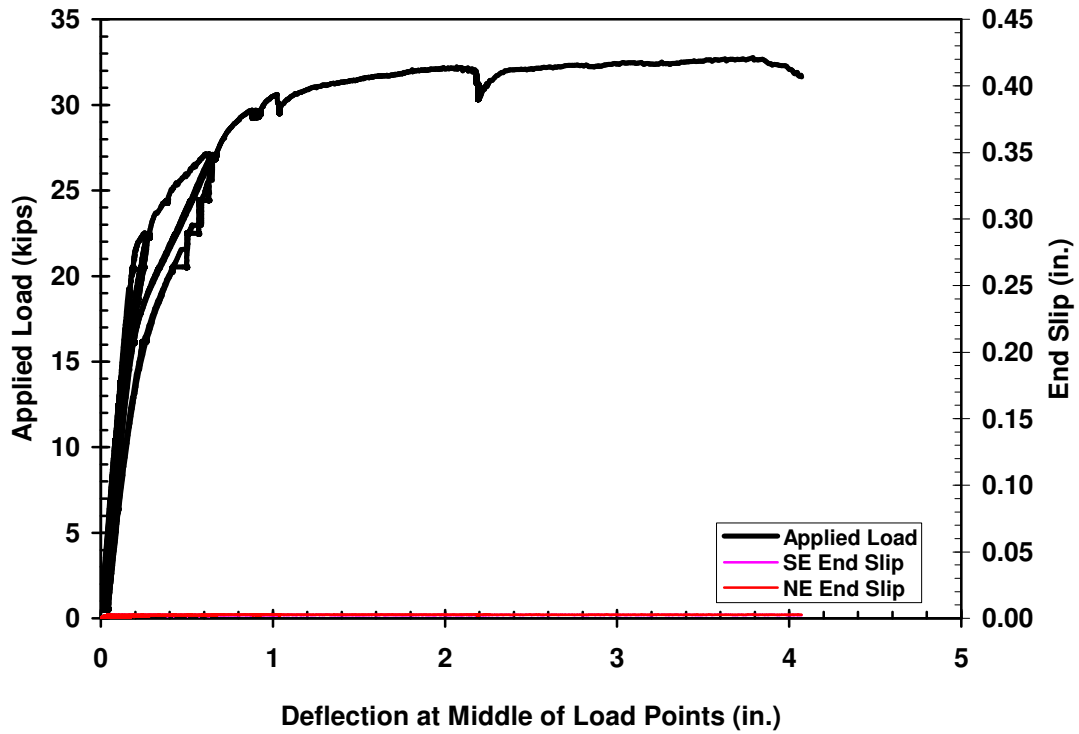


Figure B-4: Applied load and end slip versus deflection for STD-M-B

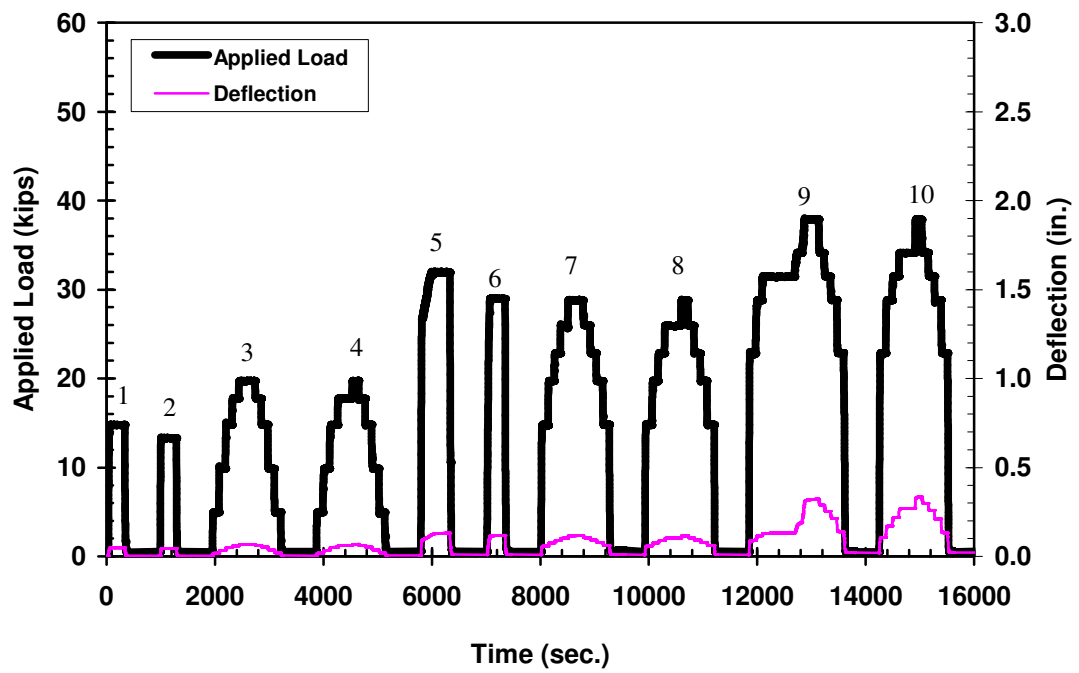


Figure B-5: Applied load and deflection versus time for STD-M-C

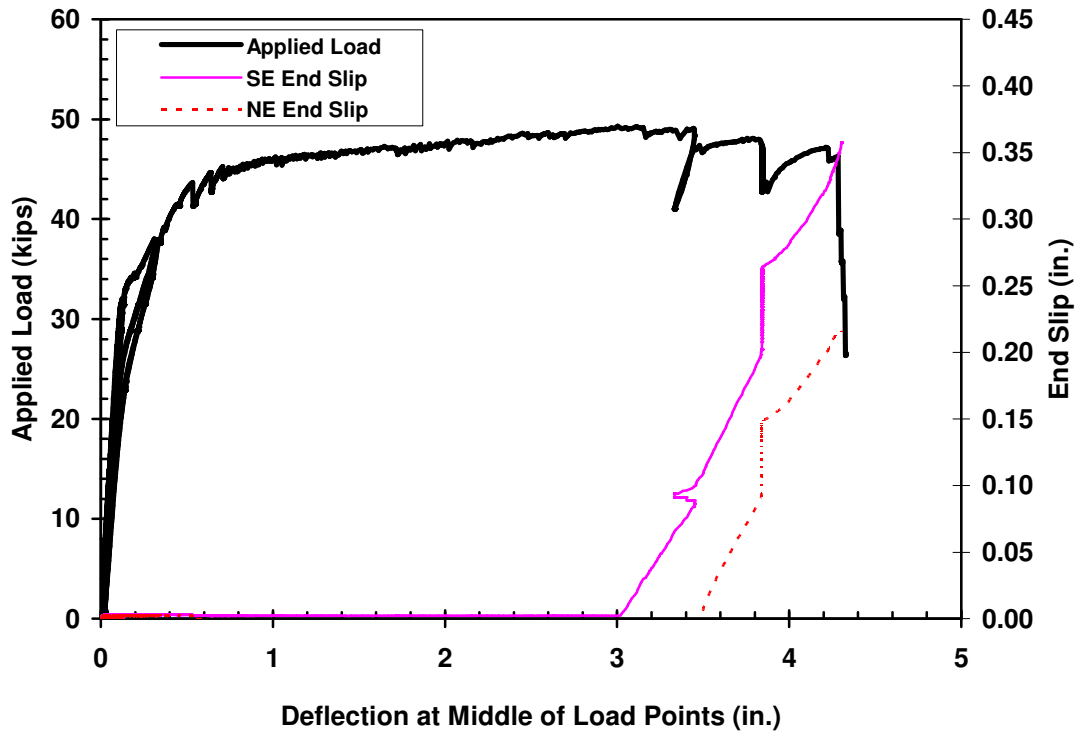


Figure B-6: Applied load and end slip versus deflection for STD-M-C

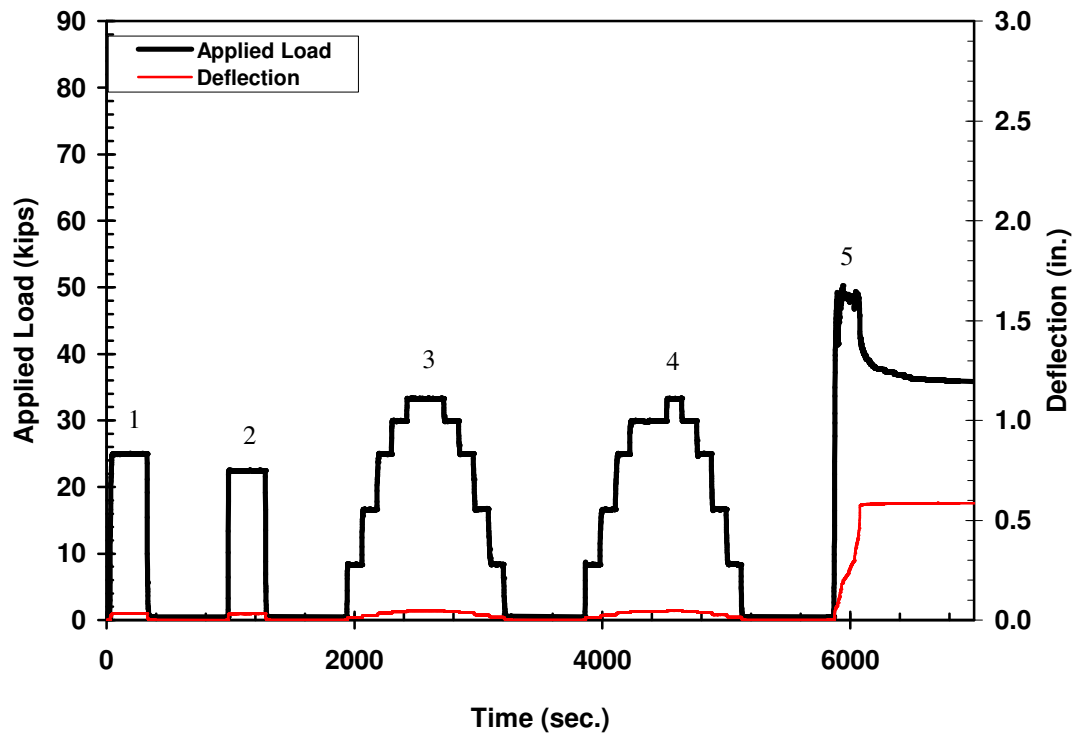


Figure B-7: Applied load and deflection versus time for STD-M-D

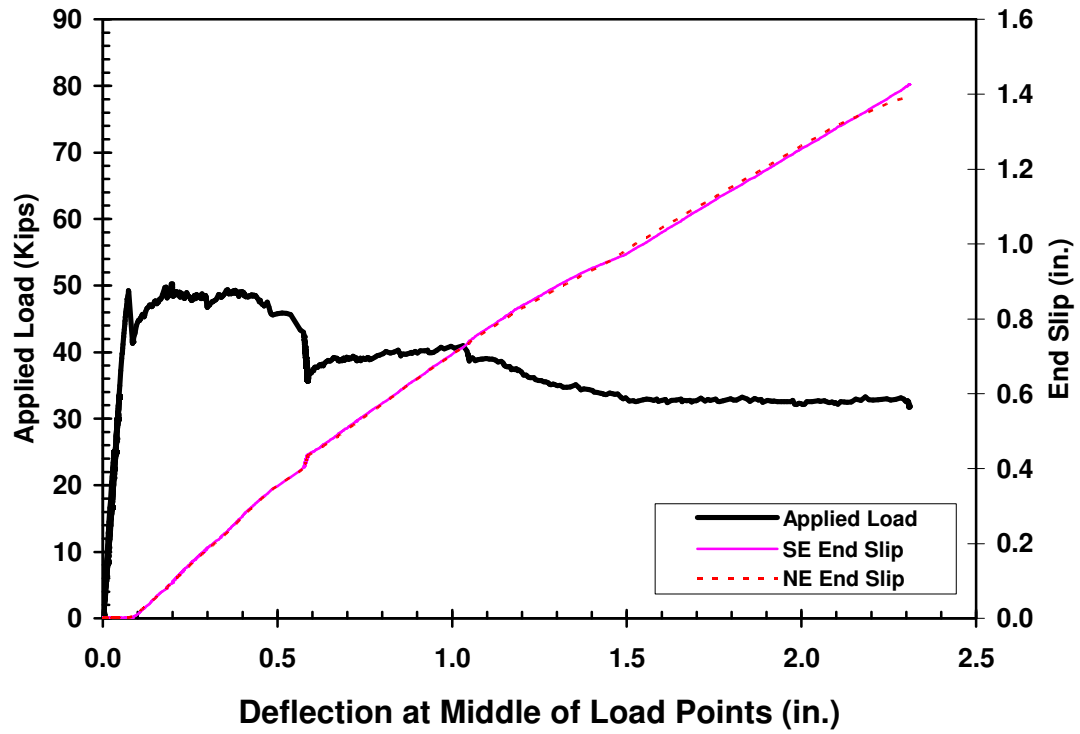


Figure B-8: Applied load and end slip versus deflection for STD-M-D

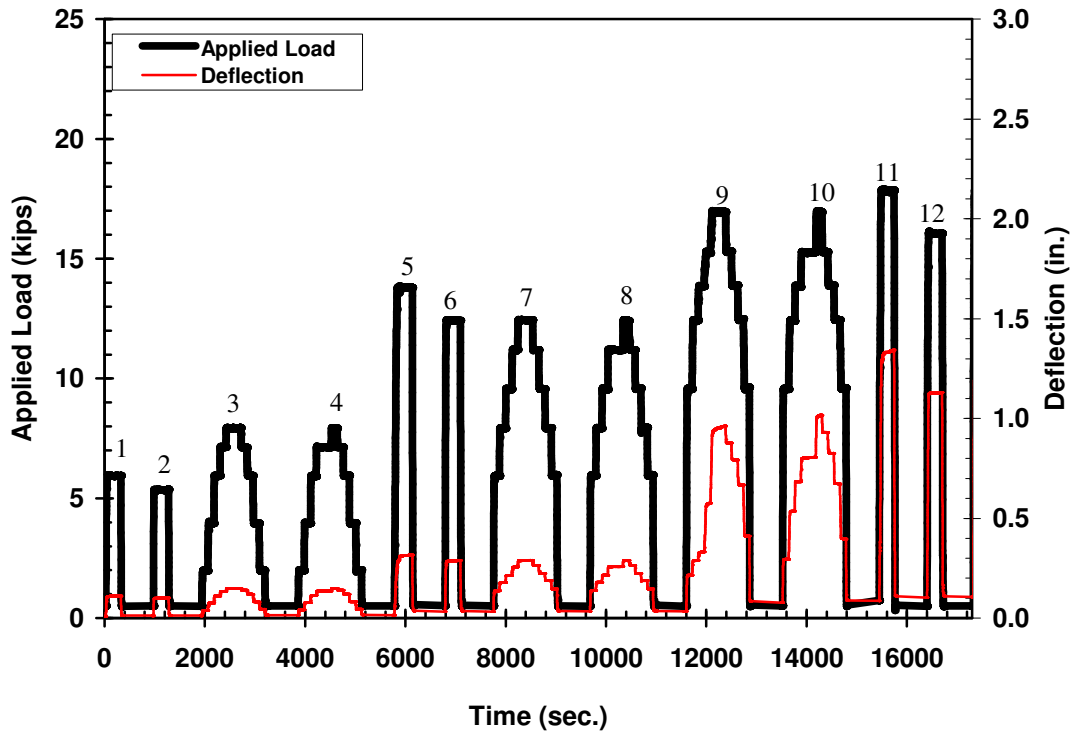


Figure B-9: Applied load and deflection versus time for SCC-MA-A

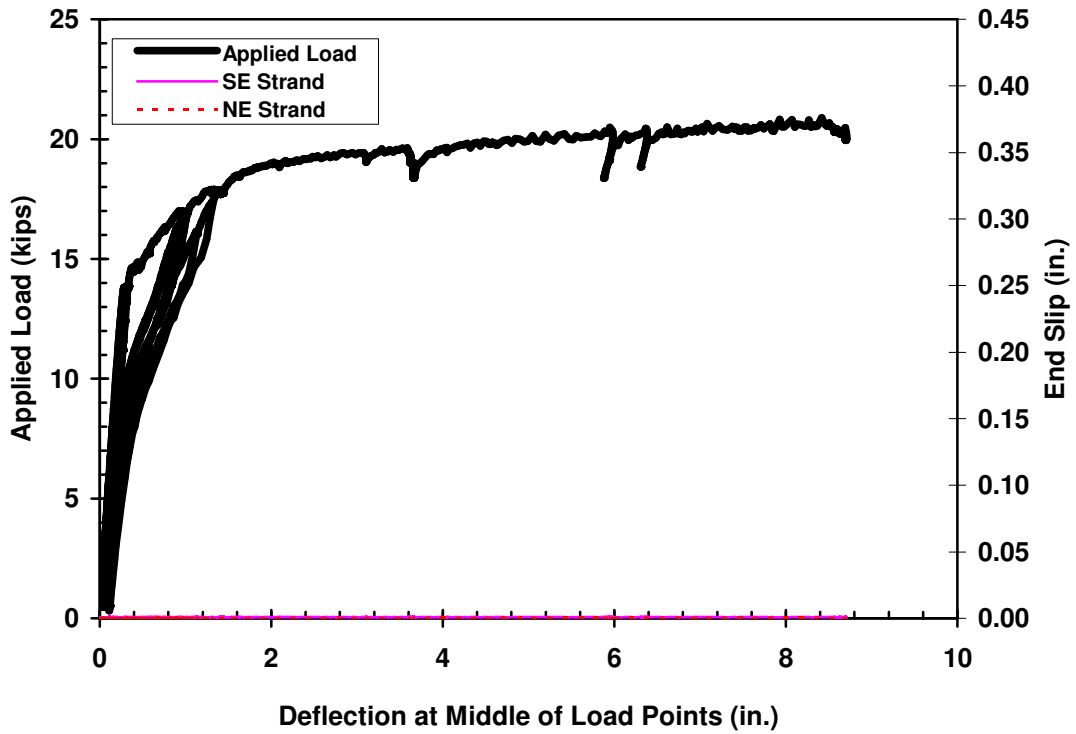


Figure B-10: Applied load and end slip versus deflection for SCC-MA-A

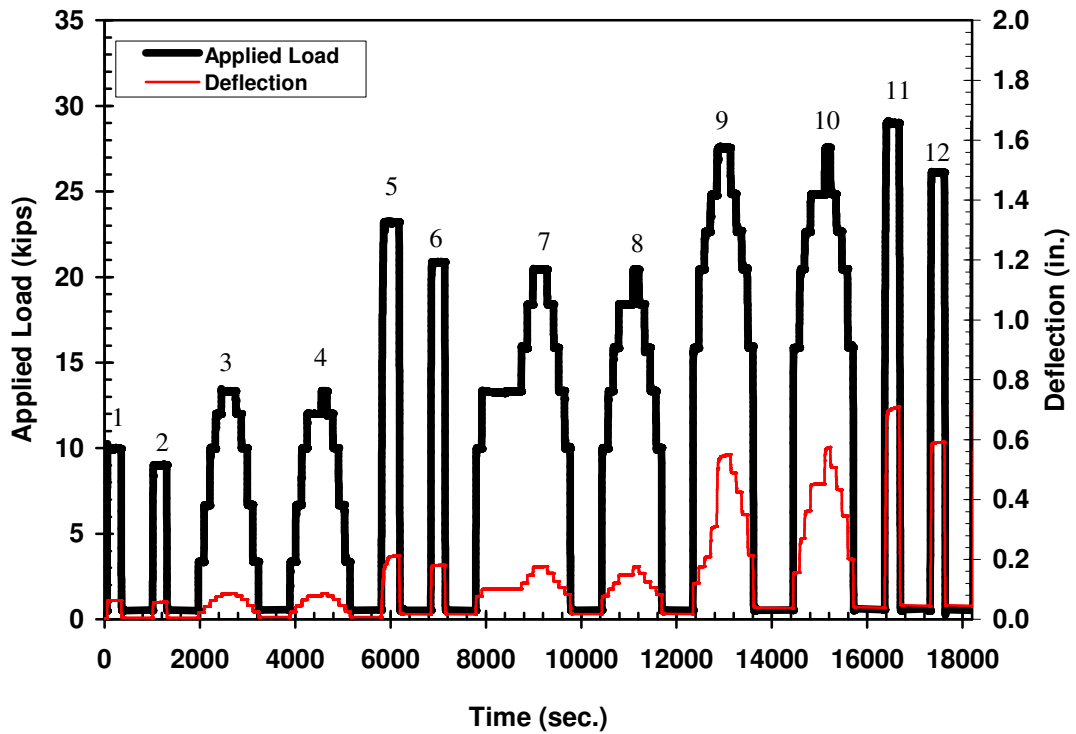


Figure B-11: Applied load and deflection versus time for SCC-MA-B

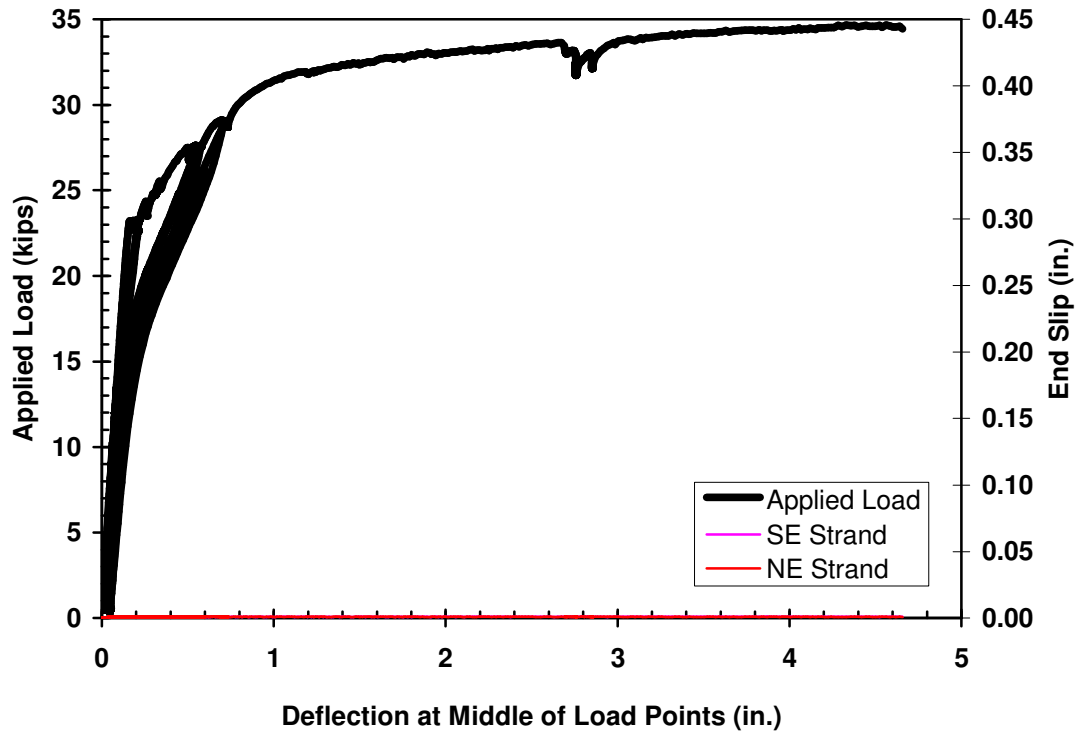


Figure B-12: Applied load and end slip versus deflection for SCC-MA-B

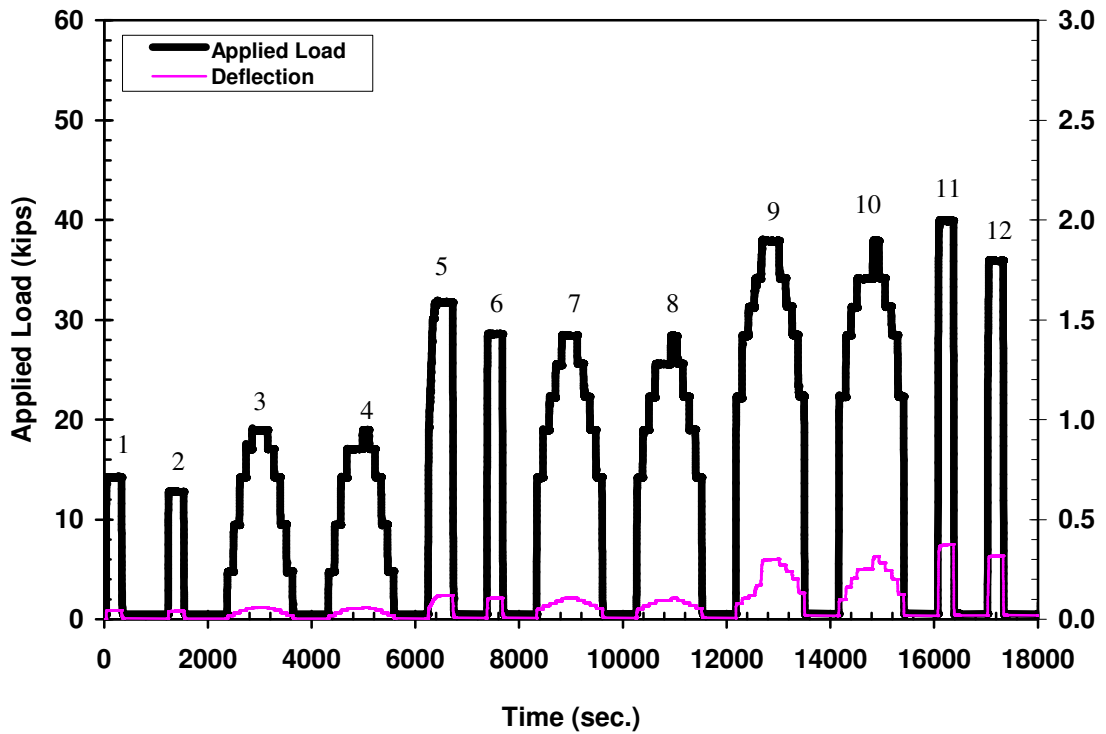


Figure B-13: Applied load and deflection versus time for SCC-MA-C

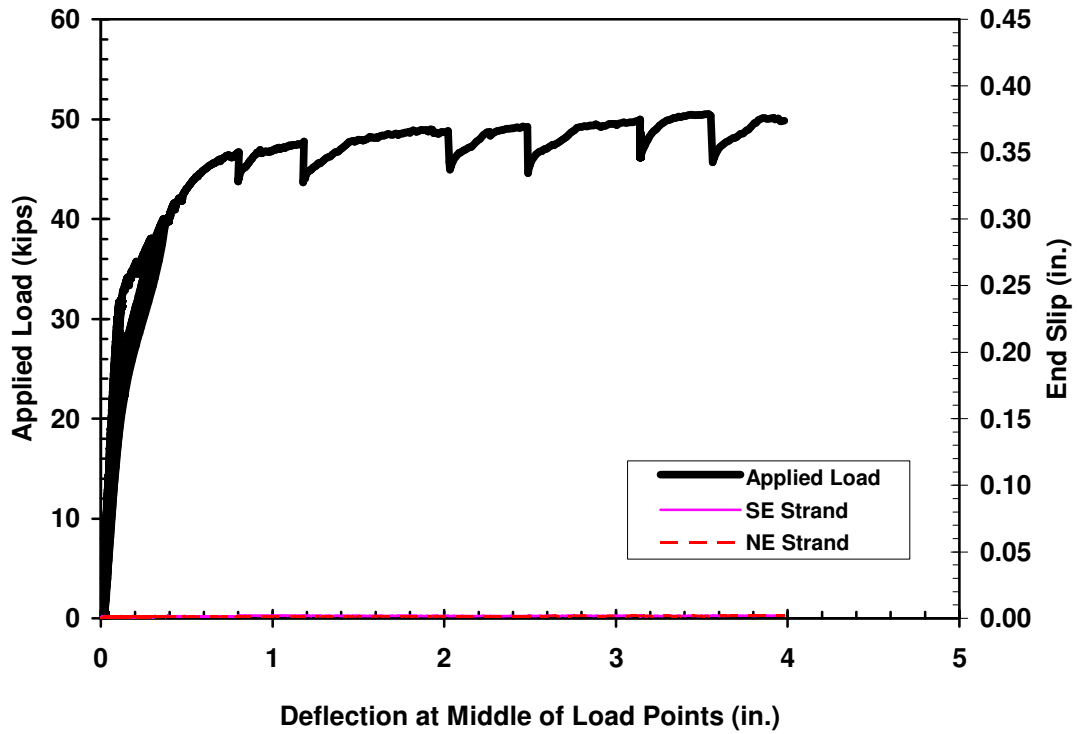


Figure B-14: Applied load and end slip versus deflection for SCC-MA-C

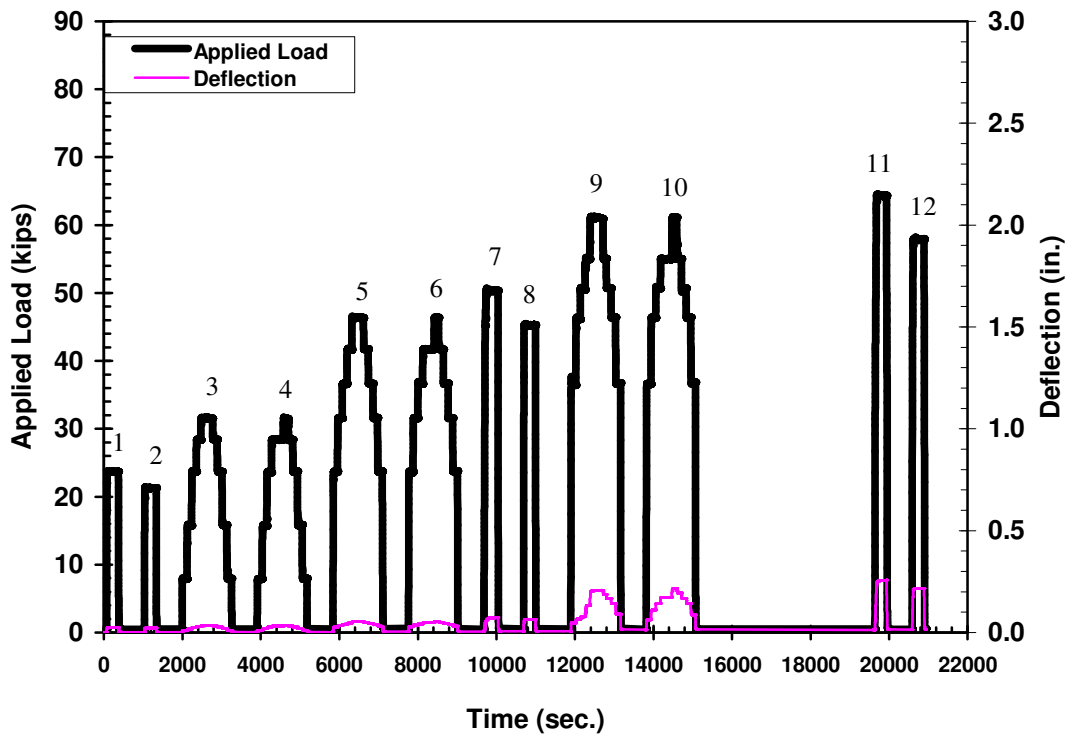


Figure B-15: Applied load and deflection versus time for SCC-MA-D

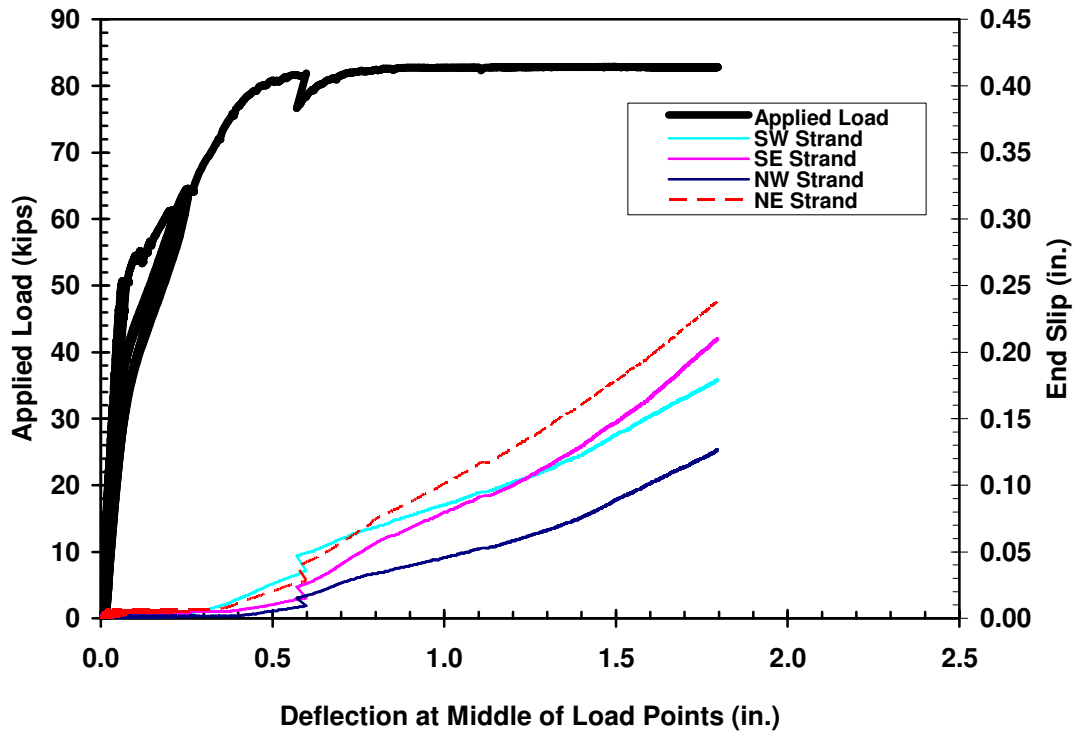


Figure B-16: Applied load and end slip versus deflection for SCC-MA-D

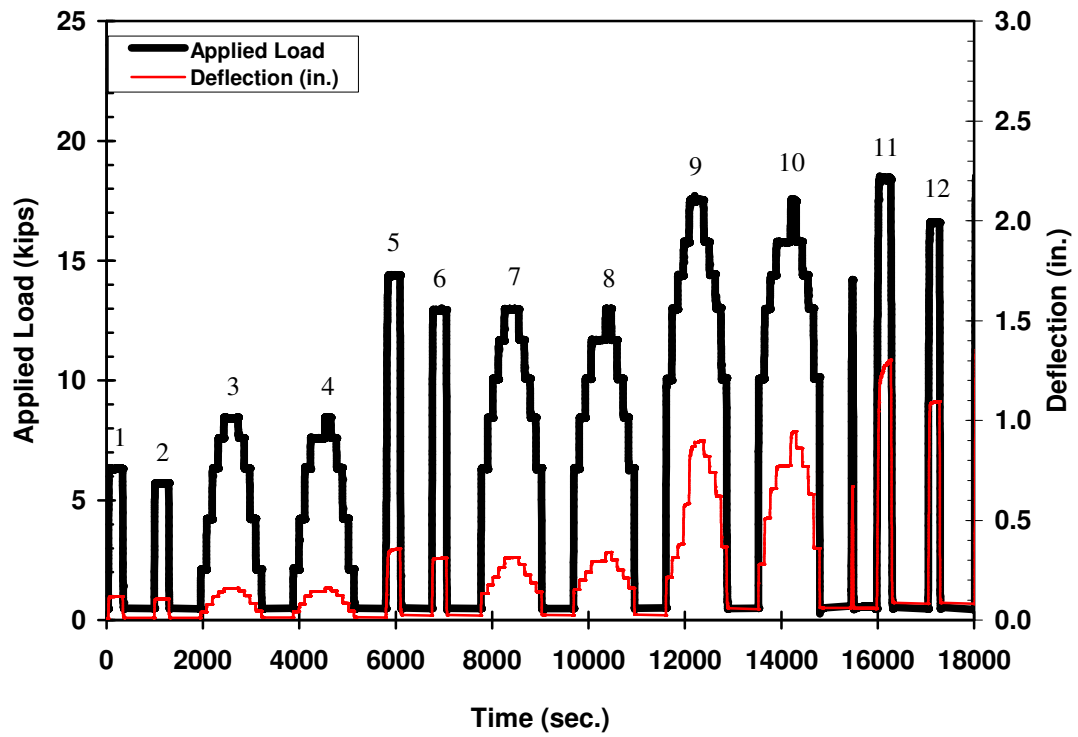


Figure B-17: Applied load and deflection versus time for SCC-MS-A

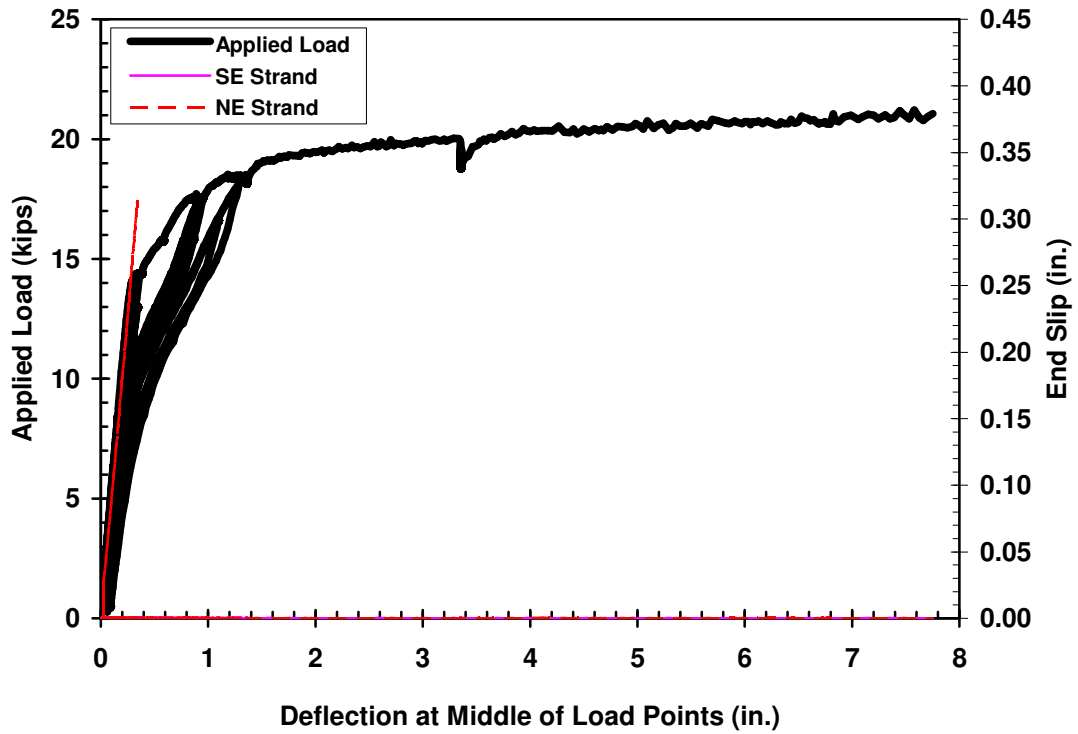


Figure B-18: Applied load and end slip versus deflection for SCC-MS-A

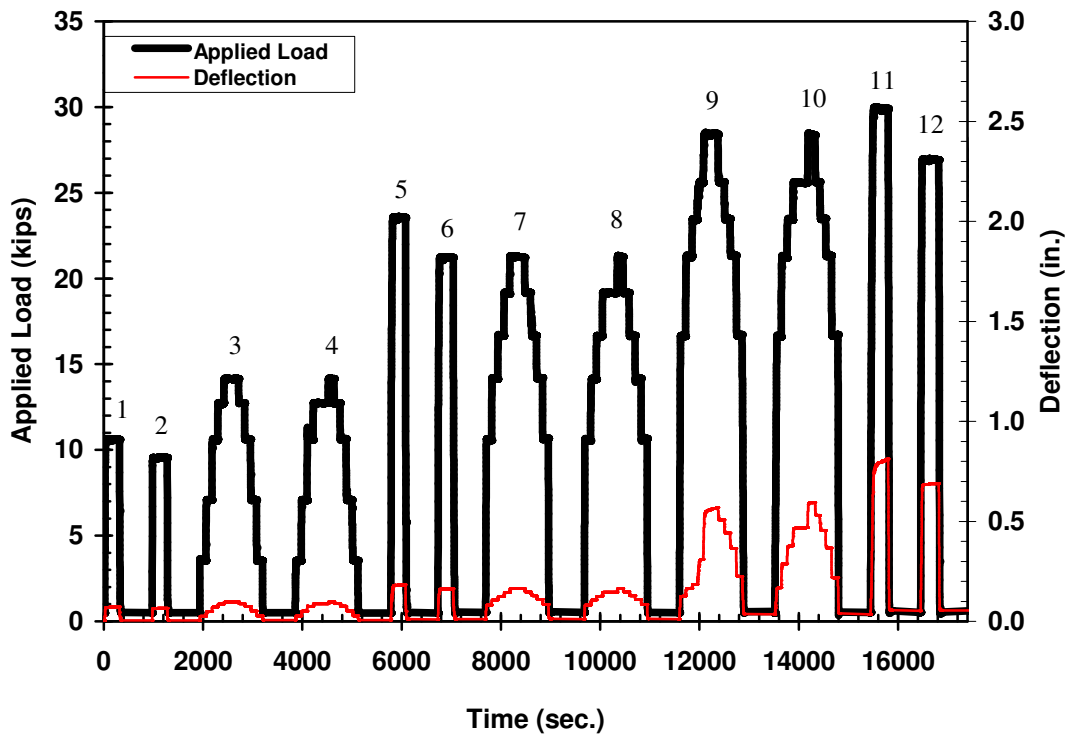


Figure B-19: Applied load and deflection versus time for SCC-MS-B

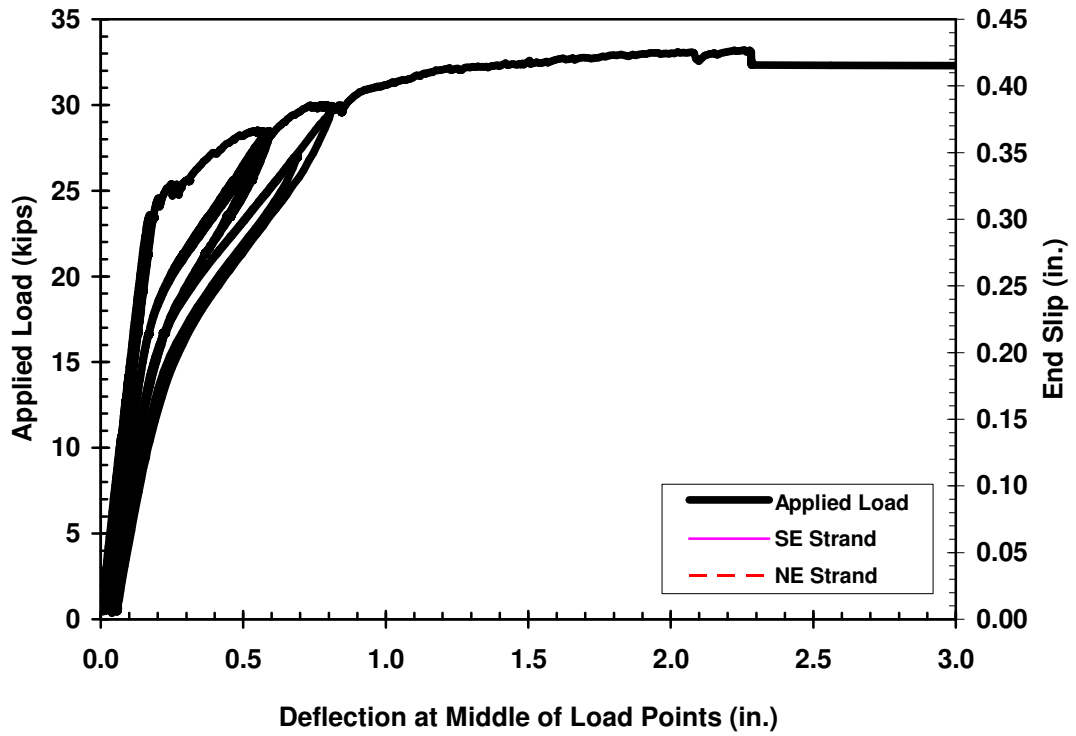


Figure B-20: Applied load and end slip versus deflection for SCC-MS-B

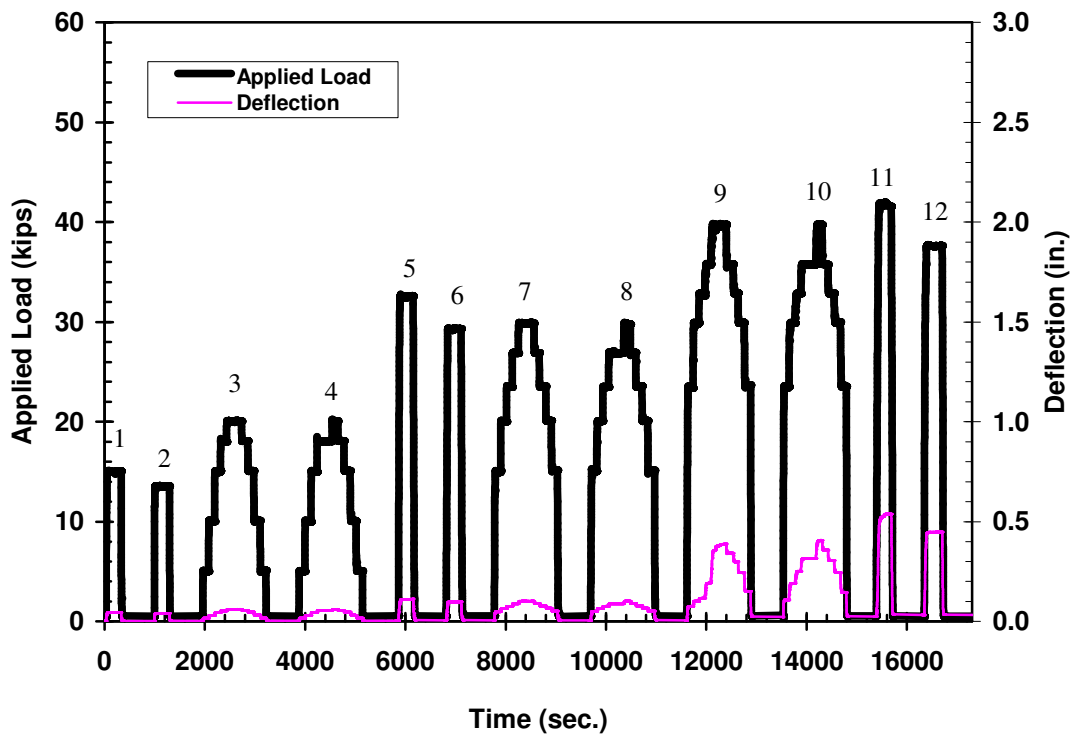


Figure B-21: Applied load and deflection versus time for SCC-MS-C

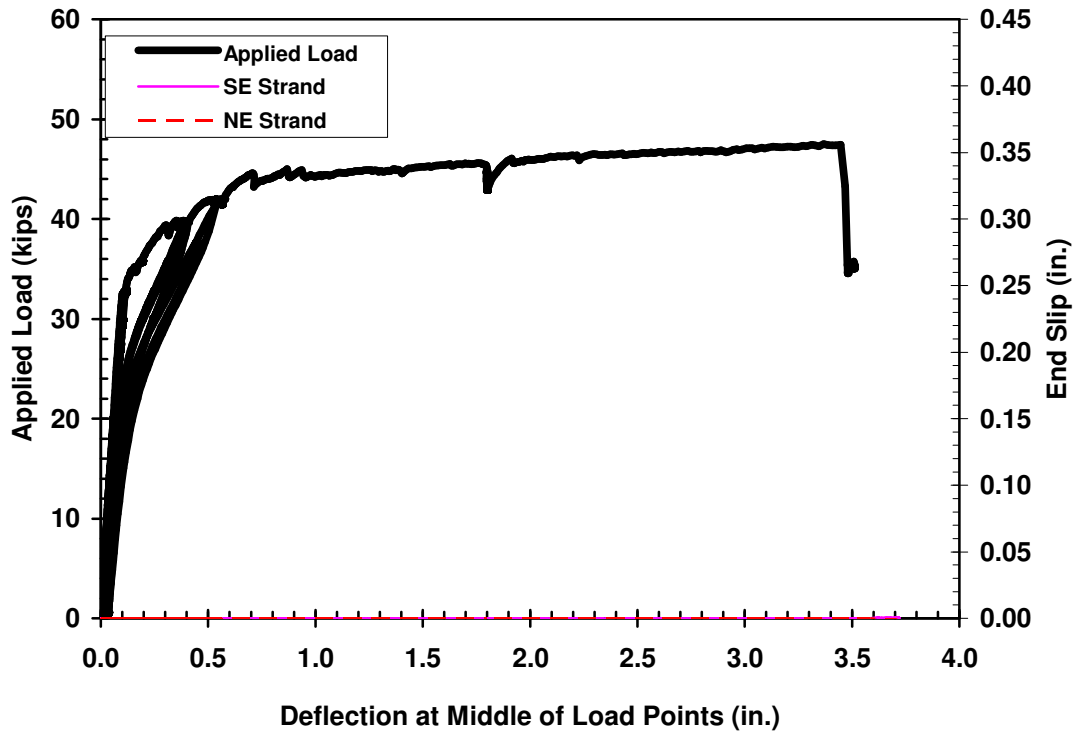


Figure B-22: Applied load and end slip versus deflection for SCC-MS-C

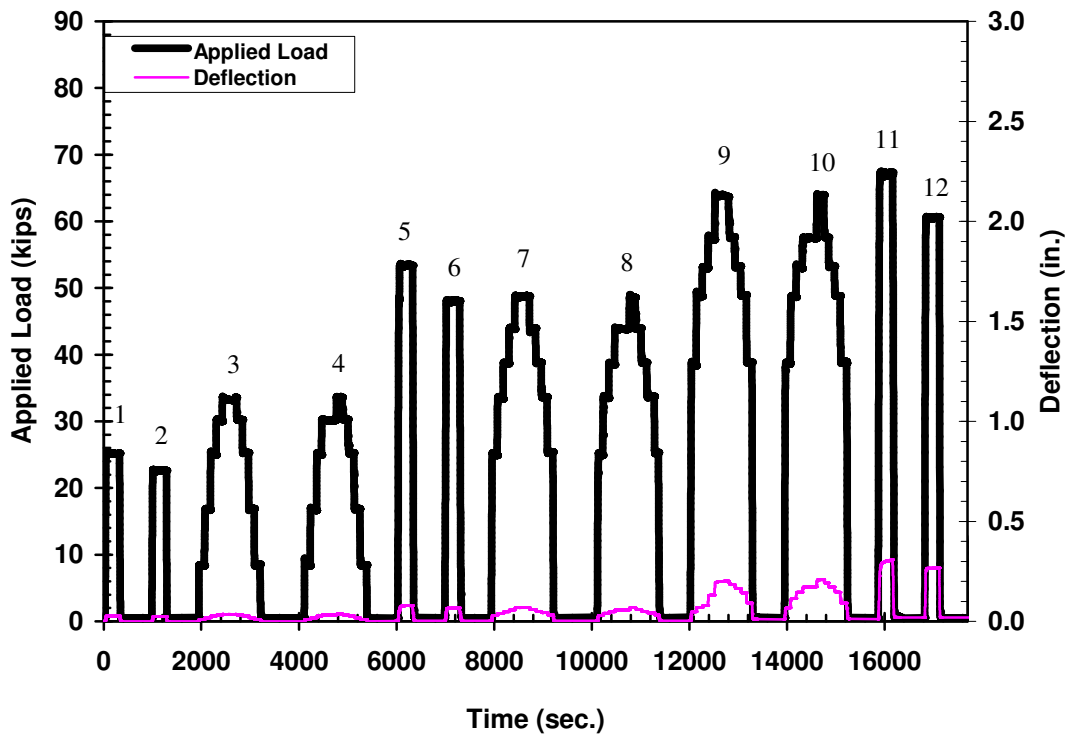


Figure B-23: Applied load and deflection versus time for SCC-MS-D

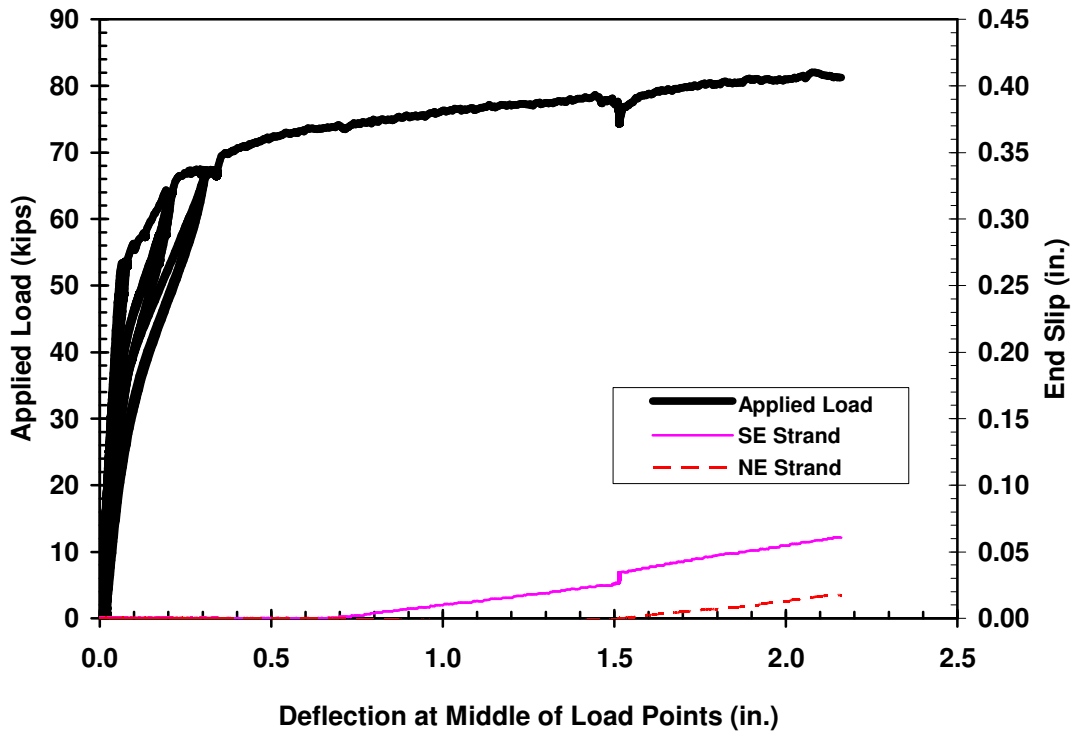


Figure B-24: Applied load and end slip versus deflection for SCC-MS-D

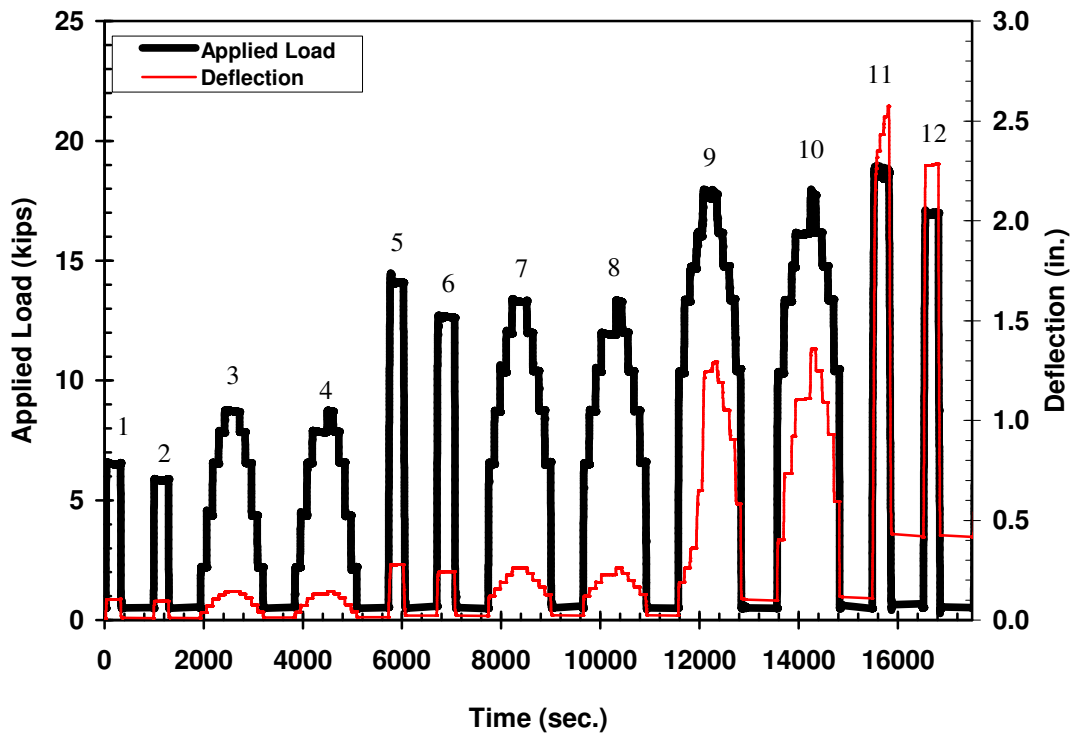


Figure B-25: Applied load and deflection versus time for SCC-HS-A

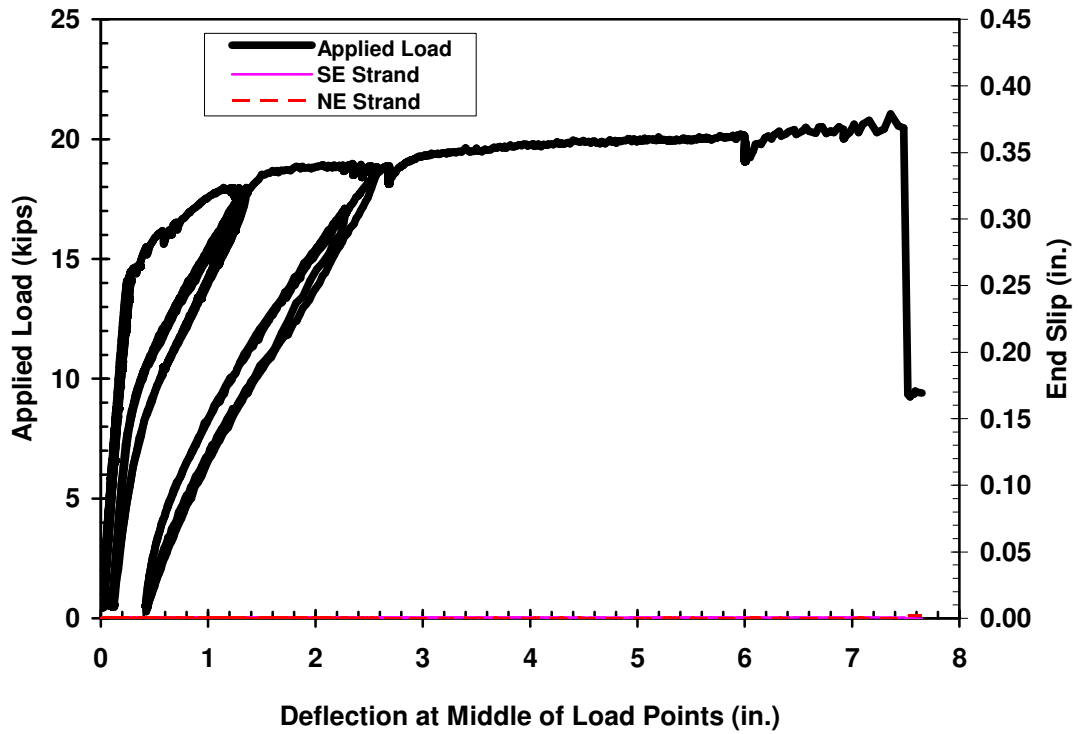


Figure B-26: Applied load and end slip versus deflection for SCC-HS-A

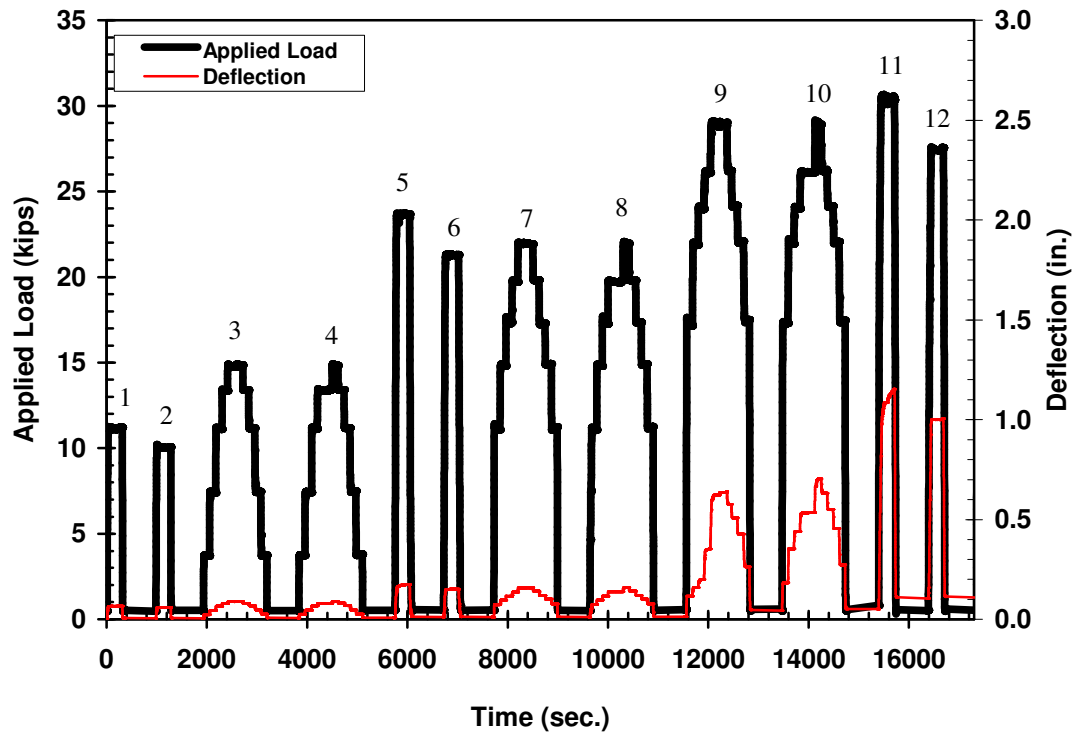


Figure B-27: Applied load and deflection versus time for SCC-HS-B

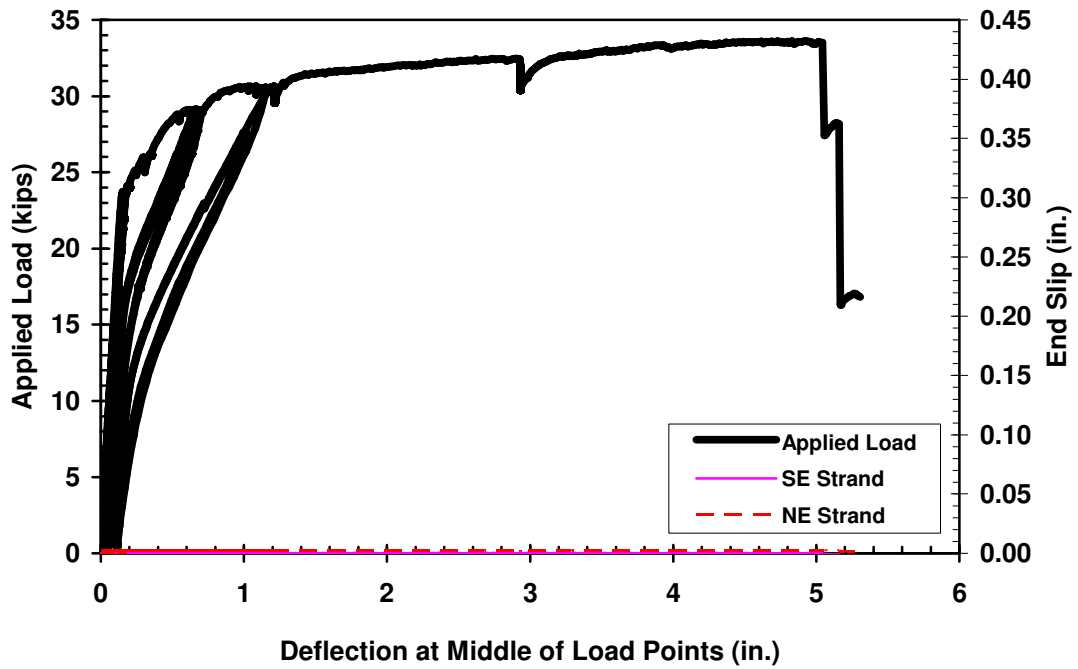


Figure B-28: Applied load and end slip versus deflection for SCC-HS-B

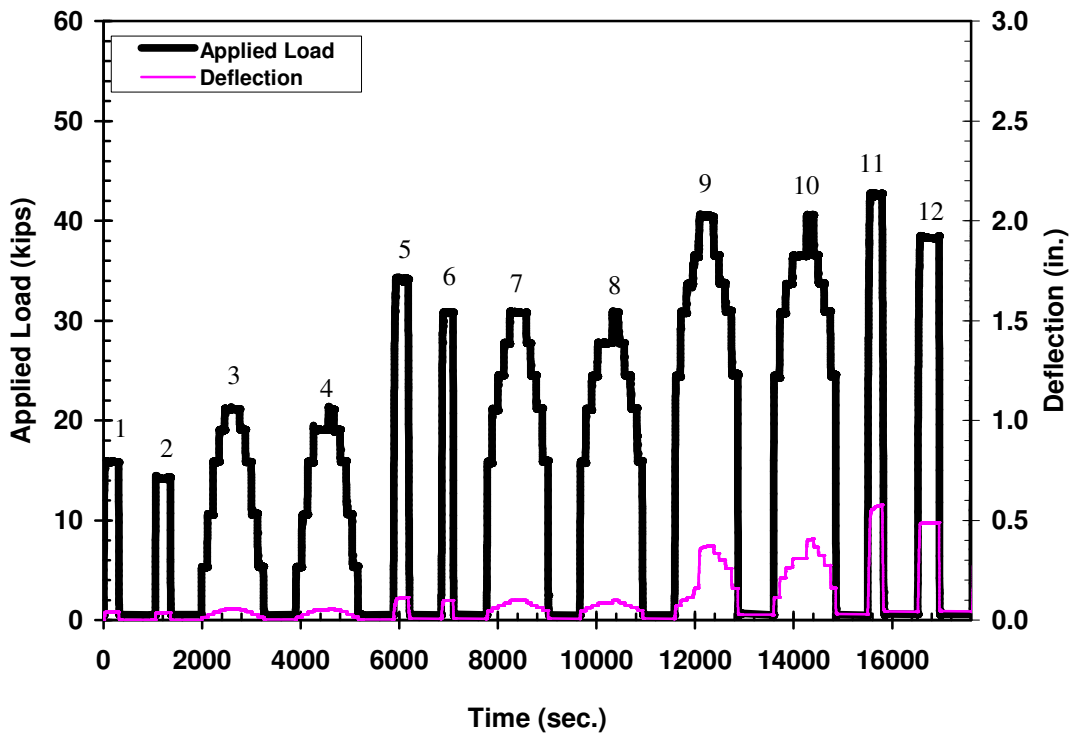


Figure B-29: Applied load and deflection versus time for SCC-HS-C

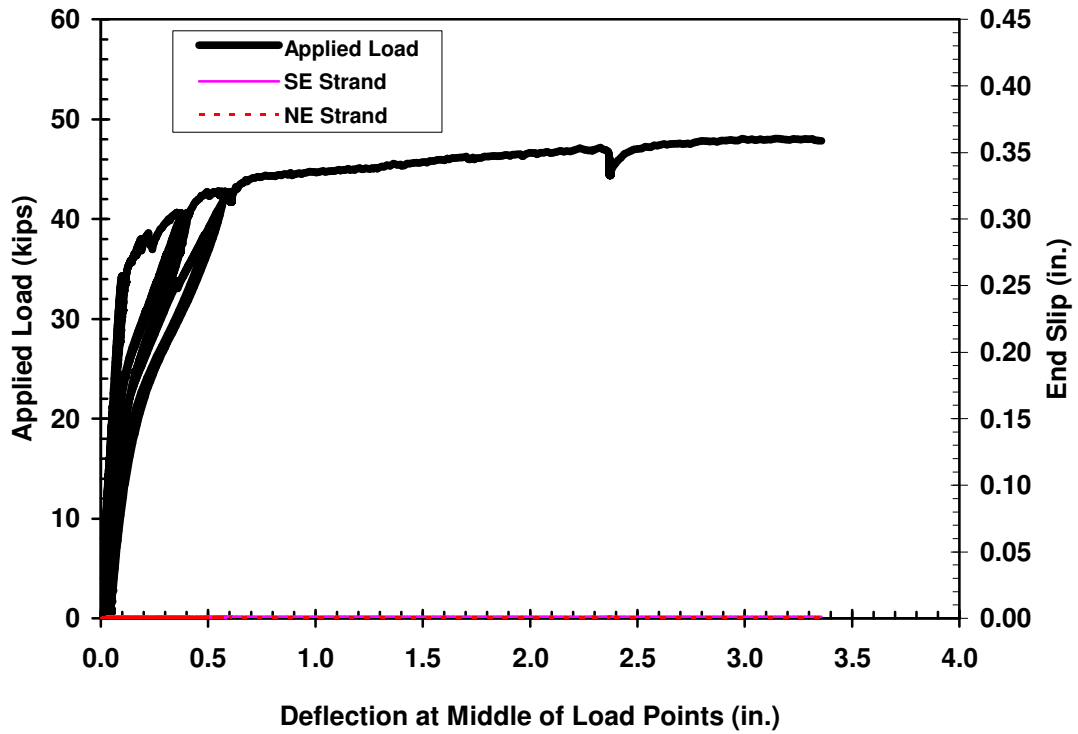


Figure B-30: Applied load and end slip versus deflection for SCC-HS-C

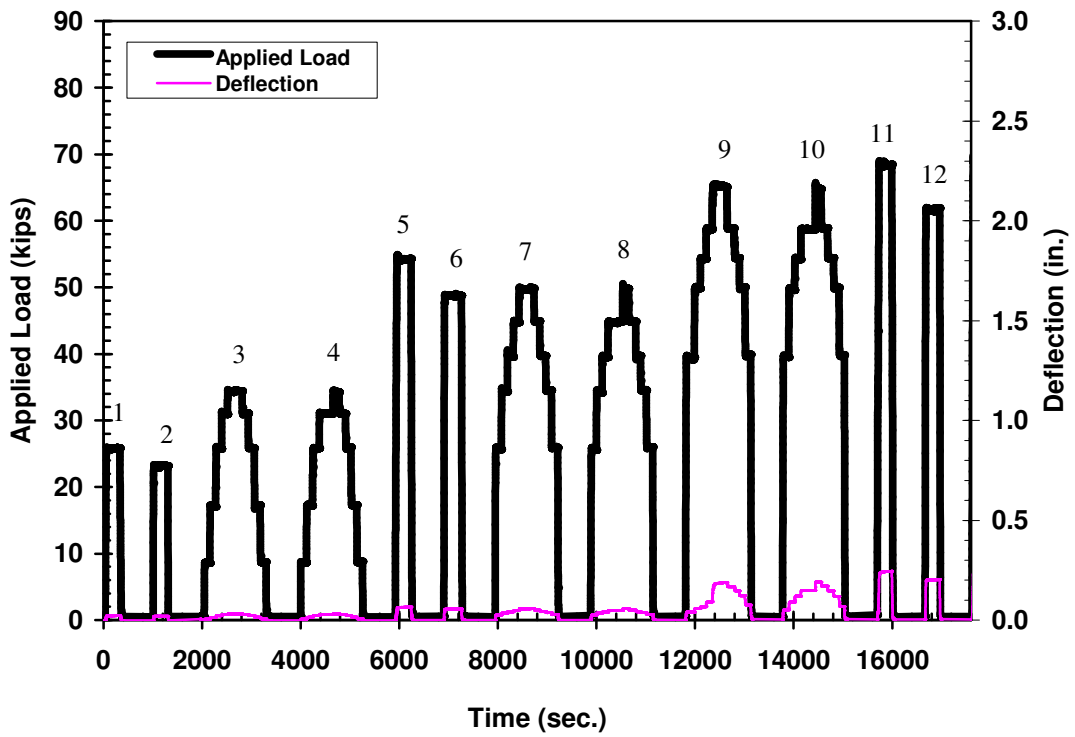


Figure B-31: Applied load and deflection versus time for SCC-HS-D

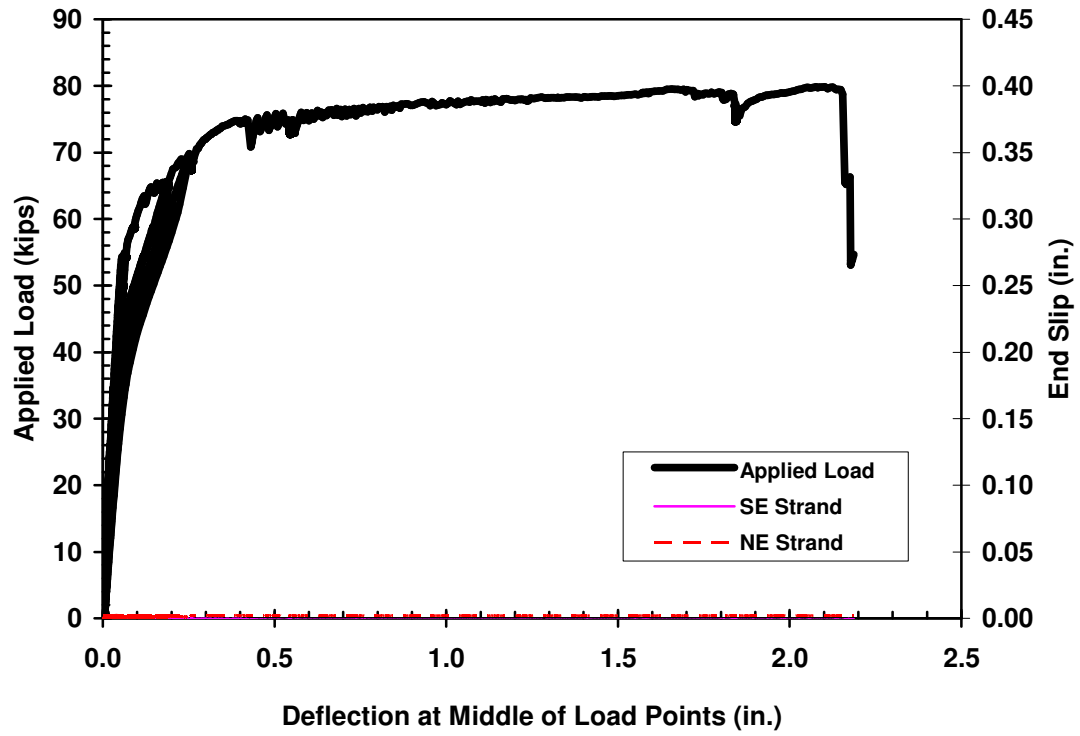


Figure B-32: Applied load and end slip versus deflection for SCC-HS-D

APPENDIX C

DURATION VERSUS AMPLITUDE CROSSPLOTS FOR LABORATORY SPECIMENS

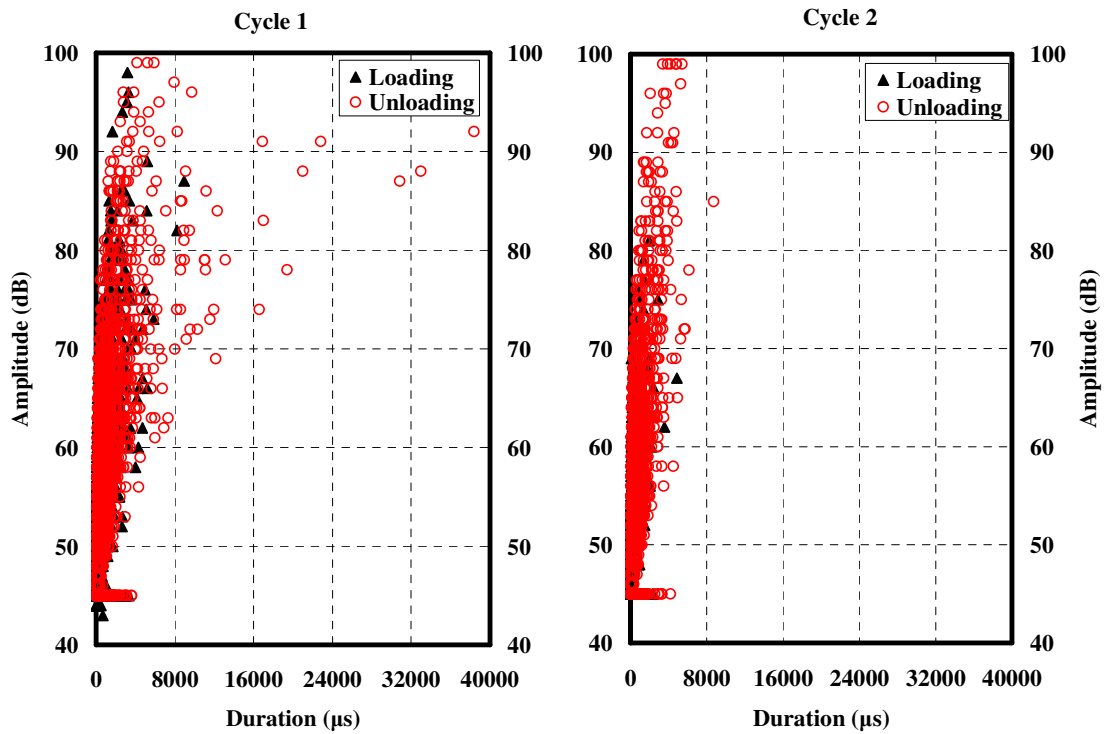


Figure C-1: Crossplot of amplitude and duration of AE signals from loadset 1-2 for beam STD-M-A

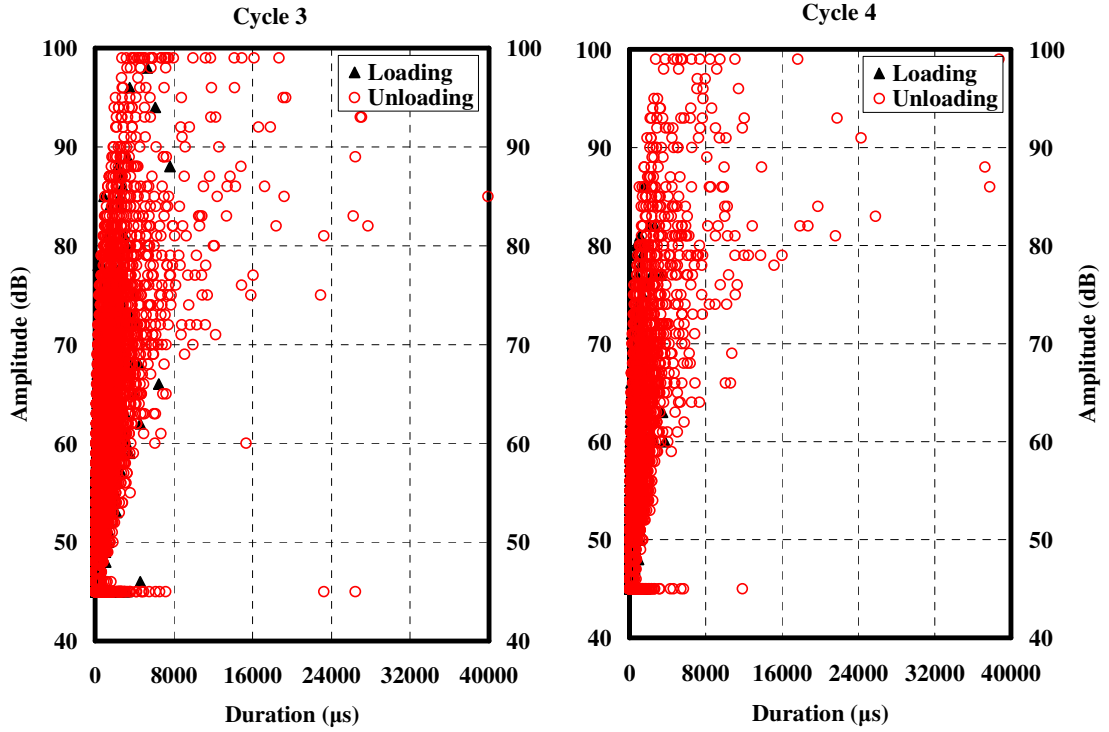


Figure C-2: Crossplot of amplitude and duration of AE signals from loadset 3-4 for beam STD-M-A

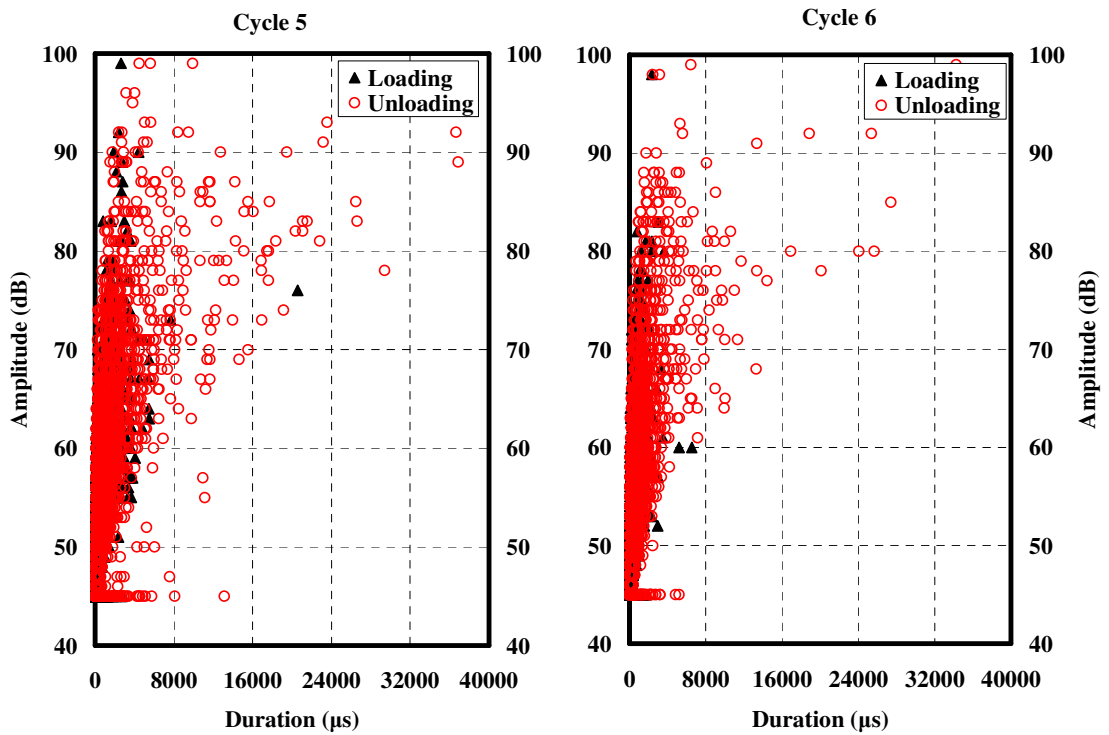


Figure C-3: Crossplot of amplitude and duration of AE signals from loadset 5-6 for beam STD-M-A

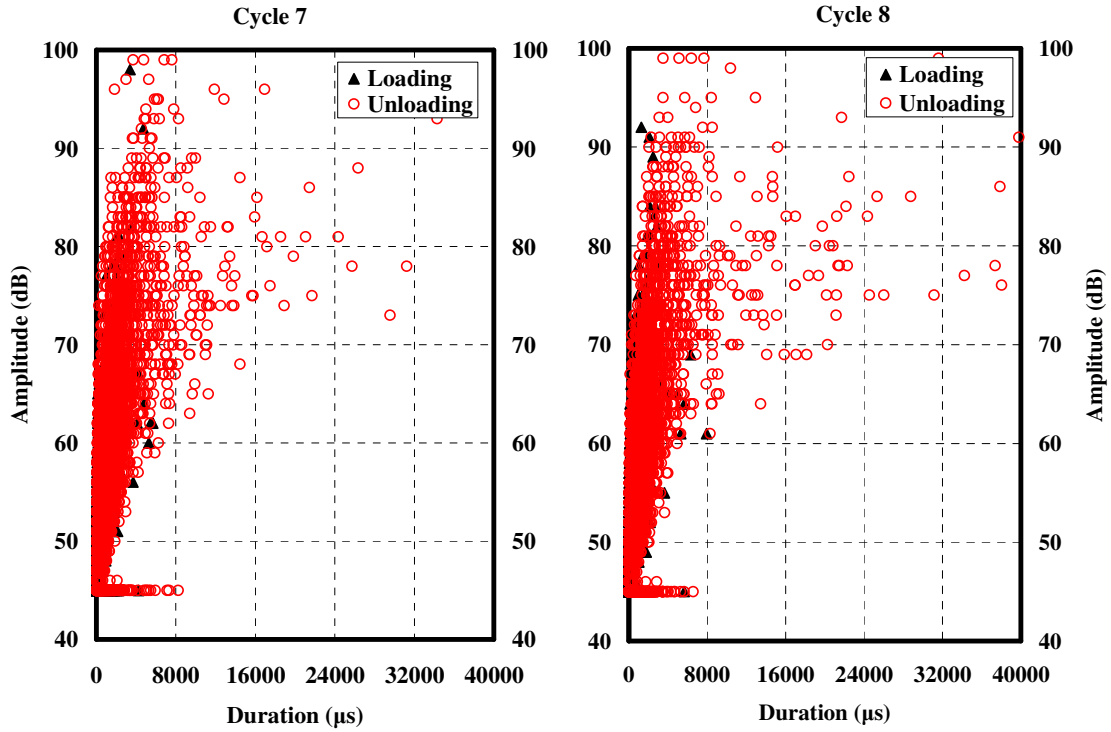


Figure C-4: Crossplot of amplitude and duration of AE signals from loadset 7-8 for beam STD-M-A

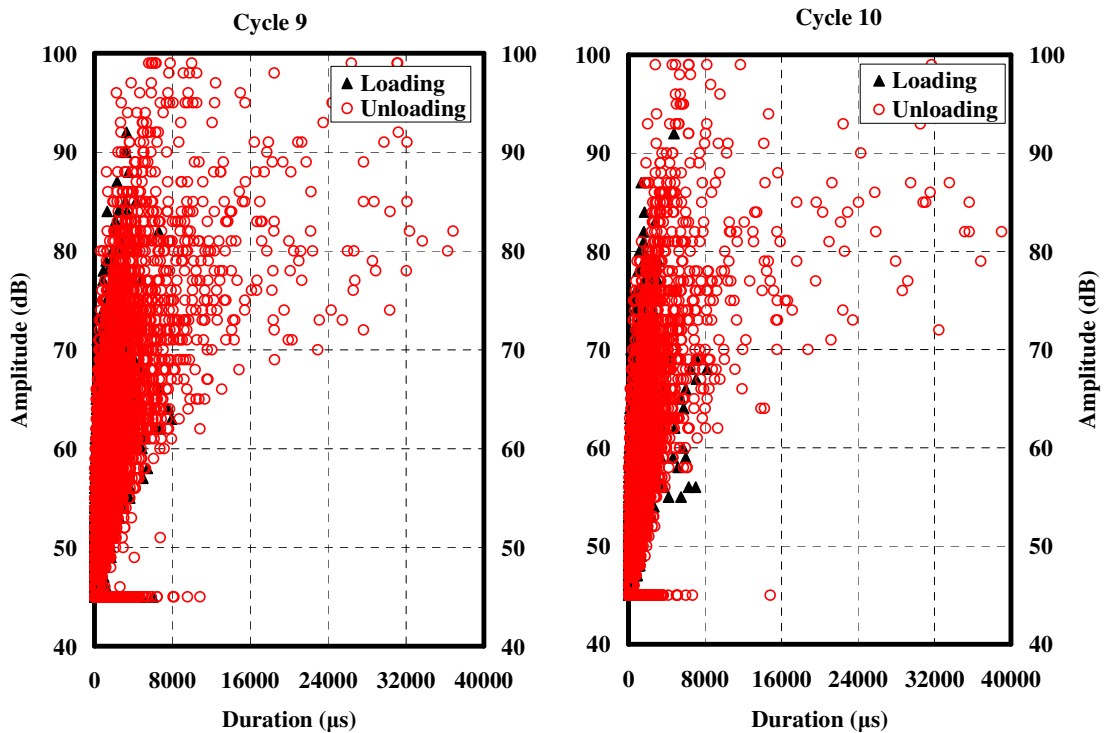


Figure C-5: Crossplot of amplitude and duration of AE signals from loadset 9-10 for beam STD-M-A

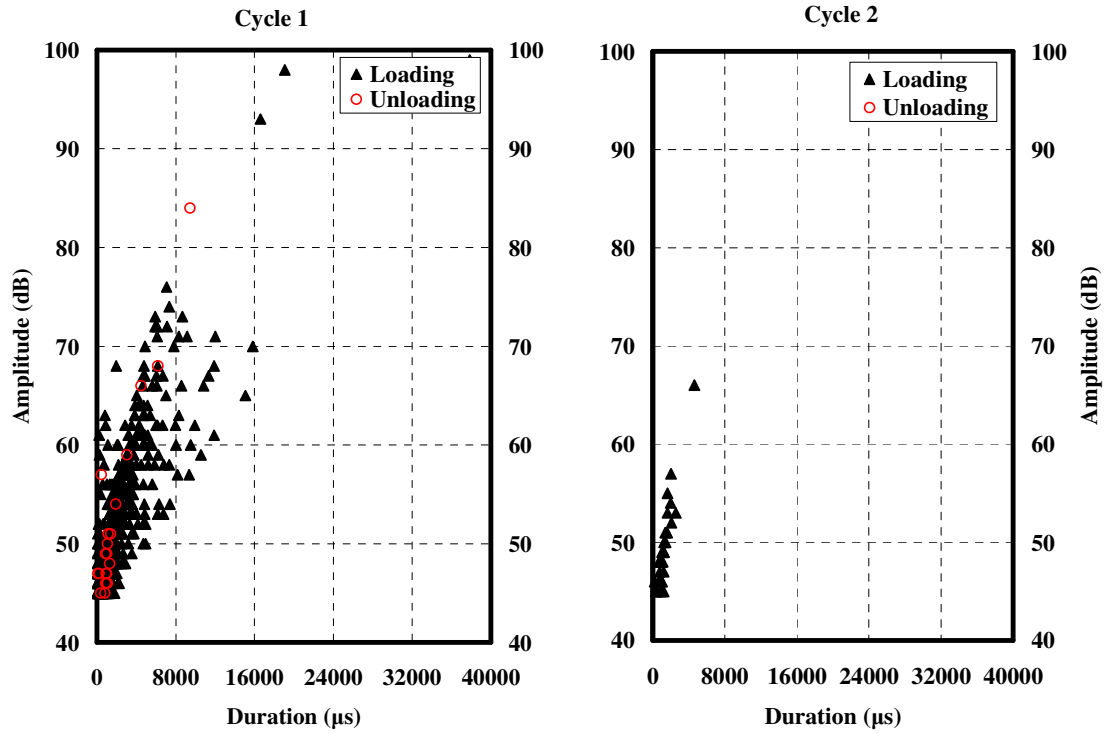


Figure C-6: Crossplot of amplitude and duration of AE signals from loadset 1-2 for beam STD-M-B

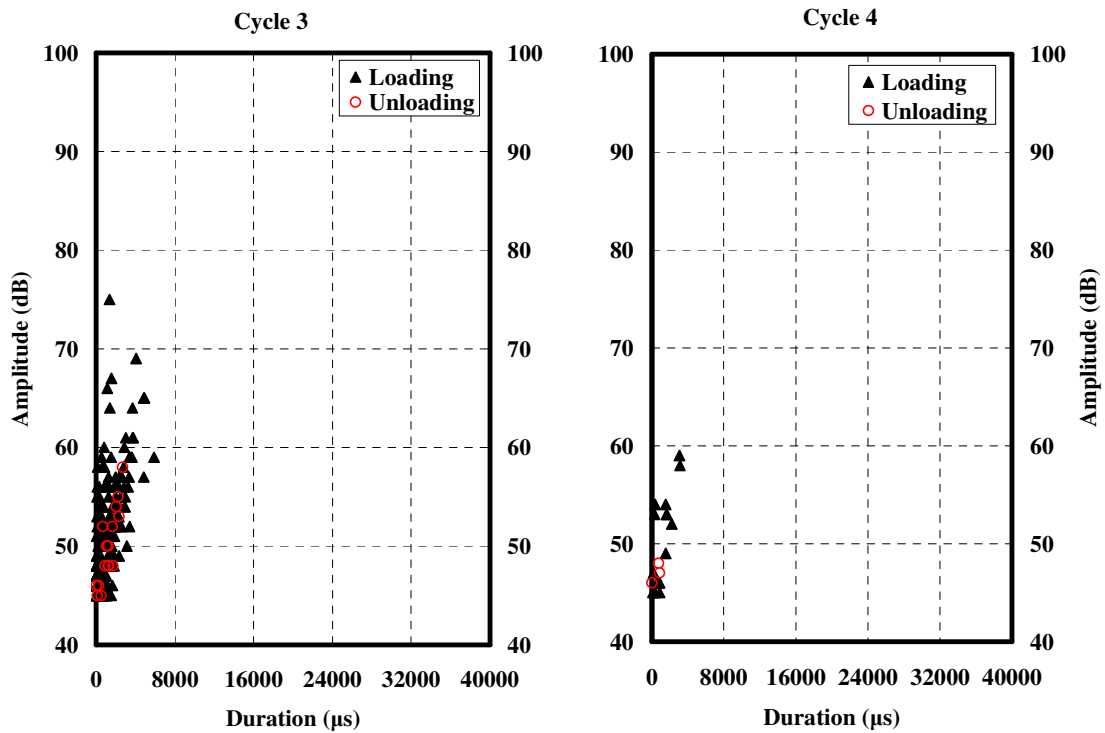


Figure C-7: Crossplot of amplitude and duration of AE signals from loadset 3-4 for beam STD-M-B

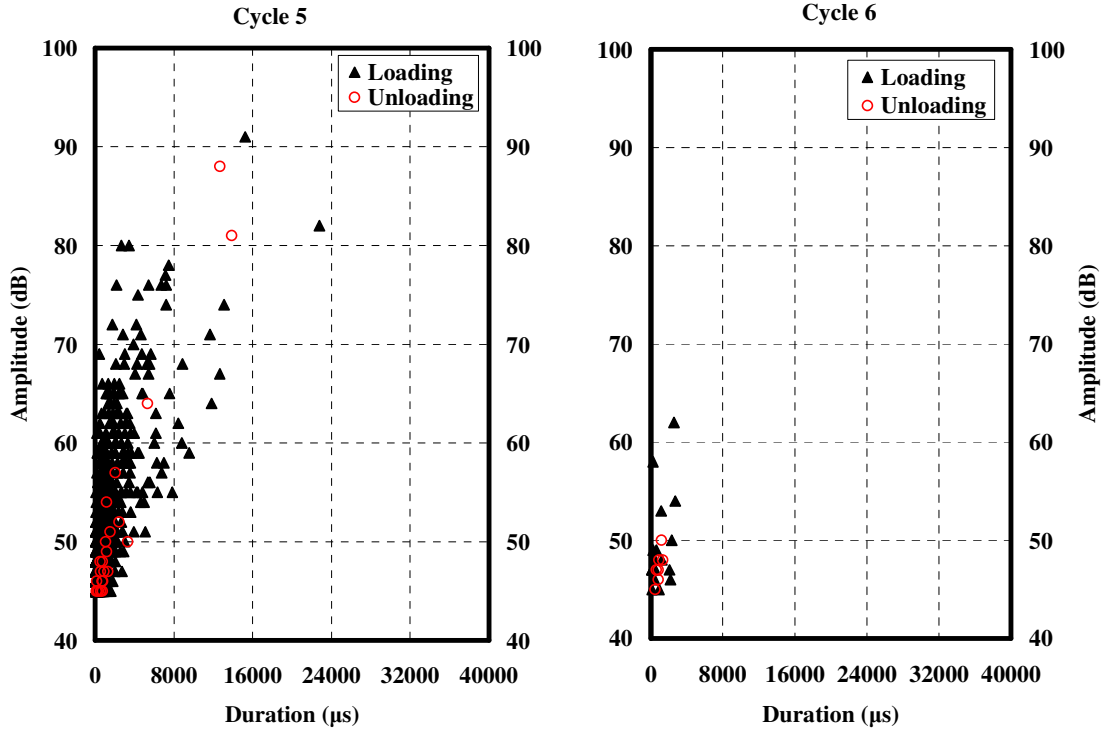


Figure C-8: Crossplot of amplitude and duration of AE signals from loadset 5-6 for beam STD-M-B

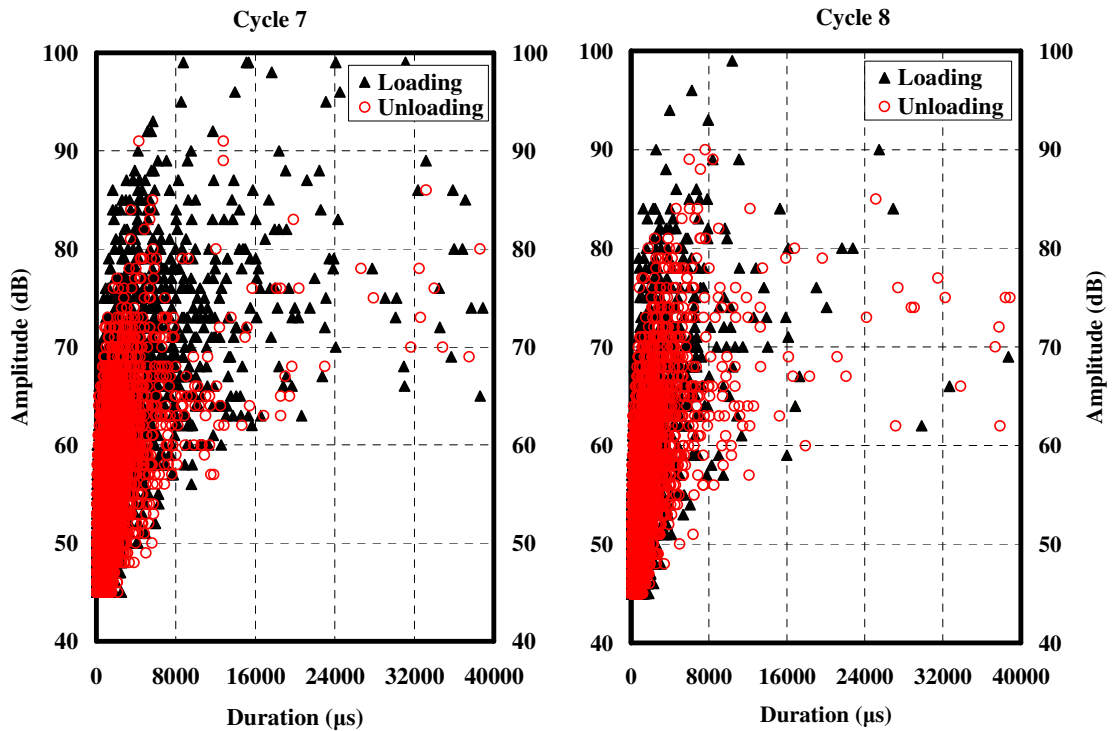


Figure C-9: Crossplot of amplitude and duration of AE signals from loadset 7-8 for beam STD-M-B

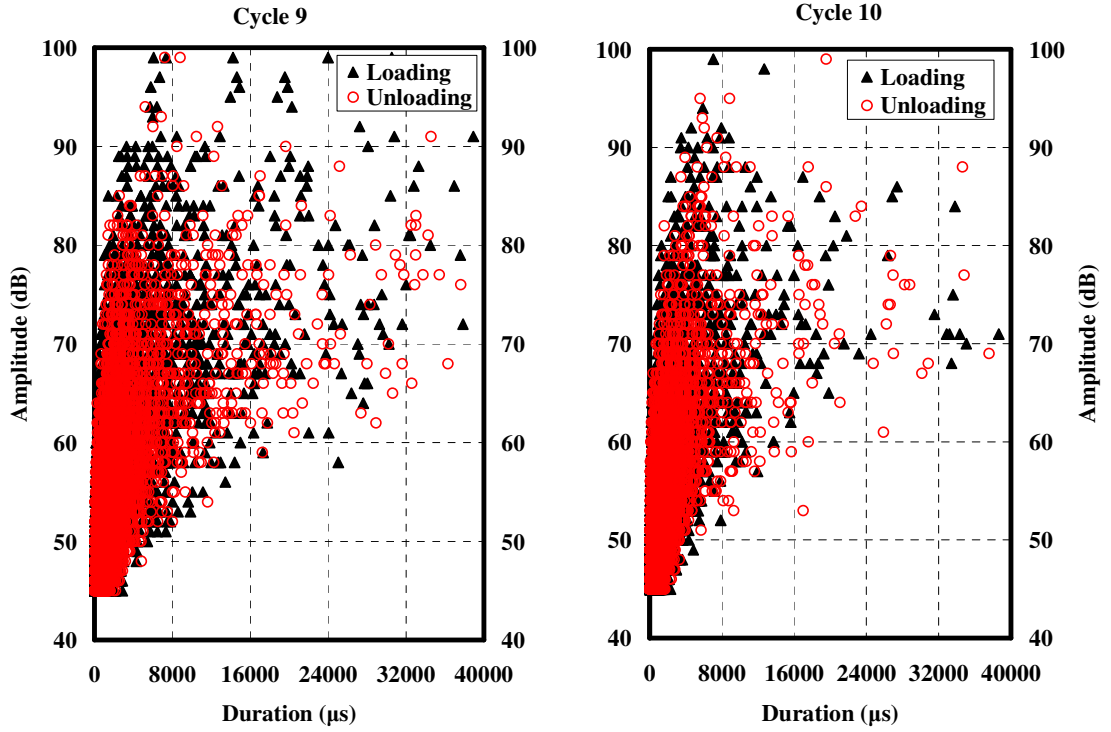


Figure C-10: Crossplot of amplitude and duration of AE signals from loadset 9-10 for beam STD-M-B

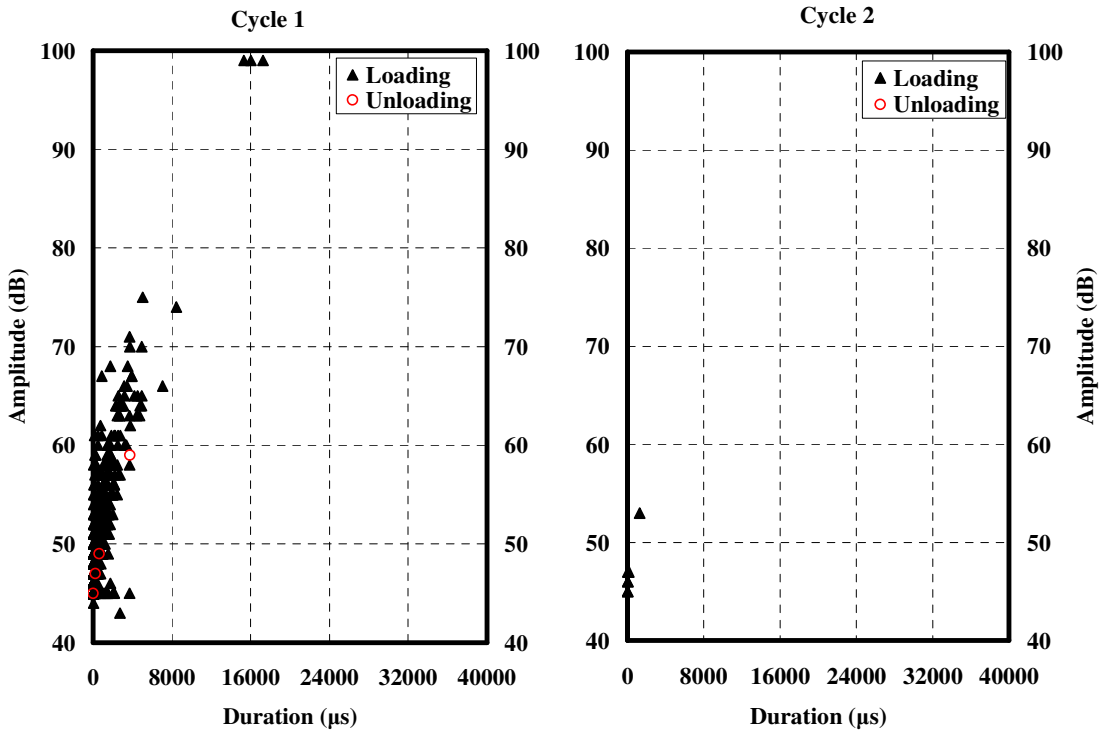


Figure C-11: Crossplot of amplitude and duration of AE signals from loadset 1-2 for beam STD-M-C

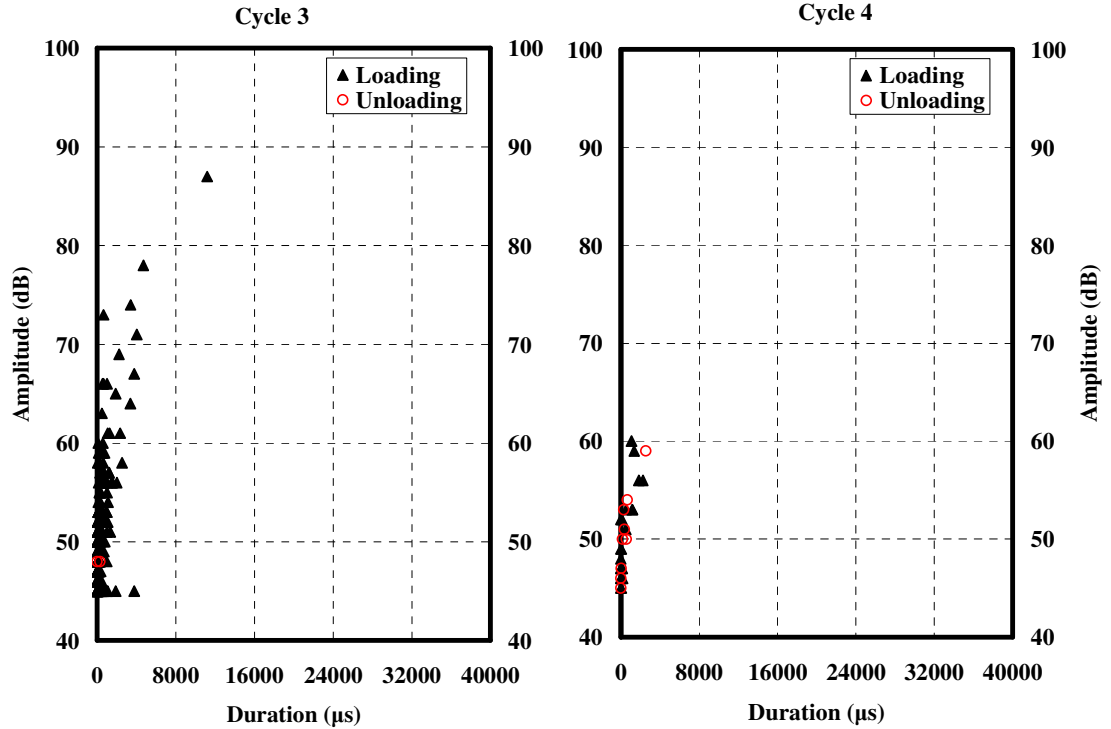


Figure C-12: Crossplot of amplitude and duration of AE signals from loadset 3-4 for beam STD-M-C

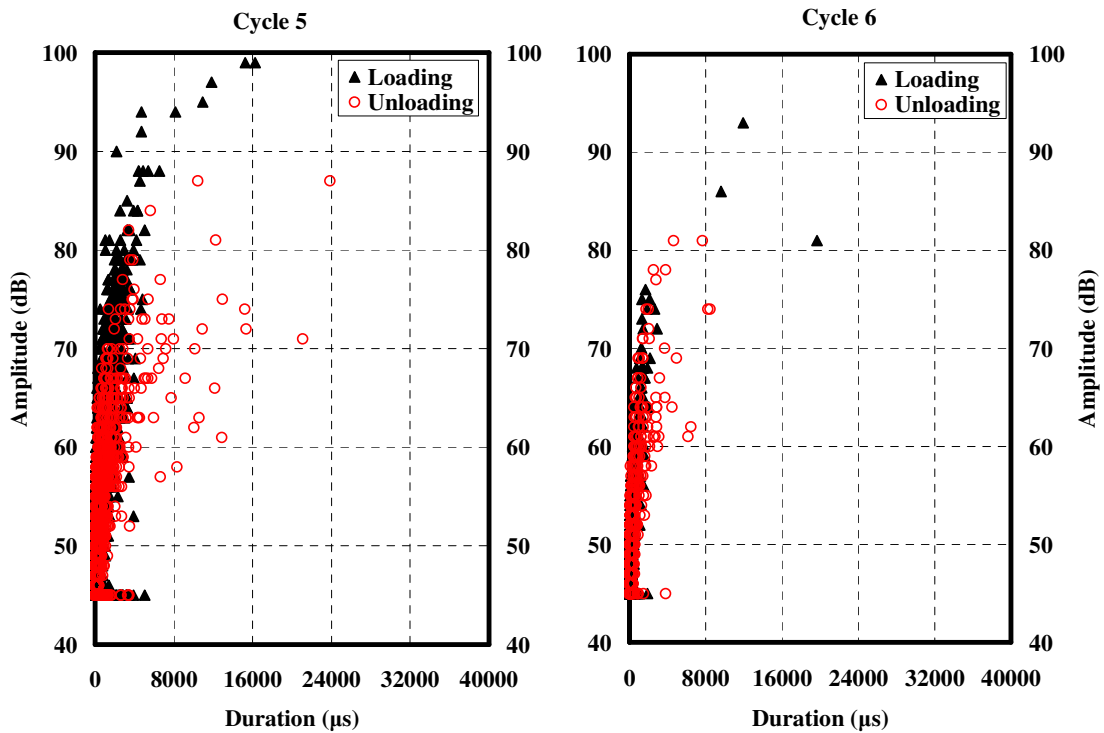


Figure C-13: Crossplot of amplitude and duration of AE signals from loadset 5-6 for beam STD-M-C

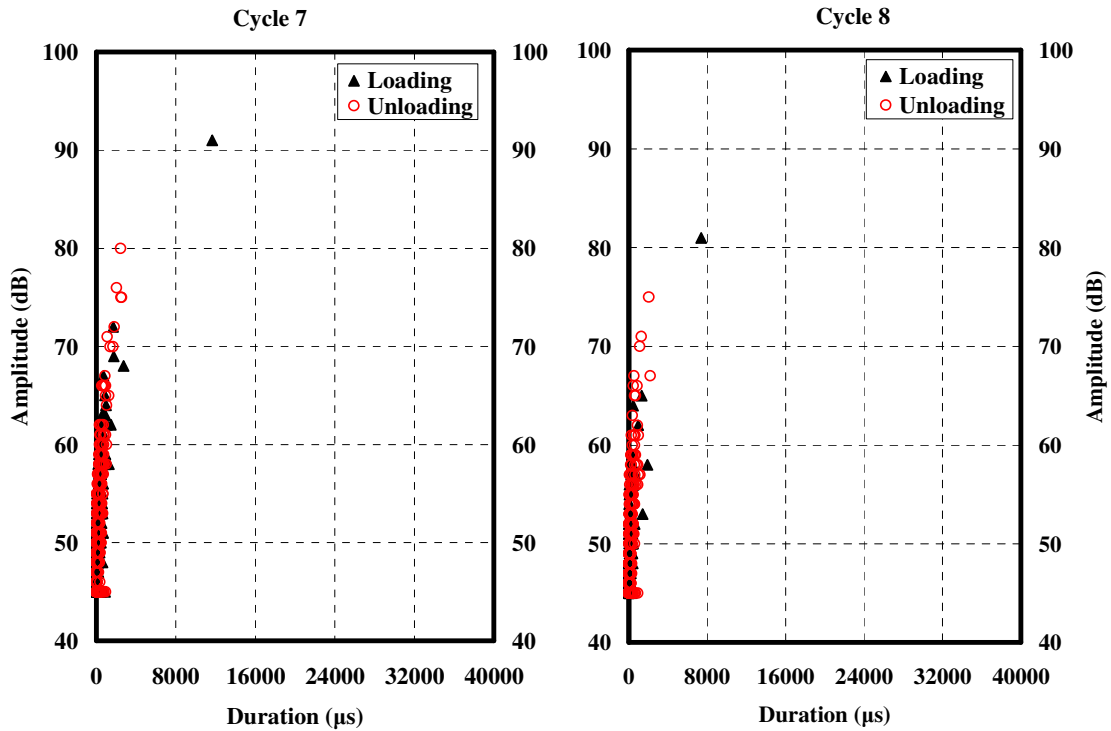


Figure C-14: Crossplot of amplitude and duration of AE signals from loadset 7-8 for beam STD-M-C

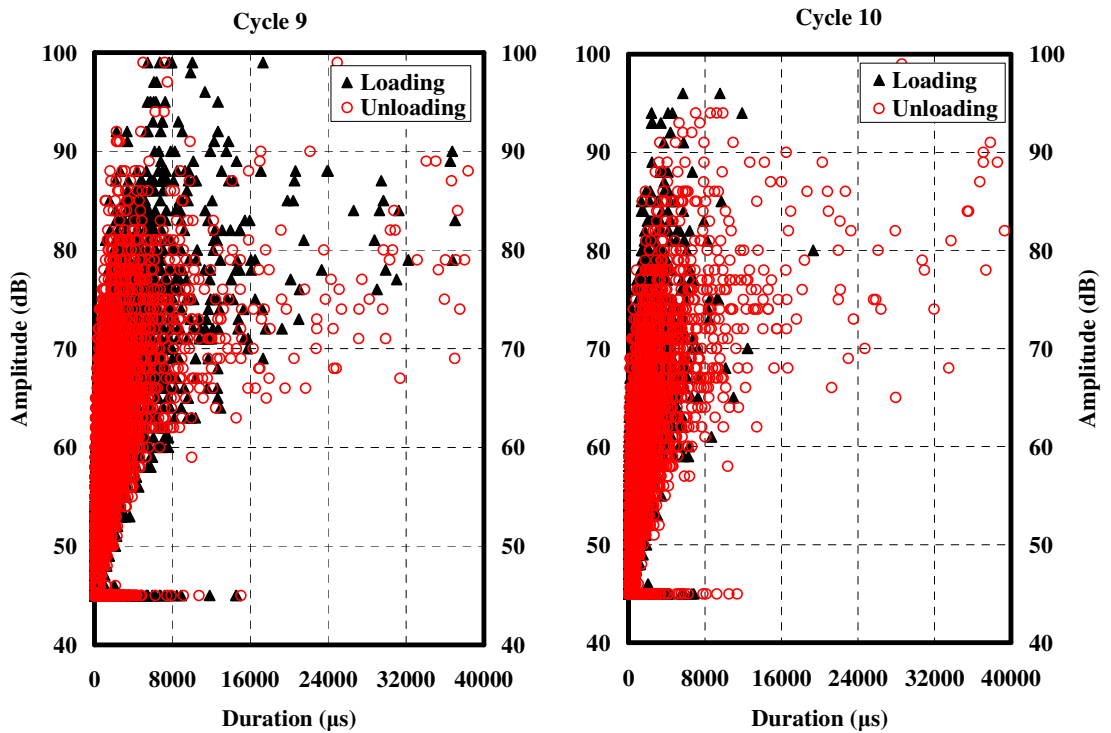


Figure C-15: Crossplot of amplitude and duration of AE signals from loadset 9-10 for beam STD-M-C

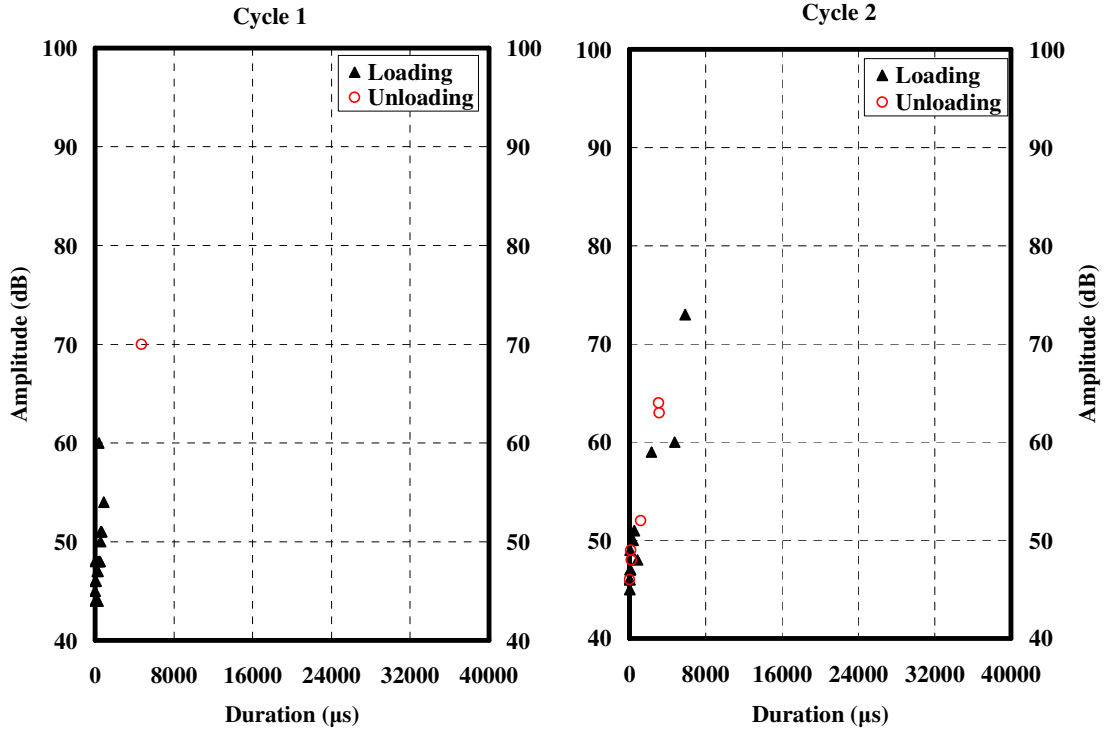


Figure C-16: Crossplot of amplitude and duration of AE signals from loadset 1-2 for beam STD-M-D

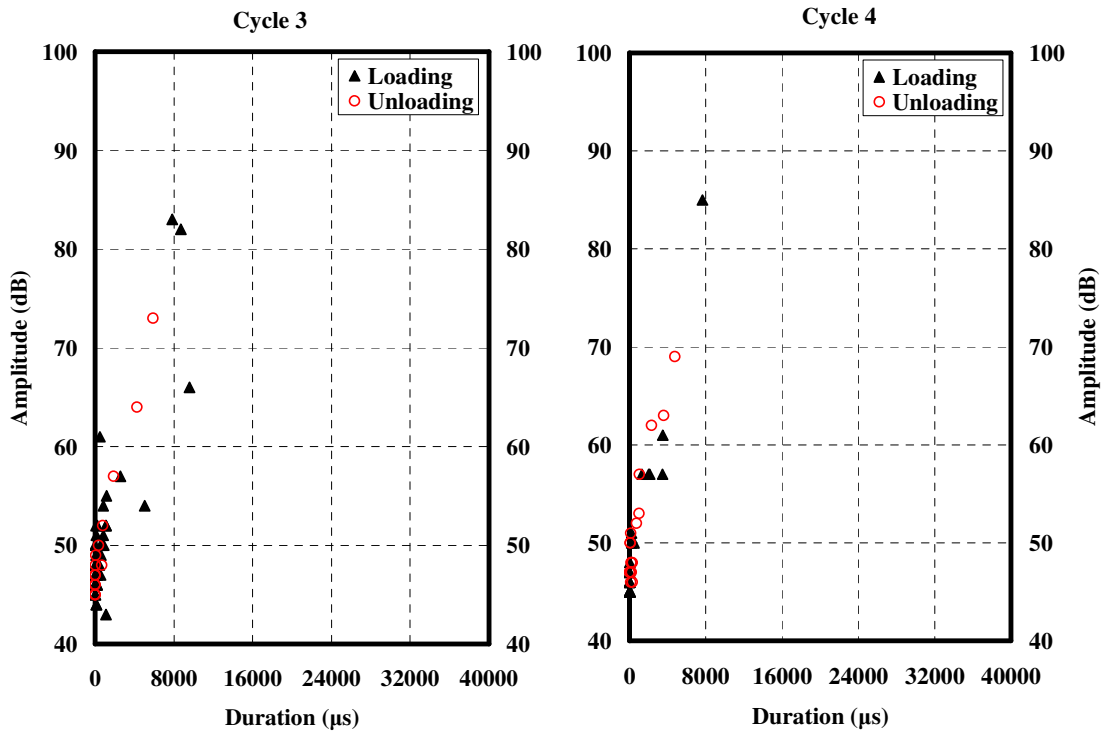


Figure C-17: Crossplot of amplitude and duration of AE signals from loadset 3-4 for beam STD-M-D

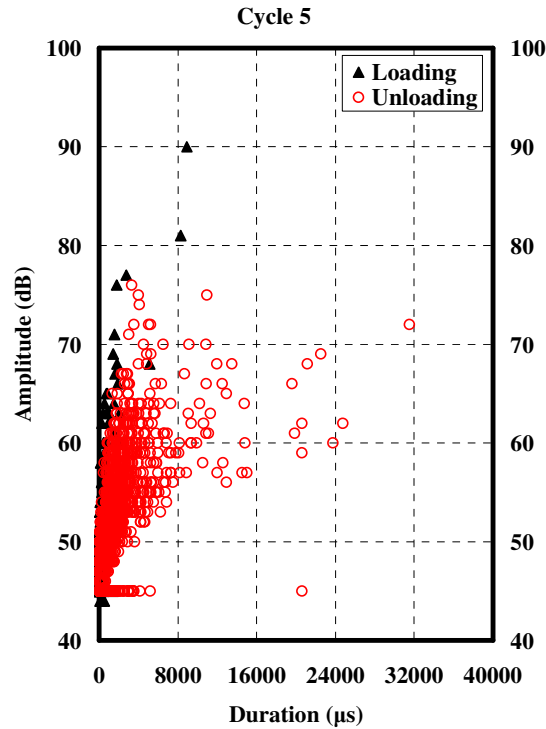


Figure C-18: Crossplot of amplitude and duration of AE signals from loadset 5 for beam STD-M-D

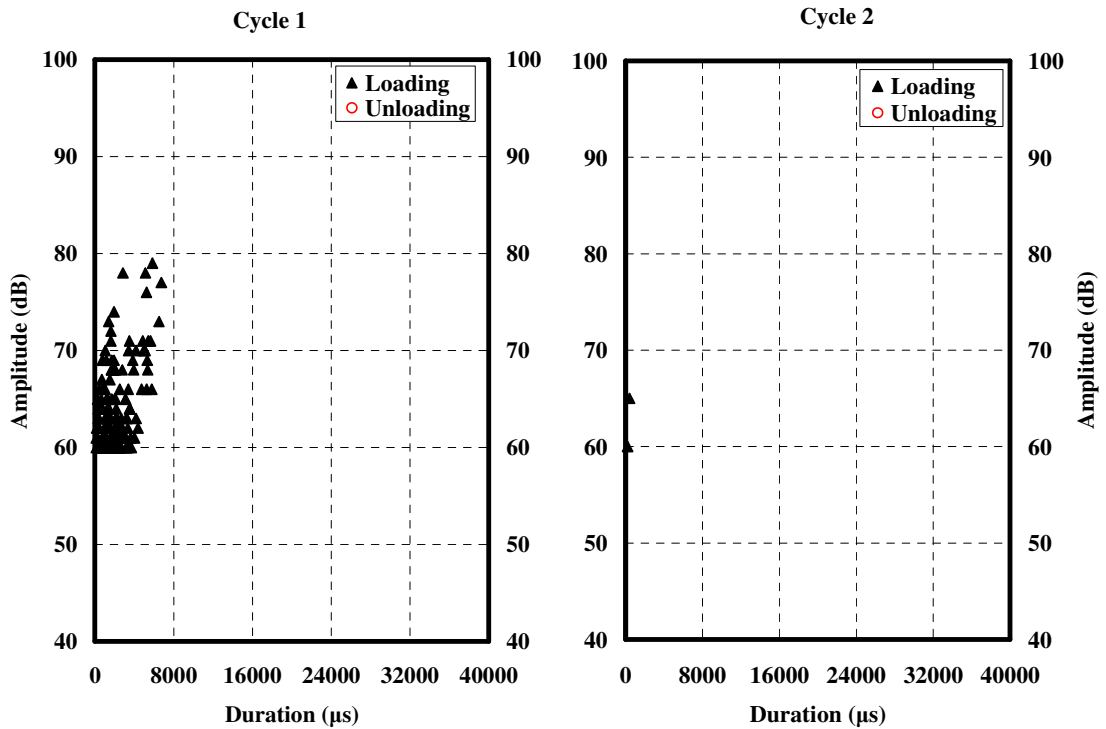


Figure C-19: Crossplot of amplitude and duration of AE signals from loadset 1-2 for beam SCC-MA-A

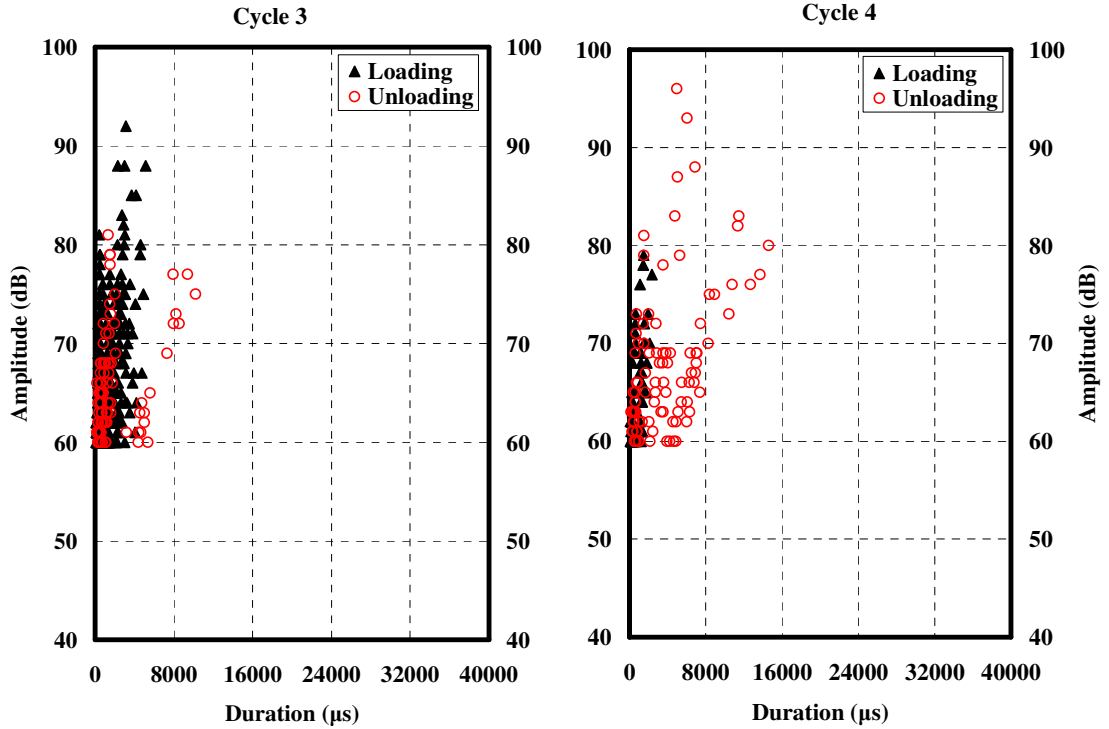


Figure C-20: Crossplot of amplitude and duration of AE signals from loadset 3-4 for beam SCC-MA-A

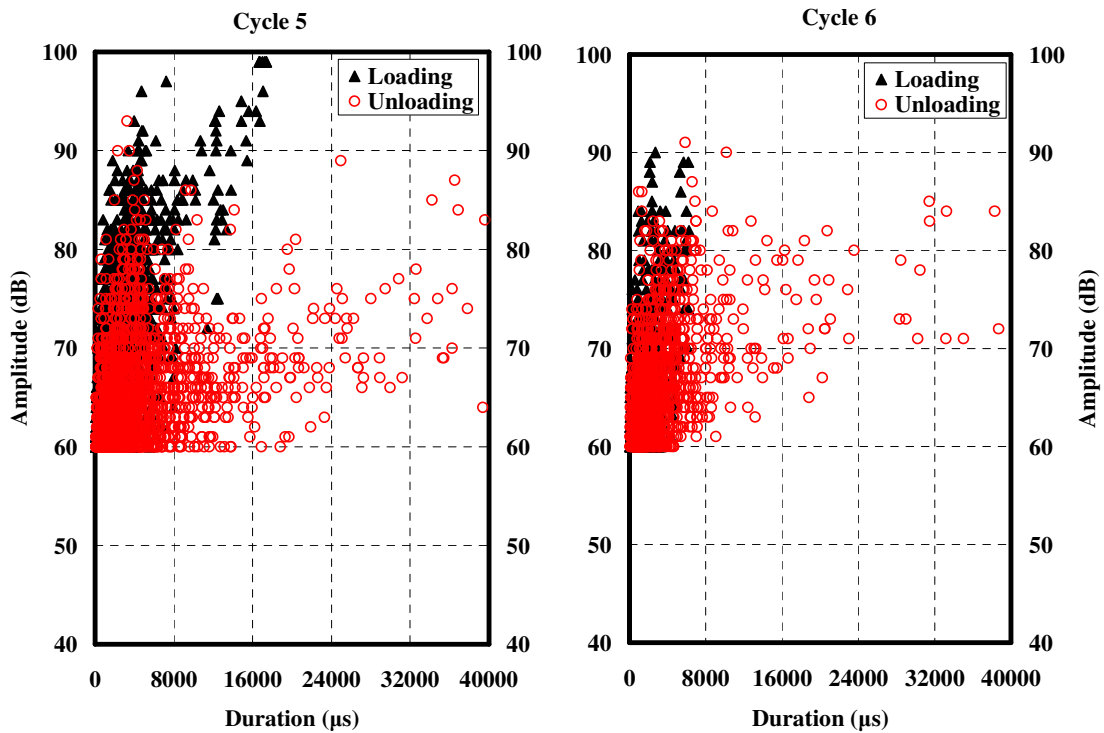


Figure C-21: Crossplot of amplitude and duration of AE signals from loadset 5-6 for beam SCC-MA-A

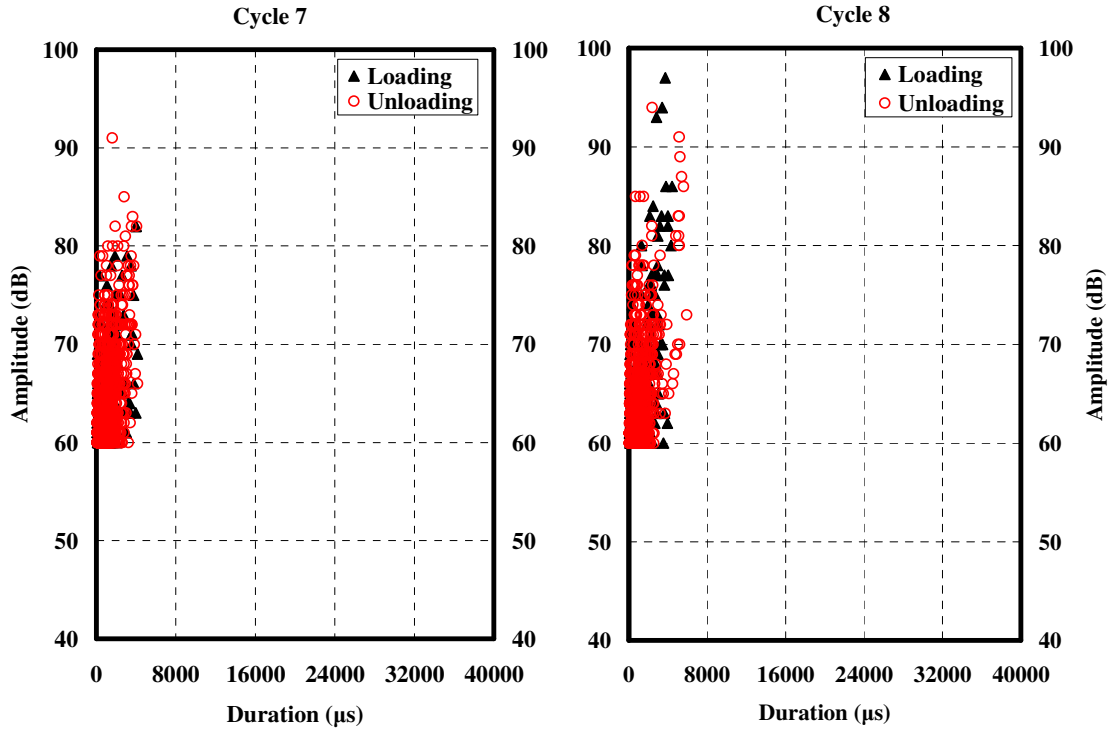


Figure C-22: Crossplot of amplitude and duration of AE signals from loadset 7-8 for beam SCC-MA-A

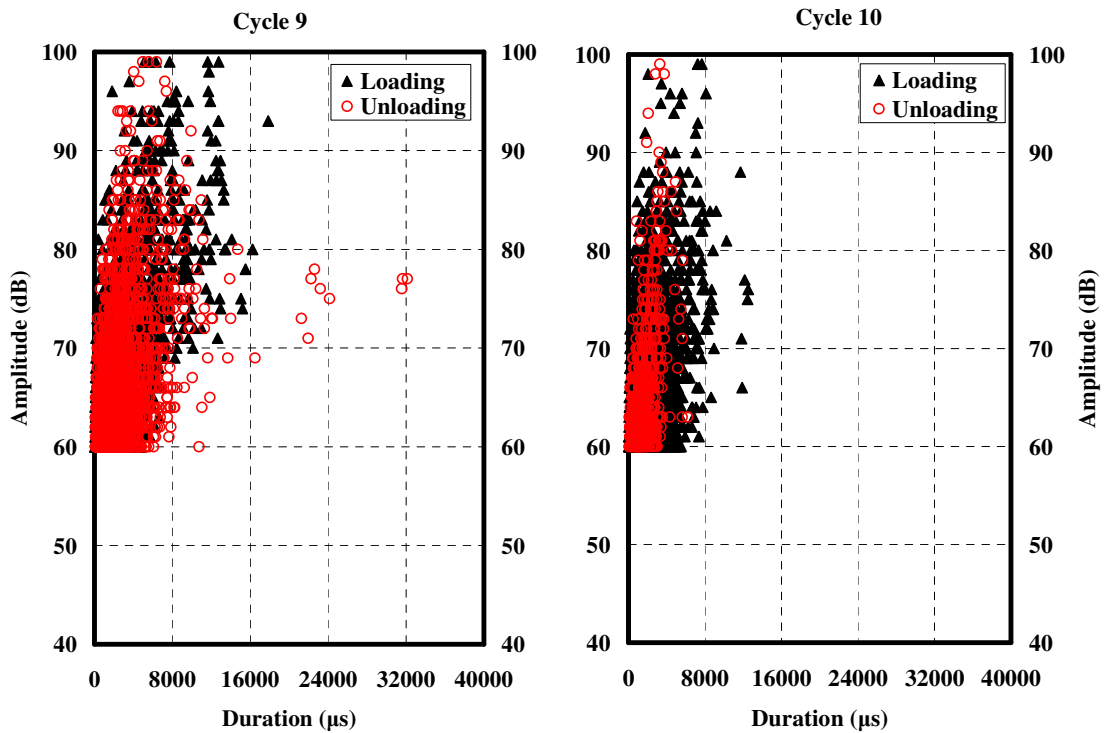


Figure C-23: Crossplot of amplitude and duration of AE signals from loadset 9-10 for beam SCC-MA-A

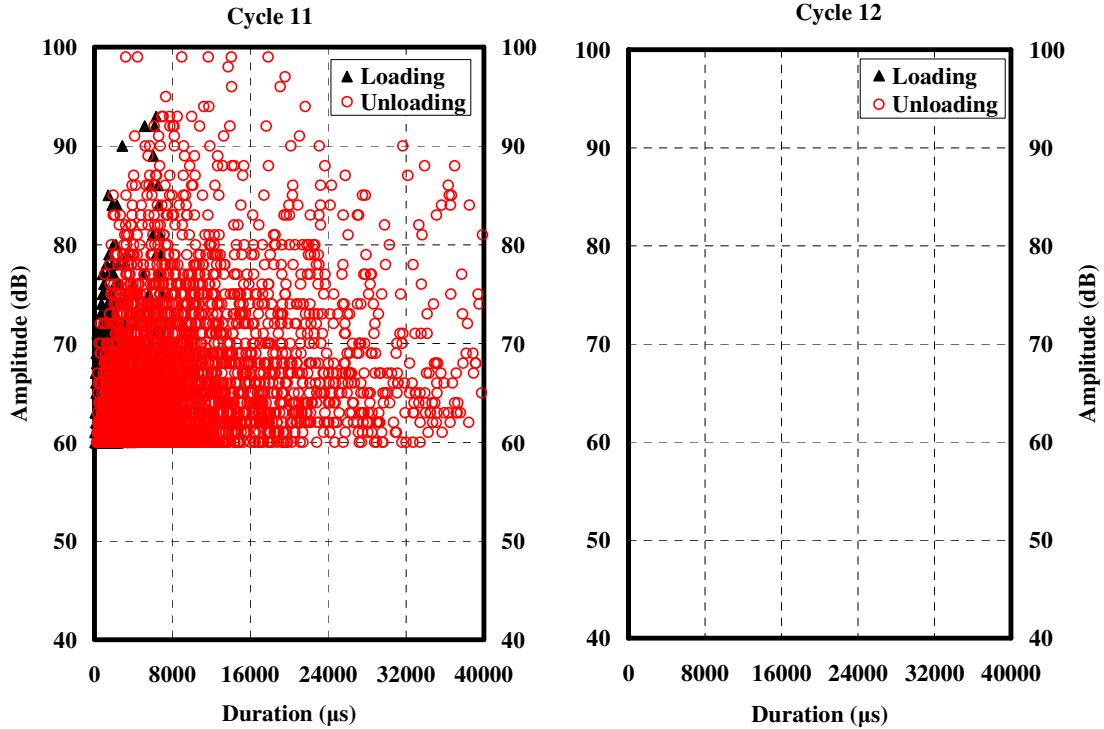


Figure C-24: Crossplot of amplitude and duration of AE signals from loadset 11-12 for beam SCC-MA-A

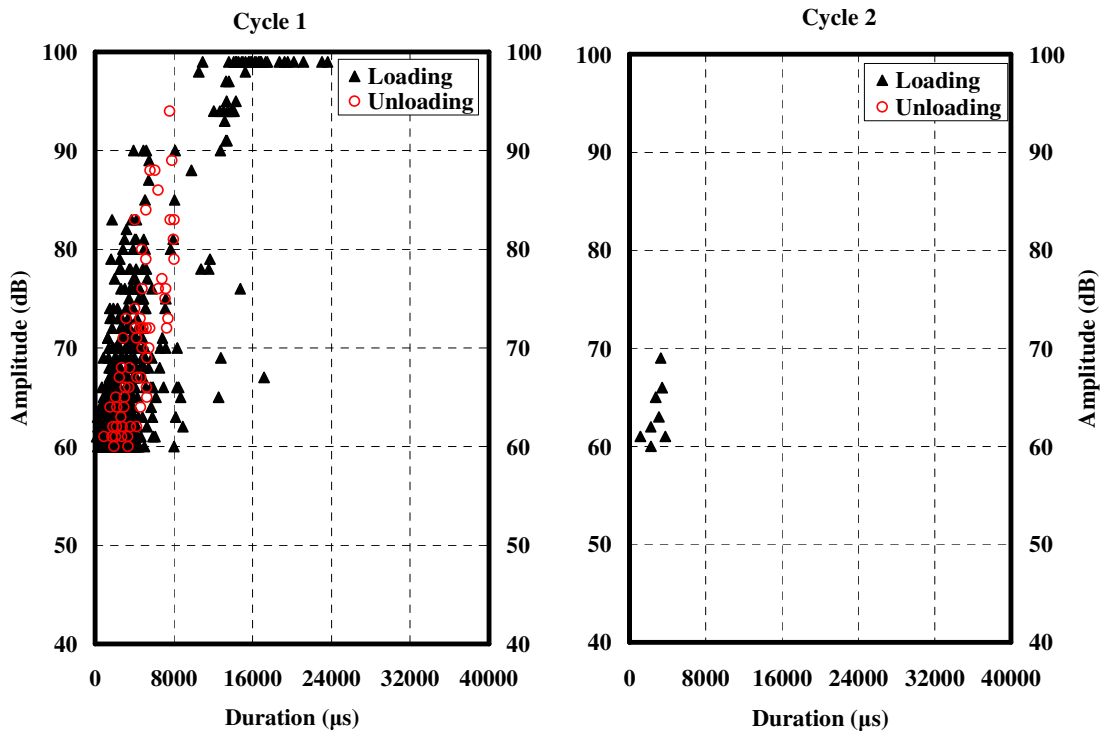


Figure C-25: Crossplot of amplitude and duration of AE signals from loadset 1-2 for beam SCC-MA-B

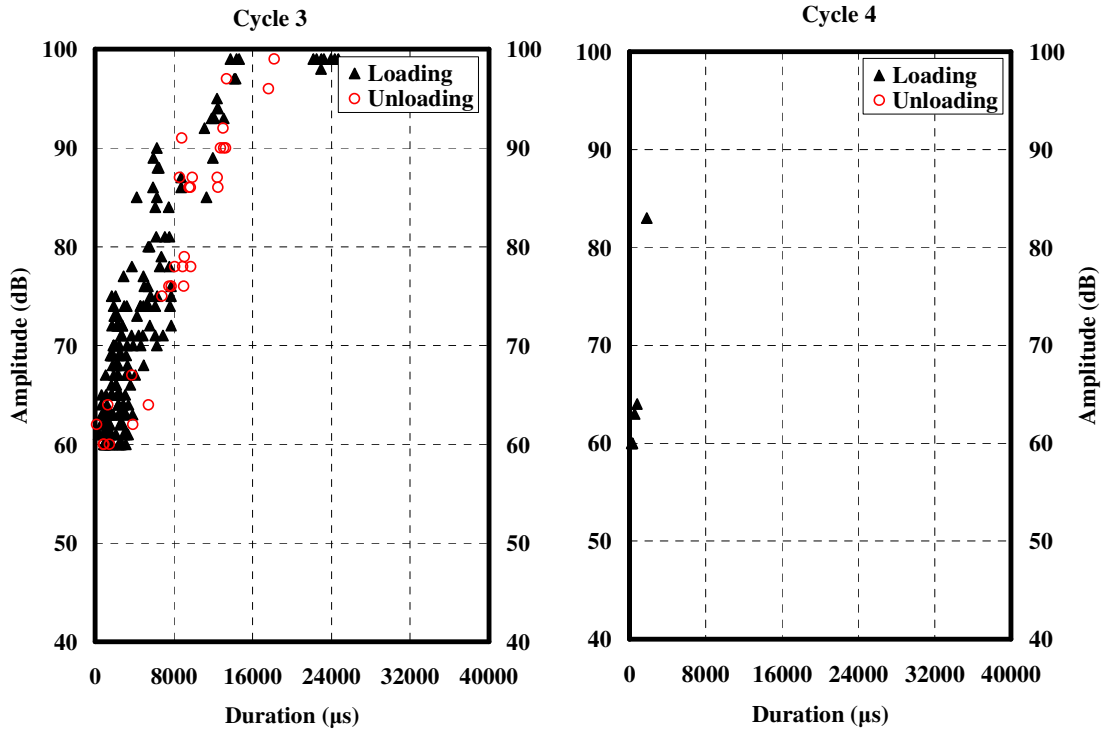


Figure C-26: Crossplot of amplitude and duration of AE signals from loadset 3-4 for beam SCC-MA-B

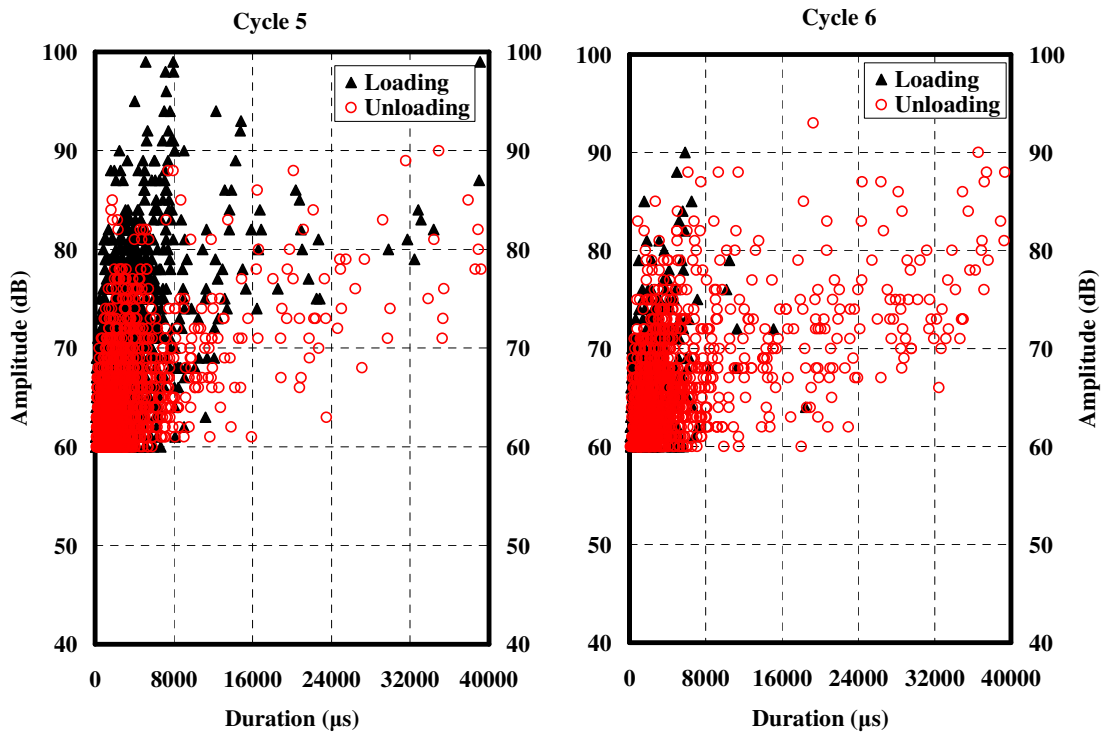


Figure C-27: Crossplot of amplitude and duration of AE signals from loadset 5-6 for beam SCC-MA-B

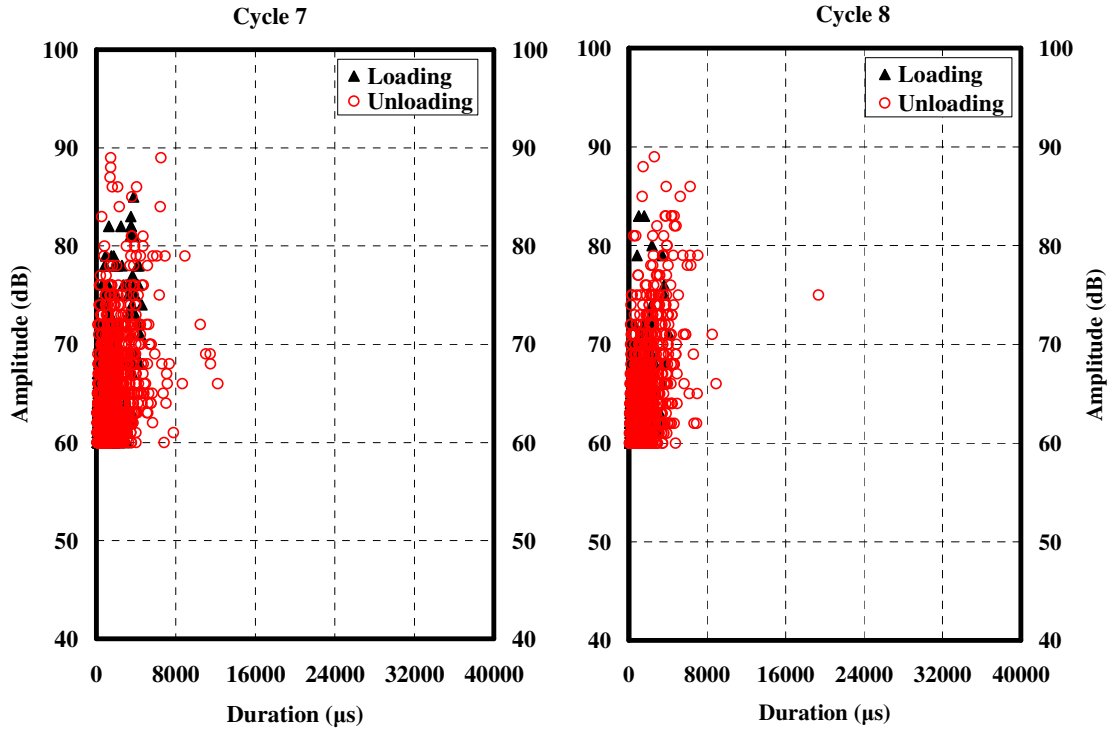


Figure C-28: Crossplot of amplitude and duration of AE signals from loadset 7-8 for beam SCC-MA-B

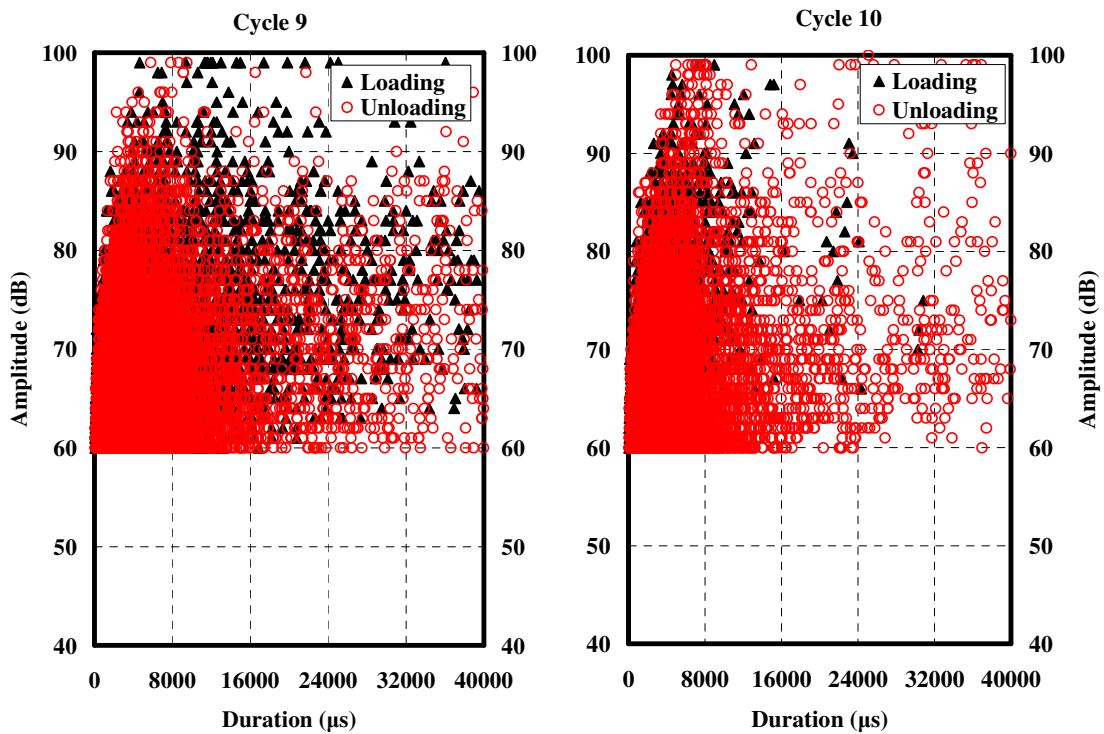


Figure C-29: Crossplot of amplitude and duration of AE signals from loadset 9-10 for beam SCC-MA-B

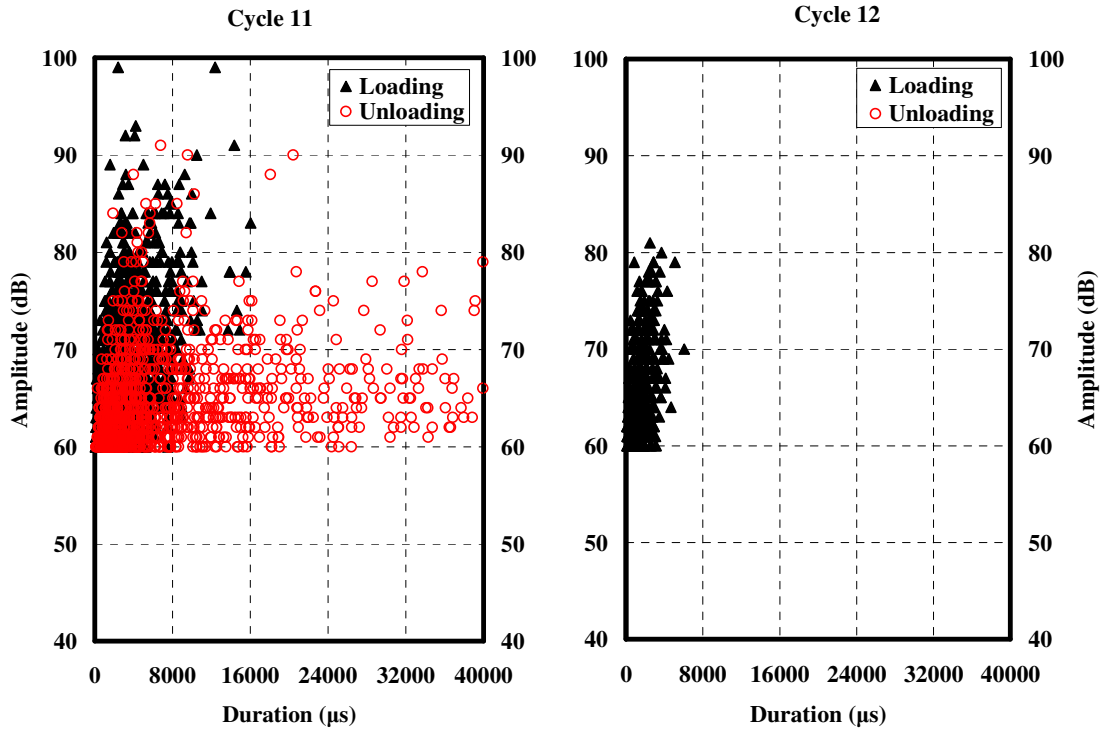


Figure C-30: Crossplot of amplitude and duration of AE signals from loadset 11-12 for beam SCC-MA-B

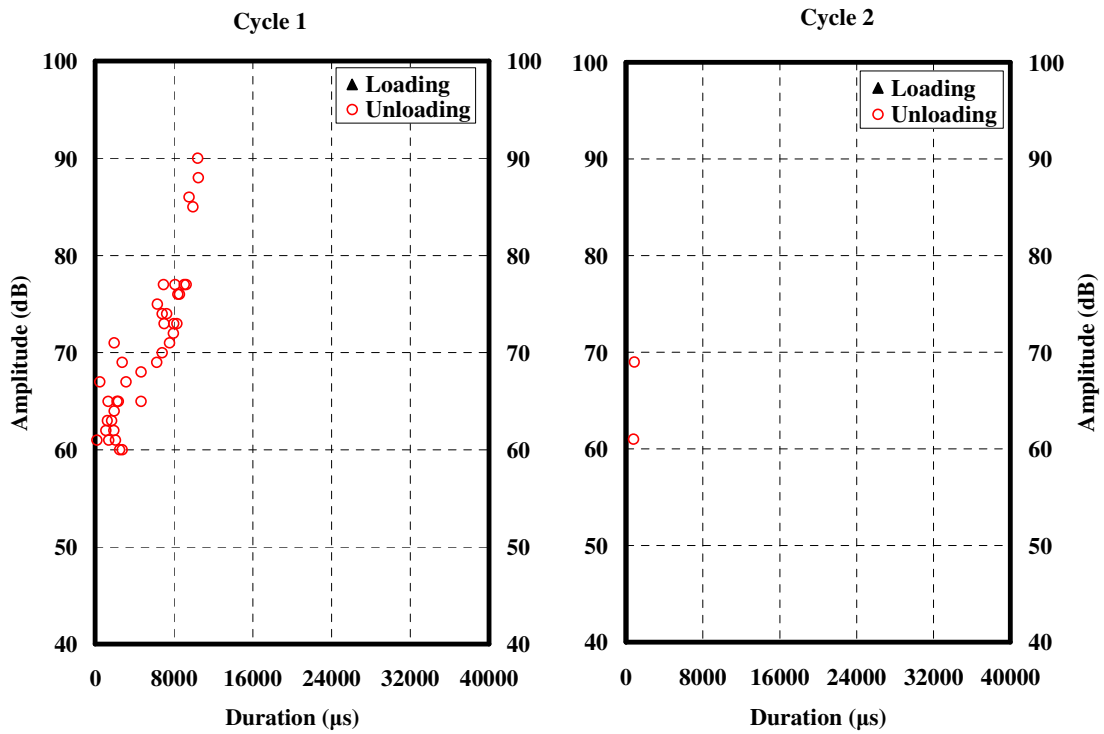


Figure C-31: Crossplot of amplitude and duration of AE signals from loadset 1-2 for beam SCC-MA-C

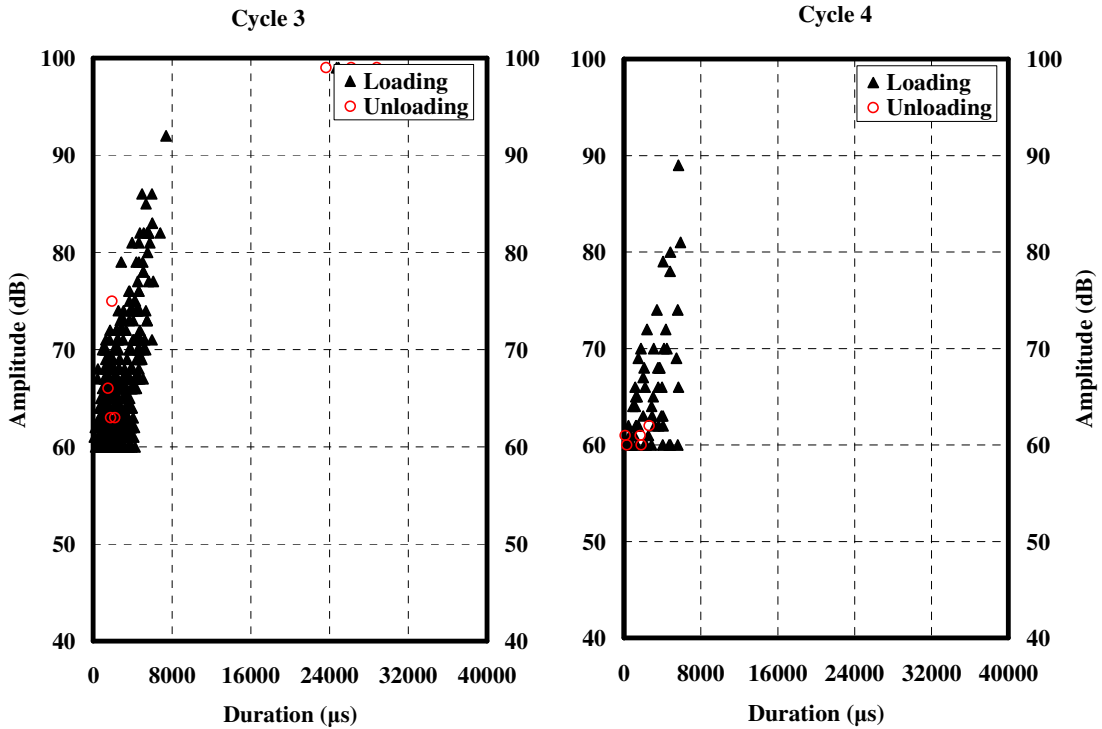


Figure C-32: Crossplot of amplitude and duration of AE signals from loadset 3-4 for beam SCC-MA-C

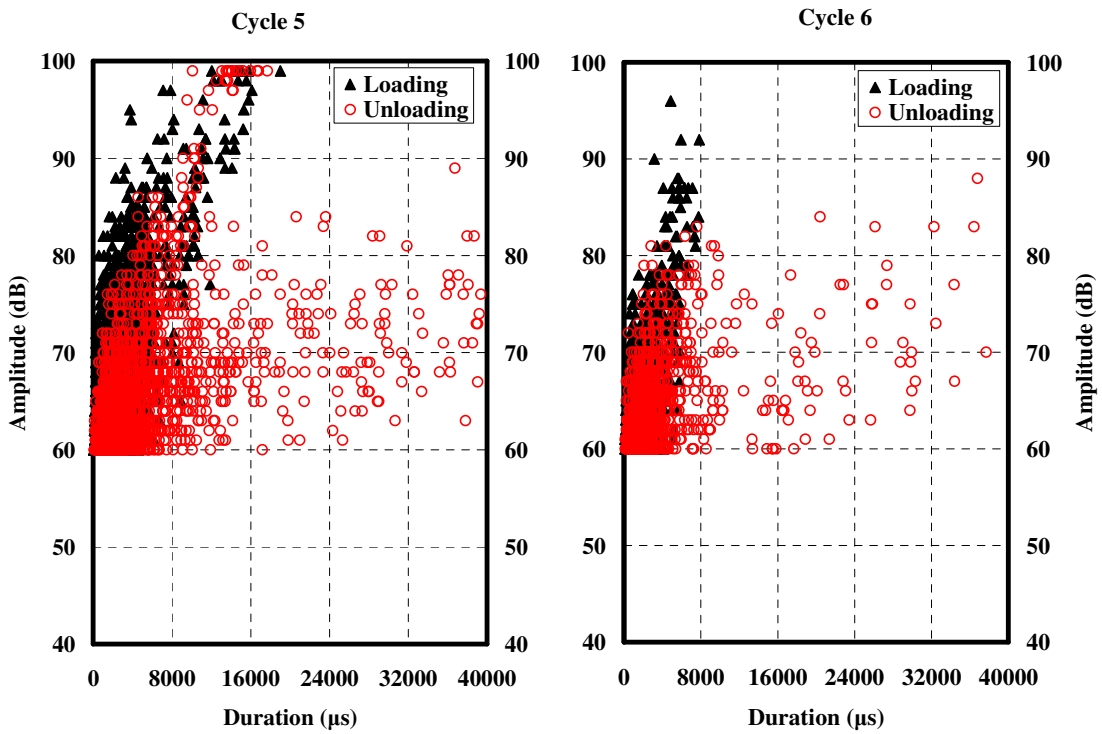


Figure C-33: Crossplot of amplitude and duration of AE signals from loadset 5-6 for beam SCC-MA-C

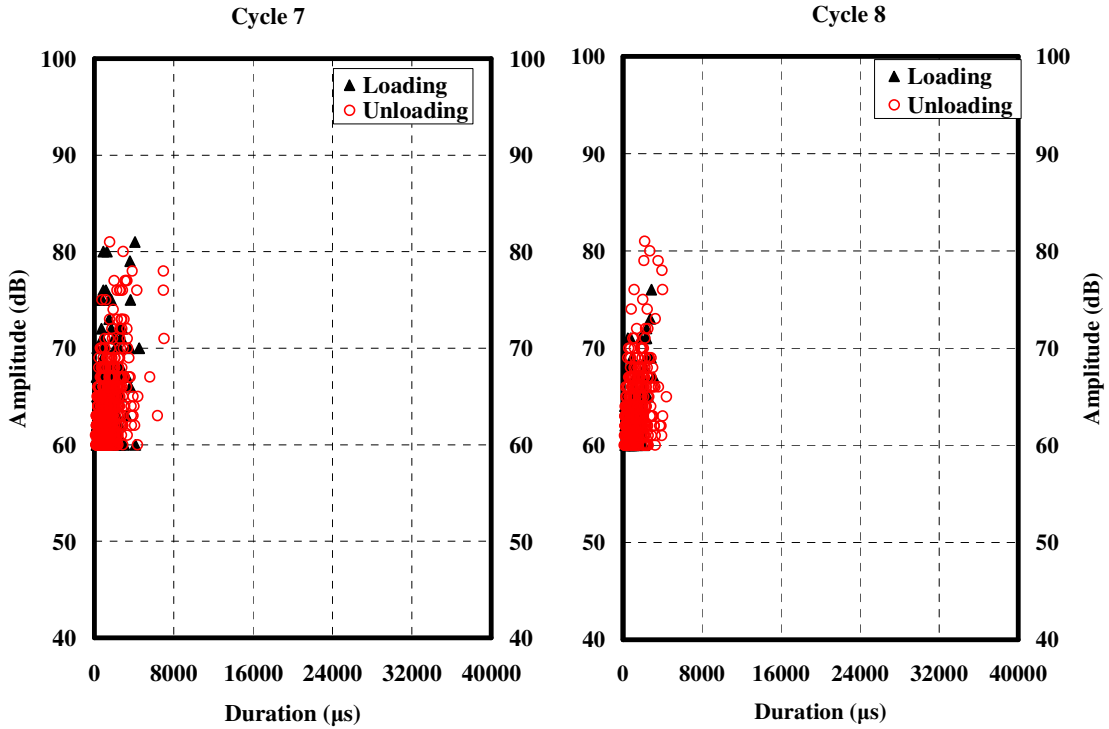


Figure C-34: Crossplot of amplitude and duration of AE signals from loadset 7-8 for beam SCC-MA-C

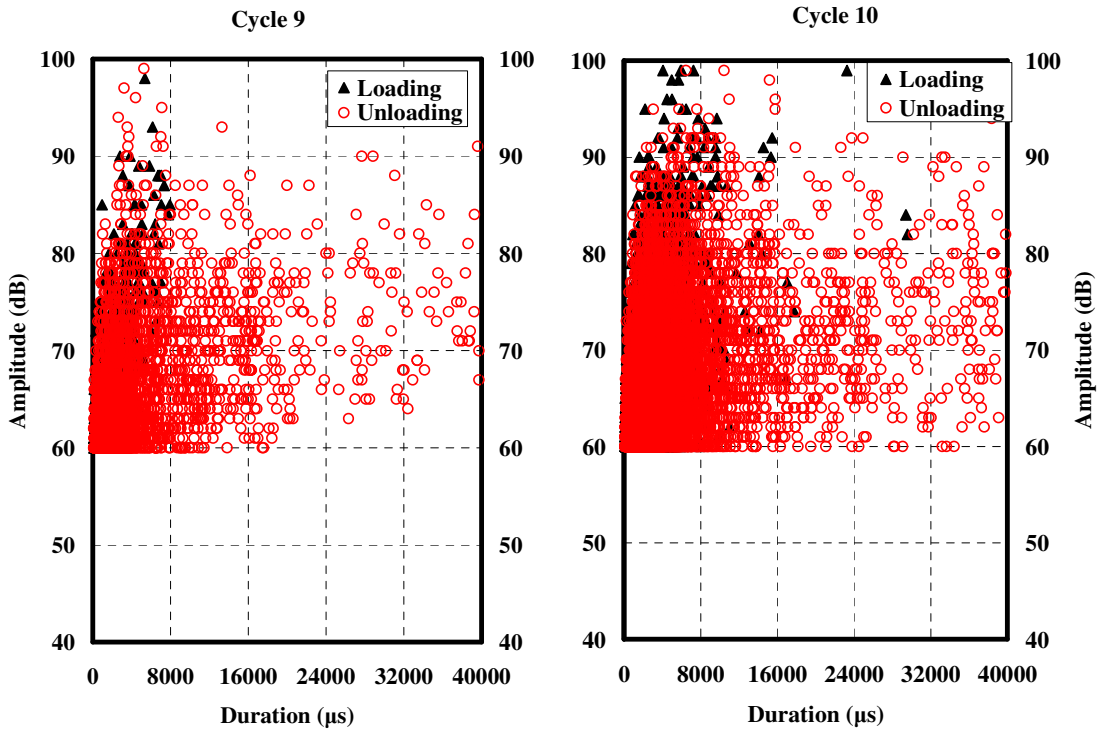


Figure C-35: Crossplot of amplitude and duration of AE signals from loadset 9-10 for beam SCC-MA-C

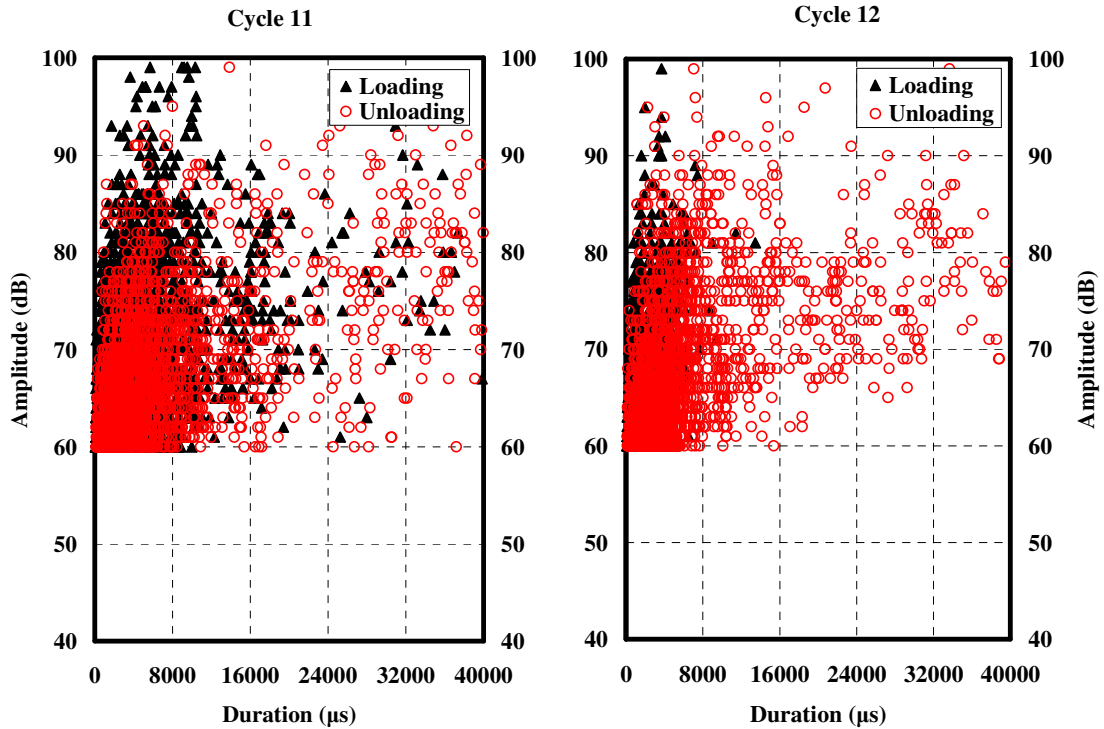


Figure C-36: Crossplot of amplitude and duration of AE signals from loadset 11-12 for beam SCC-MA-C

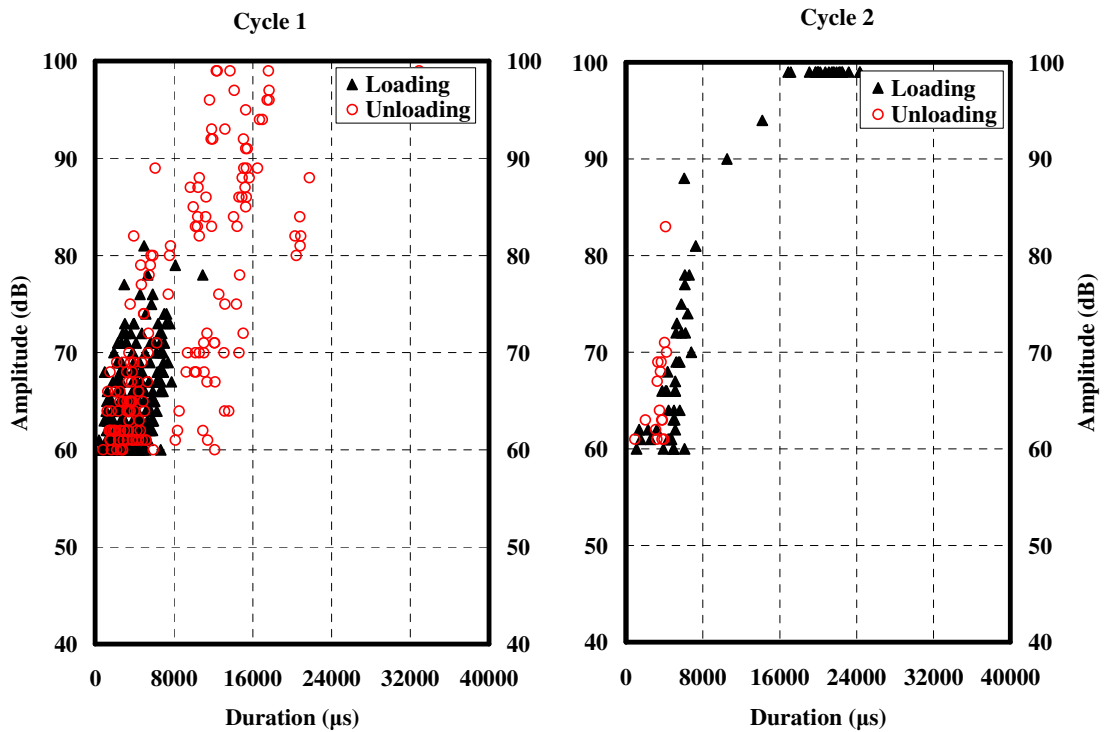


Figure C-37: Crossplot of amplitude and duration of AE signals from loadset 1-2 for beam SCC-MA-D

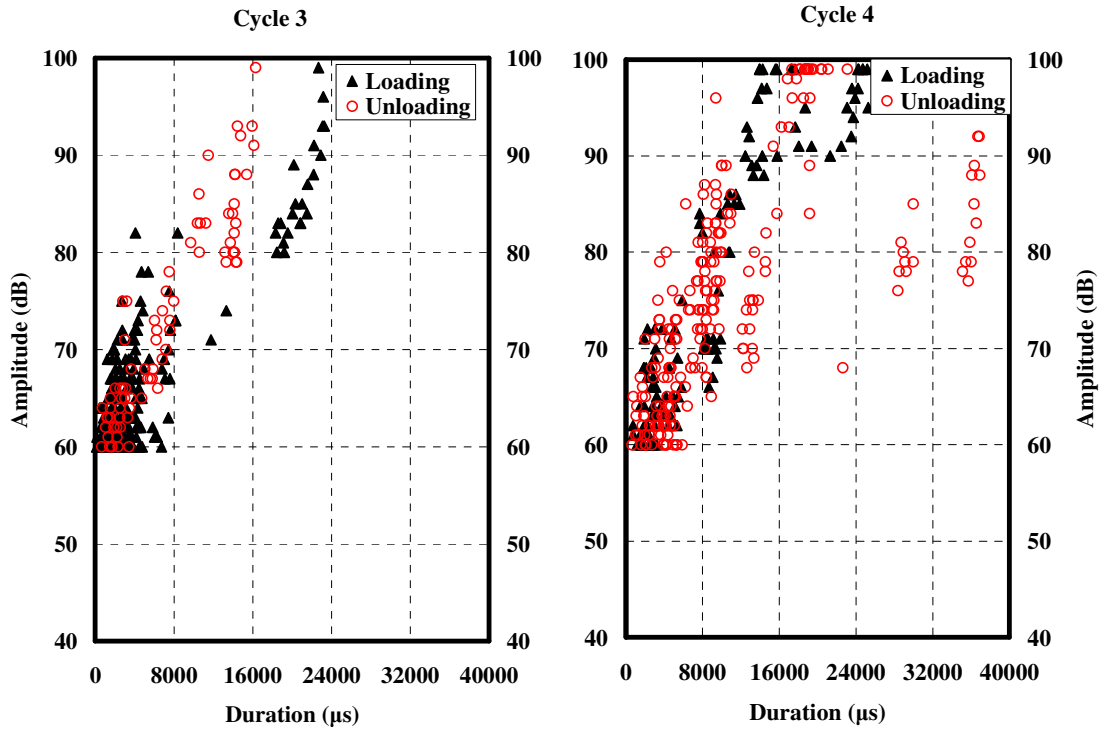


Figure C-38: Crossplot of amplitude and duration of AE signals from loadset 3-4 for beam SCC-MA-D

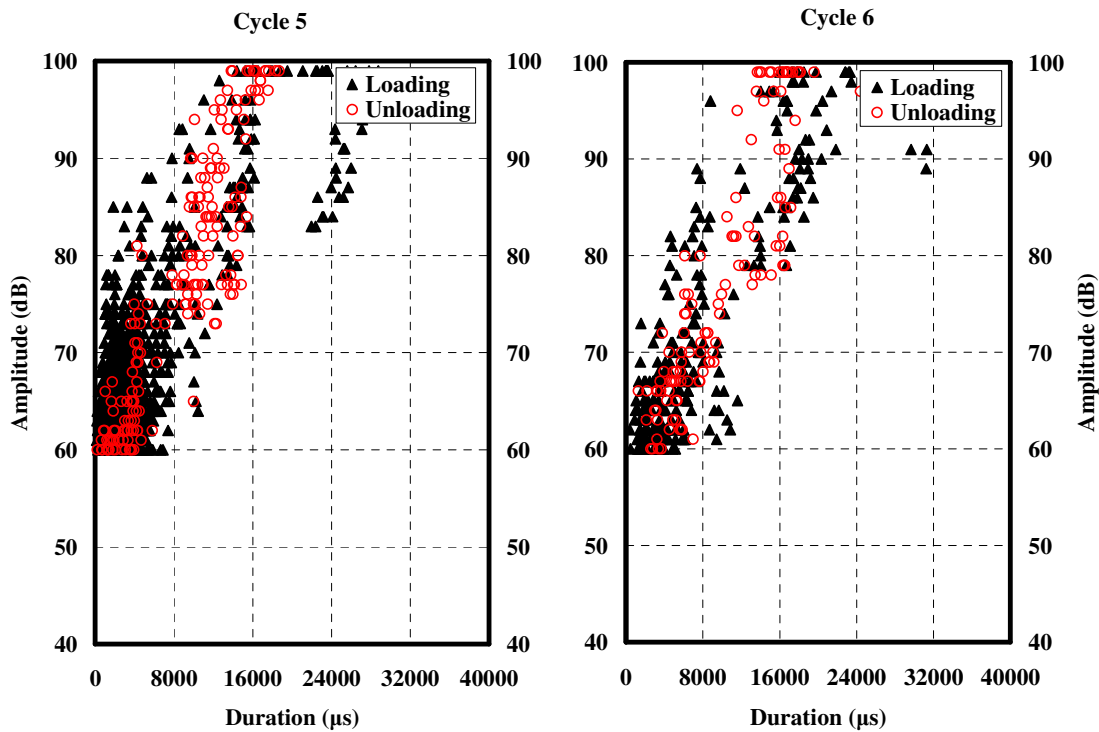


Figure C-39: Crossplot of amplitude and duration of AE signals from loadset 5-6 for beam SCC-MA-D

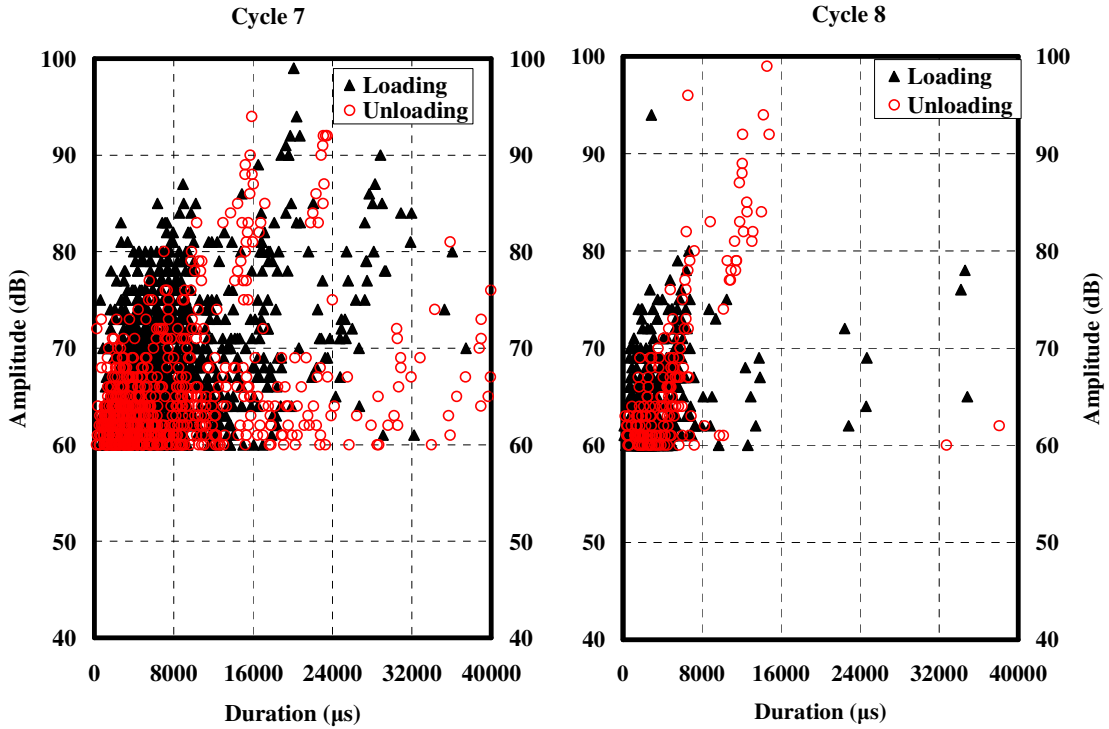


Figure C-40: Crossplot of amplitude and duration of AE signals from loadset 7-8 for beam SCC-MA-D

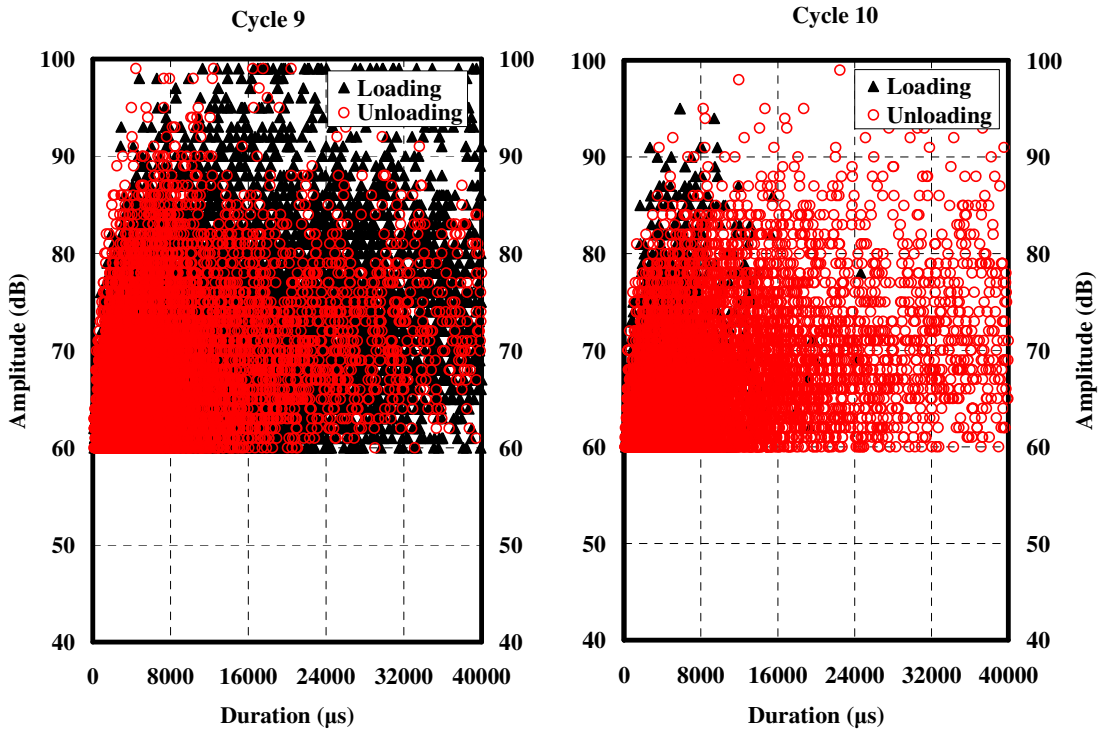


Figure C-41: Crossplot of amplitude and duration of AE signals from loadset 9-10 for beam SCC-MA-D

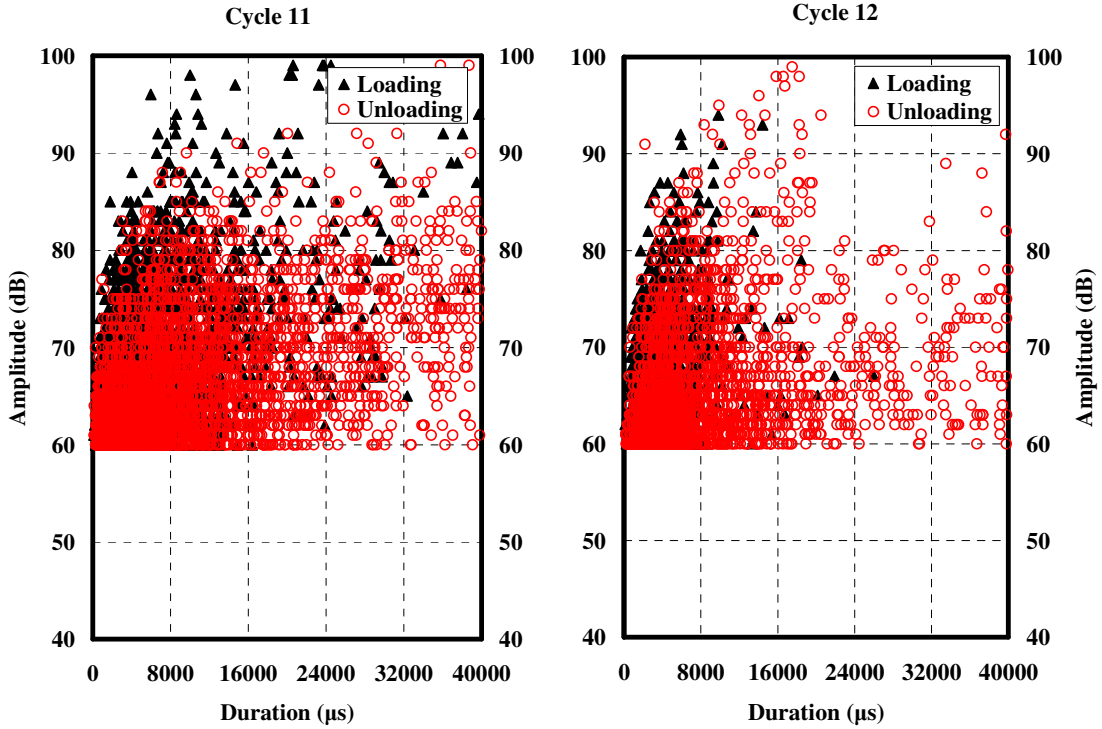


Figure C-42: Crossplot of amplitude and duration of AE signals from loadset 11-12 for beam SCC-MA-D

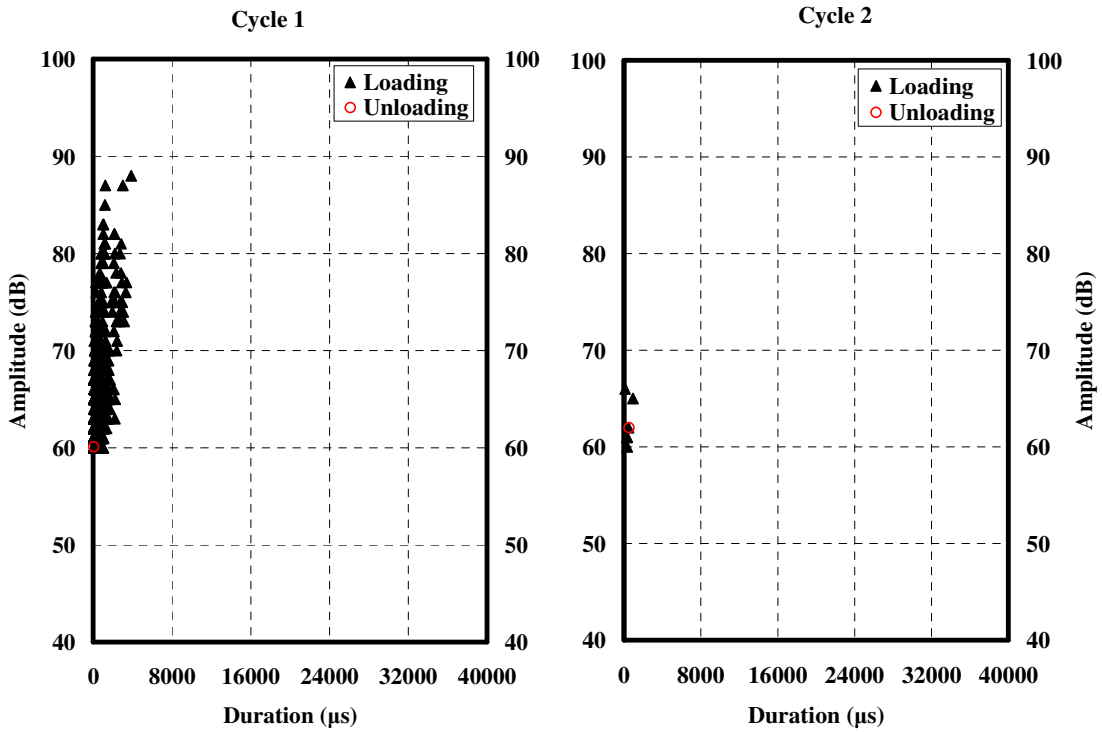


Figure C-43: Crossplot of amplitude and duration of AE signals from loadset 1-2 for beam SCC-MS-A

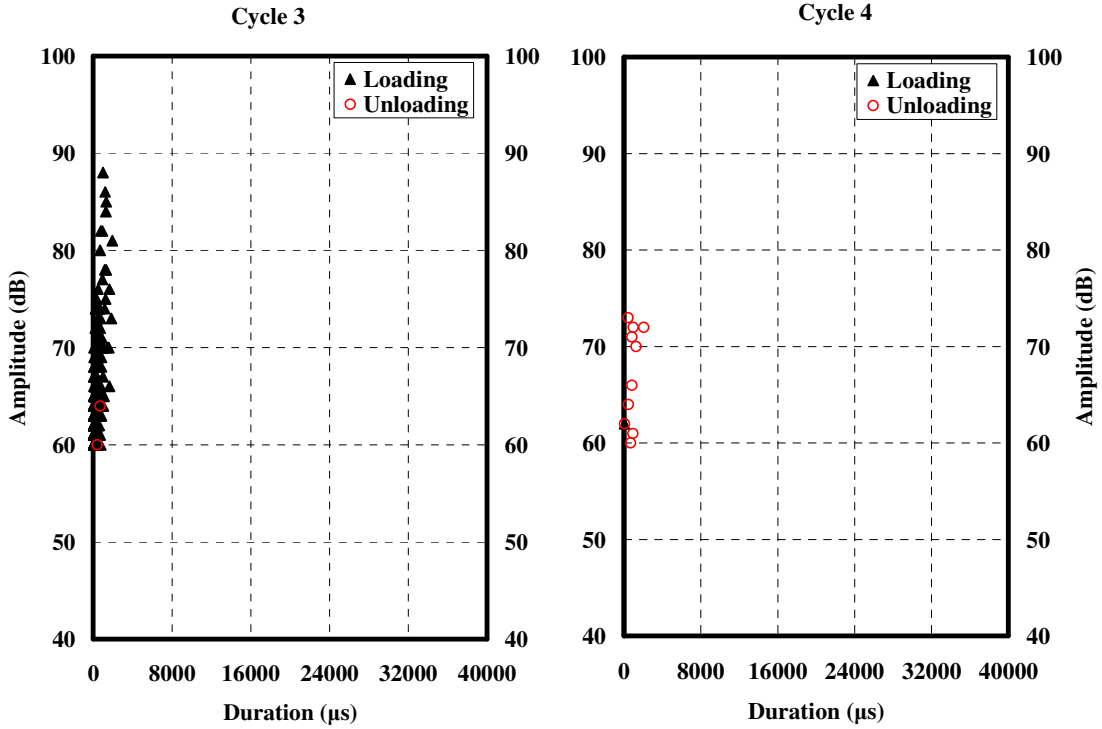


Figure C-44: Crossplot of amplitude and duration of AE signals from loadset 3-4 for beam SCC-MS-A

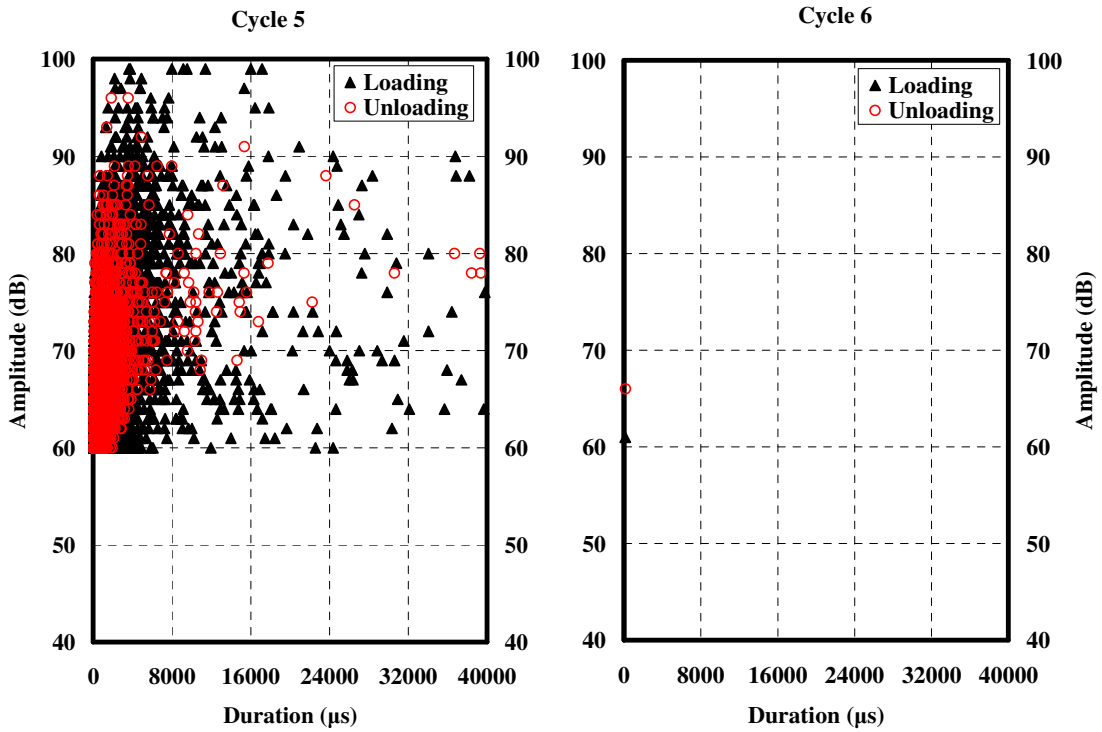


Figure C-45: Crossplot of amplitude and duration of AE signals from loadset 5-6 for beam SCC-MS-A

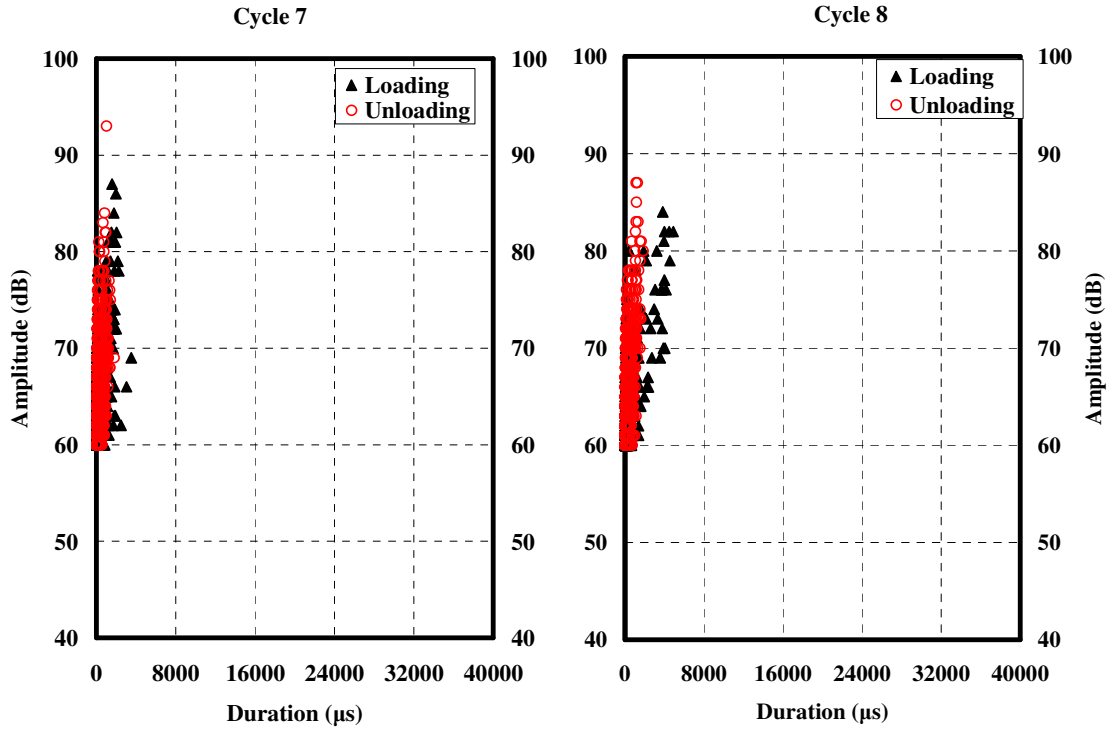


Figure C-46: Crossplot of amplitude and duration of AE signals from loadset 7-8 for beam SCC-MS-A

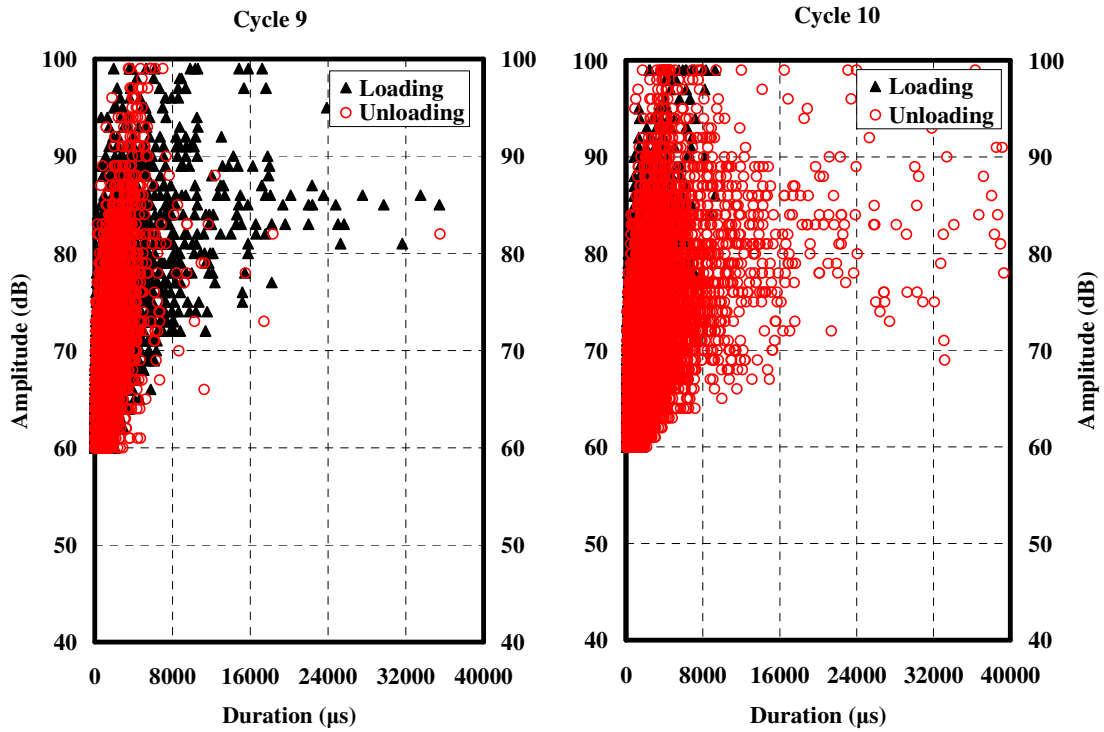


Figure C-47: Crossplot of amplitude and duration of AE signals from loadset 9-10 for beam SCC-MS-A

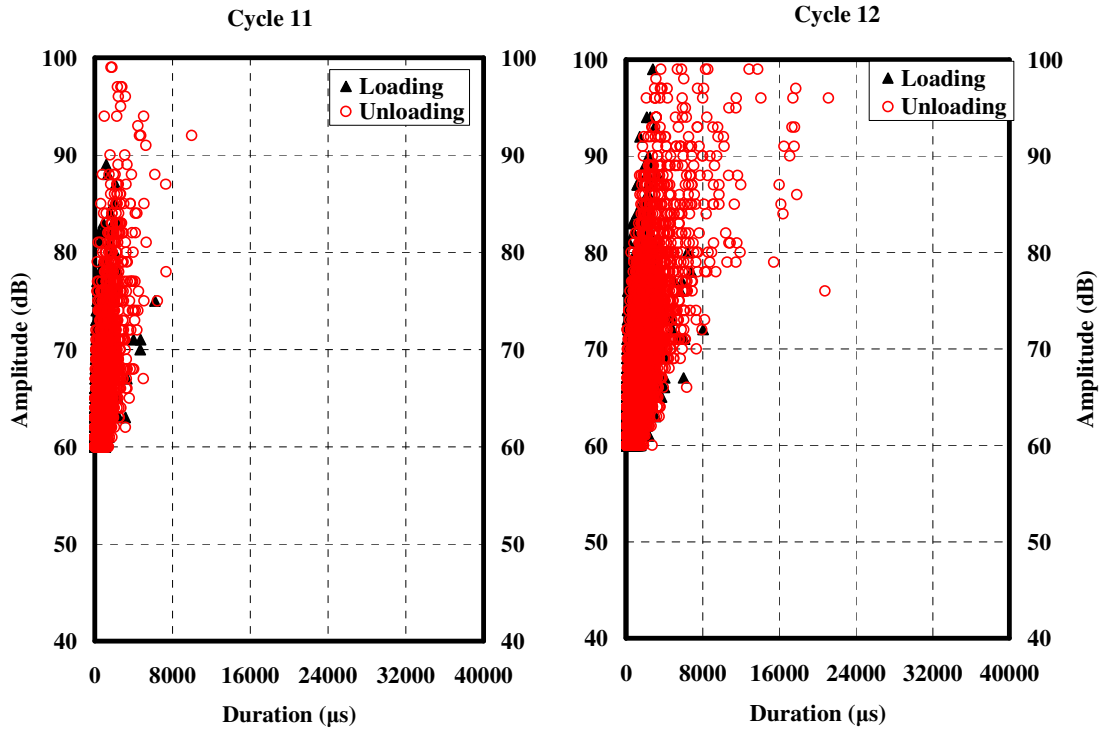


Figure C-48: Crossplot of amplitude and duration of AE signals from loadset 11-12 for beam SCC-MS-A

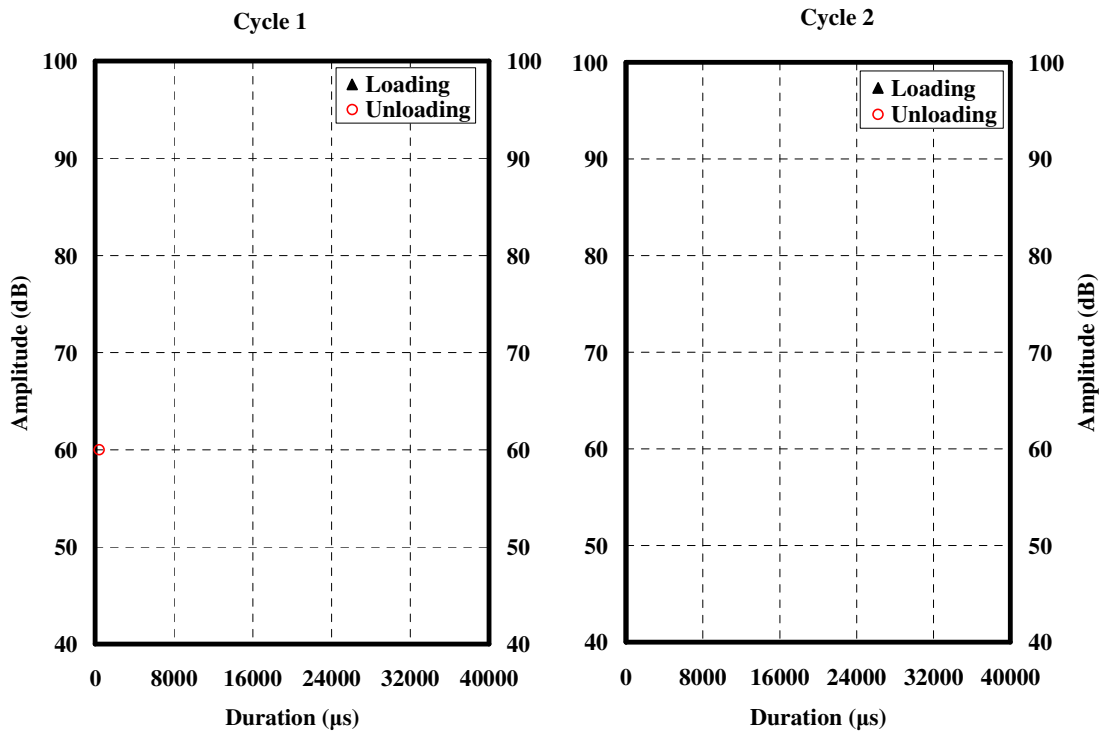


Figure C-49: Crossplot of amplitude and duration of AE signals from loadset 1-2 for beam SCC-MS-B

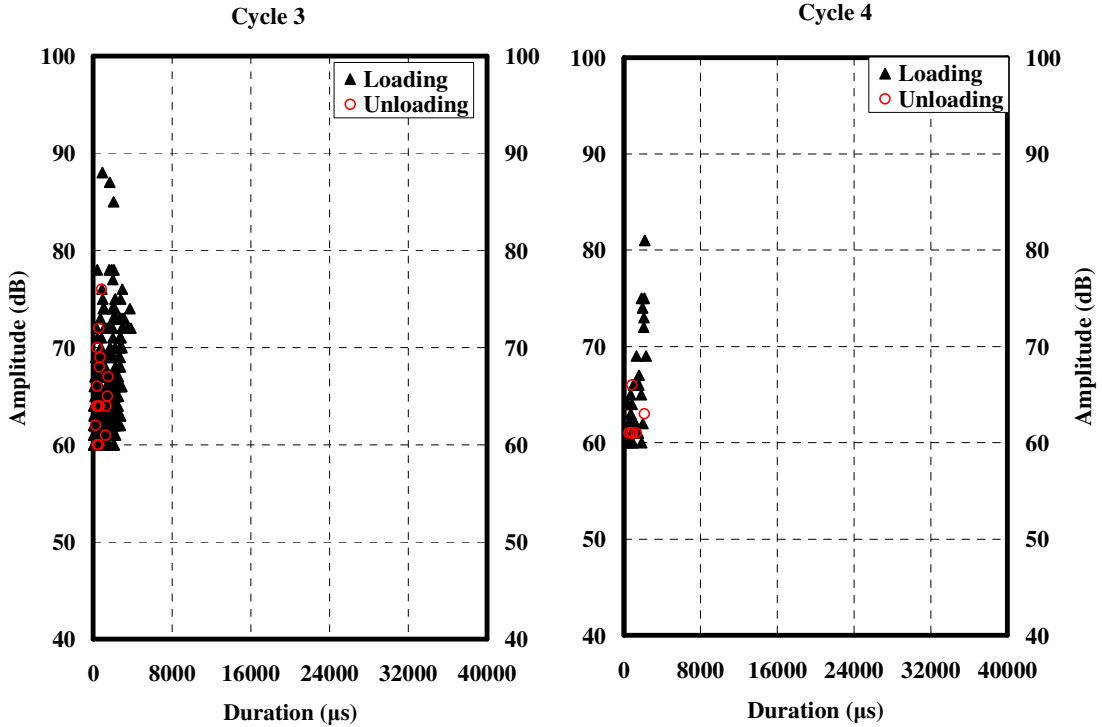


Figure C-50: Crossplot of amplitude and duration of AE signals from loadset 3-4 for beam SCC-MS-B

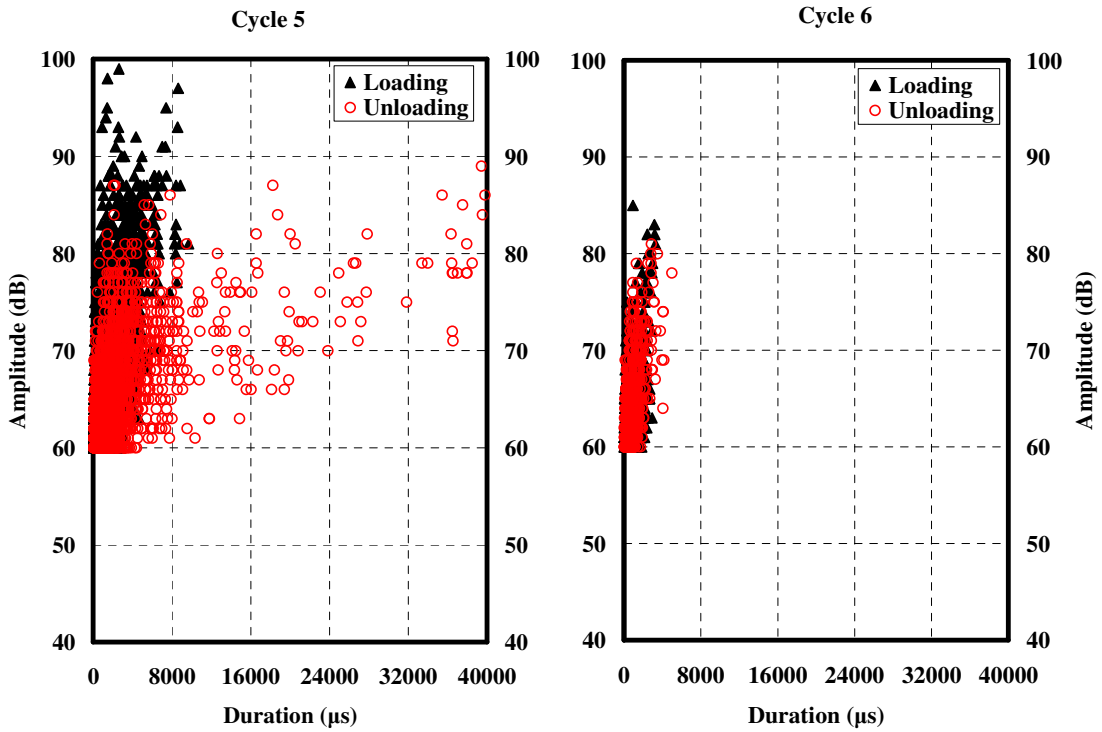


Figure C-51: Crossplot of amplitude and duration of AE signals from loadset 5-6 for beam SCC-MS-B

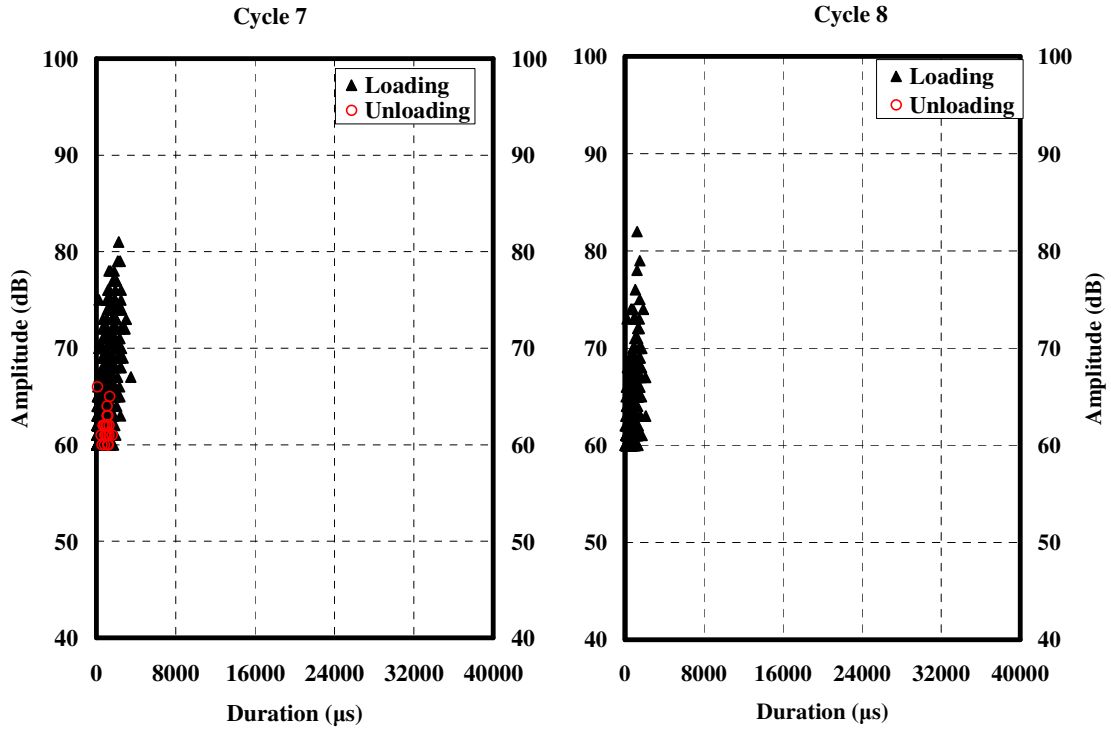


Figure C-52: Crossplot of amplitude and duration of AE signals from loadset 7-8 for beam SCC-MS-B

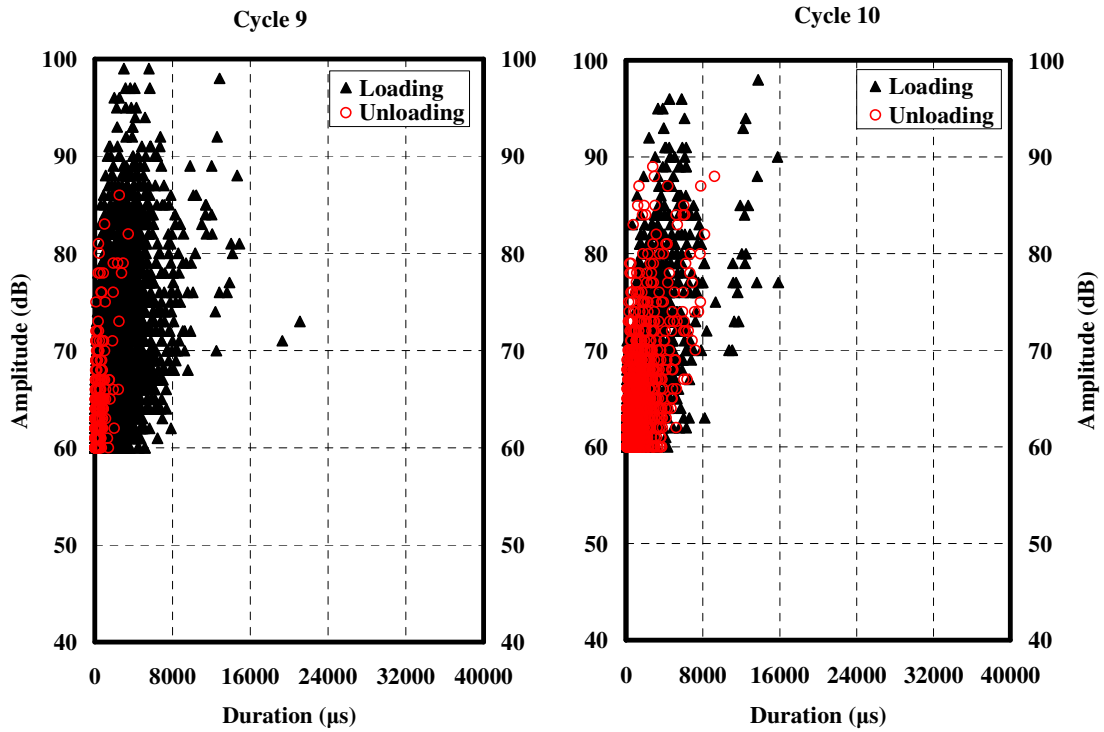


Figure C-53: Crossplot of amplitude and duration of AE signals from loadset 9-10 for beam SCC-MS-B

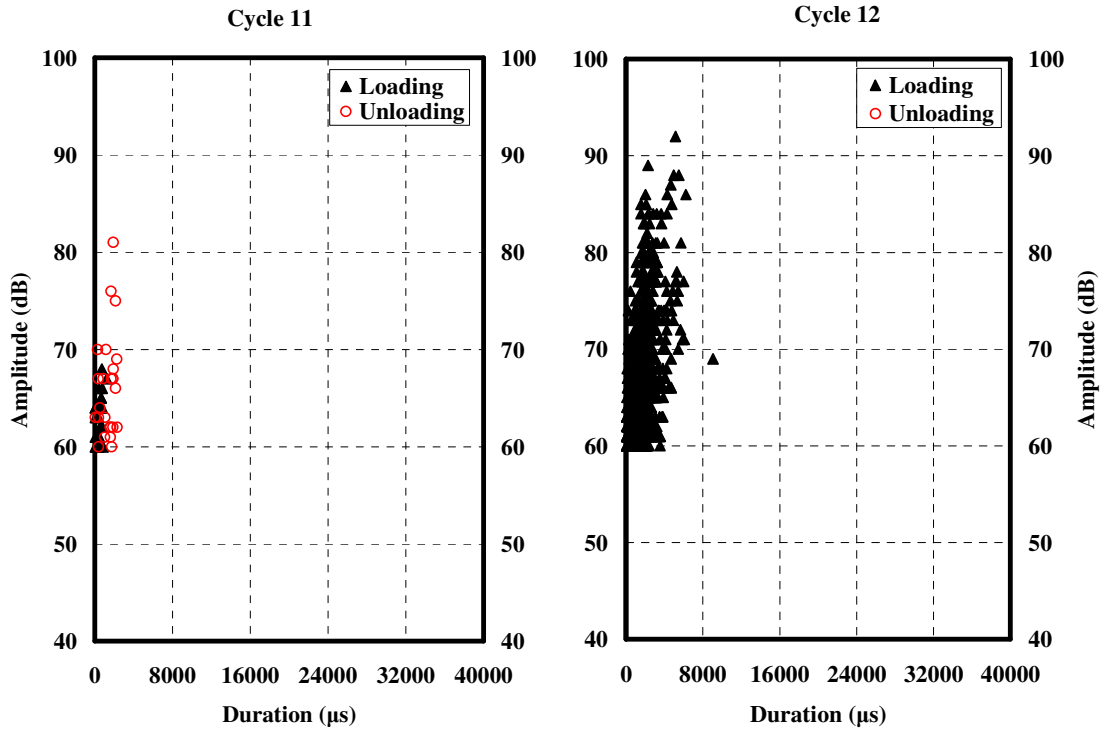


Figure C-54: Crossplot of amplitude and duration of AE signals from loadset 11-12 for beam SCC-MS-B

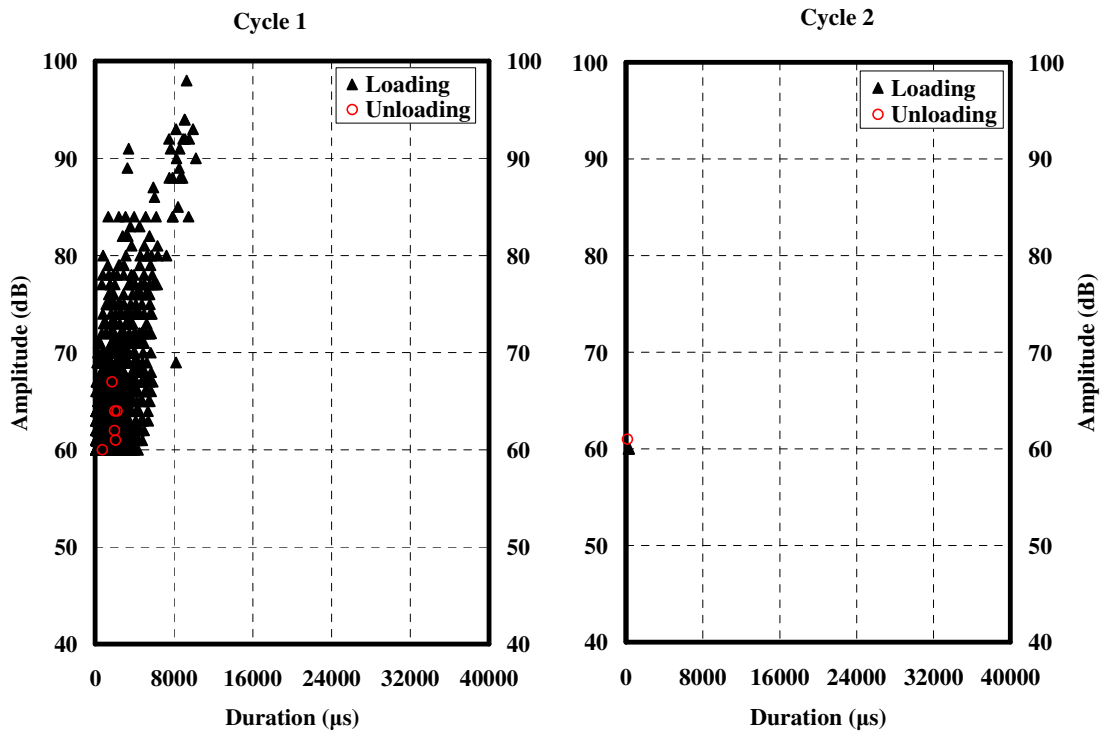


Figure C-55: Crossplot of amplitude and duration of AE signals from loadset 1-2 for beam SCC-MS-C

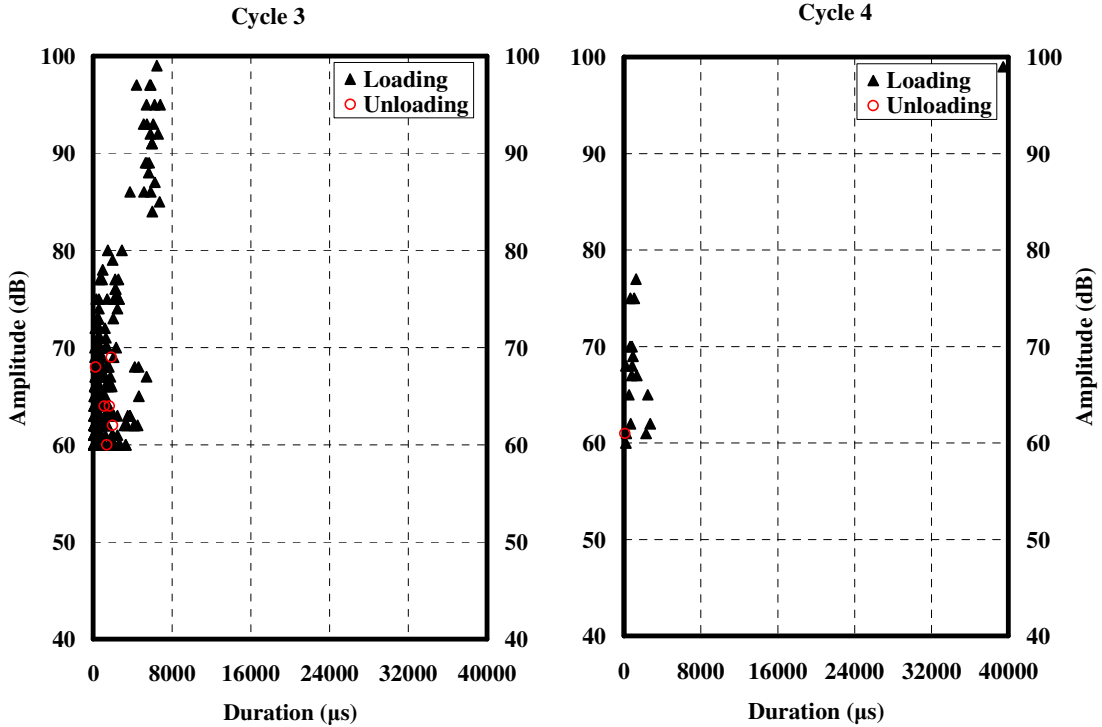


Figure C-56: Crossplot of amplitude and duration of AE signals from loadset 3-4 for beam SCC-MS-C

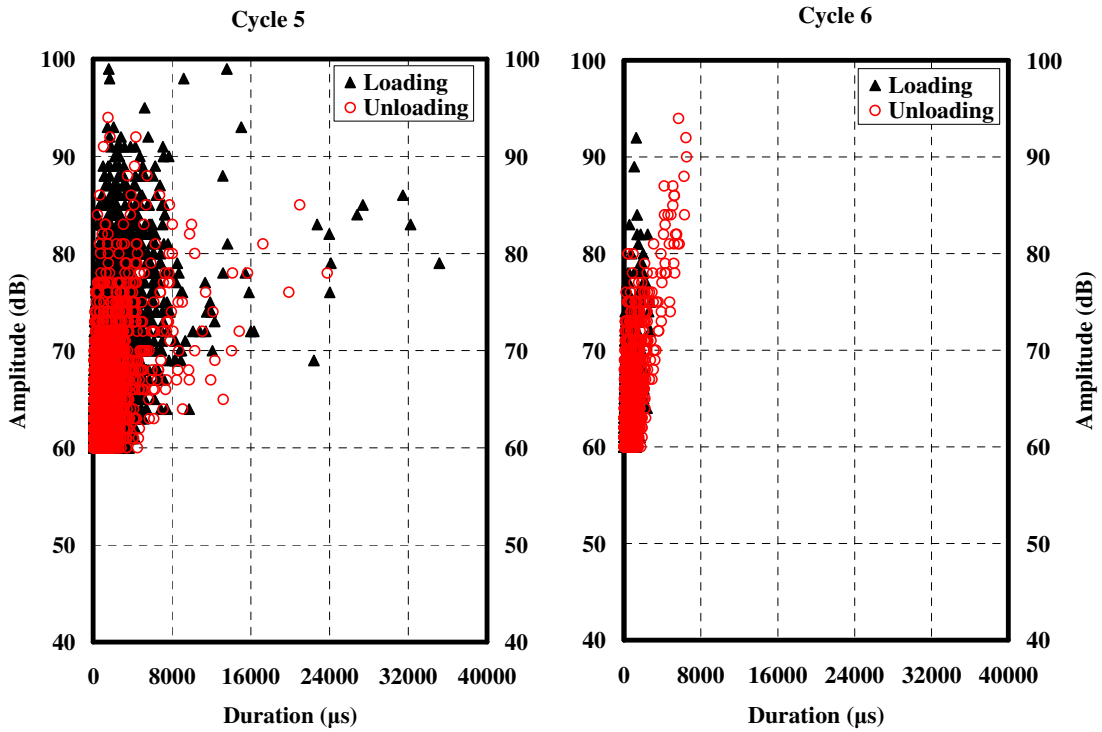


Figure C-57: Crossplot of amplitude and duration of AE signals from loadset 5-6 for beam SCC-MS-C

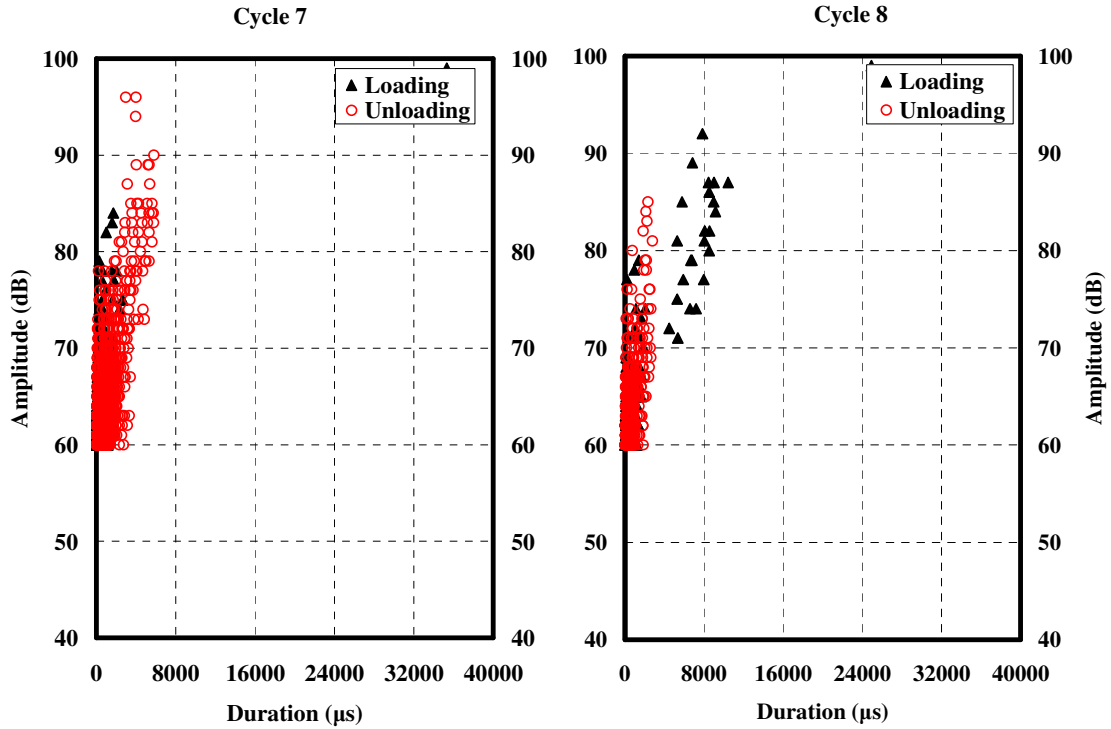


Figure C-58: Crossplot of amplitude and duration of AE signals from loadset 7-8 for beam SCC-MS-C

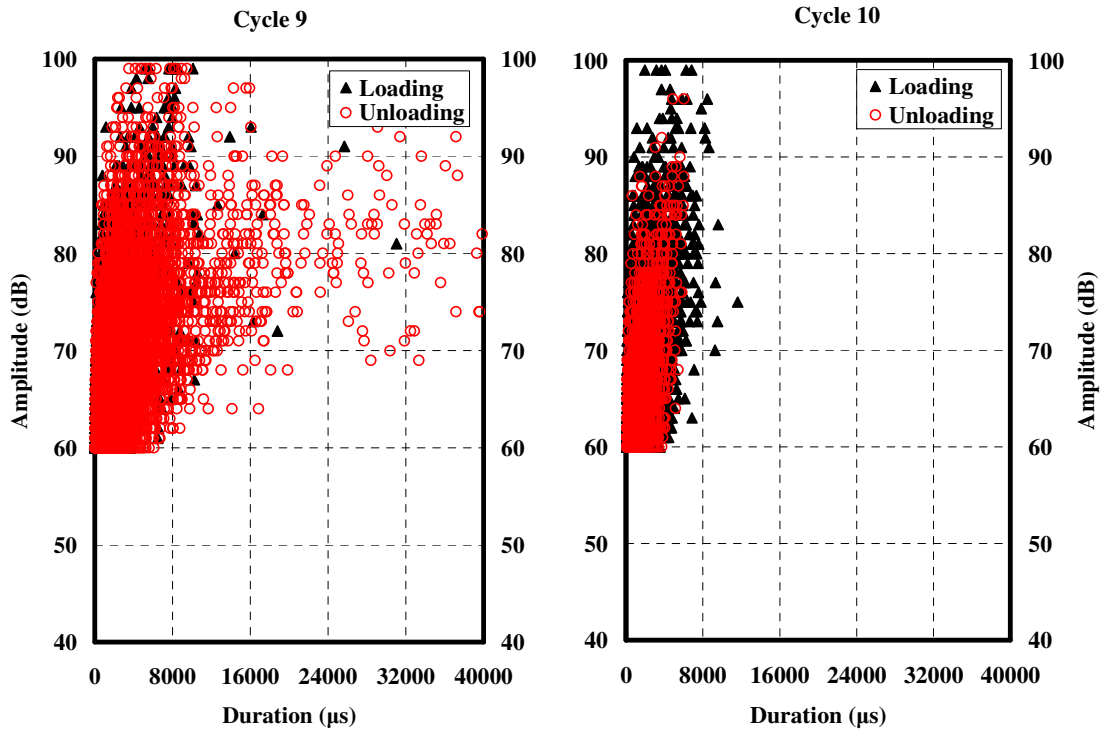


Figure C-59: Crossplot of amplitude and duration of AE signals from loadset 9-10 for beam SCC-MS-C

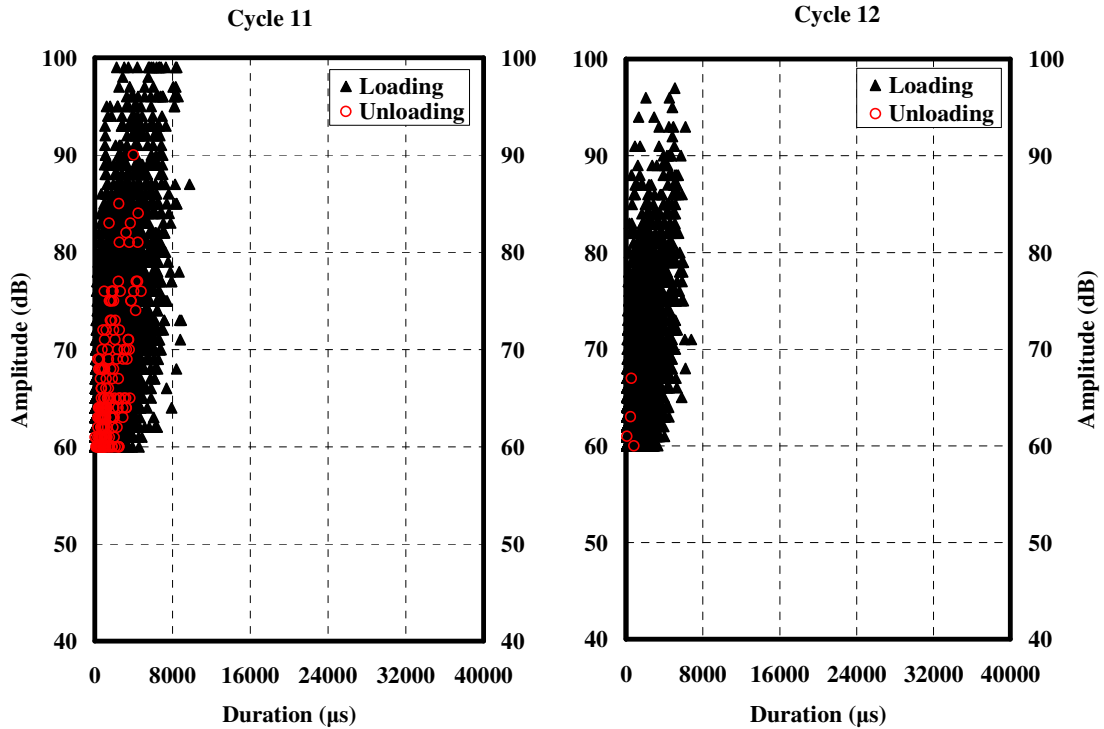


Figure C-60: Crossplot of amplitude and duration of AE signals from loadset 11-12 for beam SCC-MS-C

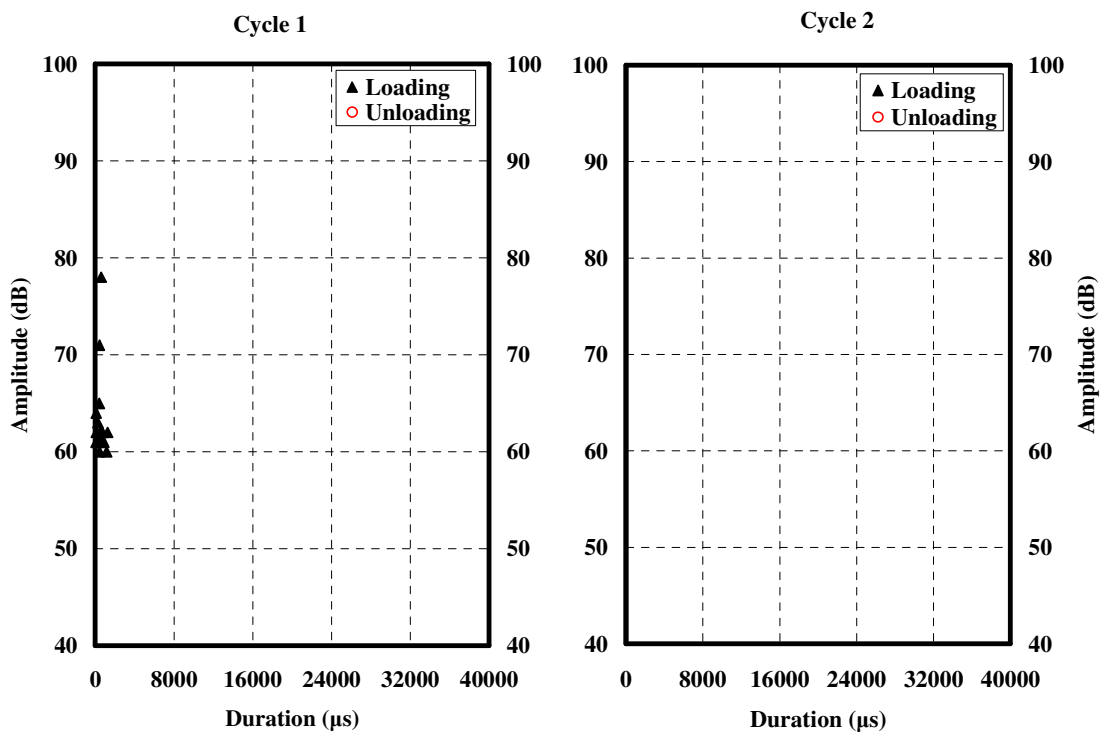


Figure C-61: Crossplot of amplitude and duration of AE signals from loadset 1-2 for beam SCC-MS-D

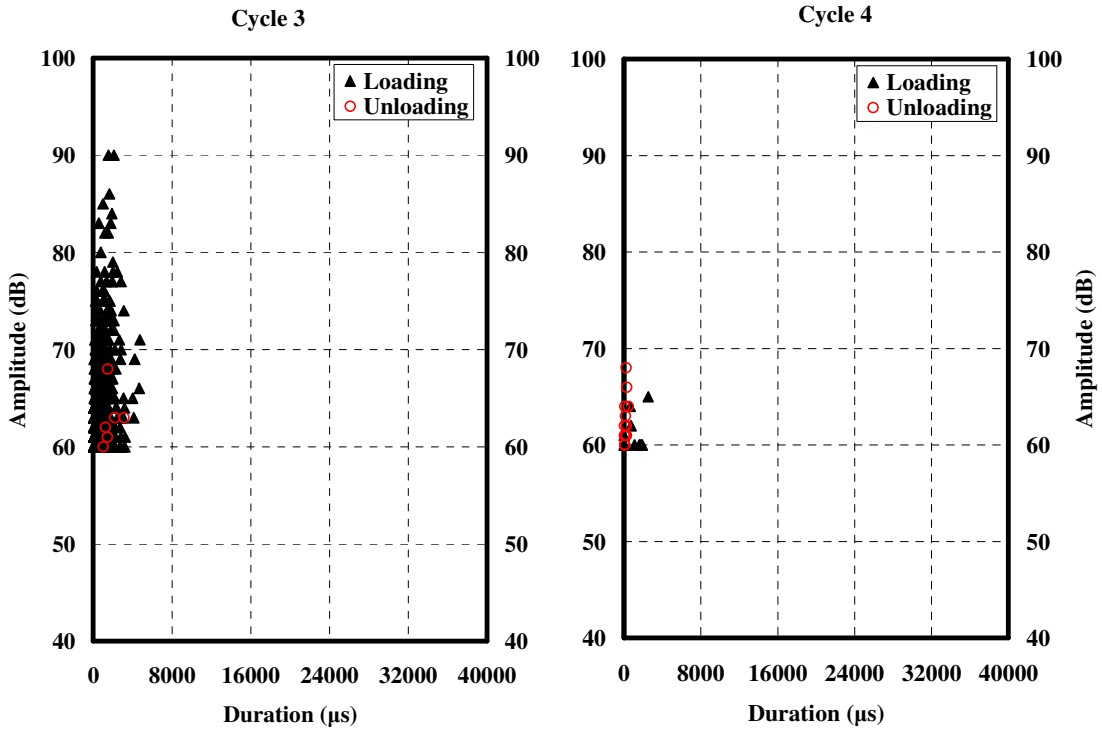


Figure C-62: Crossplot of amplitude and duration of AE signals from loadset 3-4 for beam SCC-MS-D

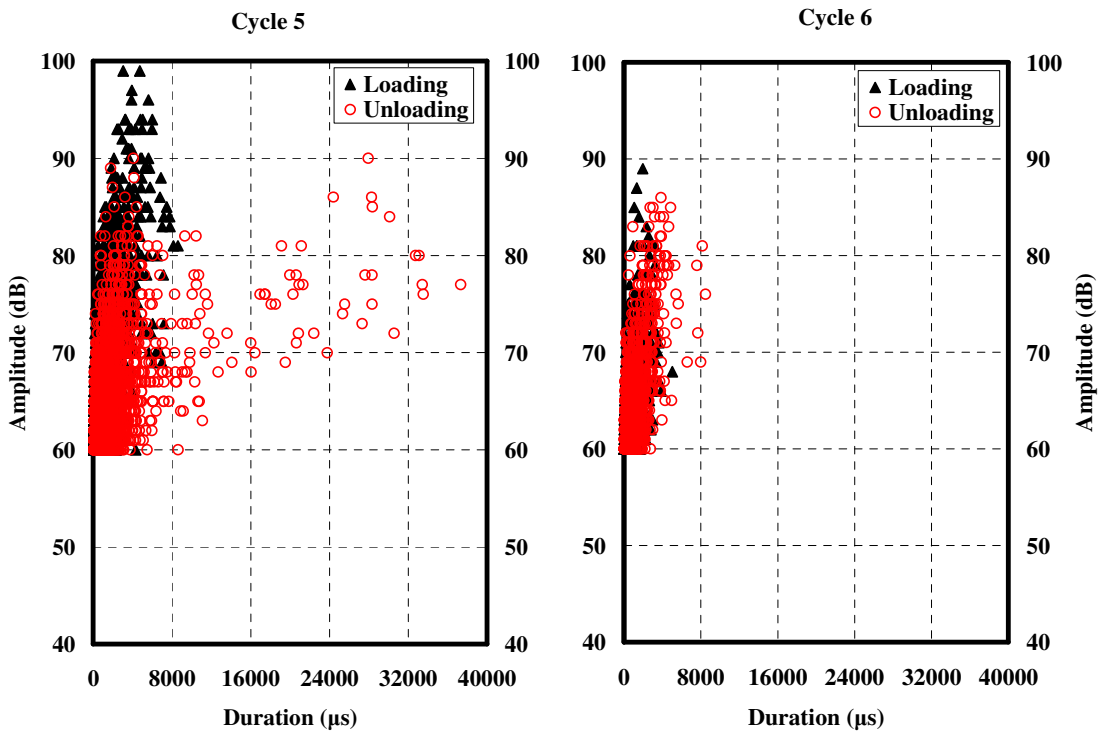


Figure C-63: Crossplot of amplitude and duration of AE signals from loadset 5-6 for beam SCC-MS-D

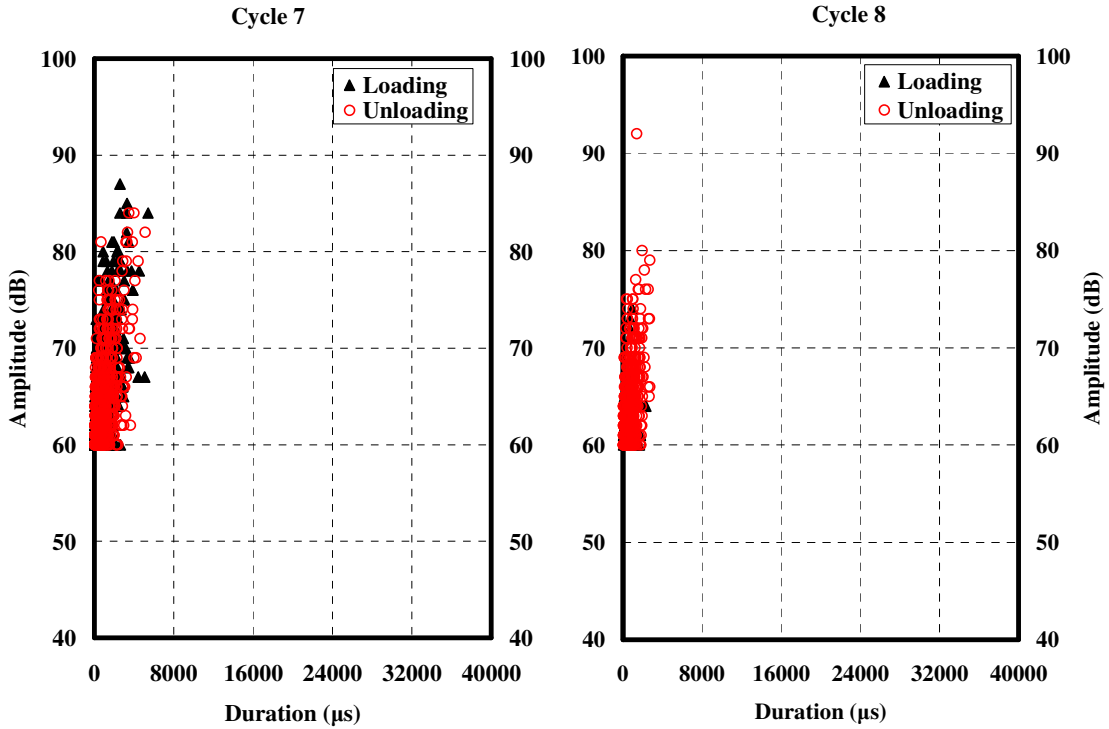


Figure C-64: Crossplot of amplitude and duration of AE signals from loadset 7-8 for beam SCC-MS-D

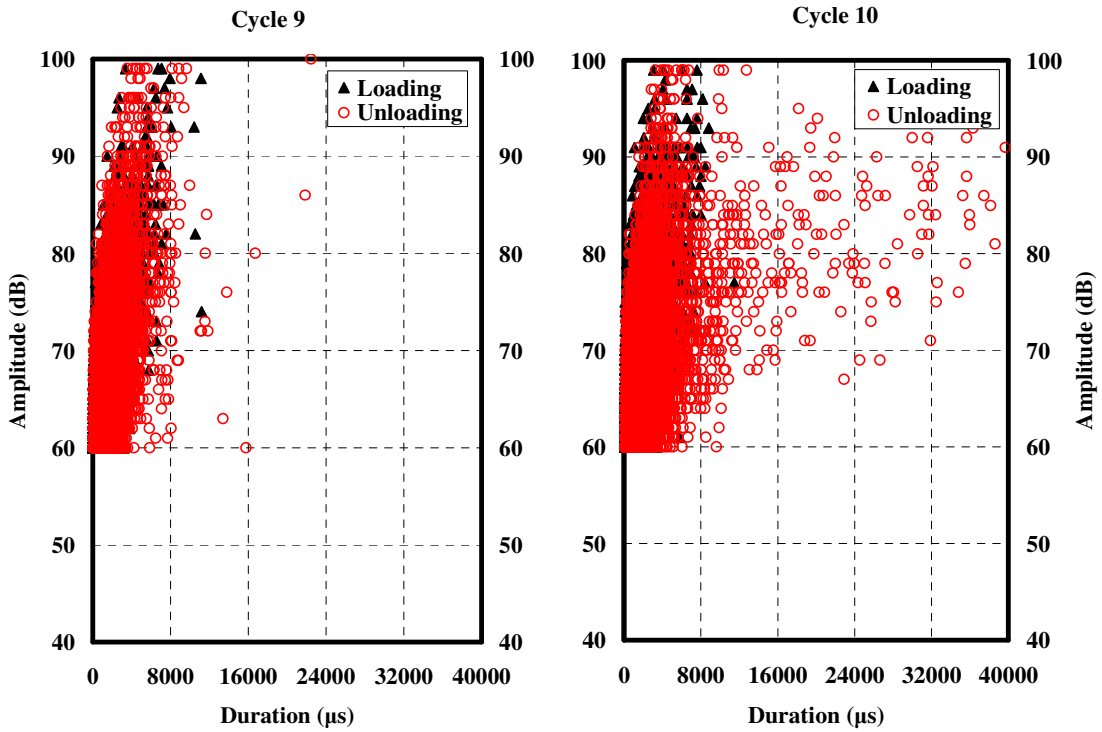


Figure C-65: Crossplot of amplitude and duration of AE signals from loadset 9-10 for beam SCC-MS-D

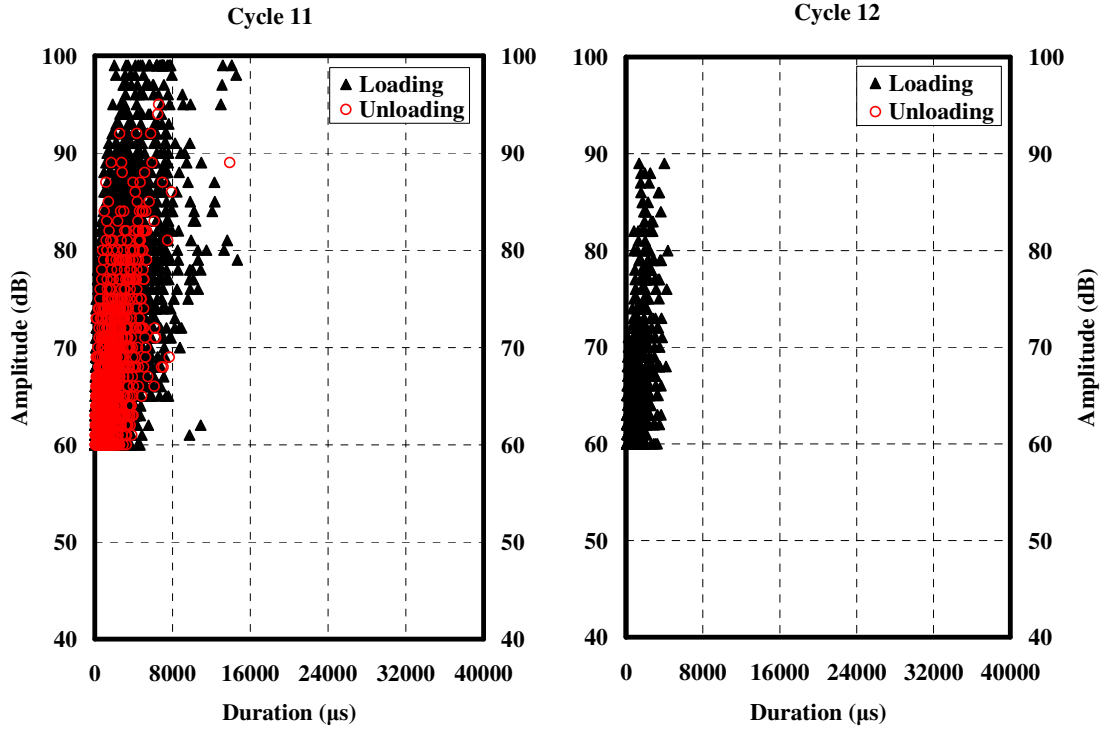


Figure C-66: Crossplot of amplitude and duration of AE signals from loadset 11-12 for beam SCC-MS-D

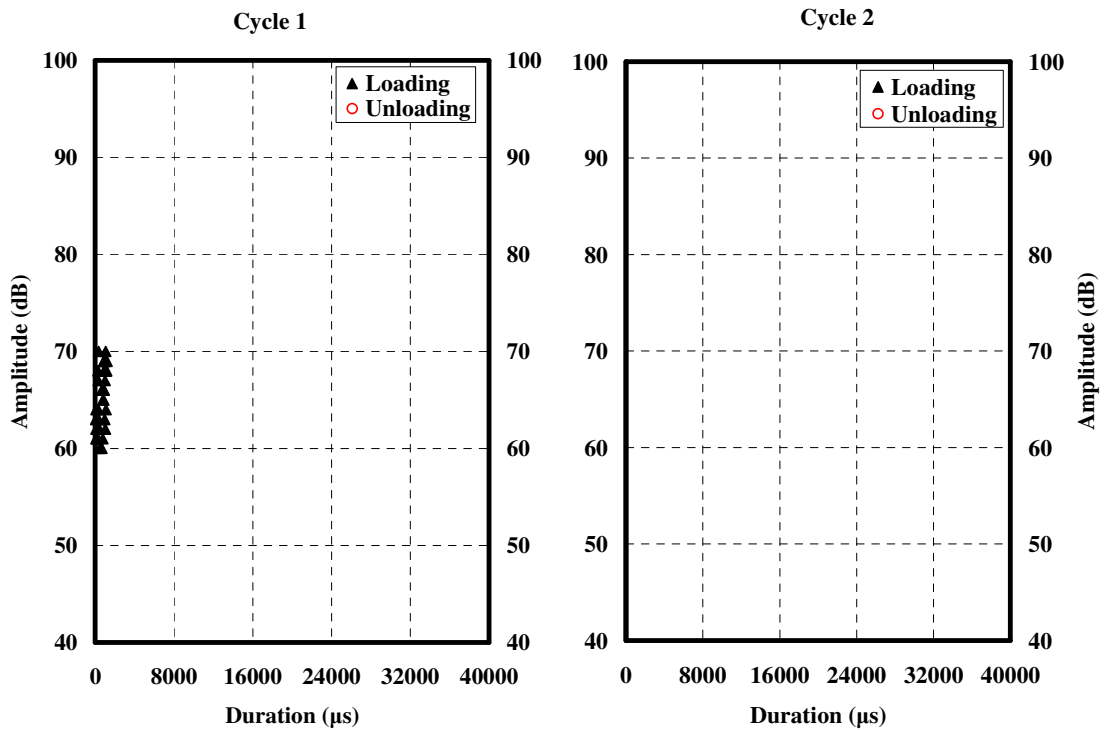


Figure C-67: Crossplot of amplitude and duration of AE signals from loadset 1-2 for beam SCC-HS-A

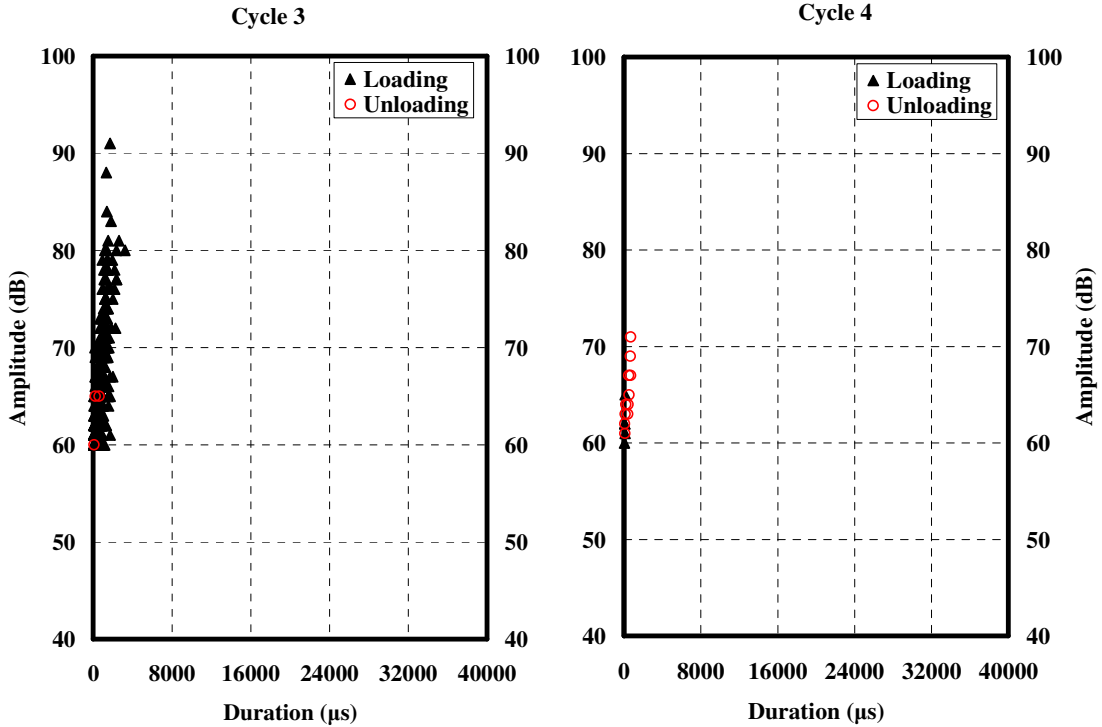


Figure C-68: Crossplot of amplitude and duration of AE signals from loadset 3-4 for beam SCC-HS-A

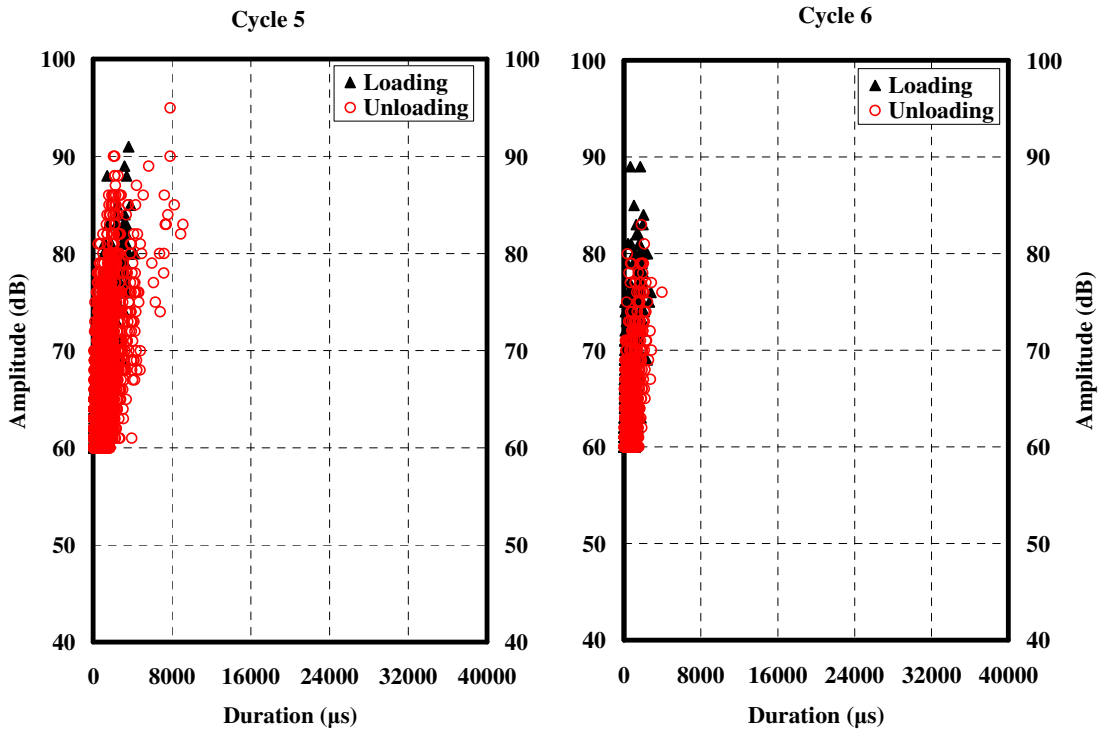


Figure C-69: Crossplot of amplitude and duration of AE signals from loadset 5-6 for beam SCC-HS-A

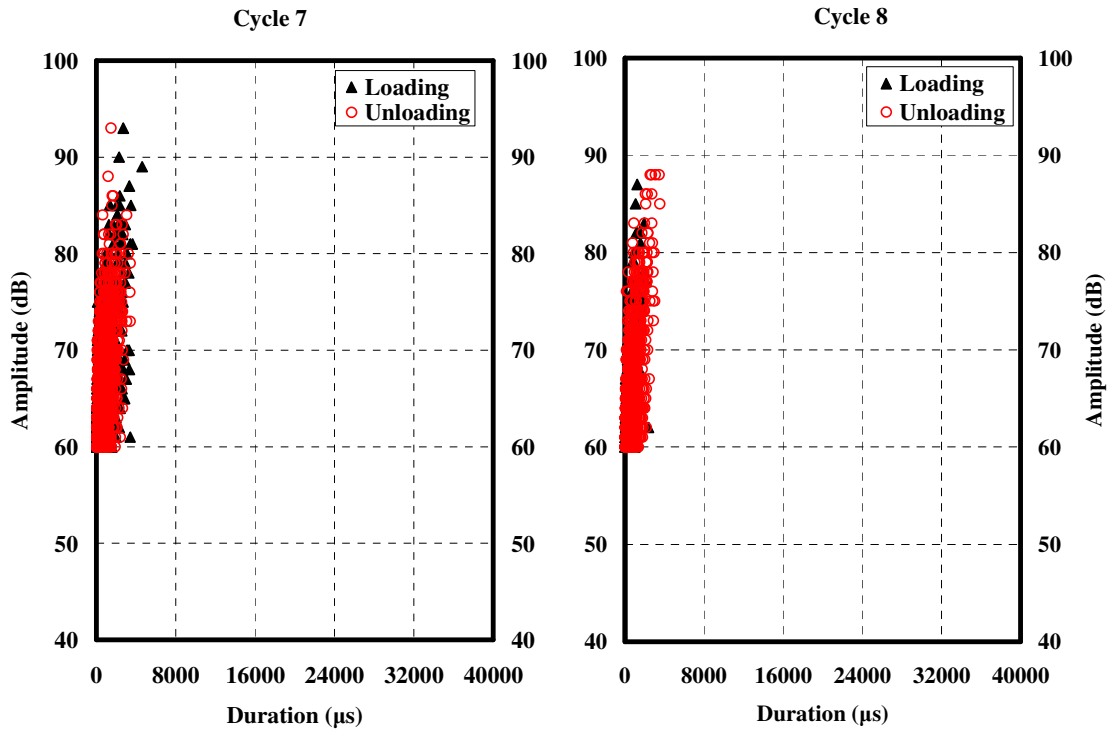


Figure C-70: Crossplot of amplitude and duration of AE signals from loadset 7-8 for beam SCC-HS-A

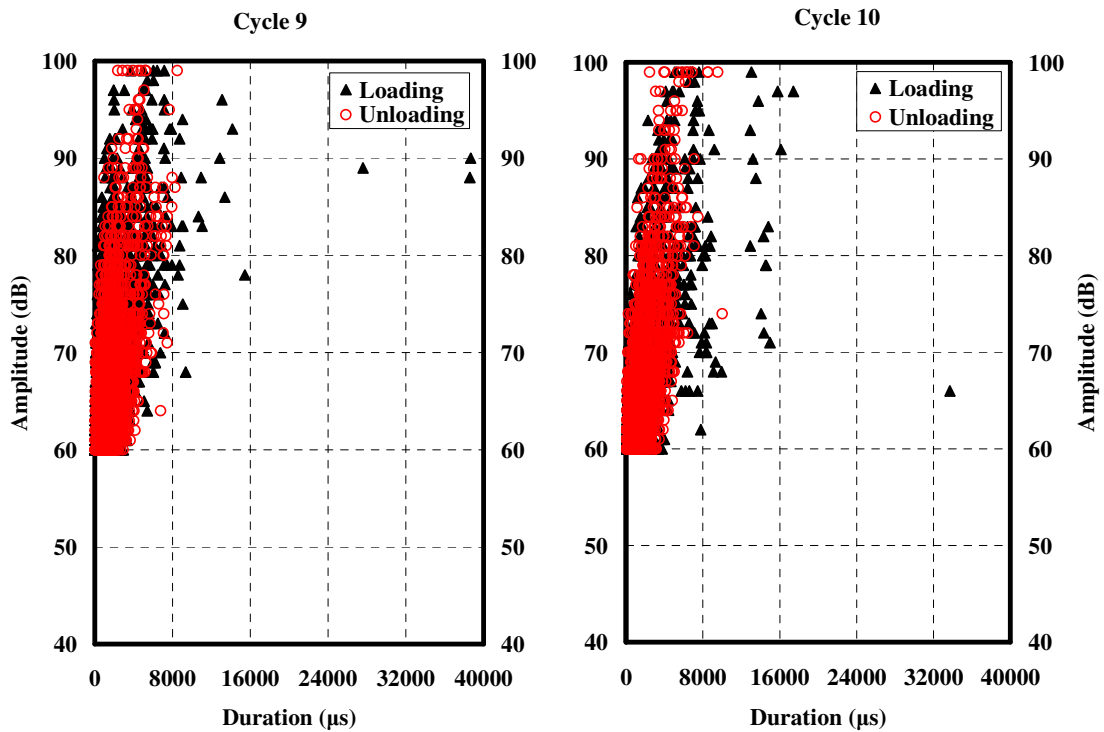


Figure C-71: Crossplot of amplitude and duration of AE signals from loadset 9-10 for beam SCC-HS-A

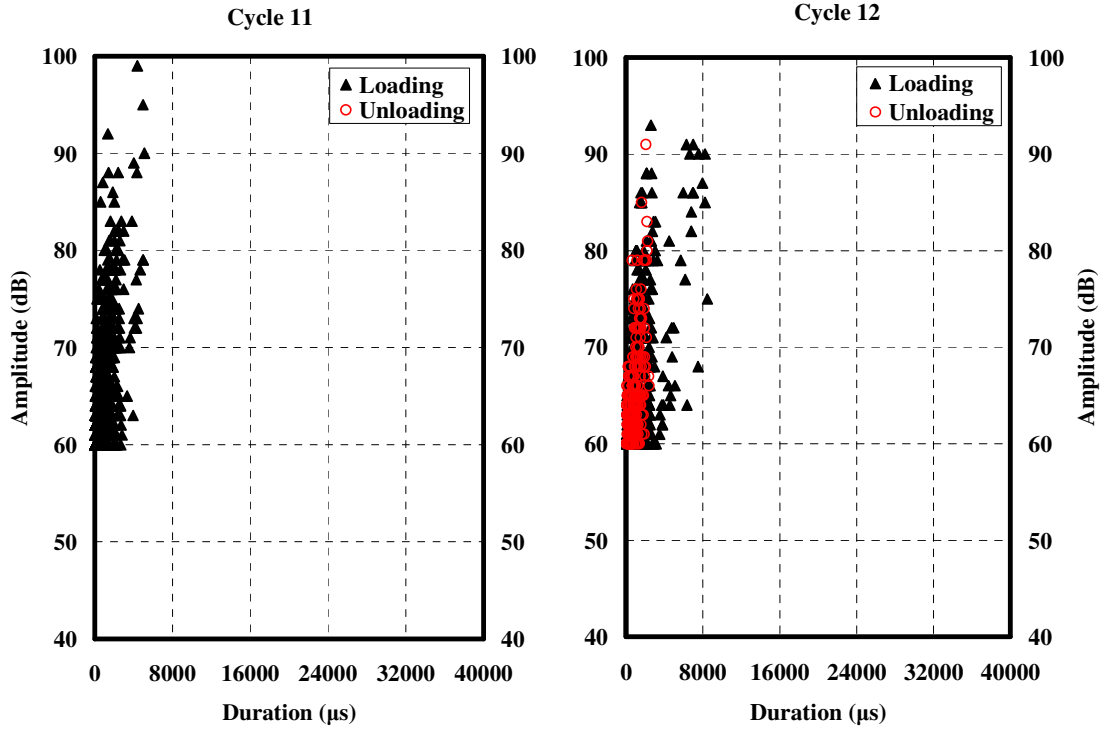


Figure C-72: Crossplot of amplitude and duration of AE signals from loadset 11-12 for beam SCC-HS-A

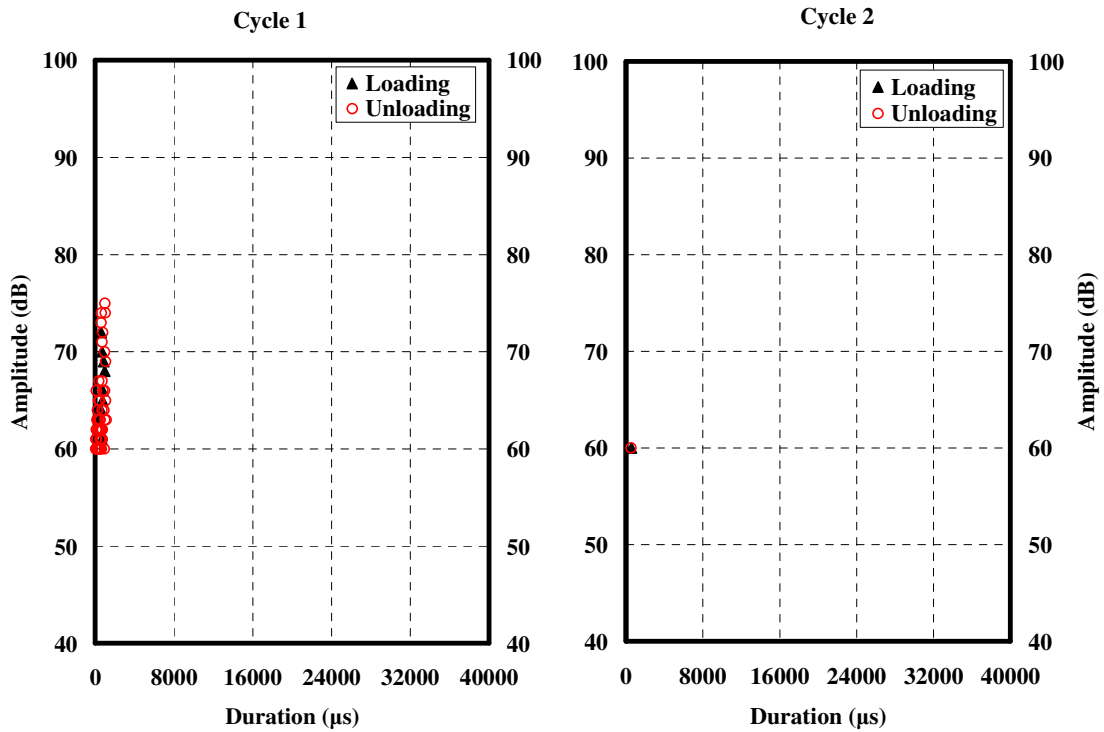


Figure C-73: Crossplot of amplitude and duration of AE signals from loadset 1-2 for beam SCC-HS-B

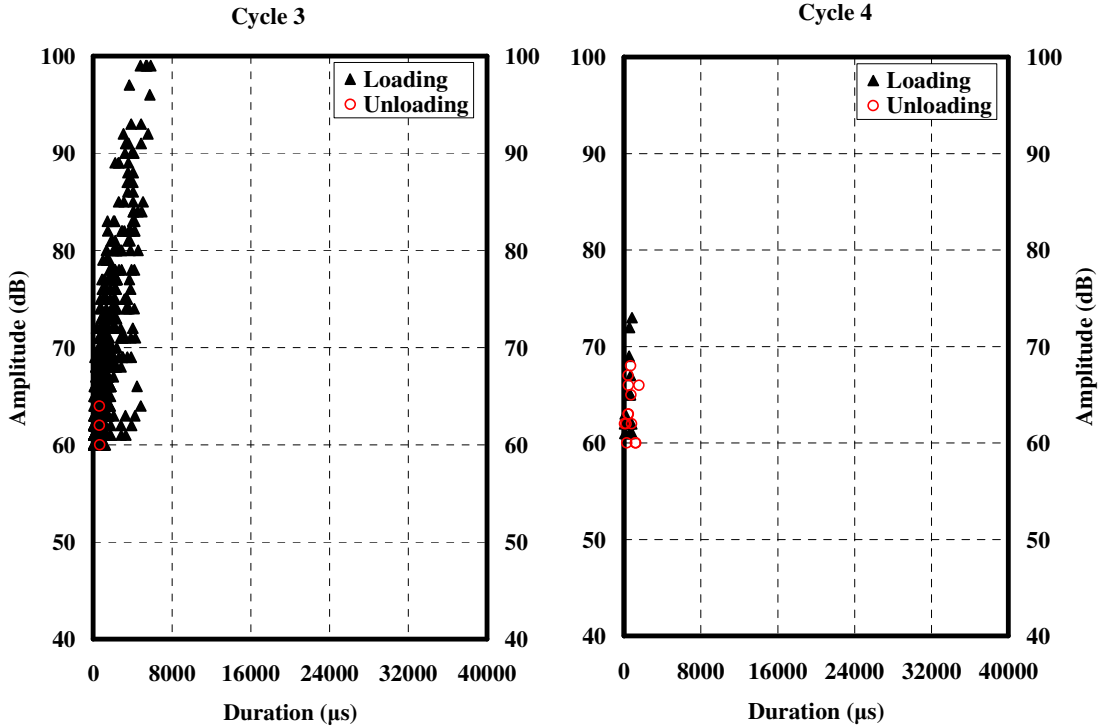


Figure C-74: Crossplot of amplitude and duration of AE signals from loadset 3-4 for beam SCC-HS-B

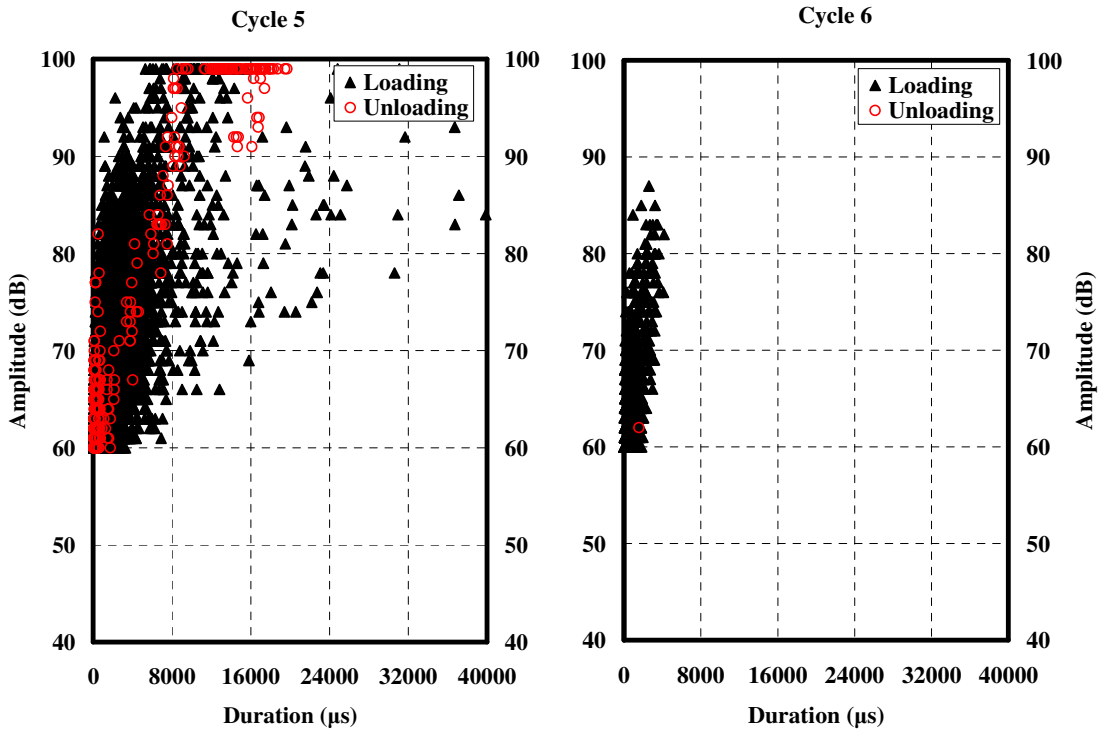


Figure C-75: Crossplot of amplitude and duration of AE signals from loadset 5-6 for beam SCC-HS-B

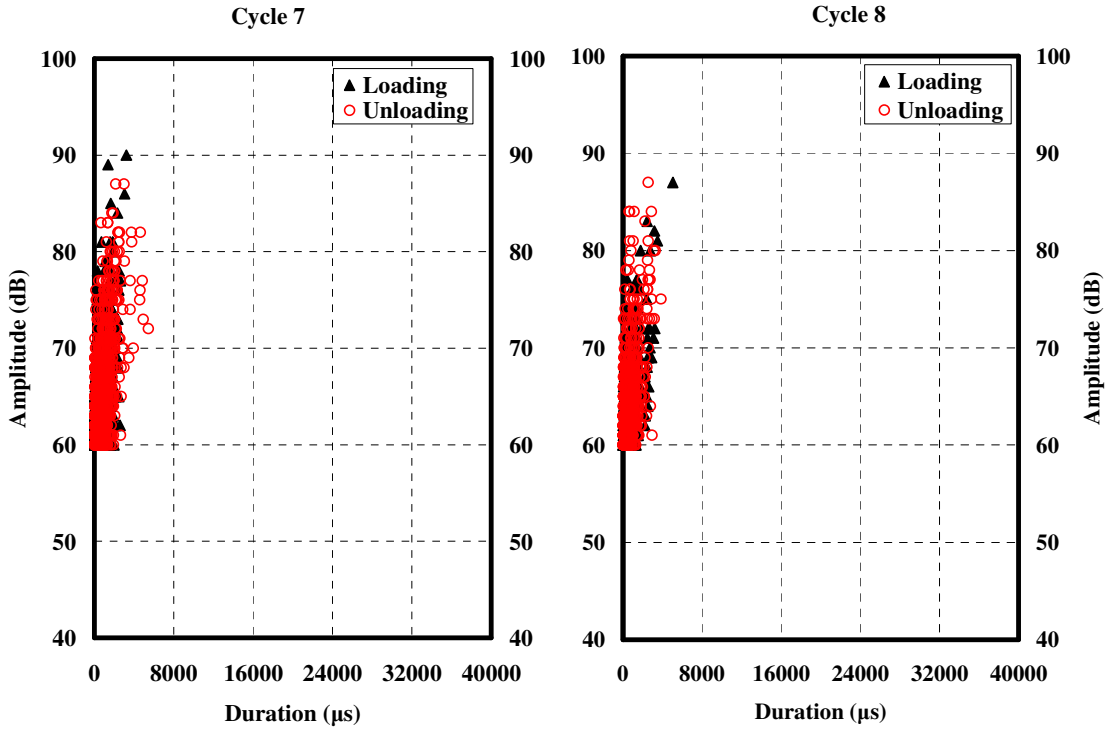


Figure C-76: Crossplot of amplitude and duration of AE signals from loadset 7-8 for beam SCC-HS-B

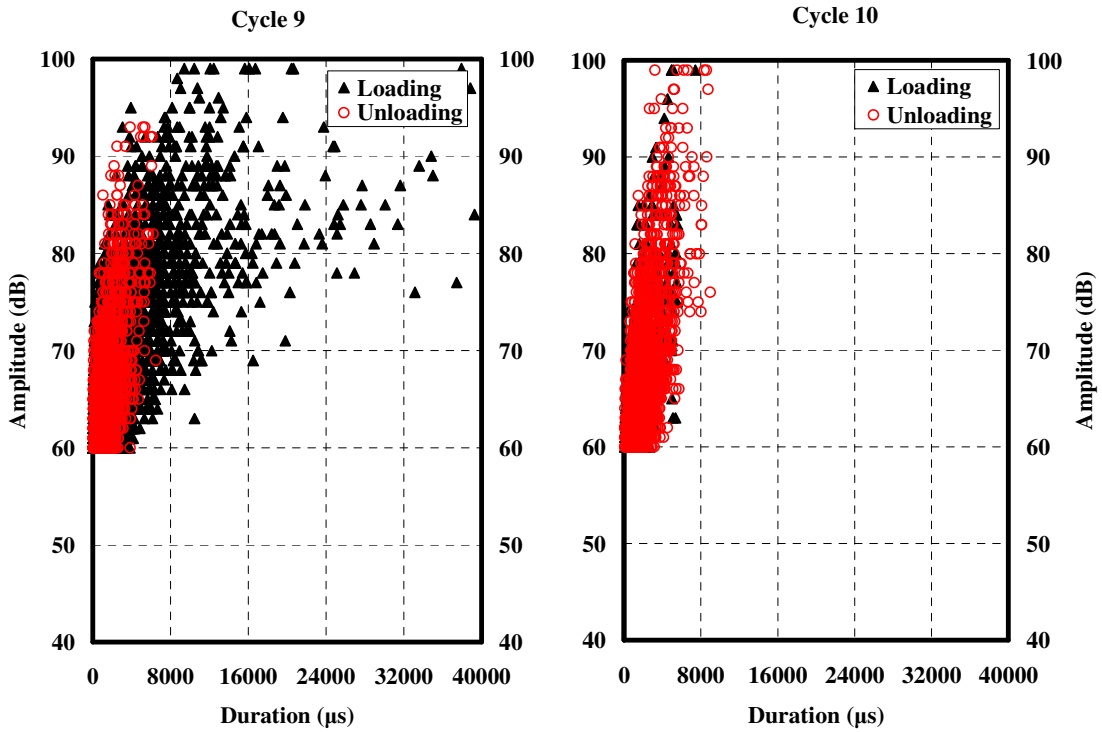


Figure C-77: Crossplot of amplitude and duration of AE signals from loadset 9-10 for beam SCC-HS-B

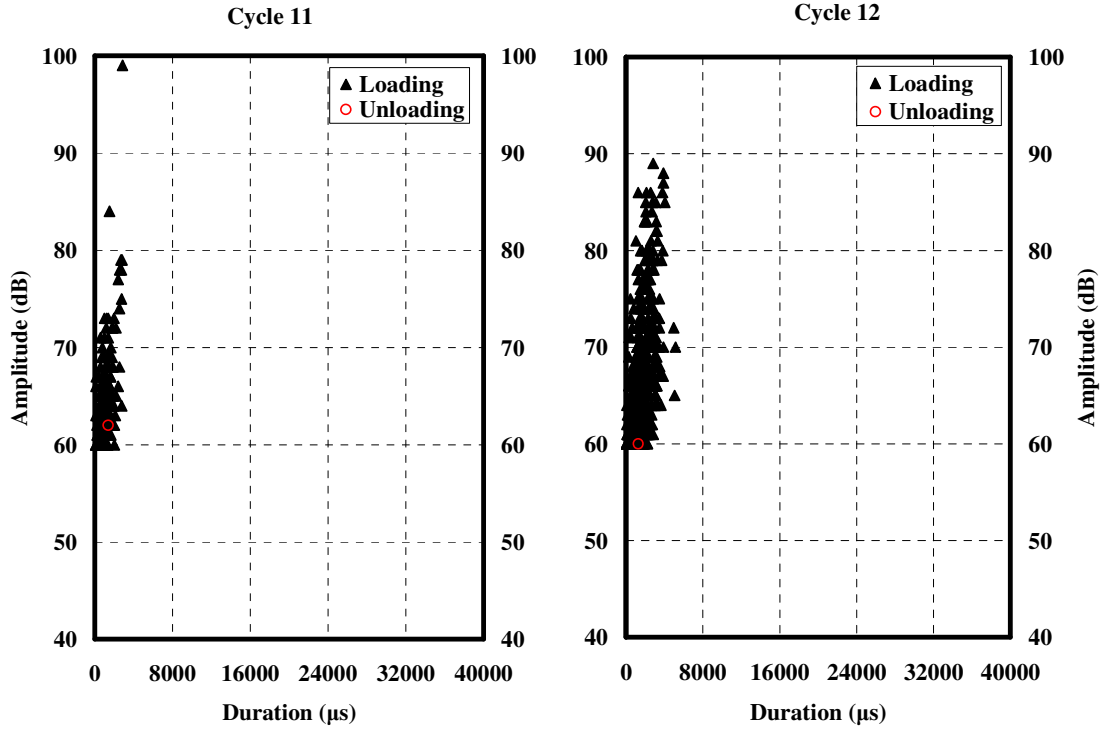


Figure C-78: Crossplot of amplitude and duration of AE signals from loadset 11-12 for beam SCC-HS-B

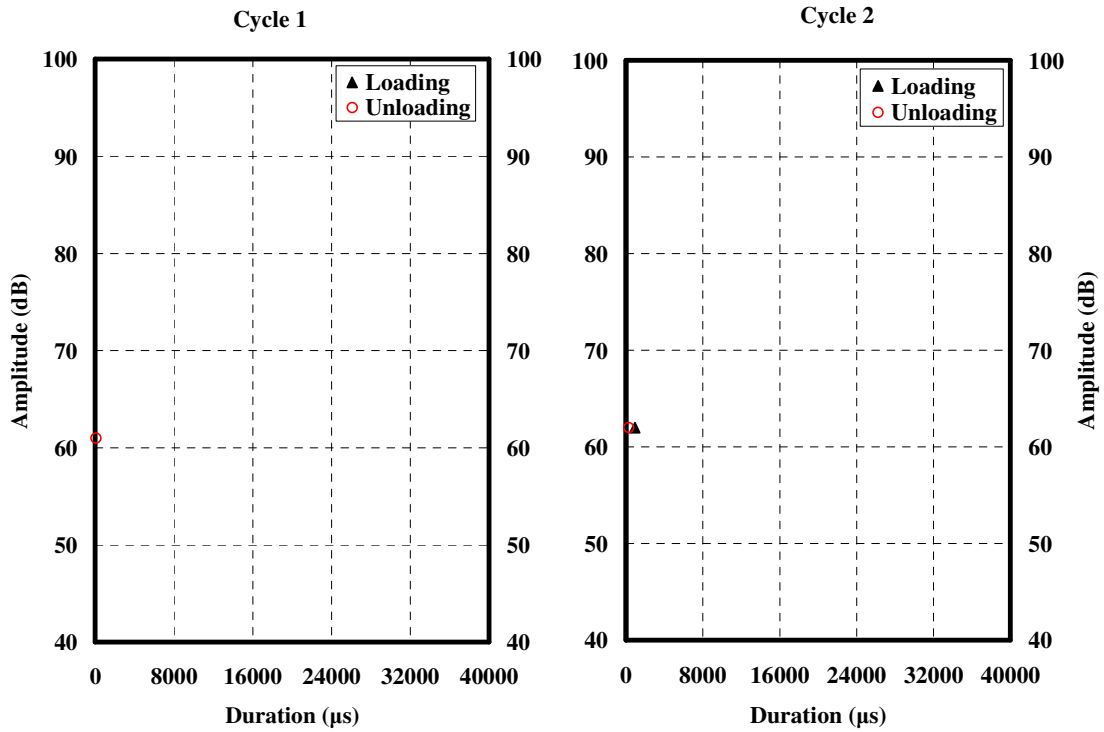


Figure C-79: Crossplot of amplitude and duration of AE signals from loadset 1-2 for beam SCC-HS-C

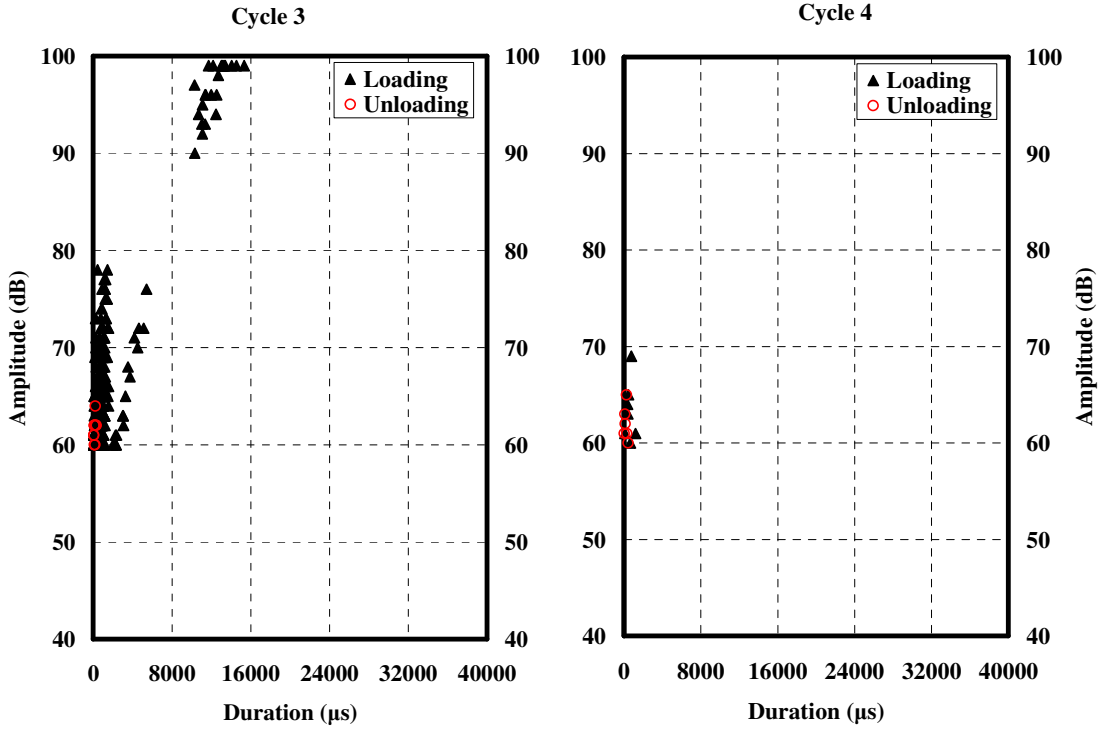


Figure C-80: Crossplot of amplitude and duration of AE signals from loadset 3-4 for beam SCC-HS-C

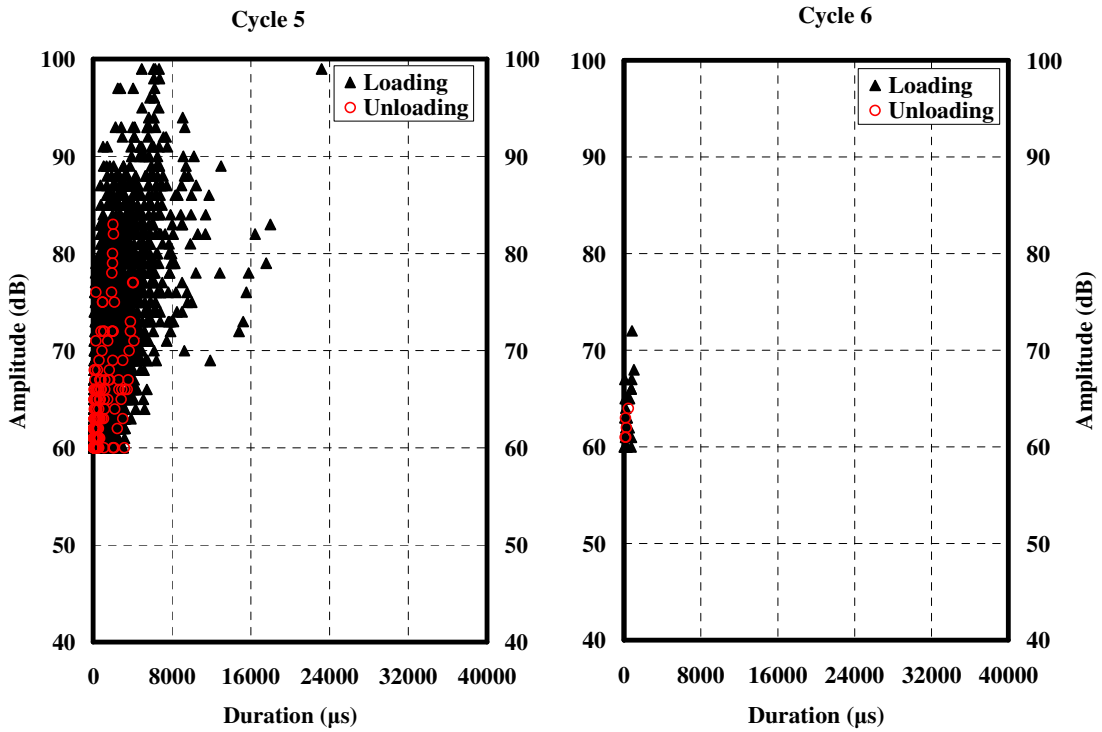


Figure C-81: Crossplot of amplitude and duration of AE signals from loadset 5-6 for beam SCC-HS-C

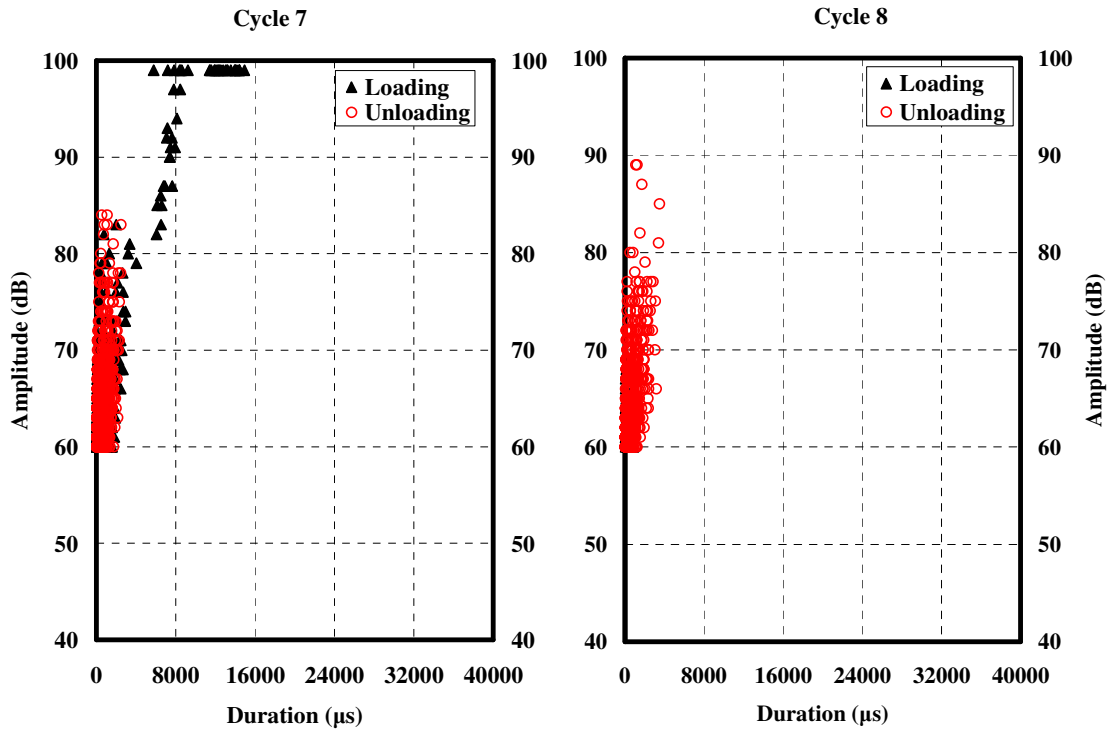


Figure C-82: Crossplot of amplitude and duration of AE signals from loadset 7-8 for beam SCC-HS-C

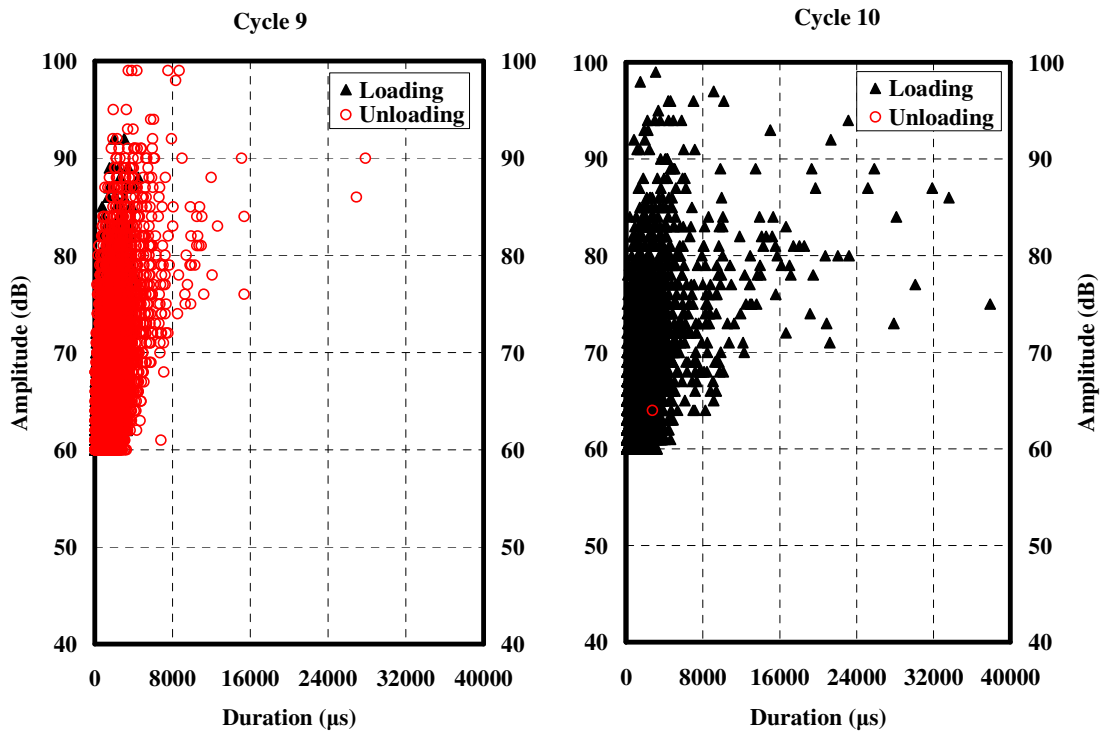


Figure C-83: Crossplot of amplitude and duration of AE signals from loadset 9-10 for beam SCC-HS-C

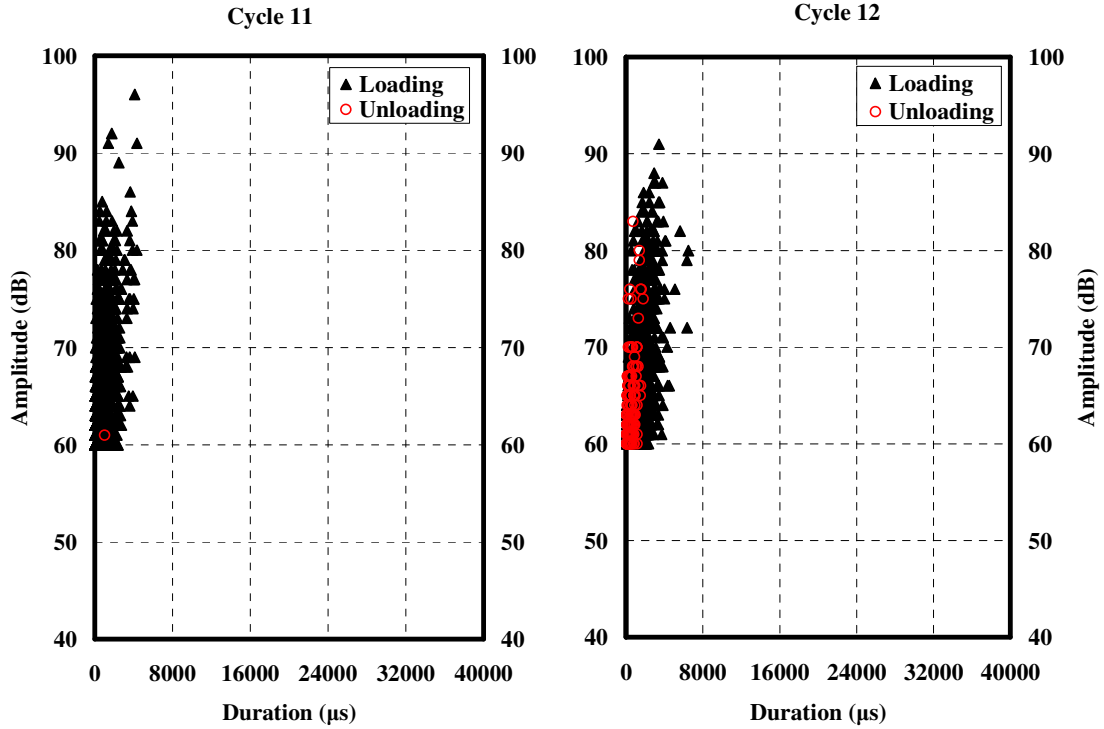


Figure C-84: Crossplot of amplitude and duration of AE signals from loadset 11-12 for beam SCC-HS-C

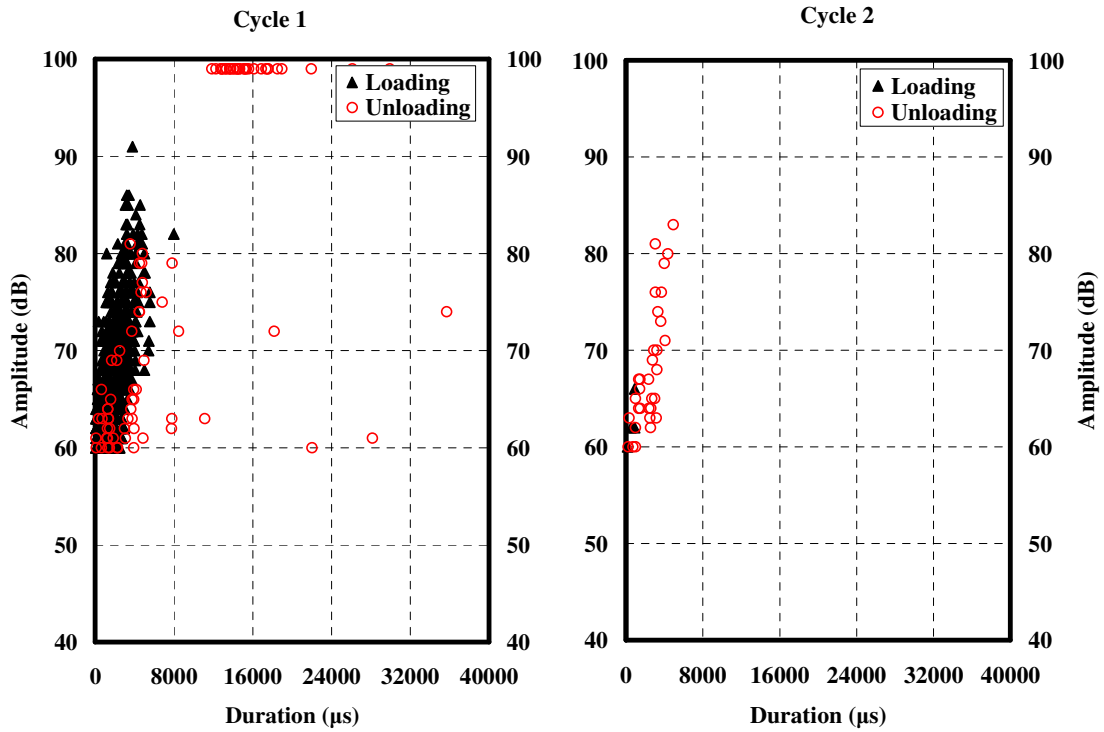


Figure C-85: Crossplot of amplitude and duration of AE signals from loadset 1-2 for beam SCC-HS-D

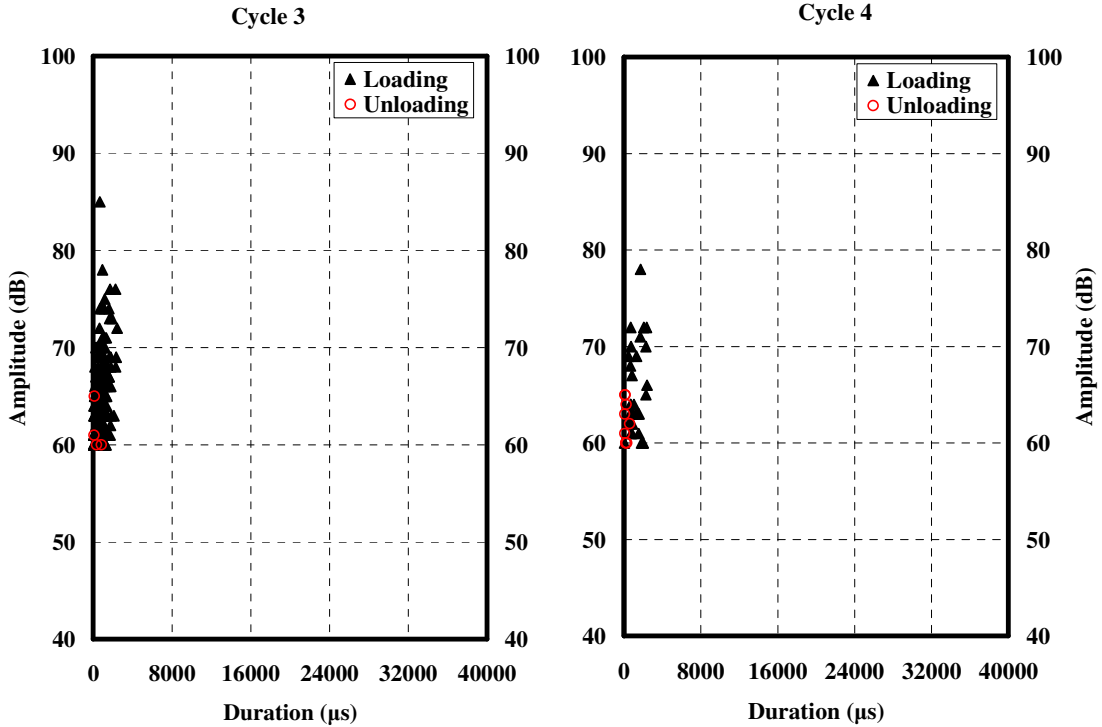


Figure C-86: Crossplot of amplitude and duration of AE signals from loadset 3-4 for beam SCC-HS-D

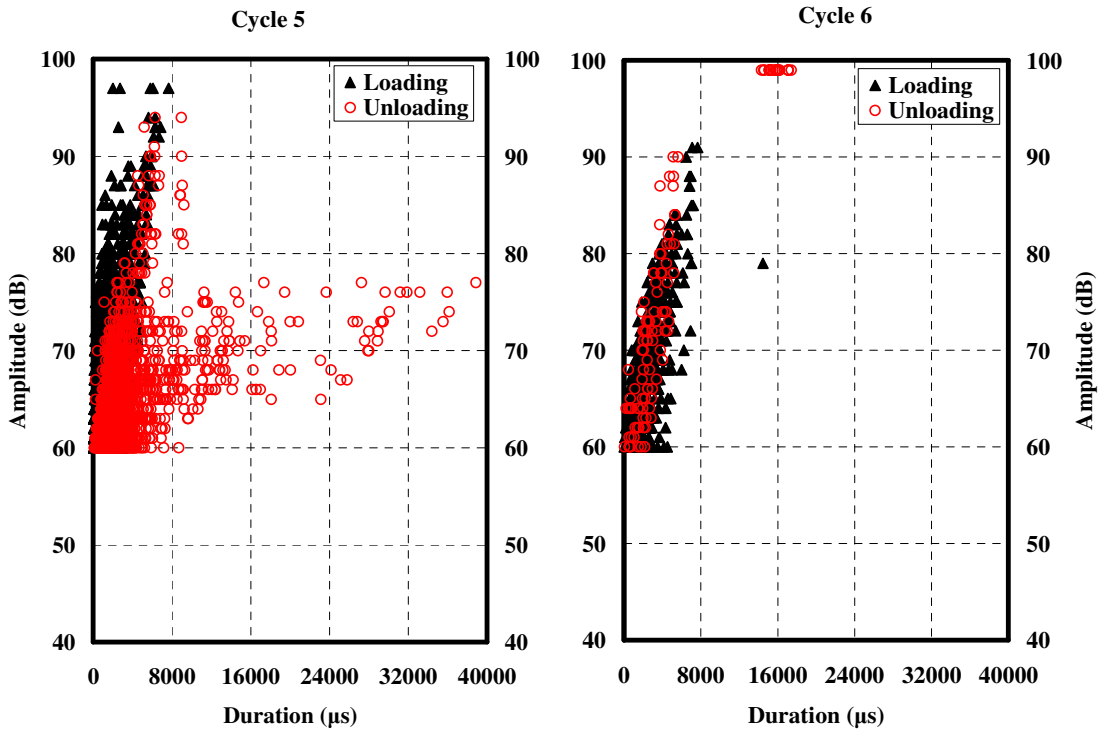


Figure C-87: Crossplot of amplitude and duration of AE signals from loadset 5-6 for beam SCC-HS-D

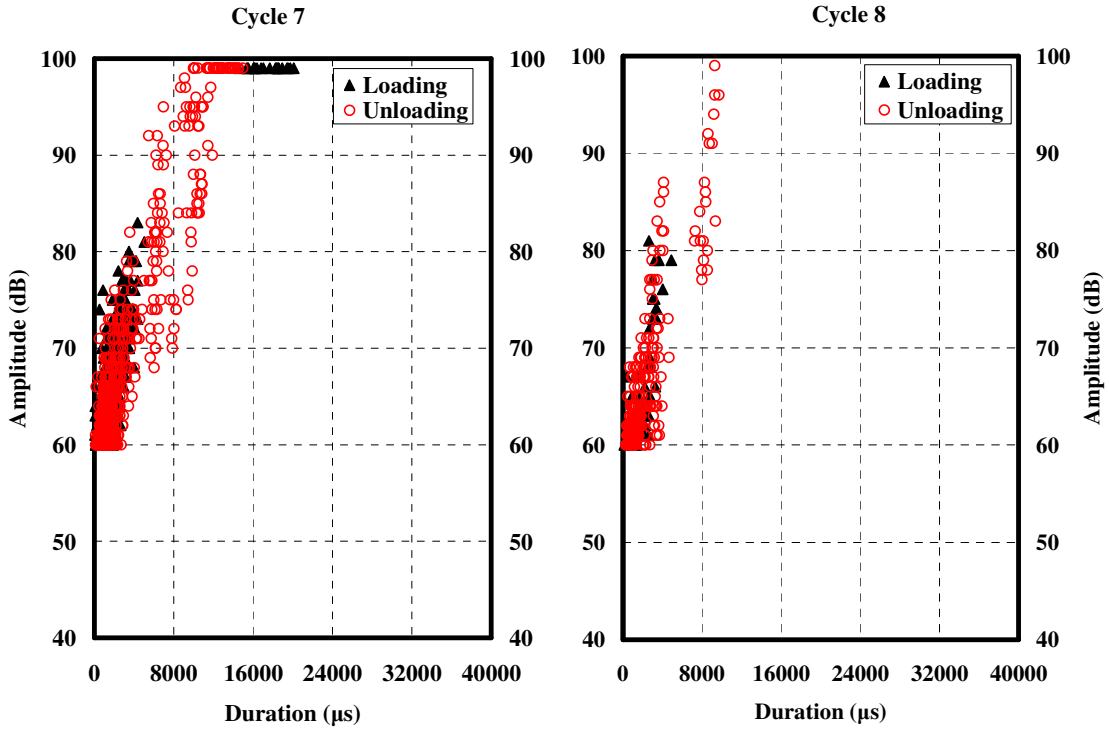


Figure C-88: Crossplot of amplitude and duration of AE signals from loadset 7-8 for beam SCC-HS-D

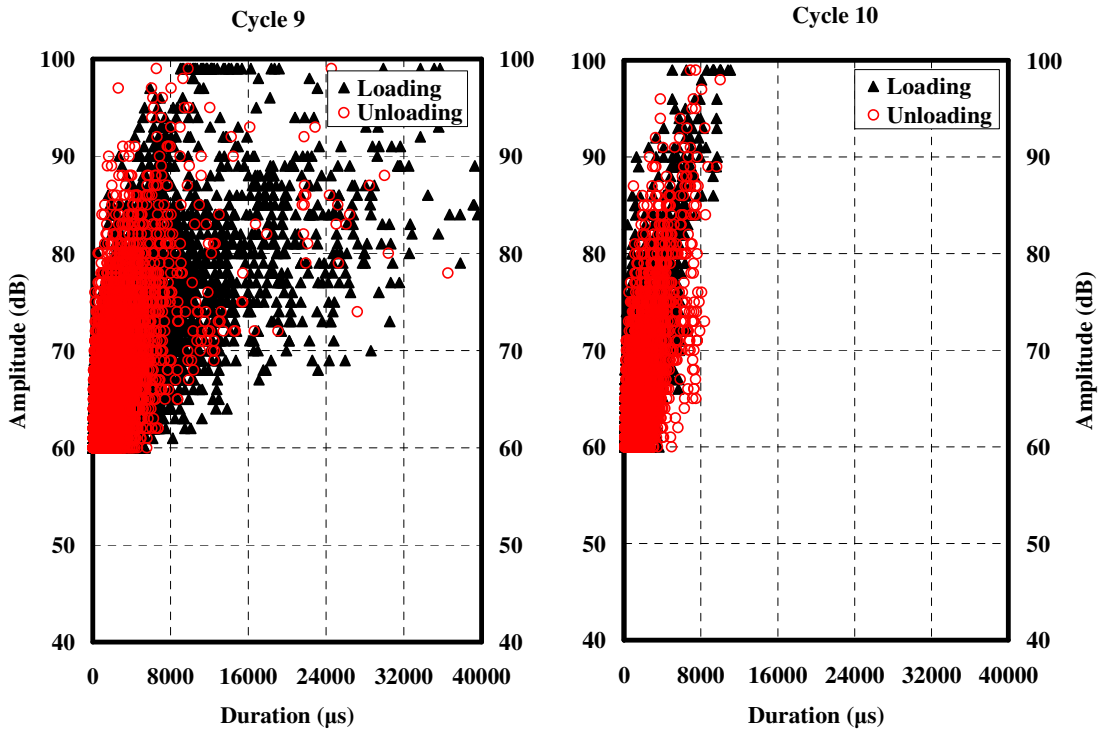


Figure C-89: Crossplot of amplitude and duration of AE signals from loadset 9-10 for beam SCC-HS-D

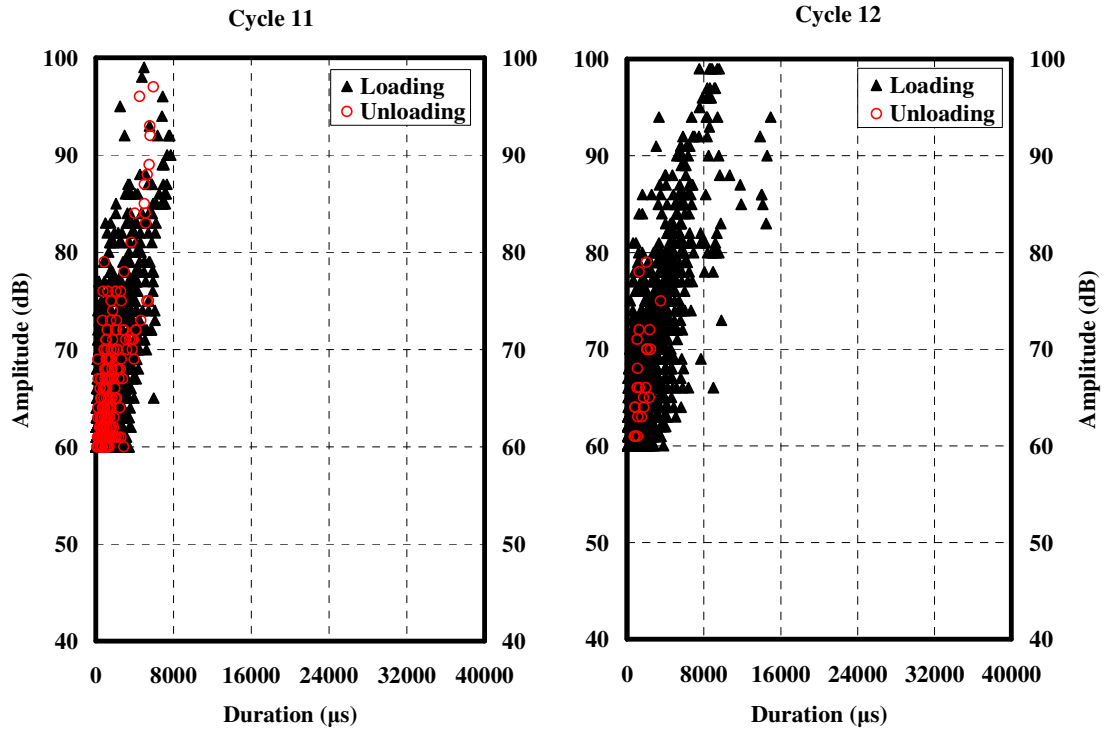


Figure C-90: Crossplot of amplitude and duration of AE signals from loadset 11-12 for beam SCC-HS-D

APPENDIX D
LOAD AND SIGNAL STRENGTH VERSUS TIME FOR LABORATORY
SPECIMENS

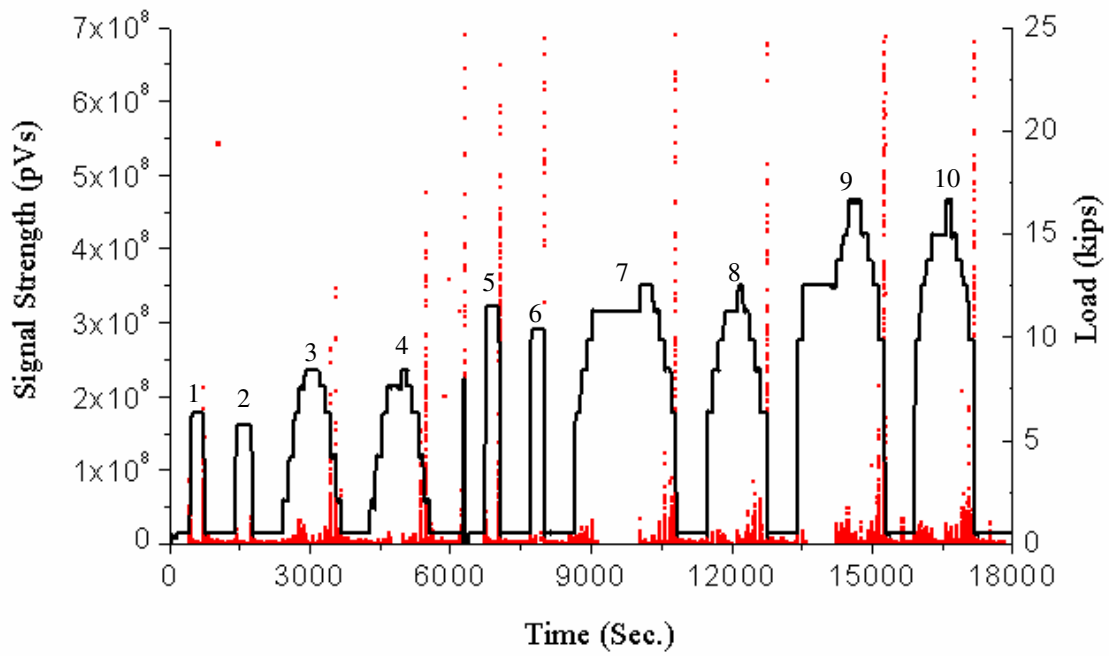


Figure D-1: Load and signal strength versus time for beam STD-M-A

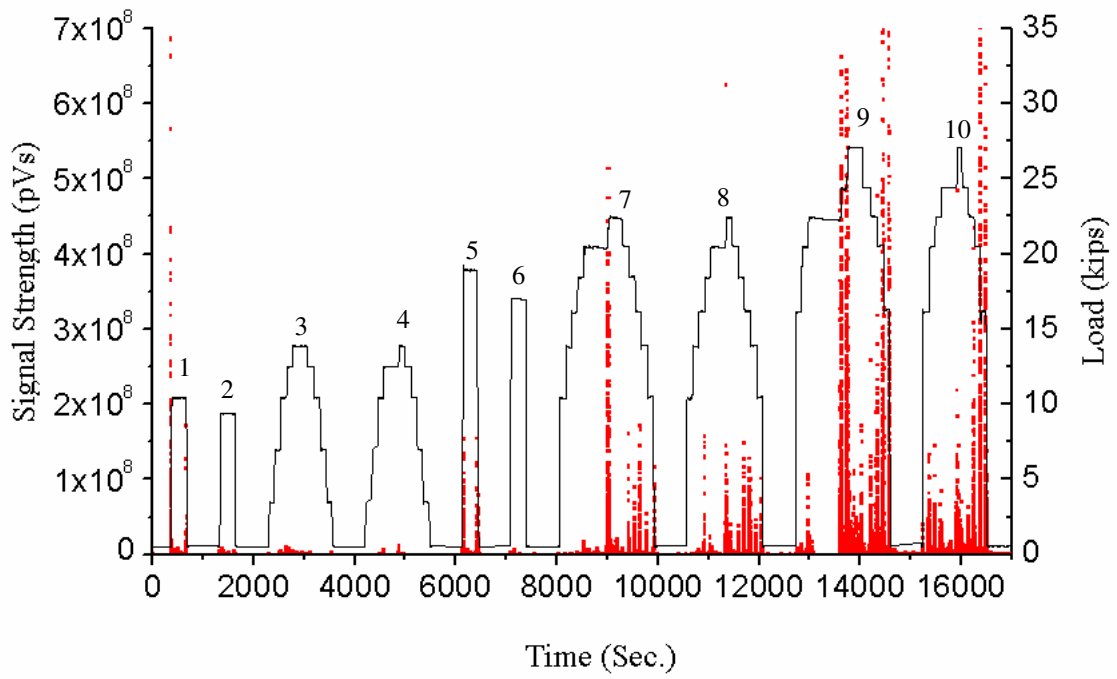


Figure D-2: Load and signal strength versus time for beam STD-M-B

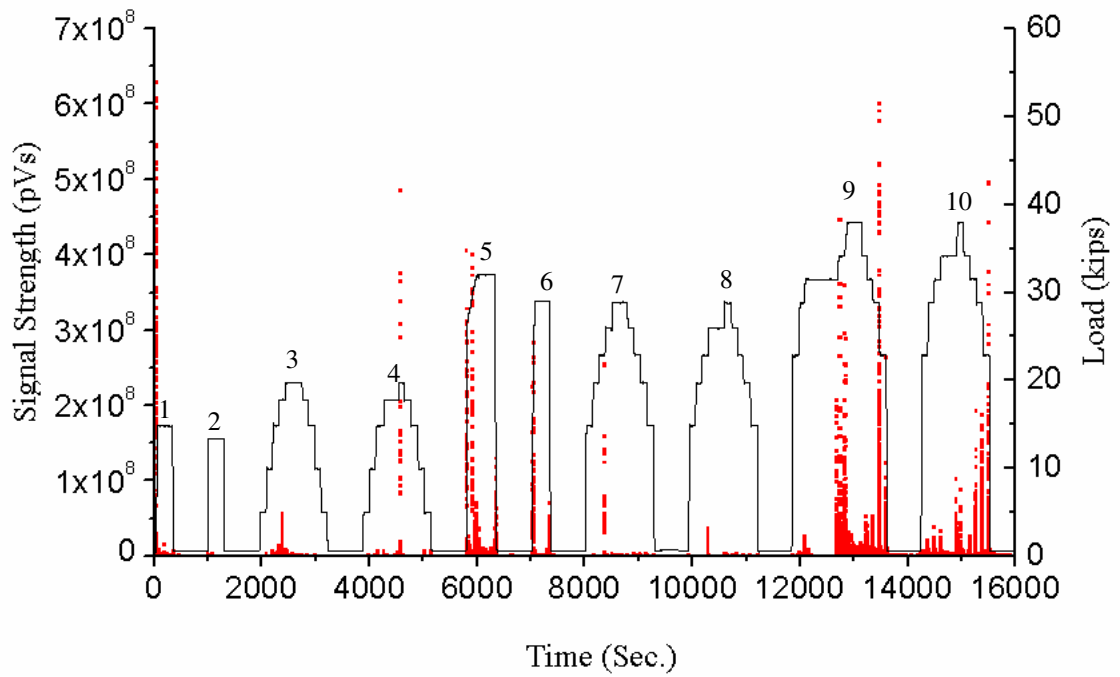


Figure D-3: Load and signal strength versus time for beam STD-M-C

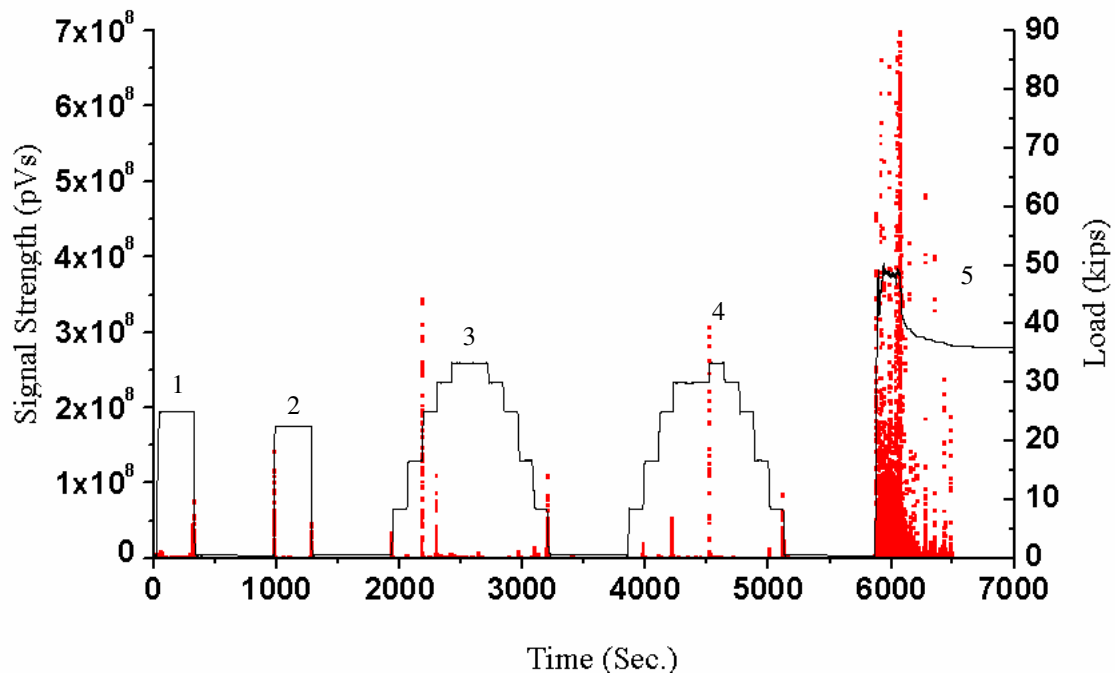


Figure D-4: Load and signal strength versus time for beam STD-M-D

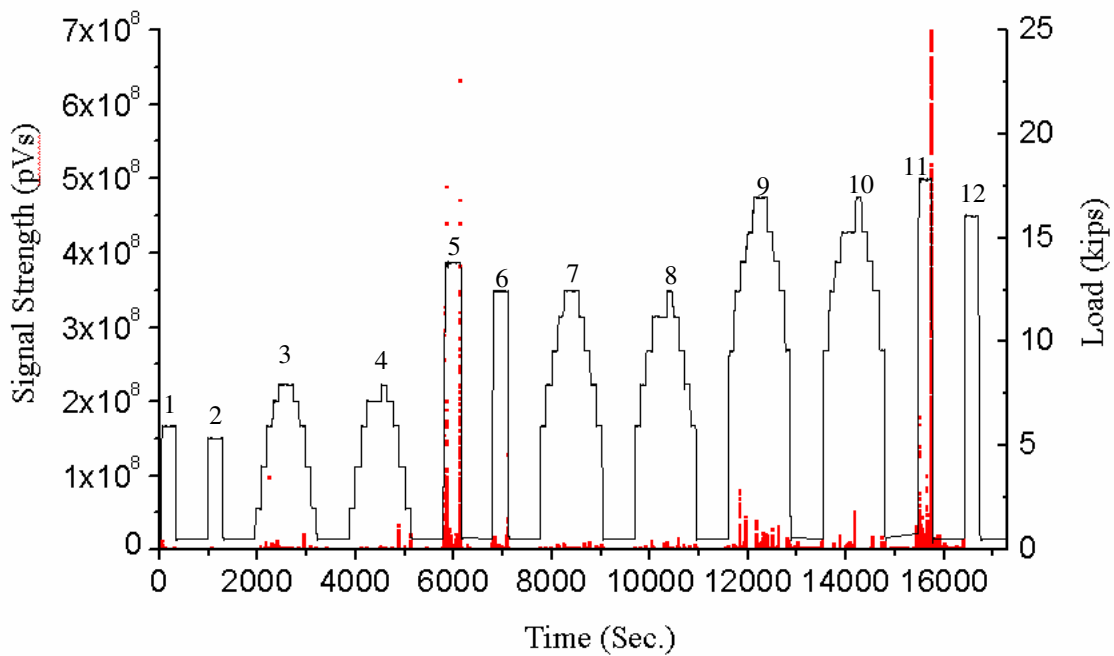


Figure D-5: Load and signal strength versus time for beam SCC-MA-A

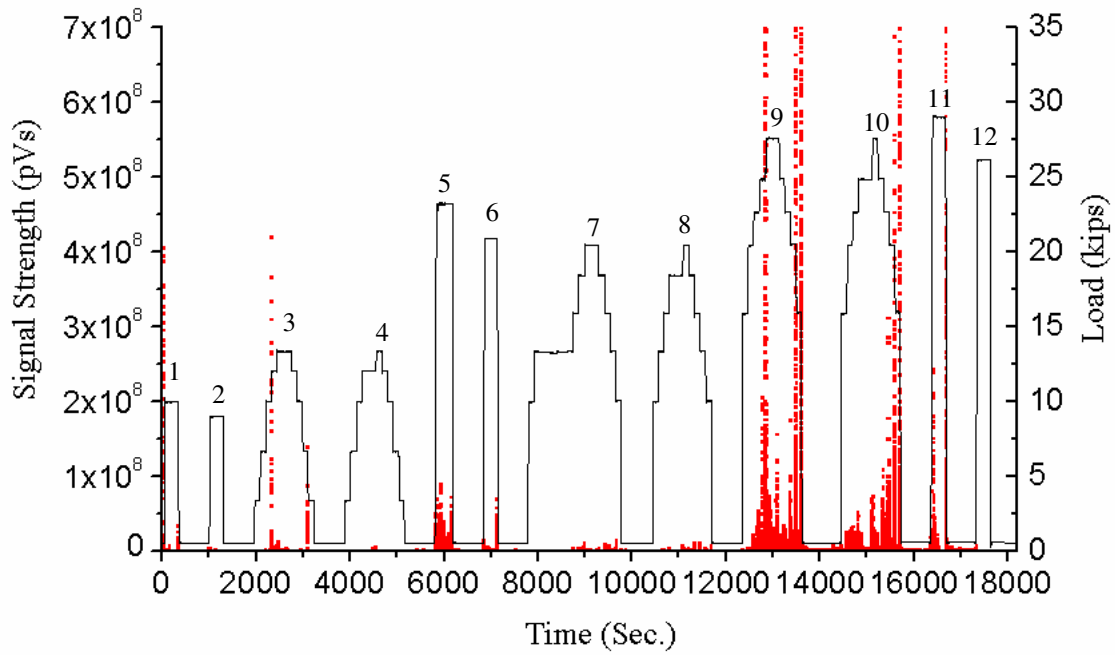


Figure D-6: Load and signal strength versus time for beam SCC-MA-B

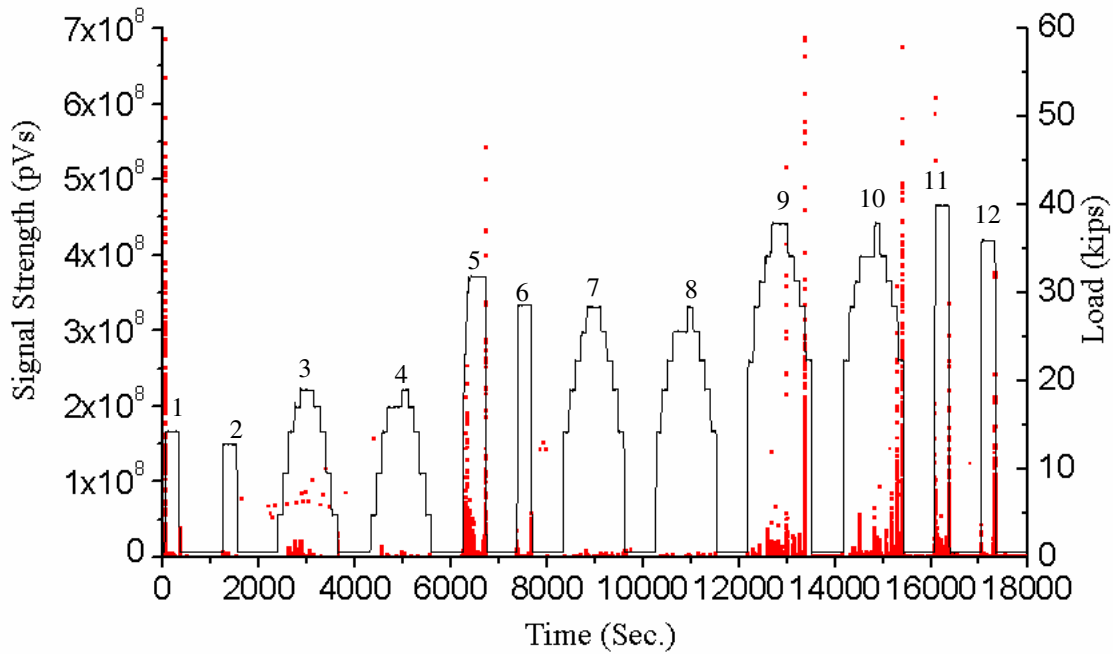


Figure D-7: Load and signal strength versus time for beam SCC-MA-C

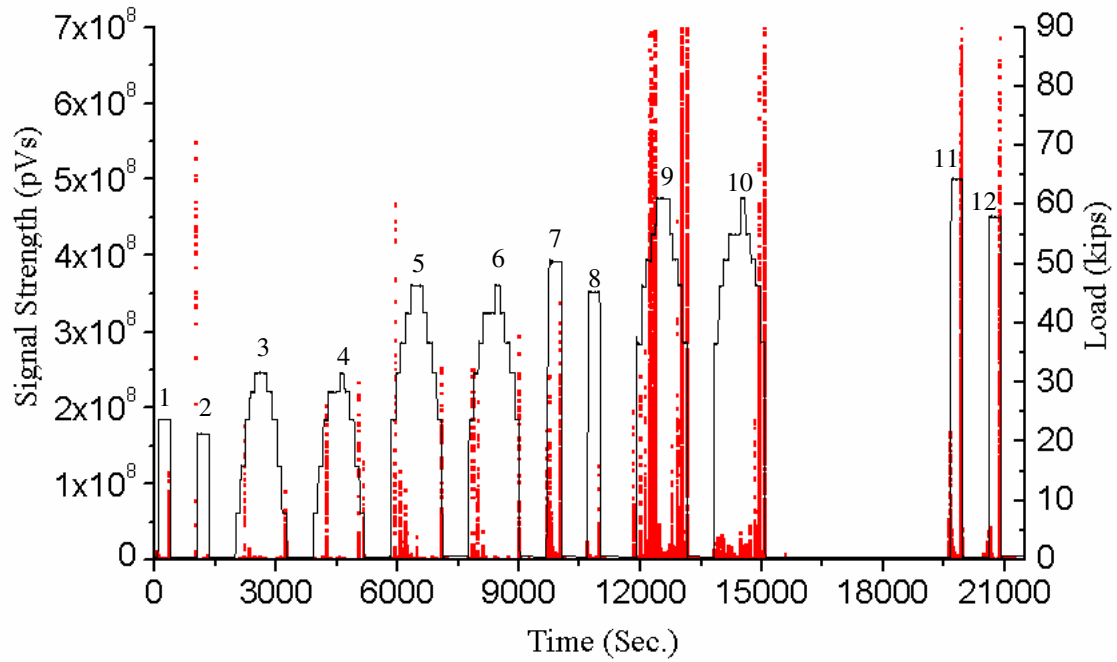


Figure D-8: Load and signal strength versus time for beam SCC-MA-D

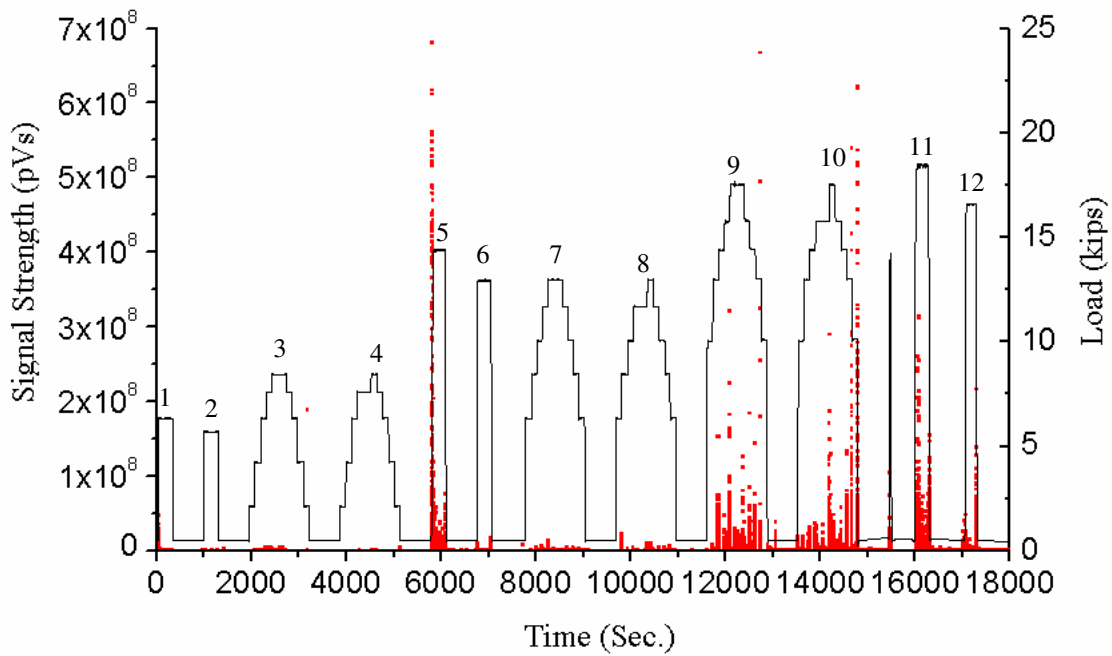


Figure D-9: Load and signal strength versus time for beam SCC-MS-A

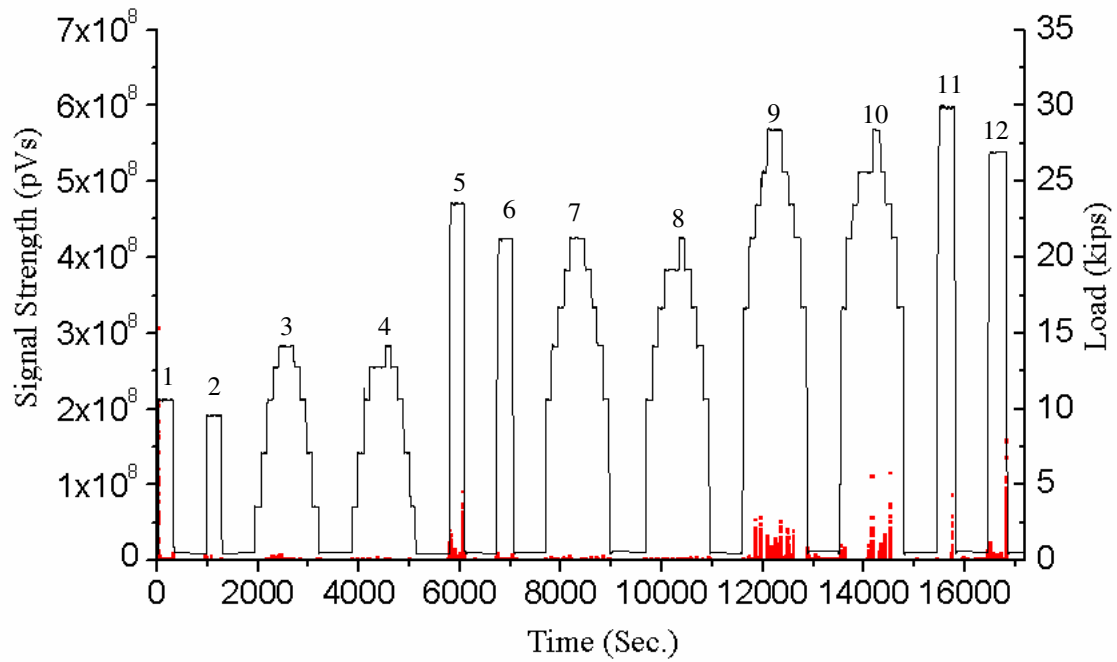


Figure D-10: Load and signal strength versus time for beam SCC-MS-B

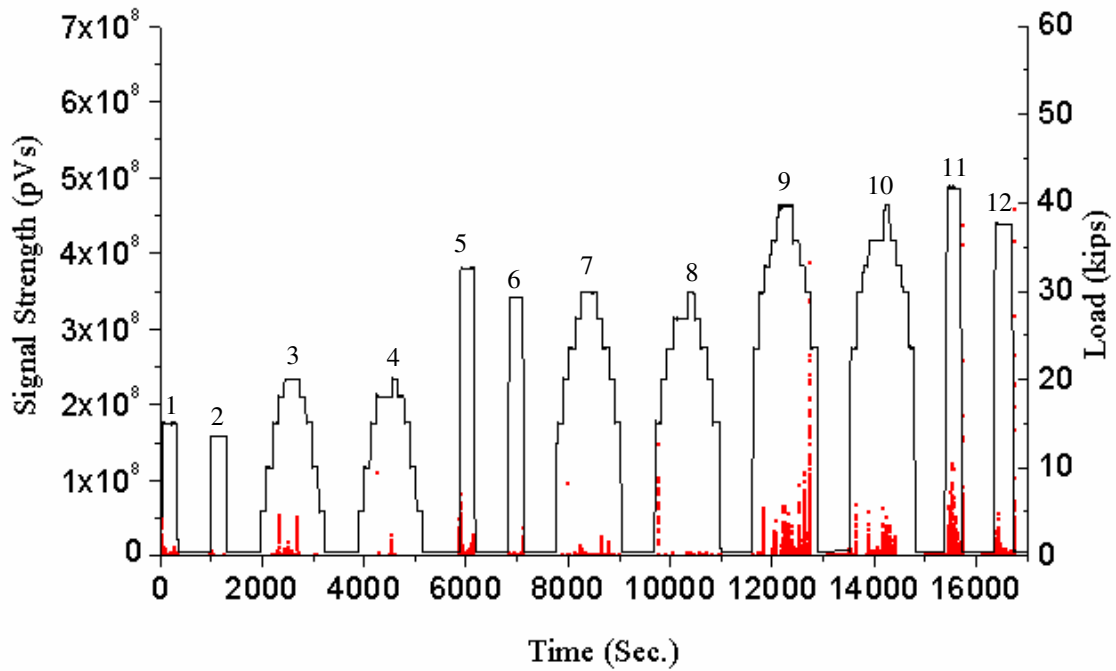


Figure D-11: Load and signal strength versus time for beam SCC-MS-C

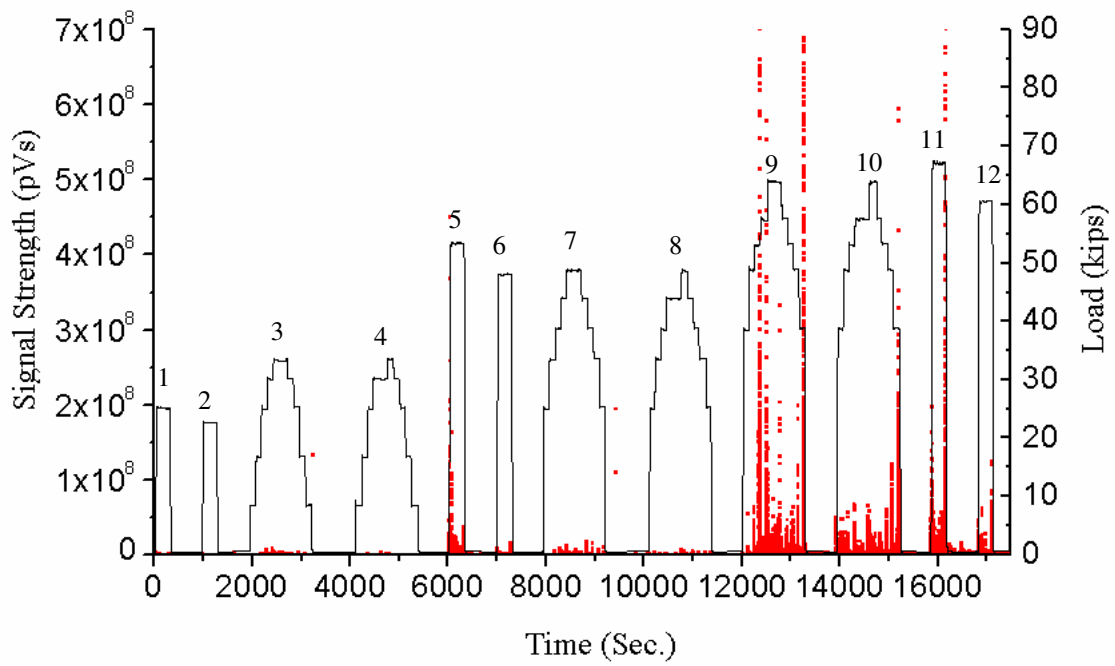


Figure D-12: Load and signal strength versus time for beam SCC-MS-D

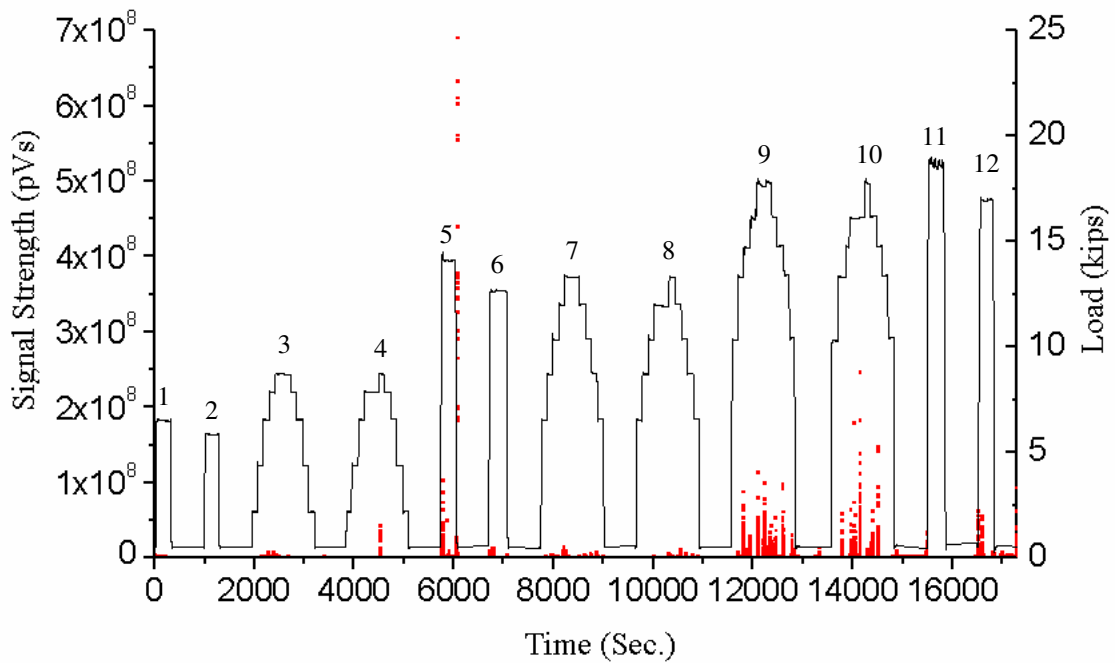


Figure D-13: Load and signal strength versus time for beam SCC-HS-A

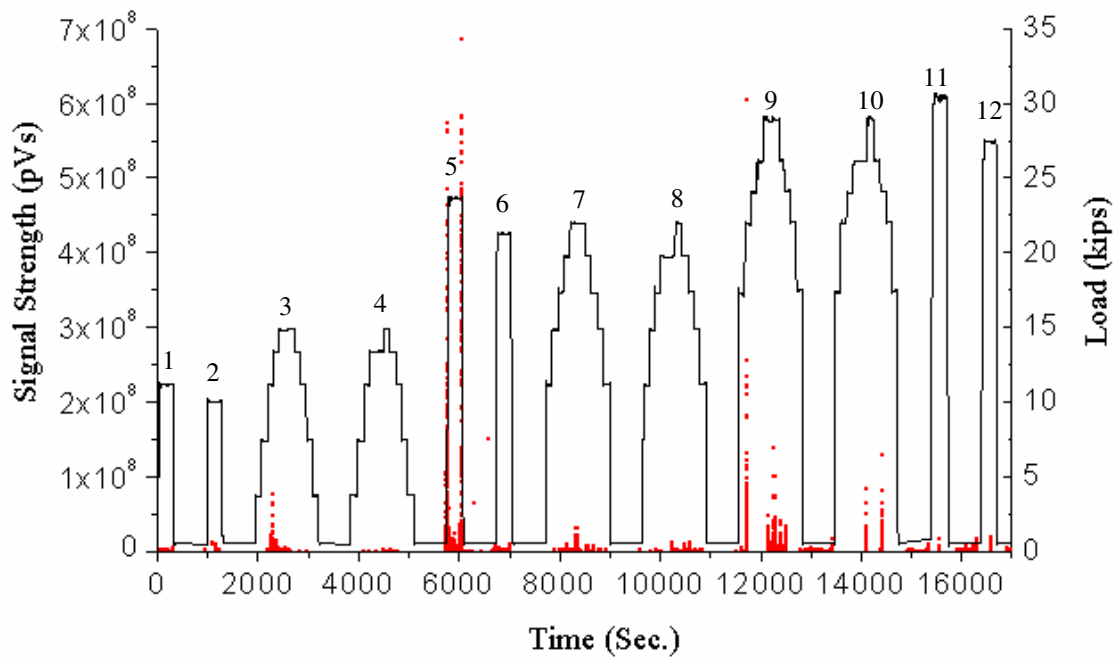


Figure D-14: Load and signal strength versus time for beam SCC-HS-B

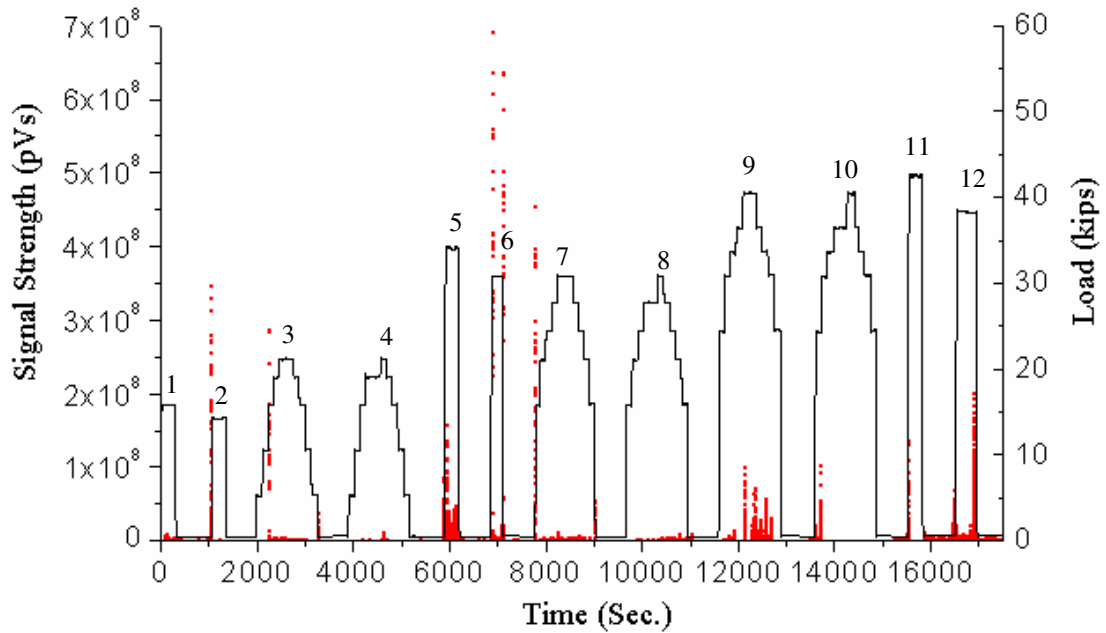


Figure D-15: Load and signal strength versus time for beam SCC-HS-C

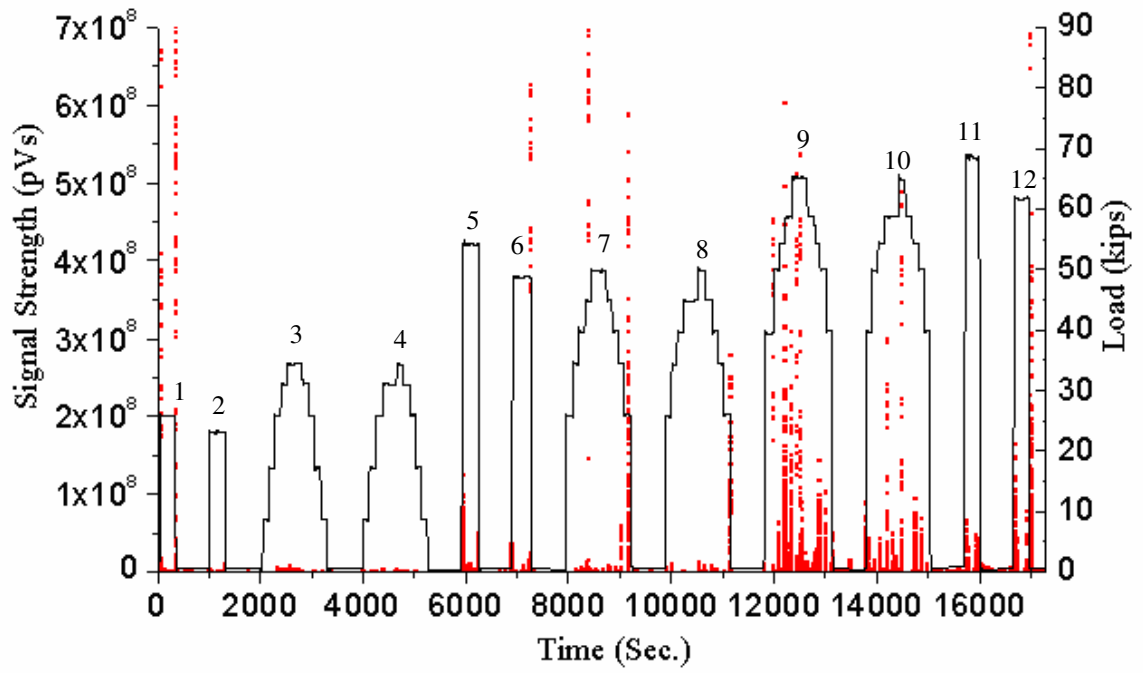


Figure D-16: Load and signal strength versus time for beam SCC-HS-D

APPENDIX E

SUMMARY OF EVALUATION CRITERIA RESULTS FOR ALL SPECIMENS

Table E-1: Summary of Evaluation Criteria Results for Beam STD-M

Beam	Criterion	Loadset Number				
		1-2	3-4	5-6	7-8	9-10
STD-M-A	Calm Ratio	2.36	12.54	19.17	36.59	13.07
	Load Ratio	0.08	0.06	0.04	0.04	0.03
	Relaxation Ratio	1.5	2.5	178.9	3.0	63.0
	CSS Ratio	12.1%	114.8%	25.7%	8.4%	16.7%
	SSM Ratio	6.0%	4.2%	6.8%	4.1%	15.1%
STD-M-B	Calm Ratio	0.02	0.05	0.45	0.27	0.78
	Load Ratio	1.00	0.83	0.77	0.68	0.54
	Relaxation Ratio	0.2	1.2	13.1	0.5	0.5
	CSS Ratio	0.2%	0.0%	0.4%	8.6%	5.1%
	SSM Ratio	0.4%	0.0%	0.8%	2.8%	4.9%
STD-M-C	Calm Ratio	0.00	0.00	0.12	0.07	0.79
	Load Ratio	1.00	0.75	0.52	0.79	0.52
	Relaxation Ratio	0.0	0.0	0.2	0.0	0.6
	CSS Ratio	1.5%	0.0%	1.0%	0.0%	6.2%
	SSM Ratio	0.9%	0.0%	2.7%	0.0%	4.3%
STD-M-D	Calm Ratio	0.44	0.21			
	Load Ratio	1.00	0.41			
	Relaxation Ratio	0.0	0.2			
	CSS Ratio	1.0%	4.7%			
	SSM Ratio	1.3%	2.6%			

Table E-2: Summary of Evaluation Criteria Results for Beam SCC-MA

Beam	Criterion	Loadset Number					
		1-2	3-4	5-6	7-8	9-10	11-12
SCC-MA-A	Calm Ratio	0.00	0.30	0.38	2.33	0.61	17.96
	Load Ratio	1.00	0.90	0.85	0.81	0.49	0.51
	Relaxation Ratio	0.0	0.3	0.4	0.8	0.6	93.6
	CSS Ratio	5.5%	0.4%	3.8%	62.7%	10.3%	0.0%
	SSM Ratio	26.1%	0.2%	1.3%	28.8%	12.9%	0.0%
SCC-MA-B	Calm Ratio	0.04	0.18	0.13	3.03	1.25	7.96
	Load Ratio	1.00	0.89	0.75	0.78	0.37	0.57
	Relaxation Ratio	0.0	0.5	0.8	1.0	0.3	63.46
	CSS Ratio	0.0%	0.0%	125.4%	103.5%	51.6%	0.0%
	SSM Ratio	0.0%	0.0%	140.1%	95.2%	36.8%	0.0%
SCC-MA-C	Calm Ratio	0.01	0.15	0.38	2.25	1.55	0.85
	Load Ratio	0.89	0.61	0.50	0.69	0.50	0.61
	Relaxation Ratio	0.0	7.8	8.9	0.9	6.6	0.60
	CSS Ratio	0.2%	0.2%	0.2%	19.2%	5.8%	6.8%
	SSM Ratio	0.9%	0.3%	0.7%	0.3%	1.3%	16.9%
SCC-MA-D	Calm Ratio	0.41	0.47	0.51	0.87	0.68	0.57
	Load Ratio	0.49	0.64	0.63	0.81	0.60	0.01
	Relaxation Ratio	1.40	1.3	3.0	2.2	1.9	1.03
	CSS Ratio	0.9%	0.2%	3.1%	5.5%	7.3%	3.8%
	SSM Ratio	0.1%	0.0%	8.3%	9.9%	3.6%	4.0%

Table E-3: Summary of Evaluation Criteria Results for Beam SCC-MS

Beam	Criterion	Loadset Number					
		1-2	3-4	5-6	7-8	9-10	11-12
SCC-MS-A	Calm Ratio	0.00	0.82	0.04	1.09	1.27	0.09
	Load Ratio	1.00	1.00	0.56	0.54	0.46	0.03
	Relaxation Ratio	0.0	130.3	0.2	0.5	1.1	4.5
	CSS Ratio	6.3%	0.1%	0.7%	1.7%	31.6%	1.0%
	SSM Ratio	5.8%	0.1%	0.7%	0.9%	9.5%	1.1%
SCC-MS-B	Calm Ratio	0.00	0.01	0.00	0.03	0.01	0.05
	Load Ratio	1.00	0.89	0.02	0.41	0.37	0.90
	Relaxation Ratio	0.0	0.5	0.0	0.6	0.1	12.3
	CSS Ratio	0.9%	13.0%	0.1%	437.9%	5.5%	17.3%
	SSM Ratio	1.1%	30.9%	0.2%	117.5%	8.0%	22.4%
SCC-MS-C	Calm Ratio	0.00	0.00	0.10	2.34	2.17	0.01
	Load Ratio	0.90	0.90	0.71	0.72	0.33	0.22
	Relaxation Ratio	0.0	0.0	0.7	0.5	1.7	13.4
	CSS Ratio	7.7%	37.1%	0.6%	0.0%	2.9%	30.3%
	SSM Ratio	2.6%	17.4%	1.3%	0.0%	2.8%	17.9%
SCC-MS-D	Calm Ratio	0.00	0.28	0.11	0.89	0.10	0.07
	Load Ratio	1.00	0.99	0.55	0.72	0.60	0.01
	Relaxation Ratio	0.0	0.3	0.4	0.8	2.1	7.6
	CSS Ratio	0.0%	0.5%	0.4%	37.9%	38.0%	3.5%
	SSM Ratio	0.0%	0.5%	0.6%	60.4%	60.9%	6.3%

Table E-4: Summary of Evaluation Criteria Results for Beam SCC-HS

Beam	Criterion	Loadset Number					
		1-2	3-4	5-6	7-8	9-10	11-12
SCC-HS-A	Calm Ratio	0.00	0.00	0.29	1.72	0.52	0.01
	Load Ratio	0.89	1.00	0.76	0.60	0.74	0.03
	Relaxation Ratio	0.0	0.2	0.4	0.4	1.8	0.0
	CSS Ratio	6.9%	0.7%	2.8%	0.3%	217.3%	N/A
	SSM Ratio	10.8%	0.1%	3.4%	1.1%	268.1%	N/A
SCC- HS -B	Calm Ratio	1.27	0.00	0.75	1.16	0.16	0.01
	Load Ratio	1.00	0.90	0.02	0.73	0.90	0.89
	Relaxation Ratio	3.7	0.0	1.1	1.0	0.0	0.7
	CSS Ratio	0.0%	0.1%	11.1%	65.9%	64.6%	488.5%
	SSM Ratio	0.0%	0.1%	37.9%	128.6%	87.4%	614.1%
SCC- HS -C	Calm Ratio	0.00	0.00	0.00	0.07	1.74	0.03
	Load Ratio	0.90	0.99	0.89	0.81	0.60	0.01
	Relaxation Ratio	0.0	0.0	0.3	0.0	2.7	0.1
	CSS Ratio	0.4%	0.1%	46.2%	7.0%	0.0%	7.7%
	SSM Ratio	0.7%	0.1%	18.1%	3.3%	0.0%	142.1%
SCC- HS -D	Calm Ratio	1.44	0.00	0.40	1.31	0.18	0.13
	Load Ratio	0.89	0.90	0.10	0.47	0.61	0.01
	Relaxation Ratio	3.1	0.2	1.2	0.8	0.1	12.5
	CSS Ratio	0.1%	8.1%	0.7%	379.8%	32.4%	184.4%
	SSM Ratio	0.2%	1.7%	17.1%	74.6%	19.4%	151.1%

APPENDIX F

NDIS ASSESSMENTS FOR ALL SPECIMENS

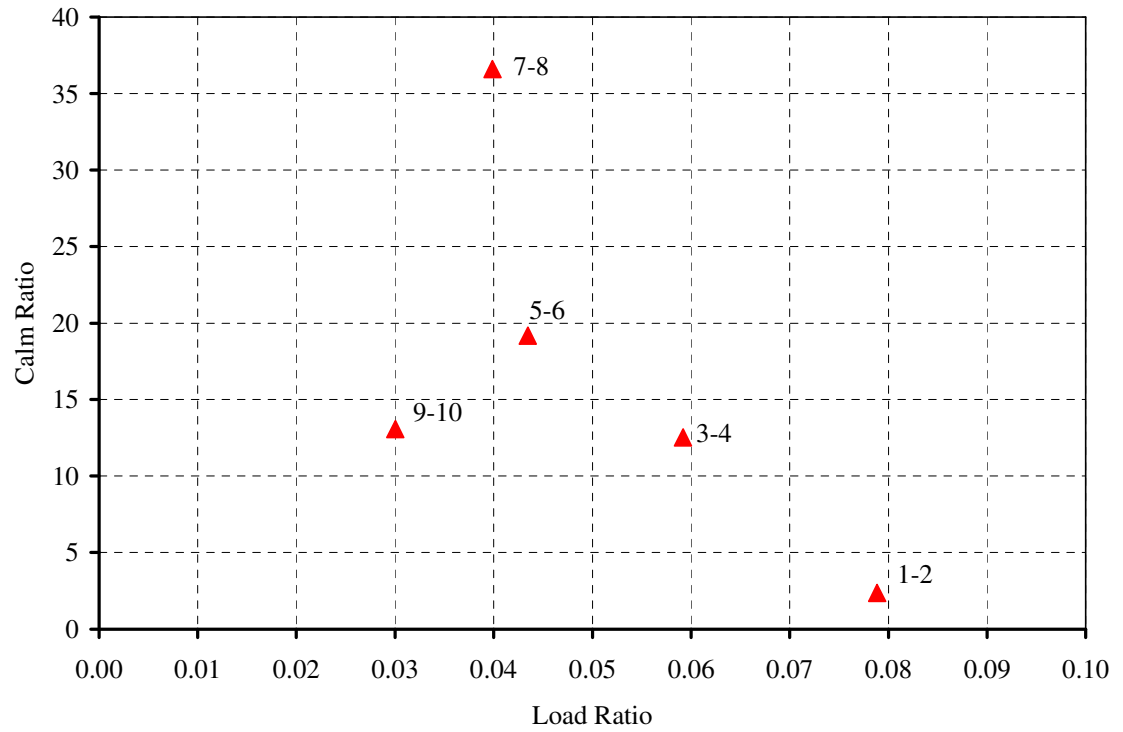


Figure F-1: NDIS assessment for beam STD-M-A

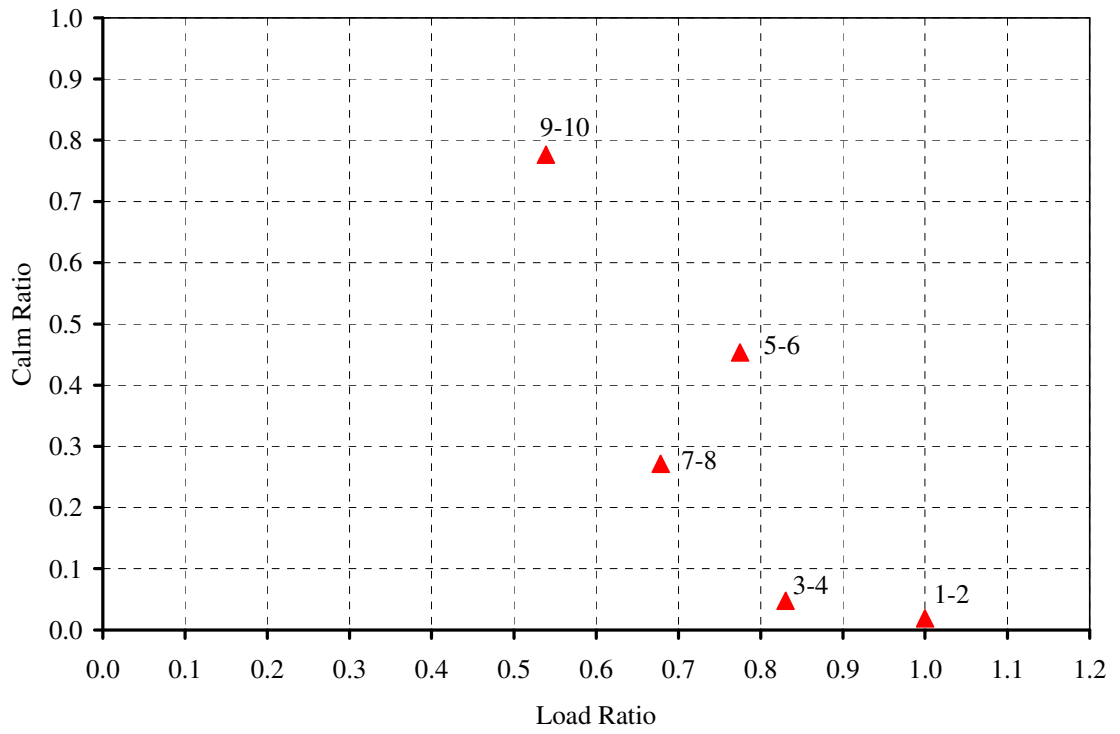


Figure F-2: NDIS assessment for beam STD-M-B

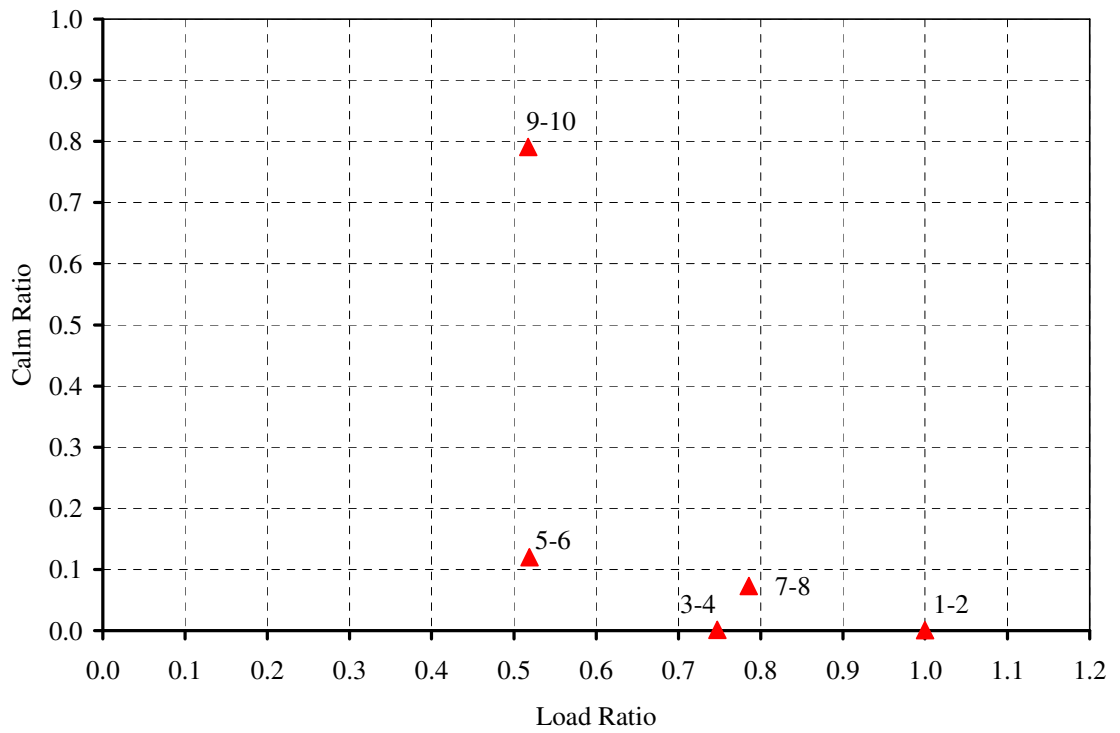


Figure F-3: NDIS assessment for beam STD-M-C

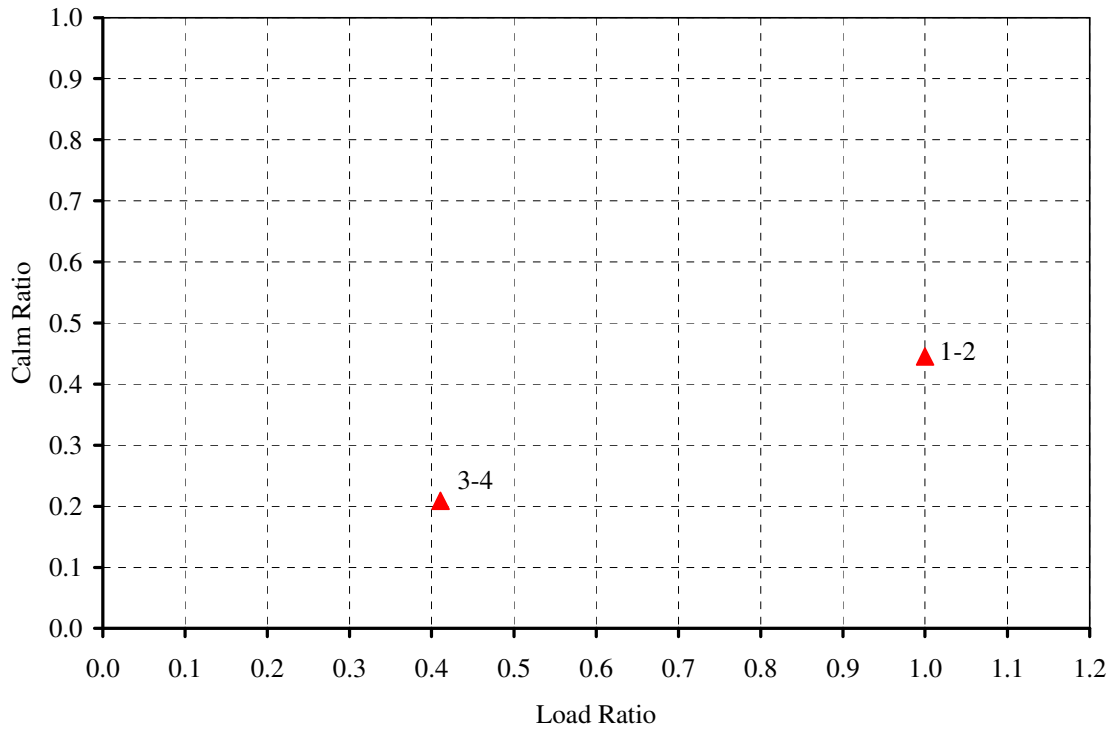


Figure F-4: NDIS assessment for beam STD-M-D

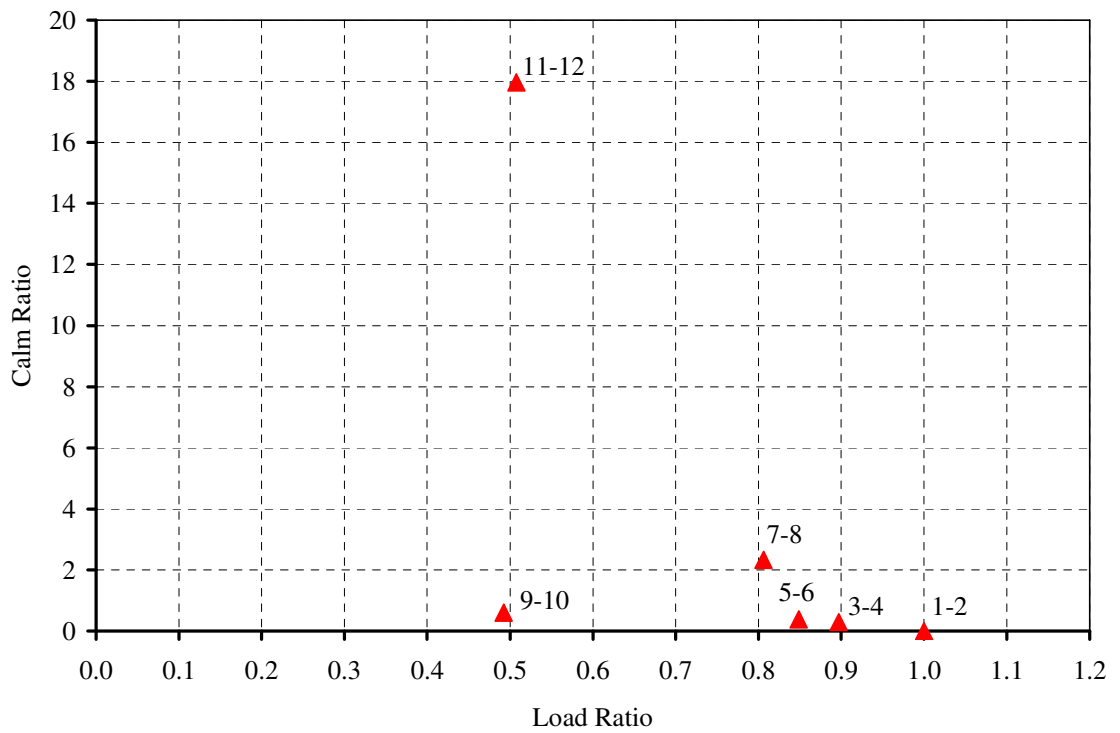


Figure F-5: NDIS assessment for beams SCC-MA-A

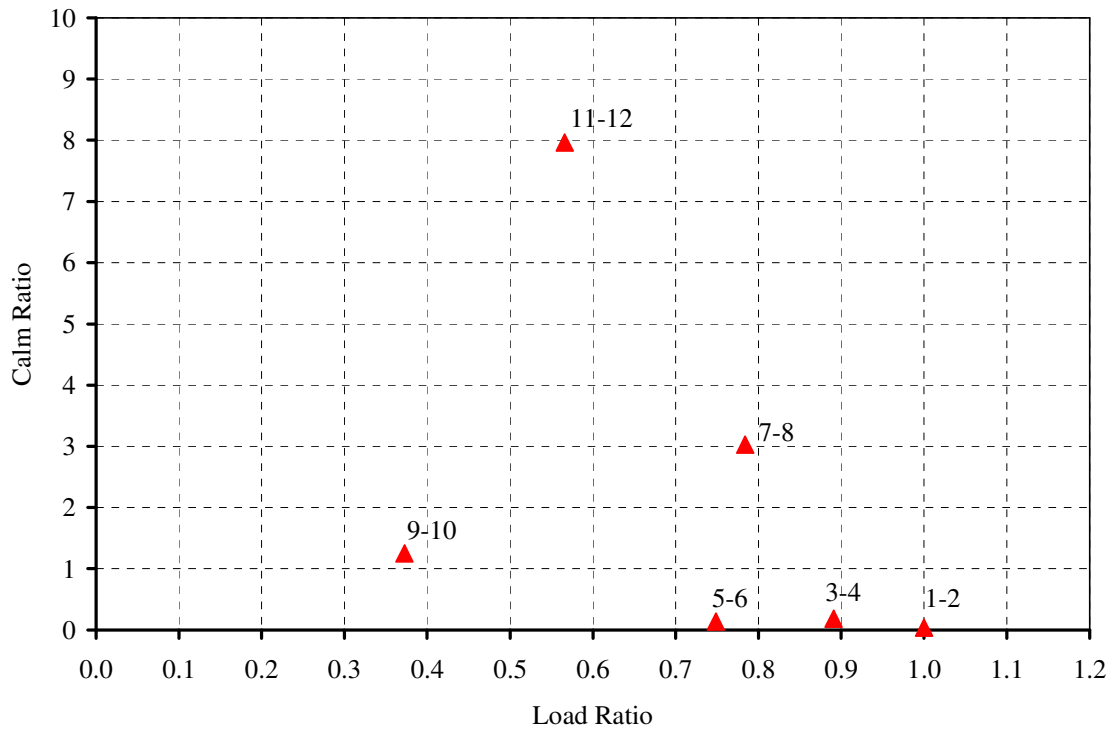


Figure F-6: NDIS assessment for beams SCC-MA-B

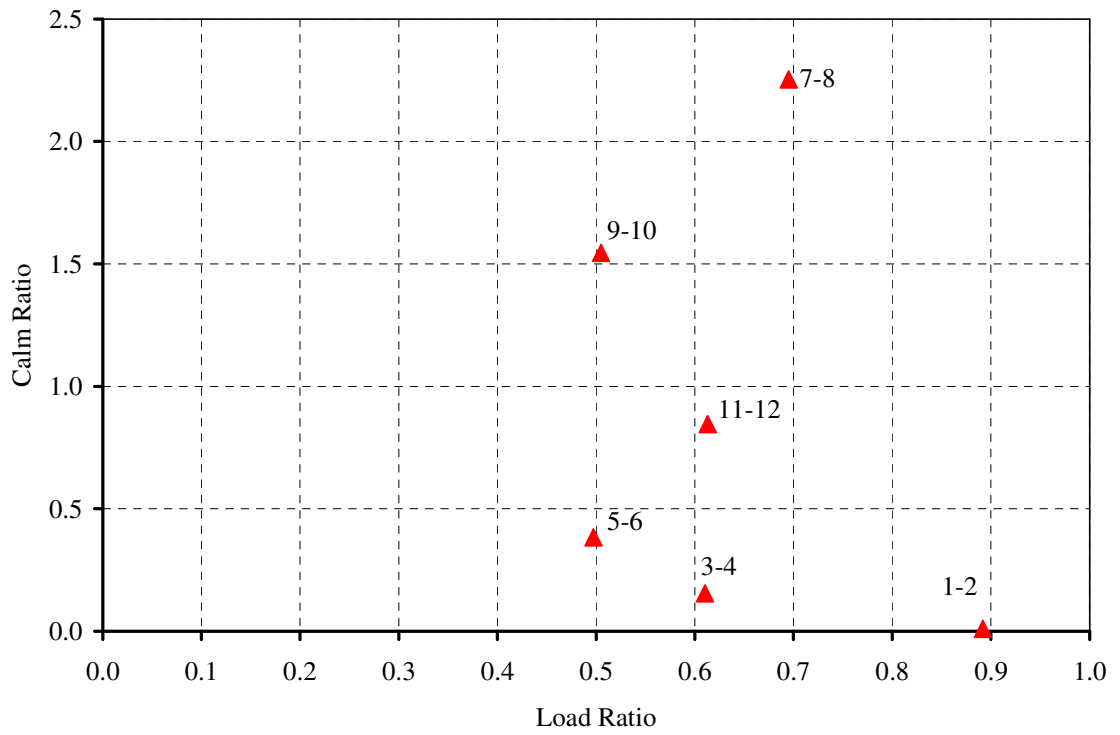


Figure F-7: NDIS assessment for beams SCC-MA-C

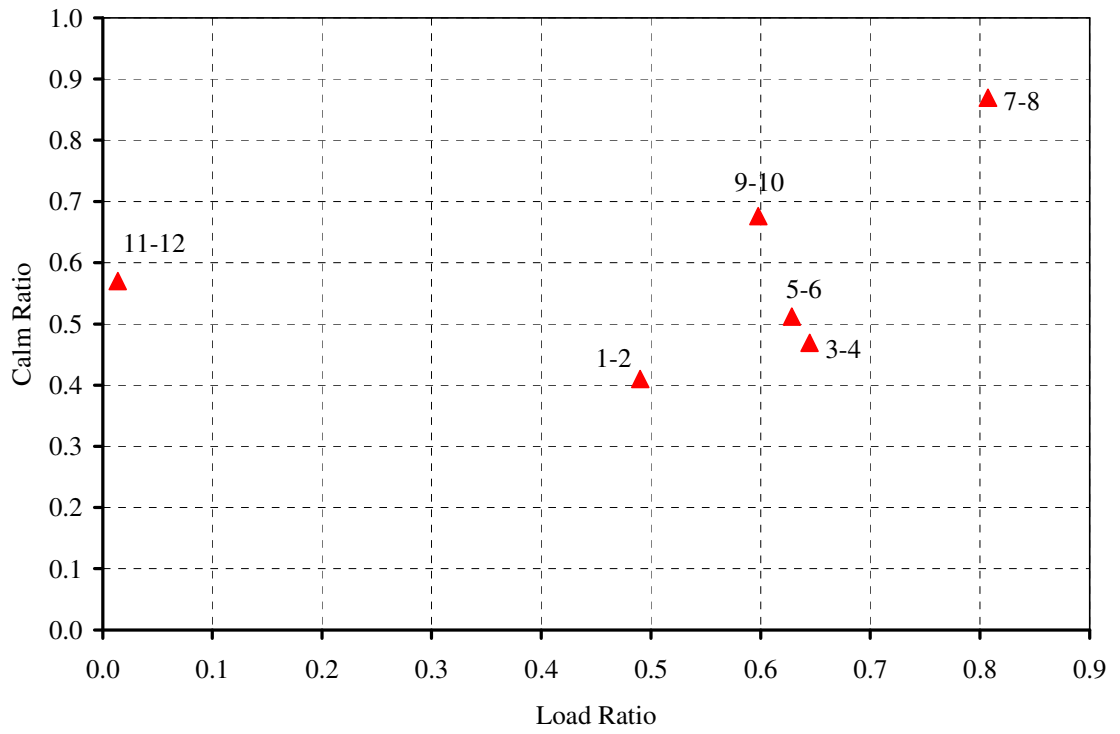


Figure F-8: NDIS assessment for beams SCC-MA-D

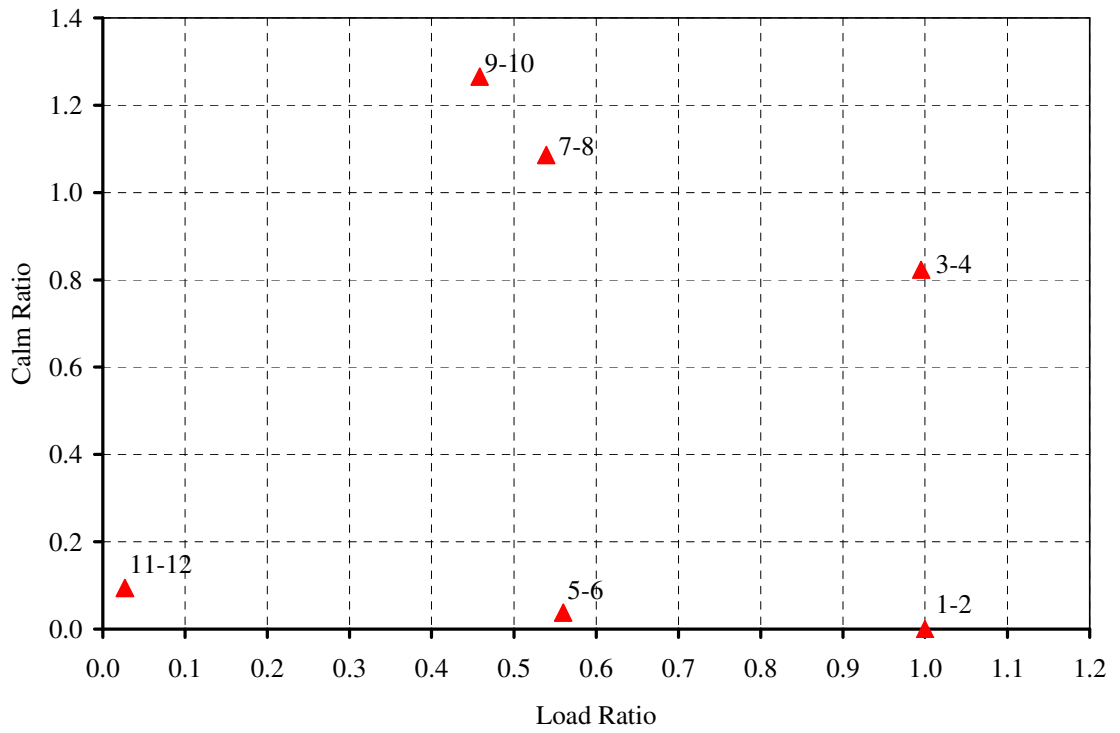


Figure F-9: NDIS assessment for beams SCC-MS-A

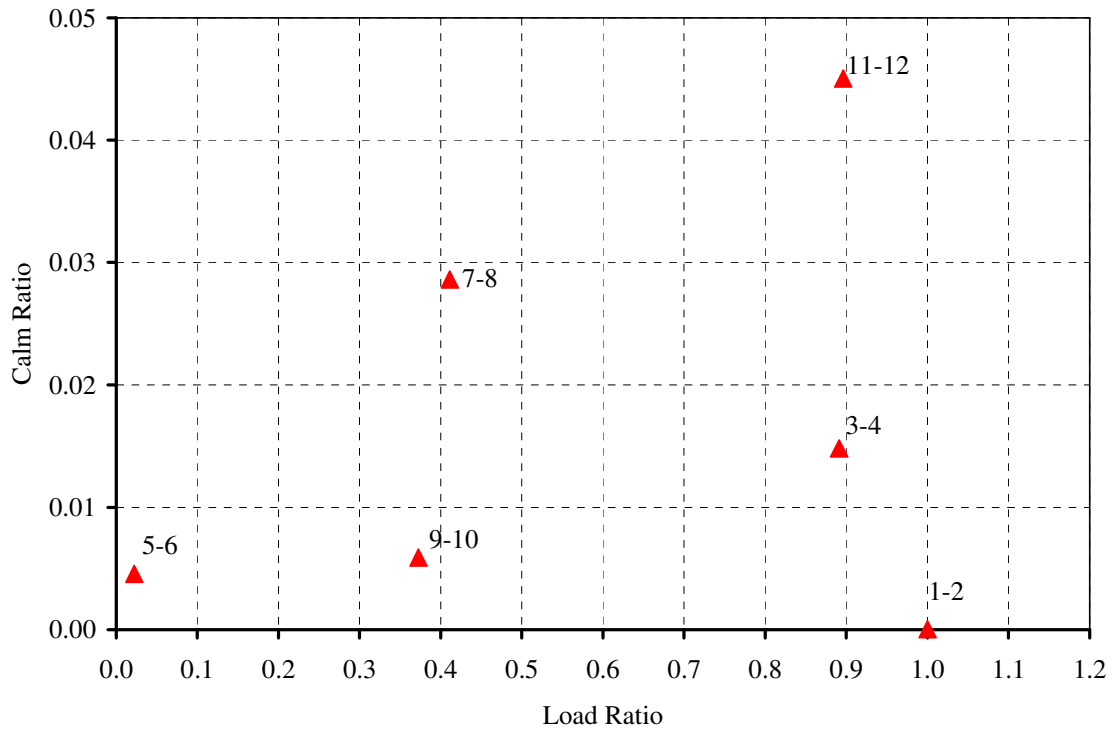


Figure F-10: NDIS assessment for beams SCC-MS-B

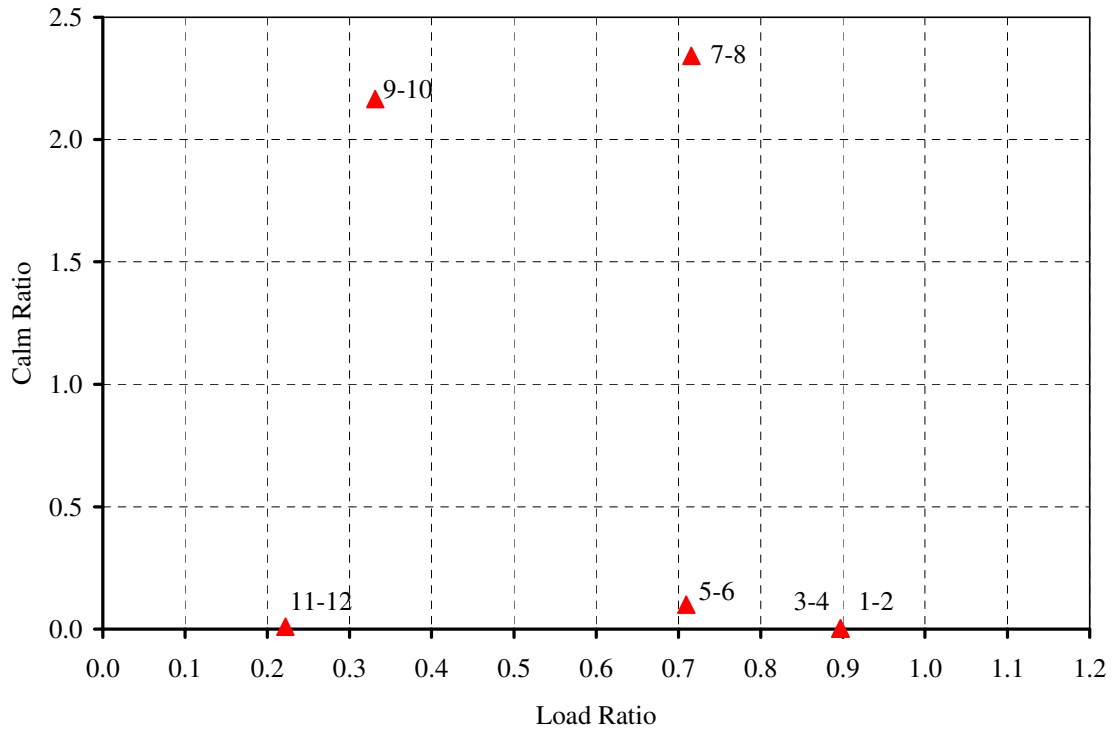


Figure F-11: NDIS assessment for beams SCC-MS-C

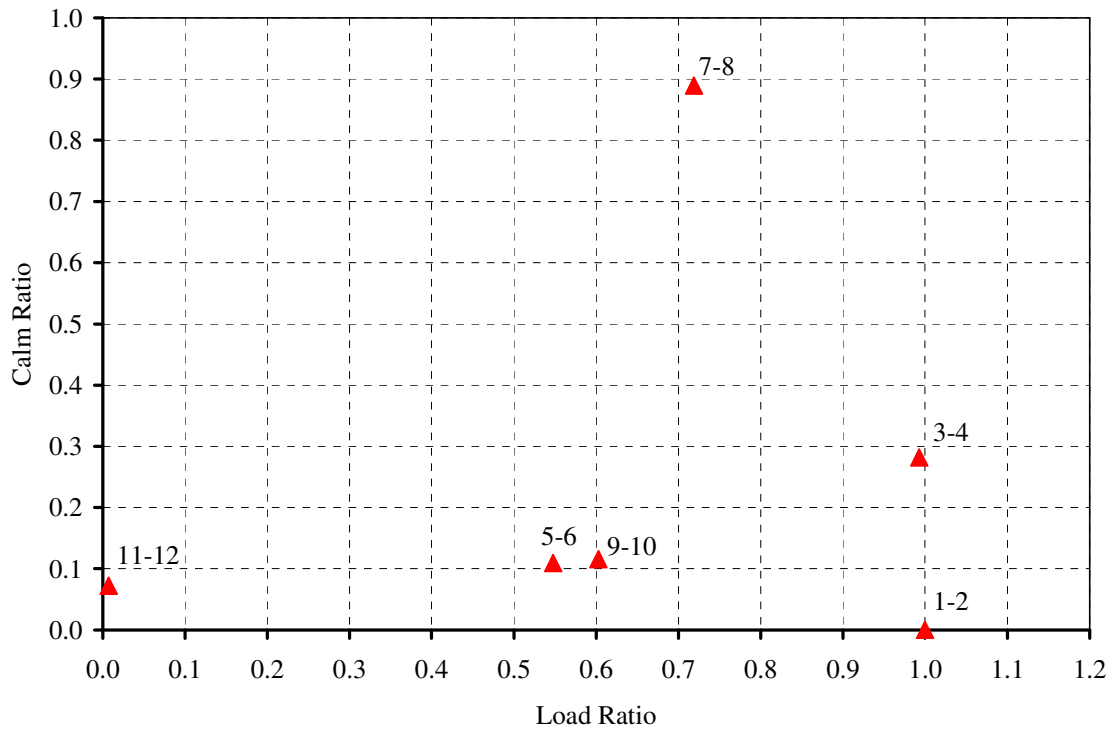


Figure F-12: NDIS assessment for beams SCC-MS-D

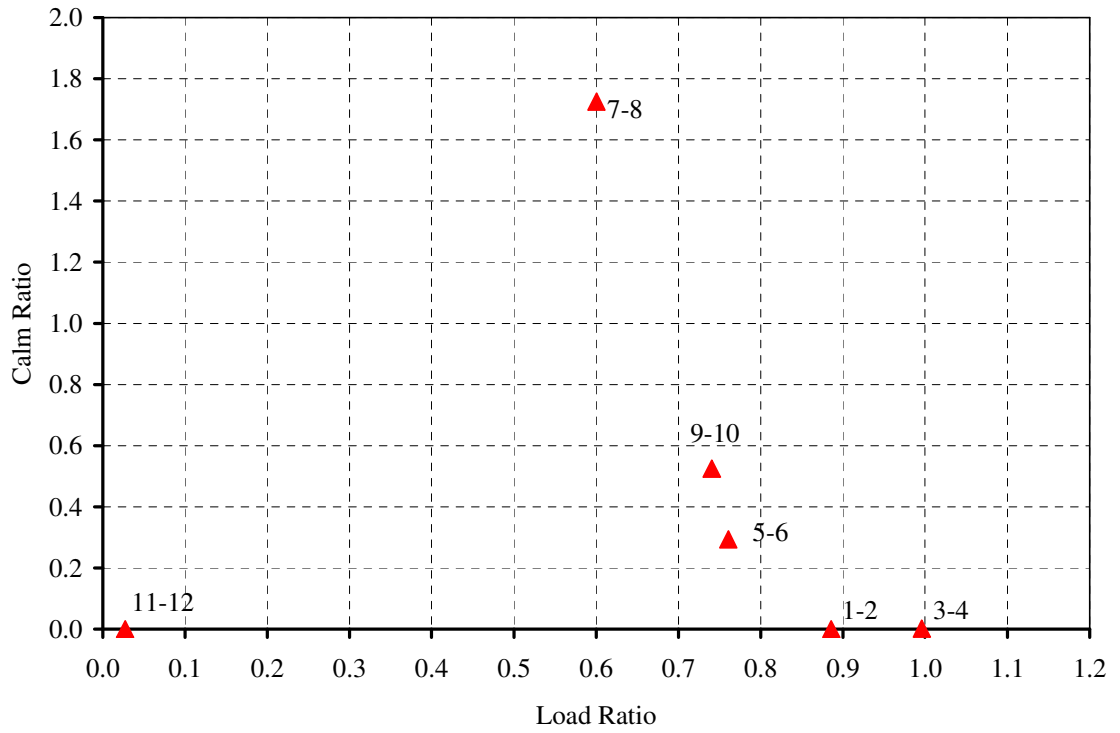


Figure F-13: NDIS assessment for beams SCC-HS-A

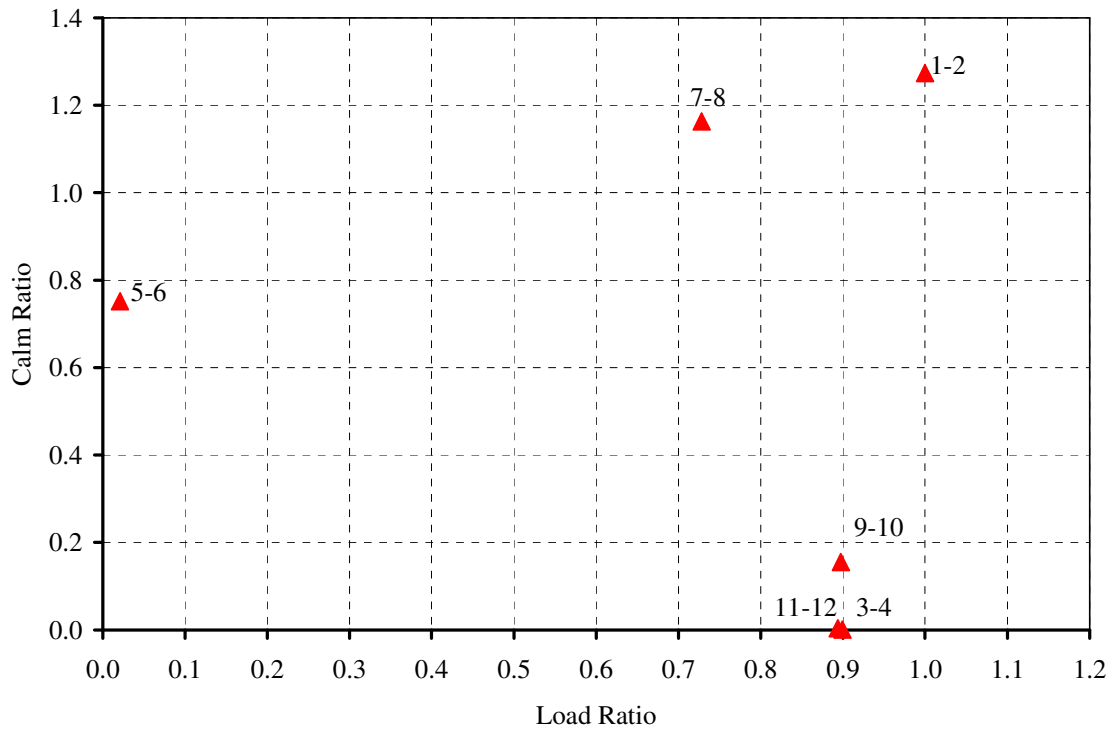


Figure F-14: NDIS assessment for beams SCC-HS-B

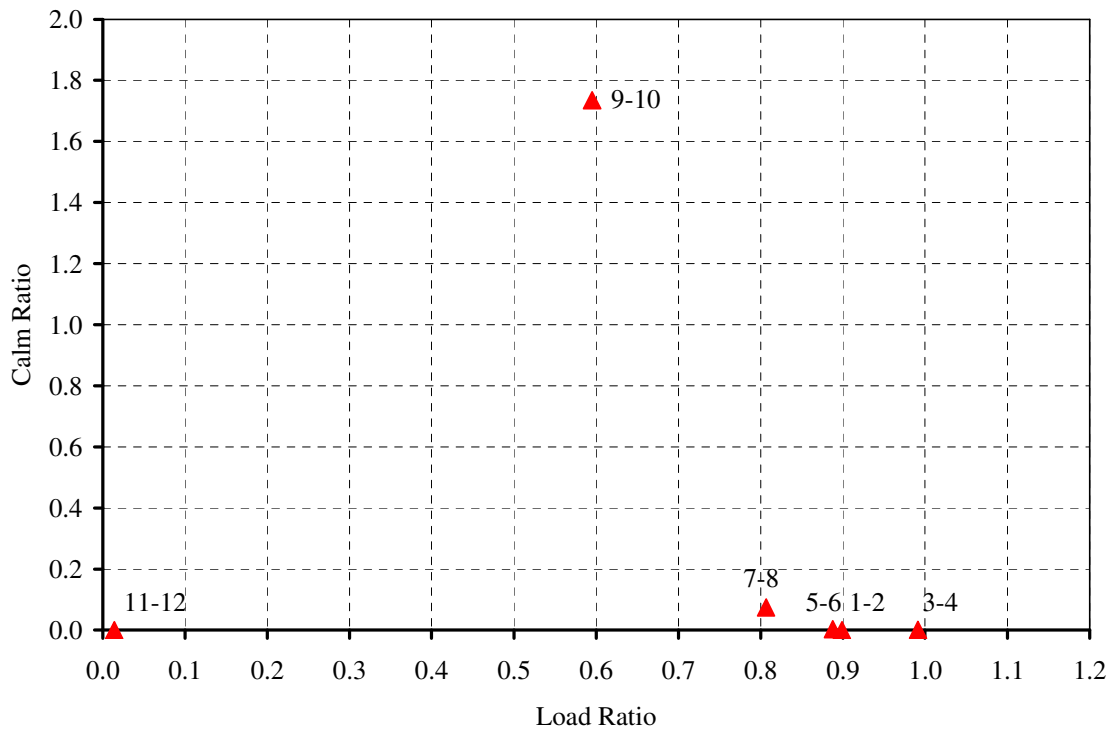


Figure F-15: NDIS assessment for beams SCC-HS-C

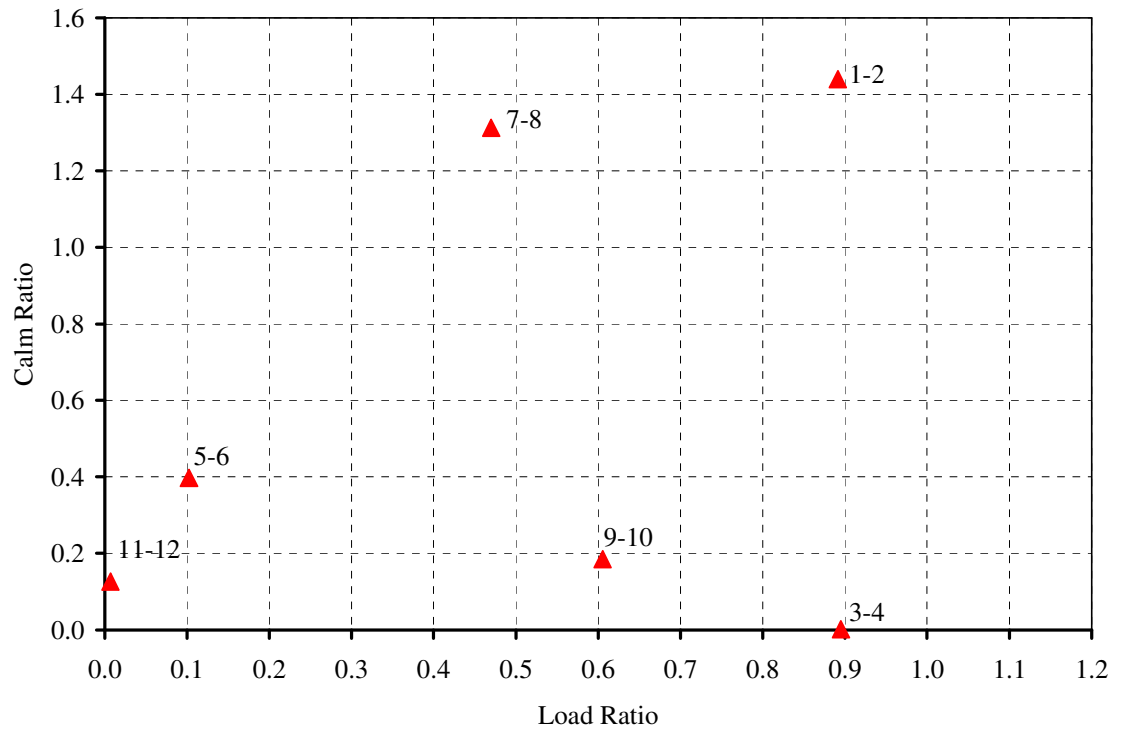


Figure F-16: NDIS assessment for beams SCC-HS-D

APPENDIX G

SSM DURING HOLD PLOTS FOR ALL SPECIMENS

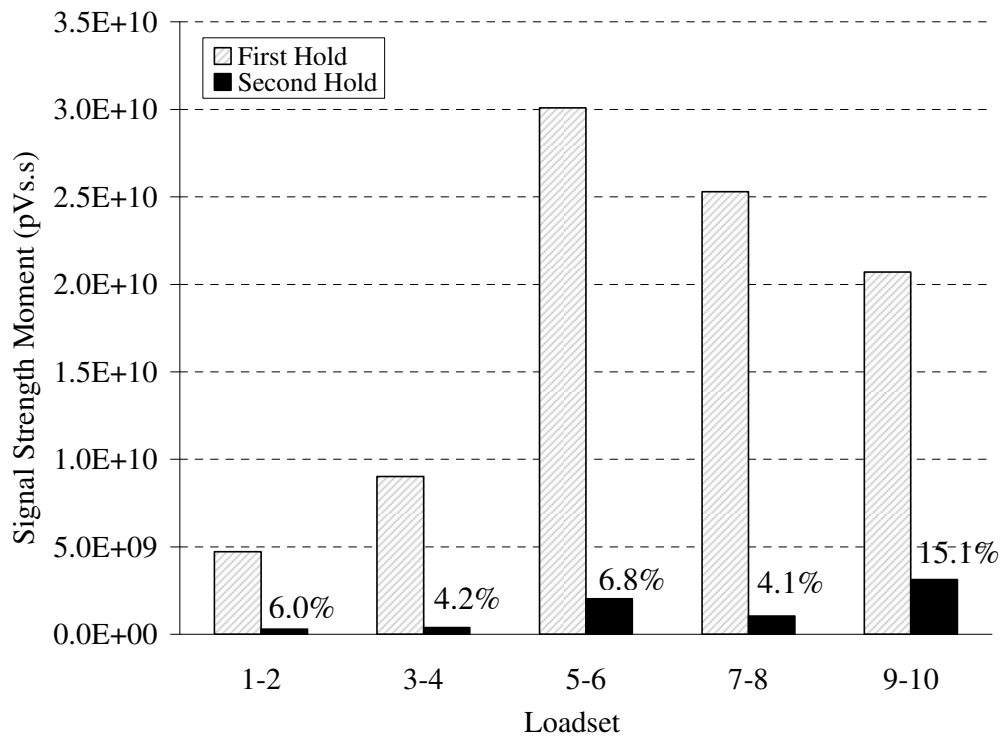


Figure G-1: Signal strength moment during holds for beam STD-M-A

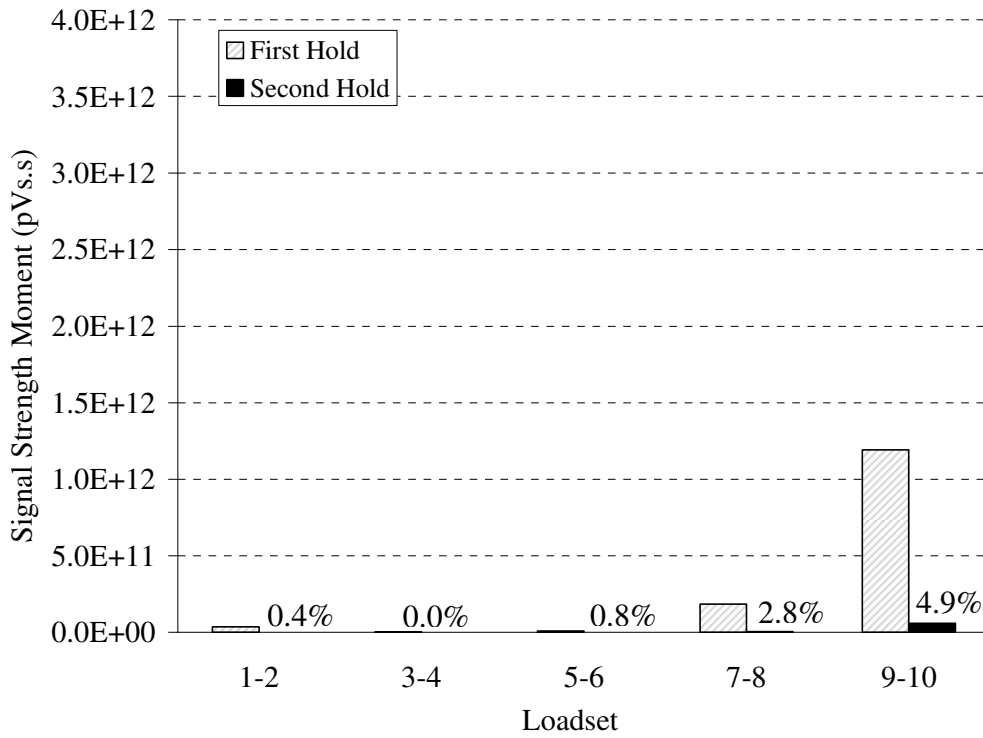


Figure G-2: Signal strength moment during holds for beam STD-M-B

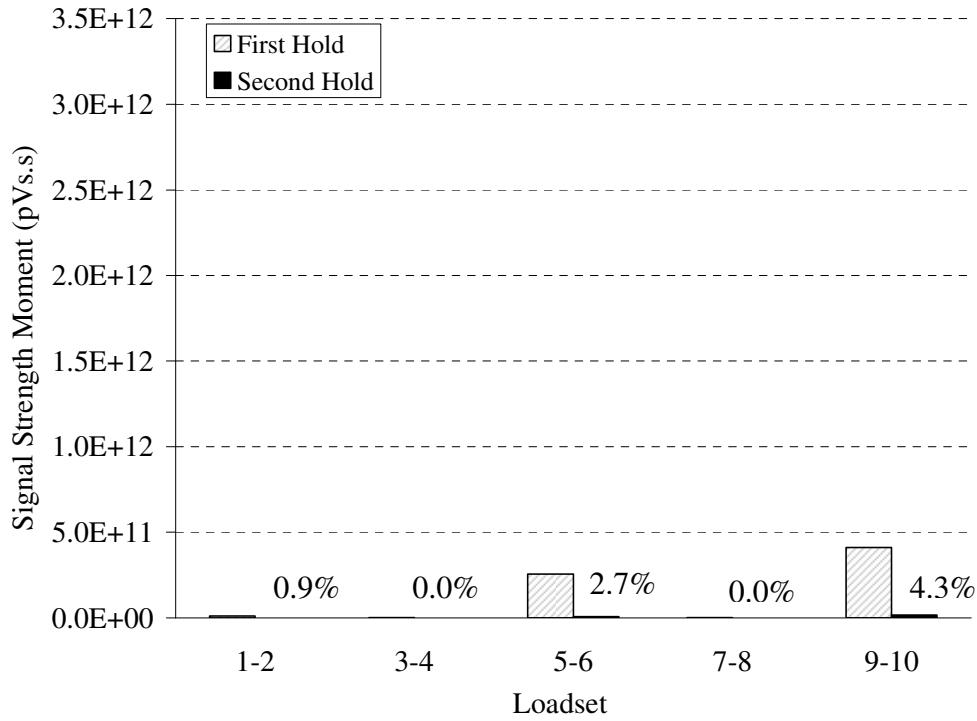


Figure G-3: Signal strength moment during holds for beam STD-M-C

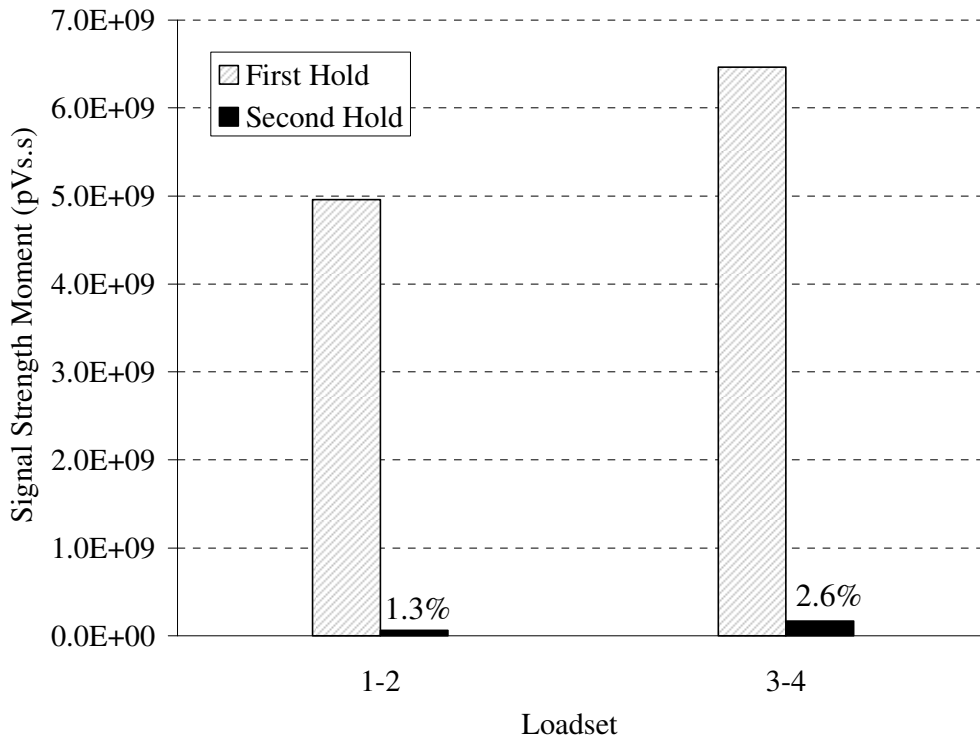


Figure G-4: Signal strength moment during holds for beam STD-M-D

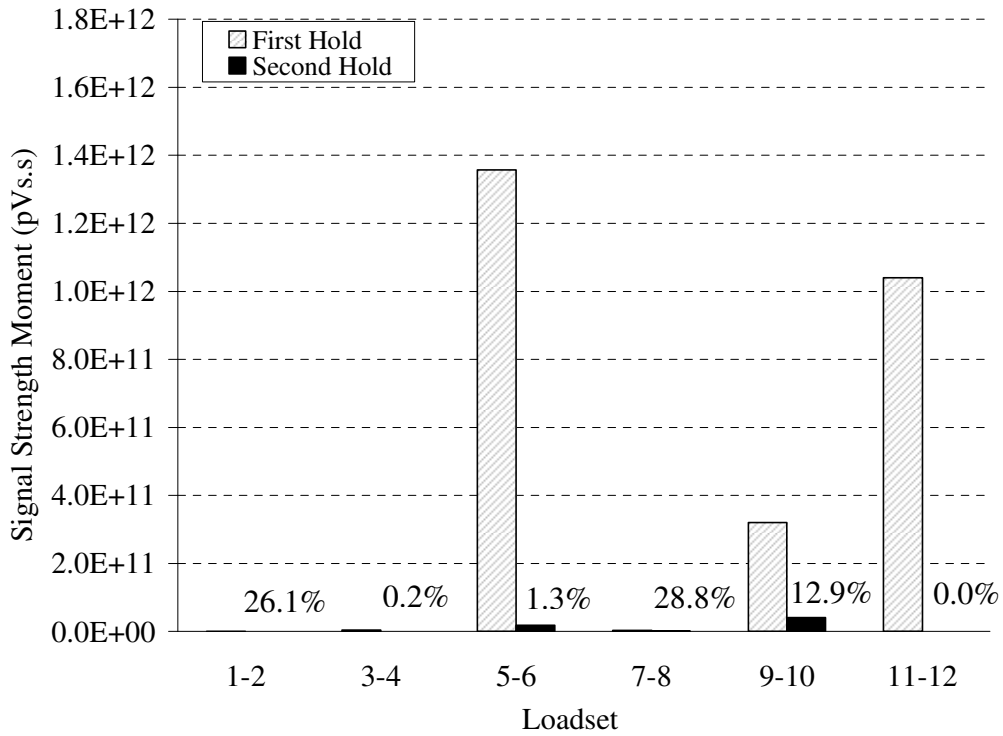


Figure G-5: Signal strength moment during holds for beam SCC-MA-A

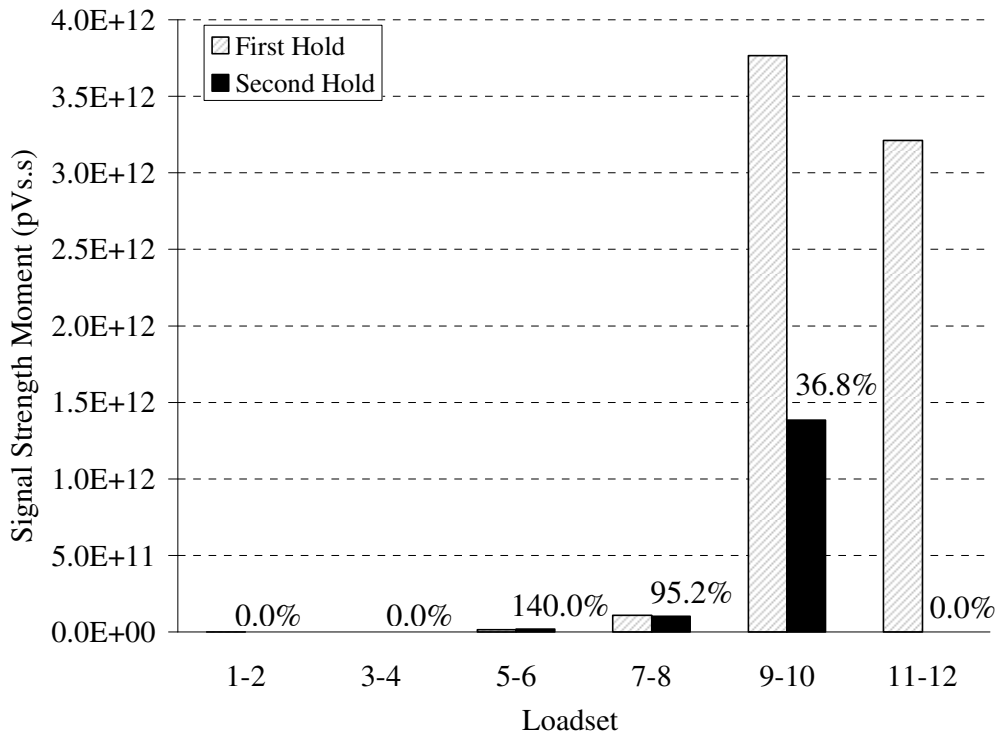


Figure G-6: Signal strength moment during holds for beam SCC-MA-B

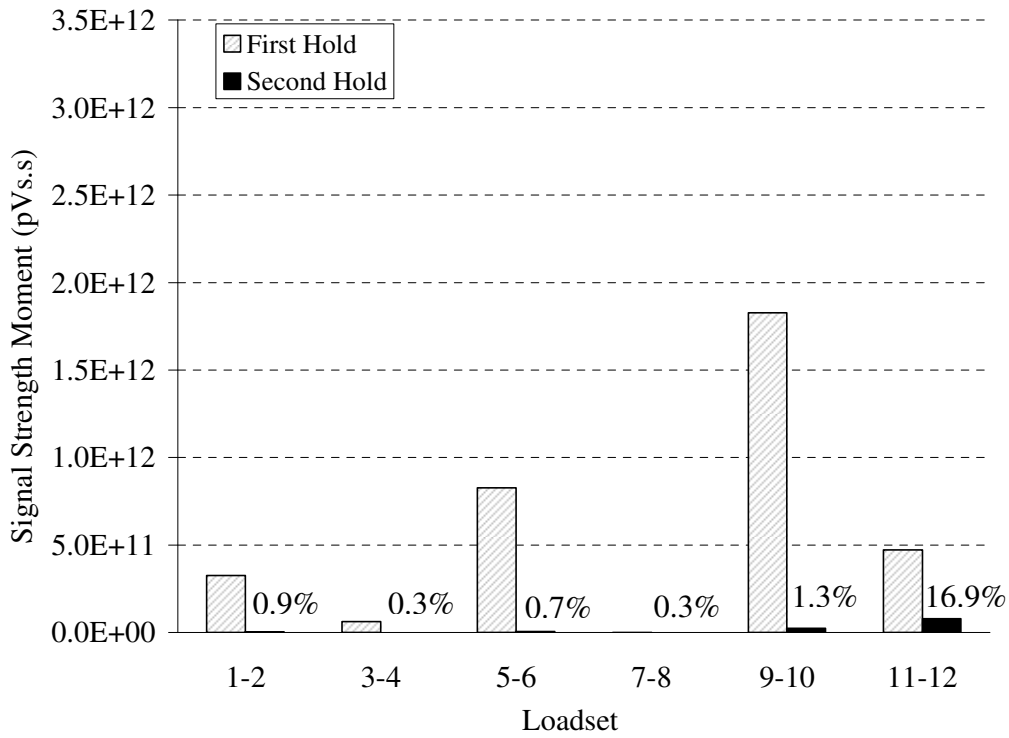


Figure G-7: Signal strength moment during holds for beam SCC-MA-C

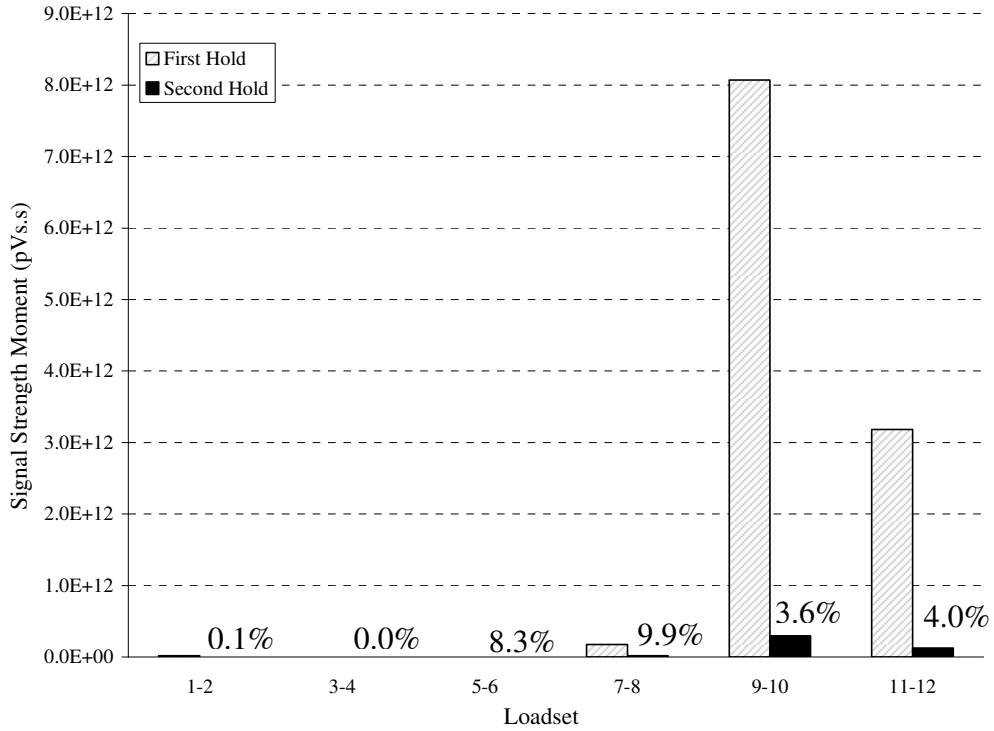


Figure G-8: Signal strength moment during holds for beam SCC-MA-D

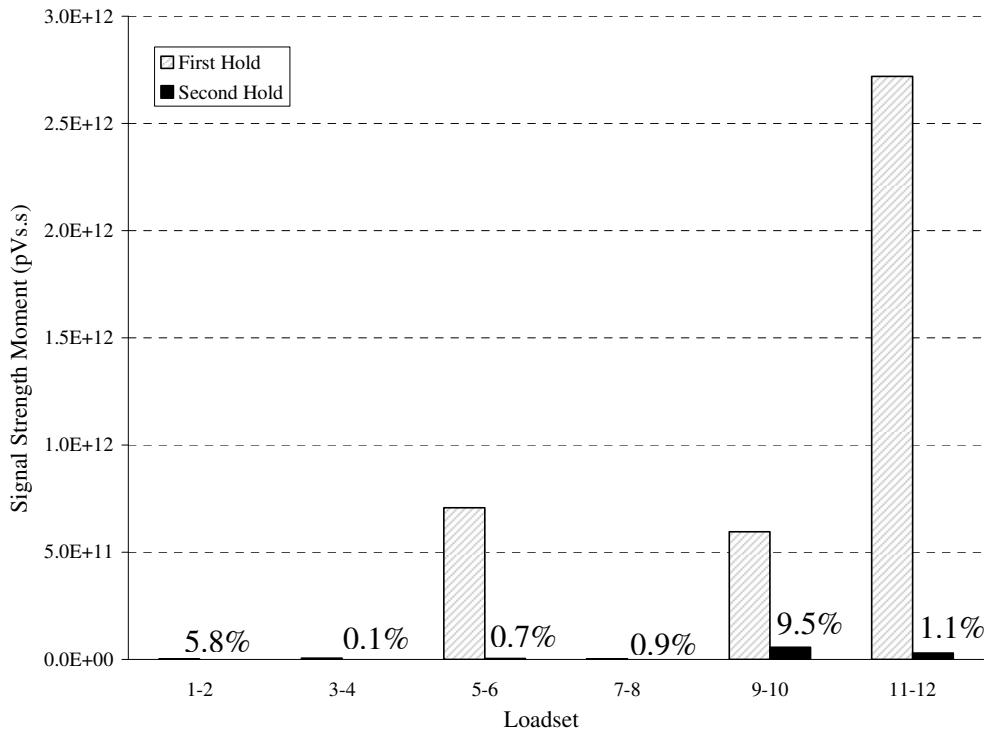


Figure G-9: Signal strength moment during holds for beam SCC-MS-A

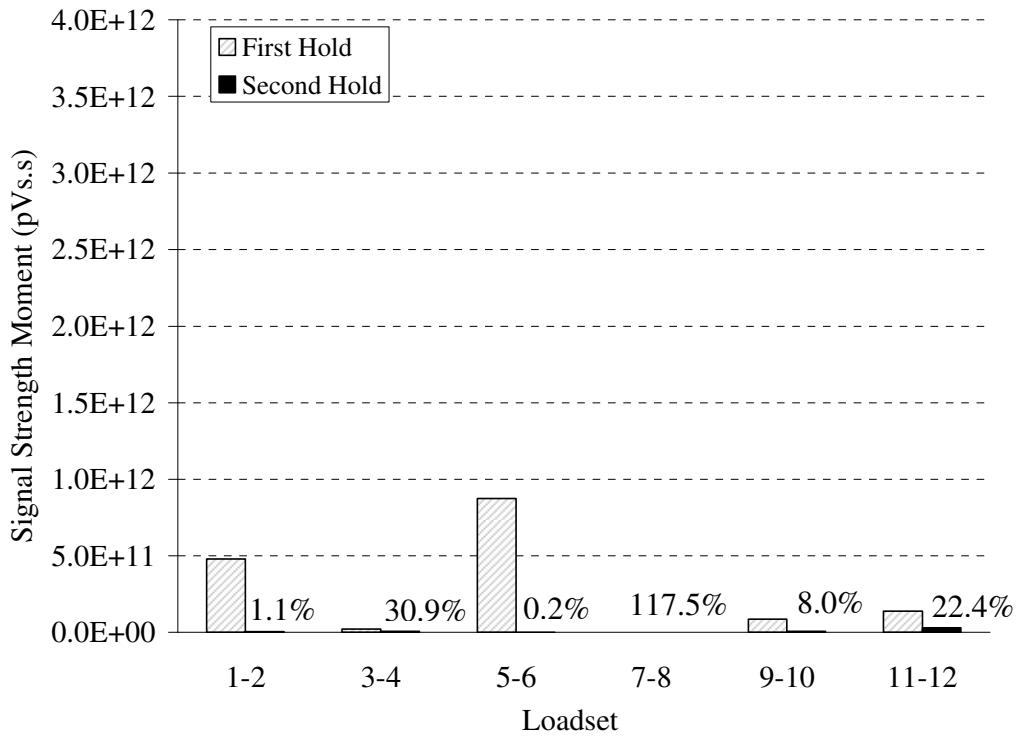


Figure G-10: Signal strength moment during holds for beam SCC-MS-B

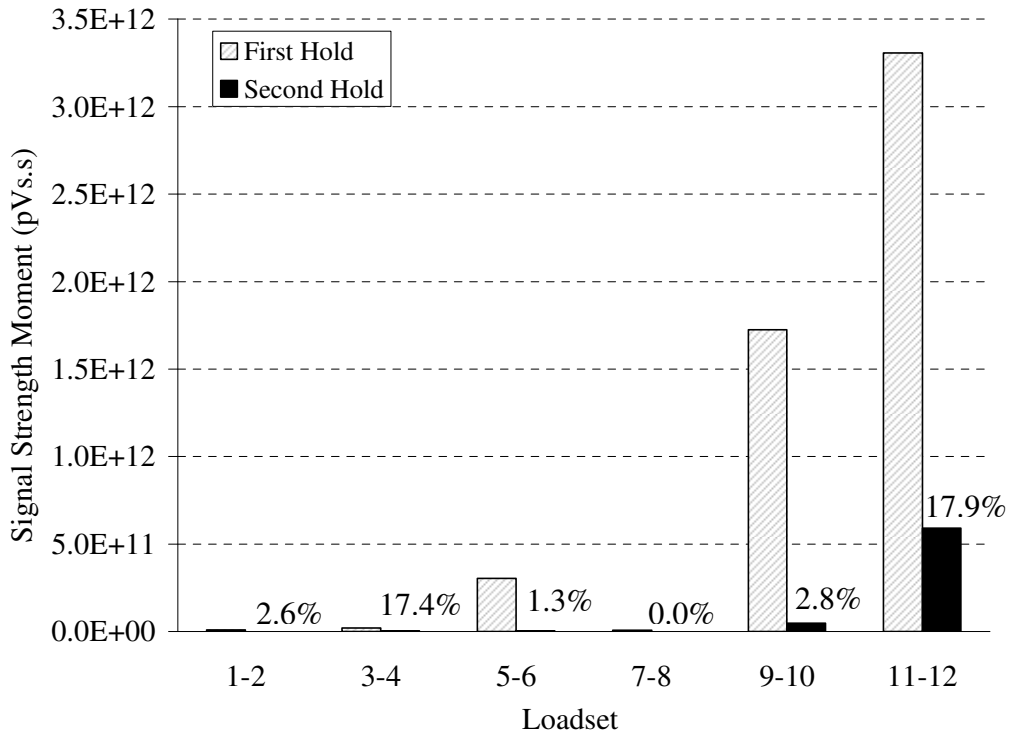


Figure G-11: Signal strength moment during holds for beam SCC-MS-C

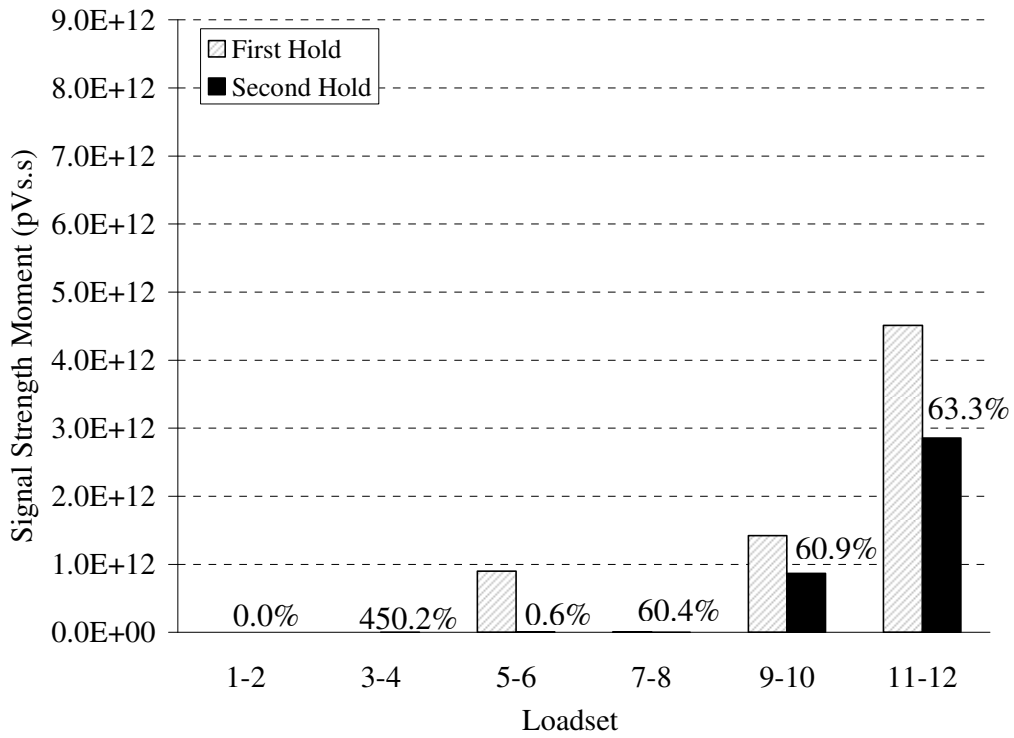


Figure G-12: Signal strength moment during holds for beam SCC-MS-D

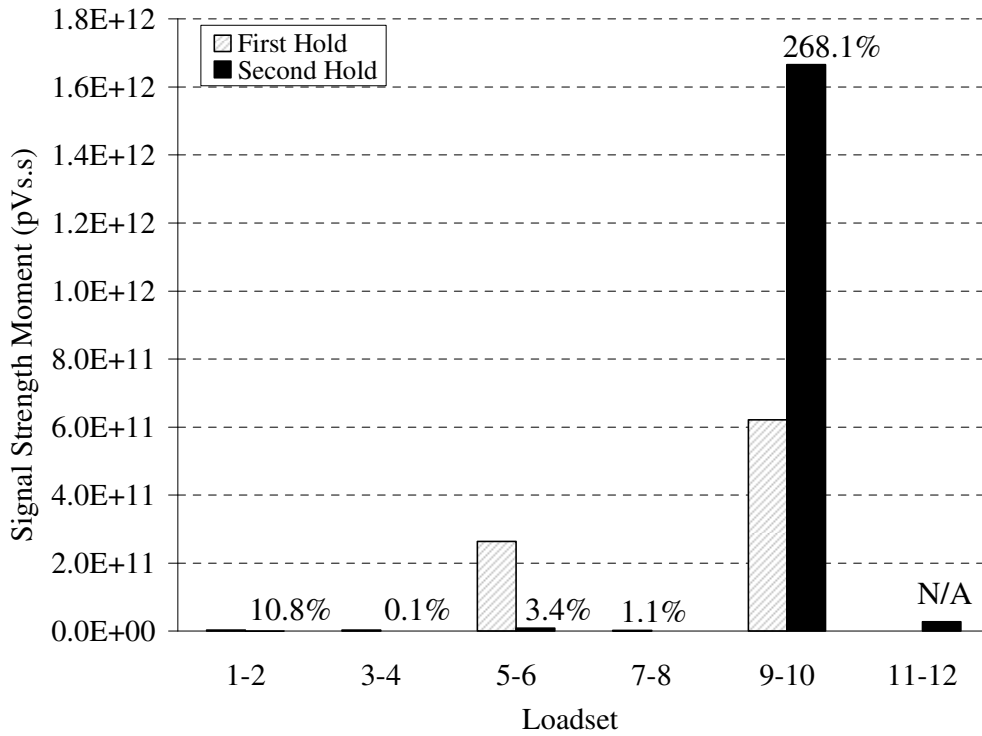


Figure G-13: Signal strength moment during holds for beam SCC-HS-A

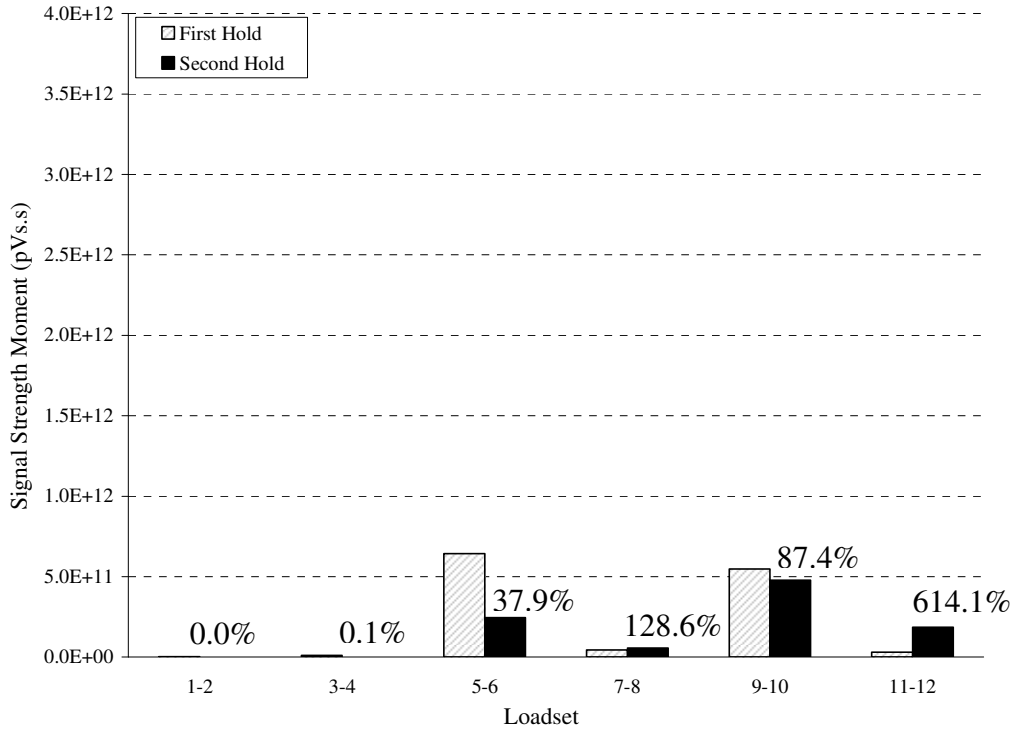


Figure G-14: Signal strength moment during holds for beam SCC-HS-B

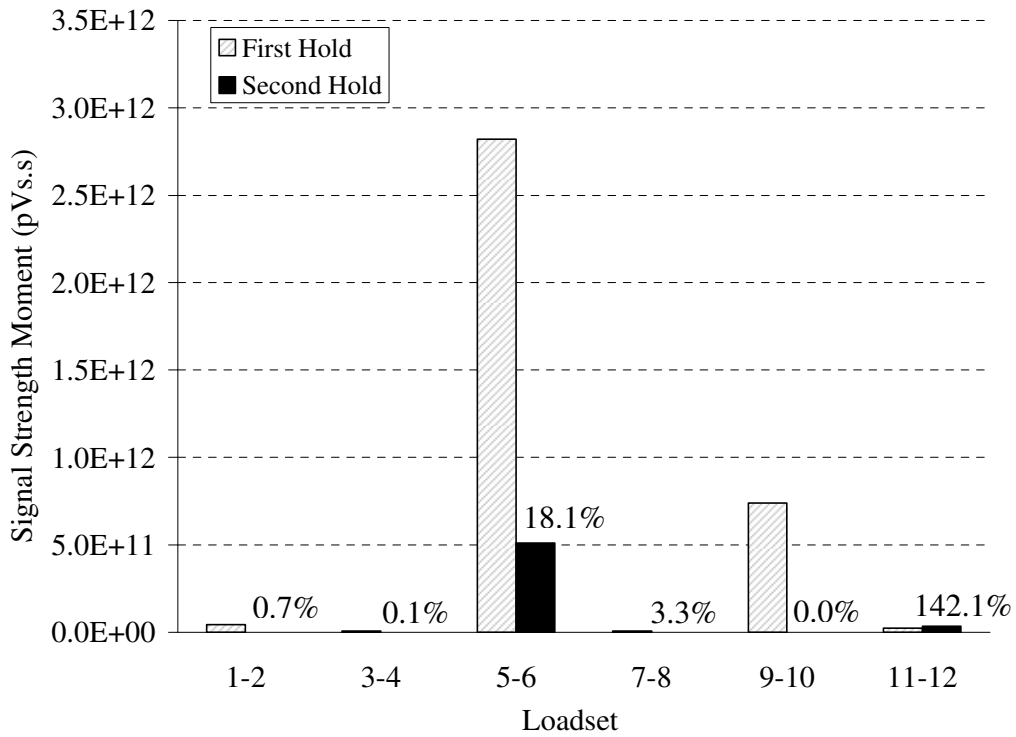


Figure G-15: Signal strength moment during holds for beam SCC-HS-C

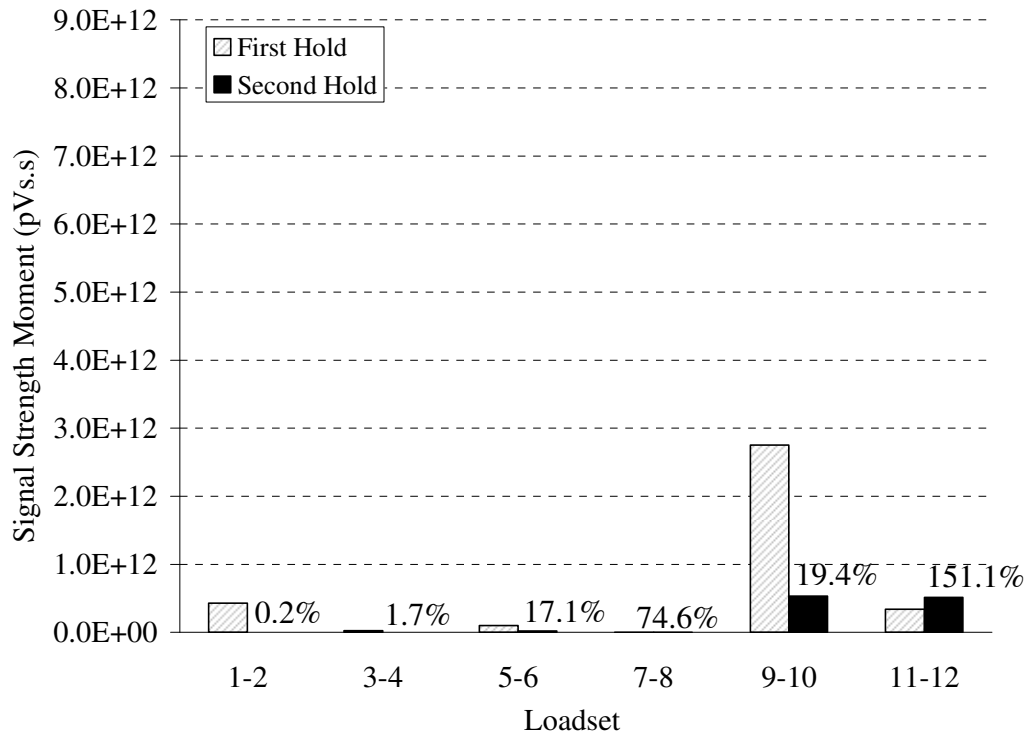


Figure G-16: Signal strength moment during holds for beam SCC-HS-D

APPENDIX H

CUMULATIVE SIGNAL STRENGTH VERSUS TIME DURING CYCLE 5

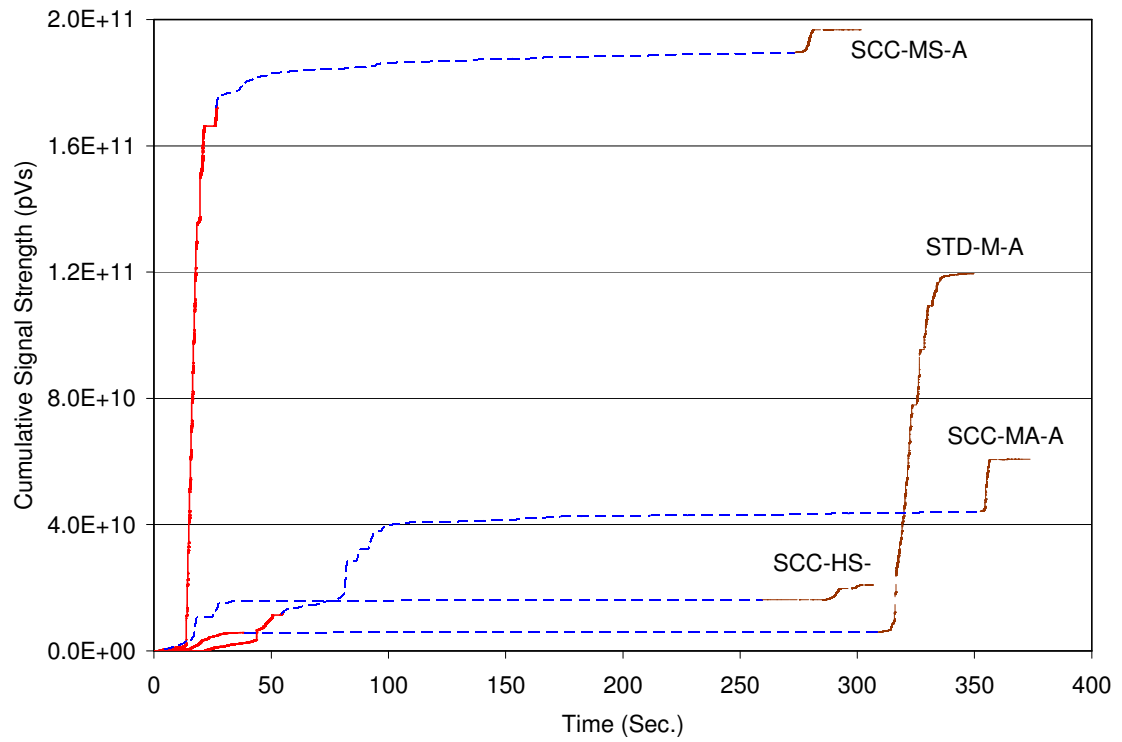


Figure H-1: Cumulative signal strength versus time for “A” beams during Cycle 5

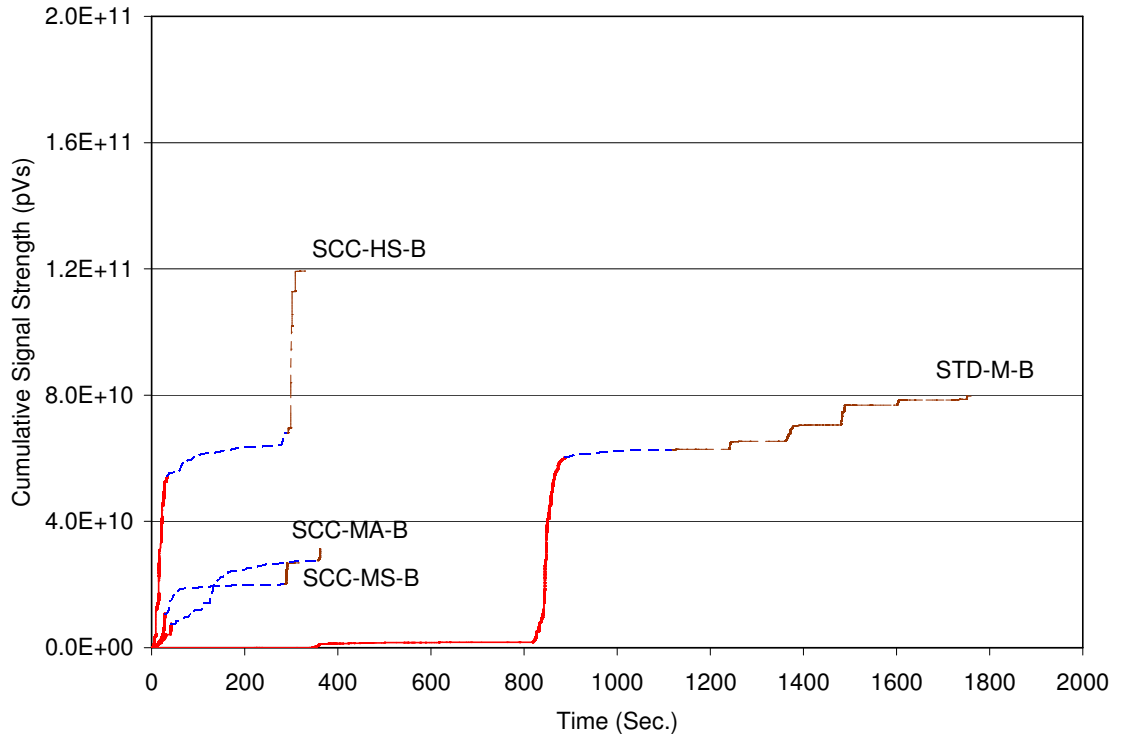


Figure H-2: Cumulative signal strength versus time for “B” beams during Cycle 5

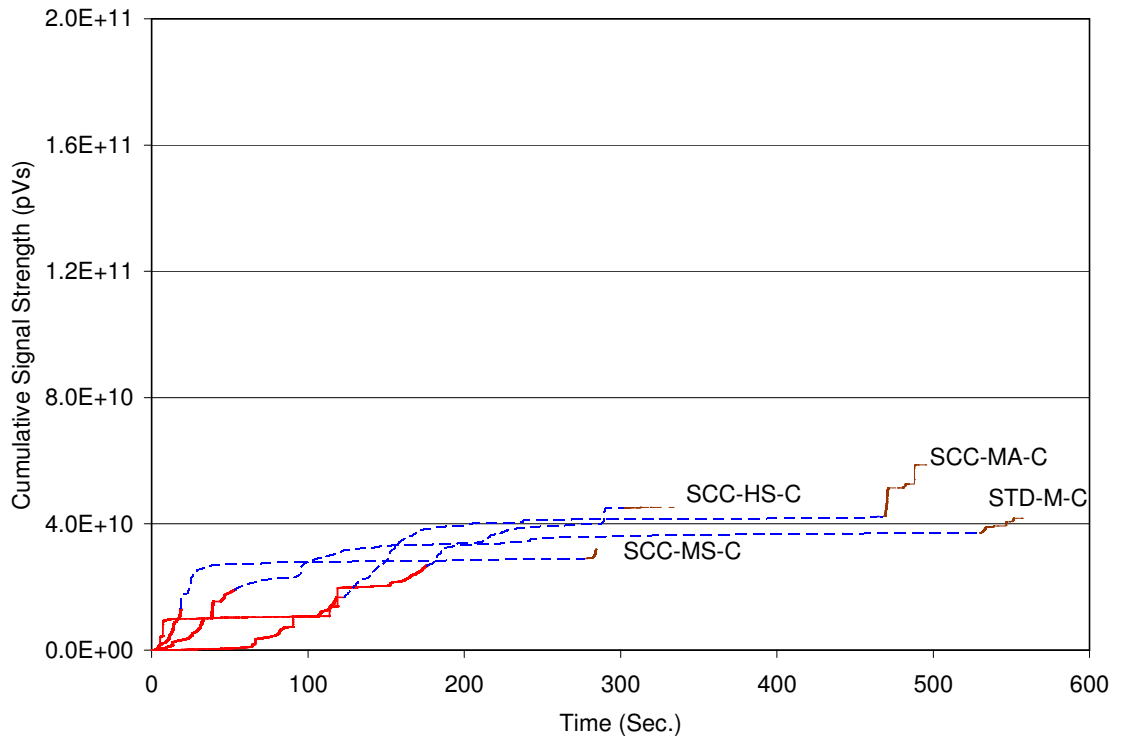


Figure H-3: Cumulative signal strength versus time for “C” beams during Cycle 5

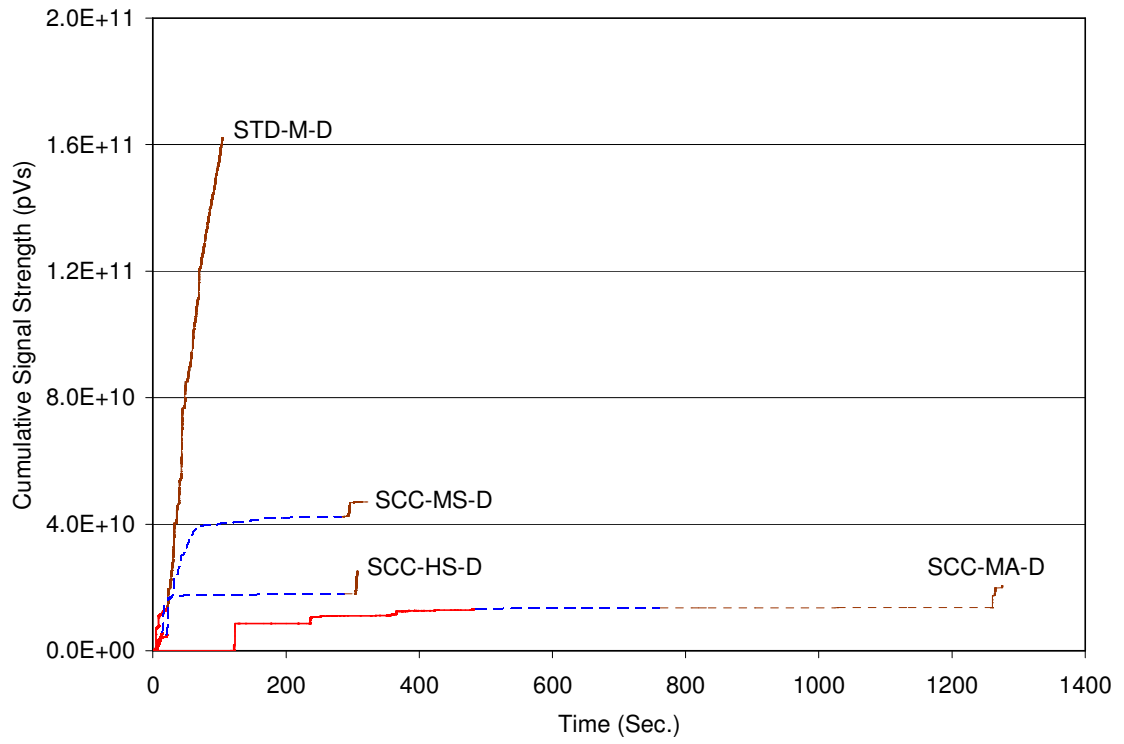


Figure H-4: Cumulative signal strength versus time for “D” beams during Cycle 5